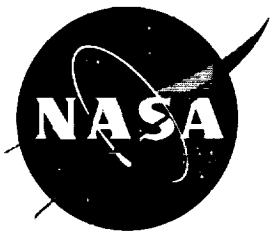
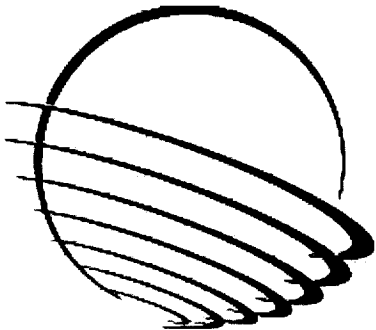


NASA/CP—2000-209895



34th Aerospace Mechanisms Symposium

Compiled by: Edward A. Boesiger



*Proceedings of a symposium held at
The Greenbelt Marriott Hotel, Greenbelt, Maryland
Hosted by the Goddard Space Flight Center
and Co-sponsored by the
Aerospace Mechanisms Symposium Committee and
Lockheed Martin Space Systems Company
May 10–12, 2000*

The NASA STI Program Office ... in Profile

Since its founding, NASA has been dedicated to the advancement of aeronautics and space science. The NASA Scientific and Technical Information (STI) Program Office plays a key part in helping NASA maintain this important role.

The NASA STI Program Office is operated by Langley Research Center, the lead center for NASA's scientific and technical information. The NASA STI Program Office provides access to the NASA STI Database, the largest collection of aeronautical and space science STI in the world. The Program Office is also NASA's institutional mechanism for disseminating the results of its research and development activities. These results are published by NASA in the NASA STI Report Series, which includes the following report types:

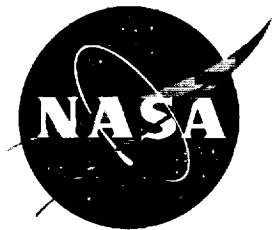
- **TECHNICAL PUBLICATION.** Reports of completed research or a major significant phase of research that present the results of NASA programs and include extensive data or theoretical analysis. Includes compilations of significant scientific and technical data and information deemed to be of continuing reference value. NASA's counterpart of peer-reviewed formal professional papers but has less stringent limitations on manuscript length and extent of graphic presentations.
- **TECHNICAL MEMORANDUM.** Scientific and technical findings that are preliminary or of specialized interest, e.g., quick release reports, working papers, and bibliographies that contain minimal annotation. Does not contain extensive analysis.
- **CONTRACTOR REPORT.** Scientific and technical findings by NASA-sponsored contractors and grantees.
- **CONFERENCE PUBLICATION.** Collected papers from scientific and technical conferences, symposia, seminars, or other meetings sponsored or cosponsored by NASA.
- **SPECIAL PUBLICATION.** Scientific, technical, or historical information from NASA programs, projects, and mission, often concerned with subjects having substantial public interest.
- **TECHNICAL TRANSLATION.** English-language translations of foreign scientific and technical material pertinent to NASA's mission.

Specialized services that complement the STI Program Office's diverse offerings include creating custom thesauri, building customized databases, organizing and publishing research results . . . even providing videos.

For more information about the NASA STI Program Office, see the following:

- Access the NASA STI Program Home Page at <http://www.sti.nasa.gov/STI-homepage.html>
- E-mail your question via the Internet to help@sti.nasa.gov
- Fax your question to the NASA Access Help Desk at (301) 621-0134
- Telephone the NASA Access Help Desk at (301) 621-0390
- Write to:
NASA Access Help Desk
NASA Center for AeroSpace Information
7121 Standard Drive
Hanover, MD 21076-1320

NASA/CP—2000—209895



34th Aerospace Mechanisms Symposium

Compiled by: Edward A. Boesiger

National Aeronautics and
Space Administration

Goddard Space Flight Center
Greenbelt, Maryland 20771

**The use of trade names of manufacturers
in this publication does not constitute an
official endorsement of such products or
manufacturers, either expressed or implied,
by the National Aeronautics and Space
Administration.**

Available from:

NASA Center for AeroSpace Information
7121 Standard Drive
Hanover, MD 21076-1320
Price Code: A17

National Technical Information Service
5285 Port Royal Road
Springfield, VA 22161
Price Code: A10

PREFACE

The Aerospace Mechanisms Symposium (AMS) provides a unique forum for those active in the design, production and use of aerospace mechanisms. A major focus is the reporting of problems and solutions associated with the development and flight certification of new mechanisms. The National Aeronautics and Space Administration and Lockheed Martin Space Systems Company (LMSSC) share the responsibility for organizing the AMS. Now in its 34th year, the AMS continues to be well attended, attracting participants from both the U.S. and abroad.

The 34th AMS, hosted by the Goddard Space Flight Center (GSFC) in Greenbelt, Maryland, was held May 10, 11 and 12, 2000. During these three days, 34 papers were presented. Topics included deployment mechanisms, bearings, actuators, pointing and optical mechanisms, Space Station mechanisms, release mechanisms, and test equipment. Hardware displays during the vendor fair gave attendees an opportunity to meet with developers of current and future mechanism components.

The high quality of this symposium is a result of the work of many people, and their efforts are gratefully acknowledged. This extends to the voluntary members of the symposium organizing committee representing the eight NASA field centers, LMSSC, and the European Space Agency. Appreciation is also extended to the session chairs, the authors, and particularly the personnel at GSFC responsible for the symposium arrangements and the publication of these proceedings. A sincere thank you also goes to the symposium executive committee at LMSSC who is responsible for the year-to-year management of the AMS, including paper processing and preparation of the program.

The use of trade names of manufacturers in this publication does not constitute an official endorsement of such products or manufacturers, either expressed or implied, by the National Aeronautics and Space Administration.

CONTENTS

Symposium Schedule	viii
Symposium Organizing and Advisory Committees	xii
A Low Power Cryogenic Shutter Mechanism for Use in Infrared Imagers	1
Scott Schwinger & Claef Hakun	
ACIS Door Failure Investigation and Mitigation Procedures	15
William Podgorski, Neil Tice & Paul Plucinsky	
Designing Spacecraft Mechanisms for Sand, Dust, Water and Frost.....	29
Kurt Lankford	
Low-Cost Ejection Mechanism for Protective Covers on Meteosat Second Generation	39
Javier Ortega, Fernando Quintana & Gabriel Ybarra	
Misconceptions in Mechanism Reliability.....	51
Walter Holemans & Donald Gibbons	
Lessons Learned from the Manufacturing and Test of the International Space Station Drive Lock Assembly	61
Curtis Allmon	
Development of an Automated Bolt Driver for the Space Station Truss Assembly.....	75
Richard Meinhold & Ken Seidner	
Design of a Power-Assisted Spacesuit Glove Actuator.....	89
Russell Howard	
Energy Absorber for the International Space Station	103
Bob Wilkes & Lora Laurence	
Friction Drive Characteristics for the Space Station Mobile Transporter	117
Richard Hughes, Daniel Hoyt & Juan Carreras	
Development of a Cryogenic Nanometer-Class Repeatability Linear Actuator.....	131
Ruben Nalbandian & Alson Hatheway	
Application of Magnetic Smart Materials to Aerospace Motion Control.....	137
Chad Joshi & Bruce Bent	
A Separation System Solution for the Interim Control Module	143
Brian Whalen	
The Development of an Ultra Low Shock Pyrotechnically Actuated Separation Nut	151
Fred Silverman & Jerry O'Quinn	

Piezoelectric Pump Development.....	157
Franklin Sager	
Miniature Linear Actuator	163
Armond Asadurian	
The Sandmeier Field Goniometer: A Measurement Tool for Bi-Directional Reflectance	167
Mark Turner & Jeff Brown	
Motor Redundancy Concept: Efficient or Reliable?.....	175
Eric Favre	
Development of a Miniature Two-Axis, Triple-Helmholtz-Driven Gimbal	189
Boz Sharif, Ed Joscelyn, Brian Wilcox & Michael R. Johnson	
Cover Drive and Lock Ring Mechanisms for Genesis.....	199
Louise Jandura	
Landsat 7 Solar Array Testing Experiences.....	213
Daniel Helfrich	
Deployment Dynamics of Solar Arrays with a Link-in-Slot Hinge/Latch Mechanism.....	225
Walter Daniel & G. Michael Bidinger	
Inflatable Boom Controlled Deployment Mechanism for the Inflatable Sunshield In Space (ISIS) Flight Experiment.....	231
George Sapna III, John Folke, Charles Sandy & Dave Cardogan	
A Novel Mechanism using Shape Memory Alloy to Drive Solar Flaps of the INSAT-2E Satellite.....	239
N. Viswanatha & T. Murali	
Evolution of an Actuator Family.....	251
Paul Stigell, Pekka Kyrenius, Tomi Ylikorpi & Kai Viherkanto	
Coaxial Cable Failure in a Spacecraft Mechanism	265
Michael Chiu	
The SeaWinds Scatterometer Antenna Subsystem on the QuikScat Spacecraft	275
Brian Workman & Eric Schwartzbaum	
Antenna Pointing Mechanism for Steerable Spot Beam Antennas	287
Manfred Schmid	
Earth Scanner Bearing Accelerated Life Test	303
Brian Dietz, Steven VanDyk & Roamer Predmore	
Measurements of Friction Coefficients between Oxidized and Contaminated Surfaces in Vacuum and in Air.....	317
Peter Frantz & Stephen Didziulis	
Marshall Space Flight Center High Speed Turbopump Bearing Test Rig.....	331
Howard Gibson, Chip Moore & Robert Thom	

Design, Development and Testing of Umbilical System Mechanisms for the X-33 Advanced Technology Demonstrator	343
Alan Littlefield & Gregory Melton	
Development of a Flywheel for Energy Storage and Attitude Control of an Exoatmospheric Interceptor.....	359
Doug Havenhill, Frank Nimblett, Steve Nichols & John Young	

SYMPOSIUM SCHEDULE

TUESDAY, 9 MAY 2000

6:30-8:30 CHECK-IN
Greenbelt Marriott Annapolis Room

WEDNESDAY, 10 MAY 2000

- 8:00 Wednesday Presenters' Breakfast
- 8:00 CHECK-IN AND REFRESHMENTS
- 9:00 **INTRODUCTORY REMARKS**
Stewart Meyers, Host Chairman
NASA Goddard Space Flight Center, Greenbelt, MD
Stuart H. Loewenthal, General Chairman
Lockheed Martin Space Systems Company, Sunnyvale, CA
- CENTER WELCOME
Al Diaz, Center Director
NASA Goddard Space Flight Center, Greenbelt, MD
- 9:30 **SESSION I – INSTRUMENTS/RELIABILITY**
Dick Casper, Session Chair
Aeroflex Laboratories, Farmingdale, NY
• A Low Power Cryogenic Shutter Mechanism for Use in Infrared Imagers
Scott Schwinger & Claef Hakun, NASA Goddard Space Flight Center, Greenbelt, MD
• ACIS Door Failure Investigation and Mitigation Procedures
William Podgorski & Paul Plucinsky, Smithsonian Astrophysical Observatory, Cambridge, MA;
and Neil Tice, Lockheed Martin Space Systems Company, Denver, CO
• Designing Spacecraft Mechanisms for Sand, Dust, Water and Frost
Kurt Lankford, Starsys Research Corp., Boulder, CO
• Low-Cost Ejection Mechanism for Protective Covers on Meteosat Second Generation
Javier Ortega, Fernando Quintana & Gabriel Ybarra, SENER Ingenieria y Sistemas, S.A., Spain
• Misconceptions in Mechanism Reliability
Walter Holemans, Planetary Systems Corporation, Washington, D.C. & Donald Gibbons,
Lockheed Martin Space Systems Company, Sunnyvale, CA
- 12:00 LUNCH BREAK
- 1:15 **SESSION II - SPACE STATION**
Manfred Schmid, Session Chair
DaimlerChrysler, Friedrichshafen, Germany
• Lessons Learned from the Manufacturing and Test of the International Space Station Drive
Lock Assembly
Curtis Allmon, Lockheed Martin Space Systems Company, Sunnyvale, CA
• Development of an Automated Bolt Driver for the Space Station Truss Assembly
Richard Meinhold, Moog, Inc., East Aurora, NY; & Ken Seidner, The Boeing Company,
Huntington Beach, CA
• Design of a Power-Assisted Spacesuit Glove Actuator
Russell Howard, University of Maryland, College Park, MD

- Energy Absorber for the International Space Station
Bob Wilkes, Lockheed Martin Space Operations, Houston, TX, & Lora Laurence, NASA Johnson Space Center, Houston, TX
- Friction Drive Characteristics for the Space Station Mobile Transporter
Richard Hughes & Daniel Hoyt, TRW Astro Aerospace, Carpinteria, CA; and Juan Carreras, The Boeing Company, Huntington Beach, CA

3:45 BREAK

4:00-5:00 SESSION III – POSTER PREVIEWS

- Christopher Hansen, Session Chair
NASA Johnson Space Center
- Development of a Cryogenic Nanometer-Class Repeatability Linear Actuator
Ruben Nalbandian, Moog, Inc., Chatsworth, CA, & Alson Hatheway, Alson E. Hatheway, Inc., Pasadena, CA
 - Application of Magnetic Smart Materials to Aerospace Motion Control
Chad Joshi & Bruce Bent, Energen, Inc., Billerica, MA
 - A Separation System Solution for the Interim Control Module
Brian Whalen, U.S. Naval Research Laboratory, Washington, D.C.
 - The Development of an Ultra Low Shock Pyrotechnically Actuated Separation Nut
Fred Silverman & Jerry O’Quinn, Hi-Shear Technology Corporation, Torrance, CA
 - Piezoelectric Pump Development
Franklin Sager, Oceaneering Space Systems, Houston, TX
 - Miniature Linear Actuator
Armond Asadurian, Moog, Inc., Chatsworth, CA

6:00-10:00 RECEPTION & DISPLAYS AT THE GREENBELT MARRIOTT

Poster Papers and invited component and software vendors display current products and provide tutorials.

THURSDAY, 11 MAY 2000

7:00 Thursday Presenters' Breakfast

8:00 SESSION IV – INSTRUMENTS & ACTUATORS

- Willie Blanco, Session Chair
NASA Goddard Space Flight Center, Greenbelt, MD
- The Sandmeier Field Goniometer: A Measurement Tool for Bi-Directional Reflectance
Mark Turner & Jeff Brown, NASA Ames Research Center, Mountain View, CA
 - Motor Redundancy Concept: Efficient or Reliable?
Eric Favre, ETEL Aerospace Inc., Boulder, CO
 - Development of a Miniature Two-Axis, Triple-Helmholtz-Driven Gimbal
Boz Sharif & Ed Joscelyn, Aeroflex Laboratories, Farmingdale, NY; and Brian Wilcox & Michael R. Johnson, Jet Propulsion Laboratory, Pasadena, CA
 - Cover Drive and Lock Ring Mechanisms for Genesis
Louise Jandura, Jet Propulsion Laboratory, Pasadena, CA

10:00 BREAK

10:15	SESSION V – DEPLOY Mark Calassa, Session Chair Lockheed Martin Space Systems Company, Sunnyvale, CA • Landsat 7 Solar Array Testing Experiences Daniel Helfrich, Goddard Space Flight Center, Greenbelt, MD • Deployment Dynamics of Solar Arrays with a Link-in-Slot Hinge/Latch Mechanism Walter Daniel, Mechanical Dynamics, Inc., Austin, TX & G. Michael Bidinger, Orbital Sciences Corp., Germantown, MD • Inflatable Boom Controlled Deployment Mechanism for the Inflatable Sunshield In Space (ISIS) Flight Experiment George Sapna III, John Folke, Charles Sandy & Dave Cardogan, ILC Dover, Frederica, DE • A Novel Mechanism using Shape Memory Alloy to Drive Solar Flaps of the INSAT-2E Satellite N. Viswanatha & T. Murali, Indian Space Research Organisation Satellite Centre, Bangalore, India
12:15	LUNCH BREAK
1:15	SESSION VI – POSITIONING/ANTENNA MECHANISMS Steve Koss, Session Chair Naval Research Laboratory, Washington, D.C. • Evolution of an Actuator Family Paul Stigell, Pekka Kyrenius, Tomi Ylikorpi & Kai Viherkanto, VTT Automation, Finland • Coaxial Cable Failure in a Spacecraft Mechanism Michael Chiu, TRW Space & Technology Division, Redondo Beach, CA • The SeaWinds Scatterometer Antenna Subsystem on the QuikScat Spacecraft Brian Workman, Honeywell Satellite Systems Operation, Glendale, AZ, & Eric Schwartzbaum, Jet Propulsion Laboratory, Pasadena, CA • Antenna Pointing Mechanism for Steerable Spot Beam Antennas Manfred Schmid, DaimlerChrysler Aerospace, DSS, Friedrichshafen, Germany
	DR. CHARLES COALE AWARD ANNOUNCEMENT
3:30	BREAK
3:45-4:30	SPECIAL PRESENTATION Mechanisms on the Next Generation Space Telescope Jon Lawrence, NASA Goddard Space Flight Center
5:30-10:30	SYMPOSIUM BANQUET AT B&O RAILROAD MUSEUM 4:45 Shuttle for guests leaves Holiday Inn for the Greenbelt Marriott 5:30 Buses leave Greenbelt Marriott parking lot 6:00 – 7:00 Reception & Exhibits at B&O Railroad Museum 7:00 Dinner & Guest Speaker – Tom Henricks: Mechanisms from an Astronaut User Point of View 10:00 Buses leave Railroad Museum and return to the hotels

FRIDAY, 12 MAY 2000

7:00	Friday Presenters' Breakfast
8:00	SESSION VII – TRIBOLOGY & OTHER MECHANISMS Edward Devine, Session Chair Swales & Associates, Beltsville, MD <ul style="list-style-type: none">• Earth Scanner Bearing Accelerated Life Test Brian Dietz, Moog, Inc., Chatsworth, CA, Steven VanDyk, Raytheon Systems Company, Santa Barbara, CA, and Roamer Predmore, NASA Goddard Space Flight Center, Greenbelt, MD• Measurements of Friction Coefficients between Oxidized and Contaminated Surfaces in Vacuum and in Air Peter Frantz & Stephen Didziulis, The Aerospace Corporation, El Segundo, CA• Marshall Space Flight Center High Speed Turbopump Bearing Test Rig Howard Gibson, Chip Moore & Robert Thom, NASA Marshall Space Flight Center, Huntsville, AL• Design, Development and Testing of Umbilical System Mechanisms for the X-33 Advanced Technology Demonstrator Alan Littlefield & Gregory Melton, NASA Kennedy Space Center, Florida• Development of a Flywheel for Energy Storage and Attitude Control of an Exoatmospheric Interceptor Doug Havenhill, SatCon Technology, Peoria, AZ; Frank Nimblett, Steve Nichols & John Young, SatCon Technology, Cambridge, MA
10:30	BREAK
10:45	VIDEO PRESENTATION: An Overview of GSFC
11:15	TECHNICAL SESSIONS CONCLUSION <ul style="list-style-type: none">• PRESENTATION OF THE HERZL AWARD• CLOSING REMARKS
11:30	LUNCH BREAK AND CHECK-OUT
12:30	BUSES DEPART HOTEL FOR GSFC TOUR
1:00-4:00	GODDARD SPACE FLIGHT CENTER FACILITY TOUR

SYMPOSIUM ORGANIZING COMMITTEE

Stewart C. Meyers, Host Chairman, NASA GSFC

Stuart H. Loewenthal, General Chairman, Lockheed Martin
Edward A. Boesiger, Operations Chairman, Lockheed Martin

Obie H. Bradley, Jr., NASA LRC
Michael J. Eiden, ESA/ESTeC
Carlton L. Foster, NASA MSFC
Robert L. Fusaro, NASA GRC
Claef F. Hakun, NASA GSFC
Christopher P. Hansen, NASA JSC
Alan C. Littlefield, NASA KSC
Edward C. Litty, JPL
Ronald E. Mancini, NASA ARC
Fred G. Martwick, NASA ARC
Martha E. Milton, NASA MSFC
Minh Phan, NASA GSFC
John F. Rogers, NASA LRC
William C. Schneider, NASA JSC
Donald R. Sevilla, JPL
James J. Zakrajsek, NASA GRC

SYMPOSIUM ADVISORY COMMITTEE

H. Mervyn Briscoe, ESA/ESTeC (ret)
David F. Engelbert, NASA ARC (ret)
Otto H. Fedor, Lockheed Martin (ret)
Angelo Giovannetti, NASA ARC (ret)
John E. Harbison, NASA MSFC (ret)
John W. Redmon, Sr., NASA MSFC (ret)
Alfred L. Rinaldo, Lockheed Martin (ret)
Sterling W. Walker, NASA KSC (ret)
Bowden W. Ward, Jr., NASA GSFC (ret)
Nathan D. Watson, NASA LRC (ret)
Edward A. Wegner, Lockheed Martin (ret)

A Low Power Cryogenic Shutter Mechanism for Use in Infrared Imagers

D. Scott Schwinger* and Claef F. Hakun*

Abstract

This paper discusses the requirements, design, operation, and testing of the shutter mechanism for the Infrared Array Camera (IRAC). The shutter moves a mirror panel into or out of the incoming light path transitioning IRAC between data acquisition and calibration modes. The mechanism features a torsion flexure suspension system, two low-power rotary actuators, a balanced shaft, and a variable reluctance position sensor. Each of these items is discussed along with problems encountered during development and the implemented solutions.

Introduction

IRAC, developed by Goddard Space Flight Center, under agreements with The Smithsonian Astronomical Observatory and the Jet Propulsion Laboratory, is 1 of 3 scientific instruments on board the Space Infrared Telescope Facility (SIRTF) to be launched in December of 2001. SIRTF is the fourth "large observatory" performing imagery, photometry, and spectroscopy of astronomical bodies over the spectral range of 3.6 to 160 μm . The IRAC instrument takes images in 4 bands centered on the following wavelengths: 3.6, 4.5, 5.8, and 8.0 μm . The major objectives of IRAC are to produce the following science data sets:¹

- Deep confusion-limited broadband (25%) surveys for high-redshift normal galaxies
- Large area shallow surveys for brown dwarfs
- Imaging surveys of star clusters to search for brown dwarfs
- Surveys of nearby stars for brown dwarfs and superplanets
- Photometric observations of selected ultraluminous galaxies and active galactic nuclei
- Imaging surveys to identify protoplanetary disks and young stellar objects

Due to its use of state-of-the-art large format infrared detectors, IRAC will be more sensitive and produce more compelling, higher resolution images than previously possible with cryogenic imagers.²

A top view of the IRAC instrument is shown in Figure 1. A pickoff mirror reflects light from the focal plane of the spacecraft telescope off of two mirrored surfaces at slightly different angles. The result is a transmission of two separate light paths into the top and bottom compartments of the IRAC structure. Each compartment has a full set of refractive optics and two near infrared detectors positioned almost symmetrically about the mid-plane of the structure.

Following the light from the pickoff mirror and into the instrument, it first travels through the aperture of the shutter. The shutter is the focus of this paper and will be addressed extensively later. After the shutter, the light travels through a doublet lens to a beam splitter. Here the beam is split into two separate wavelengths. The longer wavelengths are transmitted and the shorter wavelengths reflected. After the beam is split, each subsequent beam passes through a filter and a lyot stop and onto a detector array. There are 4 of these arrays, one for each of the stated wavelengths, each 256 x 256 pixels and covering a 5.12 x 5.12 arcmin field of view. Two detectors are Arsenic-doped Silicon (Si:As) IBC arrays and the other two are Indium Antimonide (InSb) arrays.

Along with the optics and the detectors, there are two on board calibration systems: a transmission calibrator and four flood calibrators. Each of the four flood calibrators is attached to a detector mount and project light directly onto the arrays. The intent is to flood the array with a known infrared source and confirm an expected level of response across the entire array. The transmission calibrator is designed to

* NASA Goddard Space Flight Center, Greenbelt, MD

send a known source through all of the optics and onto the detector arrays. The transmission system consists of a calibration sphere that produces a uniform source of known intensity. When the shutter is in the closed position, the light from the transmission calibrator is relayed through the optical train to the detector arrays. With the calibrator system off and the shutter closed, a dark level calibration of the detectors can be obtained.

IRAC, along with the other instruments aboard SIRTF, is a cryogenic instrument thermally coupled to a superfluid Helium dewar. Therefore, the base temperature of the instrument is expected to be 1.4 Kelvin. The mission lifetime requirement is set at 2.5 years with a goal of 5. At that time, the cryogen will be expended and the instrument chamber is expected to rise to 30 Kelvin. Two of the detectors, the InSb arrays, are still expected to work in the post-cryogen state further extending the useful life of the instrument. The shutter mechanism is expected to continue to work, as well.

The Shutter Mechanism

The requirements, design, operation, and testing of the IRAC shutter mechanism are described. The shutter has been developed over a three-year period. During that time, two ETUs were built and tested. One of these units remains in the IRAC Instrument Demonstration Module (IDM) which was built for engineering testing and proof of concept. In addition, three flight units have been designed and built and are currently in various stages of test. Two of the assembled flight units have been tested and characterized at liquid helium temperatures and one of these units has been delivered to the IRAC flight cold assembly. The test data taken includes actuator characterization, position sensor characterization, repeatability of mirror position, optical metrology, and excess actuator torque.

Functional Description

The IRAC shutter (Figure 2), approximately 0.15 m (5.9 in) in length, is designed to move a 79.8 mm by 37.1 mm (3.14 in x 1.46 in) mirror to two positions identified as open and closed. The motion is rotational and sweeps a total arc of 38 degrees (Figure 3). When the shutter is opened, the mirror is stowed out of the incoming light path. Therefore, the instrument is able to receive light from the focal plane of the spacecraft telescope and take images of the outside sky. When the shutter is closed, the outside light is to be attenuated by 1.0E06 providing a dark environment in the instrument for infrared detector calibration. To achieve this, the mirror is translated directly into the light path completely filling the aperture and interfacing with a baffle in the IRAC housing. The result is the light path being completely blocked with very little leakage around the mirror. The inside portion of the mirror itself provides a reflective surface off of which the transmission calibration source is reflected. The source then passes directly through the optical path of the instrument and onto the infrared detectors.

Requirements^{3, 4}

- Spacecraft:
- Stiffness must assure fundamental frequency > 50 Hz
 - Must survive launch loads generated by a Delta II H launch vehicle
 - Uncompensated momentum shall not exceed 200E-06 N-m-s
 - Shall operate at 1.4 Kelvin for mission lifetime and 28 Kelvin for extended mission
- Mechanism:
- Mass not to exceed 1.6 kg
 - Shall translate mirror to two positions: Open and Closed, with 0.5 deg repeatability
 - Time to close shall not exceed 10 seconds
 - Shall be failsafe open
 - Lifetime operations shall be 20,000 cycles
 - No microphonic transmission beyond 0.5 second transient
 - Maximum power dissipation shall not exceed 0.5 J/100 s (5 mW average)
 - Attenuate incoming photon radiation by $\geq 1E06$
 - Redundancy:
 - There shall be no electrical single point failures
 - Minimize mechanical single point failures

Electromechanical design and operation

A cross-section of the IRAC shutter is shown in Figure 4 and an exploded view is included as Figure 5. To facilitate the description of the component parts of the shutter mechanism, they will not necessarily be discussed in order of their assembly with the unit. The description will start with the suspension system of the mechanism, move to the actuation system, continue on to the structure and stress limiting components, and conclude with the sensory components.

Suspension System

The shaft assembly (Figure 6) provides the suspension system for the mirror panel. The shaft, itself, is fabricated of Aluminum 6061-T651. The central hub, the most robust portion of the shaft, is designed to hold the mirror and counterweight. The mirror panel is aluminum and has two diamond-turned surfaces coated with gold. An arm extends from this panel and mates to a flat surface machined into the shaft's hub. Opposite the mirror, a 0.1058-kg tantalum counterweight is attached to the shaft. This counterweight minimizes the CG offset of the shaft, which minimizes moments under 1G and vibration.

The shaft also supports the two rotors of the actuators and two A286 steel bushings. A square hole in the center of each rotor slides axially over the shaft and mates with a matching square profile. As a result, each rotor is fixed in rotation such that relative motion between the parts is not possible. The rotors are fixed axially by a nut on a threaded portion of the shaft at either end. This threaded portion also supports steel bushings that provide bearing surfaces for rotation and act as the radial centering device for the shaft. The bushings fit into holes in the end caps of the mechanism such that there is only 38.1 μm (0.0015 in) clearance radially. The mating surfaces in the end caps are plated with Teflon-impregnated anodize to minimize friction.

Finally, the shaft is machined to allow a Beryllium Copper torsion flexure to run down the central axis. This component provides the axial stiffness required to locate the shaft assembly and provides the restoring torque to reopen the shutter when power is terminated. The flexure is chemically etched out of 0.66 mm (0.026 in) thick BeCu 25AT sheet and is heat-treated at 315.6°C (600°F) for 3 hours to obtain the following strength and fatigue properties at 4 K: $\sigma_{\text{ult}}/\sigma_{\text{yield}}/\sigma_{\text{fatigue}} = 220/190/110$ ksi. It has two active portions, 0.66-mm (0.026 in) square and 52.1-mm (2.05 in) long, and three flanges for attachment to other components. The middle flange is attached to the central hub of the shaft. Two aluminum end pieces are bolted to the end flanges such that the two ends of the flexure can be fixed in rotation to the end caps of the mechanism. As the shaft rotates with the ends fixed, restoring torque is generated in both sides of the flexure to fight this motion. This restoring torque reopens the shutter when the power is off.

Actuators

The shutter contains two actuators built around each of the rotors on the shaft (Figure 7). These actuators are electromagnetic variable reluctance rotary devices capable of providing 45 degrees of angular motion, though the shutter only requires 38 degrees of rotation. They are cylindrical in design and consist of a rotor, two stators, an electromagnetic coil, and a magnetic "closeout" cylinder. These devices contain no permanent magnets. Hiperco 50A, heat treated to allow high magnetic flux density with little hysteresis⁵, provides a closed path for magnetic fields generated by an electromagnetic coil. All components of the actuator except the bobbin and the coil itself, are machined of this material. The active portions of the stators are radially contained within the bobbin. The coil is 99.99% pure 38 AWG, HAP TZ insulated copper wire precision wound on a black anodized aluminum 6061-T651 bobbin to 11,000+ turns. Passing current through the coil generates a magnetic field that is focussed by the stators and flows through the rotor. The coil was sized by analysis to provide an NI value greater than 600 with 60 mA. To complete the magnetic circuit, a closeout cylinder covers the coil and connects the two stators. The moving portion of the actuator, the rotor, is positioned between the two stators and is rigidly affixed to a shaft that runs down the central axis of the device. This shaft maintains the radial position of the rotors within the actuators and transfers rotary motion to the mirror.

Rotary motion is produced by the geometry of the device. The footprint of the rotor is best described as a bow tie. There are raised portions of the stators that match the profile of the rotor exactly, though the footprint of the base of the stators is circular to mate with the closeout. The stators face each other when the actuator is fully assembled. There is just enough separation of the stator faces to allow the rotor to pass between them with 0.33-mm (0.013-in) clearance on both sides. The rotational position of the rotor in the open state is such that its footprint is out of phase with those of the facing stators except for an approximately 30 degrees of overlap at one side. In this position, the rotor is at a state of high reluctance in the magnetic circuit. When current is applied, the rotor wants to achieve a state of minimum reluctance. Thus, the rotor is drawn between the stator faces. This motion produces a torque and rotates the shaft and mirror to the closed position.

A final component to the actuator design is paramount to achieving the 5-mW requirement. That component is a magnetic latch that extends vertically from each of the stator faces. These "tabs" are positioned and sized such that the rotor contacts the tab on each of the two stators when it is fully rotated to the closed position. With the rotor against these tabs, the magnetic flux can travel directly from stator to stator through the contacting rotor and on to the magnetic closeout. The rotor effectively completes the magnetic circuit, reducing all air gaps to nearly zero, producing a large drop in magnetic reluctance. This drop in reluctance means that the shutter can be held closed, fighting the restoring torque of the torsion flexure, with a much lower magnetic field. Since the field is electromagnetic in origin, the reduction in field means a reduction in current and less power dissipation in the coil. The result is a shutter that requires 55 mA to close and less than 1 mA to hold closed.

Of further benefit to achieving low power dissipation is the fact this mechanism operates at liquid Helium temperatures. The result is a reduction of resistance of the electromagnetic coils from 2700 ohms at room temperature to 20 ohms at 4.2 Kelvin, a factor of 135 change. This change has been verified during liquid Helium testing. Since the shutter closes in approximately 0.5 second, the control electronics sends a high current pulse, then quickly drops the magnitude to a hold current value. By including a position sensor (described later) to resolve the position of the shutter mirror, the shutter electronics immediately know when the shutter is closed and time spent at the higher pull-in current is minimized. Time averaged power dissipation can then be calculated using Equation 1. Assuming a typical shutter closure duration of 500 seconds and including margin on the current levels, the inputs to the equation are as follows:

Pull-in Current	-	$I_{\text{pull}} = 60 \text{ mA}$
Hold Current	-	$I_{\text{hold}} = 3 \text{ mA}$
Pull-in Current Duration	-	$t_{\text{pull}} = 0.5 \text{ s}$
Hold Current Duration	-	$t_{\text{hold}} = 499.5 \text{ s}$
Total resistance -	-	$R_{\text{tot}} = 20 \Omega$

$$P_{\text{ave}} = \frac{I_{\text{pull}}^2 \cdot R_{\text{tot}} \cdot t_{\text{pull}} + I_{\text{hold}}^2 \cdot R_{\text{tot}} \cdot t_{\text{hold}}}{t_{\text{pull}} + t_{\text{hold}}}$$

Equation 1 – Time Averaged Power

The result is a shutter mechanism that dissipates 252 μW , a factor of 20 less than the requirement.

Structural and Stress Limiting Components

The housing is a continuous piece of Aluminum 6061-T651. Pockets are machined into each end along the main axis to house the actuators. A gap in the structure, between the two actuator pockets, allows the rotation of the mirror attached at the central hub of the shaft. End caps on either end of the shutter housing contain the actuators within the pockets and provide support structure for several components on either end of the flexure. The actuators are preloaded against these end caps by a wave spring in the bottom of each actuator pocket. This preload maintains the position of the actuator components during launch and provides axial compliance necessary for CTE mismatched parts when going cold.

A hole in the center of the end cap provides a bearing surface for the steel bushings on the ends of the shaft. The end cap is plated with a Teflon-impregnated anodize to provide some lubricity during actuation. Precision concentricity is maintained in the position of these holes in the end caps, the interface of the end caps to the housing pockets, and the relationship of the centers of each of the pockets to ensure that the axis of rotation of the shaft is centered.

The square cross-sectioned end piece attached to the flexure in the shaft is designed to protrude through the end cap where it engages a component with a square hole, the Spring Preload Ring. This component is designed to be rotated until the proper torsional preload is imparted to the flexure. This preload is necessary to return the mirror to the open position when power to the actuators is terminated. In addition, this preload helps to ensure that the mirror does not flap uncontrollably during launch. The preload rings are set, clamped in place during preliminary assembly, and pinned to the end cap during final assembly.

To anchor the flexure axially to the end caps, a steel nut is run onto threads in the flexure end pieces. The threads extend through the square hole in the preload ring allowing the nut to effectively anchor the flexure to the end cap/preload ring stack. The nut on one side is run onto the threads completely to the preload ring while the nut on the other side is run down onto a stack of wave springs. In addition to affixing the flexure to the end caps, these nuts allow axial adjustment to ensure that the rotors attached to the shaft are in the proper location for optimal performance of the actuators. The springs under one of the nuts provide axial preload for the flexure and maintain a desired preload as the structural components shrink going cold. Since the CTE of the Beryllium Copper flexure is 25% less than that of the Aluminum of the structure from room temperature to 4 K⁶, the preload and the rotor position would be lost without the springs. This preload is necessary to maintain the rotor position during operation and launch.

A hard stop further limits the loads transferred to the flexure during launch. This component is Aluminum 7075 plated with Teflon-impregnated Anodize for lubricity. It provides a rotary stop for the mirror in the open position. In addition, it has two uprights that straddle the mirror arm throughout its entire range of travel. These uprights are positioned such that there is a 0.2-mm (0.008-in) gap between each upright and the mirror arm. This gap is sufficient to allow freedom of movement for the shaft but to restrict axial motion in the event that launch loads excite the suspended mass of the shaft components. Restricting the axial motion is necessary to prevent stress in the flexure from violating material strength limits and ensure that the rotors do not impact against the stators in the actuators.

Finally, a retaining device is mated to the end cap to capture the stack of rings at the flexure interface. The gap between the top of the stainless steel nut and the underside of the retainer is less than 0.127mm (0.005 in). This gap ensures that in the event of a breakage in one half of the flexure with the mirror in the closed position, the axial motion of the shaft in the opposite direction will be less than the gap between the mirror arm and the hard stop uprights. Therefore the restoring torque of the remaining half of the flexure will be enough to open the shutter without friction on the hard stop.

Sensory Components

There are three sensory components on the shutter: 2 Cernox resistance thermometers and a variable reluctance position sensor. The Cernox thermometers are calibrated to operate from room-temperature (300 K) down to pumped liquid Helium temperature (1.4 K). One of these sensors is located on each of the end caps. They will be used to monitor temperature on orbit and to verify power dissipation during component level testing.

A variable reluctance rotary position sensor was developed to monitor the position of the mirror. The sensor is an electromagnet in the shape of a "C." There are two electromagnetic coils wired in series, one on either side of the opening. Each coil has greater than 300 turns of 99.99% pure 38 AWG, HAP TZ insulated copper wire. The bobbins for the coils are part of the magnetic circuit and are made of Hipercos 50A heat-treated to optimize performance. To resolve position, a magnetically conductive ramp is passed through the gap in the sensor. As this ramp passes between the poles, the change in thickness of the material changes the air gap of the circuit. This change in gap changes the reluctance of the circuit. The reluctance change is measured by passing an AC signal through the coils and measuring the change in inductance of the circuit. The ramp is curved, bonded to the counterweight, and sized to be at a minimum thickness when the shutter is open and at a maximum thickness when it is closed. The raw response of the sensor is approximately 1.5 V across the full range. This response is then scaled to 1.25 to 3.75 V from open to closed position, respectively. Since the ramp is continuous, it can provide continuous position data for all intermediate positions of the shutter mirror, as well.

Under normal operation, the position sensor will provide feedback to the electronics to minimize the power dissipation in the actuator coils. The sensor position will be continuously checked after the actuator is sent the 60 mA pull-in current level. Once the sensor reads a threshold indicating the shutter is closed, the electronics will autonomously drop the current to the hold level of 3 mA. The delay from the time the sensor reaches the threshold to the drop in current is 1.0E-03 sec. When the shutter is given the signal to open, the sensor verifies the open position and returns this signal in a data packet prior to completely powering down the shutter mechanism.

Unique Operation

There are additional unique characteristics of this mechanism. As stated above, the shutter is designed to fail open if there is a flexure breakage. However, the shutter is also designed never to close again if this failure should occur. The internal forces of the actuators (discussed in the Problems section) are large and the rotor is in an inherently unstable position. Therefore, without a continuous flexure under tension, the rotor is pulled away from the failure side and large frictional loads are generated either between the rotor and the stator in the actuator, or between the mirror arm and the hard stop upright. This fiction is enough to prevent the actuator from closing.

Finally, the choice in flexure suspension system combined with the bearing surfaces as designed cause the internal forces to approach zero when the shutter is powered off and the mirror is returning to the open position. The flexure allows us to avoid conventional ball-bearing designs that are difficult for cryogenic usage and always have some level of internal friction. In addition, the fatigue properties of BeCu increase dramatically at liquid Helium temperatures. We have performed a life test on an ETU and have driven the mechanism to greater than 450,000 cycles, 22.5 times the rated life.

The bushings on the shaft are designed to have 38.1 μm (0.0015 in) radial clearance with the hole in the end caps. Careful alignment and tolerancing is performed to center the bushing within this hole as precisely as possible and limit the contact between the two parts. However, due to operation under 1 G and physical limitations in the precision of the machining, these parts do touch. As the shutter is actuated, the internal loads of the actuators pull the shaft off axis and these bearing surfaces rub. Under this loaded condition, there are frictional losses at these interfaces due to the off axis normal load in the bearing interface. However, with power off, this load goes to zero as does the friction force. Therefore, the frictional force fighting the opening of the mirror is minimized. This effect will be realized to an even greater extent in the zero-G environment of space.

Functional Testing

The shutter has been successfully tested cold many times. These tests included cold functional, position sensor repeatability, life operation for the ETU, infant mortality for the flight, and electronics board checkout. The performance during each of these tests was repeatable and consistent. In addition, life tests were completed with no apparent degradation in performance.

One additional test was in a dewar with a window to take optical metrology on the shutter mirror. Using a theodolite, we were able to measure the mirror angle relative to a starting position. This was our first opportunity to characterize the position sensor cold. The window prevented us from being able to achieve temperatures colder than 28 K, but the operation of the shutter at temperatures below 10 K had been previously verified. In addition, the shutter is actuated with a current drive system that compensates for any variance in actuator coil resistance.

The performance of both the actuator and the sensor proved to be repeatable. Mirror angles were measured at several different current inputs. At each of these current levels, the voltage output from the sensor electronics was measured as well. The results are included here as Figures 8 and 9. The response of the position sensor is second order with regard to the mirror angle (Figure 8). Figure 9 indicates that the actuator needs approximately 42 mA before overcoming the torsional preload of the flexure. Above 42 mA, the mirror will rotate according to the plot until the current reaches 53 mA. At this time, the attractive force of the actuator tabs overwhelms the restoring force of the flexure and causes the

mirror to quickly rotate to the closed position. The speed of this motion makes angle measurement difficult in this regime.

Several current input levels were repeated to verify the repeatability of the mirror position with current. The open and closed positions of the mirror were repeatable to less than 30 arcsec. However, we found that if current is stepped up to a particular level, the angle achieved by the mirror is slightly less than if the current level is input as a step function from zero. The difference in angle ranges from 0.05 to 2.2 degrees depending on location within the range of motion. There were not enough data points taken to achieve a statistical sampling. However, it seems apparent that the internal off-axis forces in the actuators are being transferred to the bushings on the shaft in the form of static friction in these intermediate positions. Since the coefficient of kinetic friction is always lower than the coefficient of static friction, the force fighting the rotation of the bushings will be lower for a moving bushing than for a static bushing under the same load. In addition, the rotational momentum of the shaft accelerating to a greater angular velocity under a step impulse rather than a slow increase may overcome more of this friction and complete a greater angle prior to stopping. Data is currently being reviewed to quantify frictional forces.

Testing has also quantified excess torque as a function of current and mirror angle (Figures 10 and 11). The test was performed at room temperature and measured the minimum excess torque in the motor to be 14.15 mN-m (2.004 in-oz) with a 60 mA input. Finally, the failure behavior of the shutter was tested on the second flight spare. The ability for the shutter to open itself if a flexure breakage occurred was verified; however, this ability is highly dependent on the gap between the flexure nut and the retainer on the end cap. If the gap is too large, the mirror arm will bear on the hard stop upright and the subsequent friction between the two parts will prevent the shutter from opening. If there is no contact between these parts, half of the flexure is still adequate to open the shutter mirror. With no axial force on the flexure (i.e. a broken flexure), the shutter is designed not to close. This behavior was also confirmed by this test. Finally, the shutter has survived a qualification level vibration test and a post-vibe life test is pending.

Problems and Solutions

During the development of this mechanism, several problems were encountered that required solutions. This section identifies the major problems and the rationale behind the solutions.

Suspension System

During the initial concept of this mechanism, we wrestled with how we could achieve 38 degrees of rotation most efficiently and repeatably at cryogenic temperatures. We wanted to avoid ball bearings because of the difficulties involved with sizing the bearings warm to achieve the proper fit cold and with lubrication at liquid Helium temperatures. In addition, our motion was not going to be continuous and we were concerned about degradation of performance over time due to displacement of bearing lubricant. A flexure seemed logical, but what should it look like?

We initially thought of flex pivots but found that the most rotation we could get out of one was on the order of 15 degrees. This would mean that we would have to gang 3 of these pivots together to achieve our 38 degrees. Our concern with doing this was losing our center of rotation during operation and maintaining structural rigidity to survive launch loads.

We then thought of using a shaft pointed on each end that engaged a jewelled cup. We thought this configuration would be a relatively low-friction interface that would maintain its center and still allow full rotation. A clock spring would provide our restoring force. This concept seemed sound but we became concerned about the wear of the jewelled cup after launch and throughout the life of the mission. In addition, the cups would have to be axially preloaded to maintain contact as the mechanism went cold. This preload would also have to be sufficient to maintain the position of the cup during launch. The design quickly became more complicated than we anticipated and was abandoned.

We finally returned to the flexure idea and decided to investigate a torsion flexure design. The concept is elegant in that the restoring torque and the axial position of the mirror can be obtained in one component. In addition, there is some heritage for this torsion flexure design in the Scanning Mirror for Infrared Sensors⁷ developed by Lockheed Missiles and Space Company. Packaging the torsion flexure required a hollow shaft and sizing the flexure for stress/strain and restoring torque was simply a matter of a parametric trade study. The axial preload of the torsion flexure was established based on predictions for launch loads and axial forces expected within the actuator. Launch loads were predicted using conventional finite element analysis. Internal actuator forces were determined using a boundary element magnetic analysis program called Amperes. The axial load was finalized by investigating combined torsional and axial stress in the BeCu flexure and confirming that sufficient margin could be obtained.

Internal Actuator Forces

Axial preload in the flexure is needed for several reasons, not the least of which is to maintain rotor position under internal forces within the actuator. The initial design had a nominal gap of 4.52E-04 (0.007 in) between the rotor and each of the stators. The rotor is in an unstable position between the stators and is pulled in the direction of the portion of the magnetic circuit that is closest. Therefore, there are both axial and radial forces on the shaft within the actuator. These forces grow by 1.751E05 N/m (1000 lb/in) of misalignment. We knew that the position of the rotors between the stators would have to be precise but we did not fully appreciate the problem until we first tested the prototype.

Initially, radial and axial motions of the shaft under these forces were accommodated by a bushing inserted into the clearance hole in the base of the actuator cavities in the shutter housing. The inside of the bushing was a toroid to limit friction radially. Axially, it had a bearing surface that the shaft hub could contact if the axial forces during operation or launch became too great. This bushing was Aluminum 6061-T651 and plated with Teflon-impregnated anodize to limit friction. The problems we discovered with this design were two fold.

First, there was very little "wheel base" as these bushings were both near the hub of the shaft. We could not limit the off-axis forces enough to prevent the shaft from tilting and the rotors from clamping against the stators. The second problem was that, to limit the axial motion, the axial clearance between the bushing bearing surface and the shaft hub had to be so small that assembly became difficult. In fact, under the initial testing we discovered that the axial forces were great enough to cause the shaft hub to clamp against the bushing seizing the rotation.

We first tried to correct the problem by increasing the axial tension in the flexure. Ultimately, we were able to make the actuator work, but not before we encountered another problem. The initial design of the shutter housing did not have the structural member between the two actuator cavities. Therefore, as we continued to increase tension in the flexure, the housing actually deformed and the gaps between the bushings and the shaft hub closed. We needed to increase tension on the flexure to maintain position of the rotors and in the process, we were deforming the housing and causing alignment problems. To correct this problem, we added a structural member that later became part of the housing design. We were then able to increase the flexure tension enough that the actuator worked.

To reduce the radial motion, we changed our bearing concept from a radial bushing capturing the shaft near the center of mass to extending the shaft and adding a precision bushing that would ride on the inner diameter of the end caps. Ultimately, this added "wheel base" and attention to concentricity sufficiently limited the tilt of the shaft. While examining the axial forces and motion of the shaft, we determined that the tolerances used to determine the actuator gap were insufficient. Therefore, we precisely measured each of the components that impacted the axial position of the stators and rotors. A rigorous CTE analysis of the shutter design to simulate the changes to the components at 2 K was developed⁸. The spreadsheets have been used for each of the shutter units developed to date and can quickly be modified for specific part dimensions.

As a result, we were able to precisely locate the rotors between the stators. With this knowledge, we were able to move away from the philosophy of limiting the axial motion due to misalignment forces and toward the philosophy of limiting the axial forces by precisely locating the rotors. In addition, we modified the actuator design to double the gaps to 3.81E-04 m (0.015 in) between the rotors and the stators. This increased gap also reduces the sensitivity of the mechanism to the forces generated by the magnetic circuit.

Consequently, we were able to lower the tension on the flexure to 111.2 N (25 lb) at room temperature. Since we improved the bearing design, began precisely measuring components, and reevaluated the cold motion, we have been 100% successful with our assemblies and cold tests.

Launch and Operational Loads

The initial design of the flexure was a parametric trade study of torsion, stress, and geometry. We also decided to limit the rotational loads the shutter would experience with an unbalanced cantilevered mirror in a vibration environment. Therefore, we counterbalanced the mirror with a mass of Tantalum. The result was a shaft that weighed 2.22 N (0.5 lb). However, the design was completed before our launch load environment was fully defined. A coupled load analysis identified that the shaft could experience loads of 100 Gs. This was not anticipated and we became concerned about the vibration load the flexure would experience due to the increased mass of the balanced shaft. The FEA on the shutter confirmed that the flexure would yield under these loads.

We looked into increasing the size of the flexure, but due to schedule restrictions we decided not to change the flexure design. Next, we looked at removing the counterweight to reduce the axial loads on the flexure. However, without the counterweight, the mirror would rotate wildly in the vibration environment. Although the axial loads would be less, the combined loading of the rotational stress with the axial was still enough to yield the flexure. The value of the counterweight was worth the added mass. We had to limit the loads another way.

We implemented a launch-load stop to capture the mirror arm throughout its full range of motion. It had to capture the mirror arm near its base due to high loads. The design resembles a goal post in football and was added as a component of the hard stop. We chose Aluminum 7075 as the material due to the high loads. Finally, the part was plated with Teflon-impregnated anodize to minimize wear and friction. The gaps between the uprights and the mirror arm were precision controlled to be 2.03E-04 m (0.008 in). This gap would sufficiently limit the axial motion of the shaft while not allowing the rotors to impact the stators in the actuators. The component has worked fine to date and has survived cold vibration testing and supports the fails safe open requirement.

Position Sensor

The development of the position sensor proved more difficult than expected. The initial design was a simple "C" shaped magnetic circuit with one large coil between the two poles (Figure 12). As stated in the description, the ramp was simply to pass through the gap between the two poles that were slightly tapered to focus the flux and fit within the shutter design. The change in the reluctance of the circuit as the ramp passed between the poles would be measured electronically. Theoretically, the design was sound. However, when we tested the prototype, we only got a response of 30 mV full range. In fact, it was difficult to measure any response at all over the noise in the electronic circuit.

Upon conducting a rigorous analysis using the Amperes modeling software, it became clear that there were large losses and fringe effects within the magnetic circuit due to the geometry. The fringe effects in the circuit act as magnetic shorts and reduce the effectiveness of the sensor. Since we only had one coil with a magnetic pole attached at either end, we generated relatively large surface areas of opposite potential facing each other. As a result, the magnetic flux simply jumped the gap between the poles all along them rather than only jumping the gap between the pole faces. Since there was less flux focused to the active area of the sensor, the response went down appreciably.

The redesign of the sensor (Figure 12) was subtle but produced much better response. Effectively, the only change was to split the coil from one large coil between the poles to 2 smaller coils moved up to the faces of the poles. The coils were then wired in series to ensure that a North and a South surface faced each other across the gap. The result was a vast improvement in response. The final design of the circuit reads the change in reluctance and is converted to a voltage response scaled from 1.25 to 3.75 V from open to closed position, respectively.

Conclusions

The IRAC shutter mechanism provides precise, repeatable, limited angular motion ideal for infrared sensing cryogenic instruments. The unique design of the actuator enables the shutter to dissipate very low power during operation. The torsion wire suspension system is elegant in its simplicity and enables the shutter to be designed to fail open and remain open through subsequent attempts to close. As designed, the shutter will survive and operate throughout all stages of the IRAC mission and remain operable in the post-cryogen environment of the spacecraft. Finally, the inclusion of a continuous variable reluctance sensor enables the shutter control to be optimized and ensures the knowledge of the mirror during a trouble shooting operation. The shutter meets or exceeds all functional and science requirements and is the result of the dedication of a talented development team.

Acknowledgements

Sid Johnson – mechanical design, assembly, test

George Reinhardt – magnetic analysis, sensor design

Chiachung Lee – mechanical analysis

Tom Hanyok, Bryan Grammer – mechanical design, drafting

Carlos Lugo, Carlos Bernabe, Gary Brown – electronics design, test

Other Contributors

Willie Barber, Willie Blanco, Derick Fuller, Paul Haney, Steve Hendricks, Dan McHugh, Dave Pfenning, Jim Towers, Steve Wood

References

1. IRAC Project. "Infrared Array Camera (IRAC) Critical Design Review Package." Goddard Space Flight Center, July, 1998.
2. Fazio, Giovanni G. "SIRTF Infrared Array Camera, IRAC Science Requirements." Smithsonian Astrophysical Observatory (January 1998), p.1.
3. Miles, John W. and Dan W Trites. "Space Infrared telescope Facility, Observatory Performance and Interface Control Document." Lockheed Martin, November, 1998.
4. Fazio, Giovanni G. "SIRTF Infrared Array Camera, Instrument Performance Requirements Document." Smithsonian Astrophysical Observatory, March 22, 1999.
5. Carpenter Steel Division. "Alloy Data: Hiperco Alloy 50A." Carpenter Technology Corporation
6. Reed, Richard P. and Alan F. Clark, Ed. *Materials at Low Temperatures*. American Society for Metals, Metals Park, Ohio © 1983, pp. 94-100.
7. Anderson, Richard H. and Sidney B. Bernstein. "Scanning Mirror for Infrared Sensors." Lockheed Missiles and Space Co., Sunnyvale, CA., 7th Aerospace Mechanisms Symposium, Houston, Texas, 1972
8. Touloukian, Y. S., R. K. Kirby, R. E. Taylor, and P. D. Desai. *Thermophysical Properties of Matter, Vol. 12: Thermal Expansion, Metallic Elements and Alloys*. Plenum Publishing Corporation, © 1975.

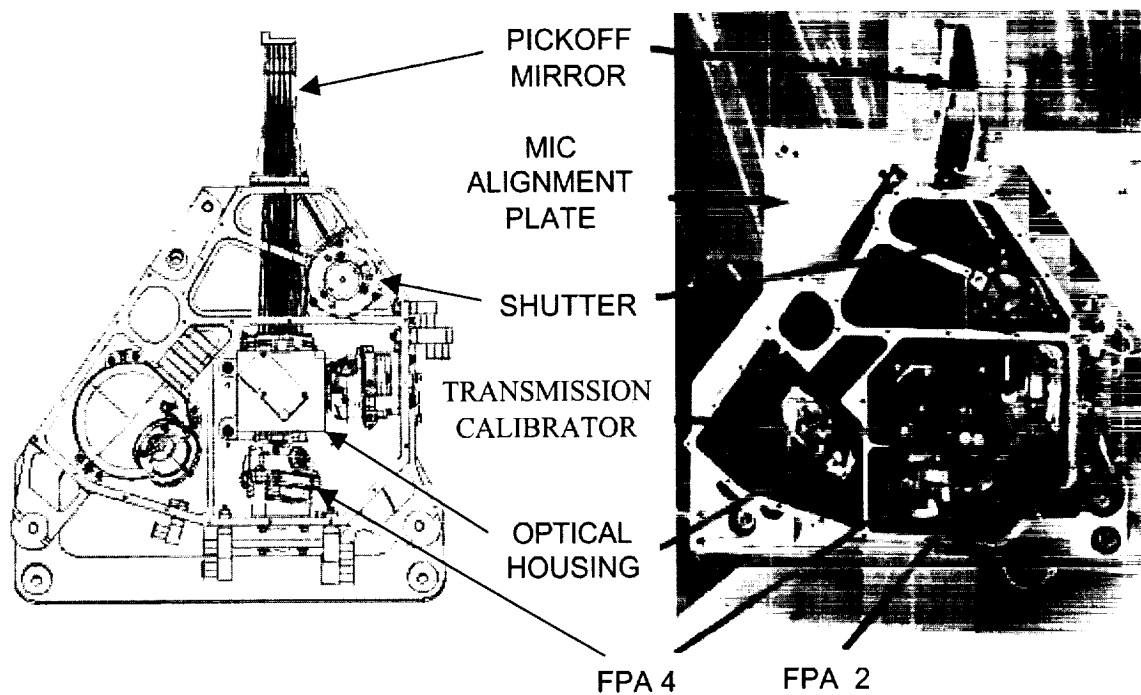


Figure 1 – IRAC Assembly



Figure 2 – IRAC Flight Shutter Unit

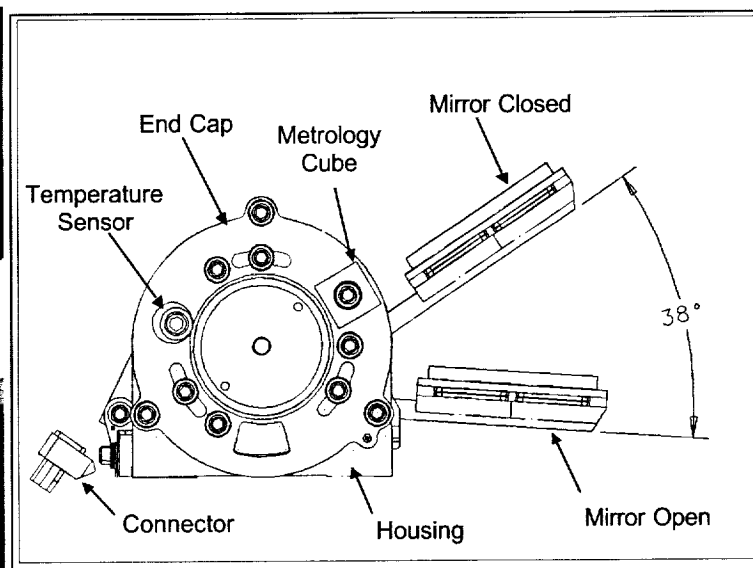


Figure 3 – End View Showing Mirror Angle

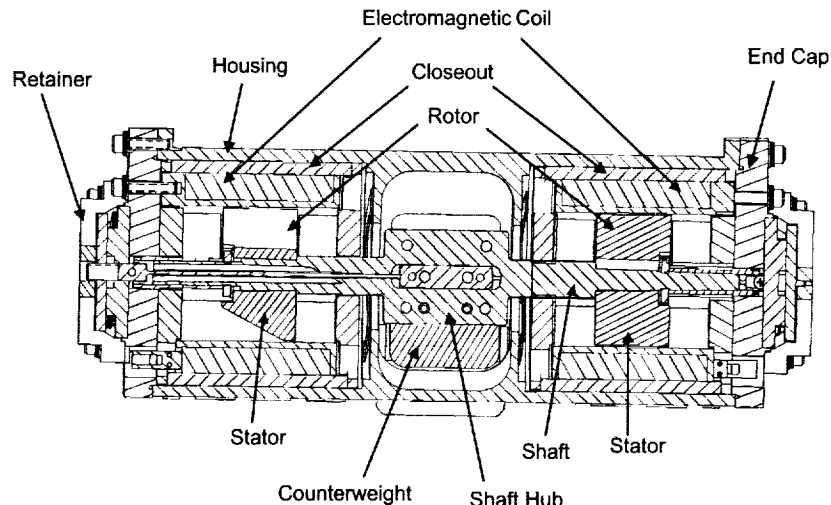


Figure 4 – Shutter Cross Section

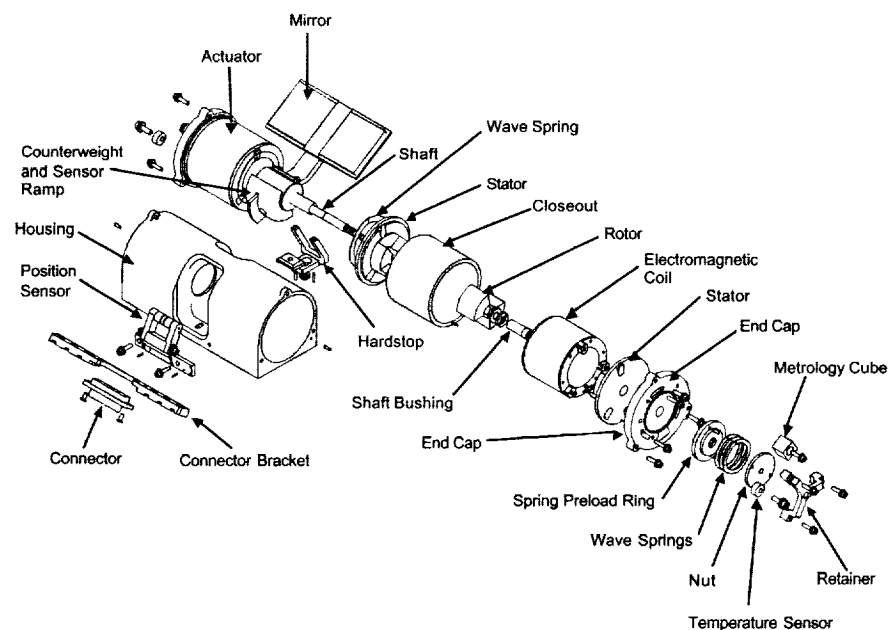


Figure 5 – Shutter Exploded View

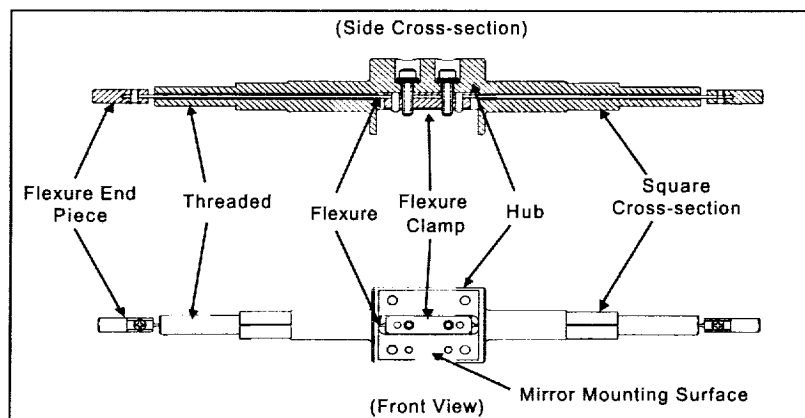


Figure 6 – Shaft Subassembly

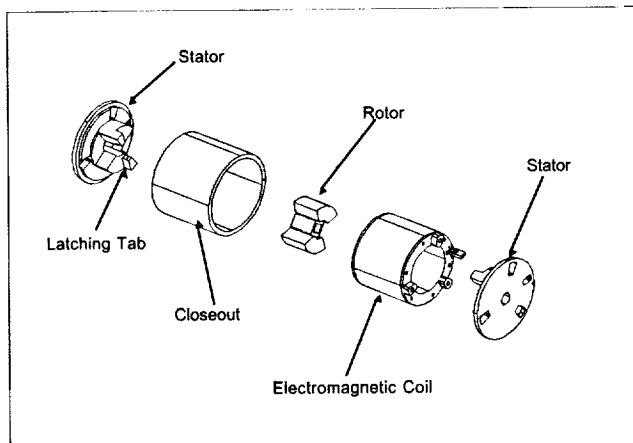


Figure 7 – Actuator Exploded View

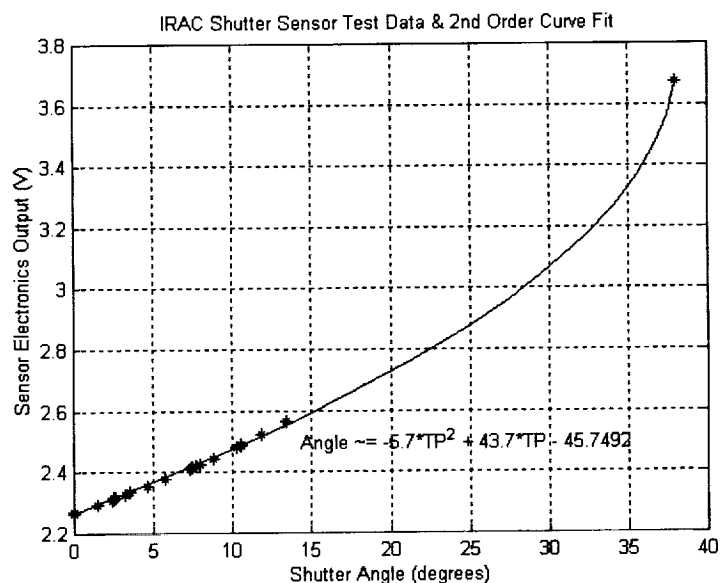


Figure 8 – IRAC Sensor Response vs. Mirror Angle

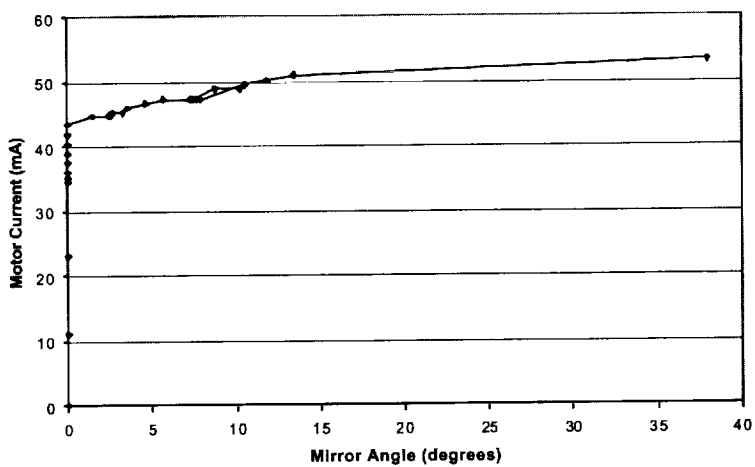


Figure 9 – Current vs. Measured Mirror Angle

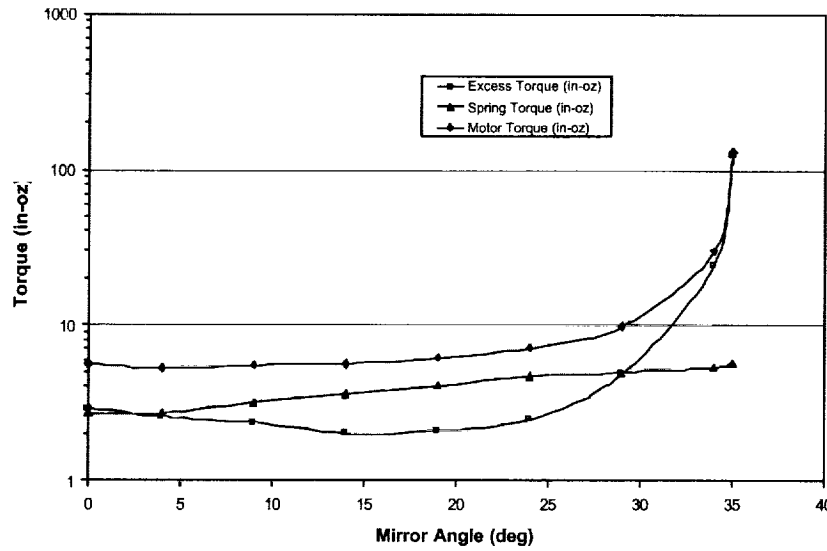


Figure 10 – Spring, Motor, and Excess Motor Torques at 60 mA

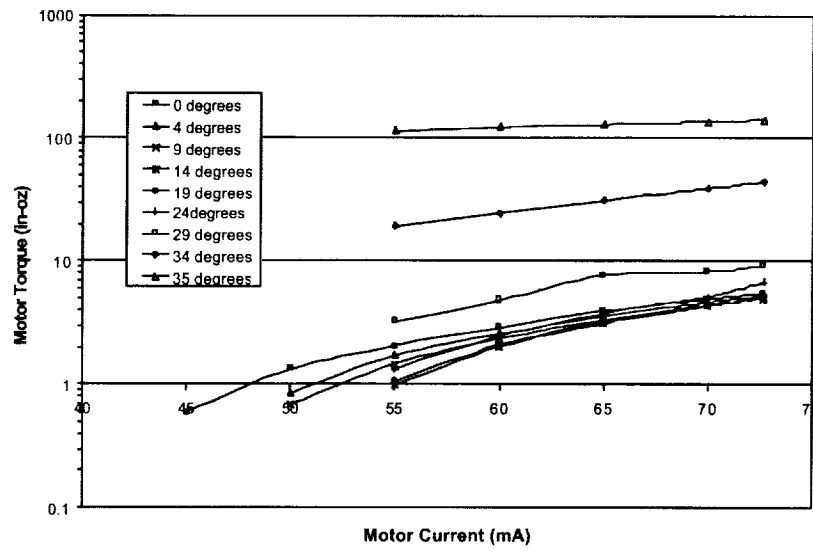


Figure 11 – Excess Motor Torque vs. Current for Various Mirror Angles

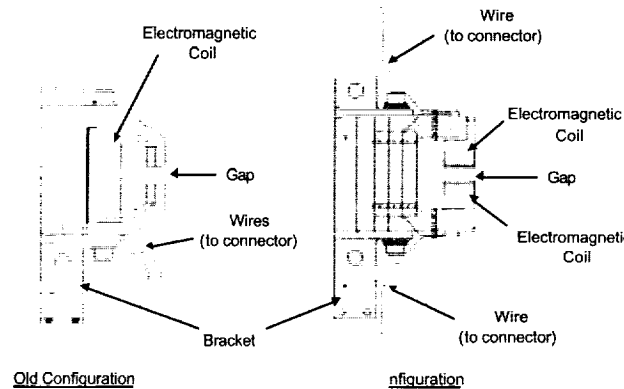


Figure 12 – Position Sensor Designs

ACIS Door Failure Investigation and Mitigation Procedures

William A. Podgorski^{*}, Neil W. Tice^{**}, and Paul P. Plucinsky^{*}

Abstract

NASA's Chandra X-ray Observatory (formerly AXAF) was launched on July 23, 1999 and is currently in orbit performing scientific studies. Chandra is the third of NASA's Great Observatories to be launched, following the Hubble Space Telescope and the Compton Gamma Ray Observatory. One of four primary science instruments on Chandra, and one of only two focal plane instruments, is the Advanced CCD Imaging Spectrometer, or ACIS. The ACIS focal plane and Optical Blocking Filter (OBF) must be launched under vacuum, so a tightly sealed, functioning door and venting subsystem were implemented. The door was opened two and one-half weeks after launch (after most out-gassing of composite materials) and allowed X-rays to be imaged by the ACIS CCD's in the focal plane. A failure of this door to open on-orbit would have eliminated all ACIS capabilities, severely degrading mission science. During the final pre-flight thermal-vacuum test of the fully integrated Chandra Observatory at TRW, the ACIS door failed to open when commanded to do so. This paper describes the efforts, under considerable time pressure, by NASA, its contractors and outside review teams to investigate the failure and to develop modified hardware and procedures which would correct the problem. Of interest is the fact that the root cause of the test failure was never clearly identified despite massive effort. We ultimately focussed on hardware and procedures designed to mitigate the effects of potential, but unproven, failure modes. We describe a frequent real-world engineering situation in which one must proceed on the best basis possible in the absence of the complete set of facts.

Introduction

The Advanced CCD Imaging Spectrometer (ACIS) is one of the four primary science instruments on the Chandra (formerly AXAF) X-ray Observatory and one of only two focal plane instruments. A picture of the ACIS instrument is shown in Figure 1. In this view, the X-rays would be imaged through the X-ray mirror, located far above the instrument, and directed downwards through the collimator and into the detector housing, where the CCD imaging chips are located. The ACIS door is shown in the open position in the picture. Due to the presence of a fragile optical blocking filter over the CCD's and the need for extreme cleanliness, the ACIS focal plane must be kept in an evacuated detector housing and launched under vacuum. The blocking filter essentially "blocks" any visible or ultraviolet light from entering ACIS's aperture. Acoustic loading during the launch environment due to presence of air in the detector housing would destroy the delicate filters. The ACIS door seals the detector housing during ground operations leading up to launch. STARSYS™ paraffin (wax) actuators are used as components in a rotary actuator, to open and close the door for ground testing and on-orbit operations.

The ACIS door mechanism, designed and built by Lockheed Martin, was fully qualified and life tested (on an engineering model) and the flight unit had been actuated at least 23 times during component testing and during system assembly and test operations. However, during the final Chandra observatory level thermal/vacuum test at TRW, the door failed to open when commanded to do so. This failure occurred in June of 1998, at a time when the Chandra launch was scheduled for early CY 1999. A similar failure of the door to open on-orbit would eliminate the use of the ACIS instrument and thereby greatly degrade mission science capabilities.

Needless to say, this failure at such a critical time in the Chandra Integration and Test cycle was extremely distressing and generated an immediate, overwhelming and ultimately successful response from a combined team of NASA MSFC, contractor and independent review team personnel.

^{*} Smithsonian Astrophysical Observatory, Cambridge, MA

^{**} Lockheed Martin Space Systems Company, Denver, CO



Figure 1 - ACIS Instrument

ACIS Door Mechanism Design

Design Requirements

The design of the ACIS Detector Assembly was performed by Lockheed Martin Space Systems Company under contract to MIT (contract # SC-A-124624), who in turn was under contract to NASA MSFC for the ACIS Instrument. Design work started in 1994 with a prototype unit built prior to Preliminary Design Review (PDR). A qualification unit was built and tested in early 1995 with the flight build and test starting in early 1996. An Engineering Unit was also built and was delivered to MIT in early 1995. There were many requirements which contributed to the final design of the ACIS Detector Assembly Door Mechanism. The key ACIS door requirements are listed below:

1. Design Life	253 Cycles
2. Operating Temperature Range	-60°C to +45°C (Qualification)
3. Flight Operating Temperature	20°C
4. Survival Temperature Range	-76°C to +45°C
5. Operating/non-operating Pressure	800 TORR to 0 TORR
6. Operating Voltage Range	24 Volts DC to 36 Volts DC
7. Actuator Min. Operating Torque	> 5.1 N-m (45 In-lb)
8. Actuator Min. Stall Torque	> 6.8 N-m (60 In-lb)
9. On-orbit Operation	One open cycle
10. Ground Operation	< 100 Cycles
11. Cleanliness Requirements	Class 100A and meet the Requirements of MSFC-SPEC-1238 and MIL-SPEC-1443
12. Internal Vacuum	Up to one atm Pressure difference Across Door
13. Seal Capability	< 1 Torr leakage per Day

Contamination control was a significant design driver for the door mechanism assembly and forced the use of materials and components that were known to be compatible with these requirements. The requirement for an internal vacuum (in the detector housing) for all ground processing and launch environments, combined with the very low allowable leak rate for such a small instrument volume, demanded a nearly perfect hermetic door seal. An unlubricated Viton O-ring was chosen as the sealing material because of its vacuum compatibility and low outgassing properties. The torque requirements for the door actuator were derived from some early development tests which showed a requirement for at least 2.3 N-m (20 in-lb) of torque capability from the actuator when using a dry Viton O-ring. Actuator trade studies performed early in the PDR design phase resulted in a decision to proceed with a Rotary Paraffin Actuator built by STARSYS Research to drive the door mechanism open and closed. This actuator (Part # HL4570B), based on a design from a previous NASA program, had redundant built-in limit switches and heaters with a positive latch at both extremes of travel. The minimum stall torque capability for this actuator was 6.8 N-m (60 in-lb), which was three times the required torque.

Door Mechanism Actuator and Linkage

The rotary actuator uses two linear paraffin actuators, one for each rotational direction. Upon actuation, heaters inside a cartridge warm the internal paraffin. As the paraffin changes phase at around 70°C its volume increase forces a steel pin outward; this linear travel is converted into rotary motion of the output shaft and coupled ACIS torsion driveshaft. The driveshaft and a folding two-bar linkage rotate the door approximately 92 degrees and out of the field of view upon opening; in the other direction the linkage is driven to a nearly straightened locking position when the door is closed. The linkage contains an adjustable turnbuckle, set to provide a calibrated force against the Viton O-ring. This force, determined through development testing, provides adequate sealing for evacuation of the instrument without additional applied forces. A "swing link" supporting the door hinge axis allows the door to seat fully on the O-ring so that O-ring compression is uniform upon preload and evacuation. An internal shear disk in each actuator prevents excessive pressure inside the actuator from causing a catastrophic failure of the paraffin actuator cartridge & protects the other components in the device from damage. However, a shear disk rupture does render the actuator permanently disabled. Figure 1 shows a picture of the ACIS door mechanism in the open position, with the access cover removed and the STARSYS actuator on the

right side of the photograph. The linear actuators are the cartridges extending from the top and bottom of the rotary actuator case.

Actuator Torque Requirement

The output torque required from the door actuator was almost entirely driven by the expected stiction that could develop in the O-ring door seal. A cross-section of the mechanism is shown in Figure 2 and shows the open and closed door configurations. The two bar linkage applies around 222 N (50 lbf) of force (1.8 N-m or 16 in-lb) output torque from the rotary actuator to the O-ring seal when in the straightened position. This force is required to compress the O-ring sufficiently so that the detector assembly can be evacuated. The mechanism itself consists of the aluminum door, dry Torlon bushings in all rotating joints, titanium/aluminum linkages, the titanium collimator, aluminum seal retainer and the 15-5ph stainless steel linkage driveshaft. The slip-fit Torlon bushings all have redundant moving interfaces which would still allow rotation if one of the surfaces were to bind. Running torque for the mechanism was very low, even in 1G environments, since the door weighs only about 0.11 kgm (0.25 lb). The total running torque for the drive train was only around 0.5 N-m (4.5 in-lb), which was mostly the frictional and spring losses inside the rotary actuator. The frictional losses in the Torlon bushings were minimal. Analysis and testing showed that there was not an issue with clearance changes which could result in any binding of mechanism components, even at the most extreme temperatures within the operational range.

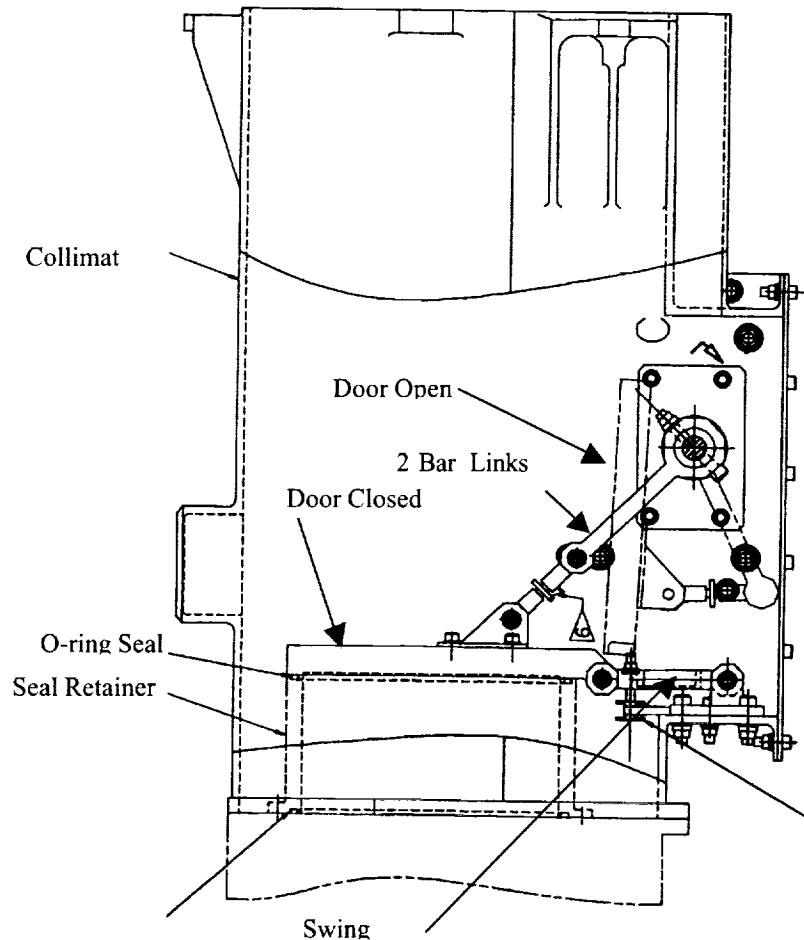


Figure 2 – ACIS Door Mechanism

Design Redundancy

As is the case with most mechanisms or structures, the door mechanism drive train components connecting the rotary actuator to the door (driveshaft, linkages, etc.) were not redundant. Rotation joints in all linkages were single fault tolerant due to the inclusion of floating Torlon bushings. Adding a second rotary actuator would have significantly complicated the mechanism. The paraffin actuators themselves contained dual sealing O-rings and redundant heaters. The rotary actuator also contained redundant limit switches. Return springs inside the rotary actuator were designed to low operating stress levels to avoid redundancy concerns. During the design phase, a single paraffin actuator with redundant heaters was deemed to be adequate for a one-time on-orbit actuation requirement. These actuators had significant flight heritage with extremely high reliability, and required only 28 volt input power to one of the redundant heaters to perform as designed. All of the electronics required to power the actuators were fully redundant and met the single fault tolerance requirement.

Paraffin actuator shear disk rupture from high internal pressure was considered a potential single point failure resulting in loss of mission. During operation, the actuator reaches a temperature considerably above the paraffin melting point. If case temperature becomes too high before heater shutoff, internal pressure is relieved by shear disk rupture. STARSYS research data showed a disk rupture threshold temperature of 154°C; the design team concluded that a shut-off of 135°C left acceptable margin for door operation, based on our development testing. To protect against failure, redundant temperature sensors were installed onto the actuator case and were monitored autonomously by the ACIS Power Supply and Mechanism Controller (PSMC). Power was removed if the actuator ever reached 133-135°C. The subject of shear disk rupture will be discussed in more detail later in the paper.

Pre-Flight Testing

Qualification Testing

Pre-flight testing was performed per NASA procedures to fully qualify the mechanism for flight. These tests included a 253 cycle thermal/vacuum mechanism life test on a special life-test unit (CAMSIM), O-ring stiction tests, acoustic tests, and random vibration tests. There were no significant issues that were not addressed in the final flight design for the door mechanism. One of the minor problems addressed was the burn-out of one of the life-cycle test heater elements. The root cause of this failure was a process change in a Minco heater that led to a delamination of the heater and subsequent burn-out as paraffin worked its way into the heater and fatigued the element. For flight, new heaters were fabricated with the original process and were re-qualified and life-cycle tested. A second problem occurred during the life-cycle test due to 1 G affects and rapid cycling of the mechanism and paraffin actuators. Convection inside the hot wax (only present in 1 G) resulted in a non-uniform re-freezing of the paraffin as it passed through the phase-change temperature. Since the paraffin froze at the bottom of the actuator first, the actuator output pin was prevented from fully retracting. This problem was addressed by procedural changes, a new retraction spring which had a higher spring constant, and an additional limit switch capability which would alert operators if the shaft was not fully retracted after a close cycle. There was a procedure in place, which never had to be used, to re-set the actuator should this problem repeat. These qualification tests showed that the mechanism was ready for flight build with no major design changes.

Flight Unit Testing

The flight unit Detector Assembly door was opened and closed at Lockheed Martin at least 12 times as part of the component level Protolight Test program under various test conditions prior to delivery to MIT. Testing included pre and post environmental exposure performance tests, random vibration tests, and thermal vacuum tests. The flight unit Detector Assembly was delivered to MIT in early 1997 and the flight focal plane and optical blocking filters were installed in April of 1997. The door was cycled open and close 11 more times in system level testing as described below.

An ACIS system level Thermal Vacuum test of all of the flight hardware was conducted at MIT Lincoln Labs. The door was cycled two times as part of the long and short form functional testing of all ACIS

hardware, at hot and cold temperature extremes, with nominal results. At the completion of this test, the integrated ACIS was delivered to MSFC for an additional one month calibration test in the MSFC X-Ray Calibration Facility (XRCF) thermal/vacuum chamber. During X-ray calibration, several additional door operations cycles were performed under flight-like operating conditions with nominal performance. After calibration activities were complete, the unit was vibration tested as part of the final acceptance test by MSFC. Pre and post test mechanism performance, which included door cycling, was nominal, thus adding four more door open/close cycles. The integrated ACIS was then shipped to Ball Aerospace in Boulder for integration onto the Integrated Science Instrument Module (ISIM). The Detector Assembly was kept under vacuum for 5 months until the ISIM was fully integrated. ISIM level thermal/vacuum testing started in October 1997. During these tests the door was opened and closed two more times under flight-like conditions. One additional successful door opening occurred at ambient temperature and pressure in January of 1998. The ISIM was then shipped to TRW for integration onto the Chandra telescope. Periodic pump downs of the ACIS Detector kept the internal pressure between 0 and 10 torr for all of the system integration and test activities (including system Acoustic test).

Related Testing

Another STARSYS HL4570B rotary actuator (same model as for door) was used in the ACIS Large Vent Valve mechanism. A failure of this actuator occurred during the ACIS system thermal vacuum test at MIT Lincoln Labs in April of 1997. This failure was due to an operator error which caused both the open and close actuators to be powered simultaneously. Under this condition, one of the shear disks ruptured and required the removal and replacement of the Large Vent Valve rotary actuator with a flight spare actuator. Corrective action was to follow procedures to prevent simultaneous powering of open and close actuators. The large vent valve was cycled hundreds of times during test and integration and was never an issue before or after this event. However, this failure on the large vent valve pointed to a potential weakness in the actuator design. As discussed earlier, disk rupture will normally occur at a case temperature of about 154°C, and the PSMC will cut-off power when the actuator temperature reaches about 135°C. However, it was discovered that this 154°C rupture temperature was based on a linear actuator in which the output pin is allowed to extend normally to full extension. Therefore, the rotary actuator must operate with stall torques less than 6.8 N-m (60 In-lb) on the rotary output shaft. If the output pin is restrained from extending, then there is no additional volume for the paraffin to expand into and the shear disk will rupture at a much lower temperature if power is not removed promptly. Thus, in the case of a restrained actuator, the temperature sensors do not provide protection from rupture except at end-of-stroke.

As it turns out, instead of a constant temperature shut-off point, each paraffin actuator could be protected by a variable shut-off temperature dependent on the amount of linear extension of its output shaft (transformed into rotary actuator shaft rotation). At zero degrees of rotation for the rotary actuator mechanism, the shut-off temperature should have been around 90°C rising to 150°C at full rotation or end-of-stroke. However, since a normal operation of the door or large vent valve would result in an actuator temperature of 105-110°C, we could not simply lower the shut-off temperature without affecting the ability to operate normally. It was also too late in the program to re-design the electronics to provide a variable shut-off temperature. It was evident, however, that in the case of a bound actuator shaft early in the stroke, we would not achieve our goal of opening the door. This potential new protection would have allowed us to try opening the door many times rather than just once. The decision not to implement this protection was based on our high confidence in our ability to open the door, since we had never observed a stiction torque above 2.3 N-m (20 in-lb) in over 3 years of testing.

To summarize the component and system level testing: the ACIS flight unit door was successfully cycled at least 23 times prior to the opening attempt at TRW under various operating temperatures and pressures. The ACIS team had confidence in the door mechanism performance for system level thermal vacuum test and for flight. There had been no anomaly in any of the previous door opening attempts. In fact, closing the door had always been of greater concern since the door was closed against a frozen (stiff) O-ring several times during these tests. Measured paraffin actuator case temperatures were always

higher when closing against a frozen O-ring but the unit was qualified to perform under these conditions so it was never an issue.

Door Opening Failure in System Thermal/Vacuum Test

Door Opening Failure

The fully integrated Chandra X-ray Observatory was subjected to over one month of thermal/vacuum testing at TRW (Chandra prime contractor). The final test planned for this period was a stray light test, in which the ACIS door would be opened and the ACIS used as a sensor to measure stray light levels within the telescope (lamp banks simulating the sun were installed in the T/V chamber). Test conditions prior to the stray light test were nominal for the telescope, with the ACIS running at cold temperatures as would be normal for observations in flight. Since there had been several past door openings with ACIS cold and a warm-up would have taken extra time, it was decided to open the door in the cold condition. At the time, there was no objection from anyone on this point.

The ACIS door opening procedure was run at 5am PDT on June 18, 1998, but the door did not open. The information available at the time was as follows: 1) Door Open Actuator exceeded its power shut-off temperature at 133°C with autonomous removal of power by the ACIS electronics (PSMC), 2) using X-ray measurements from a door mounted calibration source, it was determined that little to no motion of the door had occurred, 3) STARSYS actuator limit switch operation indicated less than 20 degrees of rotation had occurred, 4) ice had been observed on external surfaces of Observatory, indicating the presence of at least some water in the T/V chamber, 5) the ACIS door and camera body were at -60°C, and 6) the STARSYS Actuator was at -42°C at the start of the procedure.

Post-test Failure Recovery and Analysis

Initially Suspected Failure Modes

As is usual in such cases, a small "tiger" team was formed to determine an immediate course of action. Even at this early stage, the team believed there was a high probability that the ACIS would have to be removed from the Observatory. A full stall of the mechanism with no door movement would more than likely have ruptured the shear disk inside the Paraffin Actuator based on experience with the Large Vent Valve Mechanism. A fault tree was created to help determine possible causes of the anomaly. The final form of the fault tree is shown in Figure 3. The first three items were considered at the outset of the failure investigation.

Ideally, the team would have liked to see the unit left undisturbed to prevent the loss of information that could ultimately lead to determination of the failure mode. However, the MIT and Lockheed Martin team concluded that there was too great a risk of damage to the focal plane and OBF's from contamination if the door were not fully closed prior to re-pressurization of the chamber. The door provides a nearly hermetic seal that would protect the focal plane and OBF's from contamination as the shrouds and spacecraft were warmed up and the chamber re-pressurized.

Recovery from Failure in Thermal/Vacuum Test

The decision was made to warm the detector assembly and door to 25°C using heaters that were designed for baking off contamination on-orbit. To protect the instrument and get the door closed, the open actuator had to be heated to soften the paraffin. With a warm open actuator, there was a higher probability that the close actuator could re-set the mechanism and latch the door closed again. The procedure was performed at 7pm PDT without success. Neither the open nor the close limit switches changed state, and the close actuator went over-temperature at 133°C as the PSMC autonomously removed power. A nominal opening or closing would normally result in an actuator temperature of around 105°C at limit switch shutoff. Now the question was whether or not the door was sufficiently sealed to allow for chamber re-pressurization. As dry nitrogen was bled into the chamber, the differential pressure transducers on the detector assembly quickly confirmed that the door was sealed, since a vacuum was measured within the detector housing. The focal plane and OBF were in a safe condition, since one

atmosphere of pressure differential provides about 500 pounds of closing force on the door. Therefore once the door sealed, a positive latch was not necessary and the instrument could be handled safely without the fear of damage to the focal plane and OBFs.

During the next several days Chandra was removed from the chamber, the ISIM was removed from the optical bench and partially disassembled, then the ACIS was removed for shipment back to Lockheed Martin. Initial external inspections at TRW looked normal except that the door did appear to have metal to metal contact with the seal retainer. This metal-to-metal contact could support the cold welding hypothesis but later inspections and testing would discount this failure mode. The ACIS detector was then shipped back to Lockheed Martin where inspections and disassembly could occur in a class 100 clean room.

- A. Door/Seal Retainer Bound
 - Cold weld
 - Ice
 - Seal Adhesion
 - Electrostatic
 - Diffusion
 - Van DerWaals
 - Chemical Bonding
- B. Rotary Actuator Bound
 - Parts Bound
 - Mismatched parts
 - Contamination
- C. Paraffin Actuator Bound or Failed
 - Heater failed
 - Wax leak
 - Start low temp
 - Low lube
- D. Rotary Actuator Shear Disk Previously Ruptured
- E. Test Procedure not followed
- F. Retarding Torque > 6.8 Nm (60 in-lbs.)
 - Over-center
 - Seal Separation
- G. Linkages Bound
 - CTE Mismatch
 - Bushing/Linkage bending
 - Ice
 - Contamination

Figure 3 - ACIS Door Failure Fault Tree

Initial Inspections at Lockheed Martin

Failure investigation efforts centered around closing branches of the fault tree shown in Figure 3. Initial inspections of the door mechanism at Lockheed Martin did not reveal the cause of the failure. All linkages appeared to be free and the two bar link was slightly over-center, which explained why the door was able to seal. It appeared that the door was metal to metal with the seal retainer, but until the detector was re-pressurized, we would not know if the door and seal were bound to one another. Since there was still a vacuum inside the detector, as measured with the Vacuum Ground Support Equipment (VGSE), we elected to remove the STARSYS actuator prior to detector housing re-pressurization, so that it could be inspected independently of the rest of the mechanism.

Door Seal/Retainer Bound (Fault tree Item A)

Since cold welding of the gold plated door to the aluminum seal retainer was a possible failure mode, extreme care was taken as the detector assembly was re-pressurized. Dial indicators were mounted

above the door to measure movement of the door as dry nitrogen was allowed back into the camera body. The door slowly rose off the seal retainer as the internal pressure was equalized to the ambient pressure in the clean room. The O-ring was still compliant and relaxed as the external pressure was removed from the door. Cold welding and/or galling was then ruled out since the O-ring had enough spring force to push the door away from the seal retainer and close inspection revealed no signs of cold welding. This also would have been the case when the TRW thermal vacuum chamber was initially evacuated since the pressure differential across the door would have been reduced in a similar manner.

With the differential pressure equalized, the door could be opened and running torque and seal adhesion could be measured. Using a torque wrench to drive the door open, the seal adhesion plus running torque was measured to be 2.6 N-m (23 in-lb) which was near the expected value. Seal adhesions had never been measured above 2.3 N-m (20 in-lb) and with a running torque of around 0.5 Nm (4 in-lbs), the seal adhesion was 2.2 N-m (19 in-lb). The full capability of the STARSYS actuator as measured in subsequent testing, was around 10.2 N-m (90 in-lb) which gave a factor of safety of over 4 above what was measured. With running torque within normal specifications, no problems were found with the mechanism. Further disassembly and inspections showed all dimensions for bushings and other components to be within specifications at room temperature. No binding or interference was found which could have contributed to the failure. Additional testing on the Torlon® bushings showed that the coefficient of thermal expansion was as expected and that analytically there were no concerns with the mechanism binding at low temperatures.

The over-center torque on the door mechanism was also found to be within specifications at about 1.9 N-m (17 in-lb). Since this flight mechanism was set up in an over-center condition, due to normal rotational and machining tolerances, there was concern that if the over-center torque was too high then it could have combined with another failure mode to result in excessive retarding torque. This was shown not to be the case with testing on other engineering units even for an incompressible O-ring. Conservatively, the flight unit was re-assembled with the mechanism adjusted in a slightly under-center condition by building a new adapter bracket.

STARSYS Actuator Inspection and Test(Fault tree Items B and C)

Failure of the STARSYS rotary actuator was one of the failure modes identified on the fault tree. X-ray inspection of the unit did not show any anomaly. As was expected, the open actuator shear disk had ruptured due to excessive pressures inside the actuator. The open actuator output shaft was slightly extended which explained why the latch and limit switches were not engaged. Some drive shaft rotation was also observed in the X-rays of the actuator. There was no evidence of any foreign material or debris that could have jammed the mechanism. The open actuator cartridge was then removed from the actuator assembly. As the actuator was removed, the latches and limit switches fell into place. The slightly extended output shaft, which was frozen in the paraffin, had prevented the actuator from re-setting completely. The shear disk looked like a normally ruptured disk with no signs of any material weakness. Material properties were measured for the shear disk and were as expected. There were no signs of wax leakage and internal inspections of the wax cartridge were nominal. Force measurements were made to determine the running torque for the rotary mechanism and were nominal at both room temperature and at -45°C.

Prior to total disassembly, the close actuator cartridge was removed and installed onto the open actuator side of the rotary mechanism assembly. At STARSYS, the unit was tested to failure with a full stall to characterize the performance of the actuator and shear disk under these conditions. This full stall test, performed at -45°C, simulated the condition where the door mechanism did not rotate and all bushings and linkages were frozen solid. The temperature profiles were similar to those which were measured at the time of the failure up until the actuator reached a temperature of around 129°C, at which time the shear disk ruptured. This is slightly lower than the estimated failure temperature of 132°C at TRW, but would be expected with this more severe test condition. The door mechanism linkages and torsion shaft would have allowed more rotation of the rotary actuator and thus a higher temperature at shear disk rupture. It is interesting to note that both shear disks were nearly protected since the PSMC shut-off temperature was set at 133-135°C. The peak torque at shear disk function was 10.4 N-m (92 in-lb) vs.

the 6.8 N-m (60 in-lbf) specification. Material testing showed that both the open and close shear disks were similar in thickness and shear properties, so it is likely that the STARSYS rotary actuator output was around 10.2 N-m (90 in-lb) at the time of the failure at TRW. Complete disassembly and inspection of the mechanism and actuators did not reveal a problem. Nothing was obstructing the mechanism and the only discrepancy was the ruptured shear disk. This closed out numerous branches on the fault tree since everything appeared and functioned nominally.

The shear disk rupture point varies linearly depending on the amount of extension of the actuator linear output shaft, which can be anywhere from 0 to 19 mm. At 0 mm of linear extension, test data showed the actuator would reach an equivalent pressure to achieve 6.8 N-m (60 in-lb) on the output shaft at around 90°C. The rupture temperature would be higher at an equivalent output torque of 10.2 N-m (90 in-lb). For an extension of 19 mm, the shear disk would rupture at an estimated 154°C. Subsequent discussions will show that we believe the flight unit shear disk ruptured at around 132°C which also supports the evidence that the door mechanism had rotated 20-25 degrees (5.7 mm of linear extention) at the time of failure and was not locked up. The clearances in the bushings and the windup in the mechanism components could allow the actuator linear output pin to extend as much as 5.7 mm even with a stuck door.

NASA/Industry Team Formation and Failure Investigation Approach

Failure Investigation Team

Door mechanism failure diagnostics were initiated by the small team of Lockheed Martin, NASA MSFC and STARSYS personnel as discussed above. Their goal was to determine the cause of the failure, fix the problem, and then return the ACIS detector to flight configuration so that it could be reinstalled on Chandra and still meet the (then projected) January 1999 launch schedule. This team was initially given two weeks to complete these activities, based on the (optimistic) assumption that the failure mechanism would be easily identified and rectified. As it eventually became clear that the failure was not going to be quickly resolved, NASA MSFC formed a larger ACIS Door "Tiger" team which included members from NASA MSFC, the Chandra external review committee, MIT, Lockheed Martin, STARSYS, TRW and SAO. The team's function was to oversee and facilitate the ongoing ACIS door failure investigation and the decision making process. In the end, the team was to operate for almost one year, as circumstances dictated, with weekly telecons and meetings as necessary.

The situation at the time the larger team was formed, in early July 1998, was not a promising one. As described above, initial work by the smaller team had ruled out many of the proposed failure mechanisms. Also, program schedule pressure was large, even though the launch date had been slipped to mid-summer 1999 due to other factors. The team, along with senior NASA and program management, decided to pursue parallel paths of off-line failure investigation along with the re-build and re-test of the ACIS detector and then re-integration with the Chandra Observatory. It was believed that the re-test effort would also supply valuable data to the failure investigation team. As a further backup possibility, NASA-MSFC even developed an alternate actuator that could have been substituted into ACIS should subsequent problems with the above paths occur downstream closer to launch.

With more resources available now, many activities could proceed in parallel, even though the primary activity remained at Lockheed Martin. These activities included the expansion of the fault tree to include items not initially considered, investigation into the issue of ice formation, more detailed investigations into the stiction properties of Viton, a search of the prior test data to look for a possible inadvertant powering of the door actuator, development of a detailed finite element model of the door mechanism to provide additional design verification and, of course, the re-build of the flight ACIS detector for a re-test at TRW in August of 1998.

ACIS Detector Rebuild and Re-Test

In the rebuild of the ACIS detector, much attention was given to possible ways to gain information on performance of the door actuator. Instrumentation to monitor door mechanism performance was added prior to the re-test which started in August, 1998. This instrumentation included non-flight strain gages to

measure actuator output torque, a potentiometer on the torsion shaft (flight) and an additional temperature sensor to be used for "pulsed heating" of the paraffin actuator. This pulsed heating technique, in conjunction with potentiometer readings, would prevent the heating of the paraffin actuator to shear disk function. Finally, a rapid warm-up and cool-down procedure was developed and demonstrated to reduce O-ring stiction (one of the possible causes of the failure) in case the pulsed heating technique did not initially open the door.

The re-test of the ACIS door mechanism (August/September 1998) was intended to re-qualify the door mechanism under flight conditions. It was decided to re-test the ACIS door as mounted to the ISIM only, not the entire observatory. This would greatly simplify the testing and also allow work on the observatory to proceed in parallel with ACIS/ISIM re-test. A key decision of the failure investigation team and program management was that the test would take place with the detector housing warm, as was planned for the on-orbit opening. This would eliminate any issues of ice during the re-test. At the same time, since water was an issue in itself due to possible VanDerWaals forces, water was to be injected into the thermal/vacuum chamber to simulate the outgassing of the complete observatory's composite materials. Some team members would have preferred to duplicate all test conditions at the time of failure (including detector temperature), but there was concern that another failure, even under non-flight conditions, would jeopardize program schedule.

The re-built ACIS detector was shipped back from Lockheed Martin to TRW in early August 1998, and was then integrated onto the ISIM. The ISIM with both Chandra focal plane science instruments (ACIS and HRC) was then moved into the TRW thermal vacuum chamber. The subsequent test then simulated as closely as possible the projected on-orbit door opening scenario. The predicted temperature profile was closely followed. The ACIS detector housing was kept cold until about 14 days into the test, at which time the door was opened. Prior to door opening, the detector housing temperature was raised to 25°C using the ACIS bake-out heaters.

The door was opened (and then closed) a total of five times during the ISIM re-test, all using the pulsed heating technique. The first three openings were done with a bus voltage of 28 volts and the last two at 32 volts. The door angle potentiometer and driveshaft strain gages were monitored during these openings. All of the data from these openings was nominal. This successful re-qualification of the ACIS door mechanism allowed the program to proceed towards launch, but the fact that the cause of the earlier failure was still not known was troubling to everyone. The ACIS failure investigation team would work for many more months, still attempting to discover the root cause of the earlier failure.

It should also be noted that there were additional door openings in an ambient condition scheduled and executed to gain confidence in the door opening mechanism prior to launch. This was accomplished through the use of the VGSE to re-pressurize the ACIS detector housing cavity with nitrogen to equalize the pressure prior to opening. This was not originally planned due to the risk of contamination entering the cavity, but a more detailed look at showed that the risk was small enough to be acceptable given the circumstances.

Ongoing Failure Investigations

The expanded ACIS door fault tree is shown in Figure 3. This tree evolved over the course of the investigation and guided our efforts to identify the failure mechanism. As mentioned above, some of the branches of the tree were addressed by early post-failure inspections and tests.

Pre-ruptured Shear Disk (Fault tree Item D)

One possible failure mechanism which had not yet been ruled out, was an accidental activation of the open actuator under ambient pressure conditions prior to the TRW test. This would have taken place after the last opening at Ball (January 98) and before the opening attempt during Observatory Thermal/Vacuum testing. With a vacuum inside the detector, the shear disk would have ruptured if the open actuator were powered when the observatory was in an ambient environment, since the mechanism does not have enough torque margin to overcome one atmosphere of pressure against the door. Chandra flight telemetry was monitored anytime that Chandra or the ISIM were powered up. An investigation of the available telemetry data showed no time at which the actuator temperature had

exceeded ambient. However, a potential failure mode was discovered when it was determined that when the spacecraft voltage was ramped up slowly, the ACIS mechanism controller could power up without receiving a command to do so. The team was able to duplicate this condition on the ACIS test hardware and was able to show that the mechanism could have been powered up inadvertently. However, the temperature profile and limit switch actuation measured at TRW during the door open failure did not match the characteristics that would be obtained for a pre-ruptured shear disk. This conclusion is based on extensive testing with non-flight hardware and also the actual flight actuator used in the failed opening attempt.

Ice on Mechanism (Items A and G of Fault Tree)

Icing of the mechanism was thought to be a promising failure mode since the failure occurred when the door was opened cold and frost was seen on the Observatory optical bench prior to the opening failure. However, analysis showed that ice could not have caused the problem with the door mechanism. At the time of the failure, several different pressure monitors inside the chamber showed the pressure to be in the 10^{-6} Torr range. At this temperature (-60°C) and pressure, the sublimation rate for water/ice is greater than the collection rate and it was unlikely that enough ice could exist on surfaces at -60°C to cause a problem. Colder surfaces at, -90°C or less, did have visible ice because the collection rate was higher than the sublimation rate. Some water/ice was probably present on mechanism components since there were increases in pressure when the heater was turned on to warm the housing to +25°C. However, the thickness of water/ice would have been angstroms and not the millimeters which would have been required to block the mechanism. A pressure increase was also observed with the on-board Chandra vacuum monitor when the heater was turned on. However, even small amounts of water/ice could result in increased pressure at vacuum levels of 10^{-5} to 10^{-6} Torr. The local pressure around the mechanism would have had to been an unlikely 10^{-3} Torr in order for enough ice to collect to cause a problem. Analytically, this was shown to be non-credible.

To further investigate the water/ice failure mode, an engineering unit door mechanism was purposefully iced up by cooling it with liquid nitrogen in ambient pressure. The mechanism and STARSYS actuator were covered with ice from relative humidity condensation and the running torque increase was barely measurable. Other tests and studies were performed and discounted icing as a failure mechanism.

O-ring Adhesion Mechanisms

During the course of this investigation various O-ring adhesion mechanisms have been proposed as possible causes for the failure. Although none have been shown conclusively to occur under the failure conditions of the flight hardware, several remained viable possibilities. This is especially true if two or more adhesion mechanisms acted together synergistically. All possibilities focused on the properties of Viton adhering to the gold surface of the door seal under various conditions. Although this failure mode is believed to be the most probable failure mode, no test or analysis could prove that enough adhesion could have existed at TRW to prevent the door from opening. Lockheed Martin conducted many tests with engineering hardware that duplicated the environmental conditions, but not during the 7-month period that existed before and during the failure. The team was unable to reproduce, under any simulated circumstance, the failure.

Plans for Flight Opening

An immense effort was expended to identify the failure mechanism prior to launch, but despite the best efforts of many able people, we were not able to clearly identify the failure mechanism. In fact, it sometimes seemed as if the failure could not have occurred, but it had. As time went on and we approached the launch date without an identified cause, the team's (and program management's) approach was eliminate or "mitigate" all possible failure modes. The decision to open the door warm, which had always been the plan, would eliminate any potential issues with icing, however unlikely.

Since O-ring stiction seemed to be the most likely failure mechanism, even though it could not be proven, plans were developed to deal with it in the flight situation. First of all, it appeared that the stiction level

would build over time, starting out at a low value when the door was initially closed and reaching an asymptote at some later time. To minimize the potential stiction build-up, it was decided to open the flight door as late as possible in the integration process.

Another stiction mitigation technique was developed by Lockheed Martin in their testing using engineering models of the door mechanism. It was determined that thermal cycling of the detector housing would lower stiction levels. Mitigation testing on the CAMSIM test unit showed that a rapid temperature cycle to 25°C would virtually eliminate any O-ring adhesion which was present prior to the cycle. Two tests were preformed after a room temperature dwell with 1 atmosphere of pressure on the door for 21 and 172 hours. Using a prediction based on previous o-ring adhesion testing, one would predict seal adhesion of 0.6 and 1.2 N-m (5.8 and 10.5 in-lb) of adhesion respectively. After the mitigation thermal cycle described above was performed, only 0.1 N-m (0.7 in-lb) of adhesion were measured in both cases.

In preparation for flight, the Chandra Flight Operations Team (FOT) developed a procedure which was essentially identical to the multiple heating cycle ground procedure and modified the telemetry decommutation software and display pages to utilize the new information available on the door mechanism. A full end-to-end test of the new door procedure was executed on September 27, 1998 from the Chandra Operations Control Center in Cambridge, MA, controlling the Observatory at TRW. The ISIM was installed on the Observatory, which was in ambient conditions. The flight procedure utilized a library of command sequences which contained the actuator heater on command, a fixed time delay, and the actuator heater off command. These sequences were built with time delays of 50 s to 200 s in 5 s intervals and additionally 250 s and 300 s intervals. The operator could then select the command sequence with an appropriate time interval based on the starting temperature of the actuator, the spacecraft bus voltage, and the results of the previous heating cycle. On September 27, 1998 the door opened nominally in five heating cycles. The heating cycles used were of 70, 85, 100, 110, and 250 sec. and reached maximum actuator temperatures of 61.2, 68.9, 74.1, 76.6, and 99.9°C. The spacecraft bus voltage was 31.5 V and the input voltage at the PSMC was 30.9 V.

The final pre-flight door opening took place on May 10, 1999, before Chandra was integrated with the orbiter Columbia. The opening went smoothly, after equalizing the pressure with the VGSE, with all data perfectly nominal. The instrument was commanded from the ACIS EGSE at KSC. The Observatory was in ambient conditions in the Vertical Assembly Building. The door was opened with 4 heating cycles of 90, 100, 110, and 180 sec durations and the actuator reached maximum temperatures of 63, 68, 72, and 100 C. The spacecraft bus voltage was 30 V.

On-Orbit Door Opening

The Chandra X-ray Observatory was launched from KSC on July 23, 1999 in the orbiter Columbia. On August 8, 1999 the ACIS door was opened as planned, 16 days after launch. The door opening sequence is shown in Figure 4. The same procedure was used to open the door in flight as had been used on the ground test at TRW. The only difference was the timing of the individual heating pulses. The door was opened with 5 heating cycles of 90, 110, 125, 140 and 200 sec and the actuator reached a maximum temperature of 56.1, 68.9, 79.2, 87.0, and 110.3°C. The spacecraft bus voltage was 31.0 V and the input voltage at the PSMC was 30.4 V. Actuator temperature, door angles and limit switch transitions were all as expected and are shown in the figure. The Chandra X-ray Observatory was now ready for planned calibration observations and scientific studies. The stiction mitigation technique had not been required.

Lessons Learned

If there is one lesson to be learned, it is to always "test as you plan to fly" and not push the limits of a mechanism to facilitate schedule, logistics or to reduce other potential impacts to the test program. On-orbit, it was always planned to open the door with the camera body and O-ring at 25 °C. During testing, if

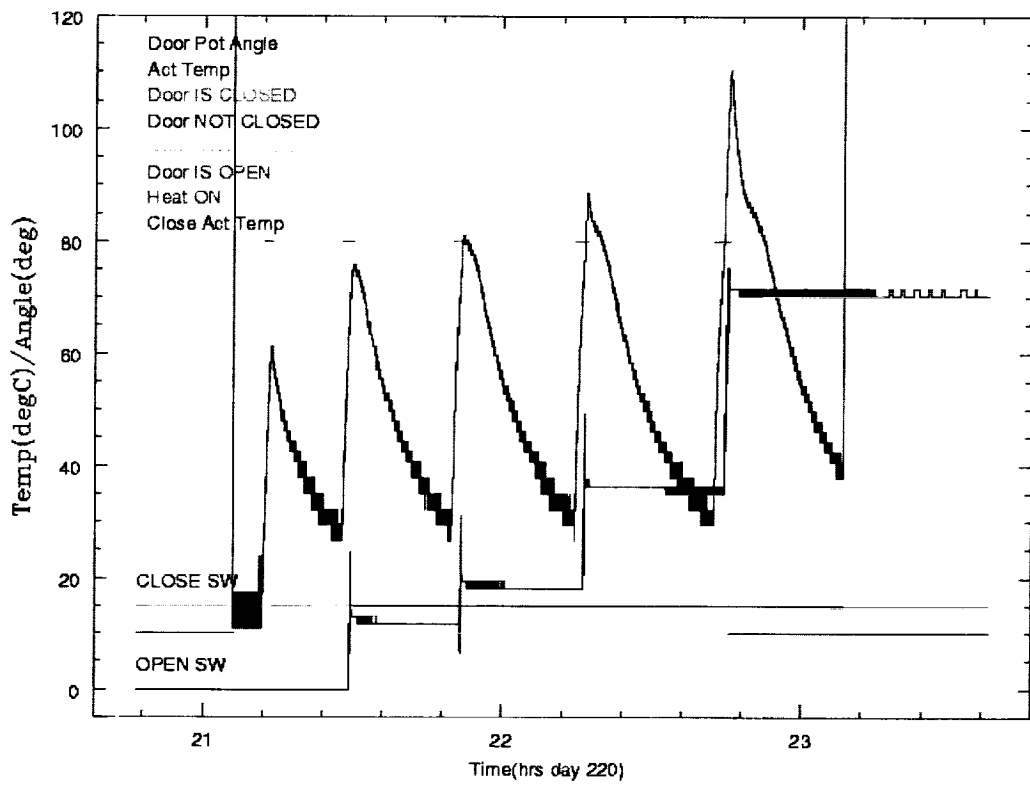


Figure 4 – On-Orbit ACIS Door Opening

we had operated the door mechanism as planned, the door may have opened and we would not have had to deal with the long and involved failure investigation. If it had failed during test, the fault tree would have been much simpler since we would not have to deal with issues related to cold operation. One positive contribution, however, was the development of a much safer, more reliable operational procedure that ultimately would contribute to a successful door opening on-orbit.

Another lesson is that either the mechanism design or operational procedure should allow for a prolonged stall condition to occur, due to possible binding or stiction, without mechanism component failure. In the ACIS door application, due to the late occurrence of the failure, the program successfully adopted an operational technique to preclude a failure due to a stalled condition, and also developed a technique to remove the cause of the stall.

The results of the ACIS door failure investigation ultimately were inconclusive and thus very frustrating. The specific cause of the test failure was never positively identified, although several potential causes were left open as possible. As it became clear that the specific cause might not be identified, much effort was put into "mitigation procedures". These procedures were developed to "mitigate", or to reduce the effect of, possible failure mechanisms such as O-ring stiction. These procedures were extensively tested on ACIS door engineering models, and later on the flight unit itself.

Acknowledgements

The work at SAO was supported by NASA Chandra contract NAS8-39073. The work at Lockheed Martin was performed under MIT contract SC-A-124624

Designing Spacecraft Mechanisms for Sand, Dust, Water and Frost

Kurt Lankford*

Abstract

This paper discusses the design trades and lessons learned in the development of a mechanisms package for the Mars Environmental Compatibility Assessment (MECA) Wet Chemistry Laboratory (WCL), an experiment on the Mars 2001 Surveyor Lander. The WCL performs in-situ wet chemistry experiments on samples of Martian soil. Designing mechanisms to handle Martian soil along with water and frost posed challenges that are somewhat unique and foreign to the spacecraft mechanisms industry. Lessons learned in the development, manufacturing and testing of the various components including the water storage vessel, soil and reagent delivery mechanisms, stirring mechanism, seals, actuators, clearances, and packaging of these mechanisms are discussed.

Introduction

In recent years, NASA has re-emphasized the exploration of our solar system. This has led to an ambitious series of exploratory missions to the surface of Mars. The desire to initially use unmanned lander probes to investigate the planet has placed unique new requirements on the designers of spacecraft hardware. The mechanisms designed for these missions must operate remotely in a poorly defined environment that includes grit and dust, a low-pressure carbon dioxide atmosphere, relatively cold ambient temperatures, reduced gravity, and in the case of the subject mechanism, water and Martian soil. This paper describes some of the issues, trade-offs, pitfalls and lessons learned over the course of a faster, better, cheaper program to design and manufacture a multifunction flight mechanism for these conditions.

Specific design challenges included measuring and delivering a relatively unknown but presumably dusty, gritty sample of Martian soil through a sealed interface. Another significant challenge involved storing water through a nine-month cruise to Mars, then dispensing it to a different container and keeping the entire apparatus sealed from the low-pressure Mars surface environment. How does one design and test a precision spacecraft mechanism for operation in dust, grit water and frost? How does one maintain effective seals under these conditions? What steps are required to perform an experiment using water on the surface of Mars. These types of design questions are relatively unknown to the space mechanisms industry and presented significant challenges to the designers of these mechanisms.

The MECA Wet Chemistry Laboratory

The 2001 Mars Surveyor Lander includes a multi-faceted instrument called MECA (Mars Environmental Compatibility Assessment). MECA is a suite of experiments that are designed to assess the composition, reactivity, and physical characteristics of Martian soil. The purpose is to assess the hazards faced by manned and unmanned mission equipment in the Martian environment. One of the MECA experiments is a Wet Chemistry Laboratory. The Wet Chemistry Laboratory is designed to measure and quantify the composition of Martian soil and assess the interactions between water and the Martian environment through simple, water-based chemistry. This type of evaluation allows for direct comparison with results from terrestrial-based soil samples. The specific function of the Wet Chemistry Laboratory then is to perform an in-situ "benchtop" wet chemistry soil experiment on Mars. The mechanisms that provide sample delivery, water transport and delivery, reagent delivery, and stirring for the MECA Wet Chemistry Laboratory are the subject of this paper.

* Starsys Research Corporation, Boulder, CO

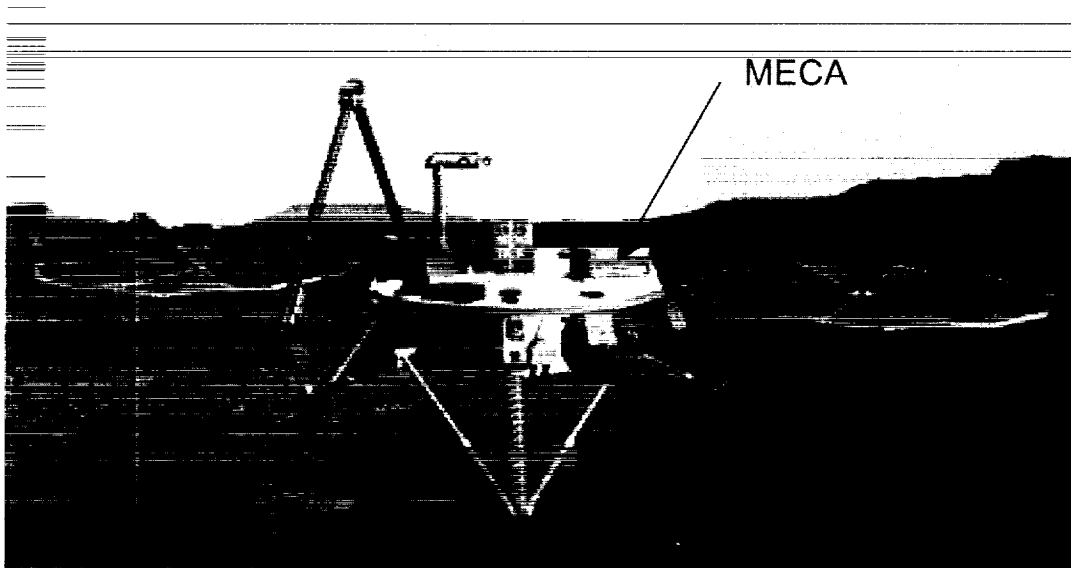


Figure 1 – Mars 2001 Lander

Figure 1 is an artist's rendition of the Mars 2001 Lander showing the location of the MECA experiment enclosure on the Lander deck. The MECA Wet Chemistry Laboratory consists of four identical (redundant) experiment cells. Figure 2 shows a photograph and schematic view of one of the four cells. In the bottom portion of each cell is a "beaker" where the experiment measurements take place. In the upper portion of the cell are the sample handling and delivery mechanisms (the subject of this paper). Four flight units, a qualification unit, and a field demonstration unit were designed, manufactured, tested and delivered to NASA JPL over the course of an 18-month program that was completed July 1999.

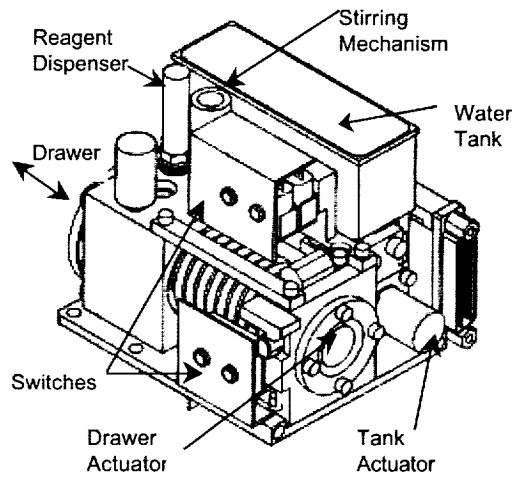
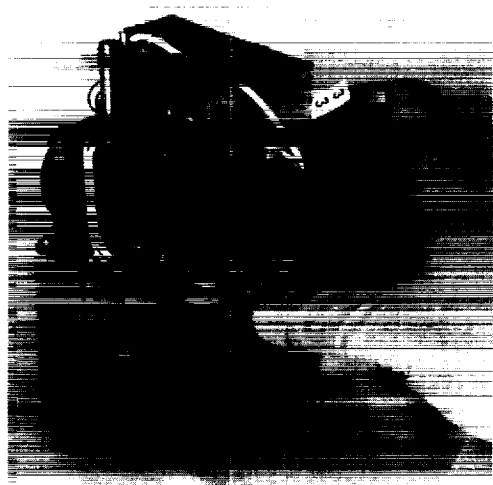


Figure 2 – MECA Wet Chemistry Laboratory

The MECA Wet Chemistry Laboratory mechanisms perform the following functions:

1. Soil Sample Measurement and Delivery
2. Water Storage and Delivery
3. Reagent Delivery
4. Stirring

Soil Delivery

The soil delivery system has the following requirements:

- Accept a scoop of Martian soil from the Lander robot arm.
- Measure a 1 ± 0.1 cc soil sample.
- Deliver the soil sample to the experiment beaker.
- Provide a means for indicating successful acceptance and delivery of the soil sample.
- Allow for up to 16 degrees of tilt in any direction.
- Work within the envelope and mass constraints of the system.
- Maintain system sealing requirements for leakage of less than 1 cc total water loss throughout cruise and less than 0.1 cc/day water loss throughout the experiment.
- Survive launch, cruise and landing environments.
- Operate in the presence of frost.

A cross-section of the final design is shown in Figure 3.

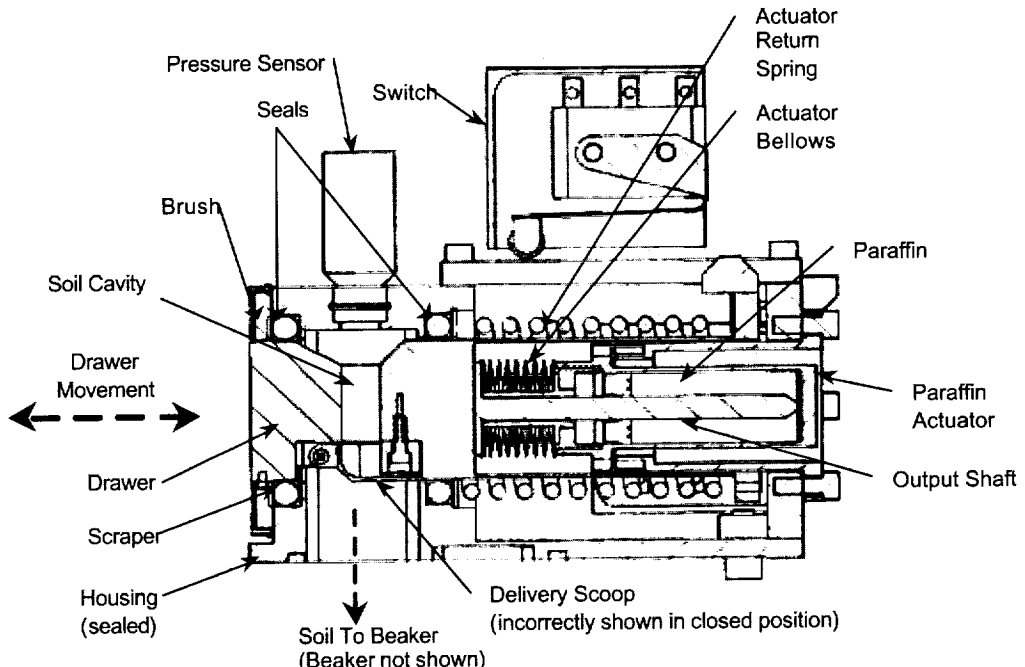


Figure 3 - Soil Delivery System

The system consists of the following components:

- Sample Delivery Drawer
- Paraffin Actuator
- Return Spring
- Brush
- Scraper
- O-ring Seals
- Extension Limit Switch
- Extension Telemetry Switch
- Retraction Telemetry Switch

The paraffin actuator provides linear stroke to shuttle a cylindrical sample drawer horizontally through a dual seal interface. Paraffin actuators are well suited to this task because they provide a slow, controlled yet powerful stroke in a relatively compact package. A resistance film heater on the outside of the actuator heats the paraffin to the melting point (70 °C). When paraffin melts, it expands approximately 15%. This expansion is used to drive the output shaft. The actuator is hermetically sealed with a welded bellows.

The drawer has a square cavity for the soil that is open at the top and has a spring-loaded trap door or scoop on the bottom. The cavity volume is 1 cc. The paraffin actuator pushes the drawer approximately 1.9 cm (0.75 inch) through the seal interface. Once extended, the Lander robot arm dumps a scoop of soil through a sieve (not shown) into the drawer cavity. During this process, a limit switch cycles the actuator to keep it in the extended position. Once complete, power to the actuator is discontinued and a return spring pulls the drawer back through the seal interface. Excess soil is removed with a brush and scraper as the drawer retracts through the seal. The spring-loaded trap door opens as the drawer retracts through the seal, dumping the soil into the beaker.

Design trades investigated a variety of drawer and seal configurations including square and round crosssection drawers, loose and tight tolerance seals, static verses dynamic type seals, compliant verses more rigid seal materials, and various seal configurations and styles. In addition, various methods were investigated to remove dust and grit particles from the sealing surfaces including brushes, scrapers and flushing.

Over the course of the program several prototype drawers were manufactured and numerous tests were conducted. Testing was done using a variety of different types of soil, sand, gravel and other materials. Official Mars simulant soil (volcanic material obtained from Hawaii that is meant to simulate Martian soil as closely as possible) was used for most tests. Sand and gravel, sieved to various particle sizes up to 4 mm, was also used. Coffee grounds and flour were tried to see what effect particle conglomeration had on the performance of the drawer. The greatest difficulty was encountered with hard crystalline materials of large particle size. These particles tended to get caught in the clearances of the seal interface jamming the drawer as it was being retracted. Early versions also had difficulty with the scoop or trap door arrangement getting caught and failing to swivel (again due to crystalline particles getting caught in the clearances). Improvements were made to the original prototype and an alternate design was manufactured and tested. The final design successfully overcame the difficulties with jamming and was able to work consistently with particle sizes up to 2 mm. For sand particles larger than 2 mm, the final design also showed the ability to recover from a jam (in most cases) by repeating the extension and retraction cycle.

Frost turned out to be less of a problem. Frost could be formed on the inside of the mechanism from condensation of the water present in the beaker. Tests with a moderate layer of frost (perhaps 1/2 mm thick) both inside and outside the mechanism showed it was easily scraped away by the force of the paraffin actuator as the drawer extended. The drawer showed no tendency to jam or freeze up on the retraction cycle. This was encouraging. However, estimating the amount of frost build up was difficult and it was not possible to rule out a much thicker layer than what was tested. It was assumed that at some point, a thicker layer would cause the drawer to jam. To eliminate the problem, a Kapton film heater was added to the outside of the drawer housing. The heater is turned on for a short period of time before the drawer is to be extended thus melting most if not all the frost on the drawer.

Initially, it was thought that the seal requirement for loss of no more than 0.1 cc/day from the system would not be difficult to achieve. Felt and labyrinth seals were seriously considered for this task. This requirement, however, turned out to be much more difficult than originally thought. Operation in a low-pressure environment meant that a positive pressure would have to be maintained between the experiment beaker and the outside environment. With a pressure difference, leakage occurs quickly through gaps or holes of any size. Several varieties of spring or elastomer energized polymer seals were tried with marginal success. The varieties that did work had too much friction to allow the drawer to

function properly. The seals with lighter springs did not have enough compliance to prevent leakage on a surface that had been scratched by particles of grit or soil. A standard o-ring seal also had too much friction to allow the drawer to function properly.

To complicate matters, changes during the course of the program placed much more stringent requirements on the seals. First, it was discovered that the ion-specific electrode sensors in the wall of the beaker are sensitive to drying out. It is therefore desirable to hold some nominal amount of water in the beaker throughout cruise to keep the sensors moist. In addition it was discovered that the sensors are sensitive to rapid changes in pressure. This meant the experiment chamber should depressurize somewhat gradually, if possible, rather than abruptly "popping" open.

The best solution turned out to be an o-ring-type seal with significantly reduced squeeze. O-rings provide enough compliance to seal around micro-scratches and particles. The light squeeze reduced friction allowing the drawer to retract with the force of the existing spring. In addition, a unique combination scraper and floating washer was used to increase compression on the o-ring and therefore provide additional squeeze at the very end of stroke. Protrusions on the outside diameter of the drawer catch the scraper/washer pulling it inward and compressing the o-ring seal in the axial direction as the drawer finishes its return stroke. Because of the resilience of the elastomer material, some of the axial compression is converted into radial compression, which improves the seal. This arrangement proved to be effective enough to meet the cruise sealing requirement. Long term testing over the course of several weeks showed an extrapolated total leak of less than 0.4 cc of water over the 9-10 month cruise. The seals were also effective after repeated soil delivery cycles using various grades of sand and simulated Martian soil.

Water Storage and Delivery

The Water Storage and Delivery System has the following requirements:

- Transport 32 cc's of water solution from Earth to the surface of Mars.
- Once on the surface, deliver the water solution to the experiment beaker.
- Maintain system sealing requirements for leakage of less than 1 cc total water loss throughout cruise and less than 0.1 cc/day water loss throughout the experiment.
- Operate in the presence of frost.
- Allow for up to 16 degrees of tilt in any direction.
- Work within the envelope and mass constraints of the system.

The Water Delivery System (Figure 4) consists of the following components:

- Water Tank
- Tank Seal Puncture Actuator
- Tank Seal Puncture Needle
- Tank Switch
- Tank Heaters
- Tank RTD

The water tank is a hermetically sealed welded titanium container. The shape of the container is dictated by the desire to dispense the water into the beaker using gravity and by the confines of the available space. At the start of the experiment the water in the tank is frozen. Heaters bonded to the walls of the tank supply heat to melt the ice. A paraffin actuator is then used to puncture a seal disc at the base of the tank. The water then flows through the hollow puncture needle, then through a narrow passage into the beaker.

Handling water in the low pressure Martian atmosphere is not as straight forward as one might first imagine. The ambient pressure on Mars is 6-10 Torr, approximately a hundred times less than the atmospheric pressure on Earth. The reduced pressure suppresses the boiling point of water while leaving

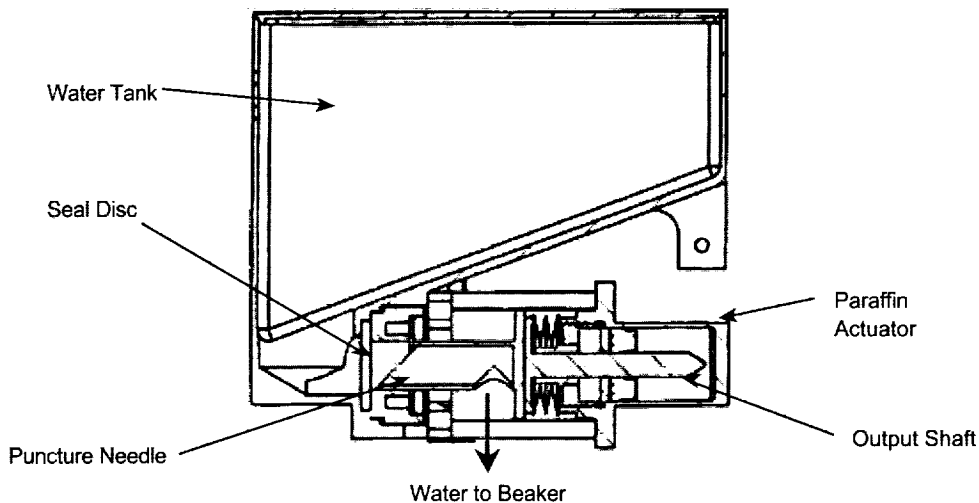


Figure 4 – Water Delivery System

the freezing point unchanged. Water cannot exist as a liquid at pressures below 4.5 Torr - ice sublimates directly to water vapor and the vapor condenses directly to frost. At 6 Torr, water boils at a temperature of only 3.5°C. This leaves a very narrow range of temperatures for liquid water and although it is conceivable to conduct the experiment within this window, the uncertainties in thermal control and barometric pressure preclude this approach. The alternative is to conduct the experiment in a closed cell that is sealed from the atmosphere. The seal integrity must be good enough to allow internal pressure to build within the cell if the temperature increases. The seal must be maintained throughout the experiment and whenever there is liquid water in the cell.

Another problem was determining the most favorable design approach for storing water over extended periods of temperature and pressure fluctuations, and then allowing a means for delivery of the water to a different container. Some of the trades investigated during the design phase included comparisons of solid tanks vs. flexible water bags, and solenoid valves vs. puncture valves. A welded tank with a metal disc and c-ring seal was chosen as the best method for transporting the water over the long cruise to Mars without leakage (leak rate <10⁻⁷ scc/sec helium). Flexible water bags in a vacuum environment were considered too risky.

A puncture needle driven by a paraffin actuator provided a highly reliable means of puncturing the metal seal disc. Paraffin actuators are well suited to this task because they provide ample force in a small package with high reliability. Various disc materials, thickness and coatings were tried. Harder materials such as stainless steel and titanium required either too much force or uncomfortably thin material thickness. The final design used a 0.38-mm (0.015-inch) thick, 1045 Aluminum disc coated with FEP. Puncture required approximately 5.4 N (24 lbf). Late in the program there were indications of corrosion in one of the tests. Speculation that the FEP coating of that particular disc may have been damaged and therefore allowed a galvanic couple to set up between the titanium tank and the aluminum disc. The corrosion could never be repeated or confirmed and a design change was deemed unnecessary.

Once the tank configuration and seal puncture method were set, the problem of dispensing the water through a small puncture hole at the bottom of the tank was addressed. If there is only a single small hole at the bottom of a container full of fluid, surface tension can prevent the fluid from exiting through the hole. When some of the fluid does come out a temporary vacuum can be created in the top of the container exacerbating the problem. The lower gravity on Mars (only about 1/3 that of Earth) makes the problem worse by reducing the pressure head available to break the surface tension. There are a

number of ways to address this problem including pumping the water out, punching a hole in the top of the container to break the vacuum or finding another means to pressurize the container. The method chosen was one that did not require additional components or space. By cracking the drawer seal briefly to reduce the pressure in the beaker immediately prior to puncturing the tank, it is possible to obtain a significant pressure differential between the head gas pressure in the tank and the pressure in the beaker. As the water flows out, the head gas pressure is reduced depending on how much gas there is in the tank to start with. If the tank is only 90 % full of liquid to start with and the rest is non-condensable air or nitrogen at Earth ambient pressure, this is enough pressure to push all of the liquid out. Testing showed that this method was indeed effective enough to dispense the entire charge of water into the beaker.

As a backup, it is possible to increase the pressure inside the tank by heating it. There are film heaters on the sides of the tank anyway to melt the ice. If you put enough additional heat in, it is possible to simply boil the water in the tank to create enough internal pressure to force the liquid out. This works quite well when the pressure is relatively low. If it is as low as the atmospheric pressure on Mars, the task is relatively easy because the boiling point of water is less than 10 °C at this pressure. Of course one doesn't want to lose the water from the beaker so the whole system needs to be resealed while the fluid is being transferred.

Systems Trades

Early stage planning for the experiment considered a wide range of sample and water handling capabilities. In addition to those previously mentioned, multiple reagent addition, pumped/metered solution dispensing, vapor interlock, stirring and multiple use capability were considered. To reduce complexity, cost and mass only the most essential functions necessary to achieve valuable scientific data were included in the initial design concepts. Water must be reliably transported from Earth and dispensed into the beaker. A soil sample must be gathered measured and delivered. Sensors must take data.

During the course of the program, however, it became evident to the lead scientists that reagent addition and stirring must also be added in order to achieve an acceptable level of confidence in the data. Reagent addition was necessary to recalibrate the sensors on Mars. The sensors were found to be sensitive to a variety of factors including pressure and temperature fluctuations and presence of moisture. After exposure to launch, cruise and landing environments, it was expected that sensor calibration would shift significantly. It was therefore highly desirable to recalibrate the sensors on Mars. Stirring was also found to be necessary to adequately mix the constituents in a reasonable period of time. Since the envelope for the experiment was already set, it was necessary to attempt to squeeze these additional capabilities into the limited space that was already available.

Reagent Delivery

The reagent dispenser (Figure 5) delivers a single reagent pellet to the experiment beaker. The pellet has to be sealed through launch, cruise and landing to prevent moisture from softening and degrading the pellet. The design is simple and very compact. The top end of the dispenser is a paraffin actuator. The reagent pellet is contained in a hollow cylindrical shear piston in the lower section. The paraffin actuator drives the shear piston in order to punch through a Kapton seal disc allowing the reagent pellet to drop into the beaker. Again a paraffin actuator is well suited to the task, providing ample force in a very compact package. Disadvantages to this design include the single pellet capability and the need to manually reset the device.

Stirring

A variety of methods were considered to accomplish stirring including paraffin actuator driven paddles, clock springs, motors, solenoids, and boiling. Although any of these methods could potentially

accomplish the task, a motor driven system was chosen because it is the most effective and versatile and also because it could fit in the available space (Figure 6).

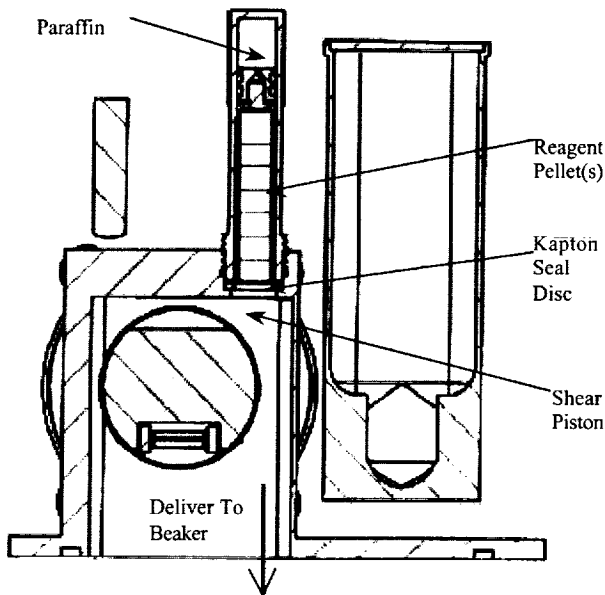


Figure 5 - Reagent Dispenser

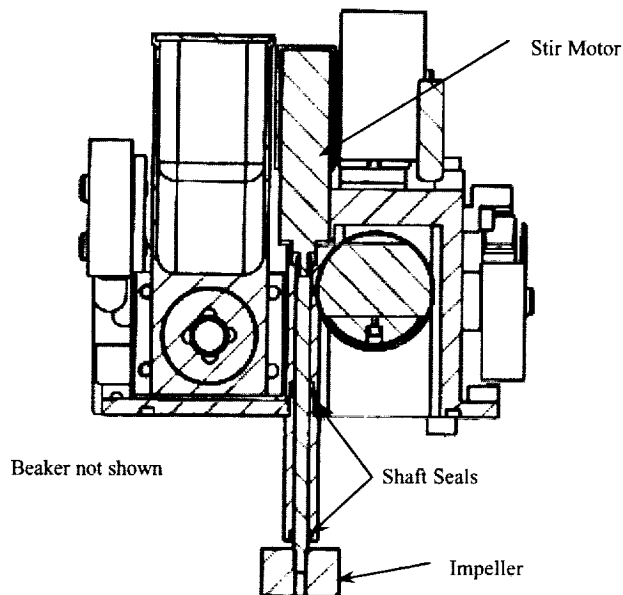


Figure 6 – Stirring Mechanism

The stirring mechanism has a small impeller that extends down into the beaker. The impeller shaft is driven directly by a Micro-Mo miniature coreless d.c. motor. The motor has precision ball bearings and vacuum-compatible lubrication for space application. The motor no-load speed as specified by the manufacturer was 16,000 rpm. The speed was reduced and torque increased by a 64:1 planetary

gearhead. Seal friction on the shaft further reduced speed to approximately 150 to 200 rpm, which is adequate to gently stir the mixture. The motor is quite small (8 mm diameter X 31 mm tall) and even with a 64:1 gearhead has limited torque. The biggest challenge was to couple and seal the shaft without introducing excessive friction or side loads. To accomplish this, the motor output shaft was somewhat loosely pinned to the impeller shaft to allow some angular misalignment and flexibility. The shaft was sealed at two locations with light squeeze o-rings lubricated with a small amount of high-vacuum perflouopolyether (PFPE)-based lubricant.

Despite early skepticism, the coreless d.c. motor performed well in vacuum. During qualification testing, the motor was operated for 16 hours continuously in a vacuum of better than 1×10^{-5} Torr. The use of vacuum-compatible lubrication was thought to be imperative for this success.

Putting It All Together

Each of the basic functions (soil delivery, water storage and delivery, reagent delivery and stirring) requires several components to complete its task and monitor the results. The complete list of components is as follows:

Water Tank	Drawer extension telemetry switch
Tank Seal Puncture Actuator 9	Drawer retraction telemetry switch
Tank Seal Puncture Needle	Drawer heater
Tank Switch	Drawer RTD
Tank Heaters	Reagent dispenser
Tank RTD	Stirring mechanism
Drawer	Pressure sensor
Drawer actuator	Electrical connector
Drawer limit switch	

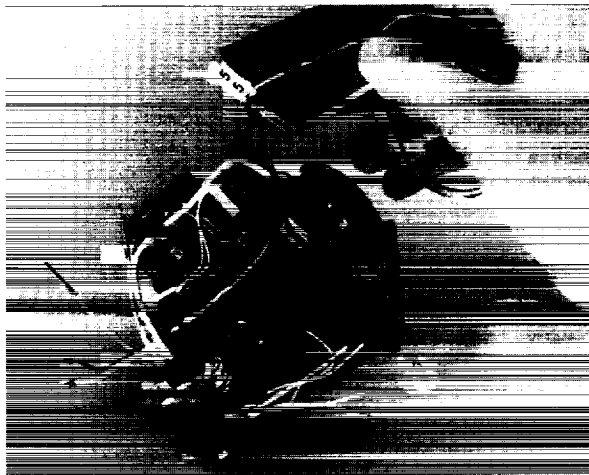


Figure 7 - MECA Wet Chemistry Lab Mechanisms with Water Tank Removed

One of the more difficult challenges of the program was to package all of these components into the 7.0 X 7.5 X 8.0 cm space available above the beaker. The mass of the combined system (excluding the beaker) was limited to 365 grams. The design process required concurrent engineering of several components. A single CAD designer was fed information from several engineers. A solid model was created in IDEAS and maintained throughout the design process. Packaging trade-offs were continuously discussed, refined and incorporated into the solid model. This process worked well and is considered one of the successes of the program. A single model created by a central designer proved to work quite well for this program. A dedicated, highly skilled designer was critical to this approach.

Despite the use of sophisticated software, the solid model should still be thoroughly reviewed for part interference. Several instances of part interference were encountered in this program. These discrepancies would have been very difficult to catch in hard copy drawing reviews. A thorough review of the CAD solid model, however, may have caught many of these errors.

Another lesson learned for this type of mechanism is to leave adequate room in the design for electrical connections and wire routing. This proved to be a difficult task that would have been easier if more time had been spent considering alternatives early in the design process.

Conclusions

Primary lessons learned and conclusions include the following:

- Paraffin actuators were found to be well suited to tasks involving linear motion in environments that include dirt, water and frost. Where actuation speed is not a concern, these simple reliable mechanisms provide high force and small to moderate length stroke in a compact, lightweight package.
- Brushes and scrapers proved useful in removing excess soil particles from running surfaces. Future mechanisms for application on Mars or similar environments should consider incorporating these components.
- Of the variety of different soil types tested, those with hard quartz or quartz-like crystals created the most difficulty for sample delivery due to the tendency for hard crystals to become jammed in tight clearances. Testing of future mechanisms for similar environments should include these types of materials.
- Frost proved to be less of a problem than soil. It was dealt with effectively by heating adjacent surfaces to remove the frost layer. It was also found that thin layers of frost were easily scraped away.
- Of the variety of seals tested, Viton™ o-ring seals proved to be the most effective for sealing linear shaft movement in a dirty environment. O-rings provide enough compliance to seal around micro-scratches and particles. O-rings however should be combined with scrapers and brushes to prevent large particles from intruding on or damaging the seal.
- Reduction of squeeze proved effective to reduce static and running friction to acceptable levels for linear shaft o-ring seals. Reduction of squeeze should be dealt with cautiously, however, because it requires tighter tolerance control and may compromise low temperature sealing capability.
- In a reduced pressure environment where the boiling point is significantly reduced, water can be pumped from a storage container quite easily and effectively by heating the container walls. This method should be considered as a relatively simple means of moving or dispensing water in reduced pressure environments.
- A Kapton™ seal disc and puncture system worked well to seal a solid reagent pellet from moisture. Kapton seal discs may be useful for similar sealing applications.
- Despite early skepticism, the coreless d.c. type motor was shown to perform well in vacuum. The use of vacuum-compatible lubrication was thought to be key to this success.
- Using a central solid model CAD designer with input from several engineers worked well in this program to fit all of the components into a very tight package.

Low-Cost Ejection Mechanism for Protective Covers on Meteosat Second Generation

J. Ortega*, F. Quintana*, G. Ybarra*

Abstract

Two covers protect the sensitive surfaces of the MSG (Meteosat Second Generation¹) satellite against possible contaminants. Once the peril of contamination ceases, the covers must be jettisoned, allowing the satellite to operate. Their failure to provide isolation or the failure of their jettisoning leads to mission failure.

The mechanisms responsible for the ejection must face severe requirements: only one pyrotechnic is allowed for the baffle cover, the acoustic environment reaches levels of 146 dB, and the allowed mass is very low. These requirements have led to the use of preloaded supports such as the "flexible releasable hinge", which is capable of supporting the cover and releasing it passively without the use of telecommand.

Introduction

MSG meteorological satellites will provide meteorologists with imagery and data. Like their Meteosat predecessors, the MSG satellites will operate from geostationary orbit. The MSG main instrument is the SEVIRI (Spinning Enhance Visible and Infrared Imager).

The MSG require protection for their optical surfaces against contaminant particles during ground operations, transportation, launch and ascent to the satellite's transfer orbit. Two independent covers provide this protection (see location of these covers on the satellite in Figure 1).

The covers isolate the inner cavities of the satellite, preventing any contaminant from entering and allowing the venting of the gas inside while the external pressure decreases. Once the peril of contamination ceases, the covers must be jettisoned, allowing the satellite to operate. Their failure to provide tightness or the failure of their jettisoning leads to the loss of the mission.

Requirements and solutions

The most challenging requirements for the jettisoning mechanisms were:

- Only one pyrotechnic was allowed to jettison the baffle cover. This requirement limits the number of supports for the cover, since these supports must be detachable in order to jettison the cover in orbit.
- The acoustic level, and the mechanical environment in general, were very severe for a high stiffness and barely supported structure.

The SEVIRI Entry Baffle Cover had to cover approximately 0.7 m², which was the aperture of the Baffle. Nevertheless, since the pressure outside the cover will decrease during launch and ascent, the cover did not close hermetically the inner cavity; a hole with a filtering device was required. The function of the filtering device was to allow the depressurization of the inner cavity and at the same time prevent the dust from entering. Dust was a primary concern and the pore size of the filter was limited.

* SENER Ingeniería y Sistemas, S.A., Spain

¹ The mechanisms & pyros subsystem for MSG is a project developed under a European Space Agency / EUMETSAT contract. The prime contractor of the MSG is Alcatel Space Cannes.

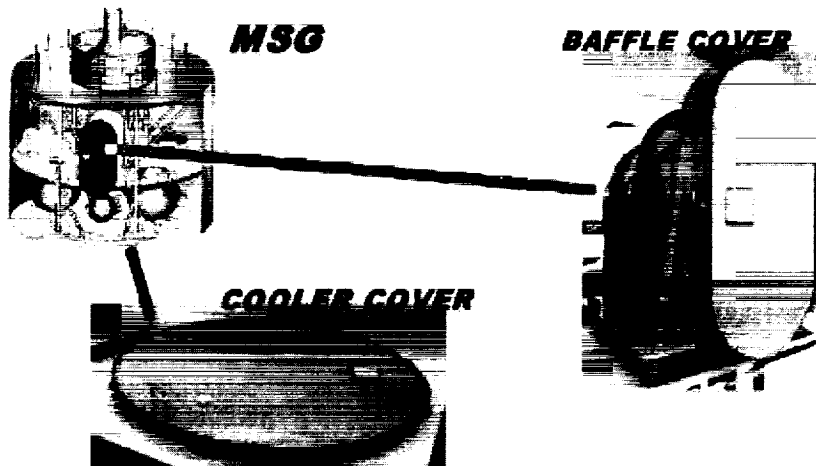


Figure 1. Covers location on the MSG satellite

The jettisoning speed was an important parameter for the Entry Baffle Cover. If it were very low, the cover could impact some parts of the satellite such as the solar panels, affecting its performance. It was defined that a jettisoning speed of 1.5 m/s would be sufficient. In the case of the baffle cover, this speed was not a primary concern because the high spin speed (the MSG is a spin-stabilized satellite) will help the cover achieve it.

The SEVIRI Passive Cooler Cover had to cover approximately 1.9 m^2 , which was the aperture of the SEVIRI Cooler cone. This cover did not close hermetically the inner cavity either. The jettisoning speed was also an important parameter and in this case it was critical for the design of the jettisoning mechanisms. The position of the cover, coaxial to the satellite spin axis, prevents it from making use of the spin.

Table 1 and Table 2 provide a summarized list of the most important requirements.

Preloading

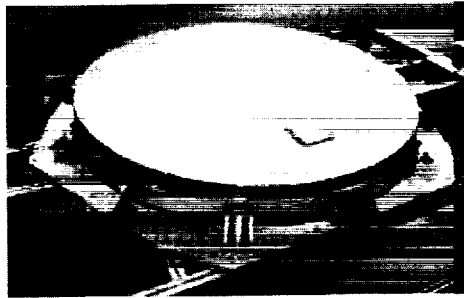
The easiest way to support a detachable cover is fixing it with several pyrotechnically removable joints. But in this case, the number of pyrotechnic devices was limited to one (baffle cover) or three (cooler cover) and these were not sufficient unless additional non-pyrotechnical supports were added. The solution chosen to solve this problem was using support points where contact was ensured applying a constant preload.

Table 1. SEVIRI entry baffle cover requirements summary

SEVIRI ENTRY BAFFLE COVER	
SURFACE TO BE COVERED:	APPROX. 0.7 m^2
TELECOMMAND:	1 PYROTECHNIC
VENTING: INNER CAVITY	1.2 m^3 $\text{MAX}(P_{\text{INT}} - P_{\text{EXT}}) = 170 \text{ Pa}$
JETTISONING SPEED:	> 1.5 m/s
MASS	$\leq 4 \text{ Kg}$
MECHANICAL ENVIRONMENT	35g QUASISTATIC 25g SINE / 27.3 g _{RMS} RANDOM 146 dB
THERMAL ENVIRONMENT	-60°C TO +60°C
STIFFNESS	FIRST MODE AT $F > 140 \text{ Hz}$

Table 2. SEVIRI cooler cover requirements summary

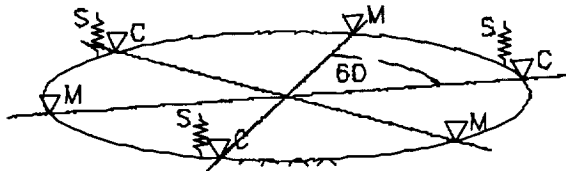
SEVIRI PASSIVE COOLER COVER	
SURFACE TO BE COVERED:	APPROX. 1.9 m ²
TELECOMMAND:	3 PYROTECHNICS
VENTING: INNER CAVITY	0.94 m ³ MAX(P _{INT} -P _{EXT})=170Pa
JETTISONING SPEED:	> 1.5 m/s
MASS	≤ 10 Kg
MECHANICAL ENVIRONMENT	15g QUASISTATIC 4g SINE / 17.3 G _{RMS} RANDOM 146dB 80g DURING 0.8ms
THERMAL ENVIRONMENT	-60°C TO +60°C
STIFFNESS	FIRST MODE AT F>60Hz



SEVIRI passive cooler protective cover.

The cooler cover is supported at six points: three preloaded points (C) and three pyrotechnically detachable support points (M). The cover is round and all the support points are distributed symmetrically on the perimeter; between each two pyrotechnic mechanisms (M) there is one preloaded intermediate hard support point (C).

COVER SYNOPSIS



M->Pyro mechanism
hard support
C->Intermediate hard
support
S->Kick springs

Figure 2. Cover support points and distribution

The preload in the intermediate hard support points is produced by deforming the cover (sandwich panel). The deformation of the cover is produced joining the two parts of the pyrotechnic mechanism (M). The gap between these two parts is calculated to produce the desired preload (see Figure 2 & Figure 3).

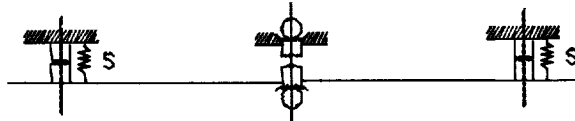


Figure 3. SEVIRI cooler cover preloading

SEVIRI entry baffle protective cover.

The baffle cover is supported at five points (see Figure 4): four preloaded support points (C and H) and one pyrotechnically detachable support point. The design of the preloaded support points ensured that if the pyrotechnic were activated, the cover would detach completely.

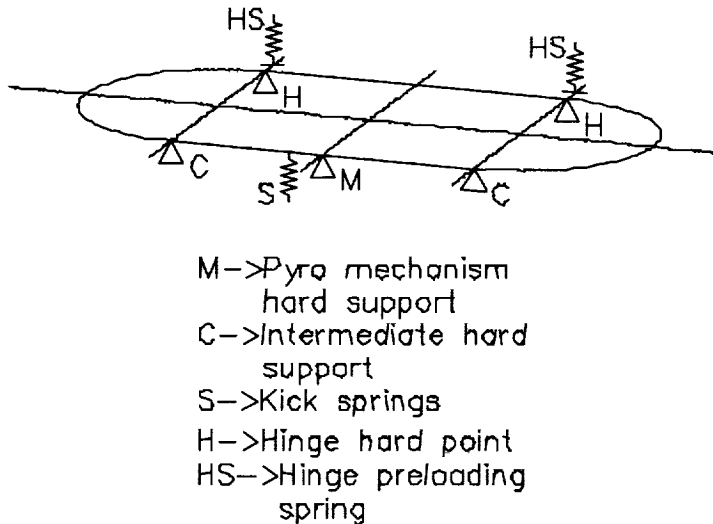


Figure 4. Cover support points and distribution

For these preloaded support joints to work properly, the following requirements must be necessarily fulfilled:

- The joined parts must be easily detached without interference and with the lowest friction possible.
- The joined parts must be kept together by the action of a force (preload). This force must be higher than the maximum separation effort that may be caused by the thermal or mechanical environments (vibration, acoustic, thermal loads).
- Cold welding must be avoided.

The preload, in these covers, is applied deforming some elements of the cover. The work sequence is 1) "flexible hinge" preloading, 2) "kick spring" preloading, 3) panel preloading, 4) launch and ascent, and 5) jettisoning.

This sequence is simpler for the cooler cover. The cooler cover is jettisoned perpendicularly to the mounting plane of the cover. After being jettisoned, the cover moves parallel to itself as it distances from the satellite.

This is not the case for the baffle cover. The baffle cover, once the pyrotechnic cutter releases the cover, rotates around the hinge support. Once a critical angle is achieved, the cover gets disengaged from the hinge and distances freely. Therefore, in addition to the translation of the cooler cover, the baffle cover has a rotational motion. Figure 5 shows this process schematically.

1) "Flexible hinge" preloading. The flexible hinge is a very simple titanium piece that allows supporting the cover at one point preloading the joint. There are two of these pieces, both of them at the same side of the cover. Once the cover is engaged at the flexible hinges, it is turned until the contact is stabilized with the "kick spring".

2) Kick spring preloading. The function of the kick spring is to provide the initial separation speed once the cover is released. During the mounting of the cover, this spring must be compressed.

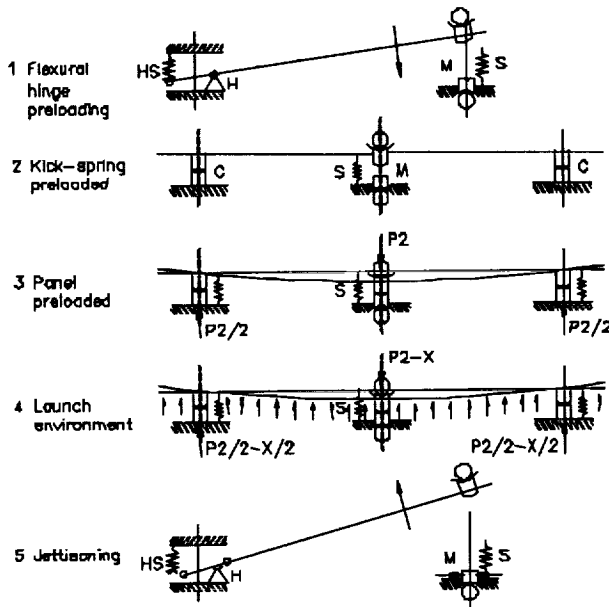


Figure 5. Structural and functional concept of the SEVIRI entry baffle cover

3) Panel preloading. The panel is the flat surface of the cover. The panel has some flexibility; when it is deformed to allow the bonding of the two parts of the pyrotechnic mechanism, which together are shorter than the lateral support points, it produces a joining preload at these lateral support points that prevents the cover from separating (see Figure 6).

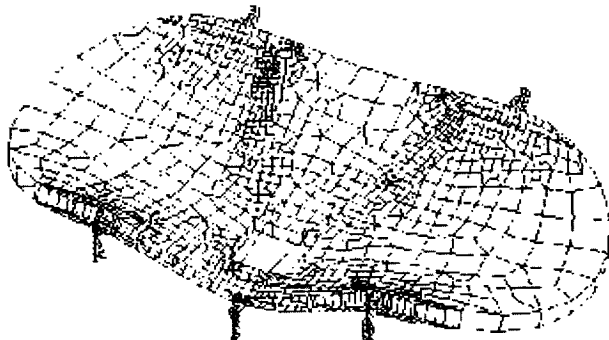


Figure 6. Baffle cover panel deformation FEM analysis (view out of scale)

4) Launch and ascent. Once all the support points are preloaded, the cover is ready for the launch environment.

5) Jettisoning. The jettisoning operation is activated by firing the pyrotechnic cutter. Once the pyro bolt is cut, all the preloads of the rest of the support points are discharged and the cover is released.

- The first preload to disappear is the preload at the hard points (points C in Figure 4). When this preload is discharged, the cover loses contact with the hard points.
- The kick spring will continue pushing the cover apart for some distance. When the contact between the cover and the spring is lost, the baffle cover will still continue rotating around the hinge for a small angle.
- The critical rotation angle is achieved and the cover is disengaged from the hinge. The cover distances freely.

Calculation

A detachable preloaded support can be treated analytically as a bonded piece if the preload is sufficient. The maximum external load must always be lower than the preload. Following this statement, calculating the preload is easy for static loads (or quasi-static). For sine and random loads it is a bit more complicated because a criterion must be defined; the preload is a constant force while the sine or random loads are not. Dynamic forces and their effect on preloads were analyzed very soon in the project and it was concluded that 2σ criterion was the optimum one. The usual 3σ criterion could have led to an impracticable design. This conclusion was confirmed later on by test.

The preloaded supports: the hinge

Design

The flexible hinge (Figure 7) of the SEVIRI entry baffle cover was designed to fulfill the following main requirements:

- Maximum allowable volume: $60 \times 35 \times 124$ mm.
- External loads: approximately 25% of the total external load -acoustic environment was the severest load case- is supported by each hinge.
- For the "cover stowed" or "hinge preloaded" configuration the hinge design considers that hinge parts will be assembled with a precision higher than 0.2 deg. This value includes all possible deviations occurring during manufacturing, assembling or integration. The hinge itself is not responsible for achieving this precision, and therefore the rest of the structure must ensure it.
- It must provide one point of support for the cover during all the phases of the mission prior to arriving at the final orbit.
- It must passively allow, without interference and with limited friction (a friction budget must be performed) the correct release and jettisoning of the cover.

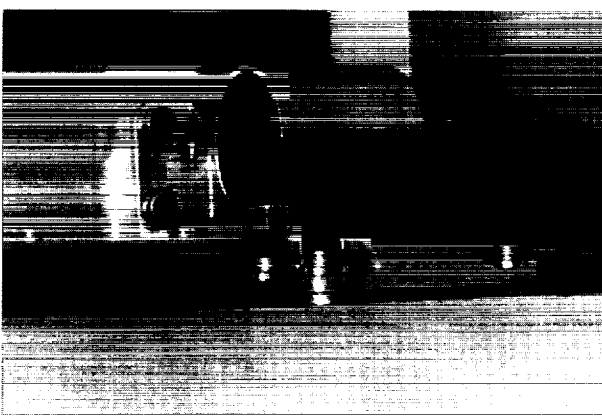


Figure 7. Flexible hinge mechanism

The most outstanding problems that were faced during the design of the hinge were:

- The allowable volume.
- The high preload required in order to overcome the acoustic environment.
- The hinge must allow the jettisoning of the cover without interference.
- Manufacturing with very tight tolerances to achieve the required stiffness and strength.
- Cold welding due to high preloads and dynamic environment.
- The friction caused by the sliding of the two contact surfaces when the cover turns during the first stage of the jettisoning.

The hinge used preloads to be a releasable hinge and a stiff point of support at the same time. The preload application is based on the lever principle so that good precision and high loads can be achieved without too much effort (Figure 8).

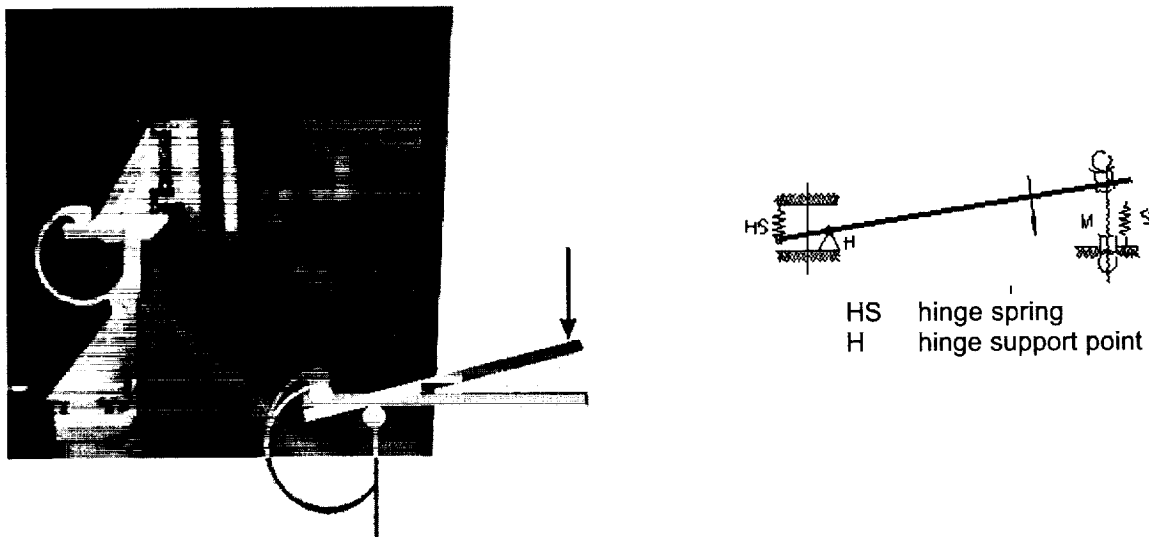


Figure 8. Hinge preloading

Precision

The hinge allows the relative movement of the connected parts on only one degree of freedom. The translation degrees of freedom are restrained, and in fact the hinge is very stiff for those translations (stiffness varies with direction). The two rotational degrees of freedom that are restrained are those perpendicular to the hinge axis. The hinge is also very stiff for those rotations.

The last degree of freedom, the rotation around the hinge axis, is free although not completely. There is a low stiffness that provides the hinge with its preload. Therefore, depending on the relative position of the hinge and its mating piece (see Figure 8), the preload will be different. In the baffle cover, this relative position was defined during the assembly of the panel and the mechanisms (Figure 5).

Geometry

The hinge has basically two different parts: the hinge spring and the support. The hinge spring is in fact a flexible Titanium structure with a nearly constant thickness, designed so that it provides the required preload with low stress and as small deformation as possible. This flexible structure has a semi-circumference shape. It can be easily modified to meet different preloads or deformations.

The support is only a preloaded detachable support, as those that will be described in "Preloaded supports: hard points".

Both parts must be located at precise locations so that absence of interference is ensured during release. An error on one of the dimensions that define the relative position of the hinge spring and the support may mean that the cover will get stuck instead of being jettisoned.

The surfaces in contact

In order to avoid the cold welding or similar undesired effects that could have an impact on the correct release of the covers, one side of the detachable pieces was coated with TiC (titanium carbide). The contact surfaces of the hinge support and its mating piece must be designed performing a trade-off between these two points:

- The contact surface cannot be a flat surface against another flat surface, since this kind of contact surface cannot withstand forces in a plane (or only by friction).

- The contact surface cannot be a cone against a cone or sphere if the aperture of the cone is small and causes bonding due to friction.

The conclusion of this trade-off must be the aperture angle of a cone:

- Closed enough so that every lateral or axial load is withstood without the surfaces detaching (for a given preload).
- Open enough so that the contact surfaces do not get stuck due to friction (for any preload).

The release

From the hinge standpoint, the functional sequence of the jettisoning is:

- Once released, the cover loses contact with the hard points and the kick spring. Up to this point, the cover has turned around the hinge.
- The cover continues rotating around the hinge up to the critical angle. During this rotation there is friction between the two surfaces in contact. The preload produced by the flexible hinge itself causes this friction. Nevertheless, since the preload decreases as the angle is changing, the friction also decreases.
- There is an angle, between the "loss of contact with kick spring" angle and the critical angle for which the preload is zero.
- The cover loses contact with the hinge and disengages.

This process was simulated with detail so that possible interference could be known in advance. As a result of this simulation, some dimensions and angles were modified in order to improve the success reliability.

Manufacturing of the hinge

Each hinge, after being manufactured, was tested to measure its stiffness on the two basic directions and its capability of being released without interference and low friction (Figure 9). With the results obtained from these tests, the mating pieces were designed and eventually manufactured.

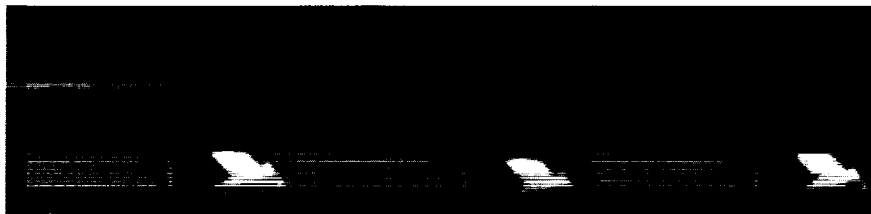


Figure 9. Hinge characterization test: release test

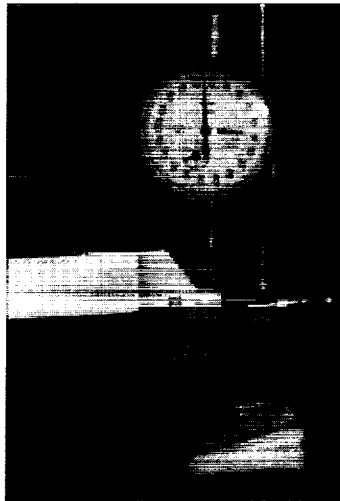


Figure 10. Hinge characterization test: stiffness test

Preloaded supports: hard points

Hard points (Figure 11) located in front of the flexible hinges, are composed of two detachable parts: on the cover side, a cone and on the satellite side, a sphere. This kind of contact provided the support of the cover when submitted to the thermal and mechanical environments and at the same time made it possible for the cover to separate without interference or friction. The aperture of the cone is designed by performing a trade-off, in the same way as for the flexible hinge support (explained above).



Figure 11. Hard points

This trade-off, performed for the hard points, concluded that there was no angle that fulfilled both conditions at the same time. The angles that are open enough not to cause friction problems during detachment were not enough to absorb the external lateral loads. This problem was solved using two aperture angles (two different cones with two different aperture angles) at the same time. One of the angles was calculated such that it would be open enough to prevent sticking during the detachment, while the other one was calculated such that it was closed enough to prevent detachment due to the environmental loads. Therefore, the cover contact surface, as shown in Figure 12, is not a pure cone.

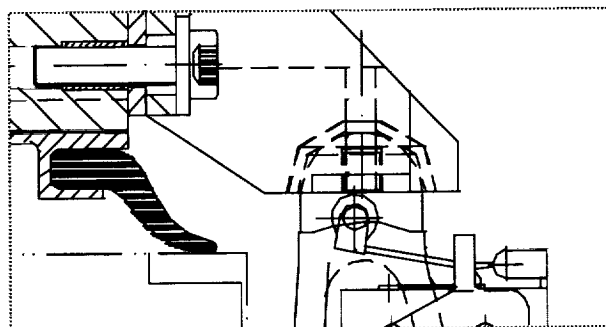


Figure 12. Hard points, contact surfaces

Pyrotechnic support

The fifth support point (see Figure 13) is mainly composed of a double pyrotechnic cutter and a rod. The pyrotechnic cutter to jettison the cover cuts the rod.

During the integration of the cover, and after supporting it by the two hinges and the two hard points, a gap exists between the fixed and jettisonable parts. This gap is absorbed deforming the panel, and therefore applying a preload to the rest of the supports (especially the hard points).



**Figure 13. Pyro mechanism and hard points
Jettisoning**

Once the covers are not needed (once in transfer orbit), they must be ejected. The main requirement of the ejection is not causing damage to the satellite. For this to happen, a minimum ejection velocity is required and the ejection direction must be such that no interference exists with any other part of the satellite.

Since the release of the covers is very important for the mission of the satellite, this operation has been designed with redundancy. In the case of the baffle cover, the level of redundancy is up to three: the pyro cutters are fully redundant and the separation is produced by three different forces, the spin of the satellite, the deformation of the cover itself, and the kick spring located next to the pyrotechnic.

The jettisoning process has been simulated using SENDAP² software. Figure 14 shows the evolution of the separation speed and distance between the baffle cover and the satellite. After performing the qualification tests, the final separation speed was demonstrated to be 15.6 m/s.

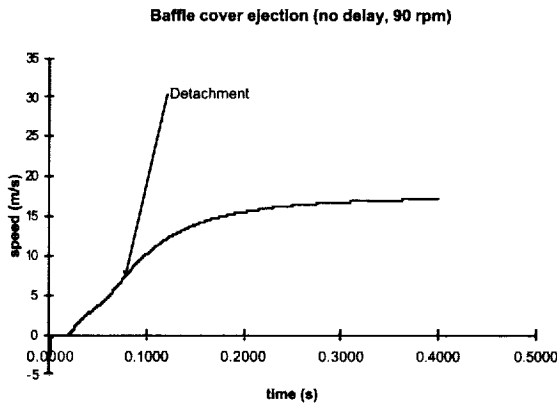


Figure 14. SEVIRI entry baffle cover ejection simulation

Figure 15 shows the evolution of the separation velocity for the cooler cover. In this case, one pyrotechnic failure has been considered. The simulations demonstrated that the jettisoning fulfilled all the requirements, namely absence of interference and minimum jettisoning speed. The tests confirmed this fact during the qualification stage.

² SENDAP stands for SENER dynamic analysis program. This software is capable of simulating very complex dynamic situations. It was designed to simulate the docking / berthing of spacecraft and it was qualified for the HERMES space plane program.

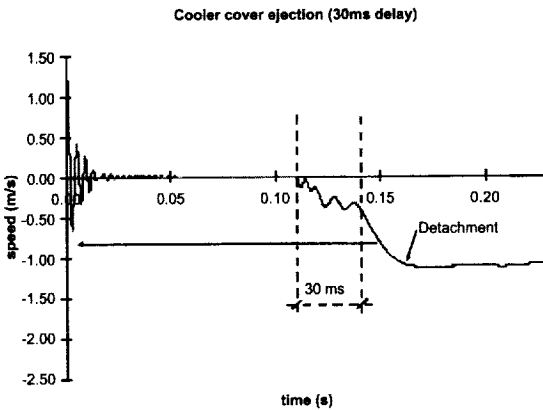


Figure 15. SEVIRI cooler cover ejection simulation

Other requirements

Tightness

So as to avoid the contamination of the inner cavities of the satellite due to the external dust, the cover provided effective isolation. A seal made of silicone rubber was designed specifically for this function. It absorbed high displacements with low sealing pressure variations.

Venting

Since the external pressure decreases during the ascent of the satellite to its first orbit, the inner pressure must be released. For this to happen, preventing at the same time the contamination of the inner satellite elements, a filtering device was built and a simulation of the venting process was performed (Figure 16). The filter provides a large filtering surface (pliable supported PTFE membrane), which was folded several times for compactness. The entire filter was sealed to avoid undesired leakage.

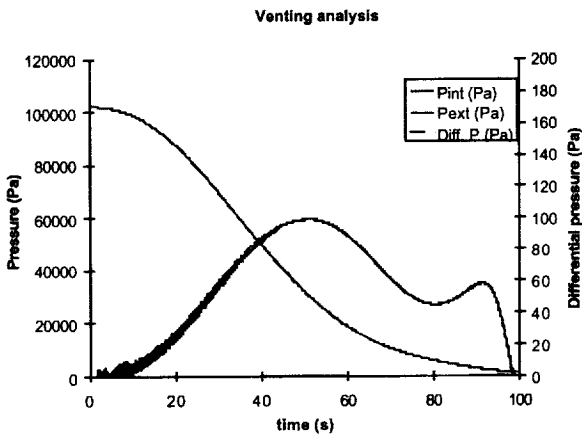


Figure 16. Venting analysis

Verification

The most important tests performed during the qualification stage of the mechanisms were:

- Environmental tests: testing the vibration, thermal and acoustic environments.
- Functional tests: the most remarkable test was the jettisoning test where the jettisoning speed was measured and the ability to release the covers without interference was proved. Another functional test proved tightness of the cover and the sealing system to be adequate.

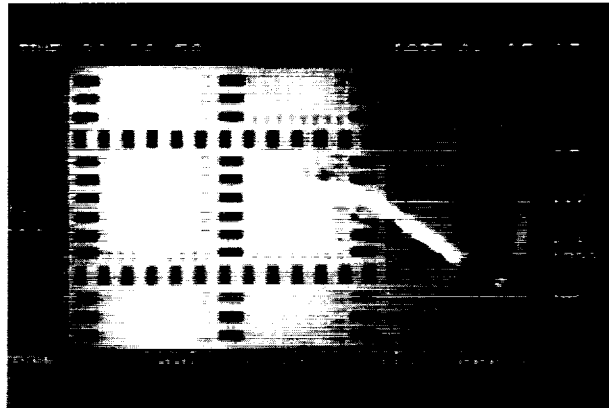


Figure 17. Baffle cover jettisoning test

All the tests were successful, and in some cases the results measured were better than required.

Conclusion

Specific lessons learned:

- Detachable preloaded structural joints can be calculated so that twice (instead of thrice) the RMS value of random external loads is lower than the preload (2σ criterion). This calculation was used for VespeI™-Aluminum and Titanium-Titanium Carbide detachable preloaded joints. If the 3σ criterion were used, it may lead to an impractical design.

Major achievements are:

- The design, analysis and test of a support concept for low-mass structures (such as protective covers), including the mechanisms to release or jettison them once they are no longer needed.
- The design, analysis and test of a hinge, capable of supporting high external lateral and axial loads (support), allowing relative rotation motion between the parts (hinge), and of eventually disengaging the parts for a predefined angle (release mechanism).

Misconceptions in Mechanism Reliability

Walter Holemans^{*} and Donald Gibbons^{**}

Abstract

Spacecraft mechanisms are in practice less reliable than intended. Today's designs are increasingly designed in shorter times with increasing reliance on historical design data. As spacecraft mechanism designs are reused in different applications and modified by engineers removed from the initial mechanism design there is increasingly more opportunity to introduce new failure modes. Several misconceptions in mechanism reliability are presented. Examples demonstrating misconceptions are provided and discussed. The misconceptions presented are: (1) reliability of a mechanism can be calculated from the reliabilities of the mechanism's components; (2) increasing force will increase reliability; (3) the more expensive and difficult the test, the less necessary it is to execute; (4) adding a back-up component will necessarily increase reliability; (5) successfully operating a mechanism once indicates high reliability.

Introduction

Continuing failures of space vehicle mechanisms demonstrate a large discrepancy between predicted reliability and actual success. Despite strong motivations to build reliable hardware, some present methods continue to yield unacceptable results. Part of the problem results from misconceptions about how reliability is attained and estimated.

In the space industry, the best-made launch vehicles and space vehicles have a failure rate of 1 in 30 while the worst see a failure rate of 1 in 3. Most new rocket companies fail on their first attempt. The majority of new endeavors in space (such as a new launch vehicles or travel to a new location) end in significant degradation of mission performance or even complete mission failure. Many failure review boards do not have difficulty in determining the cause of failure after it has occurred and many other failure review boards have too little information on which to base a cause. It is a tragedy that we continue to use the operational mission to discover these failures. The cost of these failures is significant.

Two straight years of massive claims following satellite and rocket failure have knocked several space insurers out of business and could result in a 30 percent drop in the amount of underwriting capacity this year according to US and European insurance officials....figures in the industry show underwriters paid out around \$2.5 billion in claims during the past two years.... (Ref. 9)

Misconceptions can prevent engineers and program managers from taking simple and cost-effective steps to achieve higher reliability and the ultimate goal of successful operation of the Mechanism through out its' intended mission. Until we can eliminate predictable failures from our mechanisms, including those resulting from the misconceptions presented below, our industry will continue to see unnecessary catastrophic failure of expensive satellites and launch vehicles.

The following common misconceptions often lead to catastrophic failure:

1. Reliability of a mechanism can be calculated from the reliabilities of the mechanism's components
2. Increasing force will increase reliability

^{*} Planetary Systems Corporation, Washington, D.C.

^{**} Lockheed Martin Space Systems Company, Sunnyvale, CA

3. The more expensive and difficult the test, the less necessary it is to execute
4. Adding a back-up component will necessarily increase reliability
5. Successfully operating a mechanism once indicates high reliability

Background

The space industry today (2000) has much in common with the aviation industry of 1925, the automobile industry of 1890, the steam engine industry of 1850, and the shipbuilding industry of 1500: production rates are low, failures are common, product evolution is rapid, experimentation is common, opportunities abound, and heroic efforts are required to be successful. We are in the midst of learning how to build cost-effective space vehicles well.

The unique environment of space makes reliability challenging to attain. The very different environment (vacuum, large temperature extremes, large temperature gradients, long dormancy prior to operation, and high radiation) of space travel precludes direct application of terrestrial hardware, it only allows some terrestrial concepts to be copied. Failed hardware is usually not retrievable so although it is possible to determine what happened to cause a failure, it is usually impossible to study the failed hardware and therefore determine the definitive root cause of a failure (broken automobiles and aircraft often conveniently present their failed hardware for study and subsequent prevention). A further difficulty is the very low rate of recurring production; most spacecraft are one of a kind, even when they are similar, production rates rarely exceed one per month. Even spacecraft constellations have relatively small numbers of vehicles compared to other industries. The relatively small market for space vehicles prevents the kind of capitalization to provide the knowledge of reliability that other industries enjoy. Automobile manufacturers have enjoyed this ability for nine decades and while some automobiles may not be reliable, all of the data is available to know what the reliability of the automobile is. Finally, due to both the physics and economics of present day spaceflight, spacecraft engineers must balance the required performance of their mechanisms with the need to design producible, reasonably priced, lightweight hardware.

There are several misconceptions about attaining reliability that keep space vehicle manufacturers in the dark ages. Until the space industry embraces more rigorous testing to truly determine the capabilities of aerospace mechanisms, products will continue to fail at present rates.

Misconception #1: Reliability of a Mechanism can be Calculated from the Reliabilities of the Mechanism's Components.

The knowledge of reliability of an assembled mechanism cannot be determined by algebraically manipulating the reliability of the subassemblies because the calculation relies on unproven assertions. For example: A mechanism engineer knows the reliability of a pyrotechnic bolt cutter from the lot test data and can determine the reliability of a retention bolt based on Typical material strength data and/or fracture mechanics. From statistics, the reliability is the product of the two item's individual reliability. The error is made when the engineer makes untested assumptions to carry out that calculation. When cutting a bolt with a pyrotechnic bolt cutter, these assumptions may include:

1. The bolt floats freely in the bolt cutter or rests directly against the anvil
2. The bolt has no mass or the same mass as the lot test bolt
3. The anvil of the bolt cutter must put some of its energy into completing the cutting of the bolt
4. The friction between the anvil and the bolt is negligible
5. The cut bolt fragments will not have sufficient energy to rebound or damage other parts of the space vehicle
6. The bolt is under preload
7. The pyrotechnic cutter is securely clamped
8. The flight conditions are identical to the lot test conditions

More imaginative or experienced individuals may come up with many more (hard-earned) assumptions. If any one of these assumptions is invalid, failure may result. Without verification, including process control and verification testing, all assumptions are presumptions and are subject to being wrong.

Misconception #2: Increasing Force will Increase Reliability.

There is always a balance between increasing deployment force (or torque used here interchangeably) and the structural margins in the rest of the mechanism. This method is frequently employed in hinges used on deploying solar arrays and antenna booms. High force margins are employed because retarding forces are often poorly characterized or known to vary widely over temperature. However, the employment of high force margins often produce undesired high kinetic energies of the deployable leading to high loading at the end of travel or even over travel of the deployable leading to collision and failure. When the high kinetic energy issue is recognized, it often leads to the use of dampers, which further increases complexity and can necessitate even higher forces to maintain deployment margins against increased parasitic loads and can induce even higher loading within the mechanism. As the complexity of a mechanism increases, the number of possible failure modes increases, and the ability of the design engineer to comprehensively verify the ability of the mechanism to perform its' mission is compromised.

Several deployables have failed or been damaged, not by over travel, but by the unanticipated behavior of auxiliary devices added to control deployment. On the Mars Global Surveyor (MGS) this is exactly what happened.

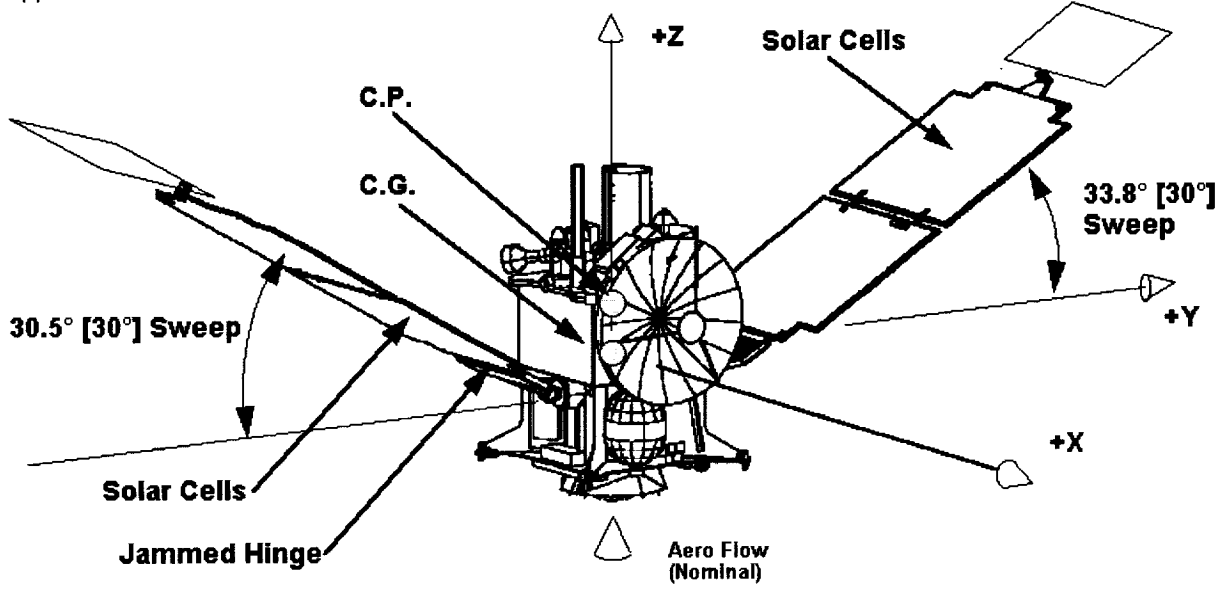


Figure 1. Mars Global Surveyor and Jammed Hinge (Ref. 6)

Telemetry from the spacecraft indicates that the inner panel is 20.5 degrees away from full deployment. Tests show that the hinge is not latched. The failure scenario that explains both the body rates during deployment and which is consistent with a 20.5 degree offset is that the deployment damper shaft sheared off during deployment and the lever that turned the shaft became wedged between the inner panel and the yoke where the damper is located. (Ref. 7)

Ultimately MGS was a success. It was only able to do so through a heroic effort to redesign the aero braking maneuvers, which originally depended on a fully deployed panel, while en-route.

On MGS a complex and unreliable mechanism resulted from the initial desire to have high torque margins. Compensating for the high energies that came along with the high torque margins led to a mechanism of unknown failure modes.

Instead of attempting to overpower friction and other retarding forces, and then needing to add controls to the driving force, a much simpler and more reliable mechanism may result through the study, test and control the source of the retarding forces.

Misconception #3: The More Expensive and Difficult the Test, the Less Necessary it is to Execute.

Program managers and customers often eliminate full systems tests based on cost and schedule limitations. Cost-Benefit analysis can be easy to sway in the direction of cost and schedule when the benefits of testing are not determined until after launch and a failure. Unfortunately no relationship exists between the cost of a test and its need which is driven by the engineering requirements. Furthermore, the more permutations of assembly, operation and environment, the more ways a mechanism can fail. Thus full systems should be tested more than subsystems, not less.

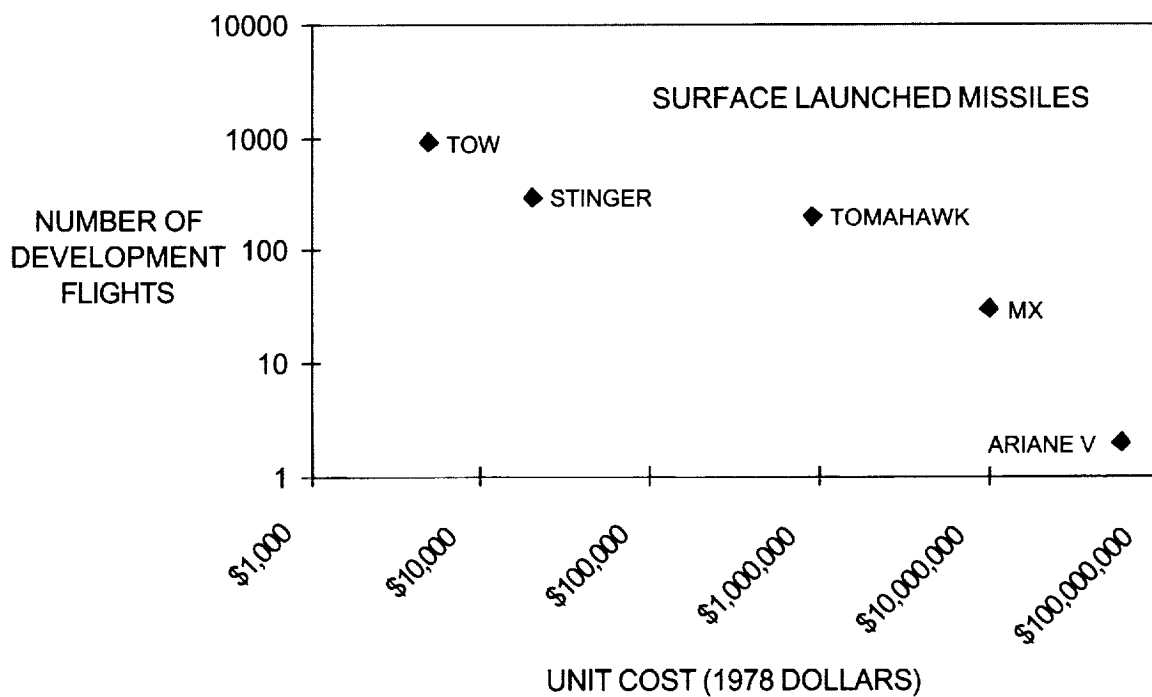


Figure 2. Development Testing of Surface Launched Missiles (Ref. 4)

Many systems in spacecraft mechanisms exhibit similarity to the testing in Figure 2: in separation systems, bolt cutters are often lot tested, but the separation system as a whole is not. It is relatively easy to test one hundred bolt cutters. Bolt cutters are not, however, separation systems.

The source of funding to pay for increased testing is not intended to be within the scope of this paper. However, testing should only be foregone when the value of an additional test is known to be negligible. This knowledge, however, can only come about from previous testing.

If there is doubt that people make this misconception, look at it another way. Is it possible that a test that is perceived as simple and inexpensive to run is run frequently without respect to the usefulness of the data collected? Although an ideal test would be simple, inexpensive, and generate a lot of useful data, most useful testing, is relatively expensive, complex and requires intimate understanding of the hardware under test.

Here is another look at why this misconception is not true. From a logical analysis perspective if the misconception is true then the contrapositive is also true. This would mean "If a test is expensive then it is not necessary to execute" and "If a test is necessary to execute then it is not expensive" are both true or both false. Necessary tests are often expensive, therefore this misconception is false.

Engineers, managers and customers must be aware that untested hardware has untested reliability, and statements of reliability about this hardware are completely speculative.

Misconception #4: Adding a Back-Up Component will Necessarily Increase Reliability.

The assumption that a back-up component will increase system reliability is predicated on the assumption the failure of either the back-up or primary component will not effect the reliability of the other. In other words, the failure modes are isolated.

One such place this method is used is with springs (Figure 3). Upon detailed examination of this design it is apparent that this design has several failure modes that would not exist in a design using one spring:

1. If one of the springs is broken it may lodge in the path of the non-redundant components, blocking motion
2. There is a significant difference in operation of the working spring when the other spring fails. This can lead to high stresses of the unfailed spring.
3. The redundant mechanism has four modes of behavior (compared to two in the single spring), all of which will need to be tested.

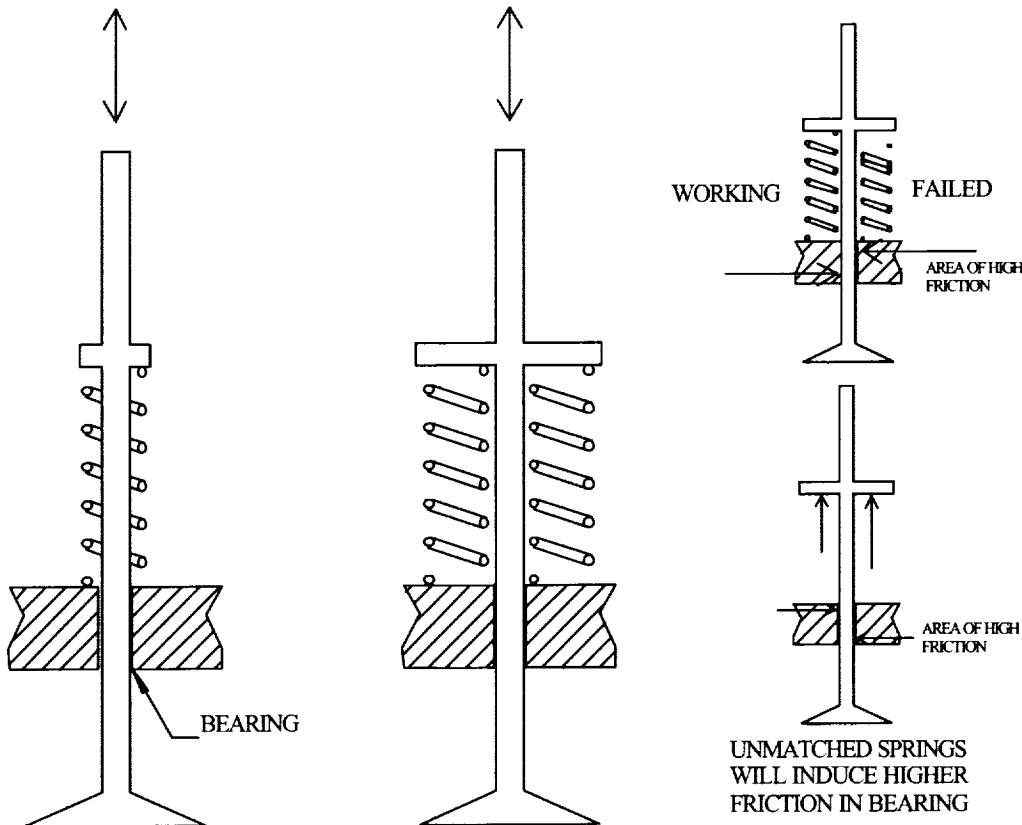


Figure 3. Illustrative Example: Comparison of a Single Spring Driven Mechanism to a Design with a Back-Up Spring

The design with the back-up spring poses several challenging problems the single spring design does not have:

1. The springs have to be well matched to avoid high friction in the bearings and high forces in the other elements of the mechanism
2. Failure of one spring will dramatically increase friction forces in the bearing
3. The springs may need additional support to prevent buckling
4. Required volume is higher
5. The number of modes of operations to verify by test increases at least 2 times
6. Mass is higher
7. The failed spring may inhibit the operation of the working spring

Although the dual spring design above (Figure 3) could be modified to use two concentric springs, the designer must consider the interaction of both failed and unfailed springs, and the need to match rate and force output to create a truly redundant system.

Without a corresponding increase in design and test effort, the design with the back-up spring may be less reliable because it can fail in many more ways.

The difficulty of anticipating and controlling new failure modes underscores the challenge of making truly redundant spring-driven mechanisms. This is because they are physically connected; no matter how tenuous that connection, there still exists many paths between the failed spring and the working one. Additionally, the introduction of new potential failure modes, and the resultant operation of with a single

component failure, requires the understanding of a more complex system as well as the need for testing additional modes of operation.

Some mechanism design practices advise at least a two to one force ratio (100% margin) for deployment in the normal operating condition. Does this choice of force margin provide redundancy? Not unless the failure of one spring does not add any additional drag to the system. Although having a positive margin with a one spring failed case is a basic tenant of mechanism design, this condition can be difficult to characterize and equally difficult to verify. Also, with the corresponding increase in energy, the impact of the deployable at the end of travel is greater reducing the structural margins or the bearing margins. Even with the addition of a damper to dissipate additional energy from added springs, the added complexity and failure modes must be taken into account.

Often the best understood and characterized components are the first components added as backups. Typical designs employ dual springs and dual pyrotechnics. Adding redundant drive springs for deployables is a confounding choice in a back-up component, because springs are exceptionally well understood components. Springs fail from overstress, corrosion, or because of inadequate manufacture, and are employed in an enormous number of applications. As a result they are well understood and can be made to last for billions of cycles (as in intake and exhaust valve springs in internal combustion engines).

A counter argument to this Misconception is that a redundant spring compensates for the probability of failure due to improper design and or improper manufacture. If we cannot make a single spring work reliably, what reason do we have to believe that we can make a mechanism that uses two or more springs work reliably?

If system reliability is the goal then why not design for reliability rather than for redundancy. If the reliability of a mechanism component item (spring, pyrotechnic, bearing, or other mechanism component) is known, then substantial information derived from either failed or thoroughly tested parts should be available to substantiate all of the failure modes. Instead of adding another component (of unacceptable or unknown reliability), why not simply remove the sources of failure of the item under consideration to be doubled up with the intent of providing redundancy? Given the high burden of achieving true redundancy, and the cost of proving the reliability of a more complex redundant system, consider the question: "How do I achieve reliability?"

It is not at all clear that in practice adding a back-up spring must increase reliability. Although it may increase reliability, it may well decrease reliability, while simultaneously increasing cost, weight and volume.

Misconception #5: Successfully Operating A Mechanism Once Indicates High Reliability

Successfully operating a mechanism once only indicates a reliability of 0.5 with a confidence level of 50%. In other words with one test you are 50% sure that the next operation will be a success. What if the next test is flight?

Table 1 lists how testing is related to reliability and confidence level. It is only valid if there have been no failures in the samples tested.

Table 1. Number of No Failure Tests versus Reliability and Confidence (Ref. 1)

RELIABILITY	CONFIDENCE LEVEL					
	50.0%	70.0%	90.0%	99.0%	99.5%	99.9%
0.999999	693,147	1,203,972	2,302,584	4,605,168	5,298,315	6,907,752
0.99999	6,931	12,039	23,025	46,049	52,981	69,074
0.99999	693	1,203	2,301	4,603	5,296	6,904
0.99999	69	120	229	458	527	687
0.99998	34	60	114	228	262	342
0.99997	23	40	76	151	174	227
0.99996	17	29	56	113	130	169
0.99995	14	23	45	90	103	135
0.99994	11	19	37	74	86	112
0.99993	10	17	32	63	73	95
0.99992	8	14	28	55	64	83
0.99991	7	13	24	49	56	73
0.99990	3	5	10	21	24	31
0.99989	2	3	6	13	15	19
0.99988	1	2	5	9	10	14
0.99987	1	2	3	7	8	10

Even testing a mechanism 10 times will not meet the reliability requirements of most missions. It is not until a mechanism is tested 100 to 1,000 times (with success) that the reliability is high enough with confidence that it may be added to the greater vehicle. Clearly, having a design that is inexpensively tested is of considerable value. Conversely, a mechanism that cannot be tested or will not be tested should be viewed with alarm.

One test of a mechanism is often better than none since many mechanisms upon initial testing have a reliability of zero. The most tragic aerospace mechanism failure in 1999 illustrates this best:

"Air Force Space Command released today the results of its investigation into the failure of the Inertial Upper Stage, or IUS, during a Titan IVB launch on April 9, 1999, from Cape Canaveral Air Station, Fla. The booster and IUS were carrying a Defense Support Program satellite. The Accident Investigation Board, convened by the commander of AFSPC, determined that the mission failed because of an incomplete separation of IUS Stage 1 from IUS Stage 2 caused when an interstage electrical connector plug failed to release. Investigators concluded that thermal wrap and tape applied to the harness and connector prevented the proper disconnection of the plug." (Ref. 5)

For DSP, their testing occurred on the flight. The cost of the spacecraft and launch vehicle is estimated to exceed \$650 million.

The Galileo High Gain Antenna (HGA) failure resulted in reduced mission performance. The cause of the failure is summarized below.

The failure of the Galileo HGA was not detectable with in-air testing, due to the choice of titanium for the pin material. Since this material reacts with oxygen so readily, the in-air friction change, due to the damaged surfaces, was not detectable because the higher friction coefficient (0.35 vs. 0.05) was not high enough to be restrained by the 90 degree included angle of the receptacles. As a result more deployment tests in air would only have worn out the drive system. Also, the vacuum deployment test of the flight antenna did not exhibit this failure mode due to the lack of pin and socket relative motion [due to shipment of the antenna

assembly]. The test conditions were not adequate for finding this problem indicating that just a functional test in vacuum is not always appropriate. (Ref. 8)

Based on this assessment, one functional test in thermal vacuum was not adequate to fully screen the antenna for the most important failure mode. Additional tests including investigation of the wear behavior on the mechanism may have been able to predict this problem.

In the bathtub failure rate model the so-called "infant mortality period" of performance is another reason to test well beyond several cycles. In many terrestrial mechanisms, the behavior of a mechanism during the first few uses is significantly different than the behavior in the next several thousand. Instead of failing on the first attempt, failure may happen in the second, third or fourth cycle. Mechanisms that are expected to seriously degrade within several tests should be reconsidered: the infant mortality period may overlap with the wear-out period, the useful life period may not exist.

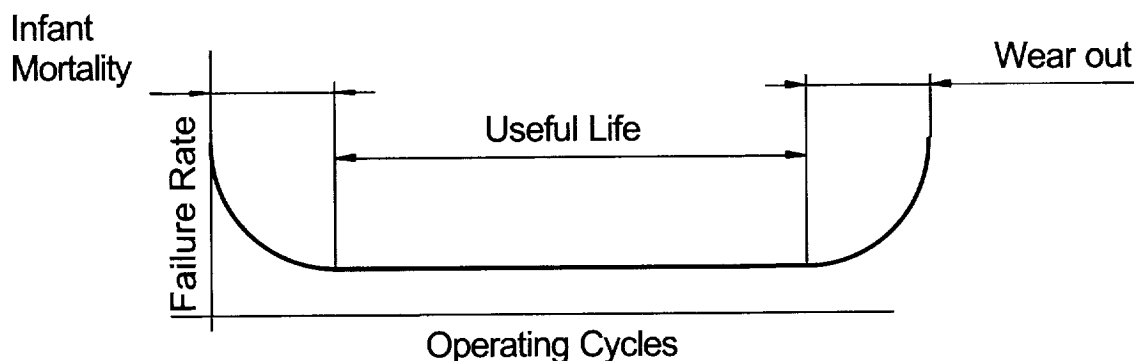


Figure 4. Bathtub Failure Rate

The Space Shuttle at the ignition event demonstrates efforts to test hardware prior to flight. The Space Shuttle Main Engines (SSMEs) are ignited and gimbaled prior to ignition of the solid rocket boosters (SRBs). This allows automated testing to determine if the engines are operating properly. If they are not, they can be turned off and the entire mission aborted. This capacity to test flight hardware decreases the possibility of catastrophic failure. Unfortunately this is not the case for the SRBs. Despite years of operational experience and well-developed inspection requirements, on several occasions it has taken until the firing of the SSMEs one second prior to lift-off to detect potentially catastrophic failure modes. The capacity to test may have saved lives and a \$2 billion vehicle on several occasions.

Conclusions

- The reliability of a mechanism or a collection of mechanisms can only be known with confidence through exhaustive testing.
- Instead of adding a back-up component (attempting redundancy) it may be easier to simply test the single string item and remove its failure modes, thus attaining the desired system reliability.
- Increasing forces of driving components of a mechanism does not necessarily increase the reliability of the mechanism as a whole.
- There is no relationship between the cost of a test and its necessity.
- Adding back-up components often only increases complexity without affecting reliability.
- Just because a mechanism worked well the first time does not indicate high reliability.
- Without comprehensive testing of a mechanism, estimates of reliability are purely speculative.

References

1. Conley, Peter (Editor). Space Vehicle Mechanisms: Elements Of Successful Design, John Wiley & Sons, 1998
2. Mosher, Todd, et al. Evaluating Small Satellites: Is the risk worth it?, Proceedings of the 13th Annual AIAA/USU Conference on Small Satellites, August 23-26, 1999.
3. Auer, Werner. Reliability and Testing, 30th Aerospace Mechanisms Symposium, NASA Conference Publication 3328, May 1996, Held in Hampton Virginia May 15-17, 1996.
4. Augustine, Norman R. Augustine's Laws, Penguin Books, 1983
5. Air Force Space Command News Service, DSP-19 Accident Investigation Board Release Results, August 17, 1999
6. Johnston, M. D., P. B. Esposito, V. Alwar, S. W. Demcak, E. J. Graat, R. A. Mase. Mars Global Surveyor Aerobraking At Mars, AAS-98-112, Jet Propulsion Laboratory, California Institute of Technology, Pasadena, CA, 1998
7. Lyons, D. T. Mars Global Surveyor: Aerobraking with a Broken Wing, AAS/AIAA Astrodynamics Specialist Conference, AAS-97-618, Sun Valley, ID, August 4-7, 1997.
8. Johnson, Michael R., The Galileo High Antenna Deployment Anomaly, Cleveland, Ohio, USA, May, 1994.
9. Spacecraft Losses Make Insurers Wary, Space News, p 3, 7 February, 2000

Lessons Learned from the Manufacturing and Test of the International Space Station Drive Lock Assembly

Curtis Allmon*

Abstract

The Drive Lock Assembly (DLA) is a part of the Solar Alpha Rotary Joint (SARJ) and functions as the primary drive for the joint and doubles as a locking mechanism (see Figure 1). The SARJ DLA (SDLA) consists of over 200 piece parts that when fully assembled, form a unique and complex mechanism. Through the course of manufacturing and test, many interesting problems were encountered, producing the need for a significant amount of troubleshooting, and in the end, leading to many important lessons learned. The focus of the paper will be these lessons learned, however, in order to familiarize the reader with the assembly, some time will be spent addressing the main design features and the design evolution.

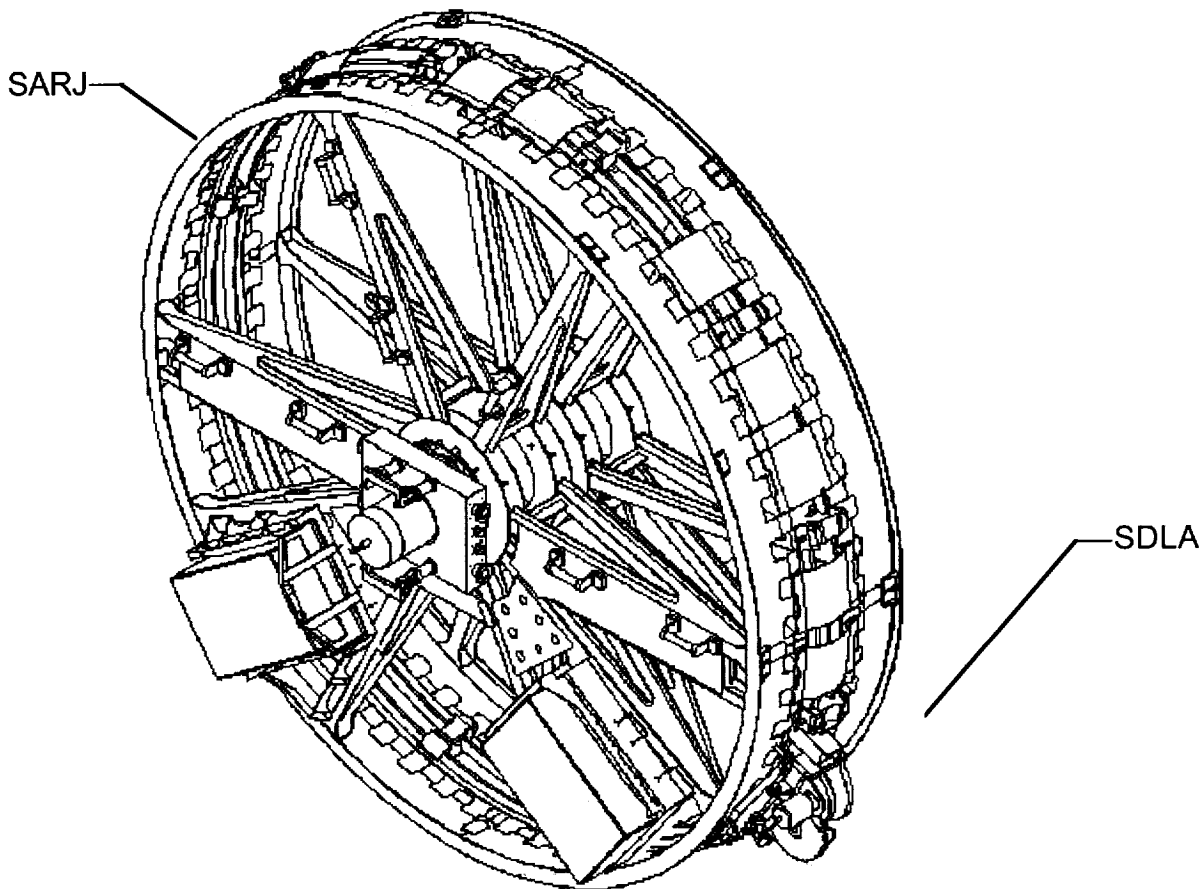


Figure 1: Solar Array Alpha Joint (SARJ)

* Lockheed Martin Space Systems Company, Sunnyvale, CA

Introduction

The International Space Station will be, when completed, the largest structure ever assembled in space. The Space Station will among other things include 8 solar arrays (4 port and 4 starboard) that will provide power to the station. To maximize efficiency of the individual solar cells, the arrays must be constantly repositioned relative to the station. This repositioning is achieved through the use of two rotary joints, the Alpha and Beta joints (see Ref. [1] for more information on the Beta joint). The Alpha joint is the larger of the two joints and is rotated by means of the DLA. Both rotary joints (port and starboard) have a primary and redundant DLA. The primary function of the DLA is to rotate the SARJ and its secondary purpose is to accurately lock the joint at specific locations to allow astronaut travel to the outer portions of the station. A similar type of design called the Thermal Radiator Rotary Joint (TRRJ) Drive Lock Assembly (TDLA) is used to rotate the smaller Radiator joint. A majority of the parts are the same, however, there is no Guide Assembly as the mating gear is much smaller and a fixed position is acceptable (4 bolts rigidly fix the TDLA to the TRRJ while the two Guide Assemblies allow the SDLA to move relative to the SARJ structure). The focus of this paper will be on the SSDLAs but a majority of the lessons learned stemmed from both units.

Design Features

The DLA consists of several significant subassemblies (Figure 2), each with a specific function:

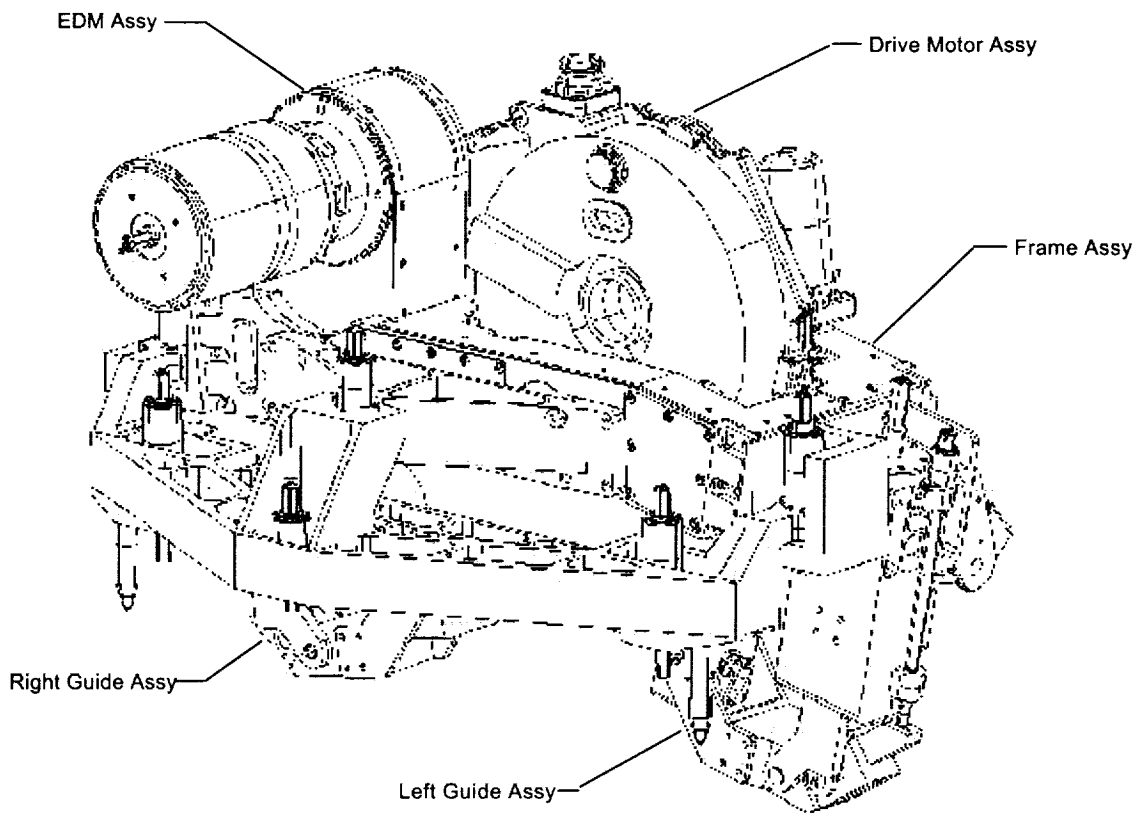


Figure 2: SARJ Drive Lock Assembly

The Engage/Disengage mechanism (EDM) (Figure 3) is a stepper motor-driven four-bar linkage that rotates the motor between its 3 main positions (Figure 4): Drive (Pinion teeth engaged), Neutral (neither Lock or Pinion engaged and within a specific band defined as neutral), and Locked (Lock rack engaged). The other two positions of the EDM are Locked and Over-center (same as the locked position except the mechanism

has traveled over-center), and In-Between (somewhere in between the other positions). The position of the EDM is monitored by limit switches. Both the pinion and lock have mechanical fuses that react the load during a tooth-to-tooth crash between the pinion or lock and the mating bull gear. The stepper motor is made up of two windings for redundancy. During final manufacturing operations, this mechanism is adjusted to ensure five degrees of over-center on each side.

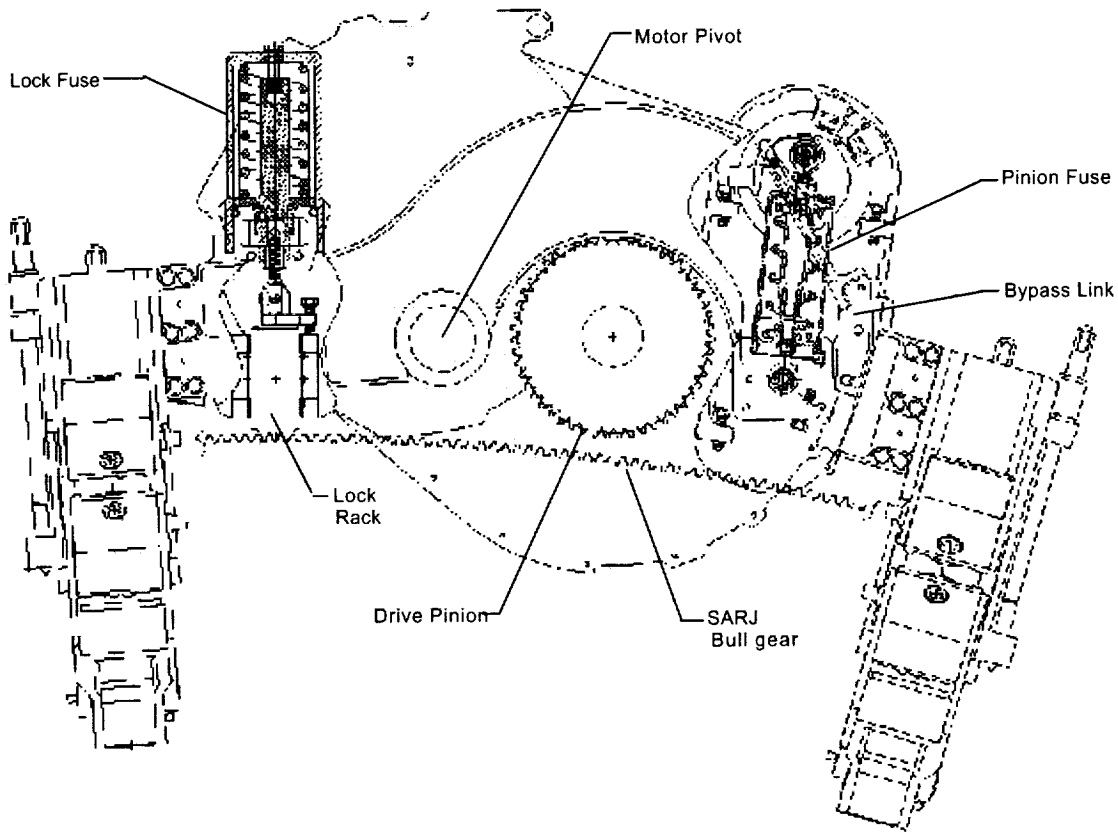


Figure 3: Engage-Disengage Mechanism

Difficulties encountered during design included configuration of assembly during launch and method of securing adjustable fasteners.

During launch, the mechanism must be preloaded in some fashion to prevent rotation of the gear train and avoid damaging the output gear. The TDLA has a rigid mount so the pinion would be susceptible to damage if the EDM shifted position during launch. The SDLA is positioned away from the race ring during launch, removing the possibility of interference between the pinion and the bull gear and allowing the mechanism to be positioned over-center during launch. The original plan for restraining the TDLA mechanism during launch was to rely on the stepper motor detent torque. It was later realized that the detent torque was not capable of restraining the estimated 1335 N (300 lb) delivered to the stepper motor by the mass of the drive motor. A trade study was initiated and an Extra-Vehicular Activity (EVA) operated pip pin design was selected. This design added an extra EVA operation but removed the need for an added mechanism.

The EDM, due to the significant number of piece parts, undergoes a series of adjustments to ensure adequate backlash, sufficient over-center capability, and reliable telemetry. These adjustments are made with standard bolts and once adjusted, get staked in place. The original design used an epoxy material but

concerns arose about its capability during thermal extremes so the design was revised to include locking nuts as a more positive locking feature.

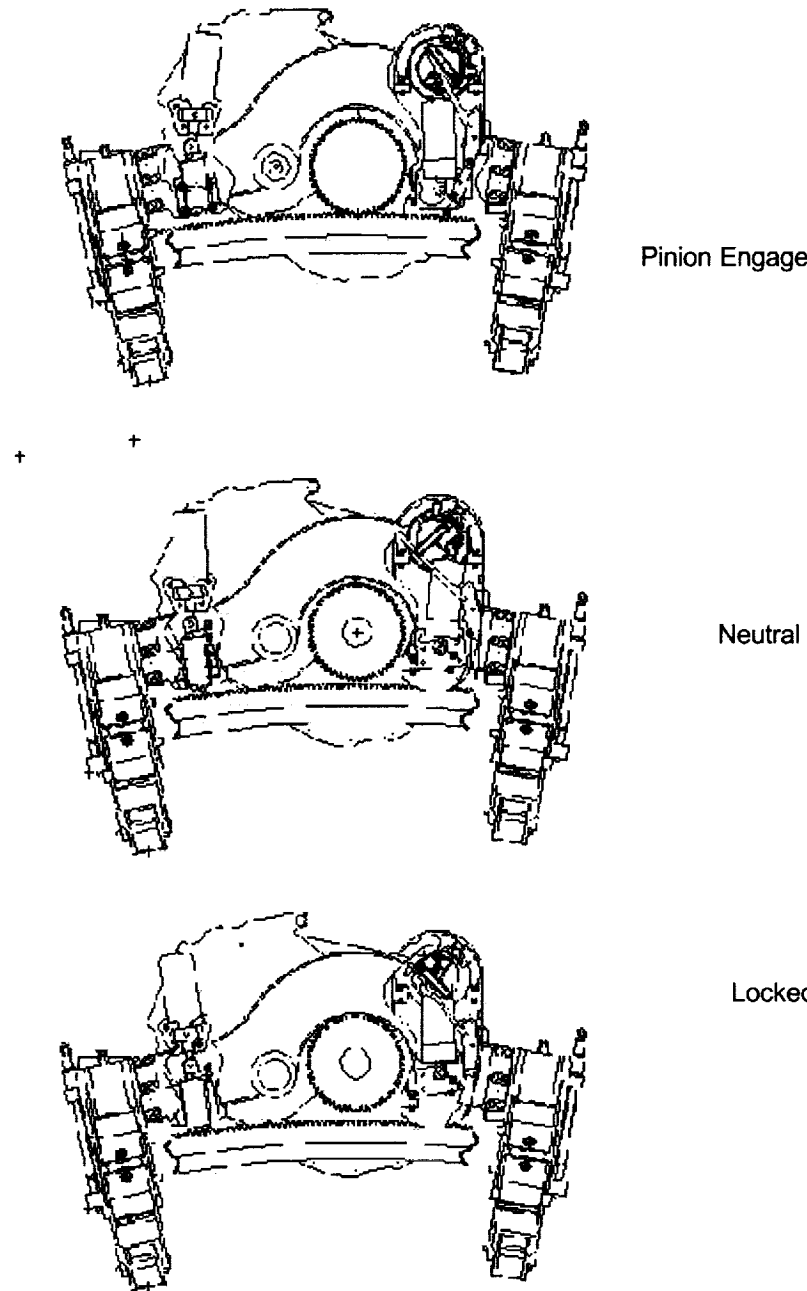


Figure 4: EDM Positions

The Motor Assembly (Figure 5) consists of a two-phase brushless DC motor pressed into an aluminum housing with a commutating resolver packaged inboard. An internal gear train produces a high mechanical advantage. The rotating shafts turn about pairs of duplex bearings with one side fixed and the opposite side allowed to float axially to accommodate any thermal distortions. The output pinion is crowned and has both its tip and root relieved.

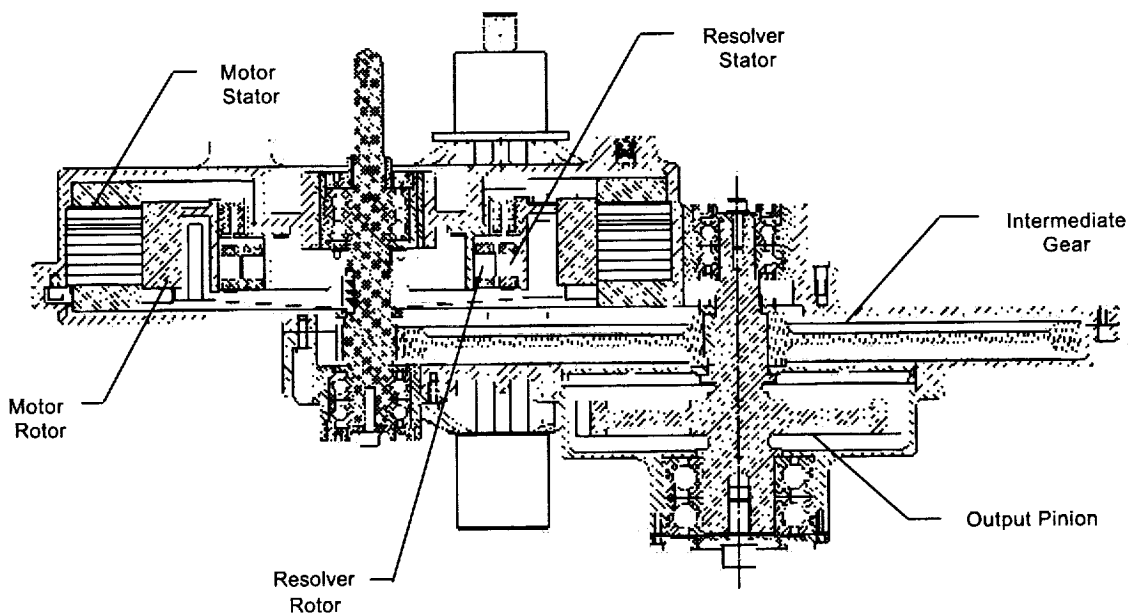


Figure 5: Motor Assembly

Early design challenges included selection of the optimum bearing preload, control of lubrication between intermediate gears, and ability to minimize resolver error voltage. Bearing preload was set high enough to prevent gapping during launch but low enough to avoid life impacts. Braycote 601 was used as a lubricant between the intermediate gear mesh with a large enough quantity to allow the formation of a grease dam to prevent loss of lubrication. A method of static resolver alignment (with respect to the motor) was devised to allow alignment to within 5-degree positional error (99.6% electrical efficiency).

Left and Right Guide Assemblies (Figure 6) each consist of 3 bearings that seat themselves on the SARJ bull gear, allowing the pinion to closely track the SARJ bull gear. Due to the large size of the bull gear (pitch diameter of 3.289 m), and the importance of maintaining a tight backlash, a rigid mount of the DLA to the SARJ structure was bypassed and instead the guide assemblies were implemented to allow the DLA to closely track the race ring and keep the backlash within tolerance by floating the DLA. The launch configuration of the DLA is different than the on-orbit position as a result of loading of the DLA during launch. The bearing assemblies (followers) are therefore not engaged during launch but require a series of EVA operations to allow repositioning into an on-orbit position (Figure 7). Preload of the bearings against the race ring is achieved by the compression of belleville washers using the main drawbolt and controlled with a hard stop. Calibration for the preload setting is performed at a component level using strain gages. Challenges included ensuring proper preload of the followers against the race ring and determination of an efficient method to reconfigure from launch to an on-orbit position.

Preload is attained by compressing belleville washers a preset amount with the EVA drawbolt. The tolerances on the desirable preload were tight enough to require use of an extra fine thread on the drawbolt. Turning the drawbolt produces motion of the follower block, which rotates the arm; once the block bottoms out on the hard stop, the bellevilles are loaded. With a standard thread, repeatability on the preload would not be attainable.

In order to avoid damage to the bearing assemblies during launch, the DLA is launched with the follower bearings removed from the race ring. This creates the need for several EVA operations to reconfigure the unit to its on-orbit position. This is achieved through the rotation of several EVA bolts that rotate the arm in two different axis.

The Frame Assembly is the primary structure for the DLA and is designed to react launch and on-orbit loading.

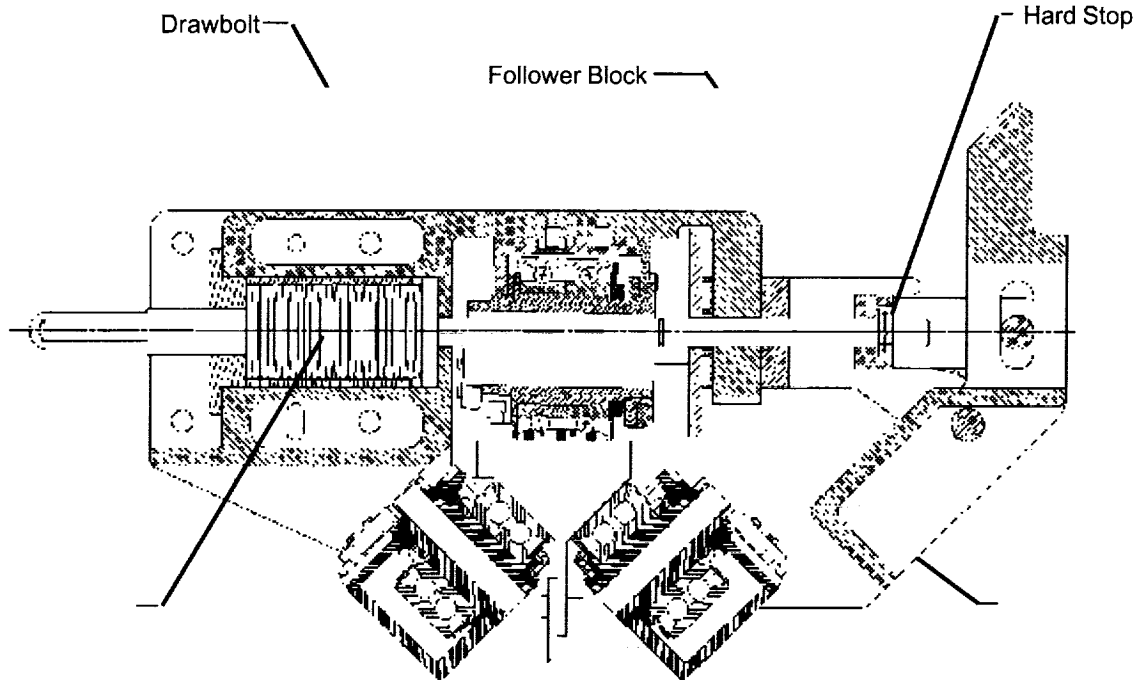


Figure 6: Guide Assembly Cross section

Design Evolution

The DLA went through a significant number of changes as the design progressed into what it is today. The early design did not consider such issues as Tooth Crashes, Gear ratcheting, Pinion crowning, and Microgravity.

A tooth crash (Figure 8) is a phenomenon in which the mating gears arrive at a tip-to-tip contact that prevents engagement of the teeth. This can occur both with the pinion and the lock rack. The original design allowed for no soft spring or fuse to react the loading and instead the loading during this event went directly into the mechanism. In order to guard the mechanism from unnecessary loading and more importantly, protect the gear teeth from damage, a mechanical fuse was introduced into the design on both the pinion and lock sides, which once adjusted, would react the loading from the tooth crash. Converting the four-bar design into a spring-loaded four bar also created a much more reliable design, as it became less sensitive to link length variability brought about by manufacturing tolerances, initial setup, and thermal distortions.

Gear ratcheting might occur if the DLA were to stall during a high speed command or if an externally applied load were encountered that tended to drive the pinion out of engagement. Typically the load from the fuse would be sufficient to react this, however, this reaction spring was designed soft enough to allow compression during a tooth crash so a large enough load would compress the spring and allow the gear to ratchet about the mating gear. A hard stop was added to the design that prevented full disengagement of the pinion and would subsequently be rotated out of the way to allow motor rotation to a neutral or lock position during an EDM command.

The need for pinion crowning was realized once an analysis on the alignment of the DLA pinion relative to the bull gear was completed. The existing design allowed the edge of a pinion tooth to directly contact the face of the mating tooth, producing high contact stresses and resulting in early surface failure of the pinion. The crowning of the teeth removed the portion of material from the pinion that contacted the face of the bull gear.

The baseline resolver did not have the accuracy required to meet microgravity requirements. A new resolver with better accuracy was installed into the unit.

1) Launch Configuration

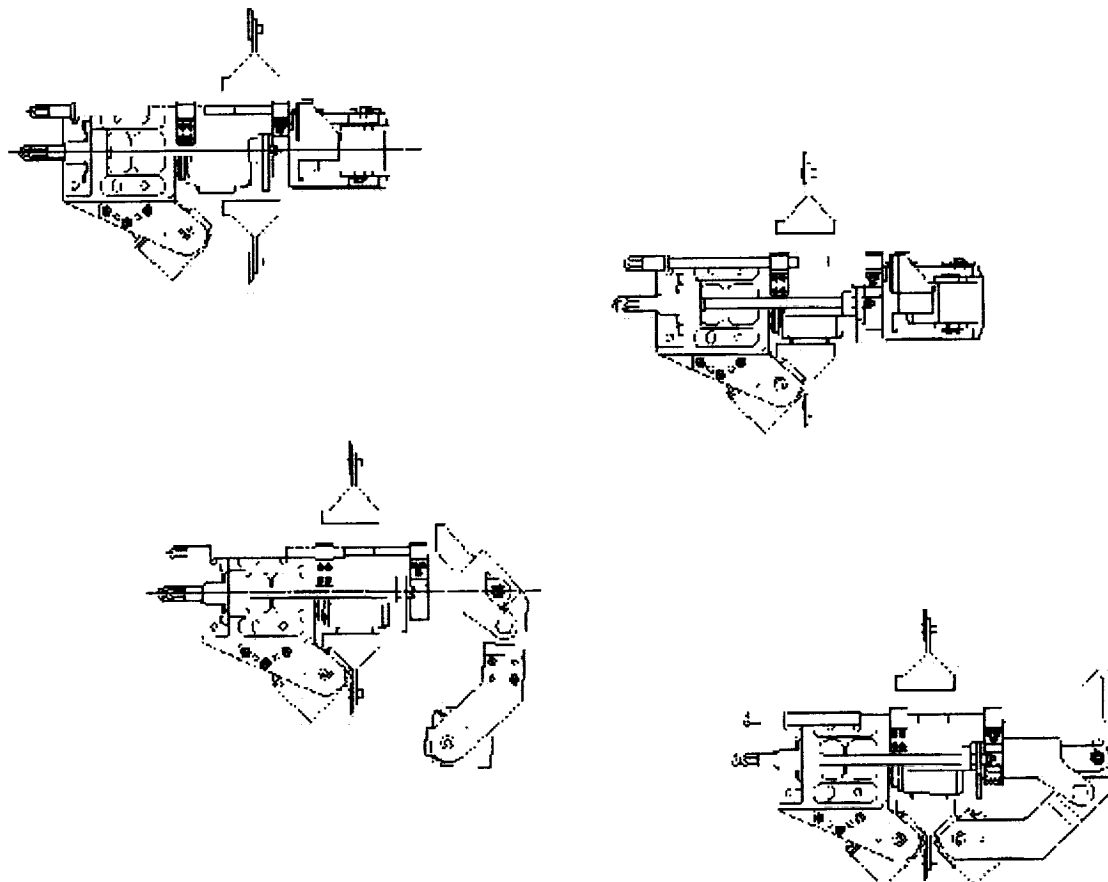


Figure 7: Steps to reposition DLA

Tooth Crash

SDLA Pinion Gear

Normal Engagement

SDLA Pinion Gear

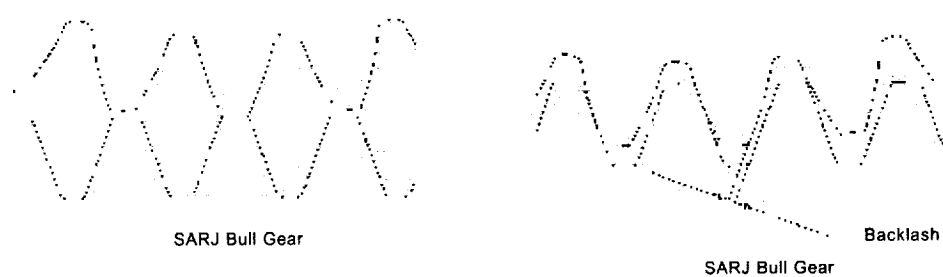


Figure 8: Tooth Crash versus Normal Engagement

Lessons Learned

During the course of manufacturing and test, a significant number of Lessons Learned were accumulated. The following is a description of some of these issues and the lesson(s) learned.

1) Pinion tip and root relief & material change

The DLA output pinion was submitted to a life test with the STA unit (Development SARJ unit with a flight like race ring). This life test used a flight pinion but was powered using Support Test Equipment (STE) with a direct drive off of the pinion shaft. The test was started with a pinion gear made of nitrided, gold plated 15-5PH that had crowned teeth. The STA bull gear likewise was made of 15-5ph and was nitrided. The test was initiated with a goal of demonstrating a 13-year life (75,972 revolutions). The rate of rotation was accelerated from normal operation to guarantee a timely completion. Normal SARJ rotational rate is approximately 0.011 rev/min. During the test, the rate was increased 186 times to 2.05 rev/min.

After only 1500 revolutions, a significant quantity of debris was discovered uniformly spread across the circumference of the SARJ bull gear. The test was stopped and the debris examined. A large portion of the debris was found to be coming from the Magnetic Particle Brake made out of Delrin. The hardware was cleaned and testing was resumed. After 4500 revolutions, testing was again stopped due to a significant increase in the formation of debris. The debris was this time found to be in part, coming from the pinion gear. The pinion gear was inspected and the tips were found to contain patches where the nitride had been blown off. A thorough investigation was initiated to determine the cause of the generation of debris. Many items were considered including gear alignment, backlash, and STE affects and their effects on the gear's surface-to-surface contact. It was discovered that if the contact patch were not controlled, the tips of the pinion were susceptible to contact with the mating gear, introducing high contact stresses and allowing chipping of the case hardened surface. Every attempt to control the contact patch including maintaining a tight backlash had seemingly been made. Although the prescribed center distance was maintained, the manufacturing errors would require running at a much larger backlash. This was considered as a potential fix, however, this would have reduced the load carrying capabilities at the high torque (stall) condition.

The root cause was determined to be manufacturing error on the SARJ race ring (as a result of its size) and lack of center distance control. After a significant amount of detailed modeling and analysis, it was decided that the introduction of a tip and root relief would eliminate the interference. By incorporating a tip and root relief (Figure 9), the contact patch was better controlled and opportunities for high contact stresses were eliminated.

The base material was reviewed as well due to the chipping discovered on a majority of the pinion teeth. The pinion, when nitrided, forms a hardened outer shell. This casing when submitted to high contact stresses due to point loading is susceptible to chipping. A change from the 15-5 Stainless nitrided pinion to a 13-8 Stainless would eliminate the need for a case hardening process as the 13-8 has a potential for higher strength. By eliminating the case, the pinion will be more forgiving to manufacturing error and failure modes will be less catastrophic since no case would be present to flake off.

The decision was made to replace the 15-5 output pinion with a tip and root relieved 13-8 pinion and restart the test. The test was subsequently completed with no significant debris created from the meshing of the gears. All flight units now use the 13-8 pinions.

This tip and root relief is not being recommended for new designs as it may increase wear due to the reduced contact ratio. It was, however, in this case a viable design alternative.

Lessons:

- *Pay attention to manufacturing techniques on large gear assemblies.*
- *Use of through-hardened 13-8 as a base material is a reasonable design alternative.*

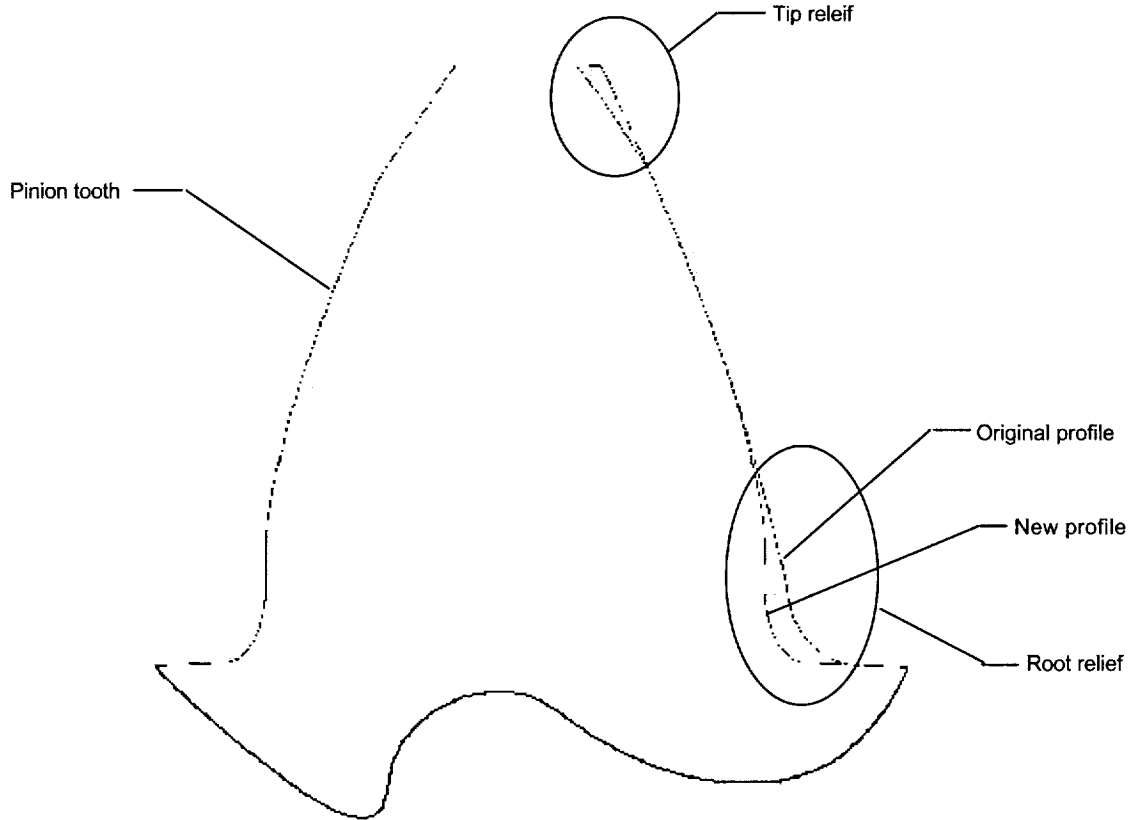


Figure 9: Modified pinion profile

2) Stepper Kickback

During Thermal Vacuum testing on one of the DLA's, a command was given to drive the unit into the locked position and then stop. The command was sent and the destination was reached. The power was then cut and immediately after the telemetry indicating position of the mechanism changed states, implying that the mechanism had moved. Troubleshooting commenced and it was later discovered that the mechanism had indeed shifted as there was no evidence of a switch failure (this was the primary suspect since only one of the two switches changed states). This was of particular concern as the mechanism could be backdriven just enough to be near going back over-center but not enough to trigger the telemetry.

The stepper motor used in the EDM is a redundantly wound 2-phase brushless dc motor. It consists of 12 poles, has a 77:1 gear reducer, runs at a nominal rate of 8 Hz, and has a torque capability of 4882 N-m (300 in-lb, which includes a 70 percent reduction due to electrical efficiency loss, which is conservative).

It takes a particular number of steps to drive the mechanism from a neutral position to a locked position. In order to guarantee that the motor reaches its destination, the mechanism is "overdriven" by approx. 10 percent of the total required steps to reach the hardstop (a step command of 110 would be given for a destination 100 steps away). Once the mechanism reaches the hard stop, the remaining steps in the command continue to pulse the stepper against the stop. Once the step command ends, the stepper holds its position as the unit is still powered, and the software then cuts the power, allowing the mechanism to relax. If a significant enough force had been built up during the last pulse into the hard stop, this relaxation would force the mechanism in the opposite direction, away from the hardstop. This "relaxation" of the mechanism was never discussed prior to this event as it was believed that since the mechanism had gone

over-center, any resistive force would be overcome by the preloaded spring in the lock fuse (especially on the TDLA that has a significantly larger preload (5338 N (1200 lb) vs. 2002 N (450 lb)).

During the troubleshooting test runs, it was discovered that there was a relationship between the time elapsed on the last pulse into the hardstop at the time of end of command and the amount of "kickback" experienced. The amount of potential energy existing at the mid-point of the pulse far outweighed the energy at the very beginning or very end. Since the number of steps required to reach the hard stop is not exactly the same for each run (the tolerance stack is too large to try and control this), the amount of kickback from run to run can vary significantly. This phenomenon was first discovered during hot testing but can be repeated at ambient as well. It was also found that the amount of kickback was related to the amount of current driving the stepper. Higher current meant potential for greater kickback.

At this point several options were considered for preventing or at least reducing the kickback. The option chosen was a zero-velocity command that allowed any energy that had been built up to bleed off prior to powering down and significantly reduce the kickback.

Lesson:

- *Use of a stepper motor in certain applications may require additional commands in order to avoid kickback.*

3) Resolver Interference

During the cold cycle of Thermal Vacuum testing on a particular unit, the motor failed to rotate after several revolutions. The chamber was brought back up to ambient and the motor was inspected with a video probe through a removable port on the motor housing. The formation of some debris was discovered and the motor was subsequently opened up. Further investigation revealed indications of an internal interference within one of the motor components. This particular vendor assembly contained a part that was not reflected in the control drawing as it was added late in the design phase. It prevented axial misalignment in one direction and was significant enough to stall the motor during cold testing. The problem was resolved by modifying the mating hardware to ensure sufficient axial growth due to thermal conditions.

Lesson:

- *Ensure Control drawings accurately reflect condition of hardware.*

4) Lock binding

The DLA, once fully tested at a component level, is installed onto the SARJ and undergoes system-level testing. During the cold cycle of system thermal vacuum testing (-42.7°C (-45°F)), an attempt to lock the DLA failed. After several attempts to get the DLA to respond failed, the chamber was brought back to ambient and additional troubleshooting was performed. The unit responded nominally at ambient and useful data was gathered during the return to ambient as the EDM was intentionally left in the failed position (commanded to lock) and at approximately -23°C (-9°F), the lock popped into position. Since the data collected pointed to a thermal issue, the areas of tight fits on the EDM mechanism came under close scrutiny.

The unit was removed from the SARJ and underwent a thorough inspection. It was discovered that the bypass link on the EDM came in contact with a tie-wrap attached to the frame as the mechanism cycled through the neutral position. It was thought that at ambient the cable was more compliant and would compress enough to allow the mechanism to push through the interference, but at cold the cable would stiffen and prevent mechanism motion. The harness was then re-routed to ensure sufficient clearances at temperature and the unit was returned to thermal conditions at a component level. During this retest, the failure was repeated, revealing either an inadequate repair or a misidentification of the root cause.

The unit was then submitted to a second thermal retest but this time with additional instrumentation added to aid with the troubleshooting. With the aid of a video camera installed inside the chamber, it was revealed that travel of the lock rack was inconsistent, jumpy, and would occasionally fail to engage and would instead send the mechanism reeling backward once power was cut. With this additional information, the main area of concern became the fit between the lock rack and its mating bushings. The unit was partially disassembled to allow inspection of the lock rack and bushings. It was found after measuring these items on the Coordinate Measuring Machine that the lock rack was oversized. At this point, several other units were disassembled to allow inspection of the same parts and similar results were obtained. A review of the history of these particular parts revealed a discrepancy in which the parts had been inadvertently completely nitrided instead of just the gear teeth. The lock rack was originally designed with a 15-5 base material that had nitrided teeth and was gold plated, while the mating bushings were aluminum coated with a Molydisulfide lubrication. This added layer of nitride was enough to throw the part out of its acceptable tolerance range. It was assumed at the time that the part still met print and it was given a use-as-is disposition.

The parts were subsequently installed into their respective units and nothing out of the ordinary was detected as the assembly is performed at ambient and the parts slipped through their mating bushings without incident. It wasn't until the unit was exposed to the cold environment at a system level that a problem became apparent. Why the interference wasn't discovered during component-level testing became an issue. A review of the component test data revealed an increase in power drawn by the stepper motor during cold testing. At first glance, this bulge in the curve wasn't noticeable and could only be truly seen if the test data was blown up. Since the unit reached its destination, a closer review of the test data was never performed.

The lock fuse on the TDLA is significantly stronger and it is believed that though the same interference existed on this unit, it never experienced the failure because its stiffer spring forced the lock though its mating bushings. Inspection of the lock racks and bushings on all units revealed a significant amount of wear. This also reveals why the failure didn't occur right away. It took the additional debris created by the interference to bind the lock.

Instead of reworking the lock rack to a smaller OD, new bushings were installed into the unit with a larger ID. The unit was then testing again at temperature and operated nominally. All units were then retrofitted with the new bushings.

Lessons:

- *Don't jump to conclusions. Consider all possible failure modes when reviewing a test anomaly. Everyone wants a quick solution.*
- *Consider harness routing and create keep out zones around operational mechanisms.*
- *Consider added thickness due to surface finishes.*
- *Use as much instrumentation as possible when troubleshooting anomalies.*

5) False Telemetry

It had been a known fact that one of the follower bearings would gap (push away from the race ring) during a tooth crash (Figure 10). It was not well understood, however, the impacts this gapping would have on the unit during system-level testing and more specifically, how it would impact the telemetry.

During an ambient system level test run, the DLA telemetry indicated successful lock engagement while it was discovered that the unit was actually in a tooth crash. The lock is not engaged when in a tooth crash so either the limit switches were malfunctioning or another phenomenon was occurring. It was revealed that as a result of the tooth crash, the follower bearing gapped significantly enough to allow actuation of the limit switches. Since this tooth crash condition was not tested for at the component level, it wasn't discovered until system-level testing. Additionally, the component test orients the unit in a more upright position

(Figure 11) while during system-level testing, the unit is positioned more horizontally. Both setups require off-loading, and the affects of the off-loading will influence the test. The offload systems in this case were completely different. This variance in off-loading methods coupled with the change in the gravity vector allowed an issue to go undetected until system-level testing.

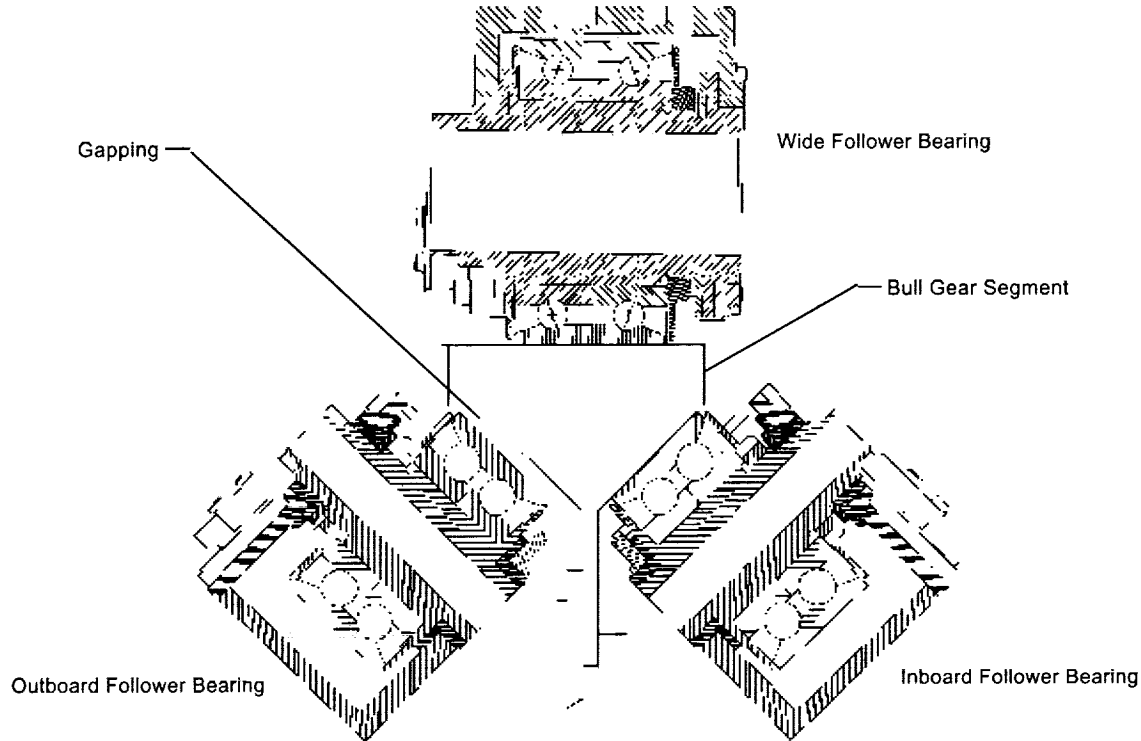


Figure 10: Follower Bearing Gapping

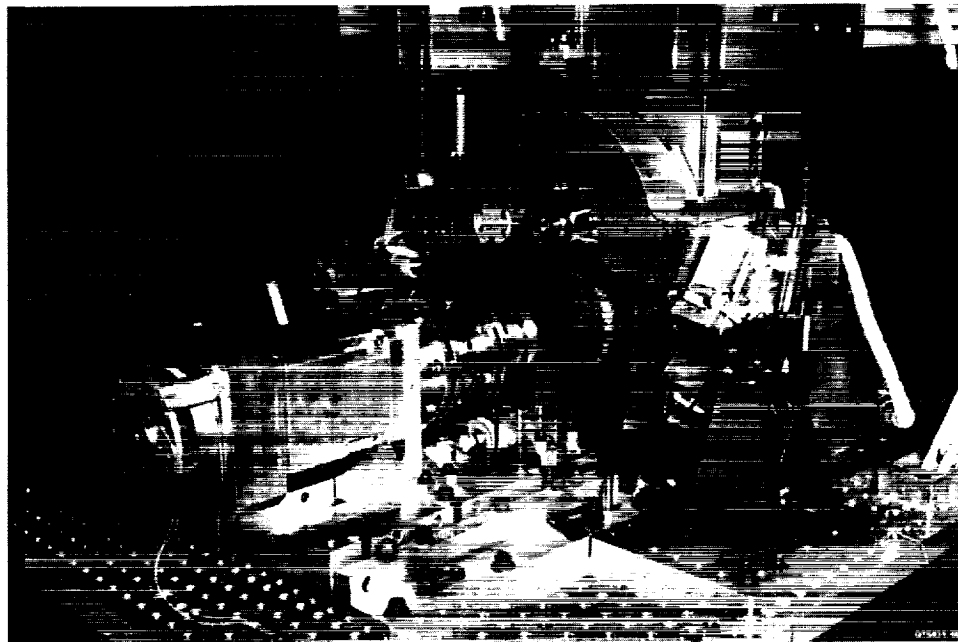


Figure11: DLA on component STE with off-loading system

After more testing and analysis, it was discovered that controlling the amount of gapping could be achieved by altering the bearing preload against the race ring. An increase in preload meant a decrease in gapping. Unfortunately, an increase in preload also meant less life out of the bearing. In the end, an optimum preload was reached that prevented this false telemetry from occurring and also allowed the bearing to stay within the required life constraints.

Lesson:

- Ensure impacts of component-level issues at a system level are well understood.
- Test the component in its flight orientation.
- If possible, test the component under all known system-level configurations.

Other lessons learned throughout the program

- *The importance of precise off-loading.* As touched on in Lesson 5 and discovered during additional system-level testing, a high priority should be given to ensuring an accurate off-loading system during ground testing. After one particular run during system-level testing, a groove was discovered on the SARJ race ring that ran a majority of the way around the unit. After a thorough review of the hardware, it was determined that the fixed DLA follower bearing was not flush with its mating surface during operation and caused the formation of the groove by applying a point load on the race ring. The offload setup was reviewed and was found to be biasing the unit in one direction and was not truly off-loading the mechanism. The method of off-loading was subsequently modified and the fixed follower bearing tracked flush with its mating surface.
- *Picture taking during manufacturing.* A person can never take too many.
- *Consideration of repairability during design.* None of us like to think our hardware will fail, but it happens.

Conclusion

The DLA is a unique and interesting assembly whose design has been refined through a rigorous test program. The problems encountered during this test program reveal the importance of test and also the impacts seemingly minor problems can have at the system level. A majority of the units have already been integrated into the next assembly hardware and have gone through system testing. The first of these units are currently scheduled to be launched in the Fall of 2000.

References

1. O'Brien, David. International Space Station Alpha's Bearing, Motor, and Roll Ring Module Developmental Testing and Results, Proceedings of the 28th Aerospace Mechanisms Symposium, 1994, pp 51-61.
2. Alchorn, Brendon. SARJ Pinion Life Test Report and Wear Analysis, LMSSC EM-02-ME-510, dated 5/6/98
3. McCully, Sean. TDLA Engage Disengage Mechanism Analysis, LMSSC EM-02-ME-422, dated 11/28/95
4. McCully, Sean. SDLA Pinion Alternate Material Review, LMSSC EM DLA-1121, dated 1/20/97

Development of an Automated Bolt Driver for the Space Station Truss Assembly

Richard Meinhold^{*} and Ken Seidner^{**}

Abstract

The Moog Space Station Bolt Motor Actuator (BMA) is a rotary actuator comprised of a brushless DC motor, controller, and 120V DC-DC power supply coupled to a four-pass planetary gear system and containing a manual override (MO) system. This paper discusses the new technologies developed and lessons learned during the BMA development. These include the use of a relatively new material, Pyrowear 675, a new Vapor Deposition coating, WC/C, and a hard-on-hard (HOH) worm drive system delivering 135.6 N•m (1200 in•lb) of torque (the primary focus of this paper).

Introduction

The BMA was a contract awarded by McDonnell Douglas Aerospace (now Boeing Aerospace, Huntington Beach) to Moog Inc. in December of 1995 for use on the International Space Station. The contract schedule detailed an 18 month start-to-finish program with one development unit, one Qual unit, and 20 "flight" units. Four of the flight units were slated for "next level assembly" Qualification. The BMA attaches to the motorized bolt assembly (MBA), which is produced by Boeing, and facilitates the actual structural connection and attachment interface load between the five truss elements inboard of the solar arrays, P3, P1, S0, S1 and S3. (P = Port, S = Starboard).

Several of the original BMA design aspects were modeled after the Moog Fluid Quick Disconnect (FQDC) program. The Moog FQDC enables the flow of liquid ammonia between the discrete sections of the International Space Station Thermal Management System. These dual-line, manually-actuated devices provide essentially zero-loss throughflow capability. Redundant seals are provided against leakage in both the mated and de-mated conditions, and the coupling is designed to limit spillage volume upon demating to less than one cubic centimeter. One FQDC item in particular that played a major role in the BMA design was a positive lock, no-backdrive device. This device allows nearly 100% of applied torque to pass from input to output and 0% torque to pass in reverse (from output to input). While not operating, the no-backdrive unit effectively uses a pin in a slot concept to prevent unanticipated rotary motion.

Unit Description

The BMA is a rotary actuator comprised of a brushless DC motor, controller, and 120V DC-DC power supply coupled to a four-pass planetary gear system. The motor runs at approximately 3400 rpm, which results in 4.1 rpm at the BMA output (a 25.4-mm 16/32 female spline) at the end of the 833:1 gear train. Dual input electrical connectors allow powered operation from either of two independent Bolt Bus Controllers (BBC's). The electrical connectors supply power (120VDC), direction logic signal, redundant heater current, redundant RTD based temperature feedback, and limit switch pigtail pass-through lines. The limit switches are part of a customer-controlled mating assembly. The RTD's are customer-supplied (Boeing Part Number 1F08041-1) and the heaters are Kapton®¹ encased, inconel element, thermal foil heaters supplying approximately 28 watts per circuit. These devices were needed to maintain the electronics at or above -42.8°C (-45°F) while on orbit.

The brushless DC controller and DC-DC power supply were totally contained inside the unit on two independent multi-layered circuit boards. The dual power line inputs were Y'd internal to the unit and opto isolated at the board level. All electronics were designated "S" class or equivalent and rated for

^{*} Moog Inc., Space Products Division, East Aurora, NY

^{**} The Boeing Company, Space Station Electronic Actuation Products, Huntington Beach, CA

-53.9°C (-65°F) operation or colder. All precautions were taken to minimize ESD susceptibility, including the incorporation of soft EMI gaskets at the side cover interfaces. The brushless motor was designed and built by Moog Inc. and had a 51mm (2.0 in) OD by ~15mm (.6 in) stack length. The motor is capable of providing more than 3 times the required torque, but is current clipped by the controller electronics at about 1.5 times the required torque.

Manual Override capability is supplied in the event of a power failure via a dual input, 10-mm (3/8 in), recess square drives. The dual input allows equal operation from two opposite sides of the BMA, meeting the requirement of a single unit to fit into one of four possible positions at the final level assembly in different orientations. The basic MO input of 50 rpm and up to 30.5 N•m (270 in•lb) of torque supply the same functionality at the BMA output as the powered main drive system. The effective gear ratio of the MO mechanism is 12.17:1. The MO utilized a unique worm drive arrangement to be able to function even with the motor through the third stage gear set jammed, and to meet the overall package size constraints.

While the maindrive is running, the MO drive is held stationary via a "no-back-drive" device. Similarly, while the MO runs, the main drive must remain stationary from the third stage planetary output (fourth stage sun gear) to the first stage input (motor shaft). There was insufficient cogging torque in the base motor design to guarantee no rotation would be allowed during MO operation. This deficiency was overcome by adding a passive magnetic "cogging" unit onto the top of the motor. The cogging unit supplies ~170 mN•m (24 in•oz) of torque statically, while only requiring 40 mA of driving force (or loss) during motor operation.

Summary of Lessons Learned

Though the originally proposed concept utilized design heritage gathered from Moog's program, several items used in the BMA design would require verification through development test before enough confidence could be gained to go to Qualification (Qual). Some items required new or unique designs and/or new material combinations that had not previously been used by any manufacturer. The bleeding edge became the cutting edge through the lessons learned as presented in this paper. These included the following items:

Package Size

The design requirement contained a rigid specification for package size. The actuator was required to fit into an existing C-channel truss structure, and the same actuator needed to fit four different locations. This constraint proved to be the major design driver. In order to obtain the specified speed and torque output within the power requirements, all available volume was utilized. Every item below was needed to make the overall design work, pushing the limits of current technology. The package weight was set at 4.5 kg (10.0 lb) max, with a 4.2 kg (9.3 lb) actual. The unit final design contained 1020 individual and over 300 unique parts.

Pyrowear®² 675 Gear Material

Originally, 440C and A286 were selected as the gear materials for the BMA. "Standard" commercial or military grade gear materials lacked the required corrosion resistance to meet space-level requirements. Plating or other surface protection could have been added to the standard materials to help them meet the corrosion resistance, but no combination found could handle the design contact stress. During the design phase, it was determined that the two selected materials may have galling problems, lacked the strength to obtain needed margins (in the case of A286), or were too brittle (in the case of full hard 440C) to survive the requirements. A relatively new material had recently been introduced by Carpenter Technologies that could answer all these issues. The material was a case hardenable stainless steel called Pyrowear® 675. It had similar corrosion resistance to 440C and answered the design strength, durability and corrosion issues. The only problem with the material was there was little to no information on heat treatment to obtain the needed 0.1 to 0.2 mm (0.004 to 0.008 inch) effective case depth. Also, all

aspects of basic machining relative to feeds, speeds and dimensional stability during heat treatment needed to be determined.

Hard-on-Hard Manual Override Worm Drive

In addition to the electromechanical actuation requirements, the BMA was also required to have a manual override input capability. Due to the multi-position final assembly requirement, the manual override interface needed to be accessible from two opposing sides (a spec requirement). The original input speed and torque requirements to the MO, to achieve same output speed and torque as the powered drive, were also very limited in selection due to the use of EVA standard interface tooling available at the start of the original contract. These factors, combined with the package size constraints, forced the use of a HOH worm drive to carry 113 N•m (1000 in•lb) output (at the worm gear) with a 50.8-mm (2.0 in) pitch diameter. The package did not have enough room to facilitate a sealed cavity in the area of the worm, preventing the use of an oil bath. Identifying a space-rated, low outgassing, -54°C (-65°F) to 71°C (160°F) operational range, high-pressure worm drive lubrication proved to be a major challenge for the program.

Brushless DC Motor and Controller

Again, due to package size and power consumption constraints, packaging a DC to DC power supply, a brushless 120 volt motor controller, and a brushless motor was a challenge. The major obstacle turned out to be lack of room to fit a resolver into the package. This forced the design to imbed an HED commutation board directly into the 50.8-mm (2.0 in) OD stator windings. The production methods used to accomplish this feat are interesting, but are not within the scope of this paper.

No-Back-drive Device

In order to interface the MO drive with the main drive, the worm gear discussed above was integrated at the OD of the planetary last pass ring gear. This required that during maindrive operation, the worm drive be positively locked to supply mechanical ground to the ring gear. Any motion allowed by the worm drive would limit the available output torque at the main drive. The FQDC program had developed a unique device that acted as a positive lock, single input, single output, bi-directional torque diode. For the BMA program, this unit was scaled down 25% in size, converted into a two input, single output device, with the potential of seeing 25% more torque. To handle the higher torque load, Pyrowear® 675 was also used extensively for this device.

Program Chronology and Illustrations:

Program Start	12/01/95
Preliminary Design Review	02/20/96
Detailed Design Review	10/22/96
Qual Test Start	08/28/97
Qual Test End	02/17/98
Delta Qual Start	08/17/98
Delta Qual End	09/08/98
First Production Unit Shipped	08/04/98
Last Production Unit Shipped	04/26/99

Figures 1 and 2 show the use location in the main ISS truss sections of the BMA Package, and Figures 3 and 4 illustrate the BMA itself.

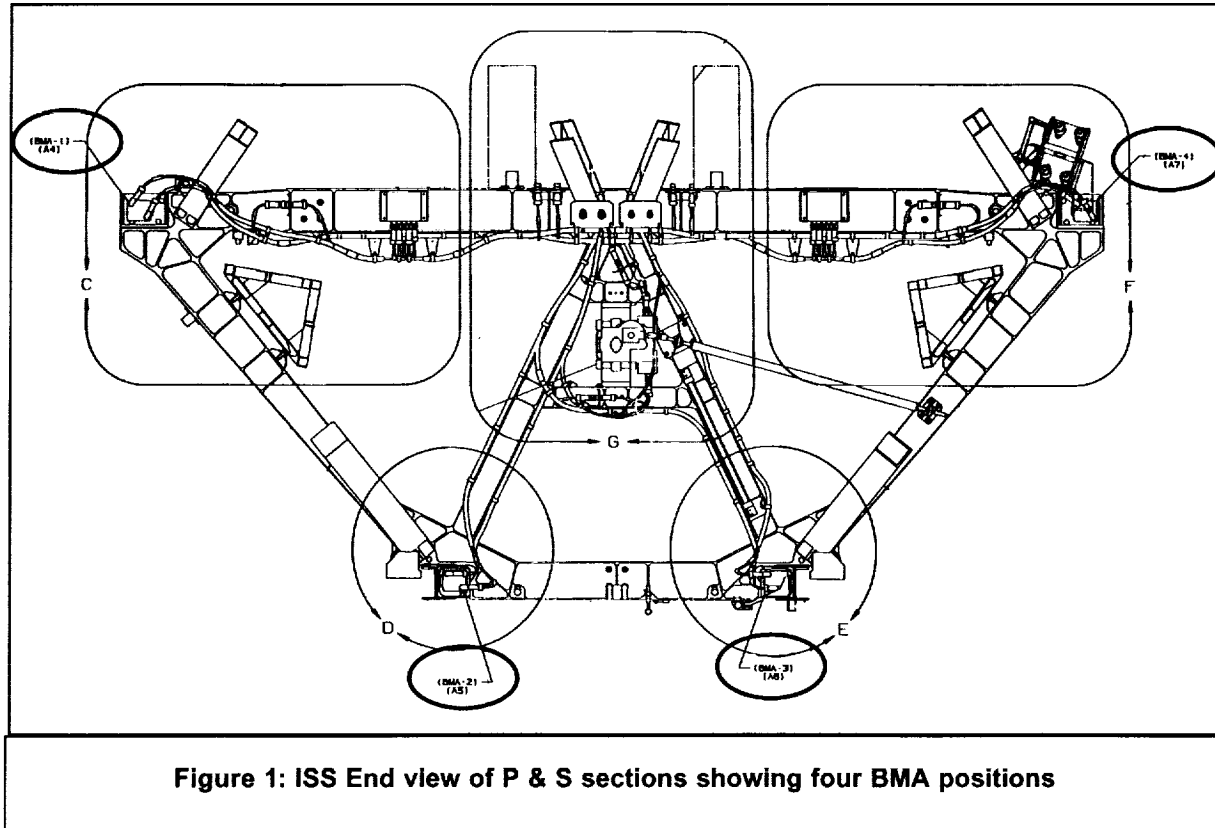


Figure 1: ISS End view of P & S sections showing four BMA positions

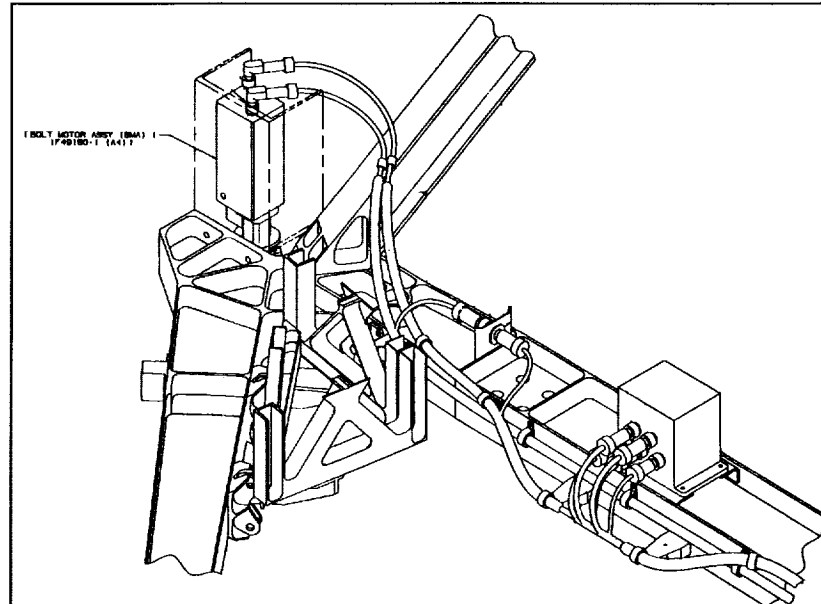


Figure 2: Truss Corner Detail showing one BMA position

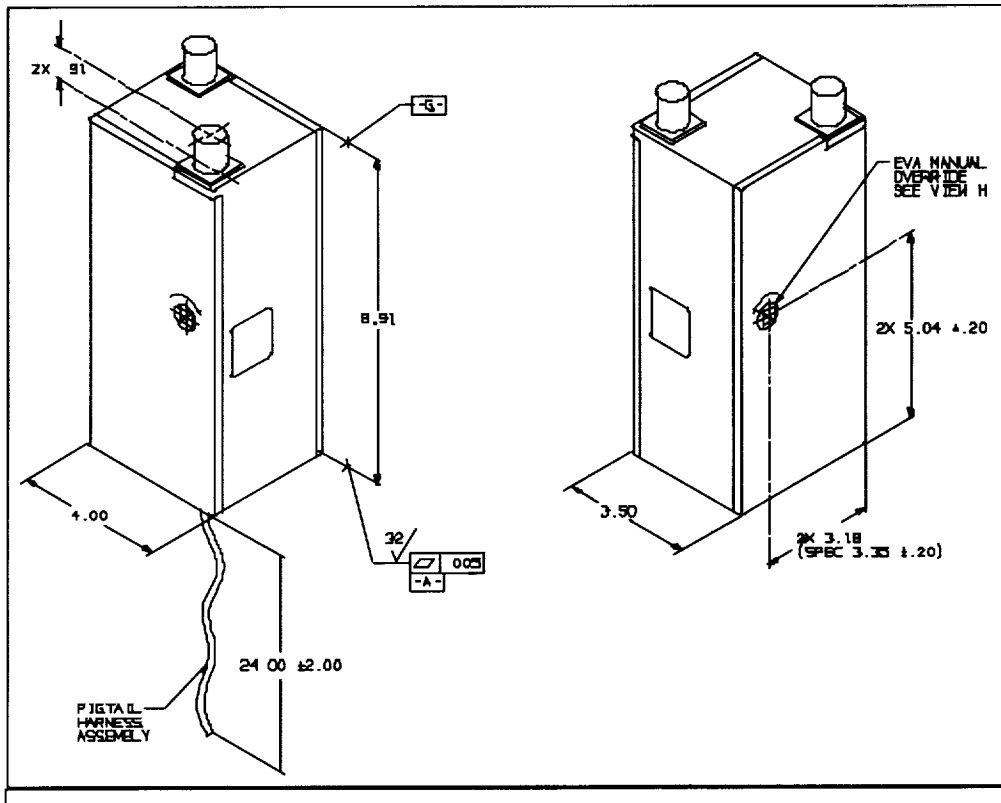


Figure 3: Overall BMA Dimensions (in Inches)

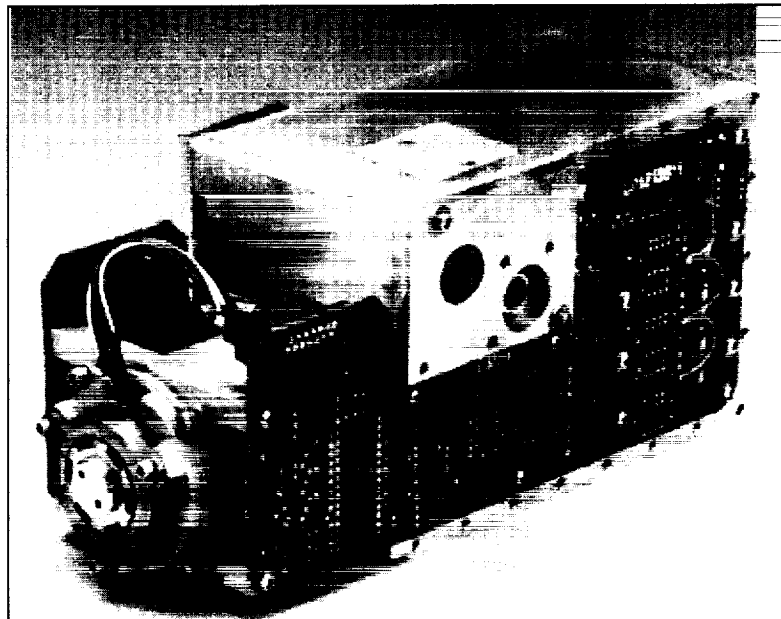


Figure 4: Photo of BMA with covers and some internal detail removed (Dev #1 Unit)

Lessons Learned

Pyrowear® 675, General Gear arrangement

All gearing in the BMA was made from Pyrowear® 675. The maindrive was a 4 pass planetary system with 48 diametrical Pitch (DP) gears and an 833:1 overall ratio (Figures 5 & 6). Stages 2, 3 and 4 were the same with the sun containing 16 teeth, planets 32 teeth and the ring gear 80 teeth, obtaining a 6:1 ratio for each 3 planet system. The MO gears were 24 DP with two spur passes before the worm shaft and had a 12.17:1 overall ratio. The worm set was a single helix, 33 tooth, 16 DP, Class C set. Because the center axis of the BMA relative to the unit outside dimensions was fixed in the specification, it was necessary to produce the last pass ring gear (at the ID) integral to the worm gear (at the OD). When running the MO, the last pass planetary set ran with the sun gear fixed, the ring gear as input and the carrier (or output spline) as output (also called a solar system). This last pass accounted for a 1:1.2 ratio. Thus, 113 N·m (1000 in·lb) input to the worm gear created 135.6 N·m (1200 in·lb) at the output. Also, the highest stressed member was the last pass sun gear which saw 22.6 N·m (200 in·lb) input for 135.6 N·m (1200 in·lb) output during both MO and maindrive operation. For this reason, the last pass gear face width was increased to 12.7 mm (0.5 in), while the other stages used a 6.35-mm (0.25-in) face width.

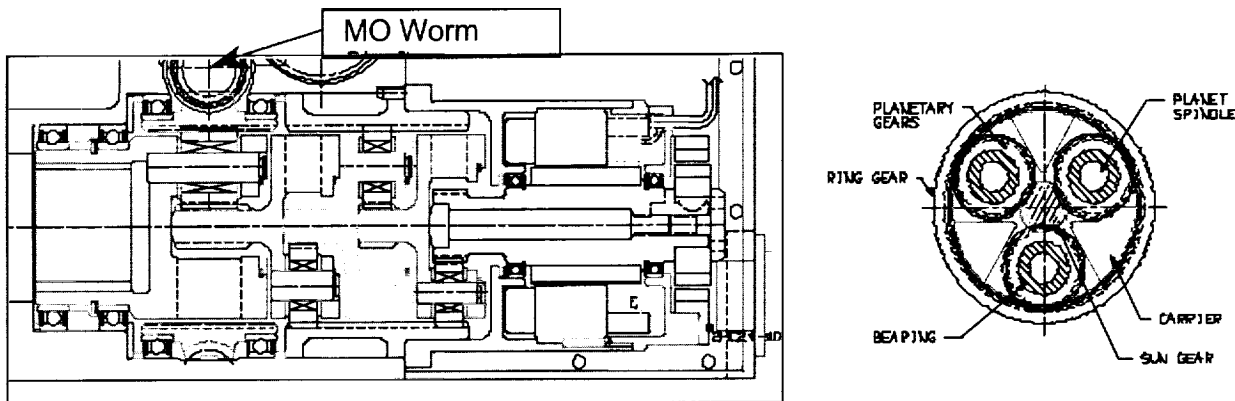


Figure 5: BMA Main Drive Gear Crossection

Gear Heat Treat

Pyrowear® 675 was a relatively new material in industry in 1996. Carpenter Technologies had developed basic material information (mechanical properties, basic heat treat, etc) but only had direct experience with 24 hour carburization cycles (equivalent to a 1 mm (0.040 in) effective case depth). In conversations with Carpenter, it was apparent that at least one major turbine engine manufacturer was using this material, but all data developed by them was deemed proprietary. Since the BMA program required a light case depth using fine pitched gearing, the detailed heat treat process needed to be developed through experimentation. Pyrowear® was selected because it had the same basic corrosion properties of 440C in its carburized state, would allow high surface hardness to carry significant contact stress, and obtain higher impact strength through its lower hardness, more ductile core. This last point was considered important since pitch diameter crosssections on the order of 0.9 mm (0.035 in) with full hard material would not allow for much energy absorption, should sudden starts or stops be encountered.

Pre-Ox

Pyrowear® 675 requires a pre-oxidation phase as a first step to carburization. The pre-ox cleans the surface of contaminants and prep's the surface for better carbon infiltration. Unfortunately, the pre-ox phase also effectively ablates (or oxidizes) the surface which results in a loss of material. Typically, a carburized material grows in net section. This did not prove to be a major problem for this program since there was no backlash requirement for the unit. A decrease in tooth thickness increased backlash and

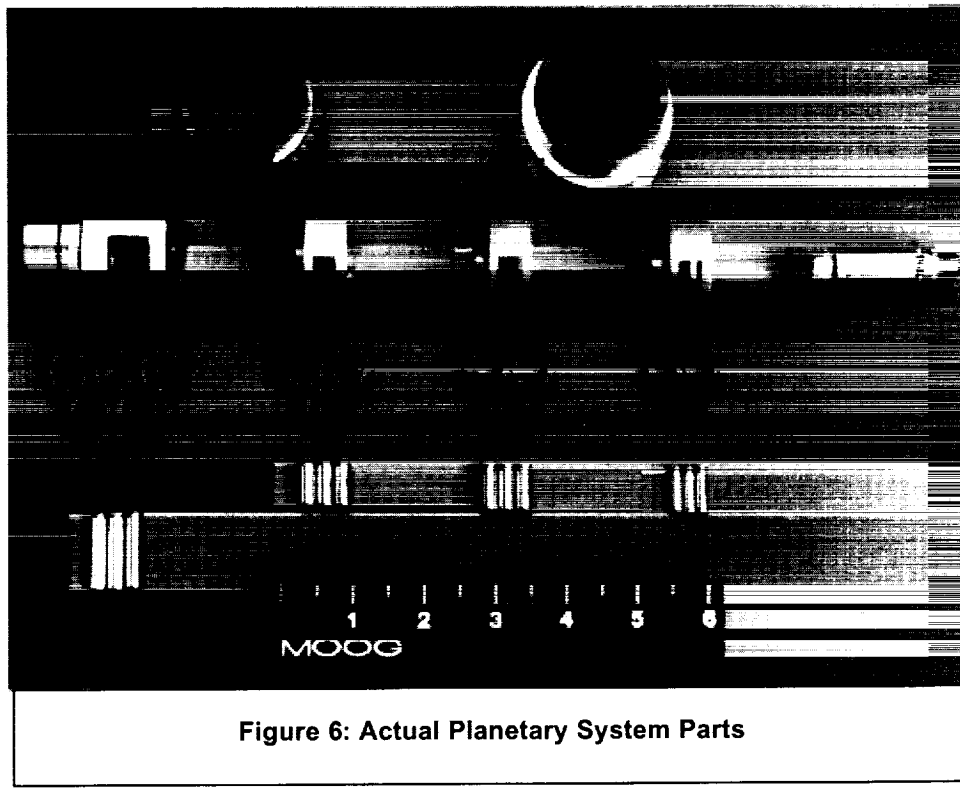


Figure 6: Actual Planetary System Parts

decreased bending strength slightly. The amount of material loss was dependent on the pre-ox temperature, which had an acceptable range of 954°C (1750°F) to 1010°C (1850°F) for 60 minutes. The low end of the range resulted in less material loss (on the order of 0.013 mm (0.0005 in) per surface) but also resulted in lower surface hardness due to less carbon infiltration during carburization. Conversely, the 1010°C level resulted in significant material loss (on the order of 0.04 mm (0.0015 in) per surface), but better final surface hardness. The scale created on the surface caused by the pre-ox phase was also very hard to remove after final temper. Due to the fine pitch gearing, the use of internal gears (ring gears) and the light case depth, post heat treat grinding was not an option. It was necessary to aluminum oxide grit blast all parts to remove this scale. Even then, the surface would not always clean up sufficiently to be continuous and smooth. One option suggested by Carpenter to obtain a better surface hardness with less oxidation was to grit blast the part prior to heat treat, and then use a lower pre-Ox temperature during processing. This avenue was investigated but showed little benefit in the final result. As a result of the increased backlash, no noise limit requirements, relatively slow rotational output and relatively low loads during the majority of its operational life, the BMA design was not affected by imperfect gear face geometry caused by oxidation scale.

Case Depth

After substantial experimentation with the heat treat process, a specific routine was developed to consistently achieve a high Rockwell hardness at the surface (R_c 58-62) and maintain an effective case depth of 0.1 to 0.2 mm (0.004 to 0.008 in) which was needed for most parts. A case depth of 0.3 to 0.4 mm (0.012 to 0.016 in) was used on the worm shaft and planet pins since finish grinding was required on these parts. The core hardness obtained was dependent on section thickness but was in the range of R_c 40-45. One key fact determined was that standard heat treat environments used during the austenitize step resulted in a significantly reduced surface hardness, and special precautions had to be taken to prevent this from happening. These precautions included decreasing the carburizing time and using a carbon atmosphere during austenitizing. Figure 7 shows a typical polished gear tooth mounted and etched with picral HCL. Two bands of micro hardness impressions are represented by the diamond shaped marks. The dark band along the perimeter of the tooth represents the zone of carbon infiltration

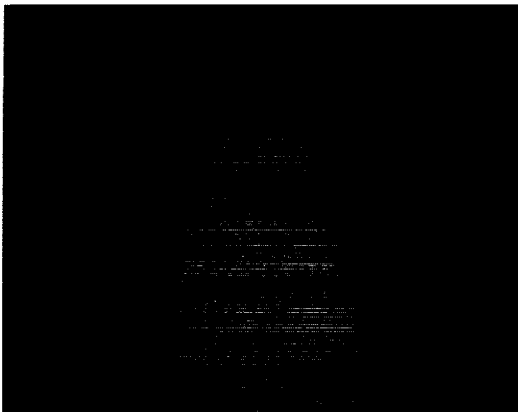


Figure 7: Post heat treat gear tooth crosssection



Figure 8: Tooth crosssection after 10x predicted Failure Load

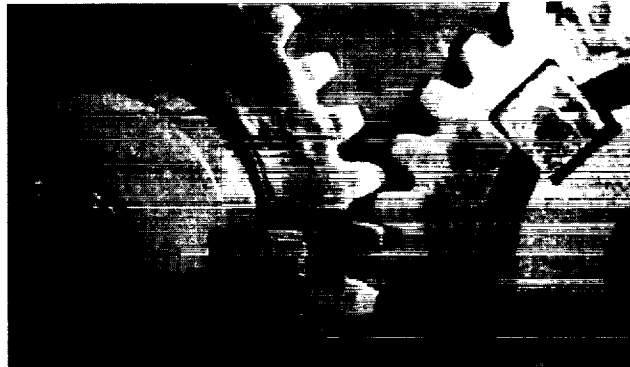
and approximates the case structure. The tooth width at the pitch line in this picture is approximately 0.8 mm (0.032 in).

Tooth Strength

Tooth strength (bending and case) was verified via static load testing. Static load testing was pertinent to this design since there would be less than 100 peak torque tooth hits during unit life, allowing yield to be used in margin calculations for design life. The planet gear contact ratio was estimated at 1.3 and a yield of 300 ksi was assumed based on a well defined relationship between material hardness and ultimate tensile strength (UTS). An Rc 60 material has an UTS of greater than 330 ksi, for which the yield was estimated as 90% of the UTS. The result of the static load testing showed no tooth deformation at 5 times the estimated single tooth in bending limit at yield. At approximately 10 times the single tooth bending limit, one gear failed at a fixture required square keyway notch (Figure 9). The tooth contact area, upon sectioning, showed some major deformation and a crack initiation (Figure 8). A supposition could be made that the crack and some or all of the deformation came about as a result of the failed keyway section and a non-centered gear-to-gear rotation. The failed gear had a fixed center and the other gear allowed rotational input. This exercise proved that the hand calculations for single tooth in bending strength, combined with the geometric contact ratio, were very conservative in a static case (by a factor of at least 5). It also showed the heat treat condition allowed adequate ductility while providing the required surface hardness to carry the contact stress. The final design last pass gear set was tested dynamically at 203 N·m (1800 in·lb) output for the equivalent of 100 torque tooth hits per tooth (on the sun gear) with no damage or degradation. The predicted lowest design margin of safety for a single tooth in bending at 203 N·m (1800 in·lb) based on hand calculations was 0.249. During the combination of actual Qual and Delta Qual testing, the Qual unit saw ~125% of the number of cycles originally slated for the complete Qual program. Also, one test equipment glitch resulted in a measured 271.2 N·m (2400 in·lb) output from the BMA for a very short duration during the Qual program. These statistics further prove the adequacy of the overall gear design, and the proof that Pyrowear® met the anticipated strength and durability required by this program.

Worm Drive

The worm drive ultimately proved to be the most challenging part of the BMA design. A great deal of effort was spent proving out the worm design early in the program. Early BMA designs considered many different alternatives to the MO drive system, but because the specification fixed the overall package size, and required one of a limited number of MO input torque and speed options, there were not many practical alternatives to consider. Any attempt to eliminate the worm drive concept added many additional parts and created a different set of unknowns. Again, because of envelope constraints, there



9: Planet gear static load test fixture

was insufficient room to package both the needed hard planetary ring gear, and desired (traditional) soft worm gear since they had to be contained on the same part. This drove the design to the "hard on hard" (HOH) approach. While there are most likely HOH worm designs that have been used in the past, they are not well documented. In addition, there was no way to incorporate any type of enclosed "gearbox" to retain a grease or oil bath at the worm surface. The temperature range of -54°C (-65°F) to 71°C (160°F) in a vacuum also severely limited the lubricant choices.

With these design parameters (they seemed more like road blocks in the beginning) in mind, the development program forged ahead. The following sections list the steps taken and details learned in chronological fashion.

Early Worm Efficiency and Strength

The first items that needed to be determined were knowing the practical static load limit and efficiency (static and dynamic) of the worm drive with no, or limited, lubrication. The original design would have used 440C for both the worm and worm gear and these were put on order as development units. In order to gain data as early as possible, several standard 303 Cres worms and Bronze worm gears (hard on soft, HOS) were ordered from Berg (#W24B37-D50, 24 DP, 3/8" Face Width, 50 Tooth, Alloy 464 Bronze gear, W24S-4D, double lead worm) as close to the actual BMA design as possible. Fixturing was created and initial static testing via hand driven input conducted. Static testing involved connecting the output of the worm system to ground (fixed) or a mag particle brake (slow dynamic). The results showed that the range of efficiencies obtained could be substantial.

Worm Gear Early Static Efficiency Test Data Results:

No lube – 12.5% (HOS)

High Pressure grease – 21-39% (HOS)

Everlube^{®3} 620C (molybdenum disulfide and graphite epoxy coating) – 45-56% (HOH)

Early in the program, at the selected MO ratio of 12.17:1 ratio and 28.2 N·m (250 in·lb) max input, the BMA had to generate 135.6 ± 20.3 N·m (1200 ± 180 in·lb) output. This fixed the required efficiency range of the MO system from 33.5 to 45.4 percent overall. Everlube[®] 620C appeared to meet or exceed this needed range repeatedly, though on the high side, with no other lubrication needed in the simplified test setup. Everlube[®] 620C was therefore selected as the baseline lubrication.

Worm gear ultimate strength was another issue that needed to be determined. Since a single enveloped worm system contains a gear that is not an extruded involute profile, it does not readily conform to single tooth in bending equations. Also, typical worm applications are used to transmit horsepower (at high speed and low torque) and are limited by the cooling capability of the lubricant. Because the basic worm design is dominated by sliding friction, heat generation can be a major failure mechanism. This

application (BMA) would be used to transmit significant torque over very short durations, with heat generation absorbed only by the thermal capacitance of the surrounding material. Research revealed no calculations were available to determine yield loads in worm drives, and a finite element analysis model for this complex geometry and contact situation would have been unruly. In order to gain confidence in design margins, a static ultimate load experiment was run similar to that for the planet gears above using the HOS sets. Again, testing showed that a factor of 5 existed above the basic single tooth in bending calculations with no apparent damage to the worm and some deformation of the soft gear. A factor of 8.3 existed in the HOS case before the teeth of the gear sheared off (using high-pressure lube, 52% final efficiency). A factor of 4 above the single tooth in bending on the gear was assumed as a conservative limit point for margin calculations for HOH systems, though a value of 5 or 6 may have also been acceptable.

Dynamic Testing

The next phase was to test the development unit using actual duty cycle inputs and outputs. Dynamic testing originally showed that the Everlube® 620C was stable and would maintain efficiency through repeated high torque cycles. The actual BMA duty cycle was 60 revs forward, noload (approx. 1.13-3.39 N•m (10-30 in•lb) in the fixture setup), 2 forward output revs ramping from 0 to 135.6 N•m (0 to 1200 in•lb), a partial revolution reverse ramping from 135.6 to 0 N•m (1200 to 0 in•lb), and 62 revs reverse, noload (again, 1.13-3.39 N•m (10-30 in•lb) in the fixture setup). When a significant number of low torque cycles were combined with the high torque ramps, the Everlube® began to show signs of distress, though it was felt that it would last for the required 16 MO Qual level cycles. This distress was most likely a result of low efficiency at noload. The lubrication properties of Everlube® actually improve with load, and the MO efficiency at noload was in the 20% range. This lower efficiency allowed more abrasion to take place which, combined with significant cycles, caused a reduction in the amount of Everlube® remaining in the worm contact zone.

During testing it was also noticed that some runs were much better than others from an efficiency standpoint, and once the efficiency dropped off, it would not return until the pieces were grit blasted and re-coated with Everlube®. After significant iterative testing, it was determined that Bracyote®⁶⁴ 601EF, which was used in all bearings and on the spur gear surfaces, had a detrimental impact on Everlube® in the sliding contact situation of the worm. A fresh worm set, carefully handled and installed into the BMA, would perform repeatedly with the expected peak torque efficiency of 40-50%. Placing one finger print of Bracyote® on the surface of the worm, and carefully installing it into the unit so as not to further contaminate the piece would result in a rapid reduction, and then degradation, of the worm set efficiency.

Since there was no practical way to prevent exposure of Bracyote® to Everlube® in this design, and there was insufficient time and resources to obtain a new grease for the bearings and gears and then prove it compatible with Everlube®, a search for a new worm lubrication method was undertaken.

WC/C Coating

A search for hard and/or lubricous coatings that could be used over the system temperature range, in a vacuum, with low outgassing, compatible with all materials in the BMA, and applied below the 315°C (600°F) tempering temperature of the Pyrowear® was undertaken. A potential solution was found at Balzers Tool Coating, Inc., (Amherst, NY) through use of a new vapor deposition coating called Tungsten Carbide, Carbon (WC/C). This coating was applied 1-4 microns thick at less than 260°C (500°F) and obtained an R_c 68 hardness. The base product reportedly had a coefficient of friction against dry steel of 0.15 to 0.30. If run against itself, the frictional values roughly halved. It did have an advertised break-in period before obtaining the lower frictional values.

Worm and worm gear pieces were sent to Balzers and coated with WC/C. It was immediately apparent that the relatively short break-in period advertised would be a significant factor in using this product. If high load was applied at the beginning of life, the WC/C coating would remove itself from the surfaces through abrasive wear. If the load were gradually increased and decreased in succeeding increments, with cool down periods in between and periodic cleaning and re-greasing with Braycote® 601EF, the system would stabilize at a 38 to 42 percent overall efficiency. The worm surfaces, once broke-in would have a mirror smooth finish, and the efficiency would be almost flat over the load ramp range. This turned out to be the best of all worlds for the BMA design, and was selected as the base BMA design.

Low Temp, Low Torque Noise

Because the BMA used a relatively coarse worm, an input torque ripple (oscillation) was always evident as the worm picked up a new gear tooth (and was less efficient) and that tooth passed through the center of the worm helix (most efficient point).

During Qual level testing at

-54°C (-65°F), it was occasionally noticed that the low load peak-to-peak input torque requirement would increase substantially, moving from an average torque of about 1.7 N•m (15 in•lb) to an average of as much as 3.4 N•m (30 in•lb) (Figure 10). This did not appear to be a problem at that time as there was no direct requirement on how low, "low" torque needed to be. However, on two occasions during Qual level testing, equipment problems resulted in a test stoppage during a MO performance test at the end of the forward ramp or at the beginning of the reverse ramp. Each time the test was reset and re-run from the beginning, repeating the 60 forward revs with no reverse revs placed on the unit. On both occasions, the forward ramp efficiency inexplicably dropped to below the required 33.5% minimum. When the unit was

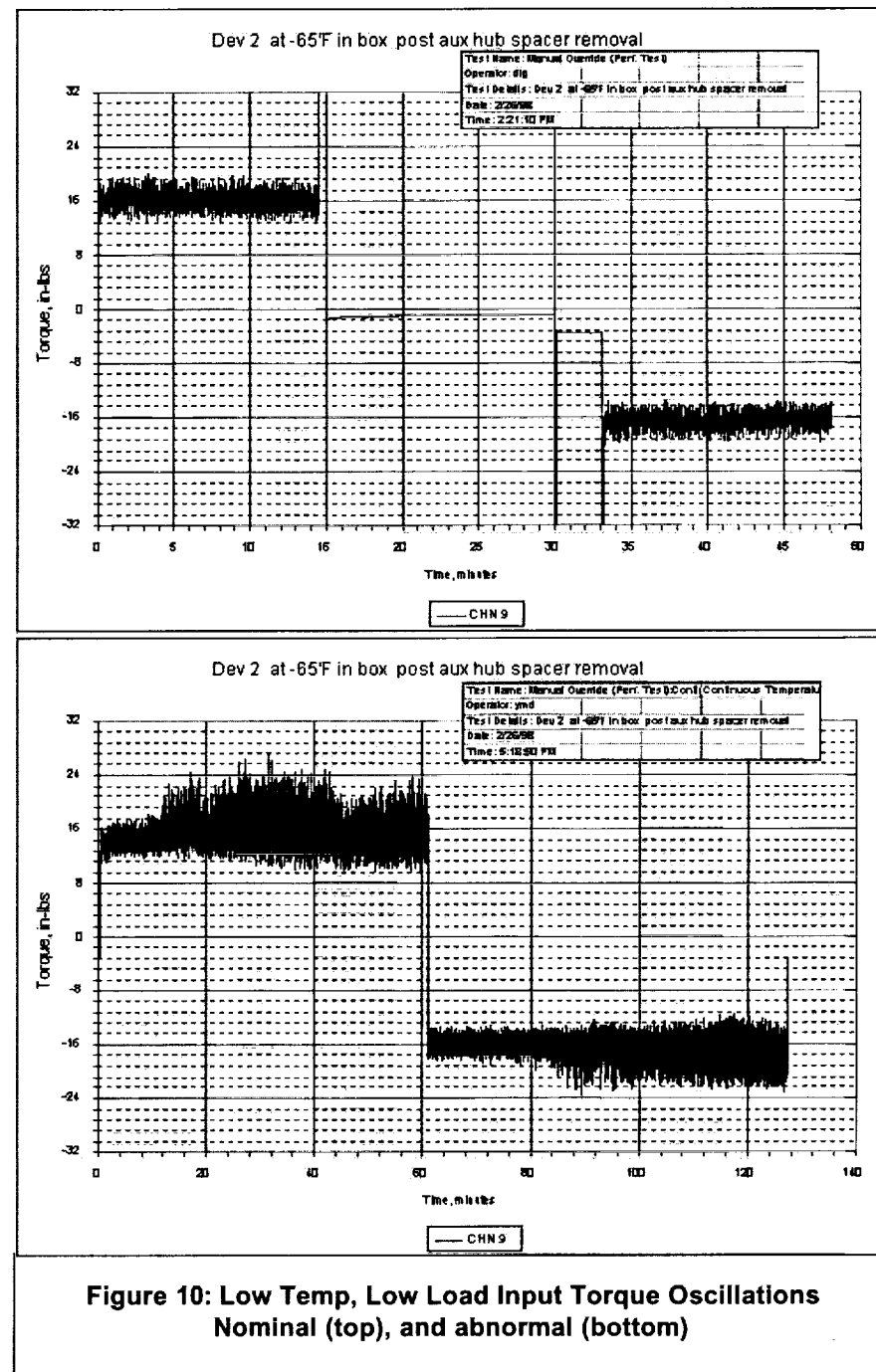


Figure 10: Low Temp, Low Load Input Torque Oscillations Nominal (top), and abnormal (bottom)

returned to room temperature or taken to high temperature, the efficiency would be exactly as expected from previous runs (no problem indicated). If the unit was again returned to -54°C (-65°F), the torque ramp efficiency would return to normal.

After review of all previous data, it was decided that the low and high torque MO issues were related, though they were previously thought to be two separate issues. This phenomena caused the program to complete the main drive Qualification, and then trouble shoot the MO issue. A freshly assembled and greased unit would run 3 mate-demate MO cycles at -54°C without issue and show good low load input torque and high load ramp efficiency. Repeatedly, on the fourth cycle, the unit would begin to show steadily higher input torque at no load. When the direction was reversed, the low load torque would start low and steadily increase in peak to peak oscillation and average. Each cycle would show a higher average start torque until the noise was sustained across the whole 30 minute test (60 revs at 4 rpm = 15 minutes each direction). Even more quizzical was that periodically, the noise would suddenly drop off significantly for some time, and then return. In addition, the forward ramp would show lower and lower (and more erratic) efficiency. When ever the unit was brought up to room temp or higher, the unit would perform nominally (both low and high load), suggesting that no problems were present and showing there was no damage to the worm surface.

An extended investigation ensued. Several suspect areas were found that might explain the reason for the torque loss through the unit. Chief among them were the several sets of uncaged needle bearings used in the MO mechanism. These bearings were selected as uncaged for load or availability reasons. Several gear and body bores contained light press fits with these needle bearings, which had aluminum bronze washers on either side. It was found that these bearings had a tendency to "walk" at cold temperature. One theory was that the Braycote® 601EF, which had a viscosity two orders of magnitude higher at -54°C than at 20°C, caused a slight drag only at cold on the lesser loaded end of the needle set. This drag caused a skew in the needles that meant they were no longer parallel to the axis of the shaft they were riding on. This forced the resultant load on the needle set to also be skewed, setting up a driving force in the bearing press fit direction. The combination of this driving force, the normal bearing rotation, and a load in direction perpendicular to the shaft axis, caused the bearing to move from its original assembly location. At room temp and above, there was insufficient drag from the grease to generate a needle skew, and thus no bearing movement would take place. The theory at the time also assumed that in the forward direction, the bearing would tend to drive the needle bearing one way, while reverse direction would force it the opposite way. Also, if the bearing had moved completely to one side during low load, it could be envisioned that high torque at low temp could cause the bearing to jam heavily against it's mating washer, accounting for the significant loss at high torque. While most of the above theories were proven as fact, there were two pieces of the puzzle that just did not fit.

First, there was the occasional sudden reduction of the large peak to peak torque oscillations at average low load input torque, which could not be explained by the needle bearing shift theory. Second, the amount of torque loss (and thus energy dissipation) during the high torque ramps did not correspond to the damage seen in the aluminum bronze washers, which tended to be noticeable but not significant. It is still suspected that these factors, while not the major players, did contribute to the problem.

In the final analysis, it was deduced that the onset of the "torque blooming" could be controlled by the amount of Braycote® placed in the worm interface. This was somewhat perplexing as the Braycote® was originally applied as a slight corrosion protection and a "nice to have". It was originally anticipated that the WC/C could have worked by itself due to its low friction nature, but was never tested early on without grease applied. In the end, it appears the Braycote® 601EF, which is a light grease and is not capable of carrying a high load, was a significant parameter in the lubrication equation. The Braycote® apparently allowed the sliding mechanism of the worm drive to work freely at low load, and added to the lubrication picture during the high load ramp. The lack of Braycote® in the interface during torque blooming reduced the efficiency of the system, but did not cause the WC/C to fail. The occasional reductions in torque noise were most likely caused by globs of grease coming back into action (back into the sliding path). Tests showed that an absence of grease in the worm interface would initiate the torque noise almost

immediately, and three times the amount of grease previously applied would allow 6 or more cycles with no onset of torque noise. The fact that this only happened at -54°C could be explained by the increase in grease viscosity. With the grease almost paste-like at -54°C , it would "push" out of the worm sliding interface to the edges of the worm and gear. When the unit warmed up, the grease would become soft again and droop back into action. Once the surfaces were re-coated at the higher temp, the unit could be taken cold again and the grease pushing action would start over.

Final Design Change

Because the design would work repeatedly near 20°C and higher, and it appeared after of intense trouble shooting at -54°C that the torque blooming mechanism was unlikely to be found, additional thermal foil heaters were added to the unit. With both heater channels on, approx. 44 watts minimum would be available to heat the unit from -54°C to 7.2°C ($+45^{\circ}\text{F}$, Qual level) in the event the MO would be needed on orbit. Tripling the amount of grease originally applied in the worm area also helped the low temperature operation. The benefit of additional grease was not realized until after the additional heaters were added to the design. The combination of these two fixes resulted in a reliable, HOH manual override mechanism.

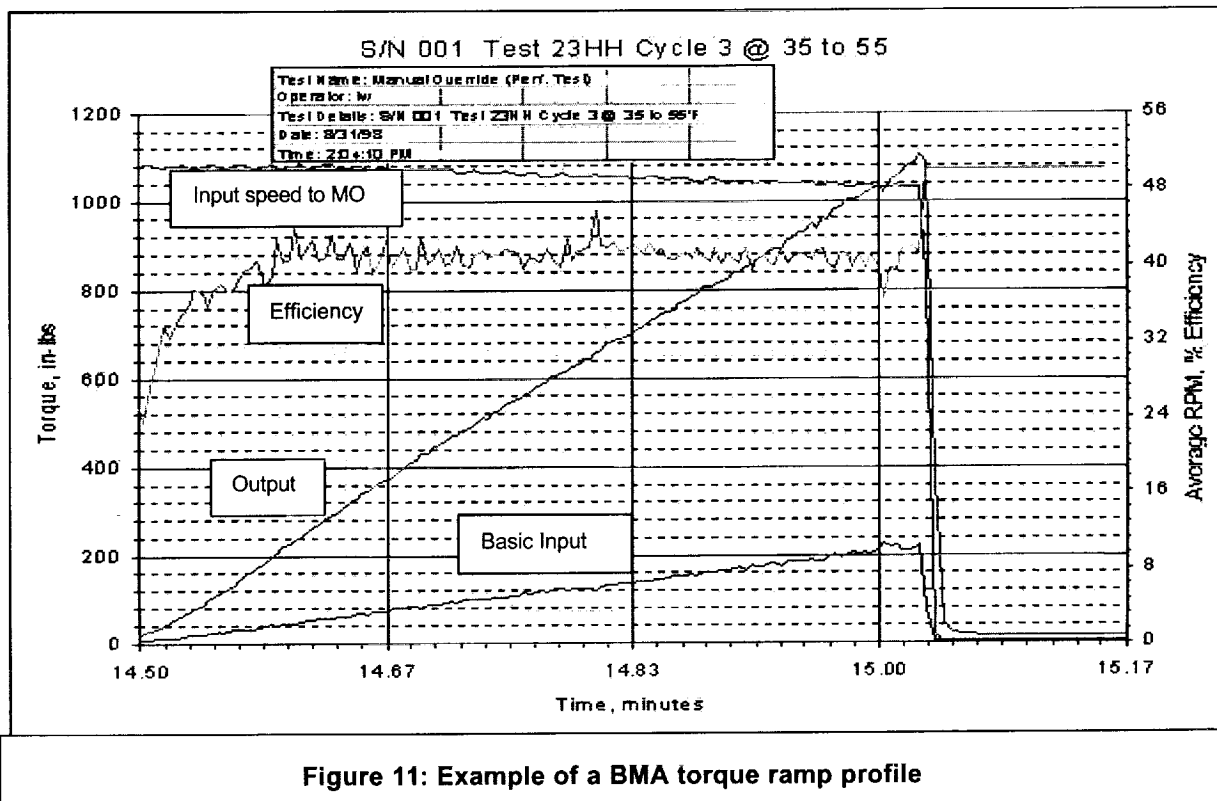


Figure 11: Example of a BMA torque ramp profile

Figure 11 shows the basic input (dark blue) and output (pink) torque for the BMA MO system. The efficiency curve (light blue) shows how the efficiency comes up quickly as load torque is applied and stays in the 40% range during the ramp period through 135.6 N•m. The input speed curve to the MO (green) shows a range from 48-50 rpm. The worm shaft spins in 162 rpm range.

Brief Mention of Other Items

Several other lessons learned were worth mentioning but will not be discussed in detail. These include the following:

Retainer Rings

MS27426 retainer rings were used to hold the carrier planet pins in the planetary system. The rings were used only on internal grooves and are comprised of two almost complete revolutions of flat stock, with a step transition from the lower leg to the upper. Unknown to Engineering early in the program, assembly took place with previously used (and distorted) rings. When combined with the needle bearing issue discussed above, a combination of planet pin rotation, axial needle bearing loads and previously used retainer rings, caused the rings to jump or twist out of their grooves. This was further exacerbated by small interruptions in the retainer ring groove, caused by the geometric intersection of the planet pin bores, which gave a rotating ring a chance to exit its slot. By eliminating the re-use of any retaining rings this problem was resolved since an undeformed ring would not come out of the groove, even if rotating.

Conformal Coat

The electronic boards were designed to be conformally coated with a low outgassing material called Conathane CE-1155. A standard military grade silicone coating (Dow Corning I-2577) was inadvertently applied to several boards. Since several components on the board were silicone based, using a silicone stripper to remove the compound was deemed a high risk. Since the lead time to replace some of the electrical components was on the order of 52 weeks, an attempt was made to vacuum bake-off the outgassing components of the silicone material. The final conclusion reached was that 180 hours vacuum bake (<1E-5 Torr) at 82 degrees C reduced the outgassing levels to program requirements.

Conclusions

The primary focus of this paper was to convey the successful design and implementation of a HOH, high torque worm drive using Pyrowear 675[®], WC/C and Braycote[®] 601EF. Empirical testing helped substantiate the ultimate load capability of fine pitch gearing and worm drives, which were values not well documented or readily determined analytically. The understanding of low temperature applications of Braycote 601EF, as related to the sliding environment of a worm drive and uncaged needle bearings, was also furthered by this study. And finally, a determination of how to successfully heat treat Pyrowear[®] 675 was obtained.

In the final design, the Bolt Motor Actuator program successfully incorporated several new technologies and overcame significant hurdles. The delivered product met the design challenges set for by the specification in a very robust package.

It is believed that several of the technologies discussed in this paper could be used to benefit the space mechanisms community.

¹ Kapton[®] is a registered trade mark of E.I. Du Pont De Nemours & Co., Inc. U.S.A.

² Pyrowear[®] is a registered trade mark of Carpenter Technology

³ Everlube[®] is a registered trademark of Great Lakes Chemical Corp.

⁴ Braycote[®] is a registered trademark of Castrol Incorporated

Design of a Power-Assisted Spacesuit Glove Actuator

Russell D. Howard*

Abstract

This paper presents the details of the design and implementation of an electromechanical power-assisted spacesuit glove actuator. The project was a joint effort by the University of Maryland's Space Systems Laboratory and ILC Dover, Inc., and involved innovative approaches to power augmentation and compact actuator packaging. The first actuator built validated several basic design concepts, and the second demonstrated improved performance and met many of the goals for flight qualification of the technology.

Introduction

A great deal of human extravehicular activity (EVA) is planned by NASA for the coming years, primarily in support of the International Space Station. Spacesuit glove design is a crucial element in the productivity, dexterity, comfort, and prevention of fatigue of an astronaut working in EVA. Improvements in glove design have been identified as a NASA priority [1] [3].

Spacesuit glove design is a difficult problem. The larger spacesuit joints (hips, shoulders, etc.) can be designed to have constant volume over their range of motion, eliminating the effect of pressure forces on joint dynamics. In the glove, however, the large number of degrees of freedom (DOF) (at least 16) combined with the small volume available and the need for dexterity make this approach difficult or impossible. Hence, the conventional spacesuit glove design is essentially a balloon, with a single carefully-selected "neutral" position. Any movement from this neutral position requires the astronaut to combat pressure forces (30 kPa (4.3 psi) differential in current NASA spacesuits), as well as the stiffness, friction and inertia of the glove material. Since the muscles of the fingers and hand are small, a significant fraction of their strength may be needed to overcome these forces, leading to limited working force capability and rapid fatigue [5]. The author's personal experience in neutral-buoyancy simulation (NBS) bears this out. It can be quite fatiguing to simply hold a wrench in a closed hand for ten minutes.

The intent of this project was to investigate the addition of power assistance to a spacesuit glove, combining the robotic actuator technology developed by the University of Maryland's Space Systems Laboratory (SSL) with the glove-design expertise of ILC Dover, Inc. To simplify the problem, initially a single degree of freedom was selected for study: the metacarpalpalphalangeal (MCP) joint. This is the motion obtained when all four fingers are closed to the palm simultaneously. MCP motion is an essential degree of freedom for gripping tasks (often required when working with tools), and one that is opposed by considerable forces due to pressurization in current spacesuits.

The power augmentation objective was not to multiply the operator's strength by a large factor, but simply to compensate for the resistance forces imposed by the spacesuit glove itself. Ideally, this would restore "nude-body" performance to the MCP joint, making work in the glove feel more natural and less fatiguing.

Other groups have previously explored augmented glove designs [2][4][6]. The approaches taken have included purely mechanical changes to the glove design, passive spring-based mechanisms, pneumatic systems, and electromechanical actuators. These systems have either failed to achieve adequate performance, exceeded the maximum packaging volume allowed by NASA EVA standards, or used technology incompatible with spacesuit operations.

* University of Maryland, College Park, MD

The concept of the SSL/ILC power-assisted glove is two-fold. The first (ILC) task was to design a glove with an MCP joint whose motion could be isolated from the rest of the glove, and a closed (grasped) neutral position when pressurized. An attachment point for an actuation cable on the dorsal side of the MCP joint, and a conformal mounting plate for an actuator on the dorsal side of the hand were also required. The second (SSL) task was to develop a small actuator with rapid response and sufficient force and stroke to allow full mobility. The actuator applies tension to a cable, which supplies opening torque for the MCP joint. The actuator applies force only in the opening direction; sufficient closing forces are inherent in the glove design. This approach keeps the palm area of the glove clear of extra mechanisms.

Actuator System Requirements

The role of the actuator subsystem in the power-augmented glove is to supply appropriate tension to the drive cable. It needs sufficient sensors to determine the correct torque, a mechanism for supplying the torque, and a suitable control algorithm.

To design an actuator mechanism, one must know the desired force, stroke, velocity, acceleration, packaging and power limitations, and the required operating environment. In this case actuator design proceeded concurrently with development of the new glove, so design work on each had to begin without details of the other system being available. Conservative assumptions were therefore made. The glove designers were asked to give us the largest mounting area they reasonably could, and we were asked to design to the worst-case glove force estimates. Frequent communication kept each group aware of updates as they came along.

Maximum glove forces were initially estimated from experimental measurements on existing Advanced Development Phase V (improved 5000 series) gloves and some theoretical work on the new design (which used an unjoined rolling convolute) to be about 31 N (7 lbf) at the cable. Cable stroke corresponding to the full range of roughly 50° of glove MCP joint travel was estimated at 2.5 cm (1 in), from the geometry of the preliminary glove design. Maximum rate of desired MCP joint motion was derived from a typical "nude-body" maximum performance rate of 4 cycles per second from fully open to fully closed and back. In this motion, the actuating cable traverses its full range in 1/8 second. Assuming constant acceleration for 1/16 second, and constant deceleration for 1/16 second, the acceleration value required at the cable is 650 cm/s^2 (256 in/s^2). The maximum required velocity for the cable is 41 cm/s (16 in/s).

Severe packaging constraints apply to spacesuit hardware. Power augmentation must be accomplished without adding objectionable bulk to the glove or restricting dexterity. The same work envelopes currently specified by NASA [9] must be usable with the augmented glove. A mounting location on the back of the hand was identified which would not interfere with the other glove degrees of freedom or violate NASA work envelope constraints. This volume was roughly 7 cm (2.75 in) longitudinal by 10 cm (4 in) lateral by 3.2 cm (1.25 in) tall. Even within those limits, it was strongly desired to keep actuator volume to a minimum, since future applications may require multiple actuators on the glove. Some components of the system (e.g. power supply, microprocessor, etc.) could be located remotely in the backpack (PLSS).

Safety is a prime consideration in spacesuit systems. This concern led to the requirement of no penetrations of the pressure bladder for this system; all components must be external. This system must also avoid creating a hazardous temperature inside the glove. A maximum temperature rise at the base of the actuator (back of glove) of 40°C (72°F) over ambient (power off) was set as a limit. The system must be designed to fail safe. Specifically, no credible failure mode can compromise the integrity of the pressure suit or prevent the operator from performing the manual tasks needed to ingress the airlock.

No strict limit on power requirements was initially set. An eventual flight system must provide sufficient power for a six-hour EVA duration, and be able to reject the heat dissipated internally. The design intent at this phase was to minimize power consumption given the required performance and other constraints.

Ultimately, the system would be required to work in several environments: the laboratory (air at sea-level pressure, room temperature), NBS (immersion in water at 32°C (90°F), up to 255 kPa (37 psi) pressure), and space (vacuum). Diver safety requirements in NBS led to a maximum voltage restriction of 30 V.

Development of the Mk I Actuator

Principle of Operation

A basic scheme of operation was needed first. How would the actuator determine what torque to apply at any given time? Once this was decided, component selection and detailed design could begin.

Several possible schemes were reviewed from the literature and our initial discussions with ILC Dover. The first is the most direct: since the goal is to reduce forces between the glove and the hand, measure those forces and control the actuator to drive them to zero. A fundamental problem with this approach is discriminating between intentional forces (such as when gripping a tool) and the unintentional ones caused by glove resistance. Another problem is sensor placement. Either you violate the pressure bladder or place the force sensors between the bladder and the restraint layer, where they would also react to inflation pressure. Since a force sensor must effectively be in series with the glove and hand (all of the forces between the glove and hand must go through the sensor), a large sensor area is required, causing further packaging difficulty.

The second possibility is a position-control scheme: sensors on the operator's hand could measure joint positions, and the actuator could drive the glove position to match. Position sensors could be much more compact than force sensors since they operate in parallel (it is just necessary to measure position at one place on a joint). Unfortunately, there is the same problem when the hand makes intentional contact with an object. The actuator would reject those contact forces as disturbances, up to its maximum torque capability. The operator wouldn't know that he or she had contacted anything until the actuator was overwhelmed. By then, excessive forces might have been exerted on a delicate component. Also, again, sensor placement is in violation of the pressure bladder, and sensors on the astronaut's hand would further complicate the (already lengthy) spacesuit don and doff procedures.

Some of the problems with these first two approaches could be solved by adding force sensors to the outside of the glove, and using the actuator to drive the glove-hand force to equal the glove-external object force. The operator would then be able to sense and control contact forces appropriately, while the actuator took care of the glove-originated forces. However, multiplicity of sensors is a serious obstacle to the implementation of this scheme, and another is that it is unstable in the 1-g laboratory environment (consider what happens when the hand is rested on a table).

Another idea commonly discussed in the power augmentation community is the use of electromyographic (EMG) sensors to measure muscle stimulation. If an accurate mapping between these signals and joint motion could be developed, the potential exists for the glove actuator to act as an extra "muscle" responding to the same signals as the operator's own muscles. If tuned correctly, the actuator would move the glove in synchronism with the operator's hand. Unfortunately, this technology is not yet sufficiently developed. EMG signals are noisy and, due to the complexity of muscle/nerve systems, only give a crude approximation of joint motion commands. They are useful for characterizing gross muscle parameters such as fatigue (see the Results section) but were not considered practical for the fine level of control desired in this application.

The above approaches were admired for their generality but found unsuitable and over-complex for the problem at hand. It was necessary to make some simplifying assumptions about the problem, which could be tested when hardware was built. First, it was assumed that the glove's forces derive from its state (DOF configuration and velocities) in a repeatable manner. Second, it was assumed that the new glove design would sufficiently isolate MCP motion such that MCP torque will only depend on MCP joint state. The angles of the fingers, for instance, would not significantly influence the glove's torque around the MCP joint, and so could safely be ignored. Third, it was assumed that the glove's resistance forces

were primarily due to (possibly nonlinear) stiffness and damping, and the inertial component due to the glove's mass was small enough in comparison to be neglected.

These assumptions allowed a substantial simplification of the system. MCP joint state could be measured with a single sensor: a position encoder or potentiometer monitoring the extension of the MCP drive cable (with velocity derived by digital filtering or numerical differentiation). This sensor could be external, located in the actuator body on the back of the glove. A mapping of joint state vs. resistance torque would be needed; once established in a lookup table the controlling microprocessor could quickly calculate the appropriate torque for any state. Since inertial forces were being neglected, no acceleration feedforward or anticipation of operator motion would be required.

Design

Due to the large number of unknowns, it was decided to approach the ultimate goal of a flight-qualifiable unit in a series of steps. The first (Mk I) unit built would be used in a laboratory setting to test the assumptions made—a proof-of-concept. The critical issues were performance and actuator packaging. The requirement to operate in vacuum and underwater was relaxed, and a laboratory power supply and desktop personal computer were used instead of miniaturized, self-contained components. Power and data systems of eventual flight units would be located in the PLSS—a more straightforward packaging problem that could be postponed to a future design iteration. Commercial off-the-shelf (COTS) components were used where possible to speed the development.

A number of actuation technologies were examined for suitability including pneumatics, hydraulics, "memory-metal" wires, phase-change actuators, and voice coils. DC servomotors were chosen for their precise controllability, speed of response and compact packaging. To simplify the design of driver electronics, a brushed DC motor (Inland Motors QT-1106) was selected for the Mk I unit. An op-amp current driver circuit was constructed to enable the microprocessor (a Gateway 2000 80486-based personal computer) to directly command motor current, which is proportional to torque.

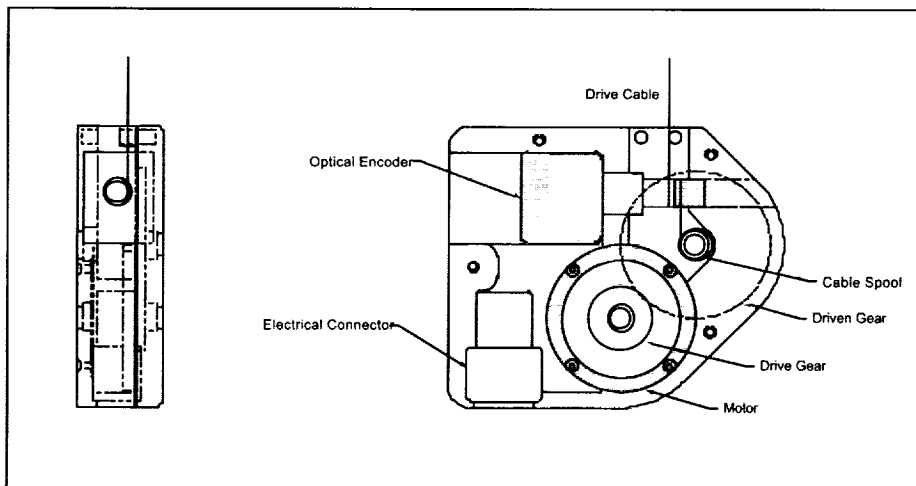


Figure 1. Mk I Actuator

The motor drove the cable capstan through a 2.5:1 single-stage spur gear transmission. The cable was secured to the 4.7 mm (0.185 in) diameter vertical spool, then proceeded around the 0.635 cm (0.25 in) diameter horizontal shaft of a 2-channel digital incremental optical encoder (Bourns ENS1JB28L00256), then on to the MCP joint attachment. Multiple wraps and passage through a transverse hole in the encoder shaft precluded cable slippage on the encoder shaft. All rotating components were supported by ball bearings.

The small bend radius on the capstan and the high forces involved made high tensile strength, small diameter and resistance to fraying the critical properties for cable longevity. A variety of cable materials were tried during development including stainless steel, Dacron™, Kevlar™, and Vectran™. A 0.69 mm (0.027 in) diameter braided Spectra™ cable was settled on as the best choice for stiffness and durability.

The housing was made of 6061-T6 aluminum. Overall dimensions of the actuator package were 7.7 cm (3.04 in) wide by 6.5 cm (2.56 in) long by 2 cm (0.77 in) tall. A 0.64-cm (0.25 in) thick aluminum interface plate attached the actuator to the glove, increasing overall height to 2.64 cm (1.02 in).

The motor was selected to produce the nominal maximum of 31 N (7 lbf) cable tension (assuming a mechanical efficiency of 70%) at a current of 1.35 A, and simultaneously support cable velocities up to 58 cm/s (23 in/s) with a \pm 30 V DC power supply. The encoder, with two channels in quadrature at 256 counts/revolution, would give 1300 counts over the nominal cable travel of 2.5 cm (1 in).

Development

While the actuator was in fabrication, it became evident that the first new glove would have significantly higher resistance forces than originally expected. The maximum cable tension required increased to roughly 70 N (16 lbf). Rather than redesign the actuator, it was decided to relax the 30 V maximum voltage requirement; a possibility since the Mk I unit would not be used in NBS. With a \pm 42.5 V DC power supply, the same motor could produce 70 N (16 lbf) cable tension at a maximum velocity of 64 cm/s (25 in/s) with a current of 2.7 A, slightly above its nominal rating. No other changes were required.

An element which could not be completed until the new glove arrived was the mapping between torque and state of the MCP joint. After delivery, the glove was integrated with the actuator on a benchtop setup which clamped the wrist ring in place and pressurized the glove to 30 kPa (4.3 psi) over ambient. With this apparatus it was not possible to perform tests with an operator's hand inside the glove, but the unoccupied glove's properties could be measured. For "occupied" tests, a glove box was used to provide the correct pressure differential, but physical access to the actuator was precluded in that situation.

Since the actuator itself includes a position sensor and a means of applying known torque, the glove's torque/state map could be generated without any extra equipment. An algorithm was developed by Dr. Robert Sanner (University of Maryland, College Park) to perform this automatic calibration procedure. Details of this algorithm have been presented in [7]. Essentially, the actuator first drives the glove to a hard stop to calibrate the incremental encoder, then relaxes to zero torque. Then it steps the torque up in finite increments to its maximum value, then back down to zero, recording the MCP positions at each step. It is expected that a similar procedure would be run operationally every time the glove systems were powered up to ensure a current calibration. It takes about 90 seconds and can be performed with the operator's hand inside (relaxed). System measurements made in this way lump together the properties of the glove and actuator, e.g. friction, damping and inertia. For operational purposes this is sufficient, since the system functions as a unit.

Results

Initial tests showed that the forces resisting MCP motion were, in descending order of magnitude: stiffness (position-dependent), friction and stiction, viscous (velocity-dependent), and inertial; as expected from ILC's previous glove investigations. The data obtained with the actuator system correlated well with ILC Dover data taken on the same glove using an Instron machine at their facility.

The observed level of static friction and stiction (some from the glove; some from the actuator) led to the addition of dither (a small-amplitude high-frequency ripple) to the torque commands. This reduced the effective magnitude of friction forces by roughly 4.5 N (1 lbf). The position- and velocity-dependent forces were mapped and compensated by the control system, and (as previously described) the inertial forces were left uncompensated. In theory, the operator would feel the added inertia of the glove (and actuator) but none of the other forces.

Glove forces were found to have significant hysteresis. The force/position map obtained in the opening direction differs from that in the closing direction, as shown in Figure 2. Even when stationary, the force required to maintain a given glove position depends on the prior direction of glove motion.

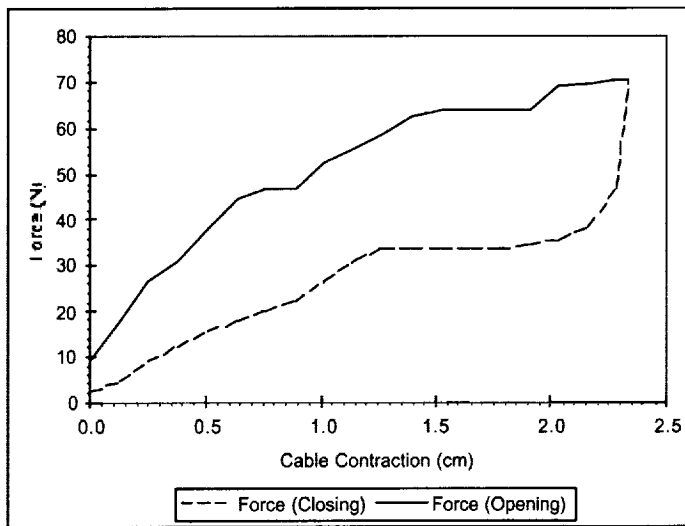


Figure 2. Mk I Glove Force/Displacement Curve

This required the control system to record and utilize two force/position maps; one for each direction. A "transition strategy" was developed by Dr. Sanner to smoothly handle changes of direction, without exciting oscillation. This algorithm is described in detail in [8].

When the system was working stably on the bench, development continued using a glove box at ILC Dover and a variety of test subjects. With an operator's hand in the glove, a number of subjective phenomena were noted which were not evident on the benchtop. This phase of testing was close enough to an operational scenario that some of the basic research questions could be answered.

The first objective was to validate or reject our overall power-augmentation approach. The three assumptions made in the design process were tested. The first two implied that MCP joint torque depends only on MCP joint state in the new glove. We had been forced to modify this a bit already when the glove's hysteresis was measured. Torque evidently depends somewhat on past state (direction of motion) of the MCP joint as well as the current state. This adjustment had been successfully dealt with in software.

With full compensation for measured cable forces, minor variations in actual glove torque inevitably cause some error in the counter-torque applied. When the compensation torque switches from being an underestimate to an overestimate the glove suddenly opens a small amount, and it closes a small amount when the reverse happens. Operators found this "uncommanded" glove motion distracting. The system was judged less intrusive when the torque maps were backed off a bit from full compensation. All errors would then be in the undercompensated sense, and "uncommanded" motion would not occur. The disadvantage of this was to somewhat increase the glove forces making it through to the operator's hand, diminishing the effectiveness of power augmentation.

The magnitude of this effect directly addresses the first two design assumptions. Any dependence of MCP joint torque on factors other than MCP joint state would result in compensation errors. If these errors were large, the level of compensation would have to be scaled back proportionally. If the original assumptions made were incorrect, the remaining compensation would account for only a small fraction of the glove forces, and the system would not significantly ease glove motion.

Figure 3 shows the results from a benchtop experiment in which the auto-calibration procedure was run with compensation turned off and on. It shows that the compensation system reduced glove force (measured at the actuation cable) from a peak of over 64 N (14 lbf) to around 4.5 N (1 lbf), a reduction of over 90%. Thus, the assumption of MCP torque dependence primarily on MCP state appears justified.

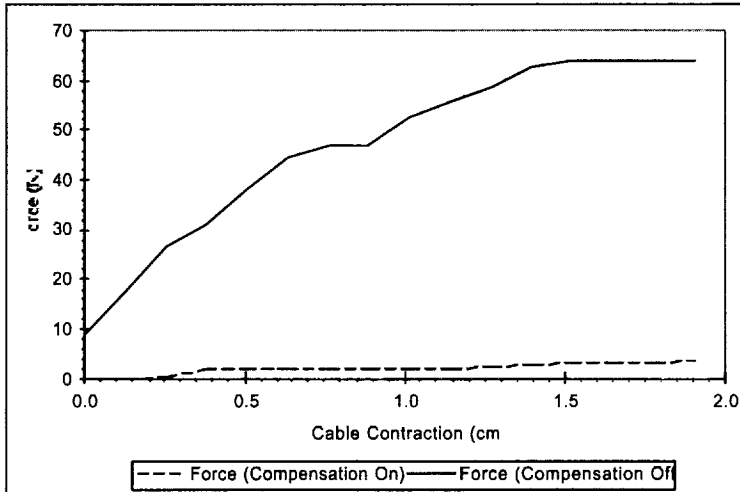


Figure 3. Mk I Glove Force With and Without Compensation

The third assumption, that inertial glove torque was much less than the position- and velocity-dependent torque, could also be tested using trajectory data from the working Mk I system. The equivalent inertia of the glove was found to be roughly 625 g (1.4 lbm) as seen by the actuator cable. At the maximum desired cable acceleration of 650 cm/s^2 (256 in/s^2) this gives rise to a 4 N (1 lbf) inertial disturbance force, comparable in magnitude to the other uncompensated glove forces. Since this peak inertial force is less than 10% of the total glove force, our final assumption appears justified as well. The topic of extra inertia introduced in the actuator is discussed later in the section on Mk II actuator design.

Extensive physiological testing documented in [7] and [8] compared fatigue (measured by EMG signal analysis and by decline in MCP range of motion over time) for a number of test subjects performing repetitive tasks with the compensation system turned off versus on. It was found that average task effort decreased 30-40% with the power augmentation. The system also enabled all subjects, some of whom had a poor fit in the glove, to utilize full mobility of the MCP joint.

Some deficiencies in the Mk I system became clear as testing proceeded. The actuator dissipated quite a bit of heat. After fifteen minutes of hard operation, the external housing temperature would reach 93°C (200°F), after which performance would degrade due to internal dimensional changes. No discomfort was noticed inside the glove, however.

Occasional "glitches" (uncommanded motion) would occur in operation. Some of these appeared to be the result of actuator internal friction changing with temperature (leading to compensation errors) and some were the result of slack in the cable (leading to errors in glove position estimation). Cable slack was seen to occur when the operator opened his/her hand very quickly; there was a time lag in the actuator's response.

In summary, the testing of the Mk I actuator and glove established the SSL/ILC power augmentation approach as a viable one. The actuator met its performance and packaging goals, and the test data refined our physical understanding of the problem. Subjectively, the system made a dramatic difference in task effort. As ILC and SSL personnel gained experience with the completed system, several ideas for improvement in both glove and actuator design emerged. These ideas led to a second design iteration.

Development of the Mk II Actuator

Objectives

The glove designers at ILC set the reduction of joint torque as their primary goal for the second-generation glove. This would have an immediate benefit in reducing the power (and heat dissipation) requirements of the actuator, and possibly allow a reduction in size. A target was set to reduce maximum cable force from around 70 N (16 lbf) to 45 N (10 lbf).

The SSL goals for the second-generation actuator were to reduce size, reduce heat dissipation, improve "smoothness" of performance, permit operation in NBS and vacuum environments (which required bringing the maximum voltage back under 30 V DC) and improve maintainability of the design, particularly the cable changeout procedure.

Design

Actuator performance parameters of maximum force capability, power dissipation, effective inertia, friction, and size all depend strongly on the motor and transmission ratio selected. From the Mk I testing we had developed a good feel for the relative importance of each of these, and carefully examined the tradeoffs between them for the Mk II design.

A central issue is the choice of transmission ratio, which includes any gearing used and the diameter of the capstan or spool that the cable is wound on. To illustrate the tradeoffs, define the effective spool radius R as the ratio between motor torque and cable force $R = T/F$. Given a motor with maximum torque capability T_M , and given that peak force F_M must be applied to the cable, the motor must drive a spool with radius $R = R_M = T_M/F_M$. In other words, an upper limit for R is set by the torque limit of the motor. What then sets a lower limit for R ?

Possibility 1: Spool size. If R is too small, it becomes difficult to attach the cable and the bend radius is too tight for cable longevity. Experience showed this limit is around 2.5 mm (0.1 in) diameter. This can be relieved somewhat by using gearing to increase the physical spool radius without changing the effective R . The Mk I actuator, for example, utilized a 2.5:1 gear ratio to increase the capstan diameter to a manageable size. Ultimately, the size and efficiency losses of a high-ratio gear train would become prohibitive, but a single stage with ratio up to 5:1 is feasible in this application. This limit sets a minimum $R = 0.5$ mm (0.02 in). The target of 45 N (10 lbf) maximum cable tension then set a minimum torque capability of 22.5 mN·m (3.2 oz-in) and consequently a minimum size for the motors considered.

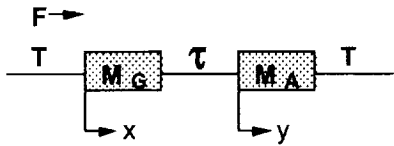
Possibility 2: Power dissipation P . $P = I^2r = T^2r/K_T^2 = R^2F^2r/K_T^2$ where I is current, r is resistance, and K_T is the motor's torque constant. Therefore decreasing R actually improves (decreases) power dissipation. This consideration drives the design toward lower R values.

Possibility 3: Motor velocity limit. As R decreases, the required motor velocity increases in inverse proportion. The highest velocity attainable occurs when the back emf plus the resistive drop are equal to the supply voltage. Higher velocities can be achieved by increasing the voltage, up to the 30 V DC limit set by NBS safety considerations. If that is not high enough, different motor windings can trade voltage requirements for current requirements. As a result, motor velocity was not a critical limitation in the regime considered.

Possibility 4: Friction. Static friction and stiction at the cable output are proportional to $1/R$, viscous friction is proportional to $1/R^2$. Therefore to reduce the effects of internal friction, R must be increased. This consideration drives the design toward higher R values.

Possibility 5: Effective inertia. The effective inertia of the actuator rotor at the cable output is J/R^2 , where J is the motor rotor inertia ($\text{kg}\cdot\text{m}^2$). If the actuator inertia becomes too high, the actuator can't keep up with the glove. The result is slack in the cable and loss of force compensation (glove opening), or

objectionable resistance to motion (glove closing). This can be quantified using the following two-mass model:



M_G = Mass of Glove

M_A = Mass of Actuator

T = Tension in Cable

τ = Tension in Cable between Masses

F = Force applied by fingers to initiate motion

x = Position of Glove

y = Position of Actuator

This simplified model assumes the cable is perfectly stiff, and that the actuator control law exactly compensates the glove state-dependent forces (T is equal on both sides of the diagram). The system dynamics are then:

$$M_G \ddot{x} = F + \tau - T$$

$$M_A \ddot{y} = T - \tau$$

Since the cable can support tension but not compression, $x = y$ if $\tau > 0$. This condition is violated when τ goes to zero. Solving for τ :

$$\frac{M_G}{M_A} (T - \tau) = F + \tau - T$$

$$\rightarrow \tau = T - \frac{M_A}{M_G + M_A} F$$

So the cable develops slack ($\tau = 0$) when:

$$F > \left(\frac{M_G}{M_A} + 1 \right) T \quad \text{or} \quad F > \left(\frac{R^2 M_G}{J} + 1 \right) T$$

where the effect of spool size is included. For smooth glove operation, therefore, it is desirable to increase the magnitude of the right side of the above equation above the level of expected human operator input forces.

Some design-relevant conclusions can be drawn from the above model. Parameters T and M_G are fixed by the glove design. To meet other objectives, glove designers strive to minimize both of these quantities. In particular, a goal for the Mk II glove was to reduce T (the magnitude of the glove resistance force) by at least 30% below the Mk I level, while M_G was likely to remain the same. Thus, slack occurrence would be a more serious problem with the improved glove.

Cable tension T is a function of MCP joint position, going to zero at the fully-closed position. Slack is therefore more problematic in that vicinity. To combat this effect, some bias force can be applied by the

actuator even when the glove is closed. As long as this force is less than the inherent static friction in the glove joint, no uncommanded motion will occur.

With fixed glove parameters, slack occurrence depends on actuator inertia. Given the minimum cable tension (the bias force referred to above) T , the glove inertia M_G , and maximum expected operator input force F , a maximum actuator inertia M_A can be calculated to avoid slack in the cable:

$$M_A = \frac{J}{R^2} < \frac{T \cdot M_G}{F - T}$$

This model also illustrates that when the system is operating nominally (no slack), the augmented glove behaves with the inertia of the glove plus the inertia of the actuator. Glove "feel" could thus be improved by reducing actuator inertia. A practical limit to improvement would occur when the level of actuator inertia fell below the inherent glove inertia. When these calculations were performed on the Mk I actuator (after testing had begun and the glove inertia had been determined) its inertia was found to be roughly four times that of the glove, clearly leaving room for improvement in the Mk II design.

Examination of the relationships described above reveals a basic design tradeoff in this application. For any given motor, decreasing power dissipation and increasing maximum force capability by adjusting the effective spool radius R is in conflict with reducing the inertia and friction of the actuator. Figure 4 illustrates this tradeoff for the motor used in the Mk I actuator.

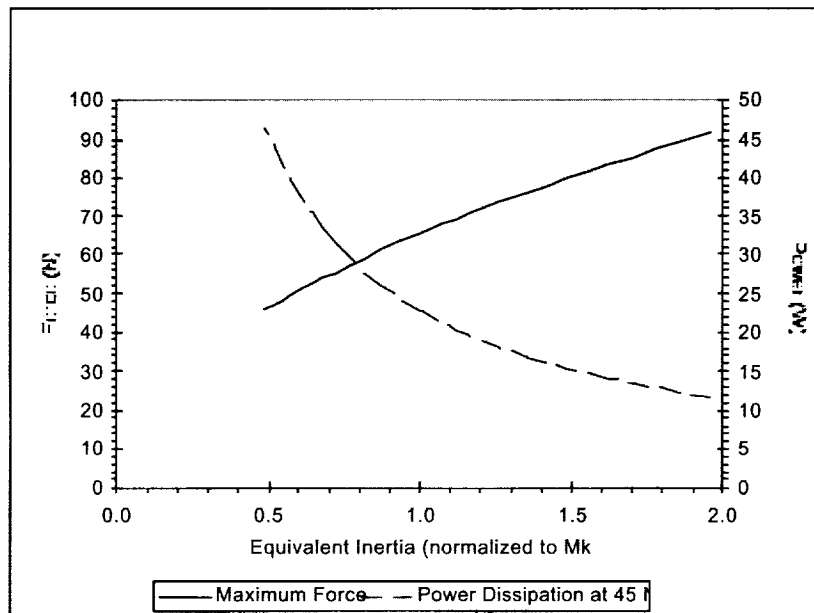


Figure 4. Maximum Force and Power Dissipation vs. Inertia for QT-1106 Motor

Since it was desired to decrease power dissipation, inertia, and friction simultaneously for the Mk II design, clearly the search for motors would have to be expanded. Given these interests, DC brushless motors had several promising properties. Their rotors carry permanent magnets instead of coils, so typically have less inertia for the same performance. Since the heat-dissipating electromagnets are in the stator they contact the housing directly over a large surface area, so thermal management is easier. They have less internal friction, since there are no brushes. Brush wear is no longer a maintenance problem, contamination from brush dust is avoided, brush arcing and welding in low pressure and dry-gas environments is not a concern, and electromagnetic interference is reduced. The drawbacks are that

several more wires are needed (typically eight versus two), more sophisticated electronics is required for commutation (typically including Hall-effect sensors inside the motor), and the aspect ratios available off-the-shelf tend toward tall cylinders rather than "pancakes," due to the added length of the sensors.

Graphs like Figure 4 illustrate the tradeoffs for a given motor, but to compare different motors, each of which might be considered with a range of effective spool radii, a different approach was needed. It was decided to compare motor/spool combinations on the basis of equal inertia—so each combination compared would produce equivalent "feel" and resistance to cable slack. The different inertias for a given motor are obtained with different spool radii. Table 1 demonstrates this method. Listed on the left are a number of COTS motors from the Inland Motors Division of Kollmorgen, Inc., in order of increasing diameter. The next column is motor constant K_m , a figure of merit which indicates the motor's efficiency at turning electrical power into torque. This generally increases with motor size, which is listed in the next two columns. Then performance figures of maximum cable force capability and average power dissipation are tabulated for each of four effective inertia levels, starting with inertia equivalent to the Mk I actuator and reducing by a factor of two in each step.

Table 1. Motor Trade Matrix

Brushed Motor	Km (mN•m/W)	Diam. (cm)	Ht. (cm)	Inertia = Mk I		Inertia = Mk I/2		Inertia = Mk I/4		Inertia = Mk I/8	
				Force (N)	Power (W)	Force (N)	Power (W)	Force (N)	Power (W)	Force (N)	Power (W)
QT-0717D	3.74	2.86	0.95	64.05	8.51	45.75	16.68	29.12	-	21.35	-
QT-1106A	11.09	3.49	0.98	65.53	7.76	45.87	15.85	32.77	-	22.38	-
T-1259A	16.95	3.81	1.30	65.85	6.19	46.34	12.50	33.81	-	23.17	-
NT-1372E	29.31	4.92	1.37	104.25	3.25	73.59	6.51	53.24	12.45	46.80	-
QT-1401D	26.41	4.92	1.37	163.83	5.45	114.68	11.12	80.48	22.59	55.94	46.7
T-1342A	28.60	4.92	2.13	107.62	5.67	74.14	11.96	52.35	23.43	36.66	-
QT-1906A	32.91	6.03	1.27	90.66	9.45	64.16	8.87	45.33	37.80	31.59	-
T-2003B	10.45	6.25	0.78	25.56	-	18.01	-	12.58	-	8.71	-
T-2509C	30.58	7.62	0.94	41.02	-	29.09	-	20.51	-	14.22	-
Brushless Motor											
RBE-00510C	7.06	2.67	1.97	117.43	2.33	73.40	5.96	58.72	9.32	39.14	-
RBE-00710B	15.82	3.78	2.16	177.00	1.58	122.54	3.30	88.50	6.32	61.27	13.20
RBE-01210B	28.25	4.92	2.10	189.84	2.72	132.89	5.56	94.92	10.90	65.36	22.9
RBE-01510B	44.98	6.03	2.10	164.03	3.19	115.78	6.40	82.01	12.76	56.78	26.6

The average power figures shown were calculated assuming a 1 Hz sinusoidal full-range MCP angle trajectory and a force model approximating the expected second-generation glove. The shaded areas designate combinations which were rejected either because they would dissipate more power than the Mk I unit on the Mk II glove (> 17 W) or produce insufficient cable force (< 45 N (10 lbf)). The double lines in each column indicate the level above which reduction gearing is necessary to obtain a sufficient physical spool diameter.

Tables of this sort were useful design tools, enabling many different potential systems to be compared quickly on an equal footing. The consequences of changing any one parameter (e.g. package size) could easily be seen.

On the basis of this information and some packaging exercises, the motor selected for the Mk II actuator was the Inland RBE-00510C, with a gear ratio of 3.024:1 driving a 2.5 mm (0.1 in) diameter spool, giving half the effective inertia of the Mk I actuator. As the table shows this gives a maximum force capability of

73.4 N (16.5 lbf), a slight increase over the Mk I value (it was considered wise to have some margin over the target 45 N (10 lbf)), and expected power dissipation of 6 W, a reduction of 65%. It was anticipated that friction would decrease also due to the lack of motor brushes. Motor diameter decreased by 23%, though this was offset by an increase in motor height of 107%.

A substantial benefit in packaging was obtained when it was realized that the three Hall-effect sensors incorporated in the motor for commutation could also be used (in principle) as an incremental position encoder. This enabled the deletion of the separate optical encoder, and a corresponding reduction in wire count (by four, to a total of eight; compared to six for the Mk I system). This innovation entailed some risk, since new electronics were needed and the net position resolution would decrease from 1300 counts over the range of travel to 216.

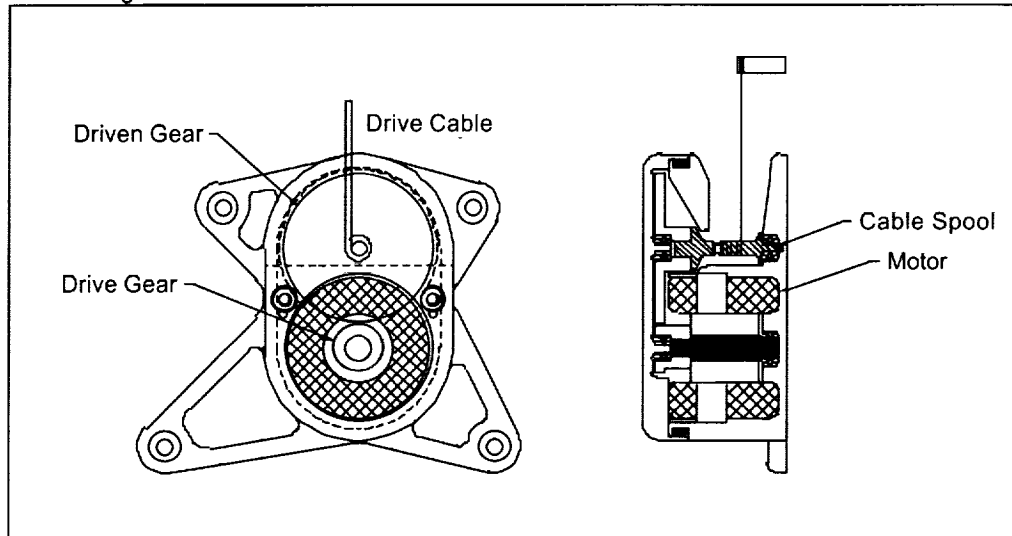


Figure 5. Mk II Actuator

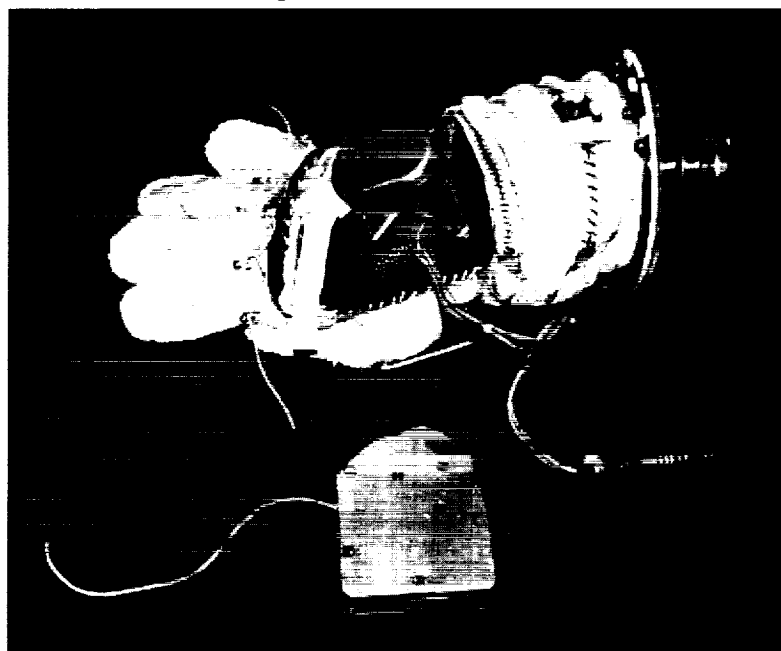


Figure 6. Comparison of Mk I and Mk II (on glove) Actuators

The new design (Figures 5 and 6) placed the cable spool outside the housing, making cable inspection and replacement simple. A shaft seal was incorporated to enable underwater use (although this actuator, with a brushless motor and no encoder, could be integrally waterproofed to operate flooded if desired). All components were compatible with vacuum operation. The electrical requirements were a peak current of 3.6 A (an increase of 33% over the Mk I) and a maximum voltage of 12 V DC (well under the 30 V DC limit for NBS and the ± 42.5 V DC needed by the Mk I actuator). The package size was 3.4 cm (1.33 in) wide (43% of Mk I) by 5.1 cm (2 in) long (78% of Mk I) by 2.5 cm (1 in) tall (same as Mk I). Overall volume decreased from 114 cm^3 (7 in^3) to 39 cm^3 (2.4 in^3), a reduction of 66% from the Mk I actuator.

Results

Testing of the Mk II glove and actuator followed a similar sequence to that of the Mk I system. Glove force calibration showed that the ILC glove designers had met their goals: 45 N (10 lbf) cable tension produced the full range of MCP joint travel. Figure 7 compares the auto-calibration results for this system with the compensation on and off. The Mk II actuator lowered peak glove resistance force from 45 N (10 lbf) to 3.3 N (0.75 lbf); a reduction of over 90%. This percentage was very similar to the Mk I value, showing that the new glove design was equally successful at isolating MCP motion.

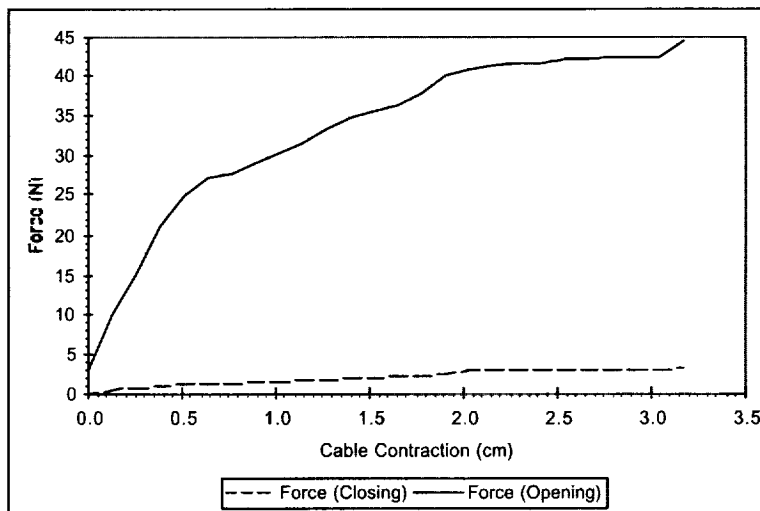


Figure 7. Mk II Glove Force With and Without Compensation

The new actuator exhibited a factor of four decrease in internal static friction. This, combined with the factor of two reduction in inertia, provided much smoother operation than the Mk I system. The anticipated reduction in power consumption by a factor of three was confirmed, although actual values for either system in heavy glove use exceeded the design-phase estimates by 66%, giving an actual average consumption of 10 W for the Mk II unit, with peaks to 25 W. The lower power consumption and better heat conduction of the new actuator made a dramatic improvement in operating temperature. The Mk II unit could run indefinitely in the laboratory without exceeding 54°C (130°F). None of the mechanical problems associated with overheating were observed with the Mk II unit.

The use of commutation sensors for encoding worked reliably. The reduction in encoder position resolution to 0.15 mm (0.006 in) steps did not perceptibly degrade smoothness. The improvement in mass and bulk over the Mk I actuator that this innovation allowed was quite noticeable to the operator in the glove box (1-g) environment.

In summary, all of the engineering goals of the Mk II development were met. Further physiological testing is planned, to quantify the potential benefits to EVA crew.

Conclusion

This project represents a significant step forward in power augmentation technology for space applications. The Mk II actuator fits easily on the back of a glove and can reduce MCP torque by 90%. These results demonstrate that a very simple system with no intrusive sensors or complicated feedback laws can perform very well. Packaging and power requirements are modest enough to allow multiple degrees of freedom on the spacesuit to be assisted; as many as three on the glove itself. Such systems could be an enabling technology for future developments such as the 55 kPa (8 psi) spacesuit and planetary exploration suits.

In addition to technology validation, several procedural lessons were learned in the course of this project. Our two-stage process was good: the first design iteration to prove out concepts and validate hypotheses, the second to explore design tradeoffs and optimize performance. Concurrent development with two teams involving industry/academic cooperation worked surprisingly well; concepts evolved that would never have occurred to either group alone. Key elements were early brainstorming sessions to cross-fertilize ideas and make sure everyone started on the same track, frequent communication, trust in the expertise of the other group, early agreed-upon interfaces, and generous design margins.

Acknowledgements

This work was supported under the 1996 and 1997 NASA Research Announcements on Advanced Human Support Technology. While the author was responsible for the actuator design work described here, that was only one aspect of an exceptional team effort. Particular notice should be taken of the contributions of David Cadogan and Robert Lingo of ILC Dover, Inc. for glove design and fabrication, the development of power and data systems and physiological testing by Elizabeth Sorenson, control software by Dr. Robert Sanner, and a fine job of principal investigating by Dr. David Akin of the University of Maryland SSL.

References

1. Callaway, R. "Advanced EVA Systems Program Plan," NASA, Washington, D.C., 1994.
2. Cleland, J., and Winfield, D., "NASA Workshop Proceedings: Extravehicular Activity Gloves," Research Triangle Institute, 1985.
3. Eppler, D., and Callaway, R., "Managing EVA Technology: the Present and the Future," *Space Programs and Technologies Conference*, Huntsville, AL, 1994.
4. Kosmo, J., "Rolling Convolute Joint for Pressurized Glove," *NASA Tech Brief MSC-21628*, 1995.
5. Lapham, B., and Lacey, D., "Astronaut EVA Symposium," Johnson Space Center, 1994.
6. Main, J., Peterson, S. and Strauss, A., "Power Assist EVA Glove Development," *22nd International Conference on Environmental Systems*, Seattle, WA, 1992.
7. Sorenson, E. A., Sanner, R. M., Howard, R. D., Akin, D. L., Lingo, B., and Cadogan, D., "Development of a Power-Assisted Space Suit Glove Joint," *27th International Conference on Environmental Systems*, Tahoe, NV, 1997.
8. Sorenson, E. A., Sanner, R. M. and Ranniger, C. U., "Evaluation of a Power-Assisted Space Suit Glove Joint," *Proc. IEEE SMC Conference*, Orlando, FL, 1997.
9. NASA-STD-3000, Rev. B, "Man-Systems Integration Standards," July 1995.

An Energy Absorber for the International Space Station

Bob Wilkes^{*} and Lora Laurence^{**}

Abstract

The energy absorber described herein is similar in size and shape to an automotive shock absorber, requiring a constant, high load to compress over the stroke, and self-resetting with a small load. The differences in these loads over the stroke represent the energy absorbed by the device, which is dissipated as friction. This paper describes the evolution of the energy absorber, presents the results of testing performed, and shows the sensitivity of this device to several key design variables.

Introduction

The energy absorber described in this paper will be used on the Crew Equipment Translation Aid (CETA), on the International Space Station (ISS). The CETA will be used by extravehicular crewmembers to move large or massive pieces of equipment needed for repair or maintenance along the ISS truss. The CETA is a human-propelled trolley, confined to ride along the truss rail system, which extends the length of the station. Crewmembers will insert their feet into foot restraints on the CETA, and pull themselves and their cargo along the truss with a hand over hand motion. The CETA, shown in Figure 1, can weigh up to 9,790 N (2200 lbf) when fully loaded with crewmember and cargo, and travel at up to 0.91 m/s (3 ft/s).

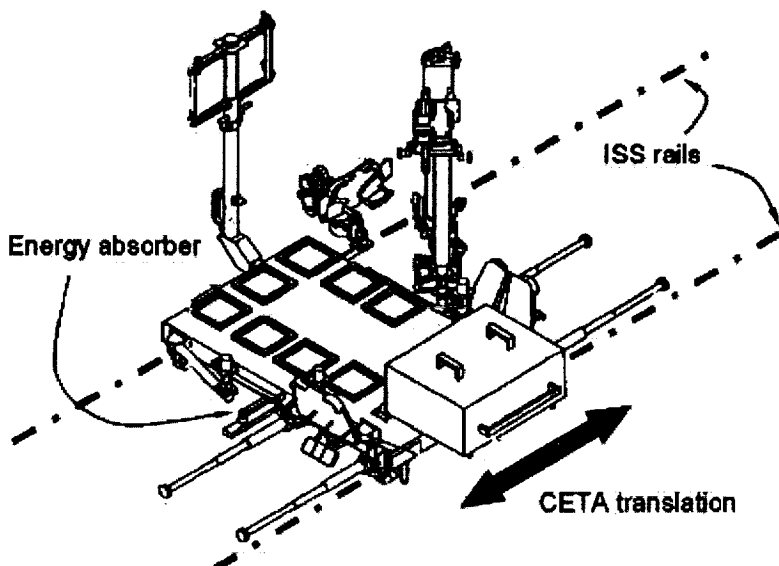


Figure 1. CETA, unloaded and without crew

The purpose of the energy absorber is to protect the CETA from inadvertent collisions with ISS rail stops by keeping contact loads to a defined maximum. It will function as a bumper, collapsing upon contact, and re-extending itself after a collision. It must be a passive device, operate for 15 years of vacuum, atomic oxygen and ultraviolet radiation exposure, and require no maintenance. Additionally, the loads needed to collapse the energy absorber must be constant and predictable over a large thermal range and

^{*} Lockheed Martin Space Operations, Houston, TX

^{**} NASA Johnson Space Center, Houston, TX

the life of the device. The load of 2535 N (570 lbf) must never be exceeded, and a minimum of 420 N-m (308 ft-lbf) of energy must be dissipated.

Background

This device is the culmination of two independent design and development efforts performed by Lockheed Martin Space Operations (LMSO) under the supervision of Crew and Thermal Systems Division at NASA Johnson Space Center. The energy absorber development effort that this paper documents began in May 1999, and resulted in ISS certification of the design in December 1999. The previous development effort and initial concept generation was largely the work of Clarence Wesselski, which culminated in US Patent 5,423,400 filed on July 29, 1993 and was described at a previous Aerospace Mechanisms Symposium as a poster paper [1]. This paper, however, will describe the changes made to the design, discuss testing of the mechanism, and explain why each change was necessary.

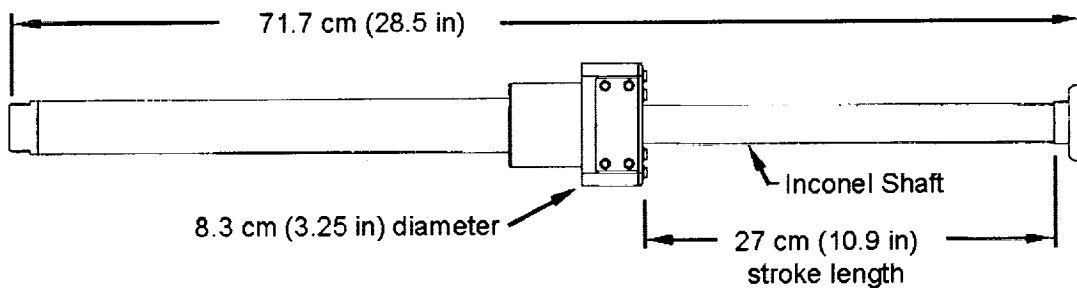


Figure 2. CETA Energy Absorber Envelope

The energy absorber is pictured in Figure 2. It consists of a telescoping shaft, which axially collapses due to an applied external load above a pre-defined threshold. The applied load is further limited from increasing above an upper bound, over the length of the stroke.

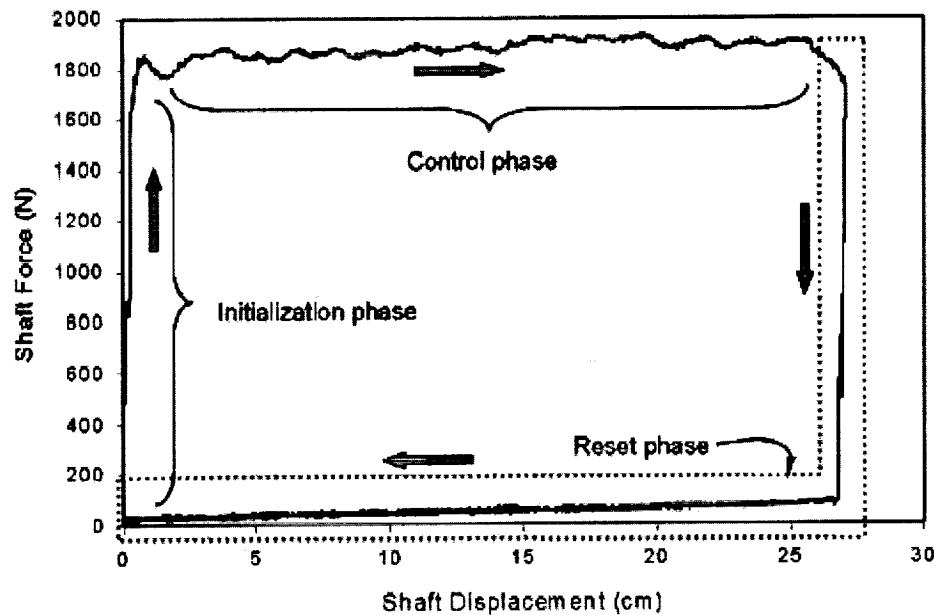


Figure 3. CETA Energy Absorber Performance

The shaft pushes through a set of beryllium copper diaphragm elements located within the housing that mechanically interfere with the shaft, producing the resistance to movement that dissipates energy as friction. The shaft is made from Inconel 718, and it is coated with a very thin film of Brayco 815Z oil. The diaphragms are C17200 Beryllium Copper, which have not been aged (precipitation hardened). On the compression stroke, a spring element that will be described later controls the deflected position of the diaphragms, which will determine the load necessary to push the shaft through them. The return stroke allows the diaphragms to flex freely. As a result, they provide little resistance to motion in this direction.

Figure 3 illustrates the CETA energy absorber performance. The three phases of operation are: initiation, control, and reset. The force required to initiate shaft motion rises sharply to the operating load of the device. It then remains fairly constant over the stroke to both limit contact loads and absorb the minimum energy required to effect a complete stop of the CETA. The reset of the energy absorber occurs automatically. The area circumscribed by the curve shown in Figure 3 represents the energy absorbed by the device. Figure 4 shows the predicted stopping distances for various CETA weights during an energy absorber impact.

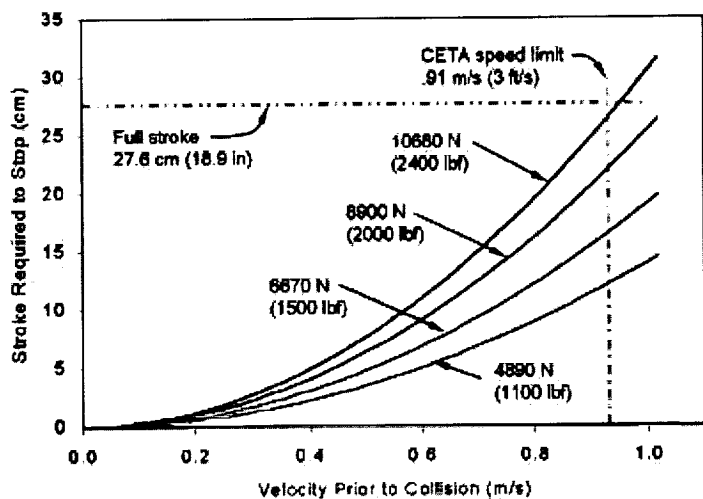
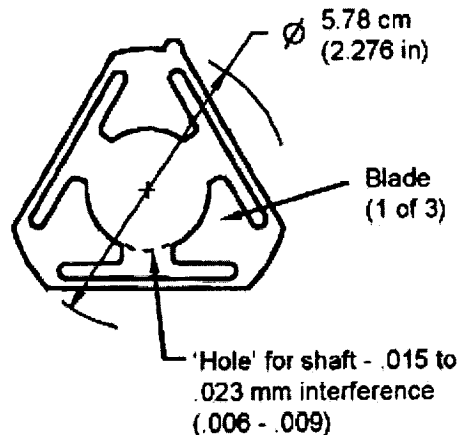


Figure 4. Stopping Distances for a 1780 N (400 lbf) Energy Absorber



Diaphragm, with three symmetrical beam elements (blades) which interfere with the shaft. Typical thickness is 0.5 mm (0.020 in). A stack of 10 is used for the CETA energy absorber.

Figure 5. Diaphragm

The operation of the energy absorber is best explained by deconstructing the interaction between the three elements (shaft, diaphragms, and spring) in each of these three operational phases. The following section will show the independent effects of each element in each of the three phases of operation.

Energy Absorber Theory

Shaft / Diaphragm Interaction

The diaphragms, shown in Figure 5, consist of 3 symmetrical blades that have a 'hole' smaller than the shaft diameter. The diaphragms are stable in either direction of shaft travel because the blades can be deflected in either direction. Changes in shaft direction result in the diaphragms 'popping through' the flat position, which is meta-stable, and inverting. This effect is similar to that which can be observed on fast food drive-through soda lids. Typically, the lid will have a series of dome shaped buttons that indicate what type of drink is in the cup. The domes are stable in two positions, the up 'as molded' position, and the inverted position that occurs when it is pushed. The flat position is unstable, and the dome will 'pop through' this position, in favor of the other two.

Figure 6 illustrates the interference fit of the diaphragms on the shaft and shows the forces acting on the diaphragms. From the figure, it can be seen that motion from right to left can occur relatively easily, as the shaft motion is in the direction of the deflected diaphragms, and sliding can begin at a low shaft load. Shaft motion from left to right will cause the diaphragms to pinch the shaft, as the diaphragm blades go into compression, and create a large normal force on the shaft. If the shaft force is large enough to overcome the resistance to motion caused by the diaphragms, they will pass through the neutral position and invert. It is only after the diaphragms have inverted that any sliding motion occurs. When the configuration shown in Figure 6 is measured in test, the force vs. displacement curve of Figure 7 results. Figure 7 shows the forces that the diaphragms exert on the shaft prior to inversion, which are equal to the housing reaction. In the initialization phase there is essentially no relative motion between the diaphragm inside diameter and shaft, and there is no significant sliding. The diaphragm edges roll on the shaft as they deflect and change position. It is important to note that the reaction from the housing changes direction when the diaphragms invert, and that the only force resisting motion of the shaft is the coefficient of friction times the normal force (μN). The shaft force cannot exceed μN . Before sliding begins, the shaft force will always be less than μN .

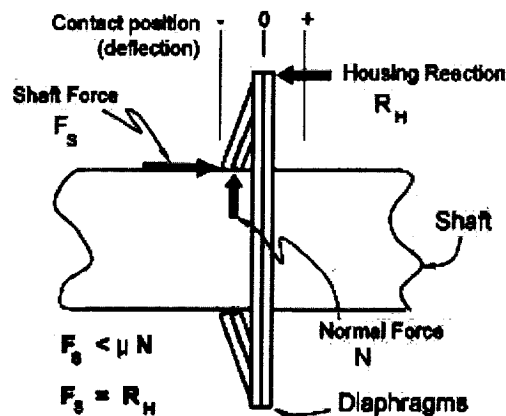


Figure 6. Shaft / Diaphragm Interaction

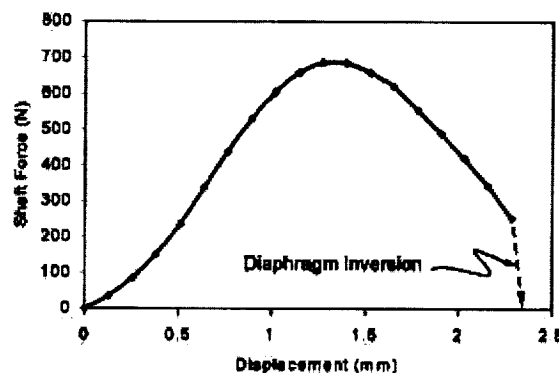


Figure 7. Housing Reaction

Spring Element

During the functioning of the energy absorber, the diaphragm deflection is controlled by the spring element. Figure 8 illustrates the interaction of the spring, shaft and diaphragms. When the shaft is being pushed past the flat position, the diaphragms 'want' to fully invert towards the direction of travel. They then hit the spring element, which provides resistance to further motion. The spring element will compress and allow the diaphragms to deflect farther if the shaft force is higher than the spring element force. Thusly, an equilibrium position is reached. The diaphragms have less normal force on the shaft the farther they deflect from the flat position due to reduced interference with the shaft. The spring element compresses, increasing resistance as the diaphragms deflect it. The diaphragms will deflect to the location where these forces and a housing reaction force balance.

Table 1 summarizes the equations that are used to model the CETA energy absorber. Figure 9 shows typical curves for the housing reaction and the spring element, and how they determine the shaft force. Note that there is a small offset between the shaft force and the spring element force, which produces a moment that is not accounted for. This contribution has been neglected for simplicity, since the offset is only 0.5 mm (0.020 in). As a result, the housing reaction force reported herein is low by about 6%.

Because of the many variables that affect the drag along the shaft, such as the amount or presence of lubrication, the surface finish of the shaft, the temperature, or the tolerance variations of the shaft / diaphragm interface, the spring element is needed to allow the diaphragms to vary their angle to the shaft dynamically during operation of the energy absorber. The spring element can be thought of as

determining the 'set point' of energy absorber operation, so that any diaphragm deflection that is needed to match the spring force can be accommodated.

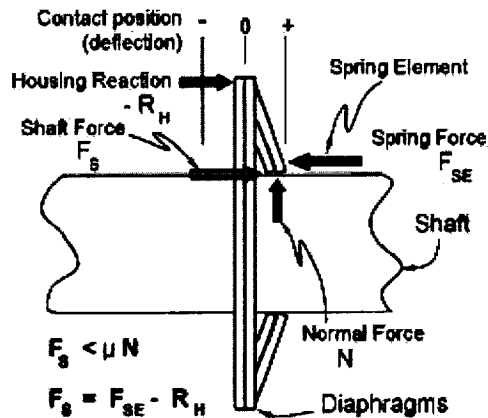


Figure 8. Interaction of the 3 Elements

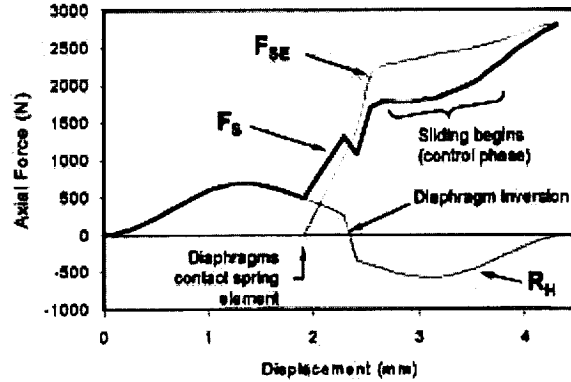


Figure 9. Initialization Model

Table 1. Governing Equations

Initialization phase	$F_s < \mu N$
1. Before diaphragm inversion & spring contact	$F_s = R_H$
2. Before diaphragm inversion, after spring contact	$F_s = F_{SE} + R_H$
3. After diaphragm inversion & spring contact	$F_s = F_{SE} - R_H$
Control phase	$F_s = \mu N$
	$F_s = F_{SE} - R_H$

Refer to Figures 6 and 8 for definition of variables

It is also the function of the spring to assure that the energy absorber resets itself after a collision. To fulfill this function, the spring must be capable of driving the diaphragms back to their original direction. Testing has demonstrated that the diaphragms must be displaced 0.76 mm (0.030 in) beyond the flat position to assure that they will energetically continue to invert. A small zone exists about the flat position that is stable due to friction within the system. Even 0.25 mm (0.010 in) less than this displacement may result in loss of reliable reset, with the shaft potentially poised in a 'hair trigger' configuration, collapsed, but requiring only a small disturbance to suddenly extend. The point at which the diaphragm deflection contacts the spring and substantial spring force also cannot occur too far from the flat position. Increasing the initial contact distance substantially to 1.5 mm (0.060 in) allows the diaphragms to contact the spring before they have developed a substantial interference with the shaft. From Table 1:

$$\begin{aligned} F_s &< \mu N \\ F_s &= F_{SE} + R_H \\ \text{Therefore, } F_{SE} + R_H &< \mu N \end{aligned}$$

Alternatively, the diaphragms have not had a chance to 'bite' the shaft and are susceptible to begin sliding motion prematurely. This type of geometry may cause difficulty getting the diaphragms to invert, and in the extreme, no diaphragm inversion occurs, and the load to collapse the energy absorber falls far below specification.

Therefore, for both reliable inversion and reliable reset, the spring element must be carefully placed with respect to the diaphragms. Both the initial contact position with the diaphragms and the spring rate must be controlled.

Control Phase Operation

After sliding motion has begun, the drag that the diaphragms produce on the shaft depends on the position of the diaphragms. Because the shaft is bigger than the 'hole' in the diaphragms, maximum interference occurs at the flat position. If the diaphragms can be kept at the flat position, maximum interference results in maximum forces at the shaft / diaphragm interface, which produces maximum drag. The drag is least when the diaphragms are fully inverted, and there is minimal force between the shaft and diaphragms. This is illustrated in Figure 10, where the calculated mechanical interference between the shaft and the diaphragms is plotted alongside the force required to push the shaft through a given set of diaphragms. The normal force generated by the diaphragms is proportional to the interference, and the friction generated is proportional to the normal force.

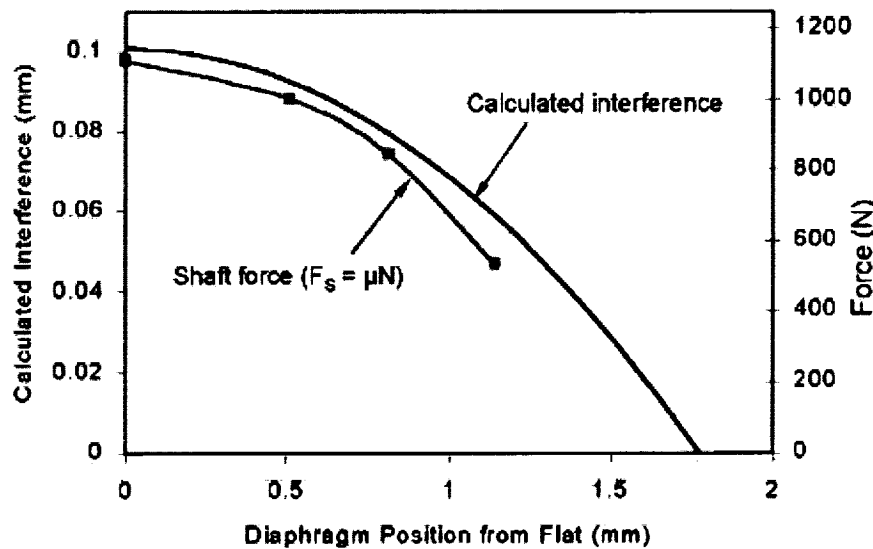


Figure 10. Shaft Sliding Through Fixed Diaphragms

In determining the configuration of an energy absorber for a given application, the number of diaphragms must be chosen such that the frictional load of the diaphragm stack in the flat position is greater than the load desired. To account for wear, the CETA energy absorber is initially set up to operate at about 1/3 the peak load that the diaphragm stack can produce when flat.

Because the shaft drag is proportional to the normal force, it does not matter if the diaphragms are on one side of flat or the other, or which direction the shaft is moving. If the drag on the shaft shown in Figure 10 is expanded to both sides of the flat position, a roughly symmetric curve results. If the conditions are then changed, such as to decrease the coefficient of friction, a second curve would result. The points at which the load is zero would remain the same, since this is a result of geometry. It is at these two diaphragm deflections where the diaphragms cease to make contact with the shaft. The peak load would still be at

the flat position. Varying the number of diaphragms, the surface finish of the shaft, the amount or quality of lubrication, or any number of other factors affecting the coefficient of friction all change the curve in the same way. Figure 11 illustrates such a family of curves.

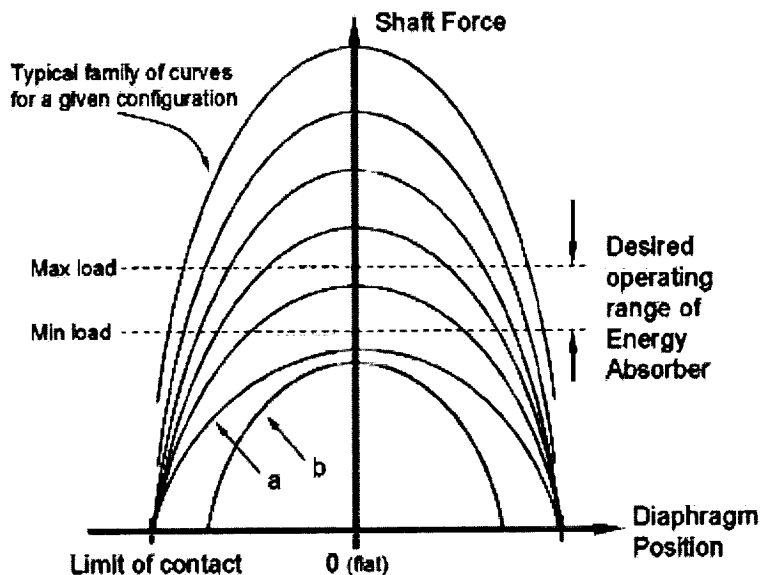


Figure 11. Sliding Frictional Drag Between Shaft and Diaphragms

Figure 11 also illustrates the desired operating range for the energy absorber. Note that all curves except the one labeled 'a' and 'b' pass through the desired operating range. Curve 'a' represents conditions that are too 'slick'. If these conditions are present, the desired load will never be reached. It is important to note that the energy absorber should be designed to allow the full deflection of the diaphragms. In this way, any condition that tends to increase coefficient of friction will be addressed. The only condition that would then be of concern is the slickest condition that can occur. Curve 'b' represents a reduced interference between the shaft and diaphragms, as would be expected due to wear or differential thermal expansion. As long as the slickest, least interference condition has a peak that is above the minimum load, all others are accommodated. This can be assured by specifying a *minimum* surface finish, by adding diaphragms, or by increasing the interference between the diaphragms and the shaft.

Design Development

The energy absorber as it existed in June 1999, is shown in Figure 12. The primary elements of the device are: the shaft, the diaphragms, and the spring element, which in this design is a single belleville spring. During assembly and test of the flight units in the spring of 1999, there was great difficulty in obtaining and maintaining the proper load setting of the devices. The first problem discovered was in the area of manufacturing of the belleville springs. The precise load needed from the belleville, combined with a sensitivity to the initial height of the spring for reliable reset made it extremely difficult to manufacture. Additionally, due to the fact that the belleville can be pressed completely flat by the diaphragms, the load of a given belleville could only be determined after 'scragging' of the part. This involves pressing it flat, which changes the peak load of the washer, but does not substantially change the spring constant. A trial and error approach was therefore necessary, with testing required before the bellevilles could be accepted from the manufacturer.

A second problem, uncovered during life cycle testing, was side loading of the shaft. As can be seen from Figure 12, the shaft is constrained simply by a hole in the housing. Deposits of aluminum from the housing and steel from a bushing (not shown in this figure) in the cover were observed. Adding Vespel bushings to both ends of the housing to support the shaft eliminated this situation.

While the above problems may be overcome by a determined design effort, the most significant problem encountered would prove to be unpredictable, and ultimately fatal to the production of a repeatable control load.

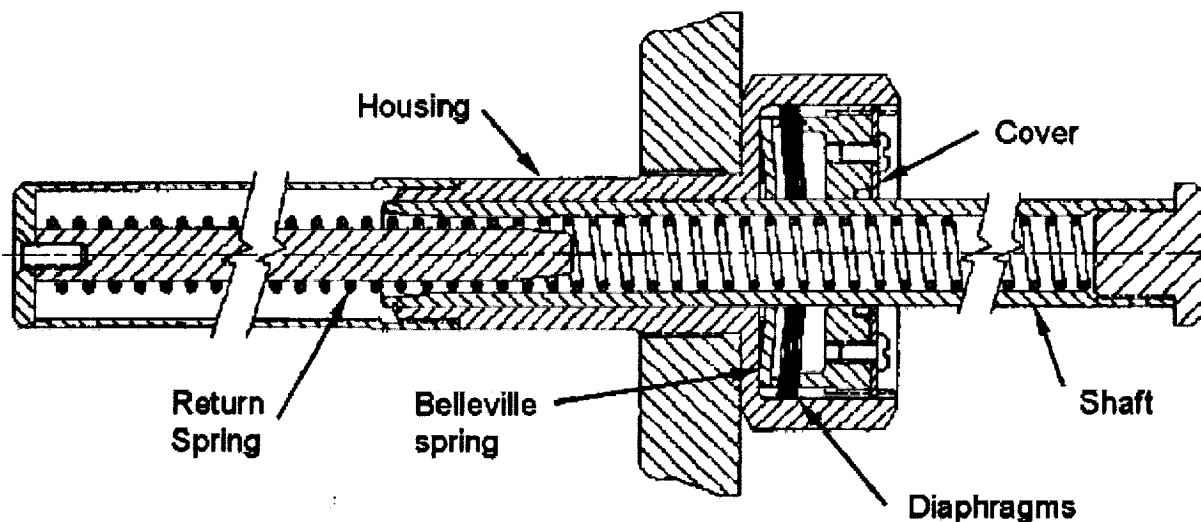


Figure 12.
1994 energy absorber using a single belleville washer to control diaphragm deflection

Referring to Figure 5, it can be seen that the diaphragm element contacts the shaft in 3 locations via three beam elements, which we call blades. While each diaphragm generally centralizes itself around the shaft, once placed in a stack, frictional forces between diaphragms during operation keep them from moving perpendicular to the shaft to balance the load between the three blades. This positional freezing of the diaphragms is combined with shaft motion due to the allowed clearances around the shaft, the possibility of off-axis loading cases, and the possible variation of friction coefficient at positions around the shaft itself. This allows the load of each blade to vary dramatically. It is this asymmetrical loading which is both unpredictable and irreversibly damaging to the belleville spring element. Belleville springs that have been subjected to this type of loading typically no longer have a consistent height, due to localized yielding. In the most dramatic examples seen, the belleville is completely flattened by one set of diaphragm blades, and lightly loaded by the other two sets of blades. Changes in set point load of 25% have been observed to occur in two successive cycles. As the asymmetric conditions may easily be found on orbit due to atomic oxygen flux preferentially affecting one side of the shaft, this aspect of the design had to be avoided.

In order to maintain the proper loading conditions for the spring element, design modifications were necessary and new components were added. One lies between the diaphragm stack and the spring element, and it rides along the shaft like a collar. The spring element then sees only uniform axial compression from the collar and is immune to asymmetrical diaphragm loading.

Attacking the problem of manufacture and sensitivity to position and spring rate of the spring element, the authors discarded the single belleville washer in favor of a spring cartridge. The spring cartridge contains a number of belleville washers which are modified from readily available stock sizes. The stack is preloaded on assembly. By adjusting the number of belleville washers and the preload via shims, the necessary performance may be obtained without requiring tightly controlled manufacturing. Also, much larger diaphragm displacements may be accommodated than were possible with a single belleville, which allows higher coefficients of friction to be accommodated.

To simultaneously achieve the goal of a reliable reset, the spring element is divided into two parts. The main load determination is done with a spring cartridge, which has a large travel, and an adjustable initial load and spring rate. The inversion and resetting is done with a second 'reset spring', in this case another belleville washer, which has an easily controlled initial position. This arrangement is shown in Figure 13.

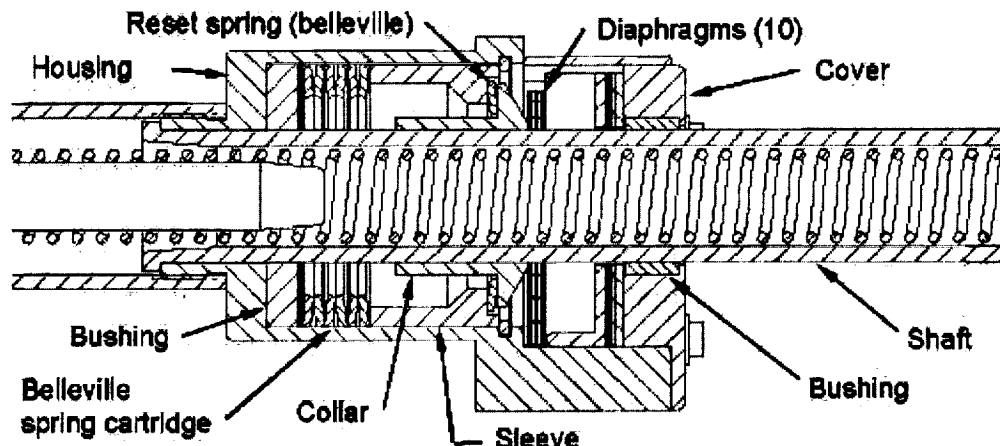


Figure 13. Spring Cartridge Implementation

A subtle but important effect is the load at which the diaphragm inversion occurs. The inversion event is characterized by a large change in the housing reaction force, as shown in Table 1 and Figure 9. If this event occurs at or near the set point of the spring cartridge, it can cause the spring cartridge to oscillate. Figure 14 illustrates one example of an oscillating spring cartridge, Figure 15 shows how the effects can be minimized by forcing the diaphragm inversion to occur well below the set point. This is accomplished by the use of the reset spring, so diaphragm inversion occurs during its travel, before the preload of the spring cartridge is reached. In the CETA energy absorber, these events occur within the first 3 mm (0.125 in) of stroke, and the load to compress the shaft stabilizes after about 6.4 mm (0.25 in).

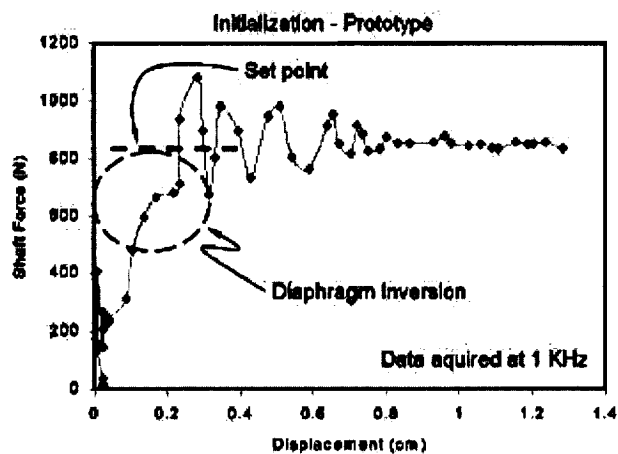


Figure 14. Oscillating Spring Cartridge

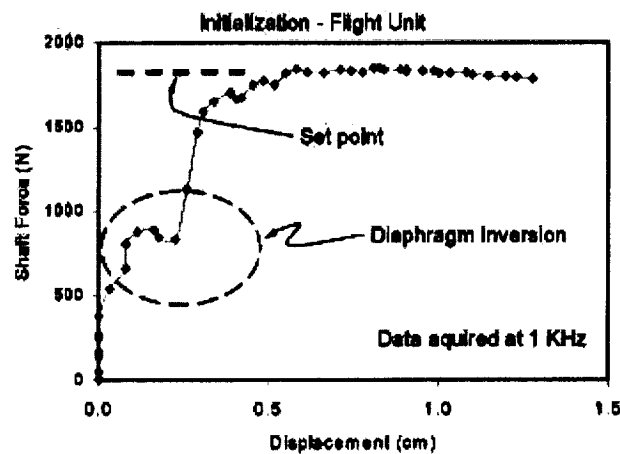


Figure 15. Oscillations Controlled

Most importantly, the force supplied by the spring element must be closely controlled, as the force needed to collapse the shaft is the simple sum of the spring force and the housing reaction. Therefore, the spring rate of the spring cartridge should be chosen such that the sum of these two is as constant as possible, which will yield a constant shaft load during operation. Figure 16 illustrates the cumulative effect of these forces. It shows how the net force in the nominal operating position of the diaphragms is determined. Figure 16 describes the energy absorber performance with respect to diaphragm deflection,

before and after sliding motion has begun. It should be noted that the force / displacement curve of the energy absorber shaft will only follow this curve until sliding begins, because the diaphragm deflection and the shaft position only coincide up to that point. The departure from the initialization phase to the control phase will occur where indicated in Figure 16. Further shaft compression will result in some shaft load variations, but a generally constant load is the result, as illustrated by Figures 3 and 15.

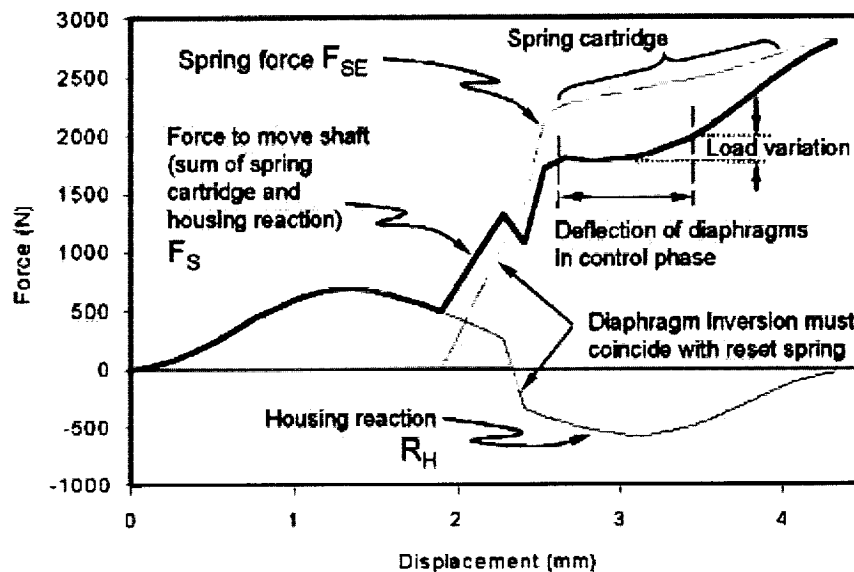


Figure 16. Initialization Phase Summary

Figure 17 shows the interaction of the energy absorber system of Figure 16 with the variable friction conditions as shown in Figure 11. The load to compress the shaft will follow the energy absorber curve, until it intersects the load limit of the diaphragm/shaft friction interface, which is represented by a series of curves. The shaft load will then remain essentially constant, because of the start of a sliding motion between the diaphragms and shaft. As the coefficient of friction varies, the load to compress the energy absorber shaft is given by the intersection of the energy absorber curve with the appropriate friction coefficient curve. This defines the predicted range of operating loads labeled in the figure.

Two impediments exist to achieving a perfectly flat force/displacement curve in the control region. The first is that the housing reaction curve changes with time. As the diaphragms wear, both the magnitude and shape of the curve changes. The material at the edges of the diaphragms is displaced, 'smeared' into the adjacent diaphragms, physically connecting them. Therefore, the slope of the spring cartridge force-deflection curve may be chosen to match the housing reaction initially, but this may change with wear. The CETA energy absorber uses non-aged C17200 Beryllium Copper diaphragms, which are significantly softer than the Inconel 718 shaft. Pairs of diaphragms were found stuck together post-test due to material displacement along the shaft interface. Although this material choice prevented any significant shaft wear, it is the authors' expectation that the aged condition would both reduce diaphragm sticking and increase overall wear life.

Use of a harder material to improve the wear properties may also reduce hysteresis by reducing or eliminating material transport between diaphragms at the shaft interface. Because the diaphragms move dynamically during the control phase to accommodate variations in conditions, hysteresis influences the degree of control that can be expected from this system. Figure 18 shows an exaggerated illustration of the possible effects of hysteresis on the shaft load. The actual effect is poorly understood at this time, since the amount of diaphragm movement that occurs during operation has not been accurately

measured. Whether sufficient diaphragm motion occurs to allow the full range of housing reaction hysteresis to be realized is unknown.

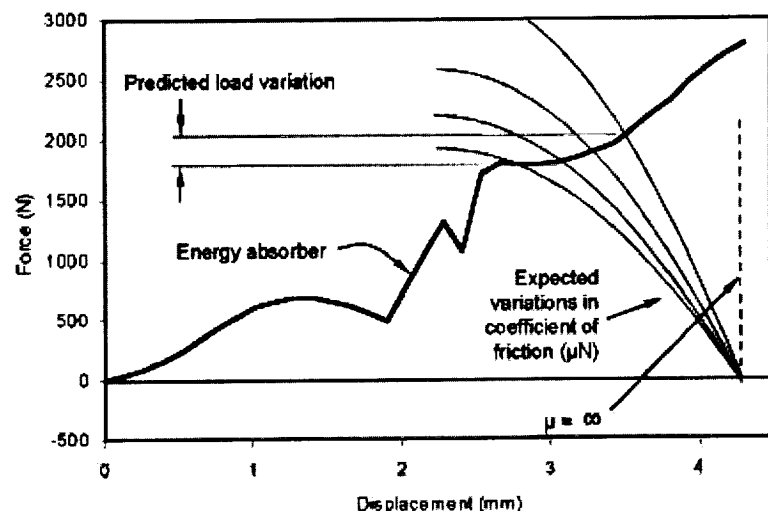


Figure 17. Predicting System Performance

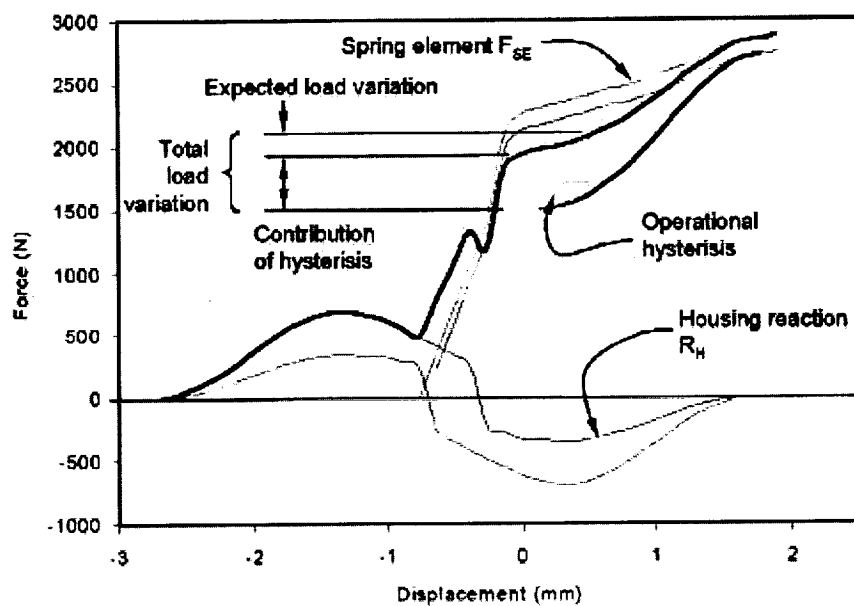


Figure 18. Effect of Hysteresis

The second impediment to more uniform load control is hysteresis. The spring cartridge consists of a belleville washer stack which does not touch the housing or the shaft on either inside diameter or outside diameter. The 304 stainless steel sleeve at the top of the belleville stack, shown in Figure 13, slides along a hard anodized aluminum bore with no lubricant. This arrangement has about 130 N (30 lbf) less return force than during compression. The housing reaction hysteresis can be determined from Figure 3.

The ratio of the housing reaction at initialization to the housing reaction at reset is in this case 83%, which is typical for the CETA energy absorber. A probable cause of this difference is that any motion of a stack of diaphragms results in a small but significant sliding motion between every diaphragm in the stack. This can be mitigated somewhat by providing lubrication between diaphragms, although no work has been done to date to find an acceptable lubricant, and none is used on the CETA energy absorber.

Testing

As part of flight hardware certification, the energy absorbers are subjected to 3 tests: vibration, thermal extreme, and life cycle. Additionally, the CETA energy absorber was subjected to impact testing to verify that it required a constant load to compress despite variations in compression velocity. This section shall describe the tests, and present how the energy absorber performance was affected by each.

Vibration testing

The CETA energy absorbers are only subject to significant vibration during launch aboard the space shuttle. The CETA itself is launched on ISS truss segment S1, with a pair of energy absorbers. The vibration testing produced no distinguishable effect on performance.

Thermal extreme testing

The nominal operating range of the CETA energy absorbers is -73 °C to +88 °C (-100 °F to +190 °F). One unit was designated the certification unit, and it was subjected to operation from -79 °C to +93 °C (-110 °F to +200 °F). Figure 19 illustrates the change in the operating set point of the device due to these temperatures. Table 2 summarizes the average loads at each temperature, over the range from 0.6 cm (0.25 in) to 26.7 cm (10.5 in) of the available stroke. Figure 19 shows these average loads as dashed lines, and the vertical bars delineate the portion of the stroke used for the data in Table 2.

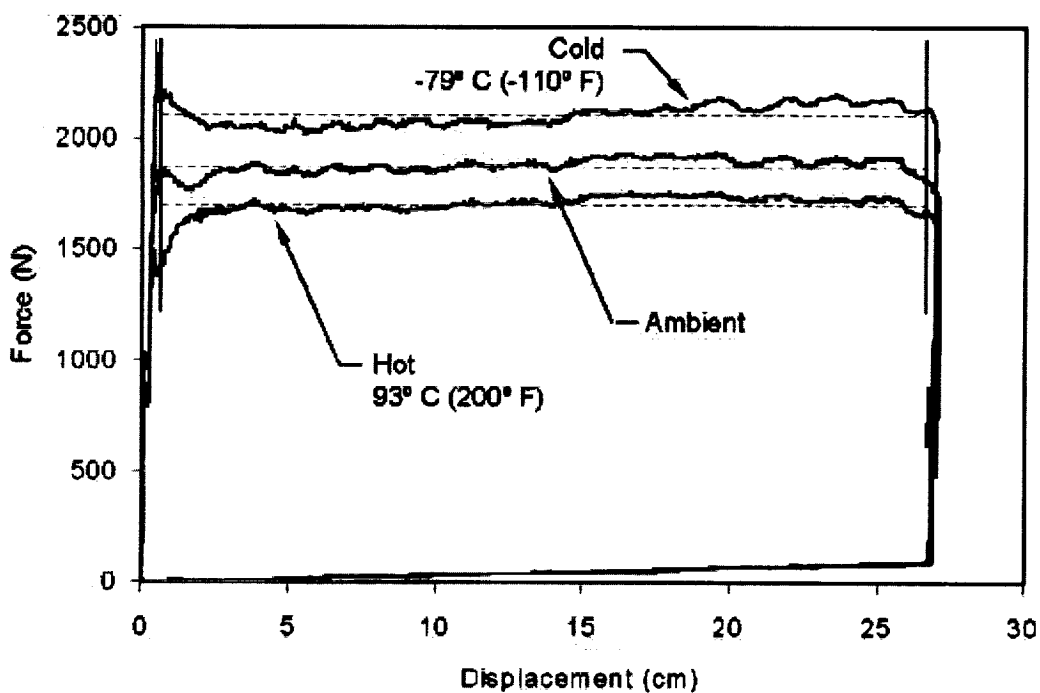


Figure 19. Performance vs. Temperature

The velocity of the shaft compression was a constant 46 cm/s (18 in/s) for each of these three tests. As evidenced by the data, variations in load due to changes in conditions along the length of the shaft are somewhat exacerbated by the reduced temperature condition. From Figure 19, each cycle increases load slightly during the stroke, with a wave like variation from 20 cm to 25 cm that is larger in magnitude at cold temperatures.

Table 2. Performance at Thermal Extreme

Temperature	Initial		Maximum	
	Force (N)	Displacement (cm)	Force (N)	Displacement (cm)
93 °C	1703 N (383 lbf)	47 N (11 lbf)	1760/1390 N (396/312 lbf)	
23 °C	1877 N (422 lbf)	33 N (7.5 lbf)	1940/1770 N (435/397 lbf)	
-79 °C	2104 N (473 lbf)	48 N (11 lbf)	2210/2020 N (498/455 lbf)	

Performance in control phase, 0.6 to 26.6 cm stroke

There are two main changes due to temperature that could be responsible for the changes observed in average load; differential thermal expansion, and lubricant viscosity change. Initially, the lubricant was thought to be the most likely cause. Brayco 815Z oil is used to lubricate the shaft, which experiences significant changes in viscosity over this temperature range, particularly at -70 °C and below. Informal tests have been conducted down to -86 °C (-122 °F), with no significant differences observed from -79 °C. The changes in load due to temperature are almost linear, which strongly suggest that differential expansion effects are more likely to be the cause. The coefficient of thermal expansion for beryllium copper is about 25% higher than that of Inconel 718, resulting in 0.1 mm greater interference at cold than at ambient. The hot temperature case results in 0.07 mm less interference. While these changes appear to loosely match the ratio of change observed in the load, additional work should be performed to verify this hypothesis, such as changing the shaft material to a different thermal expansion coefficient.

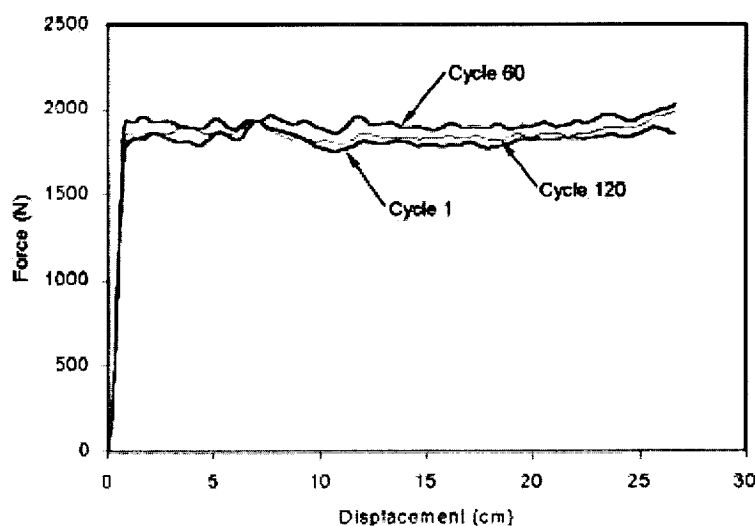


Figure 20. Life Cycle Summary

Life cycle testing

The life cycle testing requirement of the CETA energy absorber is 120 cycles. The actual number of on-orbit cycles is only 60. A summary of the certification life cycle testing is presented in Figure 20. It is interesting to note that no trend is evident from this data, which suggests that substantially more than 120 cycles could be accommodated. The maximum number of full stroke cycles tested by the authors is 240. After 240 cycles, the device demonstrated a greater variation in load along the stroke, but no significant change in the average load.

During an engineering evaluation test, an energy absorber was cycled without any lubricant. The first 60 cycles showed little degradation in load. At around 70 cycles, the load that the energy absorber would require to compress the shaft began dropping with each successive stroke, such that virtually no load carrying capacity existed by cycle 80. Subsequent measurement of the diaphragms showed that there was virtually no interference with the shaft due to material loss on the diaphragm inside diameter. The Inconel shaft was visibly coated with beryllium copper.

Conclusion

An energy-absorbing device is presented, planned for use on the International Space Station, offering collision protection for the large translating mass of the CETA. The device requires approximately 1800 N (400 lbf) to compress over a stroke of 27.6 cm (10.9 in), and will self-reset with an average of less than 67 N (15 lbf) over the stroke. The key element in the recent development has been the use of a spring cartridge to isolate and control this friction based energy dissipation system. With the use of a spring cartridge, a consistent, known spring load can be used to control a friction based interaction which may vary enormously due to many variables such as temperature, wear, surface finish or lubrication.

References

1. Wesselski, Clarence. "Energy Absorber for the CETA", Proceedings of the 28th Aerospace Mechanisms Symposium, 1994, pp141-146.
2. Boyer, Howard & Gall, Timothy, editors. "Metals Handbook desk edition", American Society for Metals (1985)
3. MIL-HDBK-5F, "Metallic Materials and Elements for Aerospace Vehicle Structures", (1990)

Friction Drive Characteristics for the Space Station Mobile Transporter

Richard C. Hughes^{*}, Daniel E. Hoyt^{*}, and Juan L. Carreras^{**}

Abstract

A friction drive system for translation along the truss structure of the International Space Station is described. All development, qualification and acceptance testing of the design has been completed and the flight article is undergoing integrated element testing in preparation for a launch in 2001. A discussion of the mechanical design, materials selection and test program is presented along with lessons learned.

Introduction

The Mobile Transporter (MT) is a robotic element, which moves along rails on the exterior truss of the International Space Station (see Figure 1). The role of the MT is to support the building and maintenance of the space station, over its 15-year nominal life, by translating payloads and robotic manipulators between fixed worksites on the station truss. At a worksite the MT supports operation of a large manipulator arm and a two-armed robot (both provided by Canada) by latching down to hard points on the truss and by plugging into station power.

Like most parts of the space station, the MT is maintainable on-orbit by astronauts through the removal and replacement of Orbital Replaceable Units (ORUs). All the avionics and major mechanisms on the MT are designed, developed and tested as separate ORUs.

When parked at a worksite for operation of the robotic manipulator, the MT is firmly attached to the truss by four Load Transfer Unit (LTU) ORUs. While translating payloads between worksites, the MT is supported by two Roller Suspension Unit (RSU) ORUs on one side and a Linear Drive Unit (LDU) ORU on the other side. The LDU provides the force needed to accelerate or decelerate the MT plus payloads and to pull against the Trailing Umbilical System (TUS) which provides power and communication to the MT.

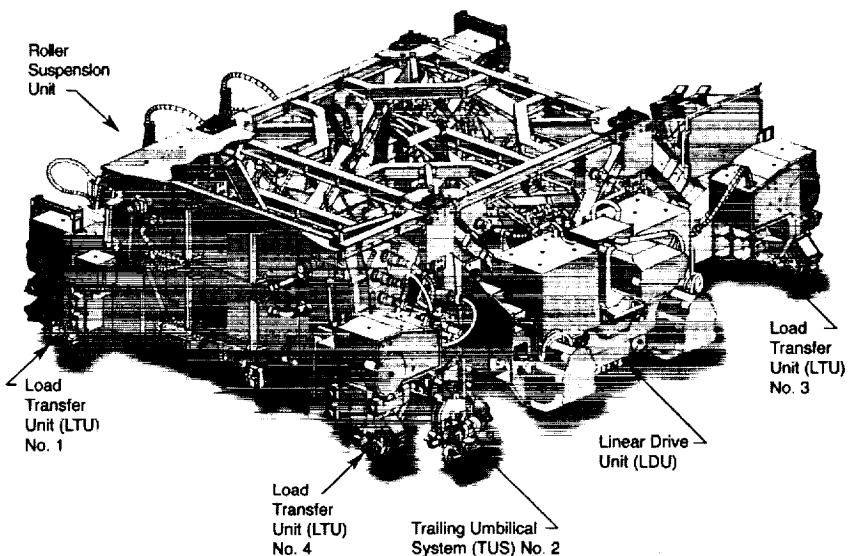


Figure 1. Mobile Transporter.

^{*} TRW Astro Aerospace, Carpinteria, CA

^{**} The Boeing Company, Huntington Beach, CA

The Linear Drive Unit is a fully redundant device, which contains two independent friction drive systems plus sensors to provide status and to detect worksites on the truss. The weight allocation of the LDU was 116 kg and the actual weight is 111 kg. Friction drives were chosen because the MT needs to navigate gaps, offsets and misalignments in the rail sections. The subject matter of this paper is the design and development of the LDU, focusing on the challenges associated with developing the friction drive.

Project Status

The basic Mobile Transporter was designed, developed and tested by TRW Astro Aerospace under contract to The Boeing Company. As the prime contractor to NASA, Boeing provides additional components (such as the TUS) and integrates the MT to the space station.

The basic MT has completed acceptance testing and was delivered to the Kennedy Space Center on 15 July 1999 in preparation for integration with the station truss segment on which it is launched. The MT is to be launched in mid 2001. The qualification program of the various components of the MT, such as the LDU, has been completed, although open issues are still being addressed.

Linear Drive Unit Description

Overview

The prime function of the LDU is to provide the translation force to move the MT along the exterior rails on the Space Station truss. The LDU, depicted in Figures 2 and 3, comprises primary and redundant translation drive systems, primary and redundant engagement/disengagement (E/D) drive systems, a bogie assembly, a booster foot assembly, a structure assembly, Extravehicular Activity (EVA) cams, EVA ORU bolts and EVA launch locks. The translation drive moves the MT along the length of the truss via a pinch-wheel system that grips a flange on a truss rail. The flange is pinched between a spring-loaded, high friction, drive wheel on one side and a pair of idler wheels attached to the bogie assembly on the other side. Only one drive wheel is engaged at a time for translation.

The E/D drive mechanism is used to engage and disengage the translation drive wheel with the truss flange using a gear-driven cam assembly. It is necessary to lift the drive wheel from the rail to eliminate any compression set of the wheel while the MT is latched at a worksite. The E/D drive also performs change-over, cam reset, and double engagement functions. The change-over function engages the secondary translation drive and disengages a failed translation drive from the truss rail to allow continued MT operation. A cam reset function is used to reposition the E/D drive cams after launch and to restore the cams to known positions after any failure scenario that leaves the

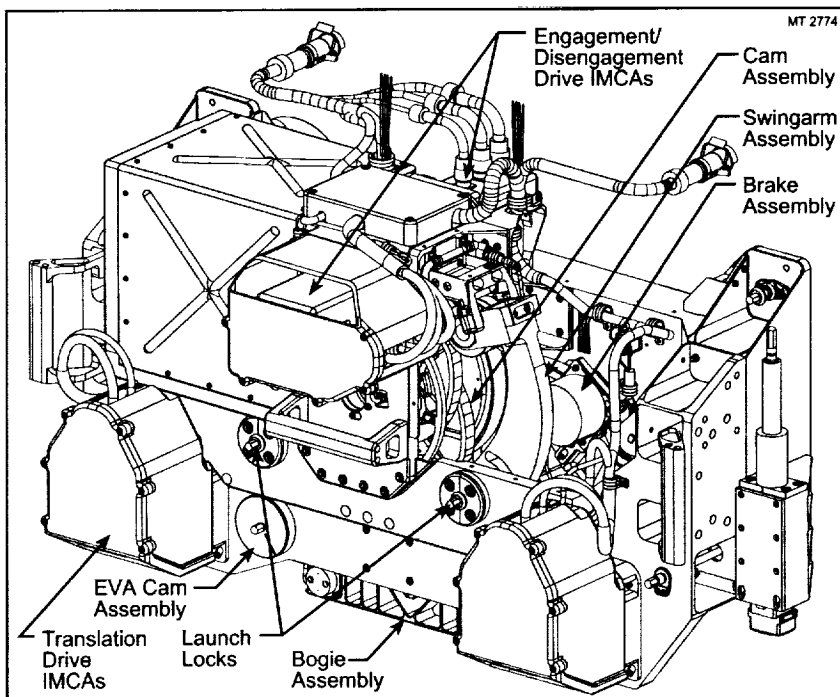


Figure 2. LDU Front Isometric View.

cams in unknown positions. A double engagement operation is performed to steady the MT during EVA replacement of a failed LTU.

During unlatching from a worksite, the booster foot assembly initially provides a vertical lifting force, by pushing on the rail with a spring load, and then lifts clear of the rail after a drive wheel is engaged. EVA cams are used to place the drive wheels in their launch positions to allow engagement of the swingarm launch locks. They also allow an astronaut to disengage both translation drive wheels and reinstall the launch locks for EVA removal and replacement of the LDU. All components of the LDU are housed in a common structure assembly to facilitate packaging as an ORU. The LDU ORU is attached to the MT structure with four EVA ORU bolts.

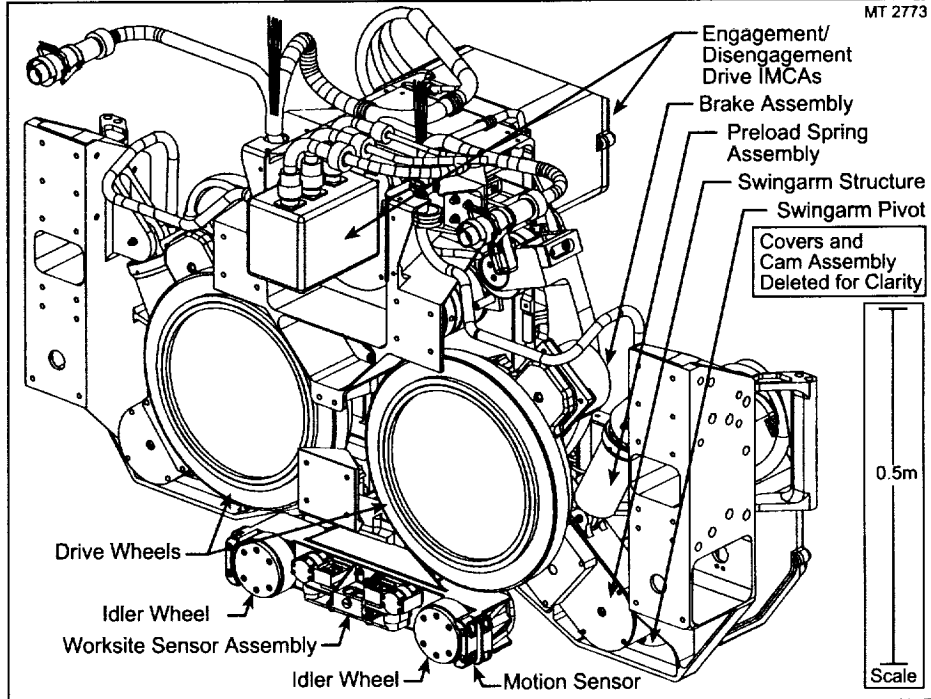


Figure 3. LDU Rear Isometric View.

Translation Drive

Each translation drive system contains an Integrated Motor Controller Assembly (IMCA), a gear train including a planetary gearbox, a preload spring assembly, a brake assembly, and a 30.5 cm (12 inch)-diameter drive wheel with an elastomer tire. The drive components are tied together by a common swingarm structure which houses part of the gear train, accepts torque input from the gearbox/IMCA combination, supports the drive wheel and brake assembly, and accepts attachment of the preload spring assembly. The pivoting end of the swingarm assembly is mounted to the main structure of the LDU. The gearbox/IMCA combination is mounted on the opposite side of the LDU structure wall that supports the swingarm. The preload spring assembly loads the drive wheel and the idler bogie wheels against the truss rail to generate the traction required for translation. Figure 4 displays a cross-section of the swingarm drive components coupled to the gearbox assembly and IMCA drive motor.

Power and communication is provided to the IMCAs in each of the two drives through dedicated electrical strings. During normal translation, only one translation drive is engaged to the truss rail and the other remains in its disengaged position as a backup. Either translation drive can be the active drive or the backup drive. The brake assembly on each swingarm provides a braking torque to the drive wheel when power is turned off in order to control MT stopping upon unexpected loss of power. Normal stopping is accommodated through controlled deceleration of the IMCA.

Engagement/Disengagement Drive

The engagement/disengagement drive assembly consists of a prime and a redundant system, each with its own IMCA, gearbox, spur gear pass, switches and cam. A third cam, referred to as the center cam, is

also incorporated between the two main cams in the E/D assembly. The cams can be seen in Figure 2. Under normal engagement/disengagement operation, the IMCA of the active E/D drive powers the gearbox, which rotates the spur gear that drives the cam. The cam lifts or lowers the associated translation drive through a cam follower attached to the translation drive swingarm.

The center cam is a contingency mechanism that enables a backup system to disengage a failed

translation drive. The center cam carries a pin that engages with slots in each of the main E/D cams. If the primary translation or engagement/disengagement system fails, power is removed from the failed system and the backup system is powered. The backup E/D cam, rotating in the opposite direction from normal wheel engagement, first engages the backup translation drive with the rail and then drives the center cam, via its pin, to raise the disabled translation drive. Translation can then be continued with the backup translation drive system.

Motion of the cams is controlled through the use of hermetically-sealed, magnetic reed switches positioned on the LDU structure and magnets embedded in the cams to indicate the translation drive disengagement positions for all three cams. Switches are also used to indicate the swingarm engaged positions.

Bogie Assembly

The bogie assembly consists of two 7.6-cm idler wheels, a bogie housing, motion sensors, and worksite sensors. The idler wheels engage the truss rail from the underside, and react the preload applied by the drive wheel during translation. When crossing gaps in the rails, one idler wheel is always in contact with a rail segment. The wheels are attached through redundant bearing sets to the bogie housing, which is a rigidly attached component of the LDU structure. Magnets in each idler wheel are used to trigger magnetic reed switches to form two motion sensors. The MT translation direction and a coarse indication of speed can be derived from the sequence and rate of switch transitions to provide an independent check of the primary sensors in the IMCA. Additional magnets and reed switches are configured into two worksite position sensors which can detect ferromagnetic strips, embedded in the rails, to signal the locations of worksites along the station truss.

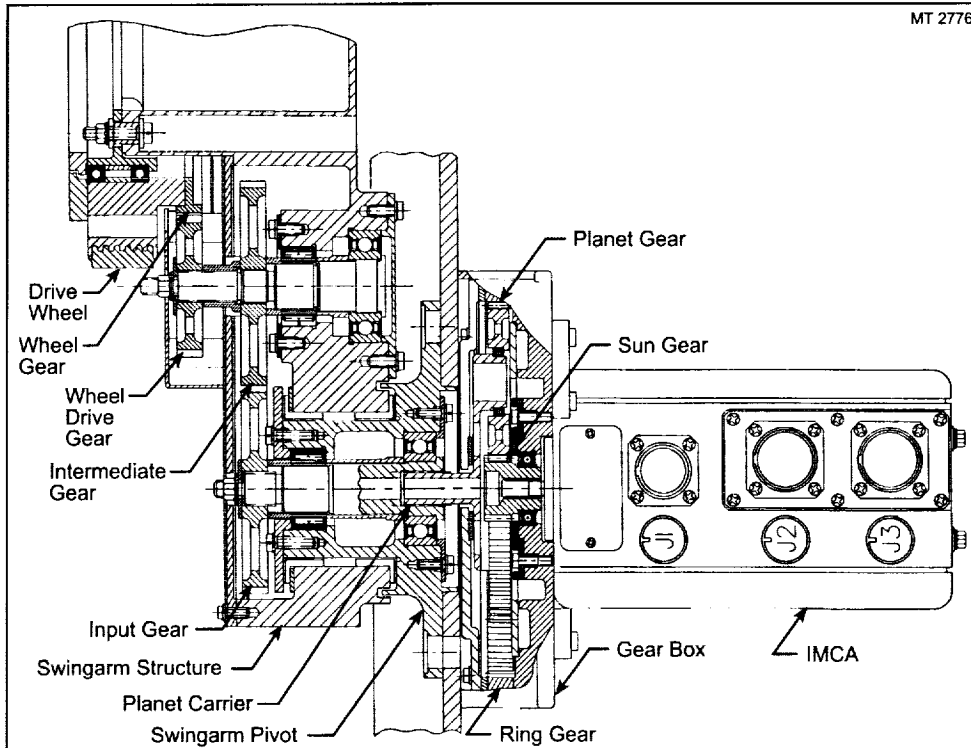


Figure 4. Translation Drive Train Cross-Section.

Drive Train Design

The primary requirements for the translation drive are to provide a peak drive force of 374 N and a continuous drive force of 156 N at controlled speeds between 0.13 cm/s and 2.5 cm/s. Drive performance has to be maintained in vacuum, over temperatures ranging between -43°C and +60°C, throughout the service life of the MT. The design accommodates a 11°C qualification margin at hot and cold.

For drive requirements, the LDU uses a Boeing/Allied Signal-provided Integrated Motor Controller Assembly (IMCA) consisting of a brushless DC motor, a motor controller, an internal 15:1 reduction gearbox, and an output clutch. Torque output from the IMCA is coupled to a 7.14:1 reduction, single-pass, planetary gearbox assembly via a splined-shaft connection. This connection drives the sun gear of the gearbox assembly subsequently rotating the three planet gears within a ring gear. Output from the gearbox assembly is delivered from a splined shaft integral to the planet carrier. Within the swingarm assembly, torque is transmitted through a spur-gear pass to a pair of coaxial gears which, in turn, drive a second spur-gear pass that powers the drive wheel. Figure 5 depicts the swingarm assembly gear train. The brake assembly is connected to the drive wheel through a separate spur-gear pass. Collectively, the translation drive assembly possesses a 51.5:1 gear ratio to provide up to a 534 N drive force from the 1.6 N·m maximum output torque of the IMCA.

To avoid drive train efficiency losses due to mechanical interference from thermal expansion, fits between mating parts of dissimilar materials were established to provide at least 0.0013 cm (0.0005 inch) clearance at worst-case temperature conditions. Axial fits were also established to guarantee minimum bearing preloads where necessary and to avoid thermal-induced interference. Unfortunately, this approach causes certain interfaces to be relatively loose under particular temperature conditions; however, qualification testing dispelled concerns of excessive wear and friction potentially resulting from this situation.

Swingarm Configuration

The LDU implements a swingarm design to allow vertical motion of the wheel when crossing steps in the rails and during MT latching at a worksite. An advantage of a swingarm design is that the drive motor, along with its planetary gearbox, can be fixed at the swingarm pivot and communicate the drive torque to the drive wheel through a gear train attached to the swingarm. An issue with this approach is that the introduction of a drive torque at the pivot axis will produce a torque on the swingarm that can increase or decrease the preload of the wheel to the rail depending on the direction of travel and the geometry of the swingarm.

Variations in wheel preload need to be minimized since decreased preload can lead to wheel slipping and increased preload causes increased drive force requirements for crossing rail steps. However, the drive wheel preload can be made independent of drive torque through a "torque neutral" design which matches the gear passes on the swingarm with the operating angle of the swingarm to ensure that drive forces result in no net torque on the swingarm. An added benefit of torque balancing the swingarm is that

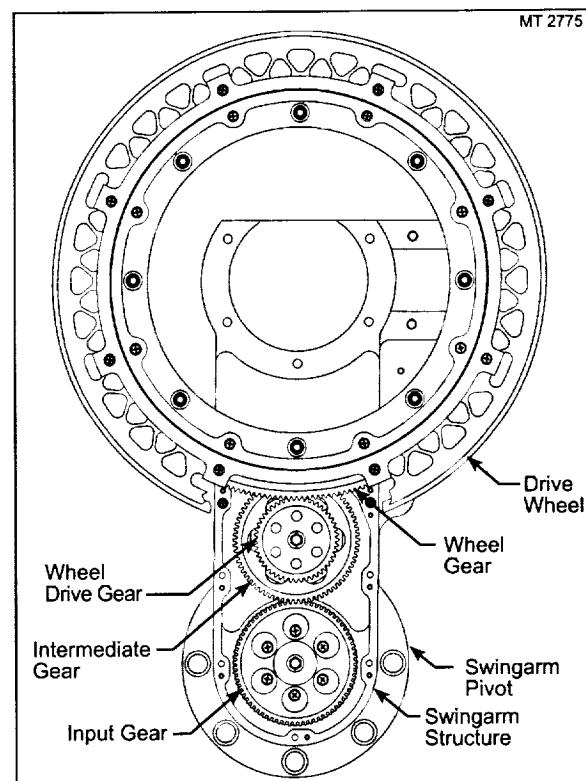


Figure 5. Swingarm Gear Train.

eliminating torque-induced preload minimizes rotation of the drive wheel due to rotation of the swingarm. This allows the MT to accurately hold its position along the rails as the drive wheel rises during a latching operation at a worksite.

The following analysis displays the dependency of wheel preload on swingarm orientation and gear train geometry. The normal drive wheel preload generated by the spring pack does not affect the torque balance of the swingarm; therefore, in the following analysis we will ignore the spring preload and only address the resulting preload due to the input drive torque and the output drive force. As indicated previously, the LDU swingarm has two passes of spur gears to increase the drive torque at the wheel. When the gears are under load, reaction forces are generated at the gear pivot points, which contribute to the net torque exerted on the swingarm. The individual forces on the swingarm (neglecting the spring preload) are represented in Figure 6 where it is assumed that the gears mesh at their standard pitch radii. The swingarm structure will only experience forces at the gear and swingarm pivot points as indicated in the resultant force diagram of Figure 7. Static balance of the swingarm requires that the net torque about the swingarm pivot be zero which results in the following condition.

$$(r_1 + r_2) \left(1 + \frac{r_2}{r_3}\right) \frac{\tau}{r_1} = (r_1 + r_2 + r_3 + r_4) \left[\frac{r_2}{r_3} \frac{\tau}{r_1} + \cos(\alpha) F_n - \sin(\alpha) \frac{r_2 r_4}{r_3 r_5} \frac{\tau}{r_1} \right] \quad (1)$$

Solving for the torque-induced preload, F_n , in terms of the input torque results in the following expression.

$$F_n = \frac{\tau}{\cos(\alpha) r_1} \left[\frac{r_1 r_3 - r_2 r_4}{r_3 (r_1 + r_2 + r_3 + r_4)} + \sin(\alpha) \frac{r_2 r_4}{r_3 r_5} \right] \quad (2)$$

Torque balance is achieved when F_n equals zero, which is achieved when:

$$\sin(\alpha) = \frac{r_5 (r_2 r_4 - r_1 r_3)}{r_2 r_4 (r_1 + r_2 + r_3 + r_4)} \quad (3)$$

For the LDU, where $(r_1, r_2, r_3, r_4, r_5) = (3.387, 4.180, 2.328, 13.600, 15.240)$ cm, torque balance is achieved for the swingarm angle $\alpha = 34^\circ$. Due to late changes in gear ratios, complete torque balance was not fully achieved with the as designed nominal 30° swingarm angle. However, the resulting preload fluctuations due to a maximum drive torque equivalent to a 374 N drive force are predicted by Equation 2 to be only ± 25 N about the nominal 623 N preload. During qualification and acceptance testing of the LDU no difference in performance was noted for changes in drive force or direction.

Material Selections

The selection of suitable materials was driven by strength, stiffness, contact stress, weight, fracture control, corrosion resistance, outgassing, atomic oxygen resistance and friction requirements.

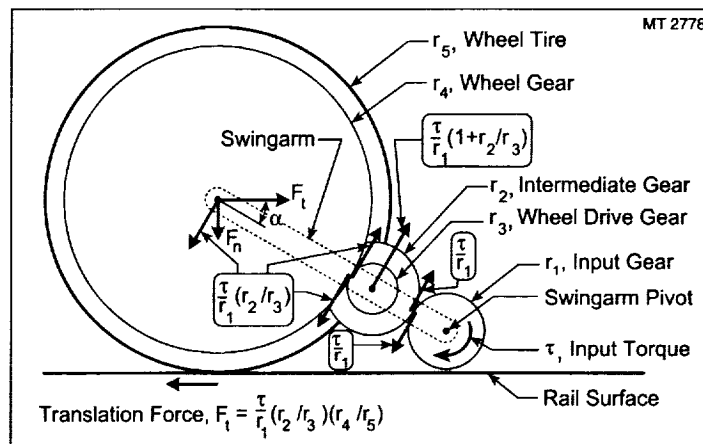


Figure 6. Torque Induced Forces on LDU Swingarm Assembly.

Structural components, such as the swingarm structure and gearbox housing, are primarily constructed of 7075-T7351 aluminum alloy while CRES Custom 455™ was chosen for gears and shafts. The structural portion of the drive wheel and its supporting spindle are Ti-6Al-4V. Bearings are of angular contact, radial ball, thrust, and needle roller design, fabricated from the traditional space-bearing material CRES 440C. The idler wheels are made of polyetheretherketone (PEEK) to avoid contact stress damage to the truss rail. A silicone material was selected for its superior friction properties and durability to use as the drive tire. Selection processes for the idler wheels and drive wheel materials are detailed in subsequent sections. Tetrafluoroethylene (TFE)-lined bushings are used to reduce sliding friction at the swingarm pivot. Also intended to minimize sliding friction, Vespel™ washers are used to line interior surfaces of the gearbox assembly.

An important selection criterion for lubricants is the ability to perform under vacuum over a wide temperature range. All gears and splines in the gearbox assembly and swingarm assembly are dry-film-lubricated with Vitro-Lube 1220C™ to reduce friction at sliding interfaces. Additionally, bearings with rolling elements are lubricated with Braycote 601™ grease. All gear trains underwent operational conditioning cycles to break-in the dry-film-lubricated components and verify basic performance.

Materials Development Testing

Idler Wheel Material

A materials development program was undertaken to identify suitable materials for the LDU drive and idler wheels. Addressing first the idler (i.e., bogie) wheels, seven candidate materials were first selected based on a review of material properties. Full size (7.6 cm diameter) test wheels, consisting of an aluminum hub with a 0.55 cm thick plastic tire, were manufactured for all candidate tire materials. In what turned out to be a poor design feature, which was corrected in the final design, the tires on the test wheels were keyed to the hub through notches on the tire rim and lugs on the hub. During testing, the stress concentration at the tire notches did initiate cracking for some materials. The test wheels were subjected to a series of tests as summarized in Table 1.

Table 1. Candidate Idler Wheel Tire Materials

Material	Impact Test	Life Test	Thermal Vacuum
Ethylene-chlorotrifluoroethylene (E-CTFE)	Passed	Distorted	No
Polyarylsulfone (PAS)	Passed	Cracked	No
Polysulfone (PSO)	Cracked	No	No
Polyetherimide (PEI), with 30% glass fiber	Abrasive	No	No
Poly(amide-imide) (PAI), 3% TiO ₂ , 0.5% fluorocarbon	Passed	Cracked	No
Polyetheretherketone (PEEK)	Passed	Passed	Passed
Polyetheretherketone (PEEK), with 30% glass fiber	Abrasive	No	No

The various tests listed in Table 1 were performed by running the test wheels with a 490 N preload against a rotating 30.5-cm-diameter anodized aluminum drum. The test wheels were first subjected to the cold temperature Impact Test, which simulated the MT crossing gaps and offsets in rail segments by

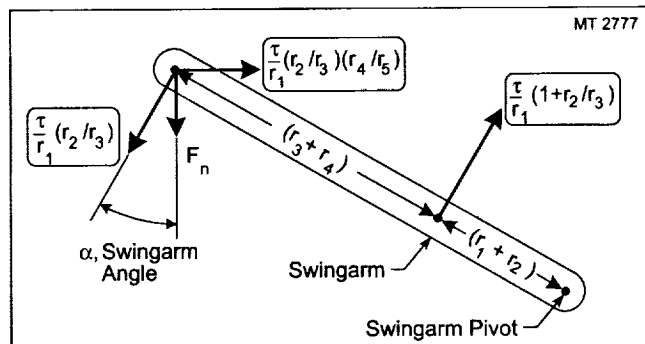


Figure 7. Moments About Swingarm Pivot.

adding profiled aluminum strips to the drum surface. The wheels were run for 124,000 cycles over steps ranging from 1 mm to 2.5 mm. As noted in Table 1, two wheel candidates were eliminated after this test because they proved to be abrasive to the anodized aluminum drum surface and a third was eliminated due to evidence of stress cracking.

The next test in the series was the life test in ambient air where the remaining wheels were run for 2,300,000 drum revolutions. During this test the E-CTFE material was dropped because it exhibited significant cold flow at the highly stressed notch area and two other materials were eliminated due to cracks developing in the notch area. The surviving PEEK material showed no evidence of cracking and suffered only minor wear.

The PEEK test wheel then underwent thermal-vacuum testing where the wheels were run for 800,000 drum revolutions at temperatures ranging between 60°C and -54°C over a 5.3-day period. Friction tests were made at the start and end of all plateaus by locking the wheel hub and measuring the torque needed to cause the drum to slip. The results show that the coefficient for sliding friction did not change from ambient air to vacuum, did not change significantly with temperature, but did consistently increase over the duration of the test. The coefficient of sliding friction at the start of the test was 0.26 (air and vacuum) climbing to 0.42 at the end of the test (vacuum). It is not possible to resolve from this data if the increase in friction is largely due to running effects, such as wear of the tire and transfer of material to the anodized aluminum drum, or if extended exposure to vacuum has a strong effect on friction.

In summary, the PEEK idler wheel tire material survived an extremely demanding set of development tests, including very high impact loads during accelerated testing. For the MT flight design of the RSU and LDU idler wheels, the stress-concentrating notches in the tire and lugs on the hub were eliminated and the tire is allowed to slip on the hub.

Drive Wheel Material

In parallel with the materials development program for the idler wheel tire, a similar selection process was undertaken to find an appropriate tire material for the LDU friction drive wheel. The general requirements dictated a compliant, temperature and vacuum stable, long-wearing, non-abrasive material with a high friction coefficient over the thermal-vacuum environment. A review of material properties narrowed the tire material to phenyl-substituted silicone elastomers, from which seven candidate materials were picked for development testing.

Two different manufacturers specializing in rubber processing were selected to produce 7.6-cm-diameter test wheels, two for each candidate material, by compression molding the elastomer tire directly onto wheel hubs. Unfortunately there is still a significant "art" to processing elastomers. Only one of our two vendors had the rubber grinding technology needed to meet our dimensional requirements, while only the other vendor had the process needed to include reinforcing belts into the tires. In preparing our test wheels, one of the vendors successfully bonded the tires to the hubs, but the other vendor had a process problem, which led to debonding of the elastomer tire from the aluminum hub for a number of test samples.

Test wheels for all of the elastomer materials were prepared without any reinforcing material added to the tire. In addition, three materials were also tested with an embedded belt of Aramid fabric reinforcement molded into the tire. The initial series of selection tests comprised compression set, joint crossing, and life/performance at temperature extremes (-54°C to 66°C in air). All of the materials passed an initial compression set test where the recovery of the elastomer was measured after being loaded for 24 hours. The joint crossing tests simulated the loading conditions experienced when crossing gaps and offsets in the rails while the life/performance test ran the test wheels under a preload of 311 N against a 30.5-cm drum at ambient and temperature extremes for a total of 120,000 rotations. At all phases of testing, wheel friction was measured by locking the test wheel and determining the force required to make the drum slip under the wheel.

Table 2 lists the various wheel candidate materials along with their hardnesses and some comments on their performance. Under sliding loads the elastomers exhibited two friction coefficients: the static friction coefficient determined by the force required to initiate sliding and the dynamic friction coefficient determined by the force required to sustain sliding. Elastomers have the unusual property that the sliding friction coefficient is generally greater than static friction coefficient. For the LDU drive wheel application, the dynamic friction coefficient was used because the MT has to produce high drive forces only for a very short duration and a limited amount of drive wheel slip can be tolerated in this situation.

In general, the softer materials have the best friction properties, but do not stand up as well to high loading conditions as do the harder materials. The very soft CV-2287 material was dropped early on as a candidate because it started to tear during joint crossing tests. The very hard M-950-A-41 material was eliminated later because its sliding friction coefficient in air had dropped from the initial value of 0.94 to a value of 0.59 at the end of extended testing, which is below the minimum requirement of 0.6. As a general comment, all of the remaining candidates showed promise as wheel material. However, the last five candidates in Table 2 were eliminated from further testing because processing problems led to full or partial debonding of the tires from the wheel hubs for all the wheels with the Aramid fiber belt and for all the wheels with the SRS 185 and SRS 105 materials. Unfortunately, the tight development schedule did not allow us to remanufacture test wheels for the debonded materials so we were unable to further investigate SRS 105 or SRS 185 materials or to resolve if reinforcing, such as embedded fabric belts or random fibers, provides any advantage.

Table 2. Candidate Drive Wheel Tire Material Testing in Air

Material	Shore A Hardness	Minimum Friction	Comments
Wacker Silicone, M-950-A-41	85	0.59	hardest material, eliminated for low friction
McGhan Nusil, CV-2287	30	-	softest material, tears under load
Dow Coming, STI LT50	60	1.04	best all round
General Electric, SE6660	60	0.71	good all round, second choice
Rhone Poulenc Rhodorsil, MM771/70	65	0.71	good all round, third choice
Rhone Poulenc Rhodorsil, MM771/70 with Aramid belt	65	-	debonding of tire from hub
Arlon SRS 185	48	0.86	very good friction, possible debonding
Arlon SRS 185 with Aramid belt	48	-	debonding of tire from hub
Arlon SRS 105	57	-	debonding of tire from hub
Arlon SRS 105 with Aramid belt	57	0.80	good all round, possible debonding

Two candidate materials, the Dow Corning STI LT50 and the GE SE6660, were selected for additional thermal-vacuum life and friction testing. Previously unused test wheels for the two materials were first vacuum baked at +71°C and then were run in vacuum against the rotating test drum over the temperature range of 66°C to -54°C, with friction measurements made periodically throughout the test. Over the 5.3 days of vacuum testing, the wheels accumulated a total travel equivalent to greater than two lives of operation of the full size 30.5-cm LDU drive wheel.

For these tests, the friction coefficient was measured by locking the wheel and measuring the torque to rotate the drum. The trends evident in the dynamic friction data are:

- The friction coefficient increases in vacuum over air (20% and 13% respectively for LT50 and SE6660)
- The friction coefficient is higher at hot than at cold (16% drop between 60°C and -54°C for both LT50 and SE6660)
- The friction coefficient decreases over life (8% and 9% drop respectively for LT50 and SE6660)

Since the final flight design of the drive wheel has a 30.5-cm diameter with a titanium hub rather than the 7.6-cm diameter with an aluminum hub as used in the development testing, bonding tests of the elastomer wheel materials to titanium were performed. Tests performed with the Dow Corning LT50 elastomer bonded to metal coupons indicated that the Dow Corning S-2260 primer used with the test wheels was effective on titanium as well. In order to qualify the drive wheel tire manufacturing process, a full-size 30.5-cm-diameter drive wheel was manufactured with the Dow Corning LT50 elastomer.

The material test wheels were manufactured in the first quarter of 1992. The initial set of tests on these wheels was completed in September 1992 with the Dow Corning LT50 material being selected as the prime candidate material for the LDU drive wheel with the GE SE6660 material being held as a backup. A wheel stiffness test, started in August 1995, of the LT50 test wheel identified a loss of wheel friction coefficient during the 3 years that the wheel had been held in storage (under ambient conditions). The friction loss was found to be permanent and could not be restored by cleaning, abrading or vacuum baking. The SE6660 test wheel still demonstrated acceptable performance. Note that, although the two elastomer formulations are both phenyl methyl-dimethyl silicone polymers, the catalysts are different for the two products (Dow Corning -T for DC LT50 and Varox™ for GE SE6660) and the quantity of free silicone oil used to disperse the catalyst was 7 times greater in the DC LT50 material than the GE SE6660 material. The unpolymerized free oil is suspected to be the cause of the loss of friction.

To address the concern that these friction tests still relied on a fixed wheel and were performed in air, a more flight-representative set of tests were initiated for the SE6660 material. For these tests the wheel was preloaded at 396 N against a flat rail surface and the friction coefficient was established by measuring the torque on the wheel required to sustain slipping. Because friction coefficients were mostly a concern at hot temperatures, these tests were conducted at temperatures ranging from 21°C to 70°C for a total of 6 days in vacuum. Friction coefficients, measured in air before and after the vacuum testing, did not significantly differ. Although the test results initially showed a drop in friction coefficient in vacuum, the friction coefficient did recover and continued to increase over the duration of the test in vacuum, with a final value of 0.82 for a net increase of 22% for vacuum over air values. The overall behavior is indicative of moisture, absorbed by the elastomer while in air, compromising the friction coefficient until the moisture is driven off. An interesting result was that when the elastomer wheel slipped on the anodized aluminum rail surface in vacuum, a luminous discharge was produced where the tire material was leaving the tire-to-rail contact patch.

Extreme Temperature Exposure

The presence of the MT tends to moderate the temperatures of the space station rails on which it runs. But to ensure that MT wheel materials will not be damaged by the MT translating onto exposed rails that are beyond normal operating temperatures, a series of extreme temperature exposure tests were performed for both the PEEK plastic idler wheel material and the GE SE6660 elastomer drive wheel material. For the hot temperature extreme, a SE6660-tired test wheel was heated to 64°C and then run under preload on a 93°C rail while a PEEK test wheel was heated to 129°C and then run under preload on a 93°C rail. For the cold temperature extreme, the SE6660 test wheel was cooled to -68°C and then run under preload on a -73°C rail while the PEEK test wheel was cooled to -76°C and then run under preload on a -76°C rail. Both wheels passed this extreme temperature testing with no evidence of damage.

LDU Mechanism Testing

Development Testing

Prior to completion of the detailed design, the LDU preliminary design went through a limited "proof of concept" breadboard test program where full size, but not flight like, swingarms, drive wheels, engage/disengage cams and a bogie assembly were fabricated and tested as a unit. This process contributed to the maturity of the design but had only limited value because it lacked much of the detail of the final design. The LDU design was also moved forward and, more importantly, the manufacturing processes were established through the construction of an LDU mass simulator for MT system level modal survey and vibro-acoustic testing. Because the LDU was big enough to contribute significant local modes to the MT modal response, the LDU mass simulator structure and ORU attachment hardware was built to early flight drawings in order to provide representative stiffness properties.

Qualification and Acceptance Test Program

At the completion of the detailed design process, a flight-like LDU qualification unit was built and tested in order to validate the design. Due to schedule pressures and the extensive qualification test program, the actual flight LDU was built and acceptance tested before the qualification tests finished. Since the purpose of the acceptance tests of the flight unit are to verify workmanship rather than to validate the design, the tests were only a subset of the qualification tests. The tests performed on the two flight-like units are summarized in Table 3.

Table 3. LDU Qualification and Flight Testing

Unit/Test	Function	Vibration	Thermal	Thermal Vacuum	Thermal Balance	Stiffness	Strength	Life
Qual.	Full	180 sec. qualification	No	3 cycles -54 to 71°C	Heater function	1.0 limit	1.1 to 1.5 limit	2x 10 years
Flight	Full	60 sec. screening	8 cycles -43 to 60°C	No	No	No	No	No

All functional testing, including thermal and thermal-vacuum, was performed on a special LDU test fixture which used a powered and instrumented rail carriage to simulate LDU operating conditions, such as offsets and gaps in rails, aiding or retarding loads, and MT latching operations. Vibration testing and stiffness/strength testing used special test fixtures with flight-like attachment hardware.

Acceptance testing of the flight LDU progressed relatively smoothly; however, the qualification test program did surface a number of problems that were resolved with fixes being incorporated into the flight hardware as well. The recovery from a vibration overtest, due to a shaker runaway, became an opportunity to fix some switch problems and correct a swingarm clearance issue. As is often the case, the test fixture, which had to work over the same extremes and was almost as complicated as the LDU itself, had numerous problems, which significantly impacted the test schedule. One lesson learned was that, overall, the test program would have been completed sooner and more cost effectively if more design effort had been invested in the test equipment.

Three major issues regarding the LDU drive system surfaced during qualification testing:

- A dependence of travel distance and velocity on load
- An increase in motor torque requirements at cold temperatures
- A loss of wheel friction during life testing

Drive Wheel Effective Radius

One of the more interesting discoveries from the LDU testing was the strong effect the drive force had on the distance traveled for each rotation of the wheel. A nominally 15.2-cm-radius wheel could behave as if its radius were between 13.5 to 16.5 cm depending on whether loads were aiding or retarding. Wheel slipping was quickly eliminated as a possible cause and the effect was traced to a distortion of the silicone elastomer at the interface with the rail. Radial compression of the wheel cannot account for the magnitude of this effect.

As illustrated in Figure 8 for a drive wheel under a preload (i.e., a normal force) and working against a load (i.e., a lateral force), the elastomer tire near the contact point on the rail will be stretched on one side of the wheel and compressed on the other side of the wheel. When the wheel turns, a spot on the surface of the elastomer tire travels faster than normal in the region of stretching and slower than normal in the region of compression; but any spot on the tire still completes one complete rotation for each rotation of the wheel. For the same wheel rotation rate, the LDU will travel more slowly if the tire rotates onto the region of slower moving tire (i.e., rotates against the lateral load) and will travel more quickly if it rotates into the region of faster moving tire (i.e., rotates with the lateral load).

The end result is that for an elastomer tire, the distance traveled along the rail for each turn of the wheel is greater for aiding loads (i.e., loads in the direction of motion) and is less for retarding loads (i.e., loads against the direction of motion). Note that the rubber is in intimate contact with the rail at all times and there is no tire slipping or scuffing, just stretching and compressing of the rubber.

The "effective radius" of the wheel, defined as the distance traveled divided by the wheel revolutions in radians, is a useful way to characterize the wheel behavior. Thermal-vacuum test data for ambient, hot and cold conditions are presented in Figure 9 as an LDU drive wheel effective radius versus drive force plot, where retarding forces are represented as negative aiding forces. As evident in Figure 9, the essentially linear dependence of effective radius on drive force is very significant but any variation as a function of temperature is within the scatter of the measured data. For predicting MT performance the following formula was derived from a linear least squares fit of the combined data.

$$\text{effective radius (cm)} = 15.52 + 0.00708 \times (\text{aiding load in N}) \quad (4)$$

This behavior is not detrimental to the LDU performance because it is predictable. The resulting alteration of travel distance is accommodated by tailoring the translation software stopping parameters.

Torque Limits at Temperature

The IMCA drive motors have considerable excess torque capability but are normally operated in a mode where output torque is limited by limiting motor current based on downloaded software parameters. At cold temperature extremes, the torque-limited motors could not complete some functions. In order to resolve this problem, the LDU output force versus motor drive current was measured over the full thermal-vacuum range with the torque/current limit off. The results indicate a linear dependence of output force on motor current with a slope which is relatively independent of temperature.

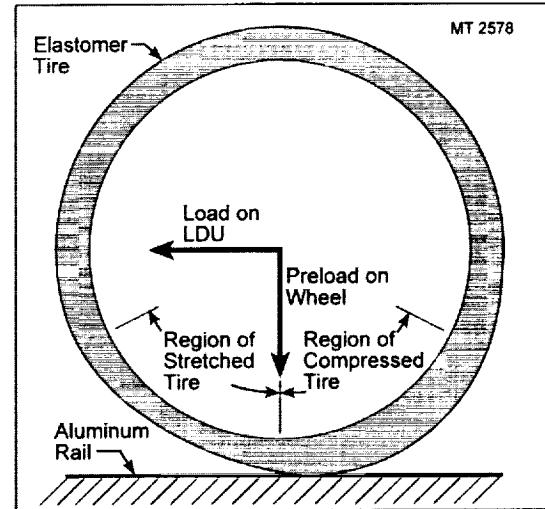


Figure 8. Tire Distortion for Loaded Drive Wheel.

The constant slope over the temperature range indicates that the gear train efficiency remains high at all temperatures; however, the intercept (i.e., starting current at zero force) increases at cold temperatures indicating a temperature-dependent drag. This behavior is reasonable because the friction coefficient of the dry film lubricant (Vitro-Lube 1220C) on the gears is not temperature sensitive but the grease lubricant (Braycote 601) in the bearings is known to increase its viscosity significantly at temperatures below -50°C. In any event, the cure to this problem was an increase to the torque limit parameters in the control software.

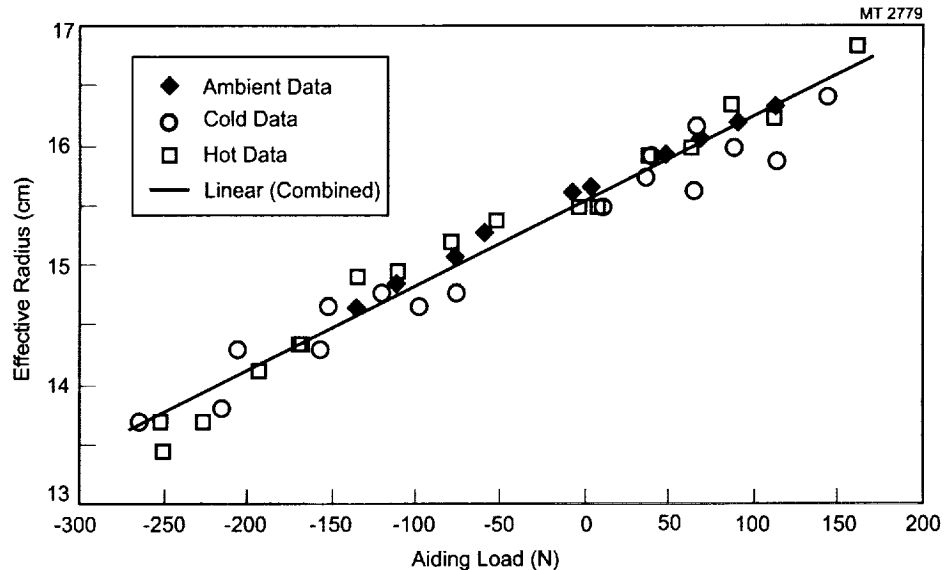


Figure 9. LDU Drive Wheel Effective Radius Versus Load.

Drive Wheel Loss of Friction

The life testing of the LDU was performed in ambient air over a 2 1/2 month period. The LDU drive wheel performance was nominal at the start and operated at a sustained force level of 423 N (445 N peak) without slipping (note that these values are not the limit of the LDU capability but just the maximum tested value). After running for 32 km of travel (1/2 life of use) under a preload of 623 N and lateral loads varying up to 375 N, the drive wheel was able to operate at a sustained force level of 400 N, but showed indications of slipping. By the end of 64 km of travel (one full life of operation), the drive wheel could only sustain loads up to 285 N without slipping, indicating that the friction coefficient had dropped to 0.46.

The low drive force experienced during qualification life testing has been traced to silicone contamination of the test rail by the elastomer tire (note that life testing consisted of repeated operations over the same, very limited sections of test rails). Chemical testing of the rail revealed silicone deposits, estimated to be of the order of 7 nm thick, only in the used portion of the test rail. Further friction tests established that the life-tested wheel could sustain adequate drive force on unused rails while the untested redundant wheel exhibited poor performance on the contaminated rail section. The source of the contamination is believed to be the free silicone oil that was used to disperse the catalyst during wheel manufacturing.

Working of the elastomer tire, as in the life test, apparently releases the free silicone oil. Over the 18 days of thermal-vacuum testing, including three hot-cold cycles, there was no indication that either vacuum or temperature extremes accelerate the release of silicone contaminants. Although the effect of long term exposure is yet to be determined, there are indications that a gradual release of a silicone contamination will not compromise MT operation on-orbit. The space station flies in a low earth orbit (400 km) which exposes surfaces facing in the direction of flight to a strong flux of atomic oxygen (AO). The LDU drive surface is normally exposed to this flux and testing on silicones indicate that the atomic oxygen will break up silicone contaminants into a residue of silicon dioxide and volatile components which rapidly evaporate. Tests have established that exposure of the contaminated test rail to atomic oxygen does maintain the friction coefficient for the drive wheel.

Conclusions

Testing of the LDU translation drive assembly demonstrates that a friction drive is a practical way to translate the Mobile Transporter along the rails of the International Space Station. Observations made during the MT program indicate that special care must be paid to the system design to maintain adequate drive force for crossing major gaps and offsets in the rail segments. Swingarm-mounted drive wheel designs with integral gear passes allow stationary attachment of drive motors and can provide a preload relatively independent of drive load. The effect of external loads on travel distance and positioning accuracy must be considered for flexible-tire drive systems.

Drive wheel and idler wheel material selection programs yielded acceptable selections for the LDU translation drive. Silicone elastomers are good choices as high-friction drive tire material; however, compounding should minimize the use of free silicone oils to prevent loss of friction over operating life. General Electric SE6660 silicone elastomer displayed acceptable performance characteristics for the LDU application, but other rubber materials also showed promise. Polyetheretherketone (PEEK) plastic, used for the idler wheels of the LDU, is recommended as a tough, nonabrasive material for use in a thermal-vacuum environment.

Translation drive testing substantiated lubricant selections. For the highly loaded interfaces and gear teeth applications of the LDU gearboxes and swingarms, Vitro-Lube 1220C dry-film lubricant performed successfully throughout thermal vacuum and life testing. Braycote 601 grease performed adequately in bearings although its viscosity does significantly increase at low temperatures.

Overall, the LDU development, production, and test program validated the choice of a gear-driven, swingarm-based, friction drive system. TRW Astro Aerospace and the Boeing Company look forward to the opportunity to validate the LDU translation drive design through on-orbit operation of the Mobile Transporter.

Development of a Cryogenic Nanometer-Class Repeatability Linear Actuator

Ruben Nalbandian^{*} and Alison E. Hatheway^{**}

Abstract

The goal of the Nanometer Resolution Linear Actuator development project was to demonstrate an extremely light weight, very high precision and high stiffness actuator capable of operating uniformly well over the temperature range of 20K to 300K. The development was a joint effort between Alison E. Hatheway, Inc. (AEH) and Moog, Schaeffer Magnetics Division (SMD), for use in spacecraft optical instruments, notably the Next Generation Space Telescope (NGST). This paper describes the design challenge of developing a lightweight, compact (35 mm diameter by 100 mm length), high stiffness, low power, thermally stable linear positioning mechanism. The key to achieving high resolution, low power, and stability is to eliminate the closed-loop control system that is normally applied to overcome non-linearities and hysteresis inherent in some technologies, such as piezoelectric and magnetostrictive transducers. This was accomplished by using AEH's patented elastic Rubicon™ transducer techniques that are inherently linear and hysteresis free.

Introduction

The linear actuator presented in this paper is comprised of two stages, a fine stage and a coarse stage. Both stages use a high reliability space-rated stepper motor designed and manufactured by Moog, SMD. The unique design features of this actuator that contribute to its light weight and extremely precise motion capability include a stepper motor driving a leadscrew through a reducing gearbox. The same motor, gearbox and leadscrew combination is used in the fine stage, but the final output motion is reduced by a factor of more than 200 by the elastic action of the Rubicon™ transducer. The Rubicon™ transducer consists of two elastic elements; a soft spring and a stiff flexural member. The soft spring exerts a force input on the stiff flexure. To maintain linearity, the displacements, and hence the stresses, developed in both elastic members are kept well below the elastic yield strength of the material. The fine stage is designed to produce a nominal axial motion of about 3 nanometers for each step in the fine motor. The materials of the actuator parts were carefully selected to provide an athermal design at the mid-stroke position and to minimize the effects of thermal expansion mismatch on the output stage.

Requirements and Constraints Driving the Design

The principal characteristics for NGST that the linear actuator must be designed to meet:

Resolution	<10 nanometers
Life cycles	1,000,000 cycles
Stroke	10 millimeters
Operating Temperature	20 to 300K
Calibration Mode (CM) Heat Dissipation	0.5 milliwatts
Observatory Mode (OM) Heat Dissipation	0.0 milliwatts
Mass	<140 grams
Outside Diameter	<50 millimeter
Creep, OM	<0.01 nanometers/day
Thermal Stability, OM	<50 nanometers/K
Axial Force, Set & Hold, OM	>1.0 newtons
Power Consumption, CM	<1 watts
Power Consumption, OM	0.0 watts
Axial Stiffness	>1,000,000 newtons/meter
Stowed Axial Length	<10.0 centimeters

^{*}Moog, Inc., Schaeffer Magnetics Division, Chatsworth, CA

^{**}Alison E. Hatheway, Inc., Pasadena, CA

Proceedings of the 34th Aerospace Mechanisms Symposium, Goddard Space Flight Center, May 10-12, 2000

Design and Development

The Rubicon actuator, a sectional view of which is depicted in Figure 1, has been jointly developed by AEH and Moog, SMD. The design consists of two stages, a fine stage and a coarse stage. Both stages are driven by high reliability space-rated stepper motors designed and constructed by Moog, SMD. The stepper motors are 15 degree two phase motors, producing twenty four full steps per revolution. Since micro-stepping is not used in the design, and unpowered holding torque is exhibited at every commanded step, the Rubicon actuator is capable of holding position with the power off. The motor for the coarse axis drives a #4-40 standard thread leadscrew nut through a reducing gearbox with a ratio of (1:45.2). With this overall rating, approximately 1085 motor steps are required to provide one revolution of the nut. The leadscrew thread pitch of 0.635 millimeter results in a resolution of 0.585 micrometer of axial movement per motor step. To achieve the 10-mm stroke on the coarse stage, the coarse actuator uses sixteen full turns of its leadscrew nut.

The fine stage of the Rubicon actuator uses the same motor and gear box, but instead of a rotating nut driving the lead screw, it rotates the screw, and the nut is allowed to translate. The plunger nut exercises the Rubicon elastic transducer (see Figure 2), to reduce the output motion by a factor of 0.00462. The fine stage is therefore capable of producing a nominal axial motion of 2.7 nanometers for each step of the fine motor. Eleven turns of the fine stage jack screw are used to produce a total stroke of about 30 nanometers.

The design is such that the output of the fine and coarse stages are summed at the actuator output shaft. This feature allows both fine and coarse position adjustment of the output.

To minimize weight and achieve the gear reduction ratio, a custom four-pass spur gear transmission was designed. The gears were machined from 15-5PH stainless steel material. Table 1 summarizes the gear reduction characteristics. For cryogenic temperature operation, it was deemed necessary to dry-lubricate the moving parts, i.e., bearings, lead-screws, nuts and gears. Tungsten disulfide (Dicronite) dry lubrication was chosen, based on the heritage of this lubrication on cryogenic mechanisms used in the COBE, UARS and AIRS programs. Dicronite offers superior performance at ambient conditions, not exhibiting the humidity absorption problems inherent with MoS_2 . The gears were manually lapped and electro-polished to accommodate the dry lubricant build-up thickness. The bearing races and balls were dry lubricated by the vendor and assembled prior to shipment to Moog, SMD. Table 2 summarizes the lubrication trade-off studies.

Table 1. Gear Reduction Characteristics

Designation	Diametral Pitch	Ratio
First Stage	120	1.800
Second Stage	96	2.929
Third Stage	96	2.929
Fourth Stage	80	2.929
Overall Gear Reduction Ratio		45.211

Table 2. Summary of Lubrication Trade-offs

Parameter	MoS_2	WS_2 (Dicronite)
Coefficient of Friction @ 300K, 760 torr	0.15	0.05
20K, 10^{-10} torr	0.05	0.05
Thickness, micrometer	0.5 to 10	0.5
Wear Rate, m/m.MPa	1.2×10^{-10}	1.2×10^{-10}
Application Method	Impingement Polymer Coating Sputtering	Impingement
Notes	Wells/Reservoirs Outgassing	Low RT Friction Molecular Bonding

The materials of the parts in the load path were carefully selected to provide for 1) an athermal design at mid-stroke position and 2) minimize frictional characteristics of the leadscrew/nut combination. Table 3 summarizes the material choices of the actuator parts. The Rubicon transducer is comprised of a 410 stainless steel helical spring and a 416 stainless steel machined flexure. The transducer was sized to achieve a relatively high stiffness (2.61×10^6 N/m) and low operating stresses (120 MPa in cylindrical shell flexure and 171 MPa shear stress in helical coil spring).

Table 3. Material Selection

Part Description	Material
General Construction	Titanium Alloy 6Al-4V
Ball bearings	Stainless Steel 440C
Rubicon Transducer cylindrical shell	Stainless Steel 416
Rubicon Transducer coil spring	Stainless Steel 410
Gears	Stainless Steel 15-5PH
Lead-screw	Stainless Steel A286
Nuts	Stainless Steel Nitronic 60
Athermalization portion of output shaft	Invar

Lessons Learned

The linear displacement input to the transducer's soft coil spring was provided by a plunger nut riding on the actuator output leadscrew. The plunger assembly was held against rotation by a pin in the housing and an enlarged hole in the plunger. The coil spring was a custom spring manufactured at SMD, with closed and ground ends. During initial performance characterization testing it was found that the fine stage actuator had a relatively large and unpredictable deadband. A closer examination revealed the following contributors:

Large diametric clearance between the anti-rotating pin and the plunger hole. A closer tolerance radial slot was machined in the plunger to reduce this problem.

The coil spring didn't have perfect ground closed ends perpendicular to the coil axis. As a result the plunger was loaded eccentrically causing it to skew and bind. A better machined spring was installed.

The Coulomb friction in the interface of the spring to plunger was unpredictable, causing the plunger to rotate back and forth as the actuator was being exercised. The large clearance in the plunger anti-rotation hole was amplifying this effect.

The next generation actuator incorporates a machined spring with integral internal threaded nut and a mounting flange to eliminate all of the above contributors to the relatively large deadband problem.

Evaluation Testing

The Rubicon actuator completed characterization evaluation testing at both room temperature and cryogenic temperature. Room temperature and cryogenic temperature testing was conducted at Jet Propulsion Laboratory (JPL), and room temperature measurement testing was conducted at Moog, SMD. The cryogenic testing at JPL used a vertical stainless steel dewar as depicted in Figure 4. The test used a Polytech Series 3000 Interferometer operating at a wavelength of 630 nanometers, with a resolution of 7 nanometers. The data were recorded on a computer workstation. For detailed analysis, the data files were converted to ASCII text and read into an Excel spreadsheet. The room temperature testing at SMD (Figure 3) used a precision capacitance gauging metrology technique developed by AEH. The capacitance was measured with an Andeen-Hagerling 2500 precision capacitance bridge that has a resolution of about two nanometers. The actuator is designed

specifically for performance characteristics independent of ambient temperatures over the range of 20K to 300K. This goal was achieved. The testing indicated that the performance of the actuator is insensitive to temperature. Figures 5 and 6 show typical room temperature behavior in the Moog SMD laboratory.

The tests were conducted at 200 pulses per second with a 0.350 ampere regulated current. Following are the overall performance characteristics of the actuator:

Coarse Stage:	Available stroke:	10.3 millimeters
	Smallest increment:	0.58 micrometer
Fine Stage:	Available stroke:	31.9 micrometer
	Smallest increment:	7.9 nanometer (two motor steps)

The smallest fine stage increment was measured at both cryogenic and room temperature at JPL. The results were not repeatable due to test equipment and test area noise levels. They were more accurately observed at Moog, SMD under more controlled test conditions at room temperature. The smallest detectable increment for the fine stage was determined to be two motor steps. For further detailed information on the test results refer to Reference 3.

References

- 1- Hatheway, Alson E. and Hammond, James C. "Passive Cryogenic Structural Actuators for the Next Generation Space Telescope", *Actuator Technology and Applications*, ed. Alson E. Hatheway (Bellingham, WA, SPIE, 1998) Volume 3429B-48
- 2- Hatheway, Alson E., "Metrology for Characterizing Actuators with Sub-atomic Repeatability," *Proceedings of the Annual Meeting*, (Raleigh, NC, American Society of Precision Engineers, 1994), pp.246-9
- 3- Hatheway, Alson E. and Owens, Daniel E. "Cryogenic and Room Temperature Testing of a Nanometer-Class Structural Actuator for the Next generation Space Telescope", *Optomechanical Design and Engineering*, (Bellingham, WA, SPIE, 1999) Volume 3786
- 4- Hatheway, Alson E., "Results of Testing a Nanometer-Class Structural Actuator for NGST," *NGST Science and Technology Exposition*, (Provo, UT: Astronomical Society of the Pacific, September, 1999).
- 5- "Rubicon" is a trademark of Alson E. Hatheway Inc.

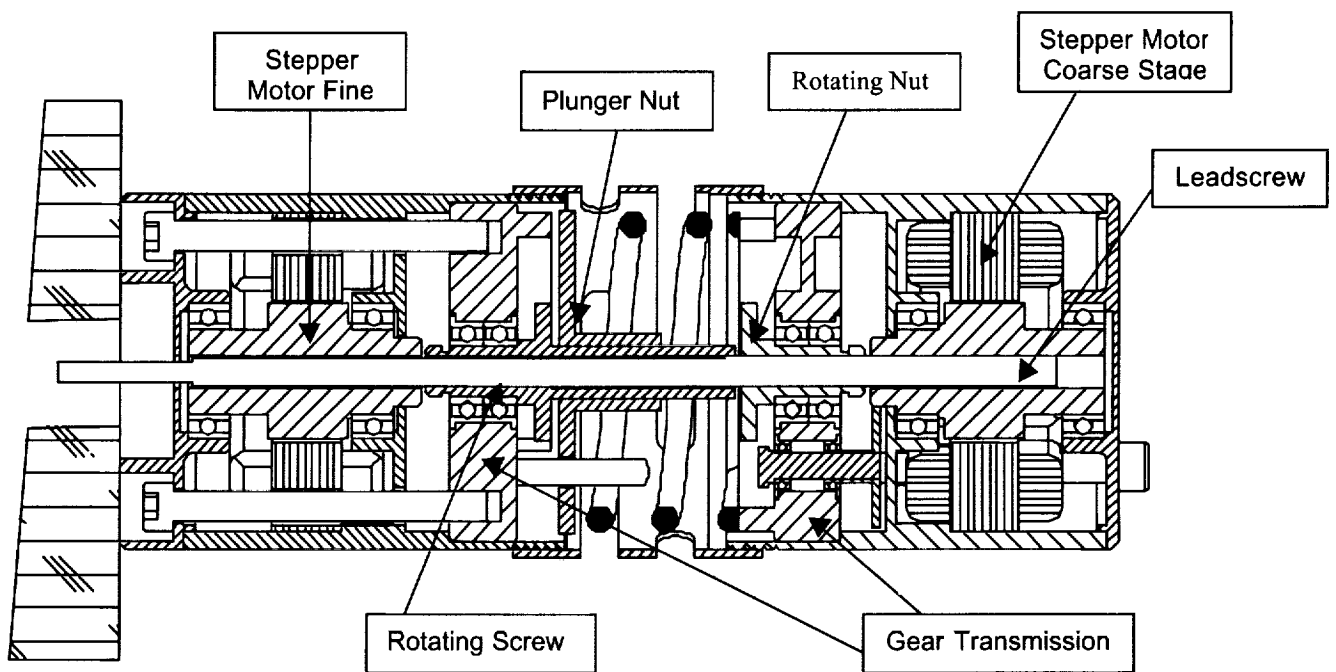


Figure 1. The Rubicon cryogenic temperature cross-sectional view

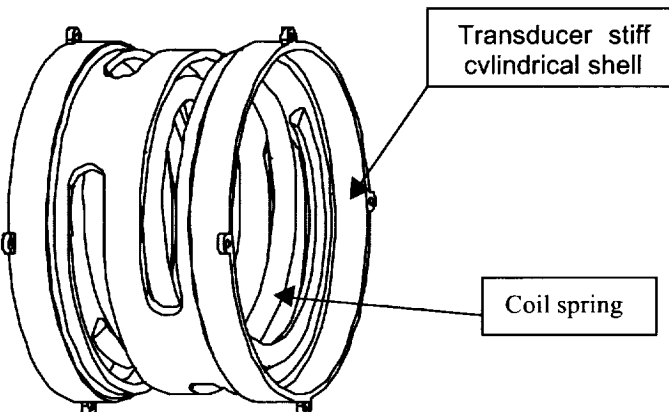


Figure 2. The Rubicon Transducer

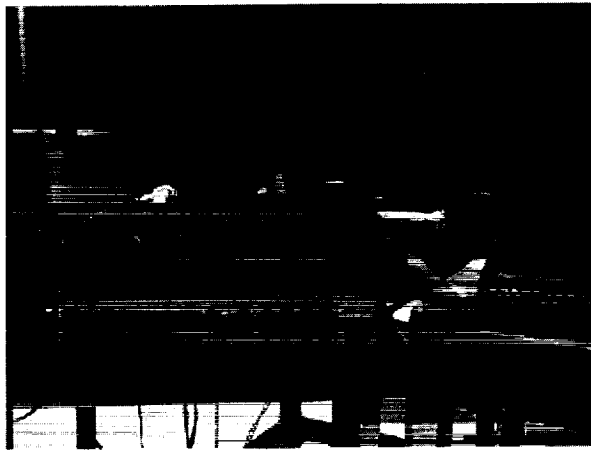


Figure 3. SMD's Room Temperature Test Facility

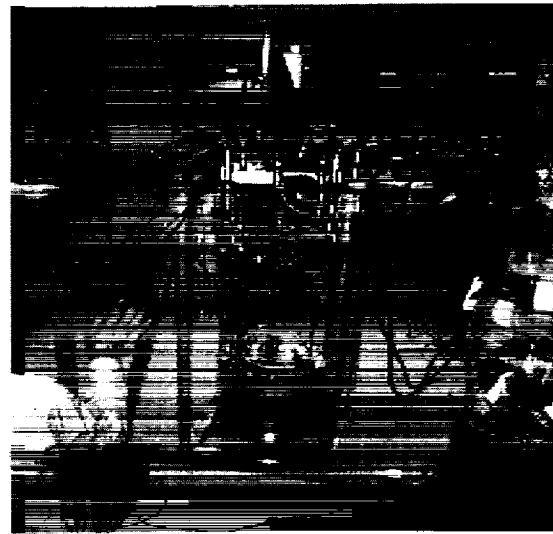


Figure 4. JPL's cryogenic test facility

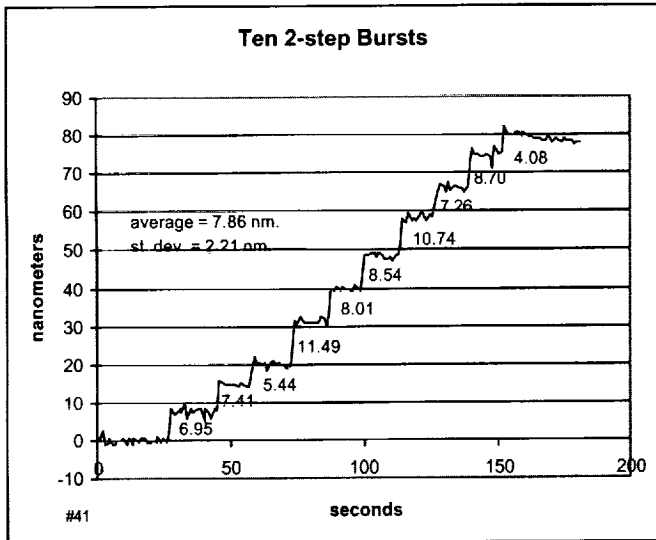


Figure 5. Fine stage, Two step increments

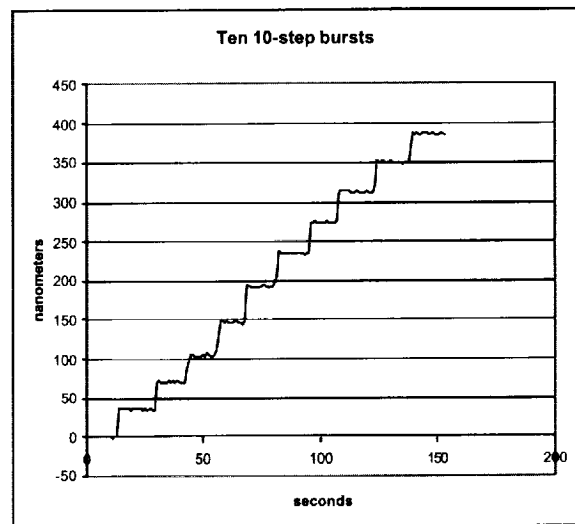


Figure 6. Fine stage, Ten step increments

Application of Magnetic Smart Materials to Aerospace Motion Control

Chad H. Joshi^{*} and Bruce R. Bent

Abstract

Energen, Inc. has developed linear actuators and linear stepper motors based on magnetostrictive materials. These devices are designed to operate efficiently in harsh vacuum and cryogenic environments. They provide submicron positioning resolution over a range of motion of 20 mm or more. The linear actuators have high bandwidth and a short stroke making them ideal for active vibration damping high speed optical positioning. The stepper motors have a long stroke and will hold position when powered off.

Magnetostrictive Materials

Magnetostriction is a change in any dimension of a magnetic material caused by a re-orientation of the atomic magnetic moments. In ferromagnetic materials, an applied magnetic field causes rotation of the magnetization towards the field direction within domains and/or motion of the domain walls to increase the size of the domains with magnetization vectors close in direction to the applied field. When the magnetic moments are completely aligned, saturation occurs and no further magnetostriction can be produced by increasing the applied magnetic field. The amount of magnetostriction at saturation is the most fundamental measure of a magnetostrictive material. The modern era of magnetostriction began in 1963 when strains approaching 1% were discovered in the rare earth materials, terbium (Tb) and dysprosium (Dy), at cryogenic temperatures. Since then, many materials (see Table 1) have been shown to exhibit magnetostrictive behavior including several materials at room temperature, but the highest magnetostriction is found in alloys with Curie temperatures below room temperatures making them ideal for cryogenic device applications.

Table 1 - Saturation strain and Curie temperatures of selected materials.¹

Material	Saturation Strain (x 10 ⁻⁶)	Curie Temperature (K)
Ni	-50	630
Fe	-14	1040
SmFe ₂	-2340	690
Fe ₃ O ₄	60	860
DyFe ₂	650	630
TbFe ₂	2630	700
Tb _{0.3} Dy _{0.7} Fe _{1.9} (Terfenol-D)	1600-2400	650
Tb _{0.6} Dy _{0.4} @ 77 K	6300	210
Tb _{0.5} Zn _{0.5}	5500	180
Tb _{1-x} Dy _x Zn	5000	200

Measurements of magnetostriction on TbDyZn alloys were made at 77 K and at 4.2 K. The data for 77 K are very reproducible and agree with data from the literature.² Figure 1 shows the measurements on one sample of the TbDyZn alloy at 4.2 K. These data are believed to be the first direct measurement of magnetostriction in this material system at 4.2 K and indicate that the high saturation strain remains at that low temperature.

^{*}Energen, Inc., Billerica, MA

¹*Magnetostrictive Materials*, K. B. Hathaway and A. E. Clark, MRS Bulletin, Vol. XVIII, No. 4, April 1993.

²A. E. Clark, *High Power Magnetostrictive Materials from Cryogenic Temperatures to 250 C*, Materials Research Society Fall Meeting, Boston, MA, November 28-30, 1994.

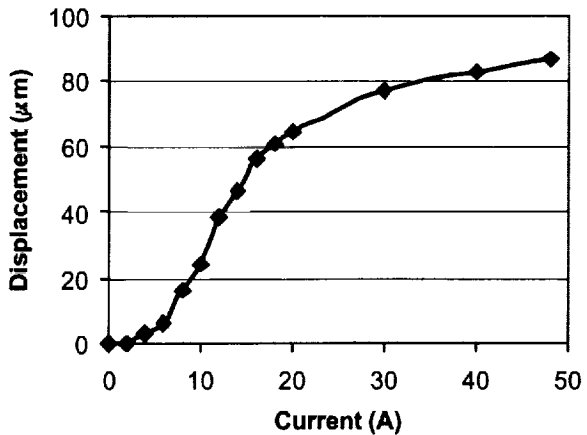


Figure 1 - Magnetostriction of a TbDyZn alloy at 4.2 K shows high saturation strain.

Actuators

A linear actuator consists of a rod of magnetic material surrounded by an electrical coil. Energizing the coil with electrical current causes the magnetic material to elongate in relation to the current amplitude. Precision positioning can be achieved by precisely controlling the current. Such an actuator can be used for precise mechanical positioning, vibration control, or switch and valve operation. Energen, Inc. has built several sizes of linear actuators that can provide very high forces in a compact device. Figure 2 shows several actuators manufactured by Energen, Inc. (the largest of which weighs only 40 g) having strokes that range from 5 to 300 microns and force capabilities up to 1200 N (270 lb).

Larger actuators can be built by increasing the size of the magnetostrictor rod. Energen, Inc. has built an actuator with a 22.2 kN (5000 lb) force capability for use in superconducting particle accelerators. Typical response of our small actuators is shown in Figure 3.



Figure 2 - Energen's linear actuators

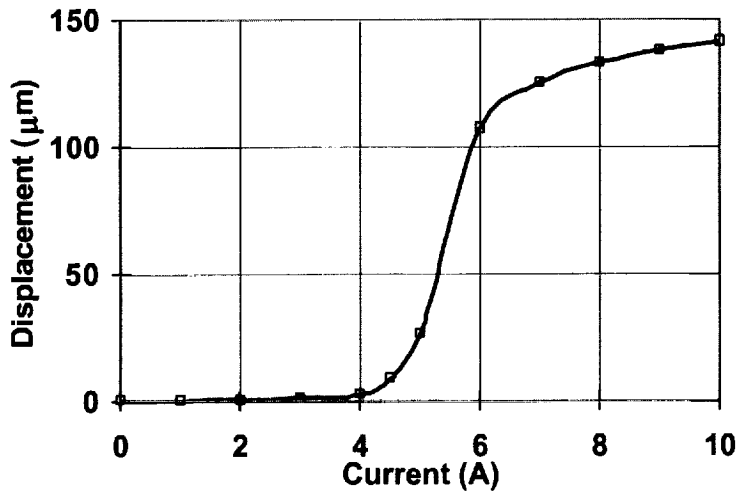


Figure 3 - Typical response of an actuator

SRF Tuners

Particle accelerators and free electron lasers are being used to generate monochromatic light sources in the infrared, ultraviolet and deep ultraviolet regions of the electromagnetic spectrum. While particle accelerators have traditionally been the tools-of-the-trade of high energy physicists, free electron lasers are finding increased applications in industrial materials processing such as polymer and metal surface processing, metal and ceramic surface micromachining, and semiconductor surface preparation.

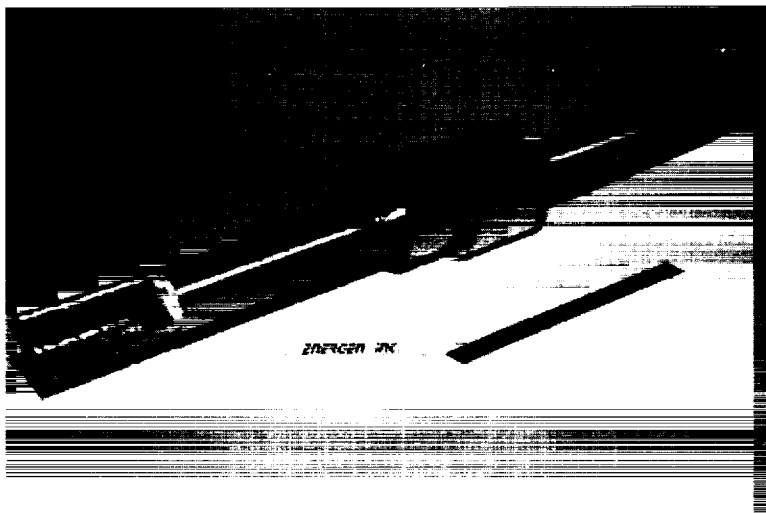


Figure 4 - Prototype cavity fine tuner.

Energen, Inc. has designed, built and demonstrated a fine tuning mechanism (shown in Figure 4) for superconducting radio frequency (SRF) cavities used in particle accelerators. This tuner was specifically designed to meet the requirement of the Continuous Electron Beam Accelerator Facility at the Thomas Jefferson National Accelerator Facility in Newport News, VA. The tuner is installed in the dead leg of the existing mechanical cavity tuning system (as shown in Figure 5) which consists of a wormwheel and ball screw assembly. The mechanical tuner is used for coarse tuning. As the magnetostrictive SRF tuner is energized, the dead leg expands providing precision fine tuning capability. Because of its high force capability, the fine tuner can overcome the 5644 N/m (50,000 lb/in) stiffness of the SRF cavity. The magnetostrictive tuner provides 2000 Hz of tuning bandwidth and can be actively controlled during the

operation of the SRF cavity. The large stroke and high force capability of our actuators makes it possible to replace the mechanical tuner with a magnetostrictive tuner thereby increasing the reliability of the cavity tuning system and reducing the thermal load on the refrigerator.

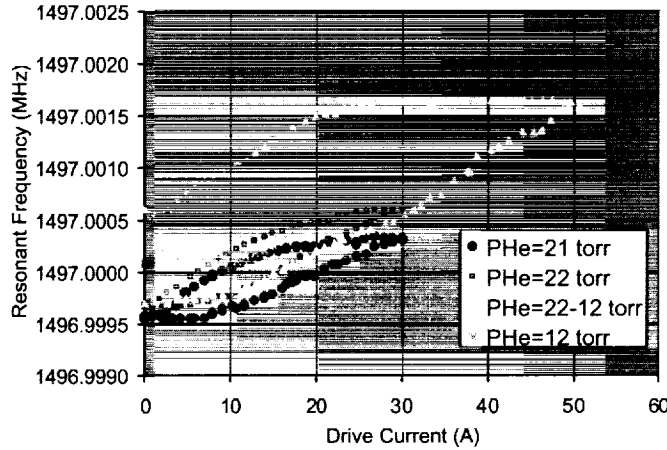
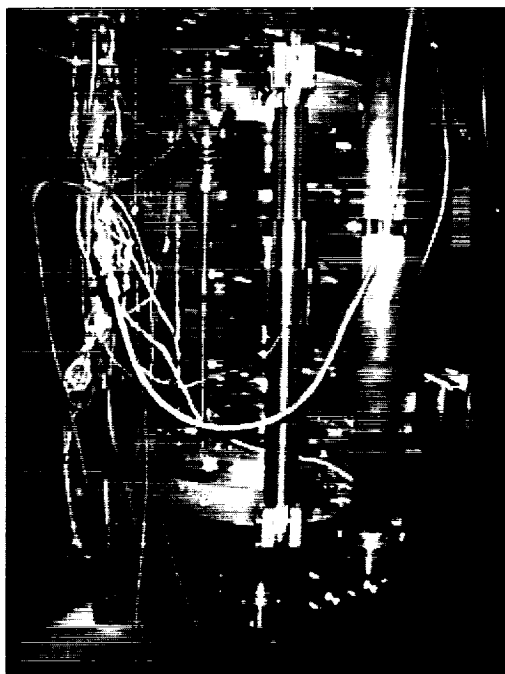


Figure 5 – The fine tuner was tested at Jefferson Laboratory and demonstrated excellent tuning capability

Linear Stepper Motor

Energen, Inc. has used the basic concept of a linear actuator to create a linear stepper motor. The linear stepper motor uses a set of three magnetostrictive actuators that enable it to move a rod forward or backward in a stepwise fashion. This motor can provide a large stroke of several millimeters. Variations on this design can yield an actuator with a stroke limited only by the length of the translating rod.

Figure 6 shows a photograph of a linear stepper motor designed for aerospace applications along with its operating sequence. The translating rod is comprised of three segments assembled end to end. The center section is a magnetostrictive rod surrounded by a superconducting coil. Clamps on each side of the actuator grab onto connecting rods. These clamps contain a magnetostrictor actuator that when energized will cause the clamp to release its hold on the rod.

The linear stepper motor can be operated in one of two modes – stepper mode or fine tune mode. In stepper mode, the clamps and translating actuator are turned on and off in the proper sequence to cause the translating assembly to index forward or backward.

Fine tune mode operation provides high positioning resolution. In this mode, the forward actuator is energized to release and the current in the center actuator is modulated thereby moving the forward end of the shaft proportionally. Under this operating mode, the positioning resolution is limited by the current regulation. Thus, this motor is capable of providing a long stroke with high positioning resolution. It is capable of holding position with zero power dissipation since the clamps hold at zero current.

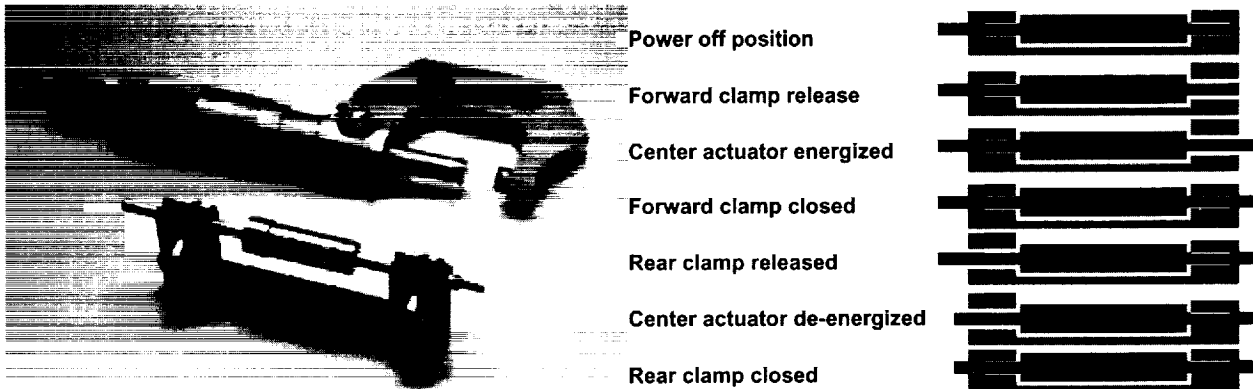


Figure 6 – Energen's linear stepper motor is capable of long strokes using a pair of clamps and a translating actuator operated in a indexing sequence.

Next Generation Space Telescope

Under contract to the National Aeronautics and Space Administration and aerospace companies, Energen has received several contracts to develop and demonstrate a series of compact actuators for use on the Next Generation Space Telescope (NGST). NGST, a conceptual design of which is shown in Figure 7, is a \$500 million project planned for launch some time in 2007 to replace the Hubble Space Telescope. It will have a large 6-8 meter diameter lightweight, segmented primary mirror that is launched in a folded configuration and then deployed in orbit. The large aperture of the telescope and passive cooling technology employed by the telescope results in a high resolution visible and near infrared observatory that operates at 30-50 K.

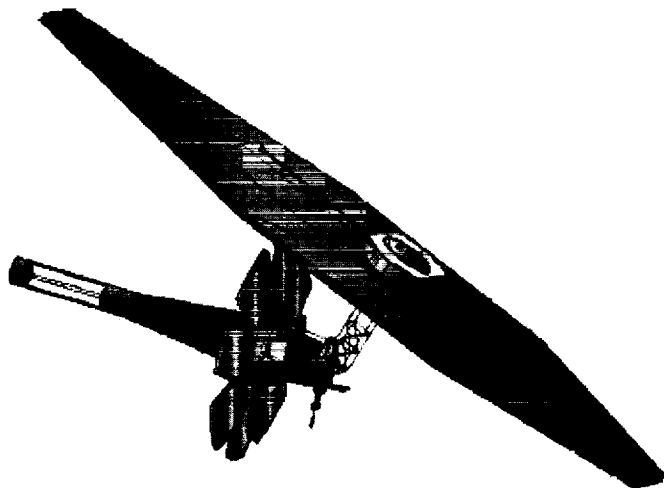


Figure 7 - A conceptual design of the NGST showing the large sunshield with the telescope behind it. The segments of the 8-m primary mirror can be clearly seen.

Whereas on the Hubble the primary mirror is ultra-low expansion glass structure similar to ground-based telescopes, the NGST will use lightweight, adaptive optics technology in the construction of the primary mirror system. The mirror will consist of several petals (or segments) that will unfold after launch. Each petal will consist of a rigid composite back structure onto which is mounted a lightweight reflective surface. An array of actuators connect the mirror surface to the rigid back structure and are used to align

the mirror segments and to correct image aberrations resulting from thermal gradients and other external phenomena.

Energen's magnetostrictive actuators are being used in the design of the Advanced Mirror System Demonstrator Project – a scale demonstration of mirror technology for the NGST. Successful completion of this demonstrator will lead to a flight demonstration to test the mirror characteristics in a zero gravity environment.

Other Applications

Other applications of these magnetic actuators take advantage of their high force capability, large stroke and repeatability. Energen, Inc. is applying linear actuators to such diverse applications as

1. High conductance heat switches for cryogenic refrigerators.
Heat switches are a critical component of low temperature adiabatic demagnetization refrigerators. They provide higher thermal conductance than other technology at sub-kelvin temperatures enabling more efficient refrigerators for high sensitivity instrumentation and detectors. These refrigerators are being developed by Goddard Space Flight Center for future space missions such as STEPS and Constellation-X.
2. Resonant frequency control of RF cavities for particle accelerators.
The high force capability combined with the sub-micron positioning capability of Energen's linear stepper motor are well suited to this application. Energen has built a proof-of-principle demonstration actuator for cavity tuning and is presently developing new generation of tuning system that will completely eliminate the mechanical tuner system presently used by Jefferson Laboratory in Newport News, VA.
3. Active vibration control.
Energen is applying its actuator technology to active control of vibration. With state-of-the-art accelerometers and control electronics, robust active vibration control systems are being developed for both cryogenic and room temperature applications. Magnetic vibration control is more efficient than the currently available piezoelectric systems for controlling low-frequency, high-amplitude vibrations.

Conclusion

Energen, Inc. has developed actuators and linear stepper motors for operation in cryogenic and vacuum environments. These systems are being applied to a variety of systems where precision positioning and high force capability are required in a compact package. The actuators and stepper motors do not use any lubricants making them excellent candidates for ultraclean environments such as clean rooms.

A Separation System Solution for the Interim Control Module

Brian Whalen*

Abstract

The Interim Control Module (ICM) is a propulsion and attitude control platform for the International Space Station (ISS) built by the US Naval Research Laboratory (NRL). ICM is delivered to ISS via the Space Shuttle, where it is separated from its structural support canister and moved into docking position using the Shuttle Remote Manipulator System (SRMS). The Pin Extraction Mechanism (PEM) is one of the mechanisms that help ensure the separation of electrical connectors and prevents re-engagement of the pins and sockets. This paper describes the ICM separation system, the PEM and operational details.

Introduction

The Pin Extraction Mechanism is a single-use mechanism that aids the Interim Control Module separation from its support canister in the Space Shuttle cargo bay. Separation is accomplished by utilizing a system of eight PEMs at the separation plane to ensure the de-mating of two 41-pin separable connectors, each shown in Figure 1. The PEM system minimizes forces on the SRMS and prevents re-engagement or re-contact of the connector halves using a ratcheting and locking plunger. Each PEM is a self-contained unit that houses a spring-loaded plunger that pushes the vehicles apart while overcoming pin and socket friction from the separable connectors. The PEMs are located on the support canister, as illustrated in Figure 2, and are returned to Earth after the Space Shuttle docks ICM to the ISS.



Figure 1. Pin Extraction Mechanism and Separable Connector Halves.

* U.S. Naval Research Laboratory, Washington, D.C.

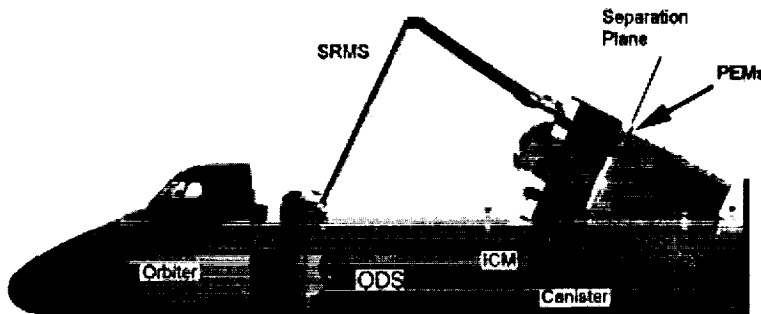


Figure 2. ICM Separation Configuration and PEM Location.

Background

The ICM vehicle is based on a previous vehicle design that was a free-flying satellite once separated from the canister. The original satellite used a spring separation system to separate the separable connectors shown in Figure 1 with no risk of re-contact.

When NASA determined that the SRMS was necessary to separate the ICM from the Canister, the separation became more complex. Due to the flexibility and configuration of the SRMS, it is highly desirable to minimize the loads at the end of the SRMS. Analysis provided to NRL by NASA predicts that the ICM vehicle will move laterally in, and rotate about, the X, Y, and Z axes. This introduces a re-contact risk for the separable connectors. Thus, new hardware needed to be developed to prevent re-contact.

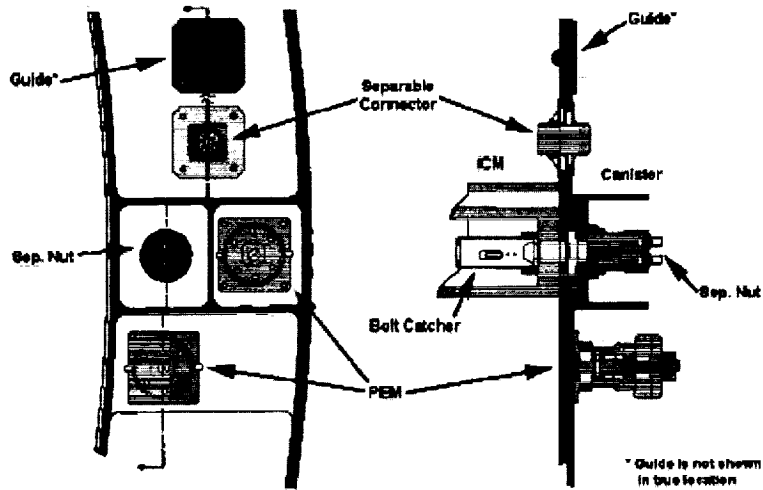


Figure 3. ICM/Canister Separation Joint.

The separation system consists of eight separation joints. At each joint, there is a cup-cone interface with a bolt through the joint as in Figure 3. The ICM side of the joint contains a bolt catcher while the canister

side of the joint houses the separation nut. On the canister side of the separation plane, in various locations, are two separable connectors, PEMs, and two separation guides.

There existed a mounting pattern for a spring separation system on the Canister, so modification was not necessary. In an effort to minimize the energy imparted into the SRMS, a trade study was performed to identify the best configuration for separation springs. Within this trade study were other options such as "connector retractors." The PEM was the best option to release the separable connector halves while preventing re-contact because PEMs are simple, they provide 3:1 force margin, and the SRMS could handle the energy. The result is eight PEMs in four pairs around the canister as shown in Figure 4. One pair of "strong" PEMs (2 springs) at each separable connector joint, and one pair of "light" PEMs (1 spring) at a joint 90° around the canister. This provides a "four-point" plane for incidental re-contact.

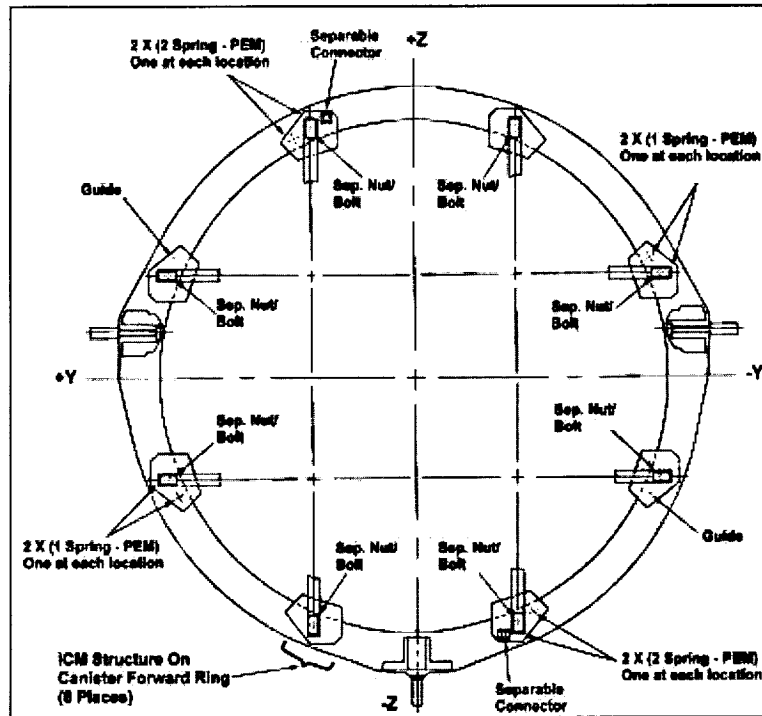


Figure 4. Canister Separation System Configuration.

The separation sequence is as follows:

1. After the Orbiter cargo bay doors open, the SRMS grapples the ICM and rotates the ICM and Canister up 25 degrees (as shown in Figure 2).
2. The Orbiter crew fires the separation nuts in a 4-2-2 sequence. This minimizes release energy imparted into the SRMS while still releasing in a symmetric pattern.
3. The PEMs push the ICM away from the Canister with enough energy to separate the separable connectors while locking the PEM plungers out.
4. The cup/cones and separation guides limit translation and rotation of ICM with respect to the Canister for up to 1.27 cm (0.5 inch) of ICM movement along the X axis.
5. If the SRMS flexes and the ICM re-contacts the Canister, the PEMs will react the loads and prevent connector or guide re-contact.
6. ICM is translated above the ODS and berthed to the ODS in preparation for ISS docking.

Requirements

The requirements to safely separate the ICM from the support canister include the following:

- a. Must prevent re-engagement of the separable connector shells
- b. Must withstand impact loading by potential re-contact of ICM and canister
- c. Maintain a 3:1 force margin on separating the separable connector halves
- d. Impart acceptably low force on the SRMS
- e. Single fault tolerant design
- f. No electrical power to function mechanism
- g. Fit existing fastener, hole pattern and pocket depth on the Canister
- h. Must be EVA compatible

The above requirements provided constraints for defining force, volume, mounting pattern, test pass/fail criteria and certain design aspects. The PEM was designed to fulfill all of these requirements with a simple passive mechanism.

Analysis

To understand the magnitude of the forces required for separation of the connectors, a pull-test was conducted using a fully populated flight Deutsch 38194-61-42PN (41-pin) separation connector selected for the design interface.¹ Test data, sampled in Figure 5, showed that the connector drag force averaged 117 N (26 lb_f) per connector. The nominal PEM output force is also shown on this graph. This shows that the PEM provides large force and stroke margins to separate the separable connector.

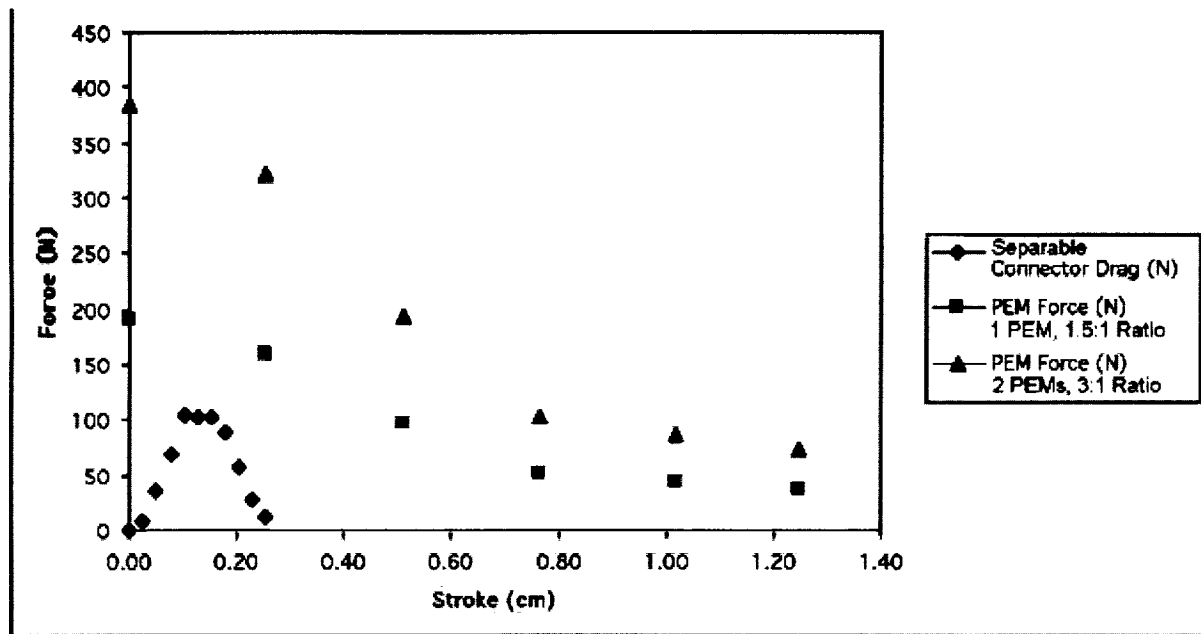


Figure 5. PEM Performance Compared To Separable Connector Drag Force.

The worst-case impact energy was calculated from the separation event, which includes activation energies of four NASA Standard Initiators and eight PEM energies. The energy from an incidental re-contact cannot exceed the energy put into the separation, so one PEM is required to be capable of reacting the total energy in the separation.

Design and Operation

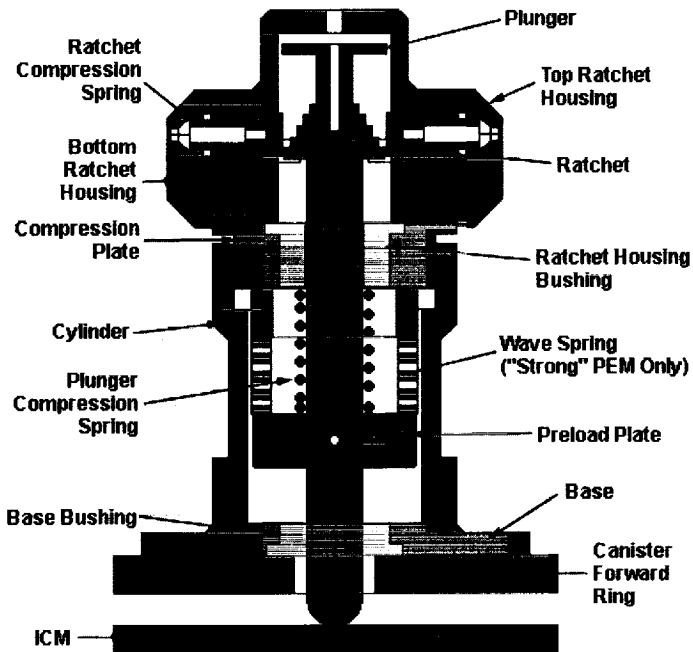


Figure 6. PEM Design.

The PEM design evolved around the requirements and available commercial springs. A sectional view of a PEM is shown in Figure 6. One key part of the PEM design process was to prototype the design to correct design flaws that could otherwise severely impact cost and schedule. Several aspects of the PEM design were changed after the prototype was fabricated, assembled and tested:

1. Improved clearance for sliding and interference fit parts. It was necessary to increase ratchet pocket volume when Bray 602 was added and the ratchet housing parts were installed. Incorrect pocket dimensions prevented proper sliding of the ratchets because it did not include enough volume for lubricant.
2. Proper surface finishes to incorporate sliding parts and part-to-part electrical conduction (grounding). Type III hard coat anodizing was applied to the flight design, with areas masked for iridite at contact points between mating parts for electrical conductivity to ground.
3. New springs with longer free length were inserted to achieve necessary margins because the original springs were outside of the catalog specifications after "removing the set."²

The prototyping process allowed developmental tests to be conducted and greatly assisted in writing assembly and test procedures as well as designing test fixtures. Part of this developmental testing included multiple impact testing at up to 10 times the impact energy with successful cycles before and after the impact tests.

The PEM is in the compressed state until the separation is initiated by release of the separation nuts that attach and preload the ICM to the Canister. Once the separation nut preload is removed, the PEM springs are free to overcome the pin/socket friction in the connector.

There is a single plunger in each PEM. The plunger is preloaded with two nested springs in the "strong" PEM; one a wave spring and the other a compression spring. The wave spring, which has a shorter stroke and a larger diameter than the compression spring, overcomes most of the pin drag with a 111-N (25-lb) force. The compression spring around the plunger applies a 77-N (17-lb) force and preloads the plunger with a 35-N (8-lb) force at the end of its stroke.

Ratchets serve as a redundant lockout feature for the plunger. There are two ratchets per PEM, each ratchet having its own compression spring, which preloads it to the steps on the plunger. As the plunger strokes out, the ratchets move in and prevent plunger movement in the opposite direction. Each ratchet operates with a single compression spring that pushes it against the plunger.

Bray 602 is the lubricant used on all metal-to-metal sliding surfaces. The plunger slides through two bushings made of Vespel SP3 and does not require lubrication.

Test

The load testing of a spring system such as the PEM is easy at a component level using a tensile / compression test machine. The wave springs and compression springs were tested multiple times prior to assembly to characterize each spring, remove the set, and group the springs into sets with matching spring constants and deflections. Since the spring values all changed when removing the set, it was necessary to test each spring instead of blindly trusting the vendor specifications. Matching spring values for groups of springs is important to ensure an even kick-off force across the vehicle at the separation plane.

Testing the PEM as a subsystem with a simulated joint has proven to be a difficult task. The test fixture shown in Figure 7 is similar to a section of the Canister forward ring. In the configuration shown, the test fixture does not work as desired. Although this is a near duplicate of a flight hardware section, it is not a good representation of the system because one fixture alone oversimplifies the separation system.



Figure 7. PEM Test Fixture.

A free body diagram showed that the PEMs only separate the plates at an angle while the separable connector stays engaged. This happens even with guide rails, which bind from the moment created by the configuration.

The solution came from the accidental wisdom of fabricating two test fixtures. The original intent was to modify one fixture for vibration, and use the other fixture for other environmental tests. Now both fixtures are

being modified to attach the fixtures side-by-side, one oriented symmetrically opposite from the other. This balances the forces and moments on the fixture and more closely simulates the system. It is now possible to separate the plates properly as a small-scale system simulation.

It is impractical to do a full system level separation test due to the size of the vehicle, risk of damaging flight hardware, and schedule limitations. There will be a system level pyroshock acceptance test where the ICM and Canister are mated and the separation nuts are released. ICM will be lifted off of the Canister to verify the PEM plungers extend and the ratchets function properly. This does not constitute a good full-scale test because it will not envelop the maximum possible translation and rotation by the vehicle while it is in flight configuration. So the qualification of the PEMs is based upon compilation of the three tests: i) PEM component, ii) subsystem separation, and iii) ICM pyroshock.

Conclusion

The Pin Extraction Mechanism is a simple mechanism that aids in the kinematics of vehicle separation. The PEM meets NRL and NASA requirements and allows the ICM and existing Canister hardware to easily adapt to a different type of separation. Prototyping the design allowed for developmental tests and design improvements. The original test fixture did not work as desired, however fabricating multiple test fixtures lead to the correct fixture design change and subsystem test approach. NRL is qualifying the system with a combination of component, subsystem and system level tests.

References

1. Whalen, Brian. *SSD-TR-IM022 – ICM Canister Joint Separable Connector Pull Test Report*. US Naval Research Laboratory, Washington, DC. 24 September 1999.
2. Shingley, Joseph and Mischke, Charles. *Standard Handbook of Machine Design*. McGraw-Hill Book Co., Inc. New York, NY. Copyright 1986. Pages 24.19-20.

The Development of an Ultra Low Shock Pyrotechnically Actuated Separation Nut

Fred Silverman^{*} and Jerry O'Quinn^{*}

Abstract

As spacecraft have become vastly more sophisticated with a myriad of sensitive and complex components, the concern caused by mechanical and pyrotechnic shock has increased. Looking for solutions to the problem Hi-Shear Technology Corporation (HSTC) is developing an ultra low shock separation nut that reduces the peak output shock by approximately 50% of the HSTC flight-qualified low-shock separation nuts, which are presently one of the lowest mechanical/pyrotechnic shock producing devices. The ultra low shock separation nut (Patent Case Number 4931) uses a rotor feature that converts much of the shock energy from an axial direction into rotation and increases the preload release time, thereby decreasing the peak output shock.

Introduction

A separation nut, which is a separable threaded fastener, is tightened to hold two objects securely together with an axial preload on the fastener. The structure of the separation nut inherently minimizes mechanical shock loads on the contiguous structure, which are developed when elements of the separation nut are abruptly separated from one another. In the early days of aerospace, reliability of separation was the primary objective. If the separation nut failed to release on command, the entire project would be imperiled. For this reason redundant fasteners were often used as a back up. Reliability is still the primary concern, but after it was solved, attention turned to the reduction of mechanical shock, which is unavoidably exerted on the surrounding structure when the separation nut is released.

Energy that is potentially a source of mechanical shock is necessarily stored in the fastener system when it is coupled to both objects that are to be held together. Customarily one part of the fastener, usually its threaded nut, is fixed to one of the objects. A headed, threaded bolt engages the other object. It is threaded into the nut and tightened. The resulting axial tensile preload stored in the nut/bolt combination is essential to the tightness of the joinder, but also must be expended when the fastener elements are separated. The resulting shock is an abrupt axial force.

Another source of shock comes from the segmented threaded part of the nut. The threads are formed on inside surfaces of segments that are held against the bolt by an external removable retainer. When the separation nut is to be released, a retainer moves away from the segments and they move away from the bolt to release it. The rapid movement and abrupt arresting of the segments and retainer thereby contribute to the shock. The final source of shock is the pyrotechnic actuator. It is evident that a shock load will be generated by its deflagration. The pyrotechnic charge load is dependent on the force required to relieve the retainer's friction force. As the preload increases, the pyrotechnic shock source increases proportionally. Although fairly large shock loads can be tolerated in heavier structures, the development of very lightweight structures such as spacecraft antennas has lowered the tolerance for such forces. Hi-Shear Technology Corporation is providing separation nut designs in both pyrotechnic and non-pyrotechnic devices¹ that can reduce this shock output.

^{*}Hi-Shear Technology Corporation, Torrance, CA

Flight Qualified Low Shock Separation Nut (SN9400 Series)

The HSTC flight-qualified SN9400 Series Low Shock Separation Nuts² were used on the Viking Lander, Mars Pathfinder, Space Shuttle, Delta II and III Launch Vehicles, and numerous other domestic and multi-national space programs. The 9400 series Separation Nut has the following general features:

- Low shock output
- Completely gas and particle containing
- Stronger than mating bolt
- Ultra-fast release (Under 5 milliseconds)
- Lightweight – predominately aluminum
- Actuates on relatively low pressure
- Thread surfaces and laying surfaces dry lubricated to MIL-L-46010 Type 1
- Multiple in-process cold gas actuations (3-5 times, maximum 25 times)
- Minimum bolt insertion required
- Large bolt tolerance
- Very low magnetic influence
- Temperature/pressure envelope limited only by cartridge

The HSTC 9400 series separation nut is constructed of anodized aluminum and stainless steel to provide high resistance to corrosive environments, and to provide the lightest weight compatible with strength and other requirements. The standard aluminum nuts can be operated between 93°C and -87°C. The efficient design of this separation nut allows the use of a low actuating pressure, which in turn allows the majority of components to be fabricated of aluminum while the high stressed parts are precision machined of stainless steel. Hence the very favorable strength to weight ratio is achieved. Actuation of the separation nut is accomplished with one or more power cartridges. Figure 1 presents the sequence of operations for the 9400 series, 0.64-cm (0.25-in) through 3.18-cm (1.25-in), separation nuts.

The low-shock separation nut design reduces mechanical shock by having the locking piston move away from the base and structure upon actuation rather than toward the base as older high-shock-output separation nuts. In addition to the reverse movement of the piston, further reduction and mitigation can both be achieved rather easily by adding honeycomb material, which cushions the impact of the actuation locking piston on the inside of the housing.

Ultra Low Shock Separation Nut

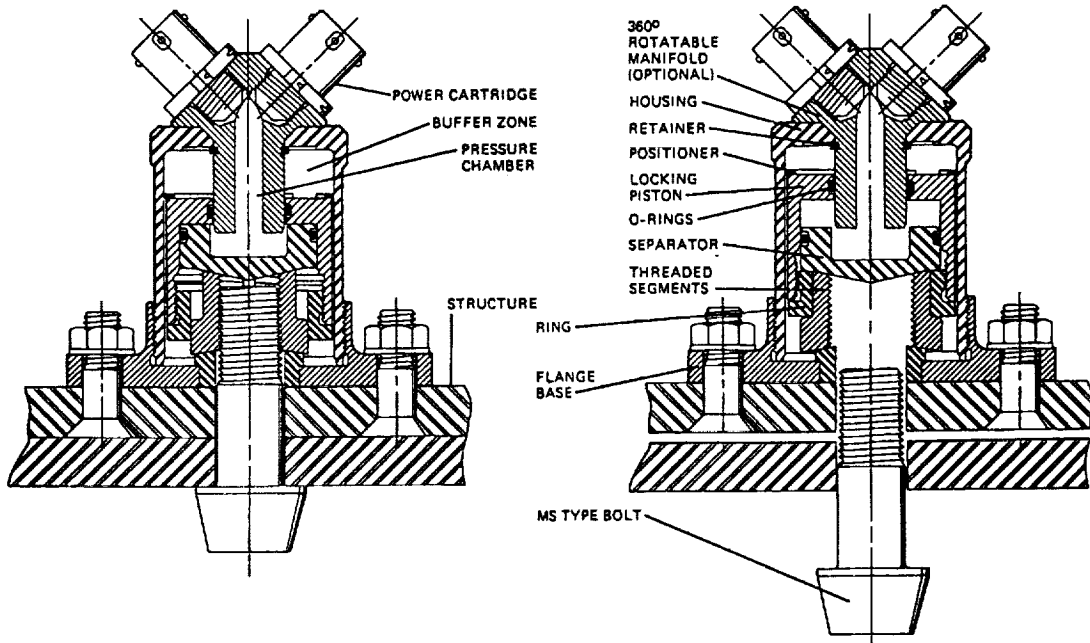
Design Definition

Output shock from a pyrotechnic-actuated separation nut has three sources: deflagration of the pressure cartridge, release of the bolts strains energy, and internal collisions of the mechanical components. It is generally accepted that the pyrotechnic shock delivered by the pressure cartridge contributes less than 10% of the total shock. It is prudent then to focus on the purely mechanical contributors making up the other 90%. Depending on the design, the contribution to mechanical shock is split evenly between internal collisions and bolt preload release. The design of Hi-Shear's Ultra Low Shock Separation Nut³ (Figure 2) addresses these two sources.

The key to its function is control of the bolt-preload release time. A rotational element (Rotor) located under the threaded segments meters preload release over a longer period of time than for standard pyrotechnic-actuated separation nuts. This longer release time minimizes bolt acceleration during the release process, minimizing the contribution to overall shock from preload release. By comparison, Hi-Shear's 9400 series nut releases preload almost instantaneously due to the sudden ejection of the retainer by high-pressure pyrotechnic gases. This sudden ejection contributes to mechanical shock twice: initially to overcome high static friction forces and a short time later when the retainer impacts the housing. The retainer in the Ultra

Low Shock Separation Nut design is simply moved out of the way by a light coil spring once the bolt preload is relieved, allowing the segments to gently separate. This reduces mechanical shock significantly.

1. High pressure gas produced by Power Cartridges is introduced into the pressure chamber.
2. Locking piston moves away from the bolt, unlocking the threaded segments engaging the bolt. Movement of the locking piston is stopped by the separator. This collision is isolated from the nut housing and surrounding structure, transmitting a very low shock level.
3. Threaded segments displace radially away from bolt.
4. Separator locks segments in open position.
5. If optional ejector is incorporated, ejector thrusts bolt out of structure joint.
6. Structure joint is cleanly separated.



BEFORE ACTUATION

1. Bolt is threaded fully into nut segments.
2. Nut segments are fully supported by locking piston.
3. Structure joint is clamped up to tension rating of bolt.

AFTER ACTUATION

1. Gas pressure acts on locking piston, moving it away from bolt to unlock threaded segments.
2. Segments displace radially away from bolt.
3. Bolt ejects and structure joint separates.

Figure 1. HSTC Low Shock Separation Nut Sequence of Operations

The Rotor of the Ultra Low Shock Separation Nut design makes all of this possible. The Rotor fits below the seat that supports the segments during preload. Both the Rotor and seat features are mating helical load-bearing surfaces. The helical surface feature optimized angles in order to cause auto-rotation under axial load. Pins lock the Rotor and seat together to prevent rotation. Actuation of the pyrotechnic initiator

withdraws the pins allowing the Rotor to turn, which allows the seat and segments to drop, relieving the preload. Although the function time of the Ultra Low Shock Separation Nut exceeds that of the 9400 series nut, it is still short enough to support the need for simultaneity in multi-nut applications.

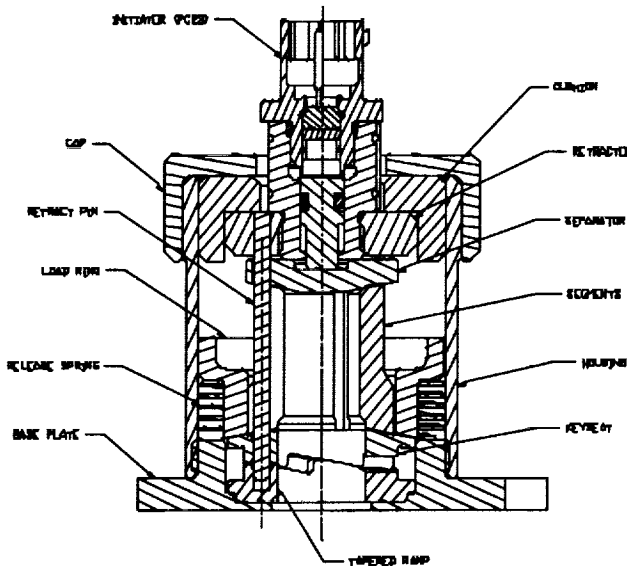


Figure 2. HSTC Ultra Low Shock Separation Nut

Shock Output Experiment

The following experiment was performed to validate the Ultra Low Shock Separation Nut concept with the standard HSTC SN9400 series separation nut. Both nuts were preloaded with a load cell to 10,000-N (2,247-lb_f) with an M12-1.75 (0.5-20 in) UNJF class-3 MS-bolt. For each test, the separation nut was centrally mounted to a 61-cm by 61-cm by 1.9-cm (24-in by 24-in by 0.75-in) horizontally suspended aluminum plate. A 2.54-cm by 2.54-cm by 2.54-cm (1-in by 1-in by 1-in) aluminum block was mounted 15.24-cm (6-in) from the center location of the separation nut on to the shock plate. Three each Model 7225 Endevco accelerometers were mounted orthogonal to the block in order to measure the acceleration output in each axis from the actuation event. Each nut was tested individually with a single initiator at room ambient condition for a total of three shots per nut. Figure 3 presents a shock response spectrum (SRS) for each of the tested separation nuts.

As each of the SRS's demonstrate that the Ultra Low Shock Separation Nut has appreciably reduced the shock output compared to the HSTC SN9400 Low Shock Separation Nut. At 100 Hz, the SN9400 Low Shock Separation Nut has a peak response of 245 m/s² (25-g) and the Ultra Low Shock Nuts is 49 m/s² (5-g); at 1,000 Hz 3,430 m/s² (350-g) and 588 m/s² (60-g); at 2,000 Hz 18,620 m/s² (1,900-g) and 3,430 m/s² (350-g); and a maximum peak response at 3,500 Hz 34,300 m/s² (3,500-g) and 5,500 Hz 14,700 m/s² (1,500-g) respectively. This is more than a 50% reduction in peak shock output in the axial direction.

TEST ITEM : 1/2" sep nut
 PART NUMBER :
 TEST TYPE : pyro output
 PROCEDURE # :

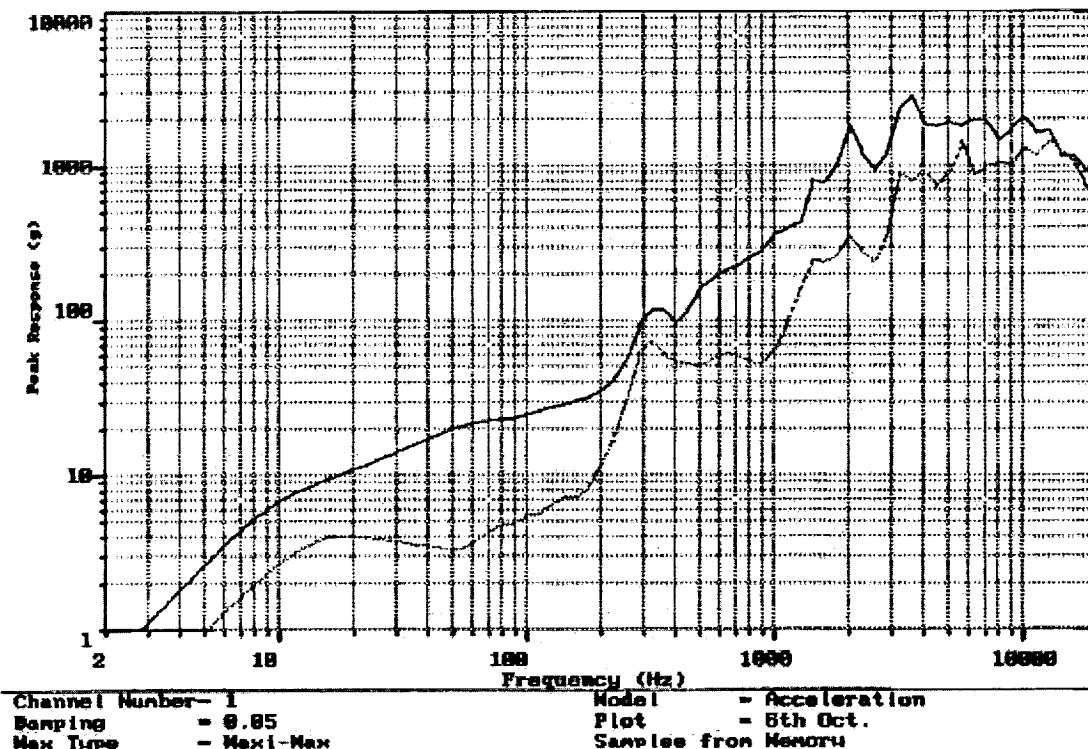


Figure 3. Axial Shock Comparison between the SN9400 and the Ultra Low Shock Separation Nut

Summary

The Hi-Shear Technology Separation SN9400 Nut Series have demonstrated low output shock performance and has been the choice on numerous critical deep space applications where shock output is critical. As the Aerospace Industry transitions to smaller payloads where shock critical devices are near proximity to pyrotechnic actuation devices, these devices' shock output become more and more critical. In response HSTC is developing a Pyrotechnically Actuated Ultra Low Shock Separation Nut (Patent Case Number 4931) that has demonstrated an approximate 50% reduction in output shock compared to the HSTC SN9400 separation nut.

The next iteration for the HSTC Ultra Low Shock Separation Nut is to handle preloads in excess of 4,500-N (20,000-lb_f) with an M12-1.75 (0.5-in) MS-bolt, and further improve on its reduced shock output.

References

1. Patent Number 5,248,233, "No-Shock Separation Mechanism", Richard G. Webster, (Hi-Shear Technology Corporation) September 28, 1993
2. Patent Number 3,926,090, "Separation Nut", James W. Bunker, (Hi-Shear Technology Corporation) December 16, 1975
3. Patent Case Number 4931, "Reduced Shock Separation Feature", O'Quinn et-al, (Hi-Shear Technology Corporation) February 1, 2000

Piezoelectric Pump Development

Franklin E. Sager

Abstract

The primary objective of the piezoelectric pump program is the development of enabling pump technology for space applications. Pumps under development are characterized by reduced mechanical complexity, increased reliability, improved efficiency, reduced volume, and reduced weight, with respect to conventional pumps. With a combination of sponsor and internal funding, two generations of pump designs were built and tested. The main products were design understanding and sizing equations, and a marked improvement in pump performance as the design evolved. The basic engineering developed on this project has broad aerospace applications.

Introduction/ Background

Conventional state-of-the-art pumps (motor and pump) are capable of achieving 18% efficiency in the conversion of voltage and current (in) to pressure and flow (out). Conventional pump technology has been under development for over 100 years. Significant improvement for conventional systems is unlikely due to the maturity of the technology. However, piezoelectrically-driven pump technology, under development for approximately 10 years, promises reduced mechanical complexity, increased reliability, improved efficiency, reduced volume, and reduced weight, with respect to conventional pumps.

This report covers work performed under two Small Business Innovative Research (SBIR) contracts and two Independent Research and Development (IR&D) projects directed toward the development of positive displacement piezo-electrically driven pumps. The initial research was more specifically directed toward the development of a Piezoelectric Water Pump for Use in Extra Vehicular Activities. The original project consisted of three major parallel efforts: the mechanical design of the pump drive mechanism, the electrical design of the drive circuitry, and the mechanical design of the pump itself. Stress Engineering Services, Inc. (SES) and Oceaneering Space Systems, Inc. (OSS) performed the majority of the work. SES has had primary responsibility for the analysis and sizing of the drive blocks and mechanical design of the pump. OSS was responsible for the drive block fabrication methodology and the electrical design and analysis. The Crew and Thermal Systems Division at the Johnson Space Center (JSC) in Houston initiated the development project as a Phase I SBIR. The conclusion of the Phase I study [1] indicated that it was feasible to build and operate a piezoelectric pump.

As a follow-on activity, OSS performed an IR&D project to confirm fabrication processes for the piezo-electric actuators. NASA awarded a Phase II SBIR to build a working prototype based on the successful conclusion of the Phase I SBIR (September 1993) and the positive results from the fabrication IR&D project. The Phase II SBIR was successfully completed in April 1997. The Phase II prototype was made with piezoelectric polymer films. Based on results from the Phase II SBIR, additional IR&D was initiated to investigate fabrication techniques and performance characteristics of hybrid PZT/thermoplastic piezoelectric bender elements. These hybrid PZT/thermoplastic piezoelectric bender elements are the primary components of the second prototype. They will allow the operation of piezoelectric devices at operating voltages on the order of 10 V. This paper describes the two

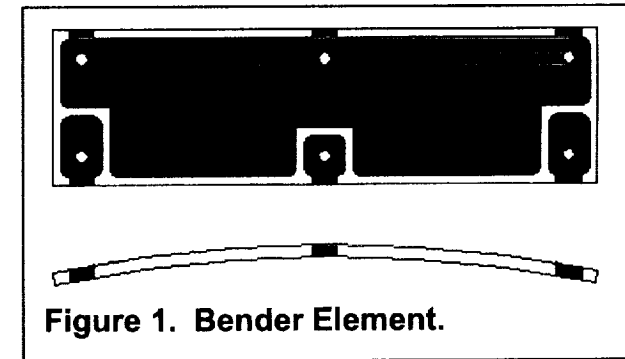


Figure 1. Bender Element.

* Oceaneering Space Systems, Houston, TX

generations of pump hardware developed during this Phase II SBIR and IR&D activity.

Piezoelectric Pump Development

Phase II SBIR Prototype Summary of Details

A double-acting diaphragm pump driven by piezoelectric polymer films was designed, constructed and tested as part of the Phase II SBIR. The initial actuators were constructed of piezoelectric polymer films that are laminated into eight forty-layer stacks, arranged so that charging the composite structure causes it to flex. One such stack is referred to as a bender (Figure 1) and two benders connected by hinges at their ends are referred to as a unit cell (Figure 2). Four such units drive the original pump (Figure 3). A novel electrical circuit developed specifically for this application (Figure 4) powers the drive mechanism. The unit cells act as capacitors, with only a small fraction of the energy input to the device being converted to flow power in each cycle. The circuit that was developed as part of this design provides switching which eliminates both the waste of energy inherent in direct-drive circuits and the need for large inductors or transformers.



Figure 3: Phase II Pump

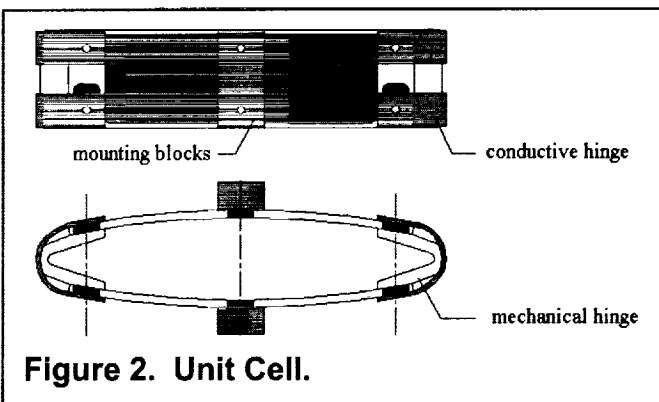


Figure 2. Unit Cell.

Tests of the pump show that it is able to pump up to 61 kg/hr of water at a differential pressure of 7590 Pa (1.1 psi) or 23 kg/hr at 20000 Pa (9 psi). These conditions represent approximately 60% of the design goals of 100 kg/hr and 32480 Pa (5 psi). The results were obtained at input voltage levels of up to 400 V. The design

eliminates both the waste of energy inherent in direct-drive circuits and the need for large inductors or transformers.

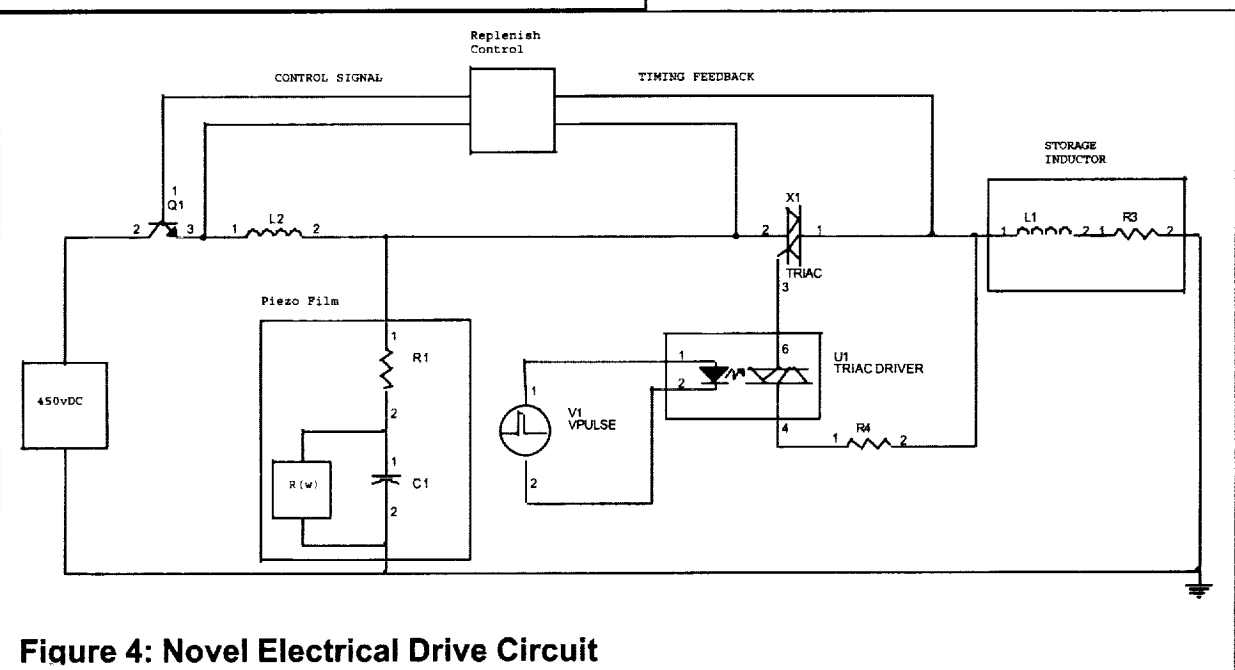


Figure 4: Novel Electrical Drive Circuit

should be stable to 800 V which would allow the design goals to be fully reached. The voltage has been limited in testing to avoid prematurely damaging the prototype.

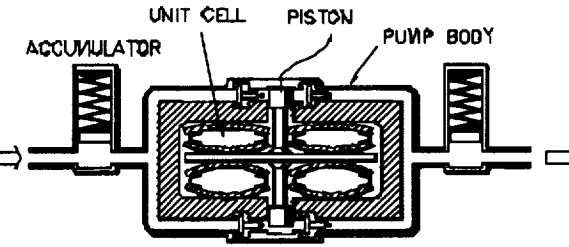


Figure 5a: Schmatic of Pump

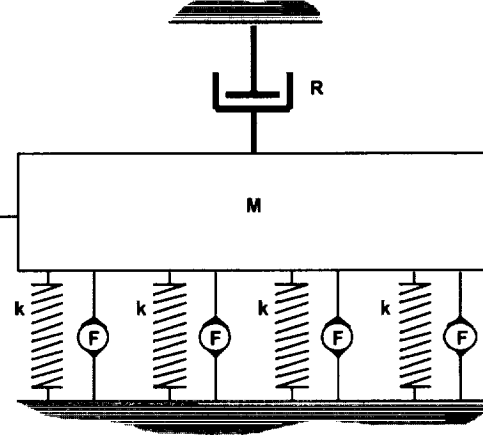


Figure 5b: Dynamic Model of Pump

Drive Block Analysis and Sizing [2]

Stacks and arrays of unit cells are referred to as drive blocks. In order to size the pump drive blocks, it was necessary to mathematically characterize the motion of the piston as a function of the geometry of the benders and the pressure on the face of the piston. In order to do this, the schematic layout of the pump shown in Figure 5a was reduced to a one-dimensional dynamic systems model as shown in Figure 5b. In this figure the springs (k) each represent the stiffness of one stack of piezoelectric benders, the mass (M) represents the mass of the piston and plate plus the effective mass of the benders, the damping (R) relates to viscous losses in the LCVG (the load on the pump), and the force generators (F) each represent the piezoelectrically-induced force of one stack of benders. This model is of value because it provides closed-form solutions which indicate the dependence of the solution upon various parameters. These solutions form the basis for the drive element sizing calculations. In addition, these calculations provide electrical impedance formulas for use in the electrical drive circuitry development. The analysis methodology is described below.

The piezoelectric force in a unit cell is

$$F = \alpha_1 e_{31} V, \quad (1)$$

where

$$\alpha_1 = \frac{3}{2} \frac{w_e h_{eff}^2}{t_f L}, \quad (2)$$

w_e is the width of the electrode, h_{eff} is the effective thickness of a bender, t_f is the piezoelectric film thickness, L is the length of the benders, e_{31} is the piezoelectric stress constant, and V is the applied voltage. The static load P which a unit cell can lift is given by

$$P = -kx + \alpha_1 e_{31} V, \quad (3)$$

where k is the stiffness of the unit cell and x is the displacement of the top of the unit cell when the bottom surface is fixed in place.

Using equation 3, the dynamic motion of the pump piston can be computed using the equation of motion given by

$$M\ddot{x} + R\dot{x} + 4kx = 4\alpha_1 e_{31} V \quad (4)$$

where the factor of 4 represents the 4 unit cells used in the design. Given a sinusoidal voltage input with a frequency ω , the piston will oscillate with an amplitude X given by

$$X = \frac{\alpha_1 |e_{31}| V_0}{k'} \frac{1}{\sqrt{(1 - r^2)^2 + \left(\frac{\omega R}{4k'} + \frac{1}{Q_m}\right)^2}}, \quad (5)$$

where V_0 is the magnitude of the voltage signal, $|e_{31}|$ is the magnitude of the complex piezoelectric stress constant, k' is the real component of the stiffness, Q_m is the mechanical quality of the unit cells, and $r = \omega/\omega_n$ is the ratio of the imposed frequency ω to the natural frequency of the system ω_n given by

$$\omega_n = \sqrt{\frac{4k'}{M}}. \quad (6)$$

The flow rate which the pump can drive is then computed as

$$Q = 4 X A_{piston} \frac{\omega}{2\pi}, \quad (7)$$

where A_{piston} is the area of the piston face. The factor of 4 in equation 7 occurs because the total stroke of the piston is twice the amplitude and there are two pump heads.

The current density i in a piezoelectric film layer is computed using the relation

$$i = e_{31} \frac{\partial S_{11}}{\partial t} + \frac{1}{t_f} \epsilon_{33} \frac{dV}{dt}, \quad (8)$$

where S_{11} is the average strain in the piezoelectric film at the point in question and ϵ_{33} is the permittivity of the film. Integrating equation 8 over the entire composite structure of a bender and totaling the 8 benders in a unit cell gives an equation of the form

$$I = [(G(\omega) + \omega C' \tan \delta) + j(B(\omega) + \omega C')] V, \quad (9)$$

where $V = V_0 e^{j\omega t}$ is the voltage signal,

$$C' = \frac{8(2N)w_e L \epsilon'_{33}}{t_f} \quad (10)$$

is the real part of the capacitance of a unit cell with $2N$ equal to the number of film layers in each bender, the factor of 8 represents the 8 benders which make up the 4 unit cells, $\tan \delta$ is the dielectric loss tangent,

$$G(\omega) = \frac{4\omega \alpha_1^2 e'^2_{31}}{k'} \left[\frac{\left(1 - \frac{1}{Q_{e_{31}}^2}\right) \left(\frac{\omega R}{4k'} + \frac{1}{Q_m}\right) + \frac{2}{Q_{e_{31}}} (1 - r^2)}{(1 - r^2)^2 + \left(\frac{\omega R}{4k'} + \frac{1}{Q_m}\right)^2} + \frac{\left(1 - \frac{1}{Q_{e_{31}}^2}\right) \frac{1}{Q_m} + \frac{2}{Q_{e_{31}}}}{3 \left(1 + \frac{1}{Q_m^2}\right)} \right], \quad (11)$$

$$B(\omega) = \frac{4\omega \alpha_1^2 e'^2_{31}}{k'} \left[\frac{\left(1 - \frac{1}{Q_{e_{31}}^2}\right) (1 - r^2) - \frac{2}{Q_{e_{31}}} \left(\frac{\omega R}{4k'} + \frac{1}{Q_m}\right)}{(1 - r^2)^2 + \left(\frac{\omega R}{4k'} + \frac{1}{Q_m}\right)^2} + \frac{\left(1 - \frac{1}{Q_{e_{31}}^2}\right) - \frac{2}{Q_{e_{31}}} \frac{1}{Q_m}}{3 \left(1 + \frac{1}{Q_m^2}\right)} \right], \quad (12)$$

and $Q_{e_{31}}$ is the ratio of the real to the imaginary parts of e_{31} .

The electrical power input to the system is given by

$$P_{in} = \frac{1}{2} V_0^2 (G(\omega) + \omega C' \tan \delta) \quad (13)$$

and the power output by the pump is given by

$$P_{out} = \frac{1}{2} v^2 R = \frac{1}{2} (\omega x)^2 R = \frac{1}{2} \frac{\alpha_1^2 \omega^2 |e_{31}|^2}{k'^2} \frac{RV_0^2}{(1-r^2)^2 + (\frac{\omega R}{4k'} + \frac{1}{Q_m})^2}. \quad (14)$$

Therefore the basic efficiency of the pump can be computed as

$$\eta = \frac{P_{out}}{P_{in}} = \frac{\alpha_1^2 \omega^2 |e_{31}|^2}{k'^2} \frac{R}{(1-r^2)^2 + (\frac{\omega R}{4k'} + \frac{1}{Q_m})^2} \frac{1}{G(\omega) + \omega C' \tan \delta}. \quad (15)$$

The above equations are used to size the pump. The critical equations are 6, 7, and 15. From equation 5 it can be seen that the maximum displacement can be obtained if the pump is run at resonance ($r=1$). This is true so long as the $\omega R/4k'$ is not too large. Large values of the viscous resistance R overdamp the system and do not allow resonance to occur. However, if the pump uses accumulators so that the piston is working against constant pressure, resonance can always be obtained. In this case the point of resonance also gives the maximum efficiency.

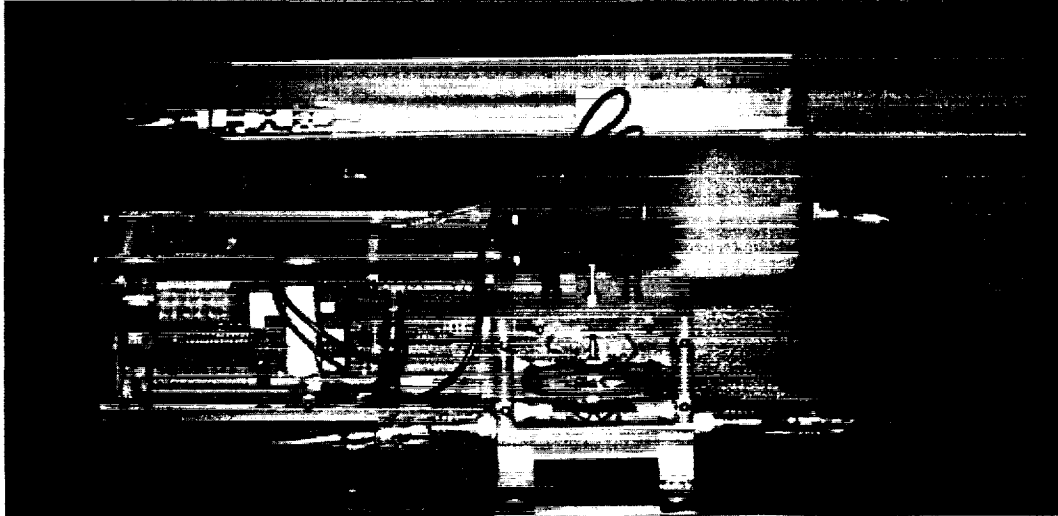


Figure 6: Second Prototype Developed Under IR&D

Second Prototype Developed Under IR&D

OSS continued the pump design with a new-generation model built under IR&D funding. The major goals of this work were to reduce the operating voltage (from the 800V first model), and to reduce the volume while improving efficiency. The follow-on work, based on the results developed as part of the aforementioned prototype, was recently completed. The work demonstrates design optimizations that allow an order-of-magnitude reduction in required operating voltages (to approximately 40V) while retaining appropriately high field strengths within the active piezoelectric material. Additional work has also been completed that demonstrates a material substitution based on hybrid piezo-thermoplastic 2-2 composites. This substitution has resulted in an order-of-magnitude reduction in the total volume required for a given unit of useful work output, with significantly improved efficiency (on the order of 65%)

with respect to the Phase II polymer designs. Additional design improvements being investigated include hinge improvements, metal bellows, and vibration elimination.

The second prototype was capable of producing half of the flow and force of the first prototype at one-thirtieth the volume and one-fourth the drive voltage. We are currently seeking funding to complete the process of characterization and to develop mathematical models for the new hybrid geometry. The preliminary results are promising.

Four patents have been issued covering the fabrication of the benders [3], the unit cell geometry [4], application of the piezoelectric unit cells to pump design [5], and the electrical circuit [6]. Additional patents based on the most recent work with low-voltage hybrid piezo-thermoplastic composites were filed last summer.

In addition to the direct application of piezoelectric pumps to active thermal cooling for life support applications, converse-piezoelectric pumps offer great potential in the dual-use area of alternative electro-mechanical actuators. As an actuator, this pump may provide solutions to control system problems in robotics, process control, bioengineering, and advanced remote control (telepresence) technologies. The advancement of these technologies is coupled to improvement in control system engineering which is a central engineering problem.

Some Space Applications

- High-reliability low-power pumps for fluid management during planetary missions
- Circulation pump for fluids in water storage system to prevent bacteria growth on walls
- General actuator for a variety of space applications including automation and robotic implementations
- Active thermal control for spacecraft
- Active thermal water loops for space refrigeration systems
- Primary flow control for space-based biological reactors
- Metering pumps to control space-based pharmaceutical production processes

Conclusion

Piezoelectrically-driven pump technology promises reduced mechanical complexity, increased reliability, improved efficiency, reduced volume, and reduced weight, with respect to conventional pumps. This paper describes characterization equations, analysis, and working hardware that illustrate these possible improvements. The hardware is currently approaching a level practical for use in space today. A concerted effort should be made to advance piezoelectrically driven pumps.

References

1. Piezoelectric Water Pump for Use in Extra Vehicular Activities Phase I Final Report NAS 9-18850.
2. Excerpt from Piezoelectric Water Pump for use in Extravehicular Activities phase II final report (NAS 9-19104). The original analysis was performed by Christopher J. Matice Ph.D., PE with Stress Engineering Services, Inc.
3. U.S. Patent # 5,761,782 for Method of Fabrication of Benders, issued 06/09/98.
4. U.S. Patent #5,889,354 for Unit Cell Geometry, issued 03/30/99.
5. U.S. Patent #5,798,600 for Application of Piezoelectric Unit Cells to Pump Design, issued 08/25/98.
6. U.S. Patent # 5,892,314 for Electrical Drive Circuit, issued 04/06/99.

Miniature Linear Actuator

Armond Asadurian*

Abstract

The objective was to design and develop a linear actuator for two different applications using one basic design philosophy. The basic design configuration was based on an incremental rotary actuator, which was derived from the family of standard SMD actuators. Linear motion was obtained from a precision ballscrew attached to the rotary output member of the actuator. This arrangement produced a linear output motion at the mating ball-nut. In one application, the actuator was used to precisely position two sliding loads within a RF Variable Power Divider. The other application required the linear actuator to rotate a reflector around a gimbal pivot point within an Antenna Pointing Mechanism.

Design Challenges

The principal design challenges were the compact and light weight arrangement, the required accuracy, and the requirement to produce relatively large linear forces within the temperature and size limitations. These performance demands were magnified by the additional requirements of meeting 2:1 torque margins within the specified power consumption requirements, redundant motor windings, redundant fine (rotary) and coarse (linear) potentiometers used for telemetry, redundant heaters, thermistors, and thermostats.

Introduction and Product Description

This design utilizes a stepper motor, which furnishes the input to a harmonic drive speed reducer. The ballscrew is attached to the output of the harmonic drive and is supported with a duplex pair of angular contact ball bearings (Figure 1). A two-track (redundant) rotary potentiometer is mounted on the output of the harmonic drive, and is housed around the rotating axis of the ballscrew, occupying only a small axial space.

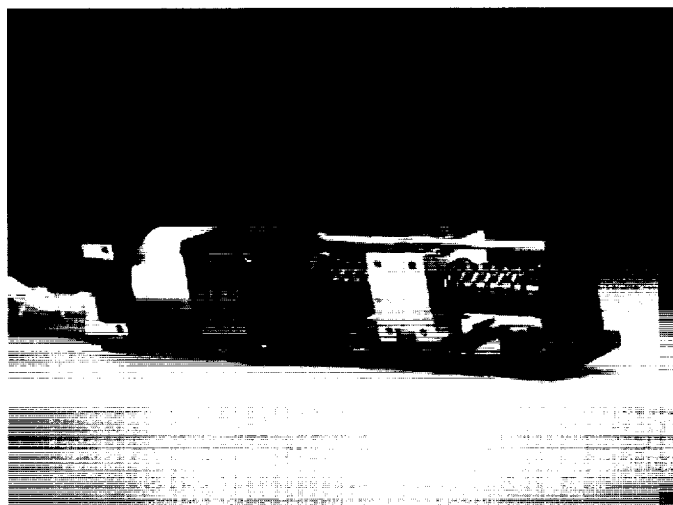


Figure 1. Linear Actuator (50-mm stroke)

* Moog, Inc., Schaeffer Magnetics Division, Chatsworth, CA

Two ballscrew configurations are available with this design, differing in the length of the ball-nut travel. The travel requirements for the two applications are 50 mm and 6.5 mm. The general ballscrew design was selected to provide the appropriate screw pitch and diameter to achieve the required speed of actuation, the helix angle for the needed efficiency and telemetry resolution, and for load handling capability. The ball-nut also carries the potentiometer wiper assembly, which is required for the coarse potentiometer located in parallel with the movement track of the ball-nut.

Providing lubrication for the ballscrew/ball-nut pair was especially challenging since the actuator configuration did not allow for an enclosed ballscrew and ball-nut assembly, and the possible use of wet lubrication. The 53R_c hardness of the ballscrew material (440C stainless steel) provided the substrate on which dry lubrication would perform and endure best. An additional design obstacle was presented by the immediate proximity of the linear potentiometer to the ballscrew, which could lead to deposits of loose dry lubricant on the potentiometer track. The dry lubrication deposit would be the direct product of intimate contact generated between the balls and the ballscrew surface, which was impregnated with dry lubricant. Based on previous experience with using dry lubrication on intimately contacting surfaces, the decision was made to use Tungsten Disulfide dry lubricant (Diconite).

A separate qualification test was conducted to determine the viability of this type of lubricant in these specific operating environments. The ballscrew was exposed to -50°C temperature with a resistive force of 93 N (21 lb) and was actuated for 1,800 cycles (1 cycle was from full retract to full extend and return to full retract), which exceeded the performance requirements of the actuator specification. At the completion of this test, it was determined that there were no deposits of loose dry lubricant induced from normal wear.

The selection of the incremental stepper motor over a brushless DC motor was driven by the incremental positioning and unpowered holding capability of the stepper motor. The stepper motor magnetic design features a number of equally spaced permanent magnets on the rotor. The interaction of the rotor magnets and the tooth structure of the stator core results in a strong attractive force, independent of any electrical excitation of the stator winding. This holding force is magnified by a factor of 100, due to the 100:1 harmonic drive gear ratio.

The ballscrew selected for this application was tested and its back-driving moment was measured to be 0.18 N (1.6 in-lb) at the worst case launch and ground transportation induced loads. In comparing this value to the actuator holding capability of 0.85 (7.5 in-lb) it was concluded that the actuator would not back-drive under the worst case loading condition.

The stepper motor was a two-phase 15-degree stepper, chosen over similarly sized three-phase stepper motors. The choice was based on its superior performance observed after motor characterization testing. The 15-degree stepping increments provided a sufficiently small linear step to meet the product requirements. The output rotary step at the ballscrew was reduced to 0.15 degree after passing through a 100:1 harmonic drive speed reducer. This then resulted in a 1.75 µm (0.000069 inch) linear step for every motor step.

The harmonic drive selected for this program was one of the "mini series" units from Harmonic Drive Technologies, which also offered a high degree of positioning accuracy and repeatability, zero backlash, relatively high torsional stiffness, and high torque capability. The small size of this harmonic drive allowed it to be used in-line with the motor, and providing a streamlined and compact assembly.

The lubrication of the harmonic drive assembly as well as the motor and output bearings was accomplished using Braycote 815Z oil and Braycote 601 grease. This lubricant was used to meet the demanding cold operation temperatures of -50°C.

Two co-molded carbon film type redundant rotary (fine) and linear (coarse) potentiometers were designed to provide the required telemetry. The rotary potentiometer was attached to the rotary output of the

actuator, and the linear potentiometer was connected to the nut of the ballscrew assembly. Combining the rotary and linear actuator resulted in a system accuracy/resolution of 23.6 μm (0.00093 inch).

Actuator Performance Characteristics

Winding resistance (ohms)	50.5
Inductance (mH)	15
Rotary Potentiometer Resistance (ohms)	9255-10544
Linear Potentiometer Resistance (ohms)	7077-7428
Power Consumption (watts)	15.44
Threshold Voltage, Hot (V)	10.0
Threshold Voltage, Cold (V)	17.0
Potentiometer Linearity	(See Figure 3 as an example)
Linear Step Size (μm)	1.75 (0.000069 in)
Repeatability (μm)	± 20 (± 0.0008)
Ballscrew Backlash (μm)	7.6 (0.0003 in)
System Accuracy over 5-cm stroke (μm)	± 25 (± 0.001 in)
Stroke (cm)	5 and 0.65 (1.9685 and 0.2559 in)
Operating Temperature ($^{\circ}\text{C}$)	-50 $^{\circ}\text{C}$ to +85 $^{\circ}\text{C}$
Mass (kg)	0.5 max. (1.10 lb)
Actuation Force requirement (N)	93 (21 lb)
Actuation Speed {(PPS) Pulse Per Second}	300

Lessons Learned

Ballscrew vs. Leadscrew

The initial design approach was based on a leadscrew (plain screw) with a Vespel material nut. This approach was considered in order to eliminate the need for a lubricated leadscrew. The Vespel material nut was selected for its self-lubricating characteristics and space environment qualification. The initial results demonstrated a nut and screw combination that was efficient enough to meet the driving force requirement without the use of lubricant yet resisted the backdriving of the overall system due to the payload reaction forces. The other advantages were light weight, and a simple and cost effective mechanism.

The mechanism was then analyzed for accuracy and thermal characteristics. The challenge was to design the Vespel nut with a specific thread shape to mitigate the effect of the thermal coefficient differences between the Vespel material and the stainless steel leadscrew. Due to the large temperature span and the tight accuracy requirement of the system, the use of the Vespel nut in combination with the stainless steel leadscrew was rejected for this actuator. The combination of these two dissimilar materials can be a viable option in the event that the payload can be constantly spring loaded in one direction producing unidirectional loading of the nut and eliminating backlash under all conditions.

Current limited system vs. Voltage driven system

The electronic interface specified a voltage driven system that was voltage regulated, with the voltage set at a specified limit and the current draw then depending on the winding resistance of the motor. This resulted in power consumption exceeding the requirement at cold temperatures. By limiting the current draw to a level adequate for producing the required torque, we were able to prevent excessive power consumption at lower temperatures.

Anti-Rotation Member

The tendency of the ball-nut to rotate due to the torque at the screw was countered by an anti-rotation bar extending along the screw axis and providing support for the ball-nut. The alignment of this anti-rotation bar to the axis of the screw is important. Any misalignment will cause a rotation of the ball-nut as it moves from one end of the ballscrew to the other end. This slight rotation of the nut will contribute to the

accuracy budget of the overall actuator. This condition will also apply to a system in which the payload is not accurately guided, allowing rotation of the ball-nut. This rotation must be identified and accounted for during the design and development phase.

Evaluation Testing

An extensive qualification testing program was performed for this linear actuator. Testing was comprised of top assembly level testing as well as detail component testing. The detail component tests were performed on the harmonic drive, ballscrew, motor, and potentiometer assemblies. The top level assembly testing consisted of functional, vibration and thermal vacuum testing.

The functional testing was comprised of potentiometer linearity, output force, step size repeatability, and backlash tests. These functional tests were repeated after vibration and thermal vacuum testing. Results indicated that actuator performance was not degraded due to exposure to vibration and environmental conditions.

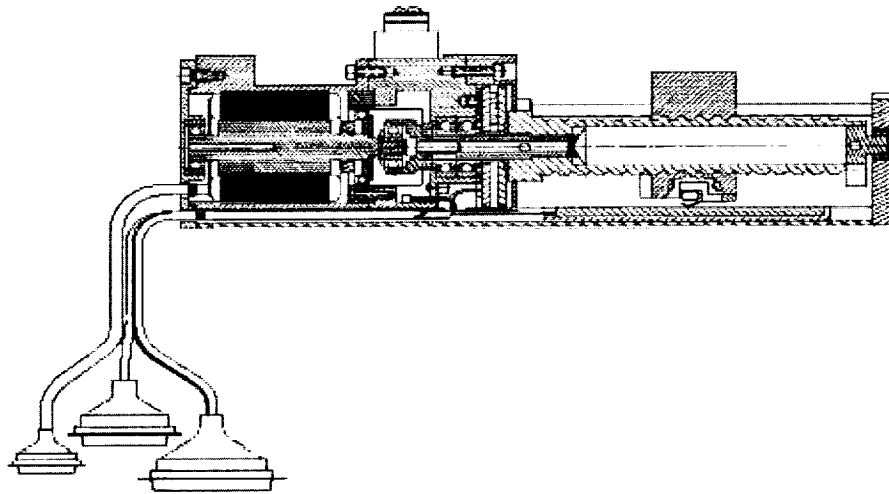


Figure 2. Linear Actuator Cross-section

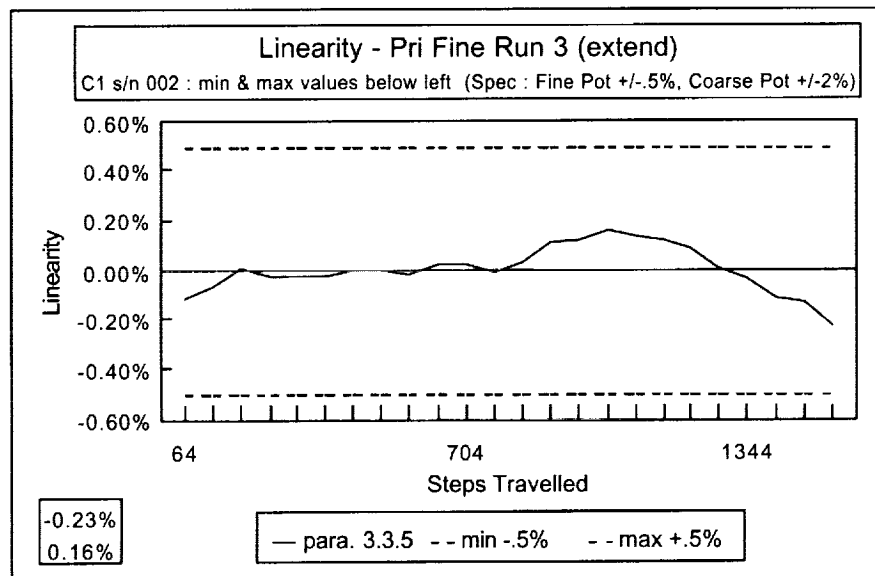


Figure 3. A Sample Actuator Linearity Test Plot

The Sandmeier Field Goniometer: A Measurement Tool for Bi-directional Reflectance

Mark Turner* and Jeff Brown

Abstract

Recent activities at the Remote Sensing Program at Stennis Space Center have identified the need to properly verify and validate data provided by the remote sensing community. One important variable, which effects remote sensing data is bi-directional reflectance distribution (BRDF). In order to quantify the effects of BRDF on man-made and natural ground targets, the Stennis Verification &Validation (V&V) team commissioned the Systems Engineering Division at NASA Ames Research Center to develop a Field Goniometer for use at the V&V Large Target Range and for various ground truthing missions.

The Swiss Field Goniometer (FIGOS) was used as a benchmark instrument to design the new state of the art Sandmeier Field Goniometer (SGF), named after Stefan Sandmeier, developer of FIGOS. After establishing requirements for the SGF, design efforts began in early May 1998. The design of the SGF was completed in September 1998. Manufacturing, construction, and testing was completed in May 1999. The SGF was shipped to NASA SSC and fully operational by June 1999.

Introduction

Depending on the viewing angle of the sensor (satellite or aircraft) relative to the target(vegetation or geology) and irradiance source (sun), the intensity of reflected radiance from the target can vary considerably. This phenomenon is known as bi-directional reflectance distribution. In addition to BRDF being caused by the variable position of the sun relative to the target, seasonal effects such as rain and snow can effect the BRDF. BRDF can also be attributed to varying viewing geometry caused when an instrument's field of view is large.

In remote sensing applications, BRDF can alter the spectral signature of the target thus limiting the usefulness of remote sensing data. By quantifying BRDF, the usefulness of remote sensing data may be improved. To measure the effects of BRDF on various targets, a Field Goniometer is used. Using a Field Goniometer, BRDF characterization of specific man-made and natural targets can be accomplished. In addition, a database of bi-directional reflectance signatures in the visible and near IR can be created for various targets. Figure 1 illustrates the general principle of measuring BRDF using a Goniometer.

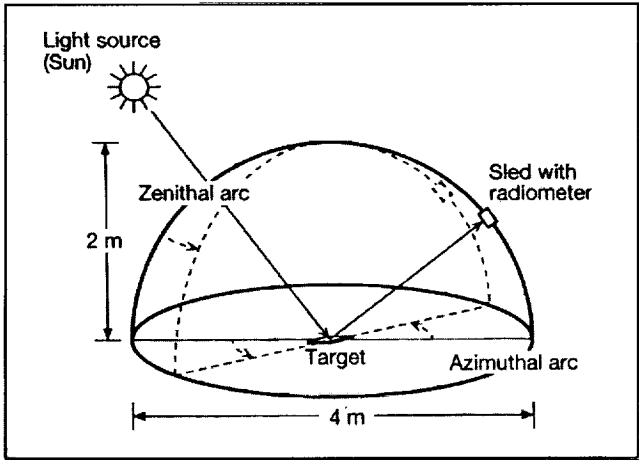


Figure 1 Measurement of BRDF using a Field Goniometer

* NASA Ames Research Center, Mountain View, CA

Sandmeier Field Goniometer Background

To support V&V efforts of the Remote Sensing Program at Stennis Space Center, the need for a Field Goniometer for quantifying BRDF was identified. The Stennis V&V team commissioned the Systems Engineering Division at NASA Ames Research Center to develop a Field Goniometer for use at the Stennis Space Center V&V Large Target Range. The Swiss Field Goniometer (FIGOS) was identified as the benchmark instrument for BRDF measurement in the field. V&V team members added new requirements to customize the instrument for their particular needs and to incorporate lessons learned during the operation of the original instrument. Figure 2 illustrates the solid model design of the Sandmeier Field Goniometer. The actual Sandmeier Field Goniometer is shown in Figure 3 undergoing acceptance testing at Stennis Space Center.

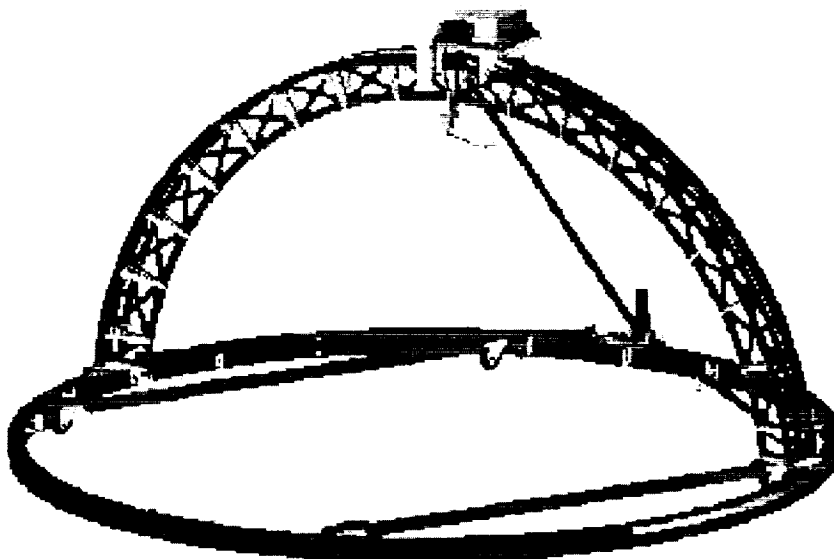


Figure 2. Sandmeier Field Goniometer

Requirements Development

To ensure consistency with data obtained from FIGOS, the new Field Goniometer maintains the same path of travel for the Spectroradiometer, the instrument that measures irradiance in the visible and infrared spectrum. The 3 degree field of view and 2 meter distance from the instrument to the target has also been maintained. The following are the key performance requirements of the SFG:

- The SFG shall be capable of providing measurements of the wavelength dependent reflected electromagnetic energy from a target on the ground in the wavelength range of 400 – 2500 nm with a constant distance between the sensor and the target of 2 meters.
- The capability shall be provided to measure a total of 66 sample locations, (11 samples per zenith arc at 6 azimuth locations) in no more than 15 minutes with a target goal of 8 minutes (The SFG should make the same standard sixty-six measurements as the FIGOS in order to compare measurements made by the two systems)
- The capability shall be provided to automatically sample at zenith angles from -75 degrees to +75 degrees in 15 degree intervals and azimuth angles from 0-180 degrees in 30 degree intervals
- The SFG shall have a pointing accuracy through all zenith (-75 degrees to +75 degrees) and all azimuth angles (0-360 degrees) of less than +/- 3.5 cm in any direction, as measured by a laser spot on the ground target, which represents the center of the spectroradiometer field of view (FOV).
- When the spectroradiometer is at nadir, its FOV of the ground target will be 10.5 cm diameter or less.

- The SFG structure shall not shadow the target when measuring in the solar principal plane, (azimuth of spectroradiometer aligned with azimuth of the sun). The spectroradiometer sensor head will be designed, to the extent possible, to reduce the amount of shadowing on the target.
- The SFG shall be designed operate on terrain with slopes of up to 10% grade.
- The SFG shall have repeatable performance throughout disassembly and reassembly in environments with a range of temperatures between -2 deg C and 38 deg C with a range of relative humidity of 10% - 95%

Additional functional and operational requirements were added which allow the SFG to be used on repeated characterization, which provide assured repeatability in data collection.

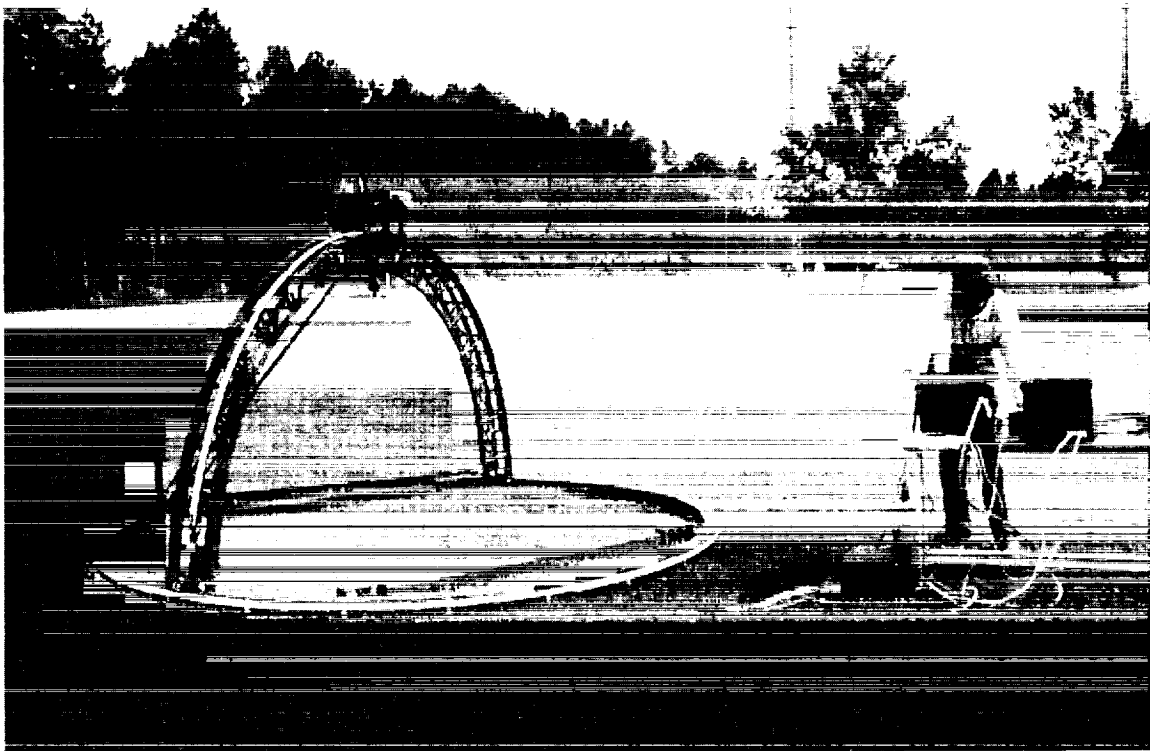


Figure 3. The Sandmeier Field Goniometer at Stennis Space Center



Figure 4. Spectroradiometer mounted on Instrument Sled

Design Description

The SFG uses an off-the-shelf GER 3700 spectroradiometer capable of taking measurements in the wavelength range of 400 – 2500 nm. A custom Fore-optic lens is mounted to the spectroradiometer to decrease shadowing effects that would occur if the instrument were placed directly over the target path. The instrument sled, shown in Figure 4, supports the GER 3700 and fore-optic lens and incorporates an alignment plate to allow for fine-tuning of the instrument's optical path relative to the target once the Goniometer is fully assembled.

Structural Design

The Zenith Arc Assembly is designed to be disassembled into two halves to facilitate transport. Since the SFG will be deployed in remote locations, emphasis was placed on reducing weight to the extent practical. The entire structure is fabricated out of 6061-T6 aluminum and each half arc weighs 14.5 kg (32 lb). To maintain a target pointing accuracy of ± 3.5 cm, the rolling surface of the zenith arc must be radially concentric to within 3 mm over the distance spanned by the rollers on the Instrument Sled. To achieve this precision, the upper rolling surface was machine screw fastened to a welded support structure. This allowed the use of shim stock to be added to compensate for any warpage experienced when the structural frame was welded. The decision to weld the main structure was made to reduce the fabrication cost, since multiple units were planned. Guide pins located at the upward mating surface allow for precise repeatable alignment (Figure 5). Captive fasteners are provided for all mating locations.



Figure 5. Zenith Arc Mating Surfaces

A design trade made with respect to the structural assembly was to consider suspending the instrument from the truss and invert the truss from its current orientation. This approach was ruled out because it would have complicated the belt drive design. The current design allows for the drive belt to be tensioned over the top of the zenith frame. The use of an all-composite zenith frame with triangular cross section was considered but was ruled out due to higher manufacturing cost and concerns about shrinkage and warpage to the frame. There was much consideration given to fabrication methods used to construct a precision welded structure. The concern was that an intricate thin wall aluminum structure would experience far too much warpage to be considered as a design choice. By using low amperage Tungsten Inert Welding (TIG), and proper sequencing of the welds, the zenith structure was fabricated with no measurable distortions in any axis. No shims were required in the final assembly.

The Azimuth Ring is 4 meters in diameter and can be disassembled into four quarter arc sections; each quarter section weighs 10.4 kg (23 lb). Four leveling jackscrews are provided to prevent rocking of the SFG on uneven terrain. To allow for assembly by two people, the Zenith Arc is attached to the Azimuth Ring Side Sleds using two pinned connections on a clevis assembly. This allows for quick assembly by one person, while the other holds the truss in position.

Drive System

The instrument sled that carries the GER 3700, and the Azimuth base ring, are driven with identical 0.4-HP brushless DC motors shown in Figures 6 & 7. The motors have a rated speed of 3,900 RPM, 0.8 N-m (7 in-lb) continuous torque and a peak torque of 3.4 N-m (30 in-lb). Each motor is coupled to the timing belt drive pulley through a direct coupled 30:1 planetary gearhead. Each end of an open-ended polyurethane timing belt is fixed at each end of travel for both zenith and azimuth drives. The timing belt selected is 30 mm wide, has steel reinforcement cables, and has an AT5 tooth design, 5 mm pitch. The toothed drive pulley has idler pulleys on each side to maintain a greater than 180° wrap around the drive pulley and provide the required tooth engagement (Figure 8). The idlers also keep the belt close to its fixed position and below the bottom of each drive sled. One end of each belt-end attachments has an adjustable pretensioning latch to pretension each belt to the required load after assembly.

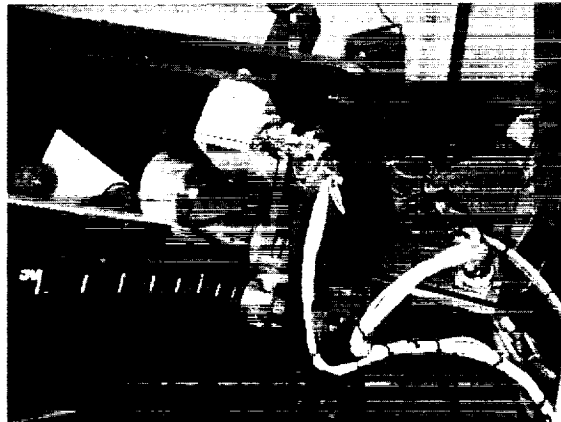


Figure 6 . Instrument Sled Drive Motor

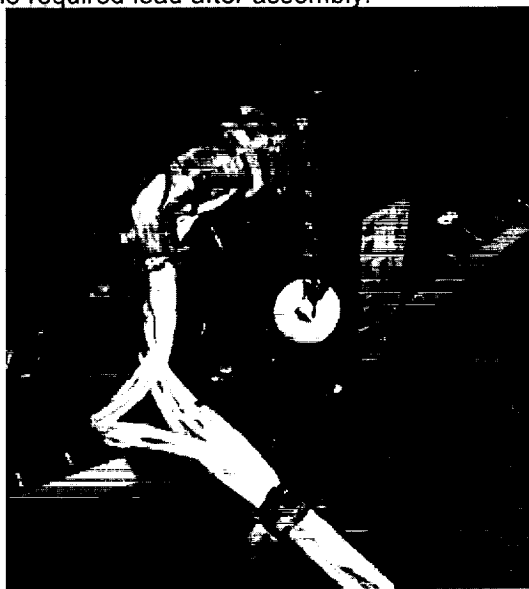


Figure 7. Azimuth Base Ring Drive Sled



Figure 8. Installation of Belt Drive

The use of guide rollers for the instrument sled and azimuth base ring was selected over the use of an off-the-shelf THK stainless steel guide track and carriage. The lead-time associated with fabricating a curved track was three months. In addition, the net cost for the structure and instrument sled would be 50% greater than fabricating components and each truss half section would have added an extra 5 kg to the structure. The SFG is intended to be field deployable in areas where dust and dirt could seriously affect the performance of a ball bearing carriage assembly. One problem that occurred during the operation of the SFG was tracking of the azimuth belt. Tension from the belt to the azimuth base ring sled would deflect the drive and idler pulleys causing the belt to track vertically downward. To alleviate the problem, a cam follower on the sled was repositioned to compensate for the tension on the belt. In addition, belt guides were added to the base ring to keep the belt centered with the drive pulley.

Motor Drives

The current control and commutation of each motor is provided by a Variable Frequency Drive. Each motor is equipped with a resolver for absolute position feedback of the motor rotor. The VFD uses a 20-kHz Pulse Width Modulated converter stage to convert the DC power source to a 3-phase variable magnitude and frequency current supply for each motor. This drive stage, commonly called a 6-pulse converter, is made up of 6 Insulated Gate Bipolar Transistors and 6 freewheeling diodes. The VFD uses the resolver feedback to commutate the 3-phase rotating current source in phase with the fixed magnetic poles of the motor. The magnitude of the motor current is also controlled by the pulse duration of the PWM converter. A current sensor in the VFD provides feedback for closed-loop motor current control. The brushless DC motor and PWM drive produce a high bandwidth torque control system with a closed-loop motor current (torque) bandwidth in excess of 900 Hz.

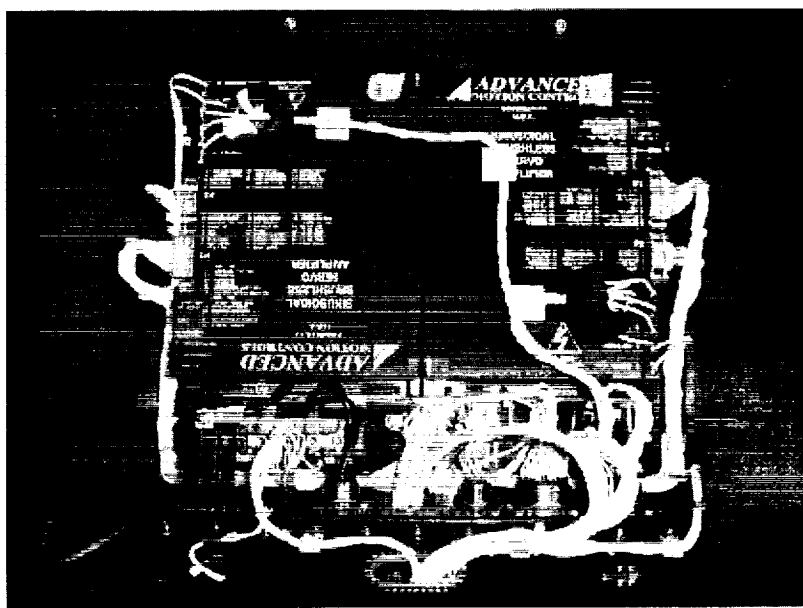


Figure 9. The Control System

Control System

The control system hardware shown in Figure 9 includes an ultra-rugged portable PC with an embedded Galil PC104 motion controller card. The PC104 motion controller is a 2-axis controller with adequate input/output channels to accommodate the instrument's operation and control. Each VFD contains an encoder emulator for converting the motor resolver data into a quadrature encoder output. The emulated encoder signals are input to the PC104 card for closed-loop velocity and position control of the zenith sled and azimuth carriage. Additionally, the PC104 motion controller performs axis homing, end-of-travel limiting, jogging functions, reference target control, VFD power up and enabling, and system fault monitoring and control. With its own processor, the PC104 motion controller executes the motion control

algorithms uninterrupted by task executed by the PC. The Galil developmental software running under Windows NT® on the portable PC provided command level programming of the motion control algorithms.

The zenith axis also incorporates two servo inclinometers, one mounted on the base and one on the zenith sled, for absolute zenith angle feedback. The inclinometers were not used for closed-loop control, but were used for display purposes only. It was found that with the motor resolver, coupled to the timing belt through the gearhead, it was possible to achieve precise position control of the zenith sled and azimuth carriage. Once the drives were homed, each axis could be positioned to better than $\frac{1}{10}$ of a degree. Once properly tuned the motion controller produced a very smooth acceleration, repositioning and deceleration down to the new position setpoint.

The portable PC provides the operator interface for operation and control of the instrument's positioning system. The operator interface for monitoring and control was developed using Visual Basic. Windows for operation and control include a checklist for startup, motion control, alarms and messages, and station editor. This motion control window allows the operator to initiate homing, axis jogging, and exercise and scan reference target. The alarms and messages window displays system faults and messages generated in the PC104 motion controller. The station editor generates and stores azimuth and zenith positioning matrices. The requirements specify that the positioning matrix with repeating 15° increments along the zenith arc every 30 degrees of azimuth base angle for a total of 66 measurements. The station editor allows any combination of azimuth and zenith angles to be entered, either manually or automatically by entering range of motion and positioning increment for each axis. Any generated position matrix can be saved and reloaded for repeated use.

Since it is desirable to take a hemisphere of data with the sun in one position the speed of instrument positioning and data acquisition were defined as key requirements. To automate the process of instrument positioning and data acquisition, the motion controller PC communicates with the spectroradiometer PC through an RS232 serial link. Parameters are passed between the two PCs to initiate motion and data acquisition. Also, these parameters contain information about reference target position and data. The motion system for either axis can reposition over a 15° arc in less than 1 sec. Data acquisition by the spectroradiometer takes approximately 3 sec., dependent on the number of integrations by the instrument. The existing system is able to exceed the specified requirements, taking the default matrix of 66 measurements in less than 5 minutes.

Auto Calibration System

Since the sun's position is always in motion and changes in the atmosphere can occur, the SFG design incorporates an automated calibration device that uses a Spectralon target that rotates into view of the spectroradiometer (Figure 10). The spectroradiometer is calibrated every time it passes the Nadir position on the Zenith Arc. The Spectralon target is placed 28 cm (11 in) from the instrument's fore optic lens, allowing calibration without shadowing when used at latitude greater than 16 degrees.

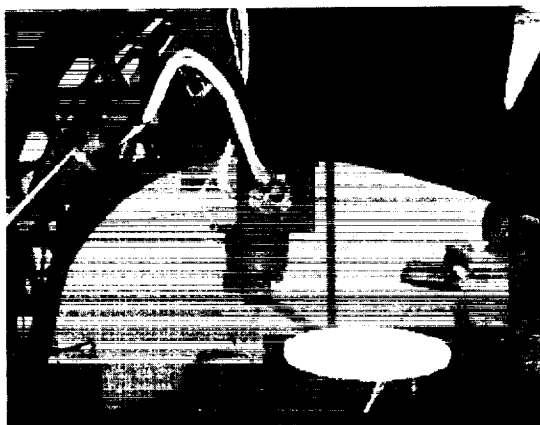


Figure 10. Calibration Arm

Operational Considerations

The SFG can be easily moved on hard surfaces using the built in caster assembly. Using C-channel rails, the SFG can be moved to different locations on uneven surfaces. All components have been designed to minimize weight to allow for assembly in remote locations. The SFG can run on 120 VAC or on supplied DC Gel Cell battery packs.

Conclusion

Manufacture of the SFG commenced in October 1998 and completed in May 1999. The SFG was delivered to Stennis Space Center and is currently operational. The Goniometer has been successfully deployed with repeatable results after being assembled and disassembled over several dozen cycles. A test of the pointing accuracy was performed using a laser to see how well the spectroradiometer could track the center of the SFG. The pointing accuracy was measured at ± 1.2 cm, which is well within the required range of ± 3.5 cm. Assembly time for the goniometer is typically under 30 minutes. Once assembled, the SFG is able to perform its default set of 66 measurements in under six minutes which is faster than the target goal of 8 minutes. Wear on the rubber rollers located on the instrument sled has occurred faster than anticipated. There is also concern regarding overheating of the computer since the instrument is used in direct sunlight for prolonged periods of time.

A sample of data obtained from the GER 3700 is shown in Figure 11. This data shows the reflectance of light at 2307 nm for various angles. The reflectance data obtained creates a spectral fingerprint that can be used to ground truth hyperspectral images taken from aircraft or satellites and correct distortions caused by BRDF.

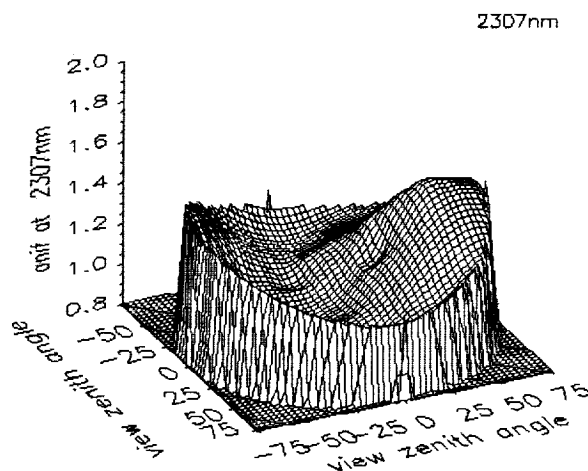


Figure 11. Spectral Fingerprint of grass at 2307 nm

References

1. Sandmeier Field Goniometer Project Management Plan, Doc # A92C-9801-X100
2. Requirements Document For Sandmeier Field Goniometer, Doc # A92C-9801-X101
3. Sandmeier, Stefan, et.al. "Acquisition of Bi-directional Reflectance Data Using the Swiss Field Goniometer System (FIGOS) in: Proc. of EARSeL Symposium, Basel, Switzerland, 1996. Balkema Publ. NL, pp. 55-61.
4. Sandmeier, St., and K.I. Itten, A Field Goniometer System (FIGOS) for Acquisition of Hyperspectral BRDF Data, IEEE Trans. Geoscience and Remote Sens., accepted.

Motor Redundancy Concepts: Efficient or Reliable?

Eric Favre*

Abstract

When a redundant electric motor is required to activate a mechanism, a trade-off is made in order to determine which type of redundancy to implement. This paper presents the five different design options available for the motor redundancy, with an emphasis on their respective and relative performances and comparing both their advantages and disadvantages. The impact of considering a redundant motor at sub-system level (mechanism) is also addressed.

Introduction

When trading-off the redundancy concepts for electric motor-driven mechanisms, two basic options are possible: to have either two separate motors on the same shaft or to have only one motor mechanical and magnetic element with built-in electrically redundant windings. For these two options, five different designs can be considered, each having different impacts on the following motor performances:

- The risk of having a failure that simultaneously damages the main and the redundant parts (single point failure);
- A global performance degradation when a failure occurs in the main winding, the redundant winding being used as the spare part;
- The motor's nominal performances (i.e., torque capability, power budget) when only one winding is energized (main or redundant winding);
- The motor's performances when the two windings are simultaneously energized (main and redundant windings for an emergency over-torque scenario).

The following main points are addressed in this paper:

- A presentation of the different available redundancy options;
- A discussion of their respective performances;
- A comparison of their relative performances;
- An analysis of the impact at sub-system level (mechanism) of considering a redundant design (i.e., cost, mass, packaging).

These inputs shall provide the rationale behind the selection of a given motor redundancy concept, enabling the mechanism designer to select the best option for given project needs.

Lessons Arising from a Motor FMECA

A good introduction to the definition of the possible redundancy concepts is provided by the analysis of the potential causes of failures observed on electric motors. Table 1 is the summary of a failure mode and effects criticality analysis (FMECA) performed on a frameless motor (electric / magnetic parts). A redundant brushless two-phase motor is considered, using permanent magnets (i.e. hybrid stepper or permanent

* ETEL Aerospace Inc., Boulder, CO

magnet synchronous motors), while failures linked to the eventual use of DC brushes are excluded. The failure causes are identified and classified into the following two categories:

Failures Causes to be Secured by Design, Manufacturing Processes & Procedures

- Stator laminations free to move within the motor housing
- Motor rotor parts free to move with respect to the sub-system rotating parts
- Loose or broken magnets
- Inadequate cable design / handling (transport, integration, tests) at motor or system level
- Mechanical shock / stress on the winding(s)

Failures that could Require the Implementation of a Redundant Path

- Failure on a winding solder joint (open circuit)
- A winding's dielectric insulation failure (short-cut)
- Thermal stress on the winding(s)
- Magnets demagnetized by over-temperature
- Input problems to the electronic driver

The implementation of a redundant winding path is a reliable option in case of (1) having an open circuit in the main winding and (2) for electronic driver failures corresponding to an open circuit.

For the failure modes leading to a partial or total main winding short-circuit and for motors with a continuously active pole excitation (i.e. created by magnets, as generally considered for hybrid stepper motors and small size brush and brushless DC motors), a braking torque occurs when the rotor moves. This braking torque is due to induced eddy currents into the short-circuited coils, the shaft motion being either created by (1) the use of the redundant path or, simply, (2) by an applied external shaft load. The value of this braking torque depends on both the speed and the failed winding electrical characteristics and is not necessarily greatest at the highest speeds. In any case, the result of a short-circuit failure is reduced motor torque when the redundant path is used, due to this braking torque component from the failed winding path. If this braking torque is not negligible / manageable, the effort to eliminate the risk associated with this degraded performance would necessitate less efficient motor technologies [1], avoiding the use of permanent magnets.

Electronic driver failures that lead to a winding short-circuit also create the degraded performance due to the short-circuited winding's braking torque. The risk of having such a failure must be mitigated as much as possible by an adequate electronic design. Generally, however, other reliability concerns prevail at a given stage and a small risk of having such a failure still remains.

A thermal over-stress has two major consequences: (1) to damage the winding and (2) to demagnetize the motor magnets, if any. In terms of a redundancy concept, the major concern is to have a design which avoids the risk of having a common failure mode (simultaneously damaging the main and the redundant paths) or single point failure. A frequently considered alternative is to secure the design by having sufficient design margins with respect to temperature.

In short, in terms of a redundancy concept, the following guidelines should ideally be considered: suppression of common thermal paths between both main and redundant motor parts; and prohibiting the use of permanent magnets if (1) the braking torque in the short-circuited main winding(s) can not be managed by the redundant path and (2) the magnet(s) maximum temperature is not secured by design margins.

Sub-System Constraints

At sub-system level and in terms of motor selection, the given torque / speed working conditions must be fulfilled with the following specified or targeted constraints:

- To have a limited power allocation
- To have limited mass and dimension budgets
- To have acceptable sub-system reliability figures
- To limit the mechanical complexity
- To have a limited project cost

Disregarding the sub-system reliability, the redundancy concept works against every other point listed above. An example is shown in Figure 1, demonstrating the voluminous cabling needed for a redundant three-phase brushless DC motor, built with an integrated Hall sensor commutation device. This picture emphasizes a somewhat obvious conclusion: a price is paid for the redundant path and the limit will be given by the trade-off between overall performance and reliability issues.



Figure 1. European Robotic Arm Frameless Motor (ETEL)

A more marginal sub-system concern is the potential increase of the motor torque demand due to the implementation of the redundancy itself. A typical case is the increase of the motor's internal magnetic friction (both detent and hysteresis torques) due to the fact that a redundantly wound motor is larger. This aspect should, at a first glance, drive the preference of motor technologies away from permanent magnets, but the larger efficiency of the latter makes it preferred.

Considered Motor Technologies

The analysis of the potential motor failure modes has shown that one should consider not using permanent magnets. A short trade-off of motor technologies is made hereafter. Readers requiring more detailed information should refer to [1]. Three different motor categories are considered here: one using permanent magnets to create a DC excitation field; one not using it; and the technologies not worth considering further due to other reasons. The targeted motor performances typically range from below 1 N·m / 50 W and marginally up to 5 N·m / 1,000 W (or 150 in-oz / 50 W & 700 in-oz / 1,000 W).

Technologies Excluding the Use of Magnets

- Variable reluctance motors (Figure 2). This technology is only used in very cold conditions (typically below -200°C) where its inherent very high copper losses are significantly reduced due to the drop of the copper resistance. This is typically a regular candidate for cryogenic applications.
- Induction motors. For space applications, its poor efficiency makes the significantly more efficient brushless DC motor a preferred solution. Both technologies work in similar torque-speed ranges and require a similar electronic driver. Indeed, the key advantage of induction motors on Earth is the availability of a 60-Hz/AC power supply, unavailable on most spacecraft.

Technologies Using Magnets

For performance reasons, the following technologies are considered in most space applications. They must be selected on a case-by-case basis, depending upon the specific mechanism's performance [1].

- Hybrid stepper motors (Figure 3), with a design often referred to as "pancake", combining magnetic yokes and axially magnetized magnets on the rotor. This design is considered further in this paper when performance comparisons are made. It is described in detail in [2].
- Permanent magnet synchronous motors, often called "brushless DC motors" (Figure 4).
- Brush DC motors.

Unsuitable Technologies

The following technologies are not considered in this paper, either because they are out of scope or due to their marginal use in space programs for performance, heritage or industrial maturity reasons.

- Salient pole brush DC and synchronous motors. This technology avoids the use of permanent magnets for the motor DC excitation for both brush and brushless technologies yet is only used on relatively large size motors. Commercial units with sizes generally required for space programs are normally made with permanent magnets.
- Single-phase motors
- Hysteresis and Homopolar synchronous motor
- Electrostatic, Piezoelectric, Paraffin or Shape Memory Alloy-actuated motors.

Conclusion on Motor Technologies

In short, for performance reasons, motor technologies prohibiting the use of permanent magnets are rarely used in space programs. The selection of the redundancy concept must, consequently, manage this practical reality.

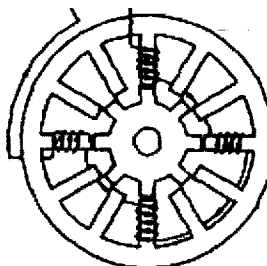


Figure 2. Reluctance Stepper Motor

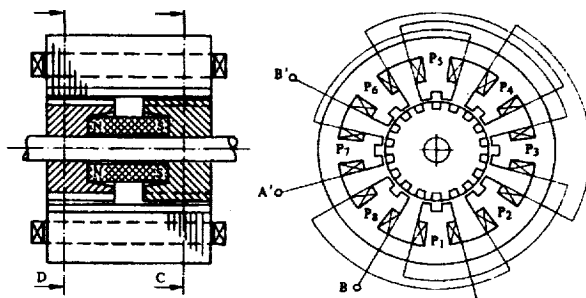


Figure 3. Hybrid Stepper Motor



Figure 4. Space-Rated Brushless DC Motor (ETEL)

Design Options for the Motor Redundancy

The following two basic options are available for a redundant motor and each option can be designed in different ways. These are discussed in detail in this chapter : having two separate motors on the same shaft (mechanical redundancy); and, having only one motor mechanical / magnetic part, with built-in electrically redundant windings (electrical redundancy).

Mechanical Redundancy

The first idea is simply to use two separate motors: one for the main and the other for the redundancy (Figure 5 - *full mechanical redundancy*). Everything is implemented twice, in particular the magnetic / electric parts, the mechanical housing, and bearings. For a given torque-to-power ratio, the budgets for the motor mass, volume and recurring costs are roughly twice those compared to non-redundant units. In case of thermal failure due to the heat rejection of the motor itself, this redundancy concept is very reliable. This reliability advantage is, consequently, lost for thermal failures due to an environmental thermal overload, likely to simultaneously heating both the main and redundant motors.

A simplified option could also be considered in this case by using the same mechanical pieces (housing and shaft) for both main and redundant electric / magnetic parts (Figure 6 - *partial mechanical redundancy*). It is, nevertheless, not always possible to reduce the number and size of the bearings in this case since the mechanical loads to be supported under vibration are similar to those encountered in the first option (Figure 5). This design simplifies, however, the mechanical interface with the sub-system by reducing the number of mechanical parts and limiting the manufacturing recurring costs. The risk of having both the main and redundant parts simultaneously damaged when a thermal stress occurs is, however, difficult to avoid.

Electrical Redundancy

The electrical redundancy consists of winding two separate sets of coils (the "main" and the "redundant") upon a single magnetic lamination stack. It can generally be implemented in three different ways, as described hereafter:

- The two sector electrical redundancy (Figure 7). This option limits the "physical contact" between both "main" and "redundant" coils, with a maximum "main to redundant mechanical interference" occurring in zero, two or a few motor slots depending upon the motor type and size. As a drawback, once the motor is magnetically saturated, this design limits the motor peak torque capability and requires more power for a given torque.
- The two wires in parallel electrical redundancy (Figure 8). The motor is wound with two wires at a time (one for the "main" coil and the other for the "redundant"). A thermal failure here represents a single

point failure. Nevertheless, it is regularly used in space applications where there is minimal inherent risk of current-induced overheating of the windings (integrated thermal sensor or low available power). Once the motor is magnetically saturated, the advantage of this solution is a significantly higher motor peak torque capability and reduced power consumption. This redundancy concept should also be considered for applications having short torque overloads (involving currents likely to demagnetize the magnets). This option still safeguards one winding in case of an electronic or wire-soldering failure.

- The shared slot electrical redundancy (Figure 9). The "main" and "redundant" coils are wound all around the motor, sharing the coil's slot, thereby limiting the physical contact compared to the "two wires in parallel" option. Performances are identical to the previous option. It is a good compromise between the first two electrical redundancy options.

Depending upon the specific motor type and size, one of these different redundancy options might not feasibly be implemented due to particular manufacturing constraints. The mechanical parts are identical to the option considered in the *partial mechanical redundancy* concept (Figure 6), except that the bearing loads in this case may be slightly lower due to possible shortening of the motor axial length. Finally, electrical redundancy options only consider one set of magnets, which represents a single point failure and must be managed via design margins as any other mechanical parts.

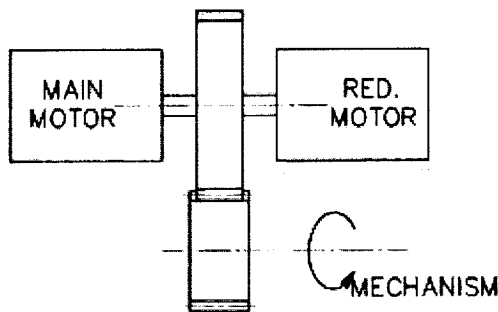


Figure 5. Full Mechanical Redundancy.

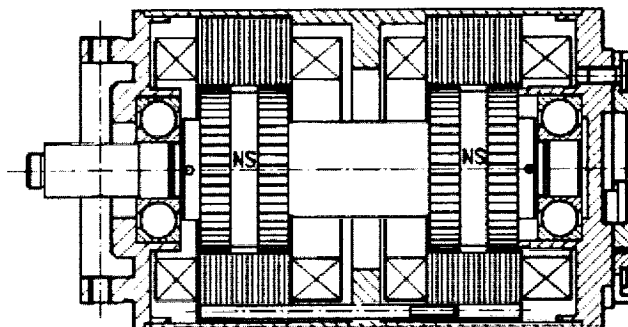


Figure 6. Partial Mechanical Redundancy.

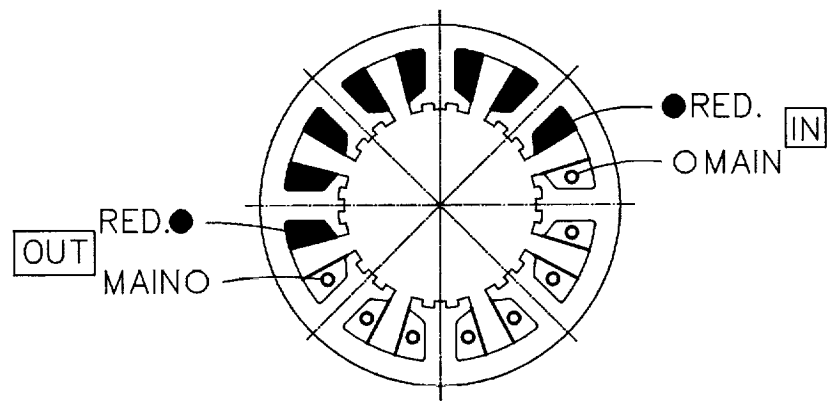


Figure 7. Electrical Redundancy – Two Sectors

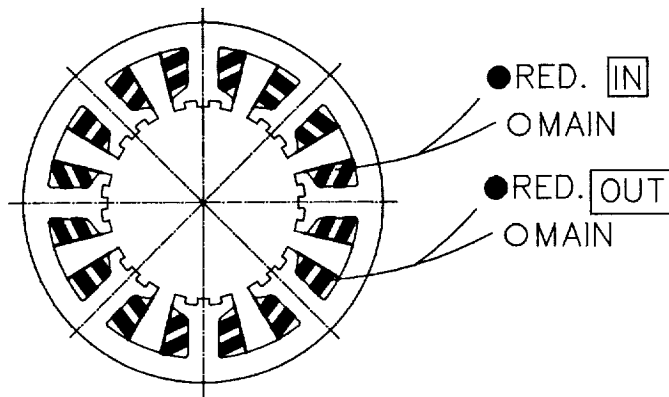


Figure 8. Electrical Redundancy – Two Parallel Wires

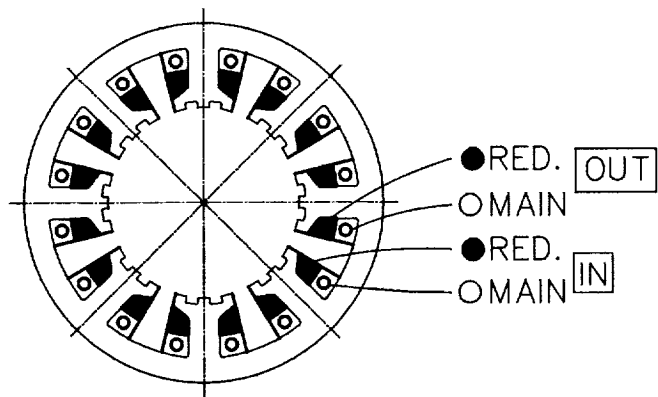


Figure 9. Electrical Redundancy – Shared Slots

Comparison of the Redundant Designs Options

The performance characteristics obtained with the different redundancy options are provided in Table 1 and are discussed further. They are based on the following assumptions:

- Only relative parameter values are given (in percents) allowing an easier comparison of the different designs. The two-sectors *electrical redundancy* option is considered as the reference case and the parameters other than the 100% reference case are in bold characters.
- The magnetic circuit is identical for all the different units, except that it is either in one or in two separate pieces. Winding changes are implemented to reflect the selected type of redundancy.
- It is not possible to compare in general the options' efficiencies since they are too dependent upon the specific speed / torque demand. The comparison is limited to the copper losses corresponding to the major loss factor for low-speed applications. Since the lamination stacks have the same size for all the different options, the iron losses can be considered identical throughout. The copper losses are provided for a given specific "nominal" working point. Nevertheless, these relative copper loss values are valid for any torque demand if the motor has a linear torque-to-current characteristic (i.e., brush and brushless DC motors). For magnetically saturated motors (i.e. steppers) and for different torque loads, more detailed information are presented later on the exact torque-to-power behavior.
- For the motor mass and dimensions, only the motor frameless electric / magnetic parts are considered (Figure 4), excluding all other related mechanical parts (i.e., housing & flanges, bearings, output shaft, output cables and connectors), which are too highly influenced by the specific application constraints (e.g., use of titanium, aluminum or steel for the housing or size of the bearings).
- A "size 23" reference motor is considered in this calculation [2], with a 0.059-m external diameter (2.3 in) and a 0.030-m total axial length (1.2 in). Adjustments may be required for motors with significantly different sizes.
- For information, a "non-redundant" column has been added, providing the performances reached by a non-redundant motor made with a magnetic lamination stack identical to the one used for the electric redundancy concepts. This motor is, consequently, more efficient since it utilizes 100% of the unit's magnetic and electrical capabilities.

Table 1. Relative Performances of the Redundant Options

PARAMETERS	<i>Mechanical Redundancy</i>		<i>Electrical Redundancy</i>			<i>Non-Redundant</i>
	<i>Full</i>	<i>Partial</i>	<i>Two Sectors</i>	<i>2 Parallel Wires</i>	<i>Shared Slots</i>	
Resistance	150	150	100 %	100	100	50
Inductance	100	100	100 %	50	50	50
Electrical Time Constant	150	150	100 %	200	200	100
Back-emf Constant	100	100	100 %	100	100	100
Copper Losses	150	150	100 %	100	100	50
Frameless Mass	120	120	100 %	100	100	100
Total Axial Length	150	150	100 %	100	100	100

Electrical Characteristics and Copper Losses

The winding designs of Table 1 options have been adjusted in order to have a back-emf constant identical for each of the different options. It reflects, in an unsaturated condition, an identical torque-to-current characteristic for all the different windings. On this basis, for a given torque the resistance is an indirect indication of the motor's copper losses. Adding the relative inductance values, it is possible to have an idea of the motor's electrical impedance, necessary for the driver design. Table 1 clearly points out the impedance increase resulting from the implementation of a redundant winding into an existing lamination stack. Redundancy options leading to a lower electrical time constant shall in some cases be preferred

(i.e., high-speed stepper motor with a voltage supply). Compared to a non-redundant design built into the same lamination stack, for a given torque or in general for motors having a linear torque-to-current characteristic, Table 1 shows that the "electrical redundancy" concept doubles the power need.

The two mechanical redundancy concepts, built within two separate magnetic stacks (Figure 5 & Figure 6), lead to a windings' "end of coil" length twice those compared to the one related to the electrical redundancy concepts (built within one stack). For the two mechanically redundant options, this implies a larger resistance and thus higher copper losses: the longer the motor's axial length, the smaller the relative impact of the end of coil length upon the resistance / power consumption. This is indirectly shown in Figure 10, which provides as a function of the motor's axial length a relative value reflecting the resistance increase. Indeed, it represents the evolution of the ratio of the "resistance of the electrically redundant unit / resistance of the mechanically redundant unit." Even for relatively long motors (up to 150 mm, or 6 in), the ratio remains below 90% and thus the electrical redundancy concept will often be more efficient, even for rather long motors.

Saturated Motor: Torque-To-Power Ratio

For a saturated motor, Figure 11 provides the torque-to-copper loss characteristics for the different types of redundancies. The most efficient designs are, in their order of importance: (1) the non-redundant design built into the same lamination stack; (2) both the two-parallel-wires and the shared-slots electrical redundancy concepts; (3) the two-sector electrical redundancy concept; and (4) both the full and partial mechanical redundancy concepts. It is important to note that the motor used in this example [2] is normally only permanently used between 5 W and 10 W, depending upon the environmental temperature. A higher power can, in this case, only be considered for a very short period (a few seconds).

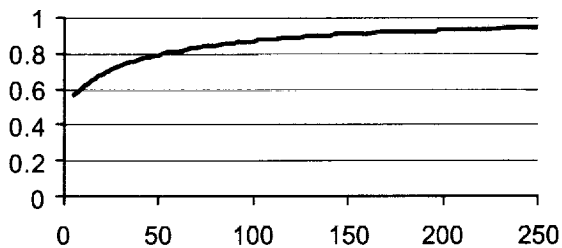


Figure 10. Resistance Ratio Between Electrical and Mechanical Redundancies.

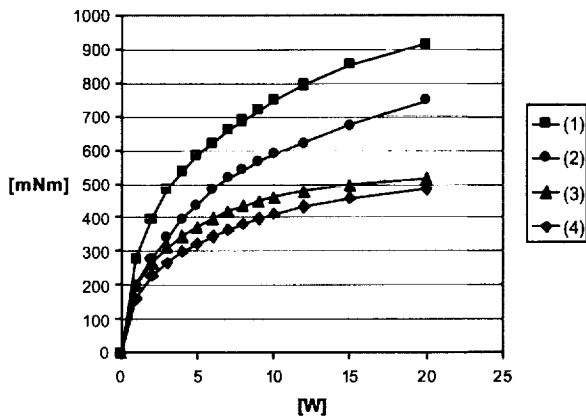


Figure 11. Torque-To-Power Characteristics

In some emergency over-torque scenarios, both main and redundant windings are simultaneously energized in order to increase the motor's torque capability. For unsaturated motors, this working mode (with twice the power) will provide twice the torque. For all the different windings' redundancy options, the torque value corresponding to the total input power can be directly deduced from curve (1) of Figure 11. A corrective factor based on Figure 10 must be introduced to reflect the larger power requirement of the two mechanically redundant options.

Mass and Dimensions

In terms of both mass and dimensions, the impact of the different redundancy options is shown in Table 1 considering frameless units and a magnetic circuit identical for all options, even if split in two in some cases. It shows that the "mechanically redundant" options are heavier (+ 20%) and longer (+ 50%) due again to the larger "ends of coils": the longer the motor's axial length, the smaller the relative impact of the ends of coils on its mass and dimensions. This is indirectly shown in Figure 12, which provides as a function of the motor's axial length two relative values that reflect the mass and the motor's axial length, respectively. In effect, it provides the evolution of the following ratios as a function of the motor's axial length: (1) the mass of the electrically redundant motor divided by the mass of the mechanically redundant one and (2) the axial length of the electrically redundant motor divided by the axial length of the mechanically redundant one. These ratios are greater than 95% for motor lengths larger than 50 mm and 250 mm (2 in and 10 in). The conclusion is that the advantage in terms of mass of the electrically redundant motor becomes marginal as the motor length increases. This is, however, not the case in terms of axial length comparisons.

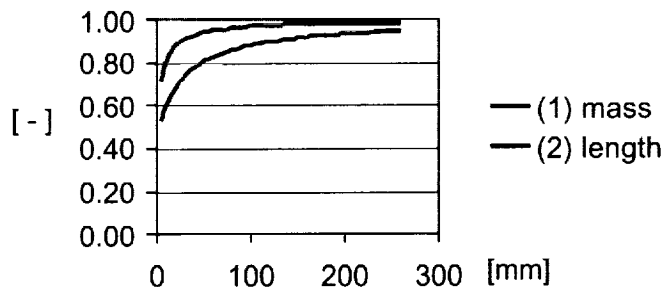


Figure 12. Ratios Between Mechanical and Electrical Redundancies

Redundant and Non-Redundant Motors with the Same Torque-to-Power Budget

At the mechanism level, the torque demands and power budgets can be seen as fixed design constraints. Thus, if a redundant motor must be selected, it will inherently have larger dimensions than a non-redundant unit. The "non-redundant" design, discussed in the previous paragraphs, always demonstrated an improved efficiency than the redundant options: thus, its design must be optimized in order to align it with the performance of redundant units.

Table 2 provides a performance comparison between two units : a non-redundant and a redundant (two-sectors electrical redundancy) motor. Both have the same power budgets and are assumed to have a linear torque-to-current behavior. The reference case is the one also considered in Table 1, the redundant unit. For motors with long axial dimensions, the relative length and mass of the non-redundant unit would tend toward 50%. For saturated units, the relative mass and dimensions of the non-redundant design must be increased.

Table 2. Performance Comparison

PARAMETERS	Non-Redundant	Redundant Two-Sectors
Resistance	100	100 %
Inductance	78	100 %
Back-emf Constant	100	100 %
Copper Losses	100	100 %
Frameless Mass	70	100 %
Total Axial Length	83	100 %

Cost Comparison

A rough assessment of the motor's cost evolution is made in Table 3 for both redundant and non-redundant units. Since it is difficult to be general on the cost point of view, the following assumptions are made: a size 23 stepper motor is considered [2]; the housed motor costs assume standard space-rated mechanical parts (without any particular complications); and both frameless and housed units are considered. It is important at this stage to emphasize the need to consider the overall redundancy costs at the sub-system level. In fact, it is likely that the major cost driver will be on the drive electronics side and not on the motor side.

Table 3. Relative Costs

PARAMETERS	<i>Mechanical Redundancy</i>		<i>Electrical Redundancy</i>	<i>Non-Redundant</i>
	<i>Full</i>	<i>Partial</i>		
Frameless motor	190	190	110	100
Housed motor	290	230	160	150

Redundant Designs – Available Statistical Data

The statistics presented here have considered the types of redundancy concepts typically selected for various space programs for the designs of more than 100 space mechanisms. These statistics take into account a wide range of electromagnetic motors including brushless DC motors, hybrid and reluctance stepper motors, limited angle torquers, mono and bi-stable electromagnets, and moving coil or moving magnet linear motors. The database is given in [3]. It leads to the proportions summarized in Table 4.

The number of known applications considering a "full mechanical redundancy" is very limited: either this option is rarely considered at sub-system level or non-redundant units are procured without informing the motor manufacturer of its intended redundant use (we nevertheless feel that this information is available). The number of applications asking for the "partial redundancy concept" is very limited. The reason can be a preference to go either toward a clear main / redundant separation (full mechanical redundancy) or toward the more efficient compromise (electrical redundancy), yet never in between. Finally, if the electrical redundancy concept is selected, the share between the three "electric options" is rather balanced, with a slight preference for the more reliable "two sectors" design.

Table 4. Selected Redundancy Concept

<i>Mechanical Redundancy</i>		<i>Electrical Redundancy</i>			<i>Non Redundant</i>
<i>Full</i>	<i>Partial</i>	<i>Two Sectors</i>	<i>2 Parallel Wires</i>	<i>Shared Slots</i>	
4 %		37 %			59 %
3 %	1 %	16 %	12 %	9 %	59 %

Lessons Learned and Conclusions

For the selection of a motor redundancy concept, an analysis of the possible failure modes on a frameless motor (FMECA) has pointed out guidelines to be followed:

- The use of permanent magnets should be prohibited if (1) the magnet maximum acceptable temperature is not secured by design margins, and (2) if the braking torque created by a failed short-circuited main winding cannot be managed by the redundant path.
- Common thermal paths between main and redundant motor parts should be prohibited.

Nevertheless, with the high performance required for space applications (i.e., mass, efficiency), it appears that motor technologies prohibiting the use of permanent magnets can rarely be considered if we except "niche" applications where reduced performance is acceptable. As a consequence, the design of redundant motors must integrate the idea of incorporating magnets and not try to avoid this practical reality.

Five redundant design options are identified and the following comments can be made:

- The full mechanical redundancy concept This is the best solution if the risk of having a single point failure between the main and redundant paths is a critical design concern, especially in terms of potential thermal stresses. Nevertheless, this "awkward" design suffers from its very limited performances and leads to a significantly higher recurring motor manufacturing costs to be balanced with the other overall project costs.
- The partial mechanical redundancy concept This is a compromised design between the previous reliable options and the other efficient options. This option is less efficient and less reliable and thus marginally considered ;
- The two-sector electrical redundancy concept As for the other electrical redundancy concepts, the risk of having a thermal single point failure needs to be carefully considered in this case. On this point of view, it is the most optimal design among the electrically redundant options. As a drawback, for saturated motors that are highly magnetically loaded (typically stepper motors), the design suffers from a limited torque / power capability. In general, this option is preferable with the brushless DC motor technology.
- The shared-slots electrical redundancy concept This option can be considered as an alternative to the previous one for applications requiring an improved torque capability, unreachable due to excessive magnetic saturation and for motor designs that cannot consider the previous option for magnetic design reasons (whereby the slots cannot be shared in any adequate way).
- The two wires-in-parallel electrical redundancy concept This option could be considered as an alternative to the last if the motor's design can't reflect the two previous options for magnetic reasons again (slots cannot be shared in any adequate way).

Finally, statistics were provided regarding the type of redundancy concept selected for various space programs (>100 mechanisms), which seem to demonstrate that half of the mechanisms have implemented non-redundant motors. The other half consider mostly electrically-redundant options, the share between the three "electric options" being rather balanced with a slight preference for the "two-sectors" options. Mechanical redundancy options seem not to be widely considered.

References

1. Favre, Eric et al. "European electric space rated motors handbook", *Proceedings of the 8th European Symposium on Space Mechanisms and Tribology*, (Sept. 1999), ISBN 92-9092-752-6, pp. 159-165.
2. ETEL Aerospace Inc. "Stepper motor performance data sheet - type #AERSM01", 4909 Nautilus Court North, Boulder, CO 80301, USA.
3. ETEL Aerospace Inc. "List of main space contracts", Boulder, CO 80301, USA.

Table 5. FMECA Entries

PART	FAILURE MODE	FAILURE CAUSE	CONSEQUENCES	OBSERVABLE SYMPTOMS	COMMENTS
Motor electric winding	The two phases of the main winding are not energized.	Problem in the electronic driver or Failure of the solder which fixes the motor copper wire to the output cable	The motor main winding has no more torque capability	No possible motion with the main winding due to the total lack of torque capability. Redundant winding can be nominally used.	Number of motor internal soldering shall be as far as possible limited. Soldering shall be made according to a suitable PA/QA standard
"	One of the two main winding phases is not energized.	Problem in the electronic driver or Failure of the solder that fixes the copper wire to the output cable	One phase of the main winding produces its requested torque contribution (i.e. a sine wave versus rotor position). The second phase of the main winding does not produce any torque. The motor main winding output torque has a zero average value with a very large torque ripple.	With the main winding, the motor may rotate degradedly and / or stop in a given position. Redundant winding can be nominally used	See one line above
"	The two phases of the main winding are short circuited	Dielectric insulation failure or Mechanical shock on the winding or Thermal stress or Failure in the electronic driver	The motor main winding has no more torque capability. For motors with pole excitation always active, typically created by magnets (i.e. hybrid stepper motors, brush and brushless DC motors), an approximately constant braking torque occurs when the rotor moves, due to induced currents into the short-circuited coils. This shaft motion can be due either to an applied external shaft loads or simply to the use of the redundant path. The value of the braking torque depends on both the speed and the failed winding electrical characteristics. It is not necessarily the highest at the highest speeds.	No possible motion with the main winding, due to the total lack of torque capability. When using the redundancy, the motor output torque is lower than initially planned due to the braking torque component to be deducted from the nominal capability. The torque loop may increase the redundant winding currents, in order to compensate the lower torque capability. It can create thermal and / or power budget problems. The specified maximum speed may not be reachable with the redundant winding. At slow speed, the motor will work nominally with the redundant path. The thermal stress that may have created the winding's short circuit is potentially a single point failure.	A double insulation is often implemented into the motor winding, for any short-circuit scenario. The system is then double failure protected. Motor integration process shall avoid mechanical shocks on the windings. Motor thermal loads shall be in line with the selected design, materials and processes.
"	One phase of the winding is short circuited	Dielectric insulation failure or Mechanical shock on the winding or Thermal stress or Failure in the electronic driver	The phase of the winding that is not short circuited produces its requested torque contribution (a pulsating component with a zero average value). The second phase of the winding, short circuited, produces a pulsating braking torque, with a zero average value. The resulting output torque has a zero average value with a very large torque ripple. For motors with pole excitation always active, a pulsating braking torque is created when the rotor moves. The amplitude of this pulsating braking torque depends on both the speed and the failed winding electrical characteristics.	With the main winding energized, the motor may rotate degradedly and / or be stopped in a given position. When the redundant path is used, all the comments made one line above are again applicable. An accurate speed / position control may be difficult with the redundant path, due to the pulsating torque disturbances created by the short-circuited coil. The mechanism may be out of micro-gravity requirements.	See one line above

Table 5 (cont.)

PART	FAILURE MODE	FAILURE CAUSE	CONSEQUENCES	OBSERVABLE SYMPTOMS	COMMENTS
Motor cables and related cable feed-through	See failures described in the "winding" section	Cable design not adequate or not well fixed / handled during the various project phases (i.e. motor transportation, integration, normal operations).	See failures described in the "winding" section	See failures described in the "winding" section	Design and procedures related to the cable aspects shall be adequate.
Magnets	One or more magnet unglued or broken	Part failure or Magnet unglued by the centrifugal rotation forces	Migrating dust into the motor / mechanism. Potential pollution of the motor bearing, a position sensor (i.e. optical) or other parts. Generally, the migration of magnet powder is very limited due to the magnetic attraction of the powder with magnetic materials (typically the stator lamination).	Potential bearing friction increase, to the detriment of the net output torque : Single Point failure	Labyrinths shall be implemented wherever possible to limit migration of dusts (any type) toward the bearings. Magnet process shall be adequate.
"	"	"	Motor produces a lower torque than it shall produce for a given torque reference value (reduced torque constant). The torque drop is given by the number of failed magnets (66 magnets in total)	Motor rotates degradedly as soon as the motor output torque can not reach a level equal to the value indirectly required by the loading torque and speed profile.	Failure detected by test if it occurs before the test of the motor unit.
"	"		In some cases, the torque loop will increase the redundant winding currents in order to compensated the lower torque capability. It can potentially create thermal and / or power budget problems. The specified maximum speed may not be reachable with the redundant winding.	Single Point failure	In some cases, the torque loop will increase the redundant winding currents in order to compensated the lower torque capability. It can potentially create thermal and / or power budget problems. The specified maximum speed may not be reachable with the redundant winding.
	Magnet demagnetized by over-temperature	Temperature exceeds the maximum magnet's rating	No more torque capability	Often a single point failure	Magnet material / design shall be adequate with the specified environment.
Stator and Rotor mechanic interfaces	Stator or rotor free to move (axial or radial)	Design inadequate	Reduced torque capability	Various	Design shall be adequate.

Development of a Miniature, Two-Axis, Triple-Helmholtz-Driven Gimbal

Boz Sharif, Ed Joscelyn*, Brian Wilcox ** and Michael R. Johnson**

Abstract

This paper details the development of a Helmholtz-driven, 2-axis gimbal to position a flat mirror within 50 microradian (fine positioning) in a space environment. The gimbal is intended to travel on a deep space mission mounted on a miniature "rover" vehicle. The gimbal will perform both pointing and scanning functions. The goal for total mass of the gimbal was 25 grams.



Figure 1

The primary challenge was to design and build a bearing system that would achieve the required accuracy in addition to supporting the relatively large mass of the mirror and the outer gimbal. The mechanism is subjected to 100-G loading without the aid of any additional caging mechanism. Additionally, it was desired to have the same level of accuracy during Earth-bound, 1-G testing.

Due to the inherent lack of damping in a zero-G, vacuum environment; the ability of the gimbal to respond to very small amounts of input energy is paramount. Initial testing of the first prototype revealed exceedingly long damping times required even while exposed to the damping effects of air and 1-G friction. It is envisioned that fine positioning of the gimbal will be accomplished in very small steps to avoid large disturbances to the mirror.

Various bearing designs, including materials, lubrication options and bearing geometry will be discussed. In addition various options for the Helmholtz coil design will be explored with specific test data given.

Ground testing in the presence of 1-G was compounded by the local magnetic fields due to the "compass" effect on the gimbal. The test data will be presented and discussed. Additionally, rationale for estimating gimbal performance in a zero-G environment will be presented and discussed.

* Aeroflex Laboratories, Farmingdale, NY

** NASA Jet Propulsion Laboratory, Pasadena, CA

Some of the physical and functional requirements are as follows:

- A clear aperture of 17 mm and a field of regard of $\pm 15^\circ$ in both Elevation and Azimuth with a 50 microradian (fine positioning) positioning increment.
- Unimpeded, full rotation in both elevation and azimuth.
- A survival temperature range of -155 to +145° C.
- An operational temperature range of -80 to +70° C.
- A maximum mass of 25 grams with a maximum total power of 0.72 watt for simultaneous 3-axis operation.
- Ability to withstand 100-G launch loading.

Introduction

- a) **Size & Weight:** As depicted in Figure 1, the gimbal is a rectangular cube with (8) integrally machined mounting ears arranged (4) to a side. The primary dimensions are 48 x 42 x 32 mm. An elliptical mirror, 18 x 25 x 2.5 mm, acts as the inner gimbal and is mounted on jeweled bearings to the outer gimbal, which is in turn jeweled bearing-mounted to the gimbal outer frame. Once allowances for the 17-mm aperture and the $\pm 15^\circ$ field of regard are considered, the gimbal structure is limited to a 3-mm square region along the edges of the allowable envelope.

Total mass of the gimbal is limited to 25 grams. The magnetic and lead wire mass is approximately 17 grams, leaving 8 grams for the mirror and gimbal structures.

- b) **Power Constraints:** The gimbal is limited to 0.72 watt peak power. Typical available power during normal operations to any pair of coils is approximately 0.10 to 0.20 watt.
- c) **Positioning Philosophy:** Three coil sets, each consisting of a pair of coils wired in series, are placed orthogonally to each other to form a rectangular box. This configuration results in a magnetic vector that is able to follow a complete spherical path. A magnet fixed perpendicular to the center of the inner axis and carried by the inner gimbal follows the magnetic vector to point the flat mirror. In theory, any point in space should be addressable as the sum of 3 magnetic vectors generated by the three coil sets. In practice, efforts were concentrated in achieving best field linearity and continuity in the field of regard.

Design Concept

Physical Form

The gimbal structure is a single machined aluminum alloy space structure that incorporates the frames for the largest pair of coils as well as the (8) mounting ears. The alloy chosen is 6061-T651, a thermally stable, iron-free alloy. The remaining (4) coils are separately wound on machined frames and then bonded to the main structure. These parts are designed to interlock and create a substantially more robust structure without adding additional mass. The structure and the separate coil housings generally maintain a 0.2-mm section thickness. The ultimate strength of the structure is obtained when all components are bonded together. The entire structure, prior to winding of the coils, weighs 4.7 grams.

Bearing Design

One of the keys to the successful realization of this mechanism was the final configuration of the bearings. In view of the minuscule levels of torque available, the lowest possible bearing drag torques were required. It was estimated that an axis drag torque of 5×10^{-5} N·m or less was necessary to achieve the required accuracy during Earth-bound testing. This level of drag torque can only be achieved with jeweled bearings.

Magnetic Design

The gimbal is driven by quasi-Helmholz coils. This is a coil set that generates a reasonably good uniform magnetic field between their centers. A Helmholtz coil has a specific dimensional relationship that is closely, but not exactly, followed by the actual gimbal design due to other optical or dimensional constraints. The field in and around the center has sufficient uniformity to accomplish the goals.

For testing purposes, the surrounding areas must be free of stray fields caused by electrical equipment or magnetic materials. One of the earliest indications of this requirement was the compassing of an early prototype to the assembler's belt buckle. One test is to position the mirror with a current profile, turn off the current allowing the mirror to swing freely as dictated by the Earth's field and gravity, turn on the currents to the same values, and have the mirror repeat its previous position to within 4 milliradians.

Early on in the program we found that the mirror would take extraordinarily large, stable offsets from the original settings. We found that even though the small springs in the bearings were made of beryllium copper as they should have been, the actual BeCu grade used contained trace amounts (0.02% by weight) of iron which, of course, causes them to be magnetic. This was found by removing the main magnet from the system and using it to search for magnetic material in the vicinity.

Thermal Considerations

The gimbal is subjected to a large temperature delta in both storage and operation. The gimbal bearings are designed to maintain consistent drag behavior and are largely immune to thermal effects in their operation. This was accomplished by spring loading of the bearing.

Specific Details

Physical

- **Optical Path:** The gimbal is required to have a clear aperture of 17 mm approaching from either side and exiting from front or back with a field of regard of $\pm 15^\circ$ in both elevation and azimuth. As mentioned earlier, this limits available space for gimbal structure to a 3-mm wide zone along the edges of the gimbal envelope.
- **Mirror Construction:** The mirror is constructed from the same alloy as the gimbal frame to maintain cohesive thermal behavior. Beryllium was not selected due to very poor reflectivity of pure beryllium at the desired wavelength. Gold plating of the beryllium mirror was not possible due to the required substrate nickel plating which would cause magnetization problems. The mirror is machined from a solid billet, including features to accept the magnet and pivots. The machined mirror is then thermally stabilized and the reflective surface is final machined via diamond turning. A dielectric oxide coating protects the diamond turned surface. The fabrication of the mirror to the required flatness ($\lambda/4$) proved to be one of the bigger challenges of the project.
- **Balance vs. Weightlessness:** The mirror as well as the outer gimbal is finely balanced to allow Earth-bound testing. The balancing is accomplished through the use of several adjustable copper screws attached to the mirror and the gimbal structure. In order to facilitate Earth-bound testing, the inner gimbal is balanced to within bearing friction levels of less than 5×10^{-5} N-m.
- **Windings Form:** The windings of all six coils are rectangular in shape to follow the perimeter of the gimbal closely. FEA analysis of the rectangular coils predicted a relatively large, uniform field in the center. By contrast, the smaller round coils, although lighter, were found to generate weaker fields with less linearity in the center region resulting in nonlinear behavior and were discarded.
- **Materials:** All major components of the gimbal are constructed from the same aluminum alloy. Components of the jeweled bearing assemblies are fabricated from a BeCu alloy. Balance screws

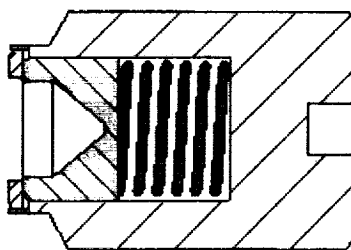
are made from pure copper. The dissimilar materials are properly coated to negate electrolytic effects.

- **Vibration Robustness:** The gimbal structure is subject to severe vibration during launch. Further, due to the limited space and mass budget, no caging mechanism was allowable. The mechanism must be able to endure the launch cycle without any degradation. As demonstrated by subsequent testing, the spring-loaded bearing design and the inter-locking structure successfully address this challenge.

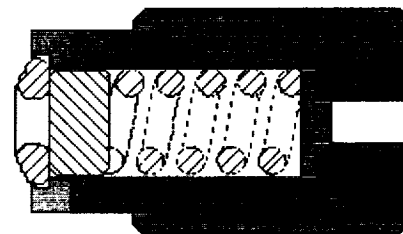
Bearings

- **Choice of Jeweled Bearings:** In 1764, when John Harrison built his famous H4 marine chronometer, he utilized a full complement of jeweled bearings in a timepiece for the first time. With the reduced friction, the H4 chronometer proved accurate enough to calculate longitude anywhere in the world. Up until the 1770's, navigation was a precarious art at best. Nautical charts for the entire world could now be accurately charted. Ever since then, jeweled bearings have been the standard in instrument-grade mechanisms of every kind. There is a wide variety of bearing designs in various materials readily available. Initially, an "olive hole"-type bearing was selected and a prototype gimbal was constructed to test the bearings. The "olive hole" design was selected to take advantage of its inherent lack of sensitivity to axial misalignment and the inherently low drag torque resulting from its "point contact" geometry. The geometry of the bearing will result in a minimum of three theoretical contact points for the axis consisting of one of the two endpoints and one sidewall. The cup portion of the bearing consisting of a toroidal ring with an abutting end plate were made from synthetic sapphire while the pivot was fabricated in several different materials including several alloys of hardened stainless steel and sapphire. Testing of the prototypes revealed a higher than desired drag torque. The test results clearly demonstrated the need for a two-point system with the smallest rotation radius possible. A second generation of bearings was developed to specifically address these requirements of the mechanism.

The final bearing design is a modified v-cup incorporating several novel features. The v-cup is spring mounted to allow a specific preload to be applied to the assembly. The spring mounting protects the jeweled bearings in the presence of shock and vibration. Additionally, the spring loading fixes the relationship between the spherical tip of the pivot shaft and the v-jeweled cup thus promoting consistent performance by maintaining a constant radius of rotation. Using this geometry, the bearings performed at lower than estimated drag torque values, helping to improve the pointing accuracy during 1-G testing. Figure 2 depicts a section view of the bearing cup assembly. Figure 3 depicts a sectional view of the mechanism with the bearings in place.



Olive Hole Bearing



V-Jewel Bearing

Figure 2

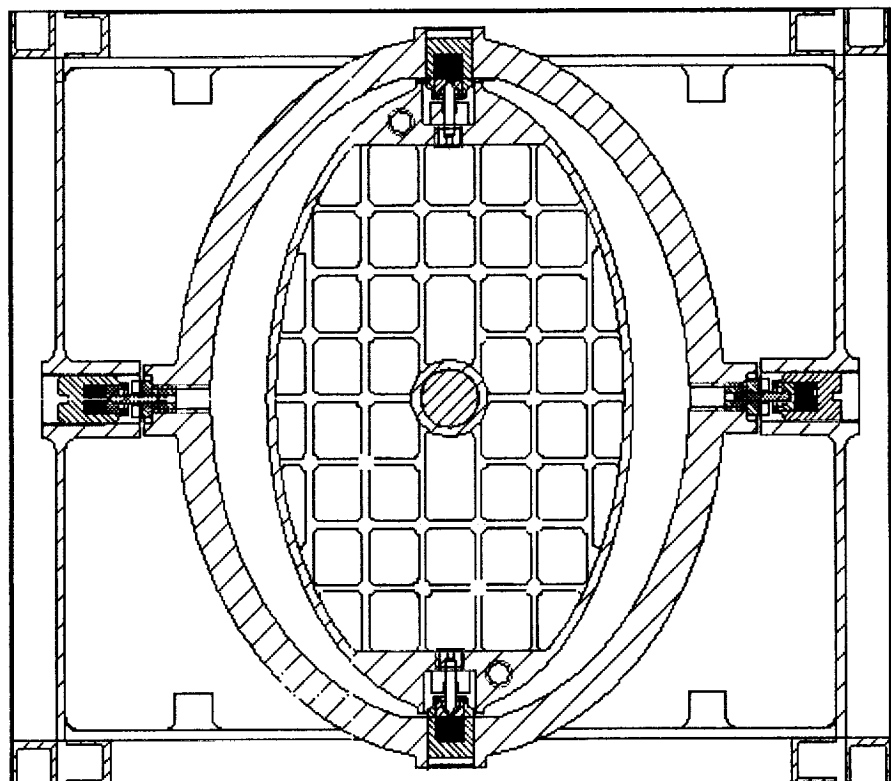


Figure 3

- **Materials:** As discussed earlier, all bearing components were fabricated from non-magnetic materials. Considerable efforts were made to obtain iron-free variants of the many "common" materials employed in the construction of the gimbal.
- **Lubrication:** No lubricants are employed. Due to the semi-cryogenic operational temperatures, no wet lubricants were suitable. The use of jeweled bearings precluded the need for any additional lubrication. The combination of the materials employed in the bearing results in a coefficient of friction of 0.15.
- **Vibration:** The spring within the bearing is a potential single point failure so that attention must be concentrated on this important aspect of the design. A reliability prediction was performed to verify a very low failure rate in the application of the spring.

The spring uses 0.2-mm diameter wire with a mean coil diameter of 1.32 mm diameter. There are 6 active coils with a pitch of 0.33 mm. The material is Beryllium-copper. The spring rate for a compression spring is:

$$R = \frac{(\text{modulus of rigidity})(\text{wire diameter})^4}{8 (\text{mean spring diameter})^3 (\text{Active coils})}$$

$$R = 4.24 \text{ lbs./in}$$

The spring concentration factor is where $r = \text{coil diameter to wire diameter}$

$$K_w = [(4r - 1)/(4r - 4)] + 0.615/r$$

The failure rate for springs is:

$$\lambda = [\text{function of (stress/strength)}^3]$$

$$\text{Stress} = \frac{8(R)(\text{compression})(\text{spring diameter})}{\pi(\text{wire diameter})^3} K_w$$

Strength for BeCu = 190 psi

$$\lambda = (3470 \text{ psi}/190E3 \text{ psi})^3 = 6 \text{ E-6 failures/million hours}$$

The springs are free floating in a cylindrical channel so that no extraordinary side loads or stresses other than the applied compression can be applied. The springs are considered to have a very good design margin for preventing failure in this application.

Helmholtz Coil

- **Field intensity:** The fields are small, approximately 40 gauss in close proximity to the coils ranging to approximately 2.5 gauss in the center for an input power in the 100 to 200 milliwatt range. By contrast the Earth's magnetic field is in the order of 0.50 gauss (0.57 gauss at plant location). Torque is produced by interaction with the field of a small cylindrical magnet (3.0 mm dia by 6.3 mm long) affixed to the back of the actuator mirror. The magnet is located at the geometric center of the inner gimbal and can only interact with the weaker fields at the center. By varying the currents in the three coils, the magnet can be made to align with the vector sum of these three fields. Figure 4 shows the FEA matrix for a pair of coils and the center magnet. The surrounding air is eliminated so the components can be seen. Figure 5 shows a side view of one pair of coils with the uniformity of the field illustrated by the mono color in the center. Figure 6 is a typical plot of the flux density through the normal to and through a pair of coils.
- **Torque Values:** The precision and friction free requirements for the bearings can be seen by analyzing the torque's generated by these weak fields. The peak torques are in the order of 3.5xE-3 N-m. The unit, when properly balanced, acts as a compass and these forces must be accounted for when testing the actuator.

Prototype performance

Precluding the use of NASA's "Zero-G" aircraft, it was not possible to test the gimbal bearing performance as it will be ultimately used. Gravity has a major influence on the bearing drag torque (due to friction) and thus some measures must be taken to reduce the negative effects of this force.

It was found that axis "stiction", the non-linear drag torque effect attributed to gravity, was far less severe when the axis of rotation was perpendicular to gravity. Further investigation revealed that the effect was due to the ability of the gimbal to roll along the inner conical surfaces of the v-jewel. The rolling effect of the bearing enabled by a level axis of rotation gave much better results than when the axis skidded at the center of the bearings when the axis of rotation is parallel with gravity. Although the difference between these two modes was significant in comparison, the gimbal easily met pointing accuracy criteria in either orientation.

- **Repeatability:** The mirror's positioning repeatability needed quantification. The first test investigated the combined effect of mirror bearing friction and field generation repeatability. The mirror was then allowed to stabilize at a position in the area of regard. No air currents or vibrations of any kind are allowed. The test bench is isolated from floor vibrations or stray air currents such as the air

conditioner or filter air streams. The drive currents of the three axes are noted. The mirror is then electrically driven so that a laser beam reflected to a calibrated target moves upward and has as near a vertical travel as possible. The mirror is then electrically reversed and brought below the initial position. The mirror is again electrically reversed and the beam is returned to the original target spot. The currents are then recorded. Knowing the gimbal's sensitivity, milliradians per milliamp, the deviations (should the currents not be exactly as they were when the beam excursion began) can then be calculated.

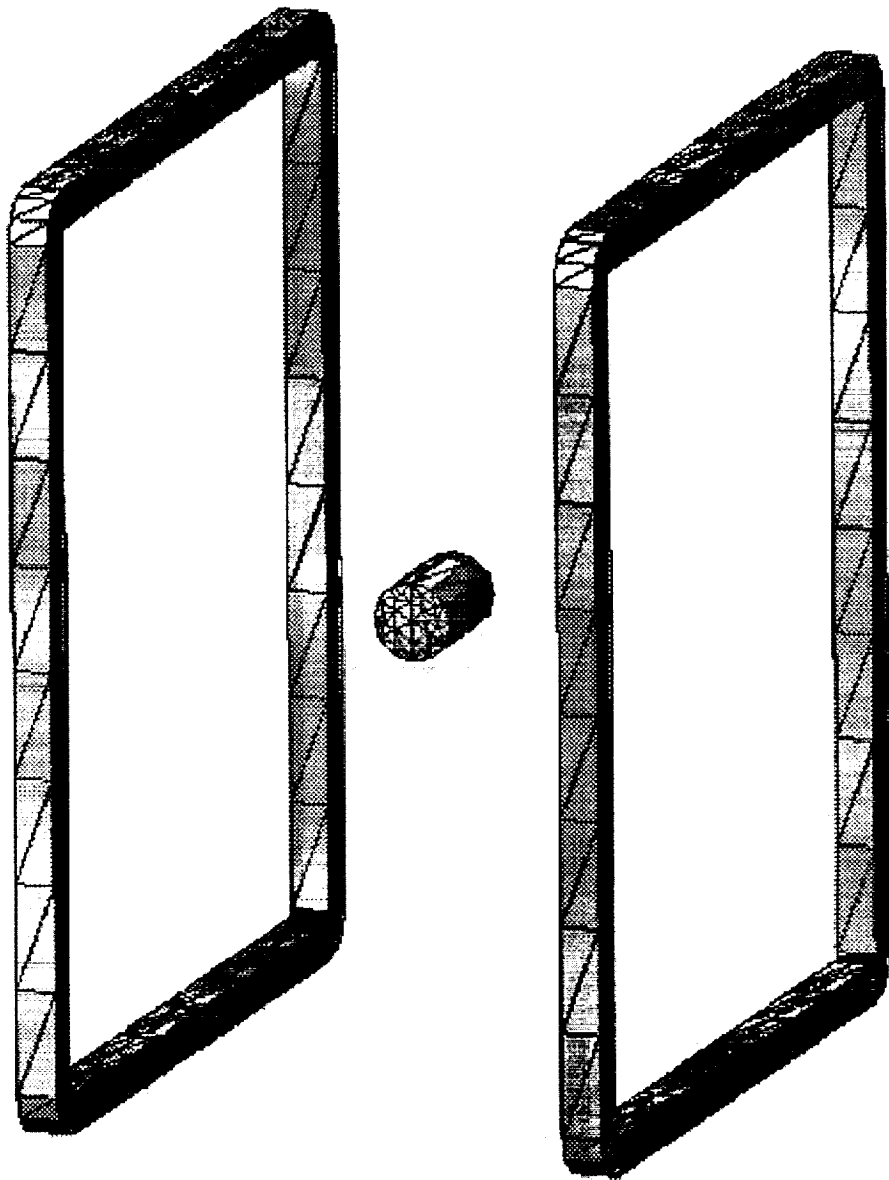


Figure 4

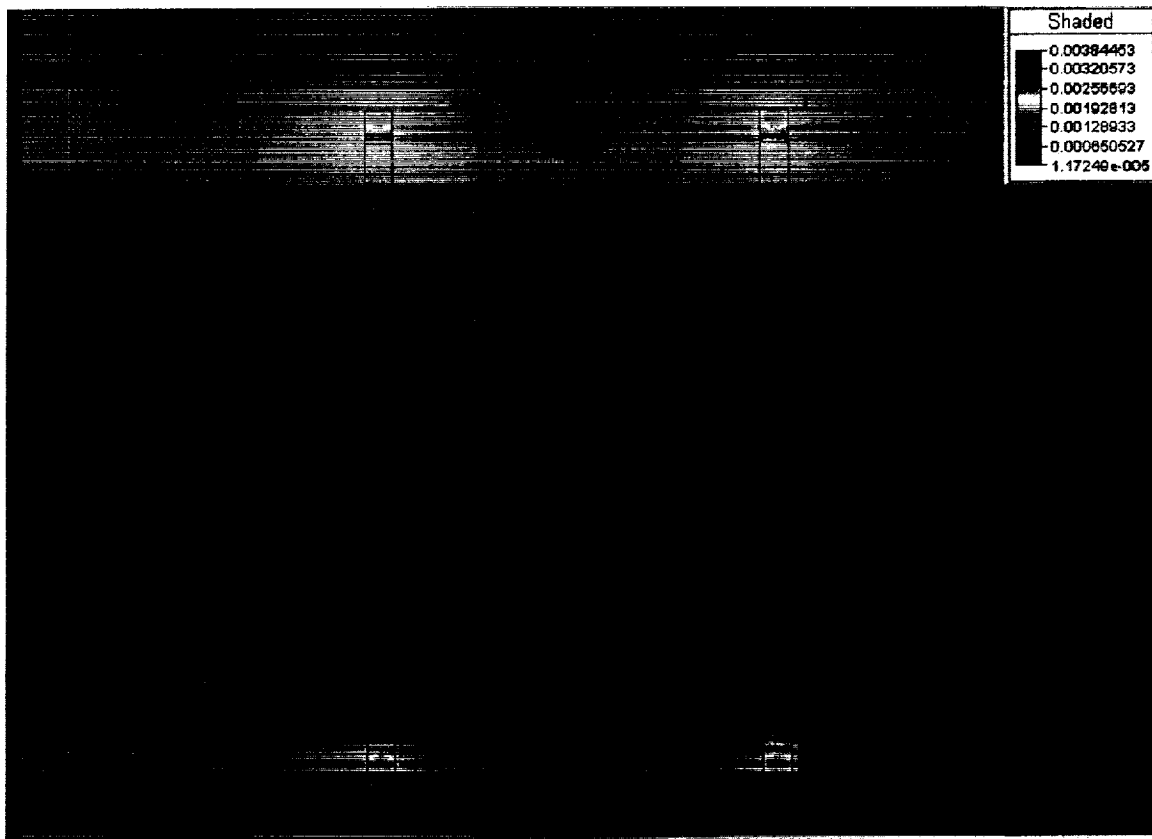


Figure 5

Typical results from a set of ten trials are shown in Table 1

Table 1

<u>Trial #</u>	<u>Axis Current</u>
1	51.2 ma
2	51.3
3	51.2
4	51.3
5	51.3
6	51.2
7	51.2
8	51.2
9	51.2
10	51.1

Given a sensitivity of 4.5 milliradians per milliamp, the maximum offset from the original spot is approximately 0.56 milliradian.

- **Accuracy:** Another test investigating the bearing friction alone was also performed. With the system set as above and the currents left unchanged, the mirror was gently moved from equilibrium using a gentle air current from a pipette. The mirror was allowed to swing until it came to rest. The deviation of a reflecting laser beam on a target calibrated at a distance was recorded.

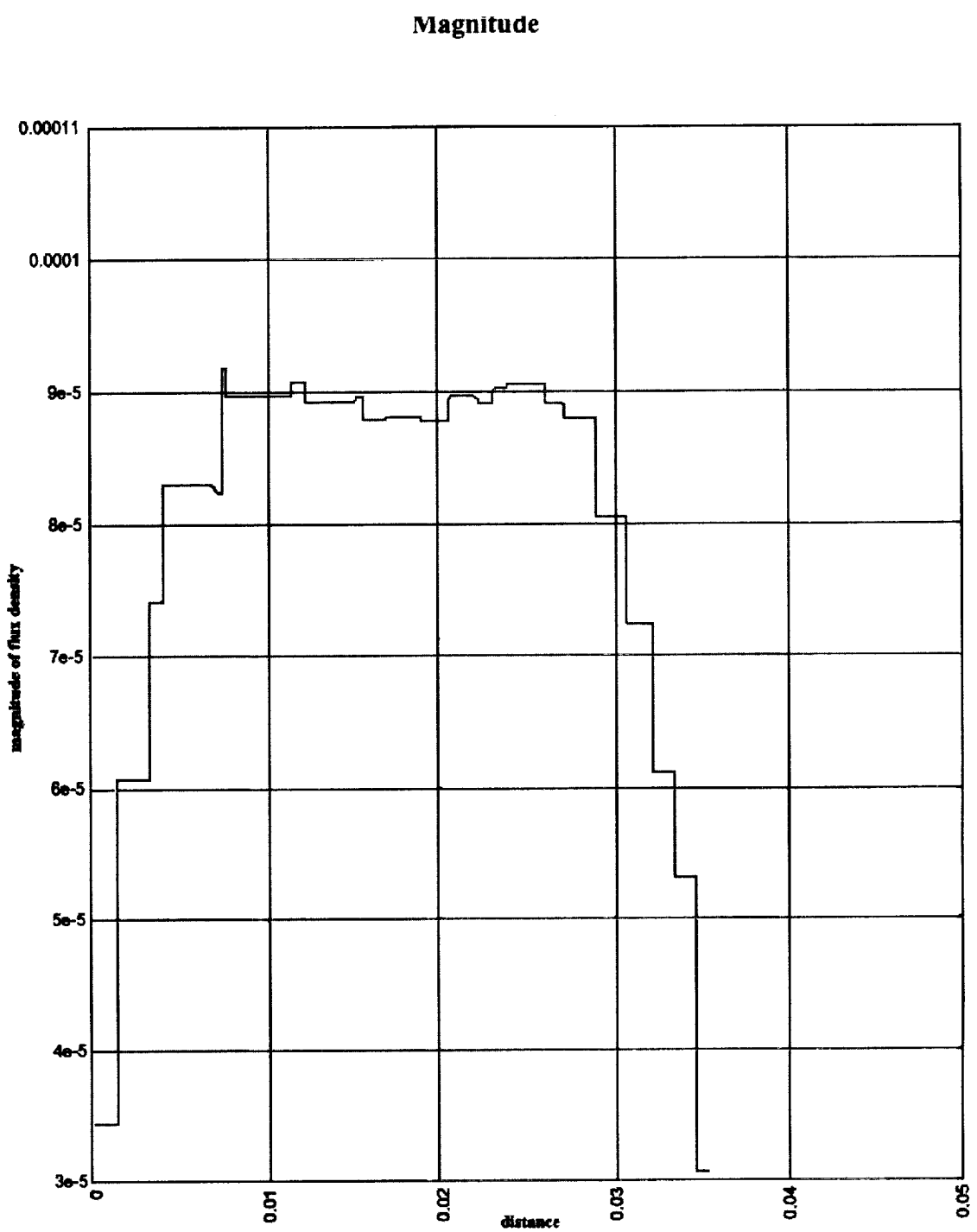


Figure 6

Table 2. Accuracy trials

<u>Trial #</u>	<u>Recorded Angles</u>
1	0 milliradian
2	-0.5
3	-2.5
4	-1.0
5	+0.5
6	-1.0
7	-0.5
8	-1.0
9	+0.5
10	0

The average deviation being 0.55 milliradian with 1.95 milliradians as the greatest from center.

- **Micro-Joule Positioning:** A third criterion for the gimbal is its ability to move in small "jog" increments. The minimum amount of energy necessary to elicit a 0.1-milliradian motion was measured as 45 microjoules. This amount of energy is equivalent to lighting a 10 W flashlight for 4.5 millionths of a second.
- **Vibration:** Of great concern was the ability of the bearings to withstand the vibration specification (27.7 g's RMS random). The bearings showed no degradation in performance after exposure to the vibration environment. For example, the first test sequence above was repeated after vibration with a maximum deviation of 0.55 milliradian.

Lessons Learned

Jeweled Bearing Performance

When testing a jeweled bearing instrument intended for micro-gravity operation in a gravity field, it is best to test with the rotation axis perpendicular to the gravitational field.

Magnetic Behavior of Non-magnetic Materials

When dealing with extremely fine magnetic fields and effects, it is best to test all associated materials and components for any latent micro-magnetism that may affect the accuracy of the instrument.

Cover Drive and Lock Ring Mechanisms for Genesis

Louise Jandura*

Abstract

The Genesis payload canister will return solar wind samples to Earth. The canister contains four mechanism assemblies: the Cover Drive Mechanism, the Lock Ring Mechanism, the Array Deployment Mechanism, and the Array Latch Mechanism. The Cover Drive and Lock Ring Mechanisms are described in detail while the other two mechanisms are briefly summarized. The Engineering Model canister has been designed, built, tested, and delivered to the spacecraft. The Flight Model is currently being built with delivery to the spacecraft scheduled for mid July 2000. Launch is scheduled for January 2001.

Introduction

The Genesis mission will place a spacecraft outside the Earth's magnetosphere and expose ultra-pure materials to the solar wind for about 23 months. Figures 1 and 2 show the stowed payload canister integrated with the Sample Return Capsule (SRC) and the spacecraft. The Electron Monitor and the Ion Monitor are sensor assemblies that provide data about the electrons, protons, and alpha particles in the solar wind as a function of time. These data are input to the science algorithm, which controls the specifics of the solar wind collection. The embedded solar wind samples will be returned to the Earth within the payload canister, safely contained within the SRC for reentry. The SRC will be retrieved by mid-air recovery.

The canister is rich with mechanisms, containing four distinct assemblies: the Cover Drive Mechanism, the Lock Ring Mechanism, the Array Deployment Mechanism (ADM), and the Array Latch Mechanism. Two key components, the Cover Drive and Lock Ring Mechanisms are the focus of this paper. These two mechanisms provide straightforward functions: a launch latch and the means to open and close the canister cover, but their requirements and design are linked together creating a much more challenging problem.

Figures 3 and 4 show the integrated canister in both the closed and open configurations. The Cover Drive Mechanism and Lock Ring Drive Mechanism are visible on opposite ends of the canister. The Lock Ring Assembly is located around the perimeter of the canister between the cover and base flanges. Solar wind is captured with both the Concentrator and the hexagonal collectors that fill the arrays. The ADM (not visible in the figures) is a stepper motor drive with separate motors used to position each of the four deployable arrays in the base. The Array Latch Mechanism secures the stowed arrays for launch and reentry.

Lock Ring Mechanism

Requirements

The Lock Ring Mechanism consists of the Lock Ring Assembly and the Lock Ring Drive Mechanism. Along with the Canister Seal, this mechanism's purpose in the canister assembly is: to provide a launch latch for the canister cover to sustain launch, reentry, and recovery loads; to prevent contamination of the canister interior; and to produce a push-off force to separate the seal interface. An additional requirement is that the mechanism must be capable of performing a functional test to verify the flight electrical interfaces and actuator operation without opening the canister to avoid contamination of the interior of the flight unit.

* Jet Propulsion Laboratory, California Institute of Technology, Pasadena, CA

Description

The Lock Ring Assembly consists of a 7075-T73 aluminum ring (81.28 cm (32 in) in diameter) with twenty-four ½-inch-diameter track roller pairs equally spaced around the ring perimeter. The entire Lock Ring Assembly is seen in Figures 3 and 4 but a more detailed view is available in Figures 5a and 5b and the section views in Figures 6a and 6b. This basic configuration was inspired by the Shuttle Get-Away Special (GAS) design. The upper row of track rollers is mounted on twenty-four bending beam flexures that create a clamping force on the joint by rolling up ramps to the locked position. The clamping force compresses the seal and preloads the joint against launch/reentry forces so that metal-to-metal contact is maintained. The two bending beam flexures located nearest the Array Latch Mechanism are stiffer in order to react the additional inertial loads of the arrays. Radial bearings at twelve locations around the ring provide both radial alignment capability and radial load capacity. The track rollers in the upper row are tilted downward in their unloaded state, 1° for the regular flexures and 2° for the stiff flexures. As load is applied to the track rollers, the bending beam flexures both deflect and rotate because the track rollers are cantilevered from these flexures. Tilting the track rollers in their unloaded state ensures that in the fully loaded state, the track rollers are loaded in the center of their outer bearing race.

Obtaining and maintaining the metal-to-metal contact during launch and reentry was the biggest challenge for the canister structure and lock ring system. This feature is a distinct difference between the Genesis payload design and the Shuttle GAS and it is an important difference because of the Genesis need for extreme contamination control. The initial design for the cover and the base consisted of simple cylinders with flanges at the separable interface. A first order load analysis that simplified the base as a rigid structure was used to estimate the clamping force required from the Lock Ring. In this simplified analysis, mass acceleration of the cover in the direction normal to the interface was reacted by the Lock Ring clamping force while in-plane mass accelerations were reacted with the shear pins installed in the base flange. The underlying assumption in this simplified analysis is that minimal coupling exists between the load directions. The inadequacy of this assumption quickly became apparent in a more detailed load analysis. Loads are transferred from the SRC to the canister base through a set of three bipods, which are partially visible in Figure 3. Because of this configuration, loads reacted into the base from the SRC create in-plane deflections of the base. In turn, the relatively stiff cover deflects in the same way as the base, absorbing quite a bit of the load and causing the tensile load at the separable interface to increase dramatically. The cover and the base were redesigned to bring the tensile loads at the interface back to an acceptable range. A kick ring was added to the base and a cover flexure was added to the cover (Figures 6a and 6b). The kick ring stiffens the base, which reduces the in-plane deflections while the cover flexure softens the cover, which reduces the transfer of load from the base to the cover. The bending beam flexures in the lock ring were redesigned to accommodate a small increase in load.

Two push-off blocks are attached to the cover on each side of the Lock Ring Drive Mechanism. Together the push-off blocks provide a separation force, if needed, at the seal interface when the ring unlocks. Push-off reaction pads, mounted on the kick ring, capture the Lock Ring Assembly when unlocked and act in conjunction with the push-off and shorting blocks to create the seal separation. The Canister Seal consists of silicone in a Gask-O-Seal configuration incorporated in an aluminum retainer. The top surface of the seal retainer is hard anodized and the bottom surface of the mating cover flange is covered with Magnaplate, a nickel-based coating, to form the separable interface. A thin layer of Braycote grease covers the seal. Tests were performed using seal samples under prolonged clamping and exposed to representative temperature, vacuum and radiation environments. There has been no sign of stiction with these material combinations. In addition, there was no evidence of stiction at this interface during the functional testing of the Engineering Model canister.

Figure 7 depicts the operation of the Lock Ring Assembly. In the unlocked position, there is no load on the track roller pair. The upper track roller is tilted downward and the lower track roller is captured between the lower bearing pad and the push-off reaction pad. The push-off reaction pads occur only in four places and they keep the Lock Ring in place when the mechanism is unlocked. During locking, the first track roller contact with the ramp occurs about a third of the way through the travel. At this point the

seal is not compressed and the lower track roller is still captured between the lower bearing pad and the push-off reaction pad. Notice that to get to the first ramp contact, the upper roller had to hit the push-off block. As the mechanism turns past first ramp contact, the flexures start to deflect and rotate, applying a force to compress the seal. When the seal is fully compressed, the lower track roller is no longer over the push-off reaction pad. Just past this point the ramp changes slope to a smaller ramp angle. In the initial design, the ramp inflection and the fully compressed seal both occurred at the same position. This was done to minimize the torque required to drive the track rollers up the ramps. When the flexures stiffened during the design iteration that resulted in the kick ring and cover flexure, seal compression occurred slightly earlier. The ramps were not redesigned since enough torque margin remained in the Lock Ring Drive Mechanism. Near the end of travel the ramp changes to a flat. In the locked position at 12.5°, the regular flexures have deflected 0.96 mm (0.038 in) and rotated through 1° to the horizontal position while the 2 stiff flexures have deflected 0.43 mm (0.017 in) and rotated 2° also to horizontal. Total preload on the separable interface is 21,218 N (4770 lbf).

During unlocking, the same force/deflection profile is followed in reverse. If there is stiction between the cover flange and the seal, the upper track rollers act on the two push-off blocks opposite the hinge line to create a significant prying force at each push-off block. The shorting block stiffens the load path so that the action of the push-off force does not cause the bending beam flexures to bend in the opposite direction, shortening the push-off stroke. The push-off stroke was measured during characterization of the Engineering Model canister. The Lock Ring Mechanism was stopped when the upper track rollers were at the center of the push-off blocks. With no sign of stiction present, the gap at the separable interface between the two push-off blocks was three times the seal crown height. The gap tapered off to 1.5 times the seal crown height at the two points halfway between the Lock Ring Drive Mechanism and the Cover Drive Mechanism. With stiction present, some of this push-off stroke would be taken up by deflection in the integral cover flexure.

In the Lock Ring Mechanism, there are design tradeoffs between the ramp profile, the torque required to lock the ring, and the lock ring flexure design. An additional tradeoff exists between the capture range of the device and the push-off stroke. In order to contact the push-off block during unlocking, the upper track roller must also contact the block during locking. This initially raises the cover a small amount during locking and reduces the capture range.

The Lock Ring Drive Mechanism (Figures 8a, 8b, and 9) provides torque to lock and unlock the Lock Ring and to operate the Array Latch Mechanism. The mechanism consists of a dual-wound, electronically-commutated gearmotor with redundant Hall effect rotor position sensors and drive electronics. The gearmotor drives into a pinion and sector geartrain mounted on the Lock Ring. The gear ratio of the pinion and sector is 22.3:1. The gearing in the motor is a four stage planetary with an overall ratio of 2160:1. Radial loads from the gear mesh are reacted into the track roller and bearing assembly of the mechanism rather than directly into the Lock Ring to minimize Lock Ring deflection and maintain the correct gear mesh. The mechanism operates by driving into hard stops at the end of travel in each direction until a timeout occurs. Microswitches provide confirmation that the mechanism arrived at the hard stop. The mechanism operates at a constant speed of about 0.0524 rad/s (0.5 rpm) due to speed control in the drive electronics. Traveling between hard stops takes about 98 seconds during unlocking and 100 seconds during locking.

The “No Open” functional test is performed to confirm the mechanism operation without opening the canister cover. During the “No Open” functional test, the cover and base are clamped together with external clamps to maintain the seal and the push-off blocks are removed. The Lock Ring Mechanism can then be operated over its full range to verify proper function.

Testing

Figure 10 shows the results of a functional test of the Lock Ring Mechanism at room temperature during both locking and unlocking. The predicted locking torque is also shown for comparison. The peak required torque of 16.5 N·m (146.4 in·lbf) occurs at 6.2° during locking. The shape of the actual locking

torque curve generally follows the predicted locking torque curve between the first roller contact and fully loaded positions. The peak of the actual curve is lower than predicted because worst case friction assumptions were used for the prediction. The actual curve is more rounded because the prediction assumed that all the track rollers reach the predicted conditions at exactly the same time. The variation causes an averaging effect. The same phenomenon is observed at the end of travel. In order to create the desired clamping force at each bending beam flexure in the locked position, the height of the flat part of each ramp is individually adjusted to nullify the tolerance stackup accumulated by the cover and base flanges, the seal retainer, and the lower bearing pad. The locking torque starts to drop off at about 10° as some of the track rollers reach the flat part of the ramp much earlier than the others do. The unlocking torque is lower than the locking torque as the clamping force on the ramps tends to help during unlocking.

During all functional testing, the highest torque required by the mechanism was 22.04 N•m (195 in•lbf) during cold operation. During dyno testing of the motors the lowest gearmotor stall value observed was 73.45 N•m (650 in•lbf) resulting in a minimum torque safety factor of 3.3.

Cover Drive Mechanism

Requirements

The Cover Drive Mechanism provides torque to open and close the canister cover. As with the Lock Ring Mechanism, the Cover Drive Mechanism must operate in 1g and must be capable of performing a functional test to verify the flight electrical interfaces and actuator operation without opening the canister (the "No Open" functional test).

Description

The Cover Drive Mechanism is illustrated in Figures 11a, 11b, and 12. The same gearmotor and drive electronics are used in both the Lock Ring Drive Mechanism and the Cover Drive Mechanism but in this case the gearmotor drives directly at the cover hinge axis using the hex drive on the gearmotor instead of the pinion gear. The drive hub turns on a lightly loaded, spring-preloaded bearing pair. The preload is not sensitive to thermal changes because of the spring preload. The hinge axis is located at the seal crown height (i.e. above the metal-to-metal interface between the canister cover flange and the seal retainer mounted on the canister base flange). Positioning the hinge axis at the seal crown height instead of at the seal retainer surface minimizes the capture range needed from the Lock Ring Mechanism, however it also requires cover translation to seal the canister when the lock ring engages. Relatively stiff cover arm flexures, integrally machined into the cover arms, permit this cover translation. The design of the cover arm flexures was a particular challenge. The torque tube is needed to stiffen the torsional load path between the two arms because only one arm is driven by the gearmotor. However, the torque tube occupies a great deal of space in the mechanism leaving little room for flexures. In order to find room for the flexures, the cover arm attachment points were changed from a more straightforward location to the more unorthodox attachment scheme shown in the figures.

During normal operation of this mechanism, the gearmotor turns the drive hub, which is attached by four fasteners to the drive arm. The mechanism moves until the hard stop arm integral to the drive hub hits either the open or closed hard stop. A timeout turns off the gearmotor command and microswitches provide confirmation that the mechanism reached a hard stop. During the "No Open" functional test, the four fasteners that hold the drive arm to the drive hub are removed. Now when the gearmotor rotates the drive hub through the hex drive, the motion occurs at the Cover Drive coupling interface (Figure 12) instead of opening and closing the canister cover. The hard stop arm on the drive hub is able to move through the full 180° of travel between the two hard stops so both the gearmotor and the microswitch operation can be verified without opening the canister cover. The mating surfaces at the Cover Drive coupling interface are treated to prevent galling and to produce low friction. The faying surfaces of the 7075-T73 aluminum arm are hard anodized and the corresponding surfaces on the 15-5 steel drive hub are covered with a dry film lubricant, Lub-Lok 4306.

Testing

Figure 13 shows the opening of the Cover Drive Mechanism under three conditions: actual in 1g, predicted in 0g, and actual during a "No Open" functional test. During opening in 1g, the maximum torque of 57 N·m (504 in·lbf) is required at the beginning of travel, decreasing in the expected sinusoidal shape as the center-of-gravity of the canister cover approaches the 90° position. Once past this position, gravity assists the gearmotor in opening the cover. The weight of the cover backdrives the gearbox, which counteracts the motor losses in the gearbox, and causes the electronics to provide less current to turn the gearmotor. This shows up in the torque trace as a negative output torque at the mechanism. The drive electronics are a unipolar drive, only controlling the gearmotor to produce torque in the commanded direction, in this case, the open direction. When the gravity-assist fully cancels the gearmotor losses, the speed increases beyond the electronics speed control value of about 0.0524 rad/s (0.5 rpm). The electronics commands no more torque and the mechanism increases in speed until it coasts into the hard stop. This is the flat part of the curve at -13 N·m (-115 in·lbf) near the end of travel. Once at the hard stop, the electronics commands the gearmotor to stall against the hard stop. It takes 49 seconds for the cover to open in 1g, which is faster than 0g operation because of the gravity-assist. The "No Open" functional test duration of 65 seconds is indicative of the on-orbit performance of the mechanism. Turning the Cover Drive coupling interface requires only about 7 N·m (62 in·lbf). The predicted opening torque in 0g is very low with a peak of 3.8 N·m (33.6 in·lbf) occurring in the first second of travel. This peak represents a worst case estimate of the Cover Drive Mechanism torque required to disengage the Array Latch crank from the Array Latch actuator block. The 0g operation of the mechanism has a torque factor of safety in excess of 19.

Array Latch Mechanism

In the stowed position, the four deployable arrays are supported at three points: the ADM, the fixed saddle, and the moving saddle. These support points (visible in Figure 4) are approximately equally spaced. Both the ADM and the fixed saddle are mounted on the inside of the canister base. The moving saddle is part of the Array Latch Mechanism, which is mounted on the canister cover. This attachment scheme creates the additional inertial load that makes the two stiffer bending beam flexures on the Lock Ring Mechanism necessary. The force necessary to operate the Array Latch Mechanism is provided by the Lock Ring Drive Mechanism through the action of the Array Latch actuator block on the crank. When the Lock Ring unlocks, the Array Latch unlatches and the canister cover is free to open. The actuator block is mounted on the Lock Ring and is therefore attached to the canister base. When the canister cover opens, the crank separates from the actuator block. This separation is mission critical. The Array Latch Mechanism must maintain its position when disengaged from the actuator block so that the crank is able to reengage the actuator block when the cover closes. As the crank moves, it drives a camshaft that controls the motion of the mechanism. A cam follower link is part of the four bar linkage that positions the moving saddle. The moving saddle engages slots in each of the four arrays by rotating through a limited angle on a simple pivot. The moving saddle on its simple pivot and a portion of the Array Latch housing are the only parts of the mechanism exposed to the inside of the canister with its extreme cleanliness requirements. The linkage that articulates the moving saddle operates through a flexible metal bellows that seals off the rest of the mechanism from the canister interior. The bellows also acts as a spring to hold the cam follower link in the cam detent when the Array Latch Mechanism is in the unlatched position. Very little of the Lock Ring Drive Mechanism's torque capability is used to actuate the Array Latch Mechanism. The peak load occurs at the very beginning of latching when the cam follower link is coming out of the cam detent. This corresponds to the beginning of locking when the torque required to turn the Lock Ring Mechanism is low.

ADM

The function of the ADM is to independently move each of the four deployable arrays between three locations: stowed, unshaded, and deployed. The latter two positions are used for solar wind collection and are 104° and 256° respectively from the stowed position. As with all the other Genesis mechanisms, the ADM is able to perform in 1g. The ADM consists of four coaxial drive tubes with flanges each

mechanically connected to an individual array and supported on bearings. Each of the tubes is separately driven by an independent mechanism consisting of a 30° stepper motor with a three stage planetary gearbox, a pinion and spur gear drive train, and three microswitches for position telemetry. The ADM joins to the Canister via a bolt circle and o-ring seal. The ADM is lubricated with Braycote grease. The Genesis contamination control requirements are met by venting the interior of the mechanism through the floor of the canister. Rotary teflon seals prevent ADM outgassing into the interior of the canister.

Additional Design Considerations

The cleanliness of the delivered Flight Model integrated canister and in particular the interior of the canister is critical to the success of the Genesis mission. All the material returned in the arrays and the concentrator will be assumed to be solar wind so it is essential to keep contaminants from these ultra-pure materials. This is accomplished in a variety of ways. The materials in the canister design, particularly within the canister interior were chosen to minimize contamination of the solar wind samples and to maximize the ability to clean the payload hardware. The only opening in the closed canister is through the filter. The processing sequence of the canister is set up to keep the canister interior as clean as needed.

The Flight Model integrated canister is built at JPL and undergoes both vibration and thermal/vacuum qualification testing at this subsystem level. The canister then goes to Johnson Space Center (JSC) where it is partially disassembled and rigorously precision cleaned. The canister is reassembled in a Class 10 cleanroom. In Figure 14, the Cover Drive Mechanism is reinstalled after cleaning at JSC. Personnel perform the operation in a Class 10 cleanroom while outfitted in Dryden suits with HEPA filters. The hexagonal collectors are replaced with new pristine collectors. The canister is closed and locked in the ultra cleanroom at JSC and it is never opened again until it is in space. The canister is purged with clean, dry nitrogen from this point until launch fairing closeout. Integration within the SRC and the spacecraft takes place outside the ultra clean environment so it is impossible to open the canister without contaminating the collectors and the concentrator. The only way to verify the flight electrical interface between the spacecraft and the integrated canister is with the "No Open" functional tests.

Conclusions

Both mechanisms have interesting design challenges of their own. In the Lock Ring Mechanism, the ramp profile, the torque required for locking the ring, and the lock ring flexure designs all interact. Key to the design of this type of mechanism is the incorporation and control of the structural compliance (flexures) that allows a controlled preload in the metal-to-metal separable seal surface. The capture range of the Lock Ring Mechanism and its push-off stroke are also directly related. In the Cover Drive Mechanism, incorporating both the torque tube and the cover arm flexures posed a particular problem. However, the most interesting aspect of all is the coupling between the two mechanisms and between the mechanisms and the structure. The canister seal is needed because of the extreme contamination requirements in the canister interior. The existence of the seal forces the Cover Drive Mechanism hinge line to the top of the seal crown height to maximize the actual capture range of the Lock Ring Mechanism. This hinge line location makes the cover arm flexures necessary. The force needed to deflect the cover arm flexures adds directly to the preload required from the Lock Ring Mechanism when clamping the seal interface. The canister cover and base structure design directly influences the loads transmitted across the seal interface thereby affecting the Lock Ring Mechanism design. Parameter changes in one area during detailed design iterations quickly rippled through all the payload design interactions. All these interactions added complexity to the overall design problem.

Status

The Engineering Model canister has been designed, built, tested, and integrated into the SRC. System level testing is in progress. The Flight Model canister will be built and tested during the year 2000 with delivery to the spacecraft scheduled for mid July 2000. Launch is scheduled for January 2001.

Acknowledgements

The work described in this paper was performed by the Jet Propulsion Laboratory, California Institute of Technology, under contract with the National Aeronautics and Space Administration.

The author gratefully acknowledges the contributions of the JPL Genesis mechanical design team: Glenn Aveni, Jim Baughman, Gus Forsberg, Gary Haggart, Ted Iskenderian, Mike Johnson, Kevin Kramer, Don Lewis, Paul MacNeal, Virgil Mireles, Pablo Narvaez, Frank Ramirez, David Rosing, Bruce Scardina, Don Sevilla, Andy Stone, George Sweeney, and Robert Troy.

The spacecraft and the SRC are designed and built by Lockheed Martin Space Systems Company – Denver Operations. The Concentrator, Electron Monitor, and Ion Monitor are provided by Los Alamos National Laboratory. The ADM was delivered by American Technology Consortium, and CDA InterCorp furnished the gearmotors.

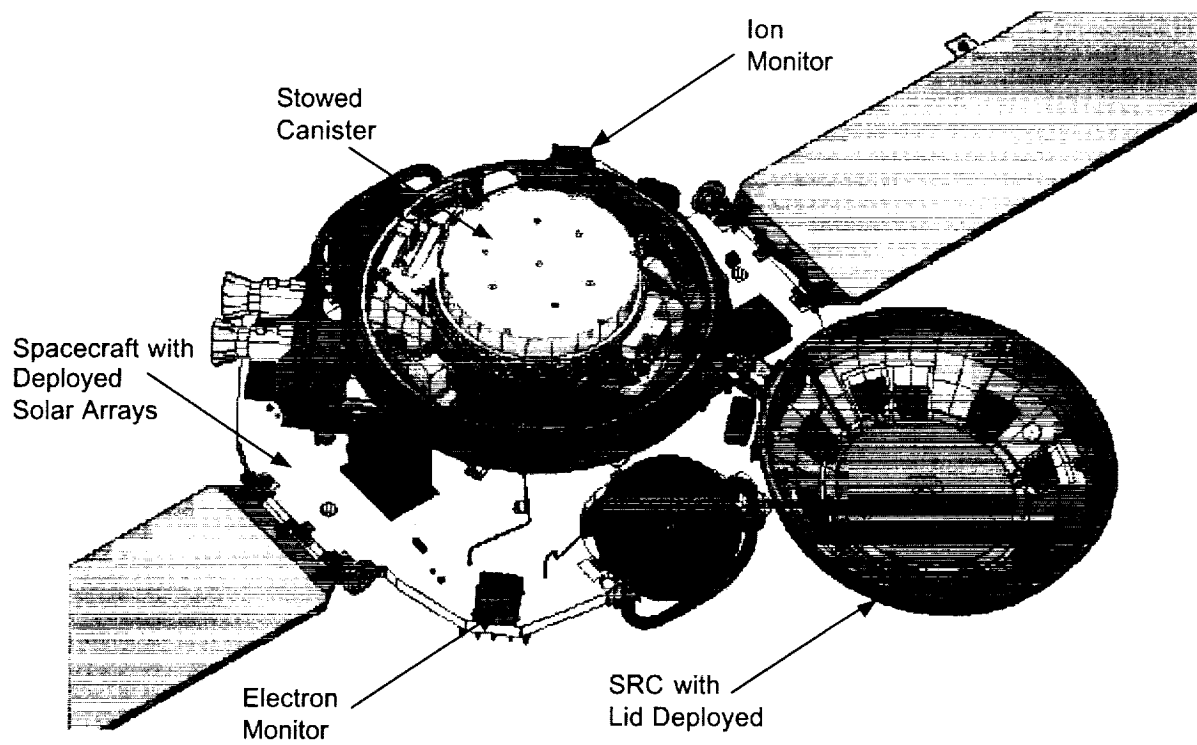


Figure 1. The Genesis payload integrated with the SRC and the spacecraft

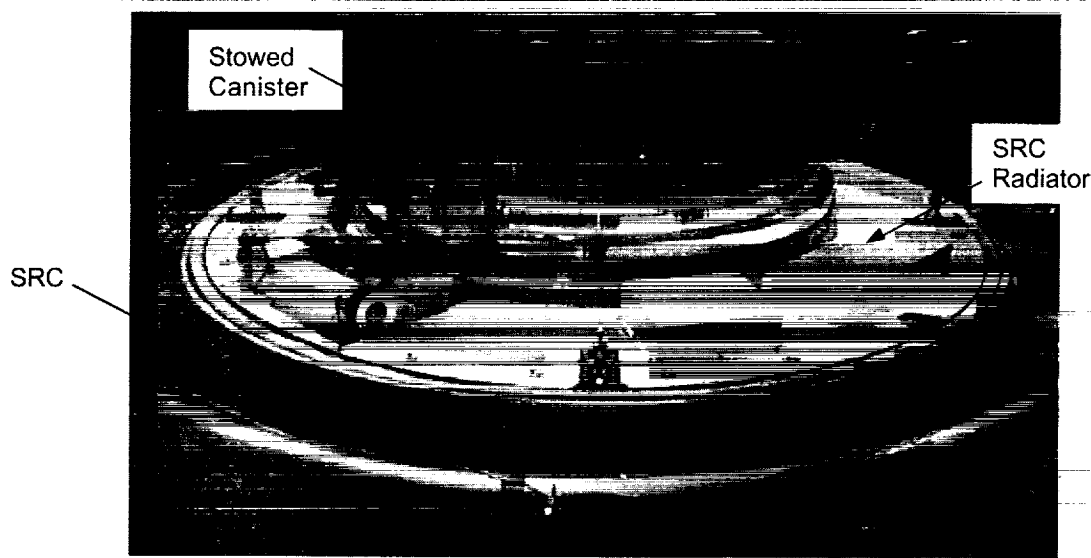


Figure 2. The Engineering Model canister integrated with the SRC

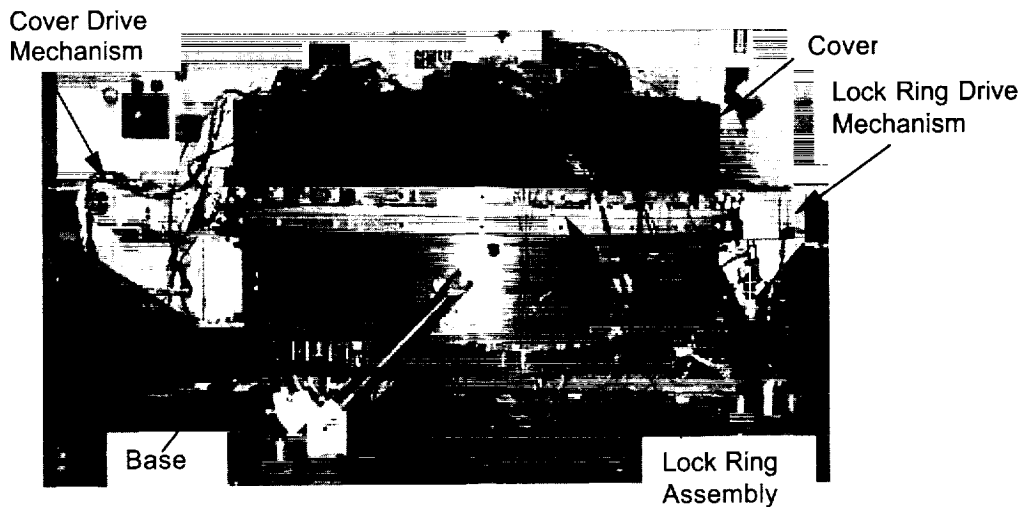


Figure 3. The Engineering Model integrated canister in the closed configuration is mounted on its vibration test fixture.

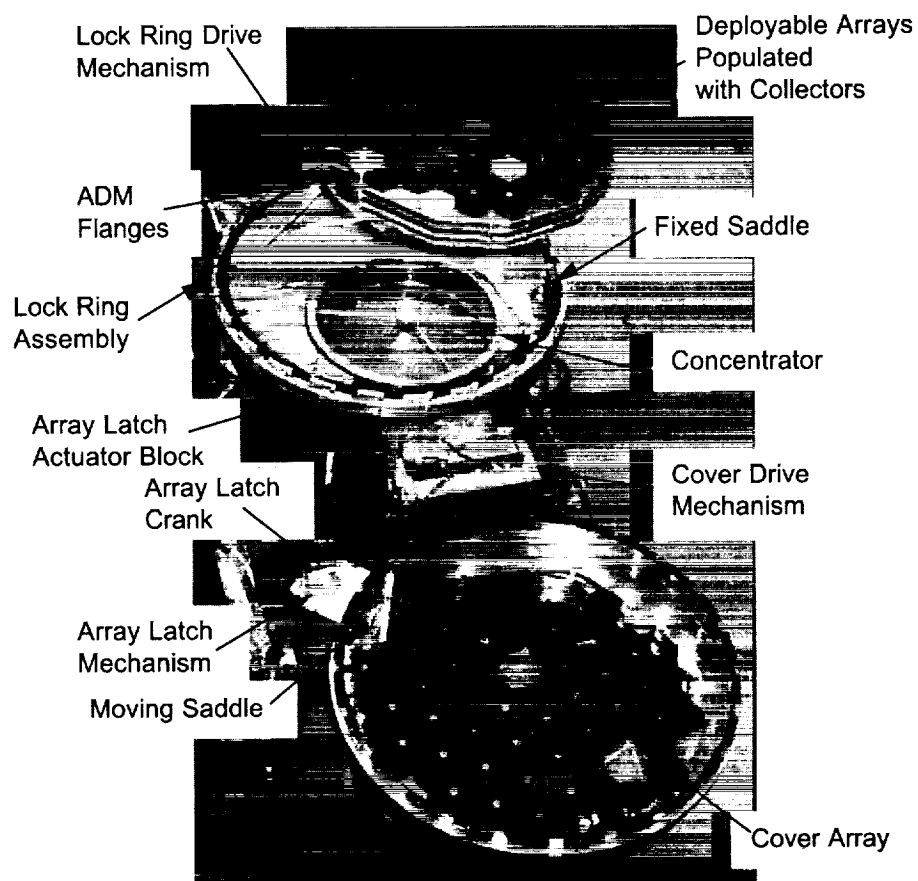


Figure 4. The Engineering Model integrated canister is shown in the open configuration.

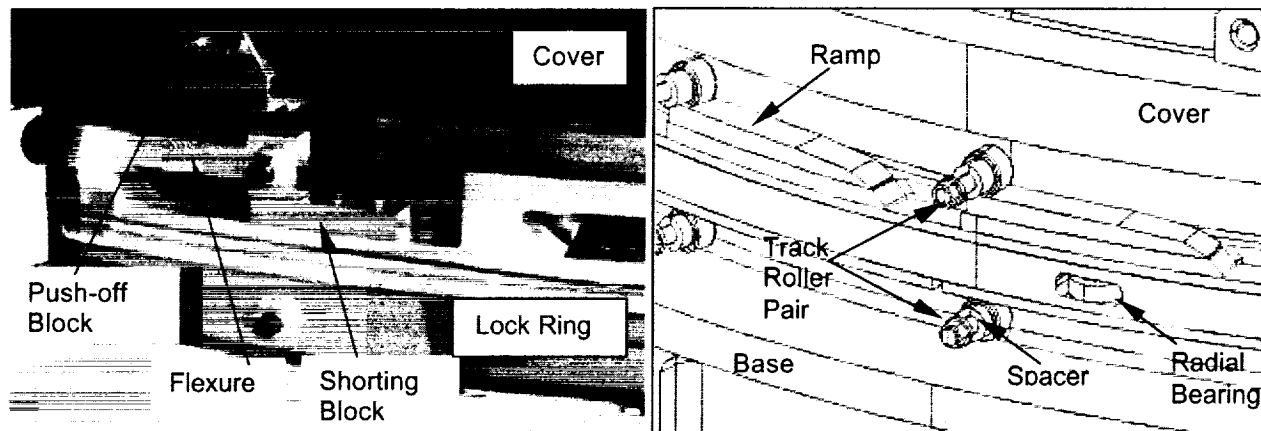


Figure 5a and 5b. A detailed view of the Lock Ring Assembly is shown. The figure on the right has the Lock Ring removed for clarity.

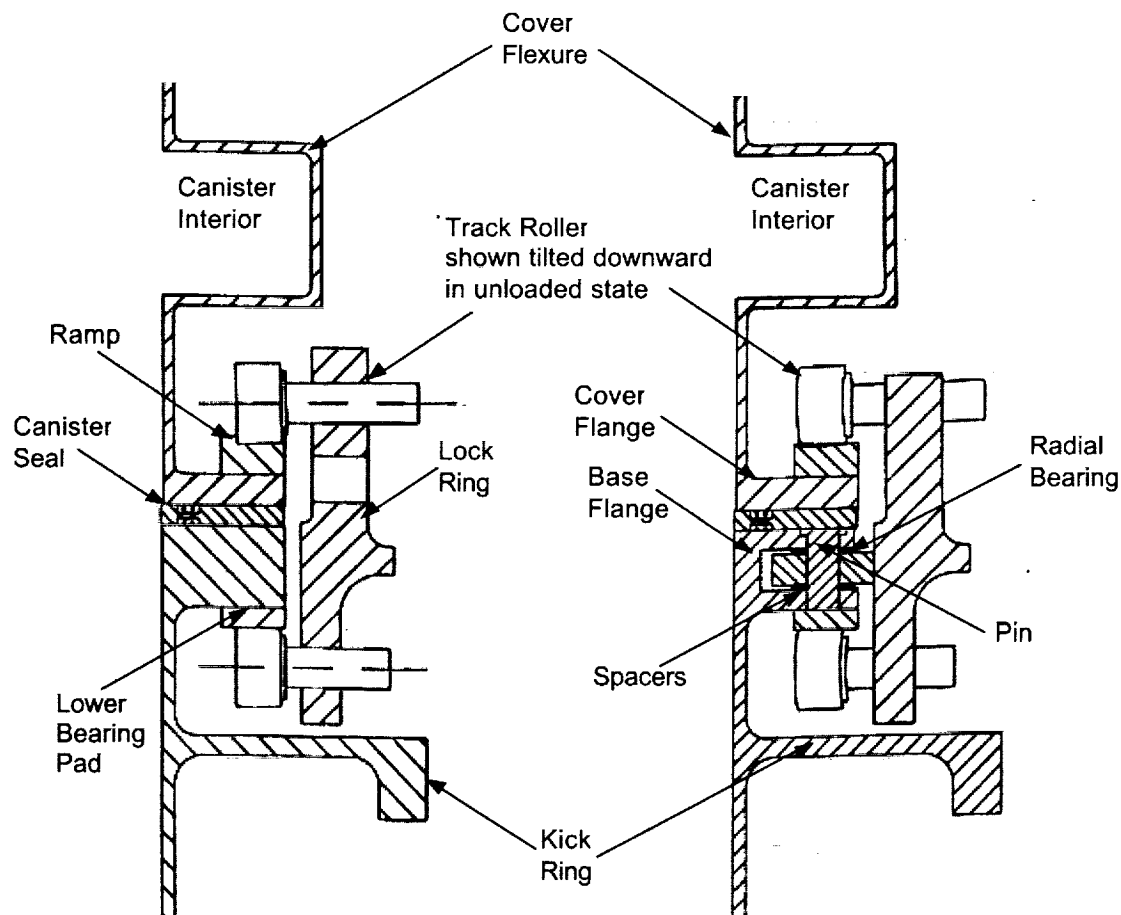


Figure 6a and 6b. Lock Ring Assembly sections through the track rollers in the left view and through the radial bearing in the right view

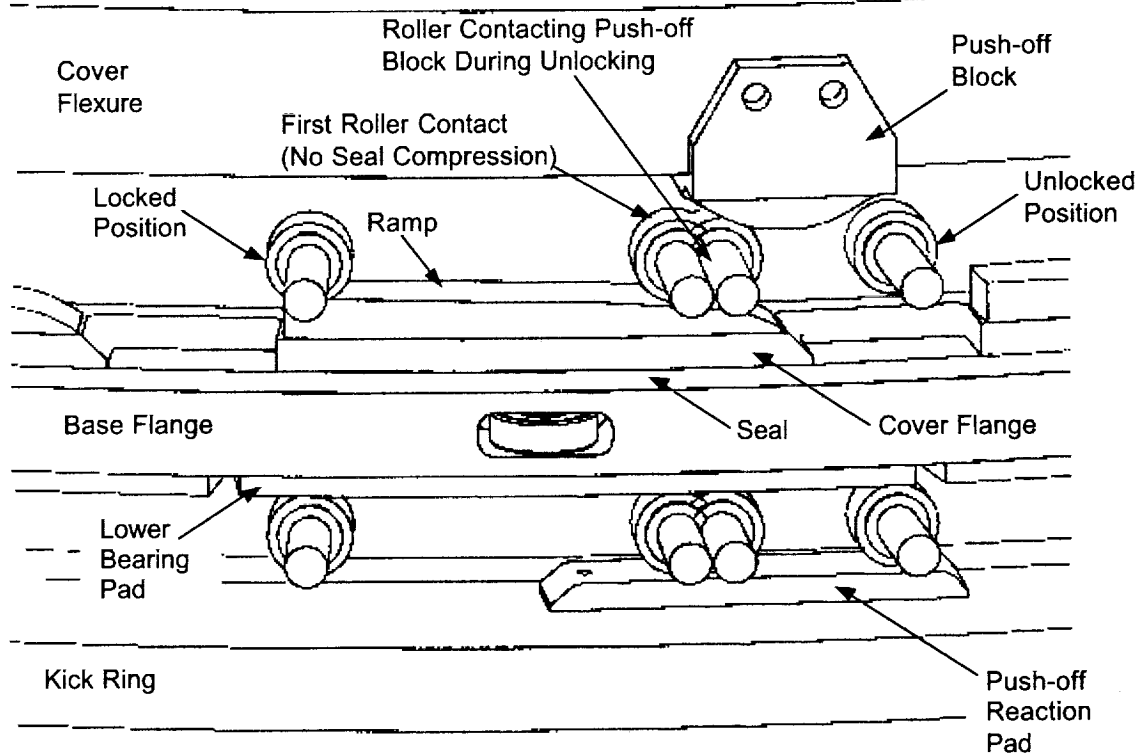


Figure 7. Lock Ring Assembly operation

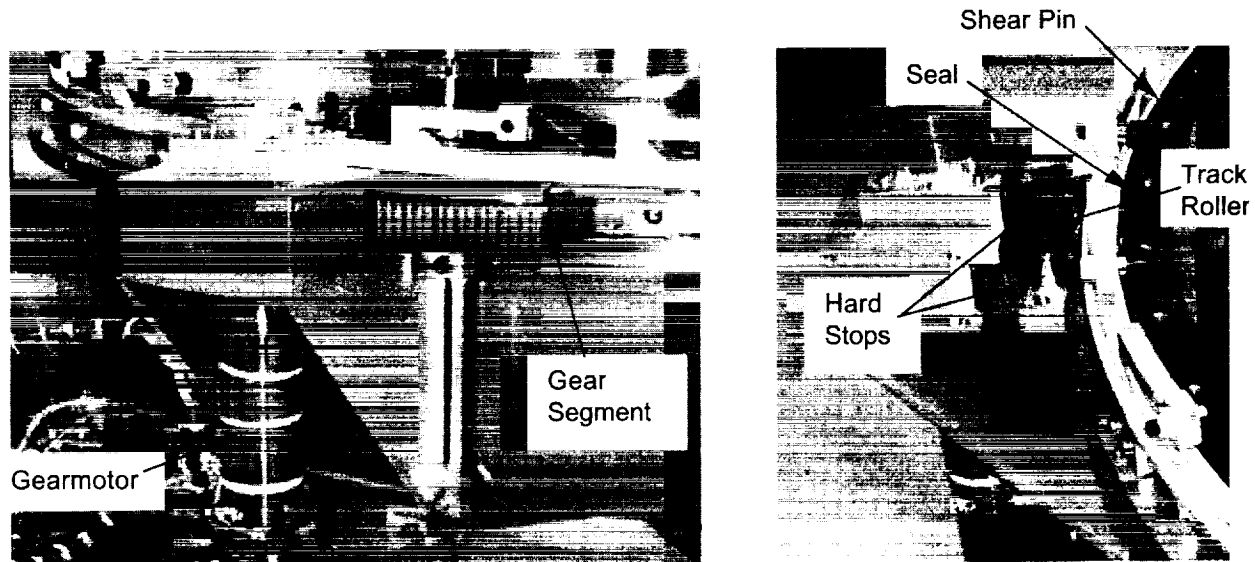


Figure 8a and 8b. The Lock Ring Drive Mechanism uses a pinion and sector geartrain to move the Lock Ring to its locked and unlocked positions.

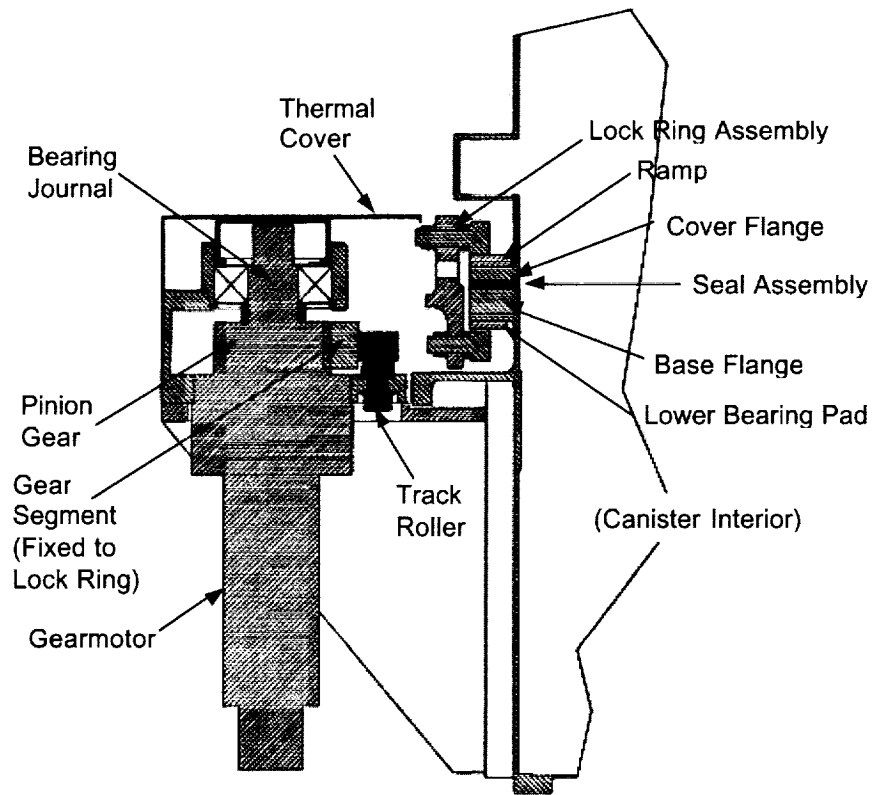


Figure 9. Lock Ring Drive Mechanism cross-section

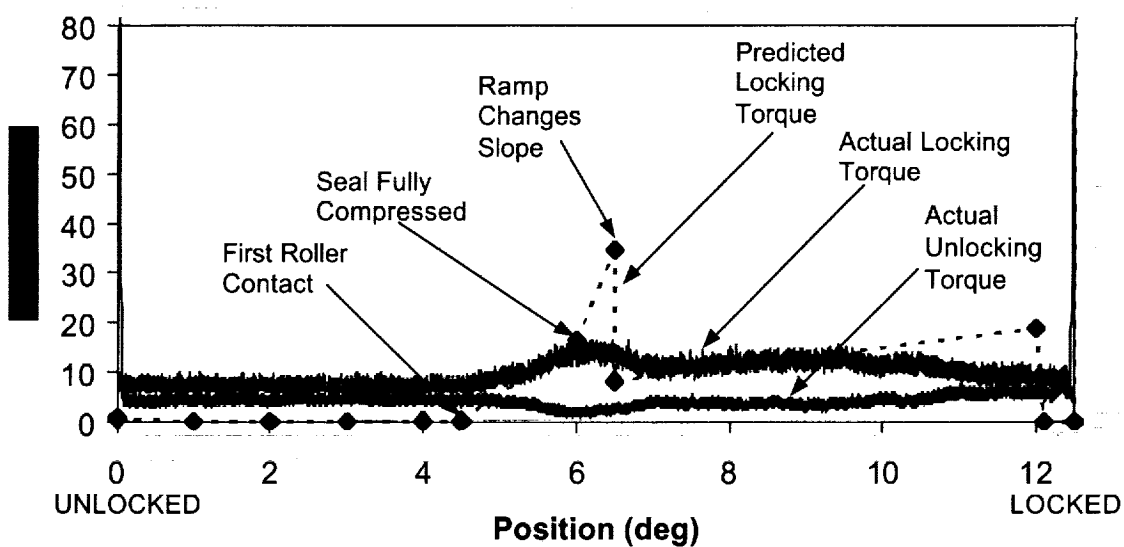


Figure 10. Lock Ring Mechanism operation

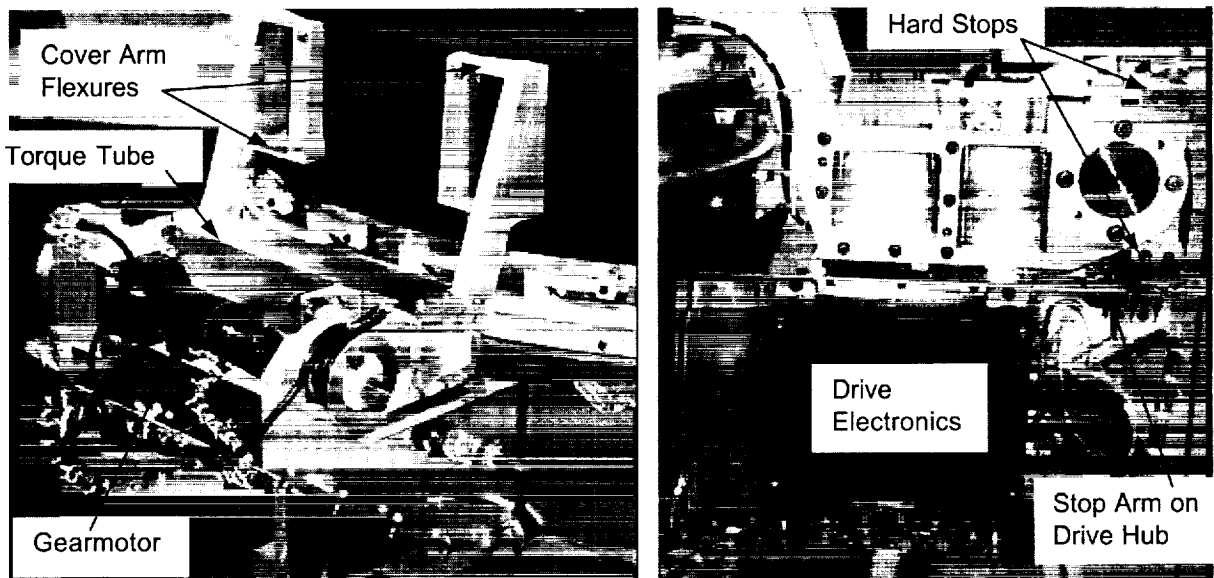


Figure 11a and 11b. The Cover Drive Mechanism opens and closes the canister cover.

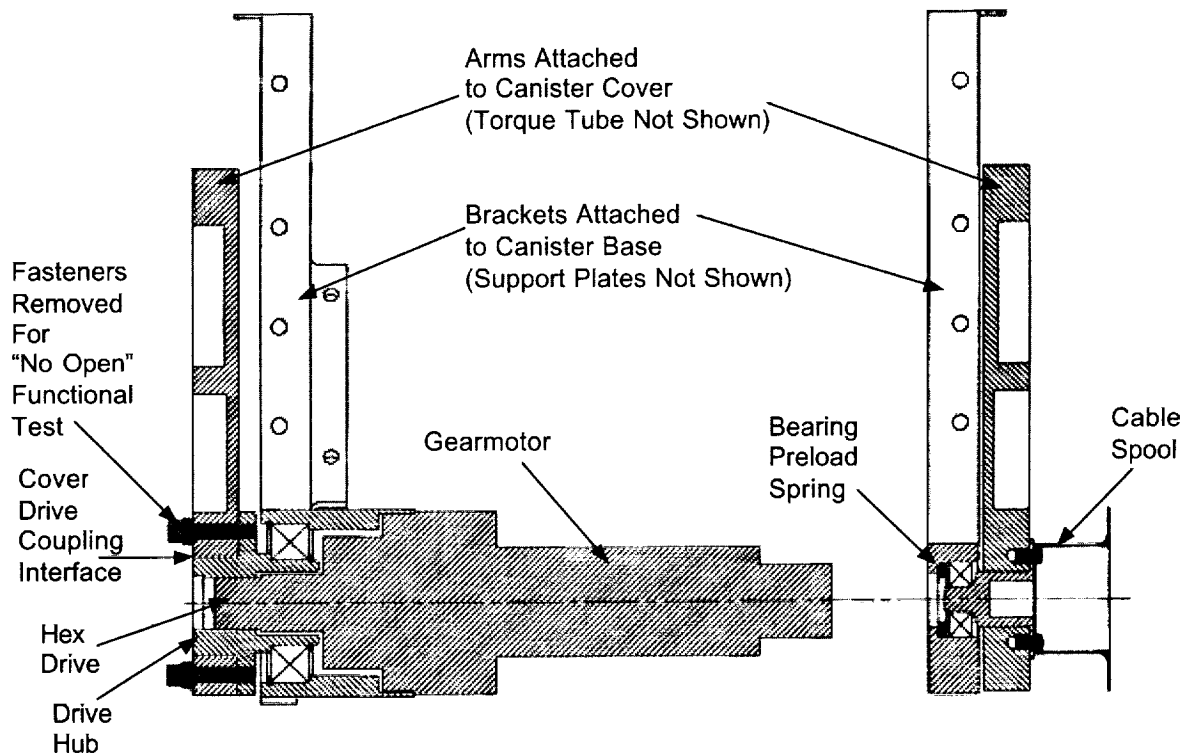


Figure 12. The Cover Drive Mechanism cross-section

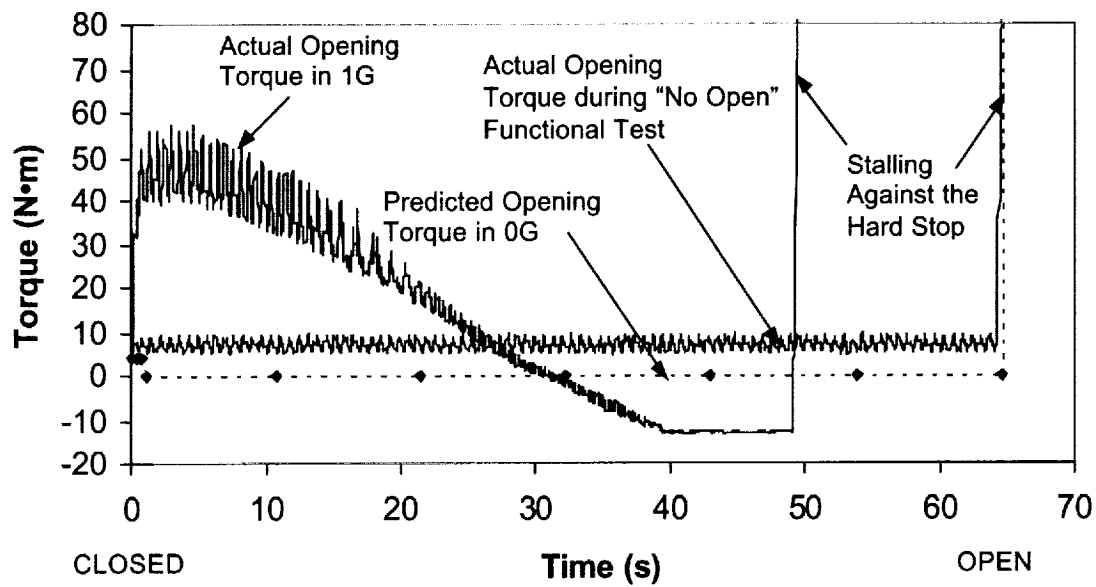


Figure 13. Cover Drive Mechanism operation



Figure 14. The Cover Drive Mechanism is reinstalled in the JSC Class 10 cleanroom after cleaning.

Landsat 7 Solar Array Testing Experiences

Daniel Helfrich*

Abstract

This paper covers the extensive Landsat 7 solar array flight qualification testing effort. Details of the mechanical design of the solar array and its retention/release system are presented. A testing chronology is provided beginning with the onset of problems encountered at the subsystem level and carrying through the third and final powered-spacecraft ground deployment test. Design fixes and other changes are explained in the same order as they became necessary to flight-qualify the array. Some interesting lessons learned are included along with key references.

Introduction

The Landsat 7 Spacecraft

Landsat 7 (L7), depicted below in Figure 1, was launched in April of 1999 into a 705-km sun-synchronous orbit. A single, huge, visible/infrared imager called the Enhanced Thematic Mapper Plus (ETM+) is the sole L7 instrument, occupying the entire forward (-Y) end of the spacecraft. ETM+ provides land and near-shore ocean imagery down to 15-meter resolution for a very diverse user community. The spacecraft was built under NASA contract NAS5-32633 by Lockheed Martin Space Systems Company (LMSSC) located in Valley Forge, PA. A comprehensive description of the spacecraft and its mission is available on the web at URL: <http://landsat.gsfc.nasa.gov>.

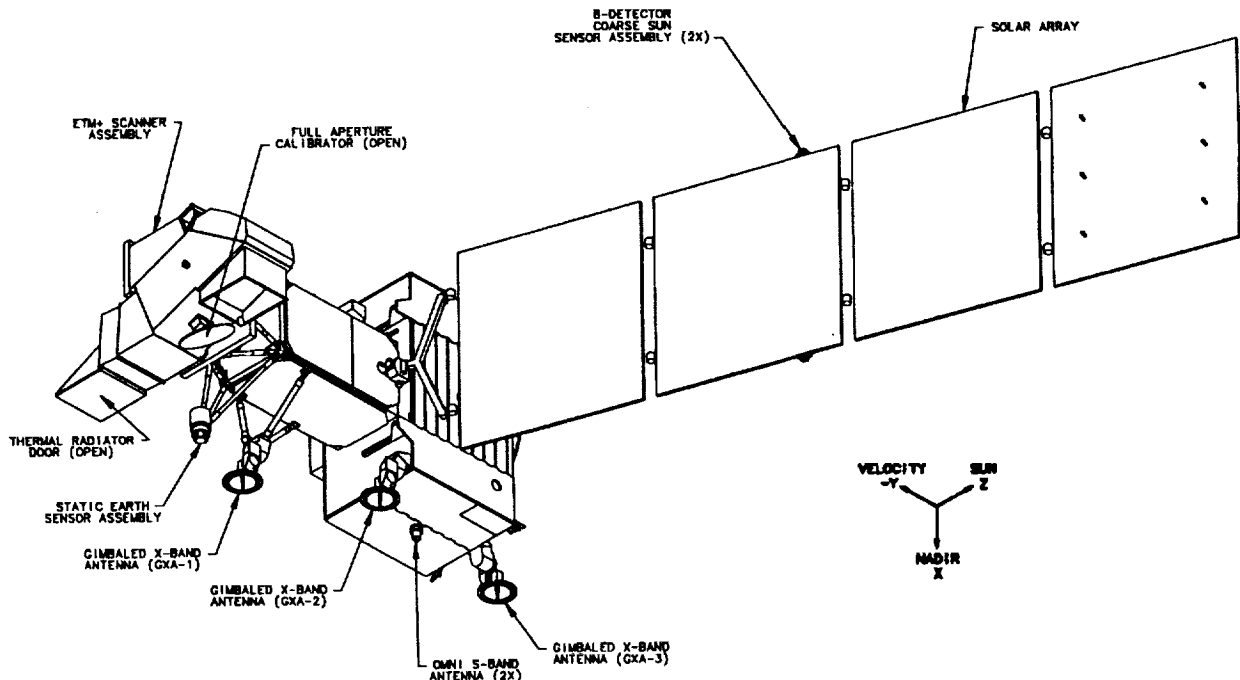


Figure 1. Landsat 7 Spacecraft and Fully Deployed Solar Array

* NASA Goddard Space Flight Center, Greenbelt, MD

Proceedings of the 34th Aerospace Mechanisms Symposium, Goddard Space Flight Center, May 10-12, 2000

The L7 Solar Array

The L7 solar array (S/A) is an assembly of four rigid aluminum honeycomb panels and an aluminum yoke with a total length of 8.5 m (335 in). Each 25 mm (1 in) thick panel weighs approximately 22 kg (50 lbm) and is 2.27 m (89.3 in) tall and 1.88 m (74 in) wide. At CDR, the end of life power requirement with one lost string at the least favorable beta angle was 1658 W. (Shortly after launch, the output was determined to be 2252 W at 32.9 Vdc.) Each hinge line latches into place at full rotation. Analytical models of the array predicted a first resonant mode of 0.232 Hz.

As can be seen in Figure 1, there are two hinge fittings per hinge line. Negator springs integral to the solar array's hinge fittings drive the deployment. The hinges all operate independently. Deployment time was originally specified to take no longer than 120 seconds with one hinge spring failed. The most recent analysis showed that the final design provided a nominal deployment time of 30 seconds and deployment in 67 seconds in the worst case single hinge spring failure. The solar array was fully tested at the factory and shipped in the stowed configuration for final spacecraft processing at Vandenberg Air Force Base, demonstrating one aspect of the "ship and shoot" philosophy.

Solar Array Restraint/Release System

The S/A Restraint/Release System (RRS) held the four solar array panels tightly against the side of the spacecraft for launch. Cables passing through the panels within cup-cone fittings in the four panels squeeze the panels together to prevent gapping of the panels during launch. Once on-orbit, pyrotechnic cable cutters inside the spacecraft are fired in pairs, releasing the four panels all at once after the final pair of cables is cut. Friction is used in the RRS to dissipate the released energy of the cut cables. Getting this friction just right in this shock absorbing device became something of a small research project, the details of which may be found in the referenced LMSSC documentation.

Ground Support Equipment for the S/A

The Mechanical Ground Support Equipment (MGSE) of greater interest is the g-negation deployment hardware which included these key items:

1. a deployment surface, which in the beginning, at least, was a poured epoxy floor,
2. four solar array supports stands, each on a set of four air pads, for a total of 16 air pads, and
3. a solar array mounting interface simulator mounted on a three-axis positioner.

The three-axis positioner was to become very useful as the need arose for unexpected test setups. The first two MGSE items are described in greater detail in the following pages.

In the beginning, the deployment of the array was a purely manual operation, requiring no Electrical GSE (EGSE). The EGSE for the solar array deployment testing later on was quite an assemblage consisting of many interconnected spacecraft test control stations. The final solar array deployments were commanded through the spacecraft C&DH system and associated flight harnessing, an important verification test to assure a successful deployment.

Testing Chronology

For the L7 solar array, what originally was a test effort spanning 6-8 months became twice that in duration. Major schedule impacts to the overall program were avoided only because the ETM+ Instrument had suffered its own problems in the power supply that had caused nearly a year-long delay. What follows in this section is just a quick summary of the flight qualification testing efforts. These activities are then more fully described towards the end of this paper.

Assembly of the solar array was accomplished at the LMSSC East Windsor plant in New Jersey in the Fall of '97. The deployment MGSE was checked out simultaneously at the LMSSC King of Prussia plant near Valley Forge, Pennsylvania. Around that time, operational difficulties with both the unevenness of the deployment floor and the stickiness of the support stand air pads were dismissed by the contractor as negligible. The first full deployment of the array on November 6, 1997, a manual operation before its installation on the spacecraft, suffered as a result. Corrective actions included additional floor smoothing and a changing of the air pads.

On April 28, 1998, the first powered-spacecraft deployment including the firing of live cable cutters was attempted before a large audience. The array released only partially due to RRS problems that had caused insufficient cable preload and had resulted in inadequate extraction of some of the cables. The RRS was manually released after a full inspection of the failed hardware, allowing numerous failed manual deployment attempts several days later, which demonstrated the epoxy floor was still a problem. Individual hinge lines were tested on a granite table within a week just to show those components were working properly and wouldn't need to be reworked. More corrective actions on the RRS and the deployment MGSE were also implemented as part of a multi-faceted failure recovery effort.

With many issues from the April deployment failure closed, on August 24, 1998, the solar array was successfully deployed off the spacecraft and became fully qualified for flight. But that test revealed yet another flaw in the shock absorber mechanism, requiring even more testing on the bench and a third pyrotechnic deployment on December 8, 1998. This final full deployment was completely nominal and laid to rest the remaining concerns about the design of the RRS.

Landsat 7 Solar Array Restraint/Release System

General Characteristics

The S/A used on L7 had six stainless steel wire cables to restrain it to the spacecraft; each cable is chopped into two pieces by pyrotechnically driven cable cutters. Each cable was really a custom assembly, fabricated by Brown & Perkins, Inc., consisting of two different threaded end fittings swaged onto a 5.5-mm (7/32") diameter, 7x16 wire rope cable.

The pyrotechnic cable cutter used in the RRS is a Hi-Shear Corporation product specifically built and tested for LMSSC. It has been used on numerous programs within the US. An explosive charge drives a chisel into an anvil within a cylindrical housing 19 mm (0.75 in) in diameter. It was also used on the 4-mm (5/32") diameter restraint cables in L7's three (3) X-band antenna gimbals. In both applications, two cutters are provided for each cable; the second, redundant, outboard cutter is the backup if the first cutter fails to fire.

Figure 2 shows the RRS hardware in cross-section. Unlabeled on the right (outboard) side of the figure are the four solar array panels and the cup-cone fittings through which the cable fits. The assembly on the left of those four panels mounts with four bolts to the inside of the body of the spacecraft, the edge of which is approximated by the heavy dashed line.

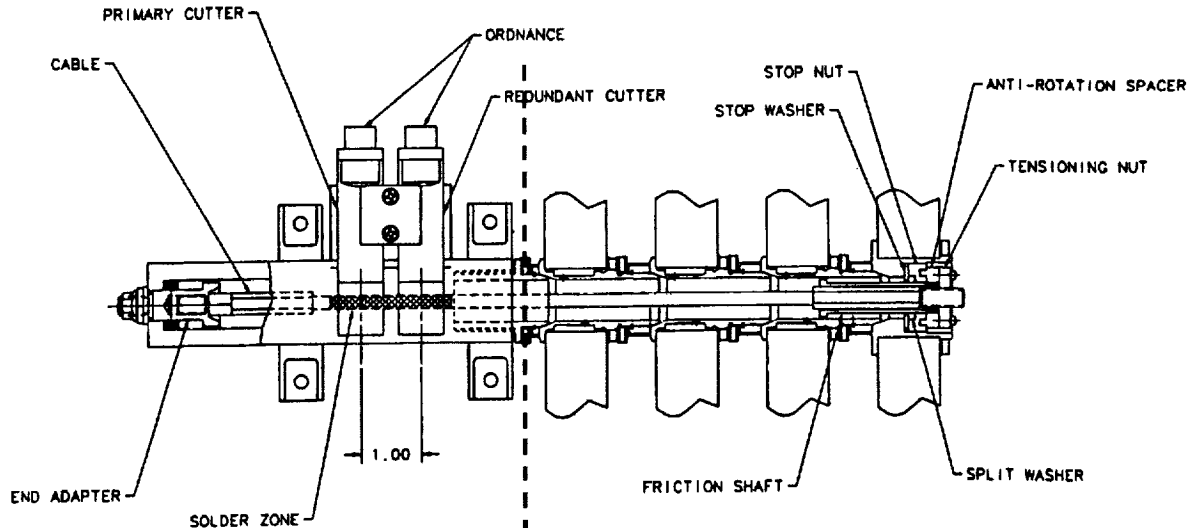


Figure 2. Cross-sectional view of Restraint/Release System

Functional Details

Figure 3 depicts the functional design of the shock absorber mechanism. At the moment of cutting, substantial strain energy is released and the outer portion of the cut cable shoots rapidly outwards. In fact, adequate preload in the cable is essential for this self-extraction of the cable. But the cable must remain constrained to the outer panel to prevent the cable from flying away into space and becoming orbital debris. At least 25 mm (1 in) of travel is required.

Friction is used to dissipate the kinetic energy of the cable so it won't deliver a large shock pulse to the outer panel at the end of the cable's travel through the panel fitting. Enough shock in the outer panel could cause the silicon solar cells mounted out there to crack and thereby degrade the power output of the solar array. Friction between the cable fitting's *friction shaft* and a *split washer* captured in the outer panel dissipates the energy released when the *cable* is chopped by the *primary cutter* and the preload is suddenly released.

Full travel is important to the overall reliability of the RRS. Without full travel, the splayed end of the cut cable will remain in the path of the *redundant cable cutter*. In such a situation, firing the redundant cutter can entrap the cable and prevent the array from releasing. This very problem arose during the failed powered spacecraft deployment attempted in April 1998. Firing some of the redundant cable cutters before all the primary cutters had been fired entrapped several already cut cables and prevented the deployment from proceeding normally. This firing sequence was subsequently revised for flight.

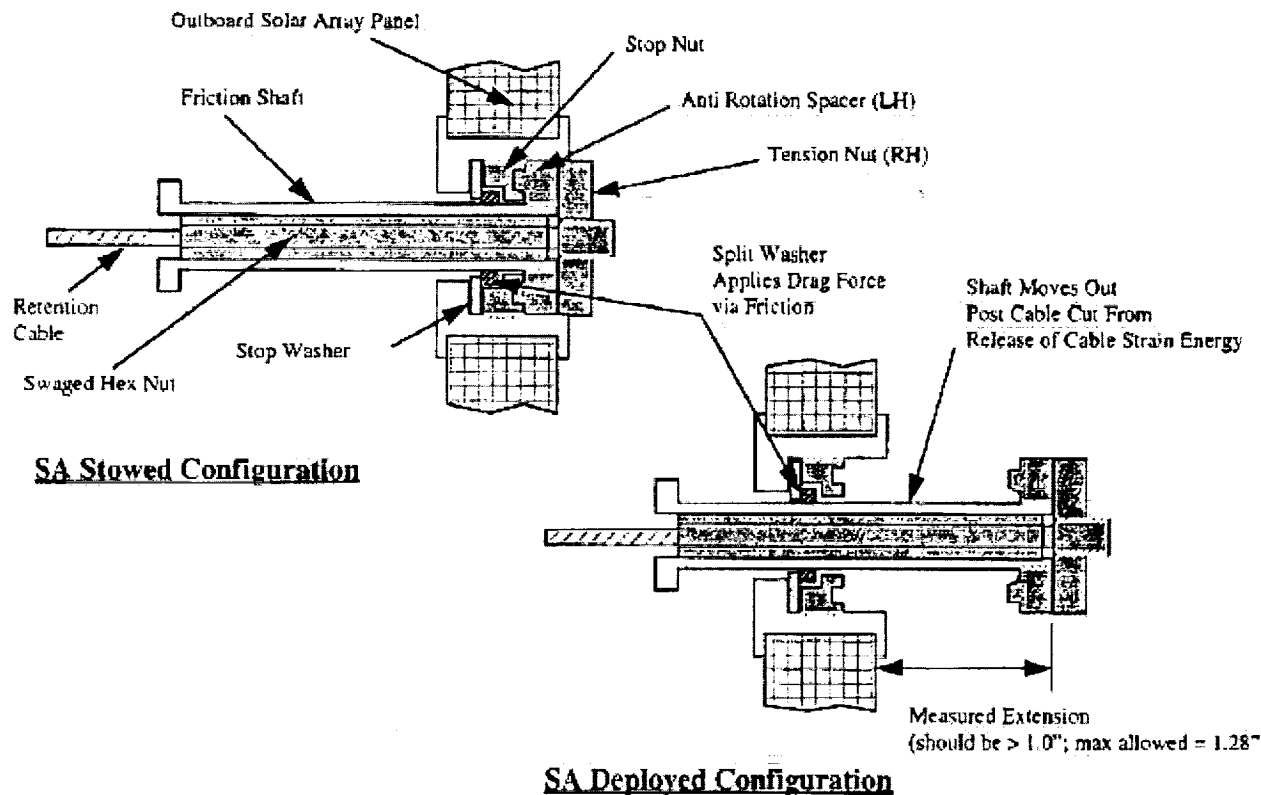


Figure 3. Shock Absorber Functional Diagram

Design Heritage and Intentional Adjustments

The RRS used on L7 has been used in a variety of configurations for GPS, Landsat 6, A2100, and other LMSSC-built spacecraft with rigid panel solar arrays. Parameters that are intentionally adjusted include the restraint cable tension and diameter, the orientation and firing sequence of the pyro-cutters, and the material and dimensions of the split washer and sleeve. For Landsat 7, launch vehicle design loads drove the RRS cable tension high enough to require a cable diameter of 5.5 mm (7/32 inch). To compensate for the additional strain energy stored in the system, the end fitting was designed with tighter clearances--and a resulting higher friction--to dissipate the greater kinetic energy.

The functionality of the RRS was actually modified for Landsat 7 in two ways, both of which contributed to the initial deployment failure. First, the frictional drag force in the shock absorber was raised too high by the selection of tighter dimensions. Bench testing early on showed the higher friction prevented end of travel shock, but it was not realized at that time that full travel was a desirable aspect of the design, so that wasn't a bench test pass/fail criteria. Second, the firing sequence was modified for what seemed like a good reason: to address a concern of panel racking in case one of the corner cables was not cut by the primary cutters.

So the firing of the primary cutters on the two central cables was purposefully sequenced AFTER both the primary and redundant cutters were fired on the four corner cables. Ironically, this sequence helped reveal two part fabrication problems in the RRS which otherwise probably would have been overlooked. The firing of the corner redundant cutters entrapped the inadequately extracted cables before they had a chance to pull out of the way, which probably would have happened if only the last pair of primary cutters had been fired first. After these shortcomings were discovered, it was back to the bench for design changes and re-qualification tests at the component level, explained in detail later in this paper.

Deployment MGSE

Deployment Surface

Originally, the L7 deployment surface was a pit in the concrete floor of the LMSSC high bay. Self-leveling epoxy was poured into the pit, smoothed out manually, and left to cure. This was put in place several years prior to the actual need date. When the time came to use the deployment floor and difficulties arose; variations over the surface were measured to be as much as ± 6.4 mm (0.25 in). This may have been in part due to the unwise use of the epoxy floor for temporary storage, but it is not known for certain that an acceptance inspection was performed when the floor was first poured. Subsequent discussions with epoxy vendors revealed the flatness requirements were pushing the limits of the technology.

Support Stands

Each panel moves independently during deployment, so four independent support stands were designed to spread out the weight of the array panels onto four low-friction air pads each. For many years prior to L7, the same square air pad design had been used successfully at LMSSC for antenna deployment tests on smooth granite tables. A compressed air leveling system was also designed into the stands to ensure that they worked properly. The stands worked well except that on the epoxy floor, there was enough unevenness in the floor surface to hang up on the corners of the square air pads. Also, small bits of dirt and particulates gathered more easily on the floor, requiring frequent wipedowns to prevent additional air pad hangups.

Air Delivery System

A tricky problem arose later with the air delivery system, consisting of flexible plastic tubing stiff enough to handle compressed air at about 100 psi. It was found that without very careful handling, the tubing could introduce lateral loads into the four floating support stands that were not insignificant. The lateral loads were measured with small force gauges and it was found that only with great care could the effects on the movements of the panels be minimized. In time, it was realized that achieving repeatability was not going to be easy, if not impossible. This problem was never fully resolved.

Solar Array Drive Bearing Protection

Floor flatness and best possible alignments were evaluated by the LMSSC stress engineer to determine what loads might be imparted to the duplex bearings in the L7 solar array drive (SAD). It was found that there was a real (worst case) possibility of the bearings being overloaded. To prevent this from happening without making Herculean efforts to level the deployment floor, strain gages were installed on the yoke and calibrated to permit a direct measurement of the forces going into the SAD. (The interpretation of the strain gauge readings became a very difficult task, but eventually the strain data were successfully post-processed and found to be below the limit loads for yielding.)

Initial Solar Array Testing

Initial Bench Testing

Engineering bench tests of the RRS performed in 1997 had two purposes: calibrating the torque required on the cable tensioning nut to achieve proper cable preload, and selecting the proper split ring washer for the shock absorber assembly. An Instron machine was used to develop the relationship between nut torque and cable tension. A unique torque was developed for each cable.

A test fixture with a gas actuated separation nut was used repetitively in statistically meaningful tests to determine the proper split washer needed to dissipate the 5.3 kN (1200 lbf) preload that was to be applied with each cable. The test objectives were met, but there were some interesting and important details that were overlooked. No emphasis was placed on demonstrating 25 mm or greater travel of the released cable, and the split washer was not adequately inspected after the test, which would have showed they were yielding due to the excessive interference. In the adaptation of a heritage design to L7, subtle yet critical details were missed that could have easily been documented on the engineering drawings of the heritage design.

Manual Deployments

In October and November of 1997, the solar array was deployed manually prior to installation on the spacecraft. It was soon realized that the slight slopes of the uneven floor had led to lateral forces once the array was deployed out over the floor on the low-friction air pads. The hand-held force gauges were utilized once again to measure the lateral component of the downslope force. Up to 2 N (0.44 lbf) was measured in some of the worst locations on the epoxy floor.

At the closest-in hinge line, with a moment arm of several array panel lengths, and multiple panels, the slope-induced torque was an order of magnitude greater than the torques the two hinge springs produced, drastically affecting the deployment paths of the panels and invalidating measurements of deployment time. In fact, the panel assembly clearly deployed downhill into the low spots on the deployment floor. The contours were measured and plotted to gain an understanding of the degree of unevenness of the floor. An attempt at filling the lowest spots on the floor was made using a low viscosity epoxy, but the labor involved was intense and less than a square meter (~10 sq ft) was so treated.

As the array deployed across the floor on its original square air pads, the corners of the air pads would come into contact with the floor as they tried to span small fluctuations in the floor's surface. This caused the assembly to stop repeatedly in various locations. Smoothing at these locations was attempted but it became obvious that this would not be practical across the entire floor measuring 4.9 m (16 ft) wide by 9.1 m (30 ft) long. When the problems with the square pads were heard of back at NASA Goddard Space Flight Center, it was suggested that round air pads left over from TRMM spacecraft's solar array deployment testing be employed. The proper fitting adaptations were implemented by Swales Aerospace and the round air pads were added to the support stands in time for the next deployment test.

Major Problems Surface

On April 28, 1998, the first pyrotechnically initiated deployment from the spacecraft was attempted. This major test involved almost the entire I&T team at LMSSC and was attended by numerous managers. The spacecraft was powered up and loaded with flight software. Special test equipment included the yoke

strain gauges and a computer-based data system to monitor them, accelerometers on the spacecraft tied into a multi-channel high-speed data collection system, local RF intercom headsets for key test personnel, and three VHS video cameras. After everything was checked out and everyone was synched-up, the countdown began and the spacecraft software operated just as if it were in flight. At the appropriate time, shortly after simulated separation from the upper stage of the booster, the pyros were fired in the corners-first sequence. The array panels popped out about a centimeter (0.4 in), but that was all they moved. The test was aborted at that point.

Close up inspections of the jammed hardware initially indicated several possible causes for the failure of the cables to release fully. One thing became clear: firing the redundant cables cutters had jammed some of the cables even though they had been fully severed by the primary cable cutters. But a full inspection was thwarted because access to all the hardware was not possible with the arrays still held close to the spacecraft and with the RRS cables themselves entrapped. Before unjamming the hardware, numerous measurements were taken of the configuration just as it was to prevent the loss of any potential evidence.

Meetings were held frequently over the next several days, giving everyone present the opportunity to consider the mounting evidence, suggest and study possible causes for the failure, and develop deliberate plans on how to proceed. The entrapped cables were removed from the hardware one by one, measuring the force required to pull them free. It was decided that the test should be resumed with an attempt at a manual release of the array.

A test plan was quickly pulled together and the GSE was set up in record time. But the team's hopes for a smooth deployment were just as quickly crushed. Numerous failed manual deployment attempts over the next two days revealed the floor was still a problem. The numerous orientations into which the solar array deployed were plotted on top of a map of the floor contours. Two such plots are shown in Figure 4. The solid dark lines show the final positions of four deployments of the array assembly. Note the relative smoothness of the upper right of the floor that is due to the filling that was attempted previously.

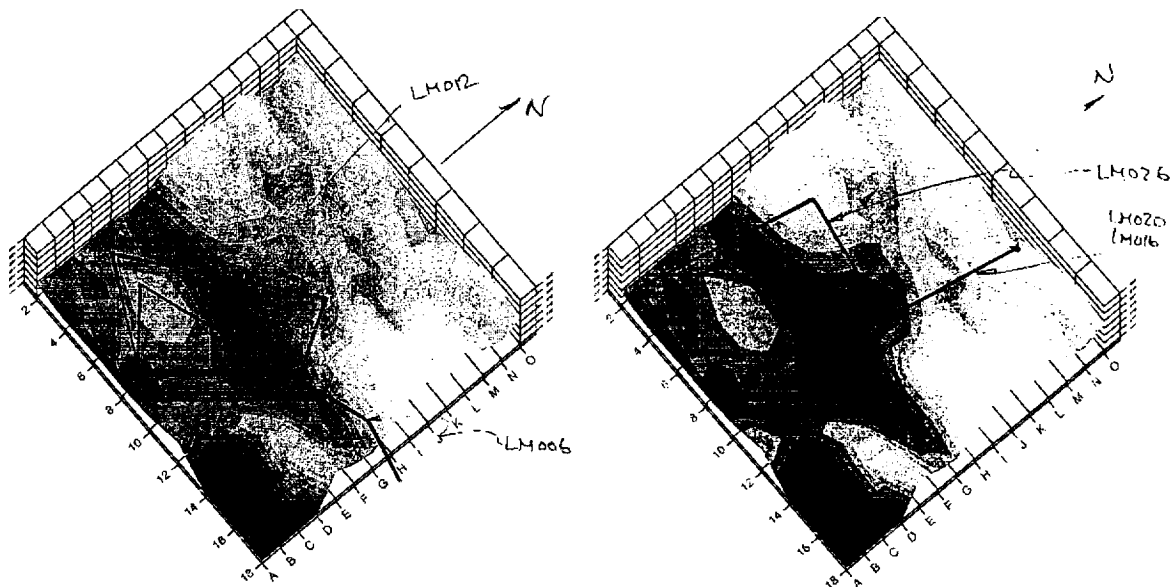


Figure 4. Solar Array Deployment Maps

A complex failure recovery plan evolved over the days and weeks following the failed deployment. Simultaneous activity in quite a few technical areas was required to resolve all the issues in a timely manner.

Failure Recovery Testing

Individual Hinge-line Torque Tests

Individual hinge lines were tested on a nearby high-precision granite table within a week just to show those components were working properly and wouldn't need to be reworked. It was quite fortunate that other deployment testing was ongoing on another program and was being performed in the same building. The granite table used for those tests provided a suitably flat location to begin the recovery testing. More corrective actions on the RRS and the deployment MGSE were implemented while the spacecraft and array were dispatched for system-level environmental testing in nearby facilities.

Restraint Cable Preload

With the removal of the cut cables, it was possible to examine them closely. When the cable fittings were compared to their drawings, some important dimensional discrepancies were discovered. The length of the cables had been unwittingly increased! The discrepancies had been overlooked during the incoming inspection and source inspections at the vendor. (The statistical sampling approach in place at the time did not uncover the part problem.) The carefully determined torques applied to the restraining nut were invalidated with the lengthened cables, which had allowed the tensioning nut to bottom out and induce a counter-twist in the cable, reducing the estimated preload by an unknown amount. With the proper functioning of the RRS directly dependent on the preload, this was a very serious problem indeed.

It was decided that it would be better to rely on load washers for determining the preload in the cables, so this design change was immediately implemented. Simultaneously, a thorough analysis was completed by LMSSC to make sure that the new cable configuration wouldn't lose its preload due to flight vibrations and cup-cone settling. The load washers were checked several times over the remaining months before launch, and they showed the expected minor relaxation over that time which was entirely tolerable. Just before the final closeout of the launch vehicle fairing, the load washers were read for the last time, confirming that full preload was still intact for all six cables. The electrical leads were then clipped off, leaving the load washers in place for flight.

Shock Absorber Redesign

The extensive investigation following the April 1998 deployment failure concluded that the two primary causes for the failure were:

1. Inadequate cable release movement due to low cable preload and excessive shock absorber friction, and
2. Firing the corner redundant cable cutters prior to firing all six primary cutters and allowing the solar array to deploy and complete the extraction of the successfully cut cables.

At first, it was thought that the counter-twist induced in the cables was a primary cause for the excessive splaying of the cable ends, and that the splaying was a condition for jamming. Bench testing was undertaken to test this theory. Cables with a normally cut end were positioned in the path of a second cutter, which when fired still entrapped the pre-cut cable. The conclusion was obvious: splaying from a normal cut like what would be seen on-orbit was enough to interfere with the cable cutting of the redundant cable. Therefore, to truly retain redundancy, after commanding the primary cutter, each cable must be cut and fully extracted, or not cut at all. To be cut and only partially extracted was never seen in any *properly configured* tests, so this redundancy-threatening failure mode was labeled "non-credible".

The following design modifications were implemented as a result of the follow-up investigation:

1. Decrease the friction drag force between the cable fitting and the split washer, using a series of bench tests prior to installation of hardware on the spacecraft.
2. Increase the strain energy stored in the cables by increasing the flight preload.
3. Change the firing sequence to fire all primary cutters first in three pairs, followed much later by an automatic firing of the redundant cutters if needed or abort by command.
4. Change the cutter installation procedure to get better alignment of the cable in the cutters.

Granite Deployment Table Expansion

A trade study began shortly after the failure of the epoxy floor to support the full manual deployments. As much filling and sanding had already been done as seemed practical, so other alternatives were brought up for consideration. Besides adding new granite blocks to the existing granite table and repouring an epoxy surface over the old one, options considered included machining the existing floor, transferring an existing deployment table from the East Windsor facility, and laying out inexpensive honeycomb panels over the existing floor or on sets of individually adjustable jack stands as had been done successfully for TRMM deployment tests. With the greatest confidence held for the expanded granite table, and without substantial cost savings presented by the other options, the decision was made to obtain three new granite tables to adjoin the existing table yielding a surface with enough area to meet the deployment test objectives. On July 22, 1998, the solar array was manually deployed on the expanded granite table proving its effectiveness for when the next pyro-initiated deployment test could be performed.

RRS Problems Live On

On August 24, 1998, the solar array was successfully deployed off of the spacecraft in a second deployment test of the entire system. With that success, the array deployment system became fully qualified for flight, but unfortunately the test revealed yet another flaw in the shock absorber mechanism. Full extraction of the cables was not achieved at all six restraints, nullifying the benefit of the redundant cable cutters, as previous testing showed the cables had to fully extract or become entrapped upon the firing of the redundant cutters. Even more testing on the bench and some additional design changes were required before the six shock absorber mechanisms could truly be considered single fault tolerant and thereby flight-worthy.

It was found in bench tests that there was frictional variability that could cause greater energy loss (and less extraction) than expected. Increasing the preload was not perceived as the best way to ensure full extraction, so that route was not traveled. Three final modifications as shown in Figure 5 were implemented on the bench and incorporated into the flight design to reduce frictional variability:

1. Stepping down the diameter of the friction shaft for the first inch of travel, reducing its role in the energy dissipation to help ensure maximum travel through the split washer.
2. Adding a short taper between the stepped-down diameter and full diameter regions.
3. Adding an elastomeric O-ring at the end of travel to absorb impact shock.
4. Adding an elastomeric O-ring to keep the stop washer in better alignment.

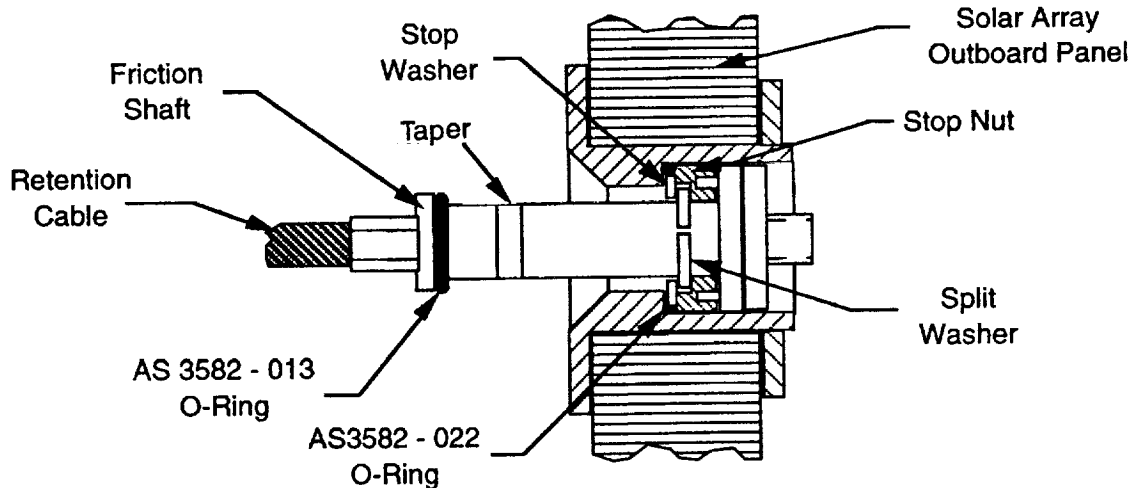


Figure 5. Final Design of Shock Absorber Mechanism

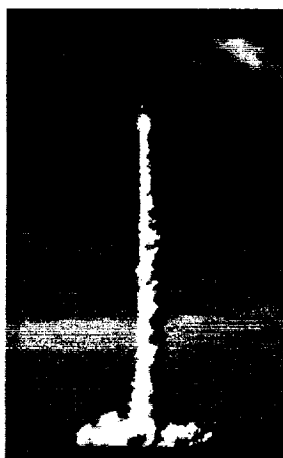
Lessons Learned

- As seen in the tailoring of the Restraint/Release System to Landsat 7, is it unwise to change critical functional dimensions such as those in the shock absorber mechanism. If you must do so as an element of the design, document such seemingly unimportant things as bench test procedures and known design limits and be sure to record them in the assembly drawing. It is essential to indicate key functional dimensions as such so they won't be treated lightly. Keep in mind that friction is present when you don't want it, and disappears when you do!
- Testing deployables early in satellite I&T can uncover problems before they affect the critical path. If the choice had been made to defer the Landsat 7 S/A deployment test until later in the I&T flow, shipment could have easily been shifted out in time, ultimately leading to a slipped launch date.
- Test g-negation MGSE ahead of time and even so be ready for problems, especially when taking a new approach. Don't ignore or brush off seemingly minor checkout issues with MGSE unless there is more than enough time to correct unforeseen problems when its used the first time. If you check out MGSE way ahead of time, make adequate plans to fully protect the MGSE while it's in storage.
- Load washers can be a very helpful element for assurance of cable preload. Don't use nut torque only when preload is as critical as it was in this application.
- Using a rigid granite deployment surface (even if it is comprised of several large granite blocks with seams) beats a cheap epoxy floor. In addition, elevated surfaces are easier to clean and stay cleaner.

Conclusion

As can be seen from the monumental effort expended to get the friction force in the shock absorber mechanism just right, it can be unwise to rely on friction in mechanisms. To dissipate energy, other approaches such as crushable honeycomb should be considered. The third pyrotechnic deployment of the Landsat 7 solar array occurred on Dec. 8, 1998. This final full deployment was completely nominal and laid to rest the remaining concerns about the L7 RRS.

Many hours of problem solving, brainstorming of new ideas, and hardware re-testing were consumed in the flight qualification testing of the Landsat 7 solar array and its restraint/release system. It took the concerted teamwork of both prime contractor and government engineers to get the job done as well as communicate the progress of the recovery efforts back to NASA Goddard Space Flight Center.



In resolving the numerous testing problems that arose, the importance of well-tested MGSE was re-enforced in the minds of all involved, and it is hoped that this paper extends that message to many more in the aerospace mechanisms community. Finally, it should never be forgotten that heritage hardware is often taken for granted and that it requires special consideration unless it is truly an exact copy of what was previously used and it will be applied very similarly.

Epilog

The Landsat 7 spacecraft was launched on a Delta 7920-10 booster from VAFB Space Launch Complex #2 (SLC-2) at 11:35 am (1935Z) on April 15, 1999. The solar array released correctly approximately 12 minutes later and deployed successfully. The deployment time was estimated at 40 seconds, \pm 20 seconds, based on a rough plot of ACS telemetry of the spacecraft attitude rates. To date, the solar array performance has been flawless, both mechanically and electrically.

Acknowledgements

The author wishes to recognize the outstanding technical efforts of Mr. Hugh McMenamin, LMSSC, under the very capable management of Mr. Robert LeRoy. Also at LMSSC, Mr. Neal Shepard contributed his expertise across the board and left the author in awe of his ability to cut through the noise and churn out new knowledge on a steady basis. Finally, for his ability to analyze a situation and quickly get to the root of any mechanical problem he was presented with, the author gratefully acknowledges the talents of Mr. Charles Teleki of Swales Aerospace. The success of the solar array on-orbit speaks to the value added by the members of the entire team of technical managers, engineers, and technicians who brought the flight qualification of the array to a successful conclusion.

References

(All references are available from the EOS Library at GSFC, (301) 286-5641, or from the author.)

"Critical Design Review Package for Electrical Power Subsystem, Solar Array Assembly" CDRL-A059, 5 May 1995. (EOS Library# 6200)

"First Solar Array Manual Deployment", LMMS PIR U-S/C-L7-1195-SYS Rev A, Neal Shepard, 2 February 1998. (EOS Library# 9482)

"Design and Development of an Improved Landsat 7 Solar Array Retention System", LMMS PIR U-S/C-L7-1340-SYS, Neal Shepard and Hugh McMenamin, 24 March 1999. (EOS Library# 11421)

"Landsat 7 Failure Modes and Effects Analysis – Solar Array Panel Deployment System (PDS)", LMMS PIR U-S/C-L7-0158-SYS Rev. A, G. Smith and R. Haffery, 18 April 1995. (EOS Library# 5883)

"Landsat 7 Solar Array Pyro Release Anomaly Review" presented to NASA GSFC Code 300, DRAFT, 29 June 1998. (Available from the author.)

"L7 PDS Restraint Cable Development Test Results" LMMS PIR U-S/C-L7-1144-MECH, Tony Kull, 13 March 1997. (EOS Library# 9503)

"Landsat 7 Solar Array Attachment Loads", LMMS PIR U-S/C-L7-1275-SYS, J. Ferraro, 27 July 1998. (EOS Library# 10866)

"Updated Results of Solar Array Panel Deployment Analysis", LMMS PIR U-S/C-L7-0119-EPS, C.K. Lo, 19 January 1995. (EOS Library# 6452)

"Solar Array Retention Cable Development Testing", LMMS PIR U-S/C-L7-0389-MECH, C.K. Lo and R.Coscia, 8 November 1994. (EOS Library# 7300)

"Cable Cutter, Ordnance Activated Device (OAD)" LMMS Dwg# 23023463, Issued 5 May 1995. (EOS Library# 10592)

Deployment Dynamics of Solar Arrays with a Link-in-Slot Hinge/Latch Mechanism

Walter K. Daniel^{*} and G. Michael Bidinger^{**}

Abstract

A solar array mechanism with both hinge and latch characteristics has been designed, developed, tested, and flown in orbit. Dynamics analysis of this link-in-slot device showed that no over-deployment took place when the dynamic coefficient of friction was higher than 0.4. The mechanism design has been verified in ground-based deployment tests and proven in flight.

Introduction

Orbital Sciences Corporation has developed and patented a combination hinge/latch mechanism for solar arrays that has been used on flight programs. The device allows for secure stowing of folded arrays and high stiffness when opened. Panels can over-deploy and rebound during deployment so analysis was performed to understand the dynamics. Loads during deployments were also studied.

Hinge/Latch Mechanism Design

Each hinge/latch mechanism has three types of components: two housings, one link, and four pistons. The housings are attached to the two bodies that will be connected by the device (body-panel or panel-panel). Each housing contains two spring-loaded pistons that pull the link into a slot. The link is connected with a pin to the pistons allowing rotation of the two bodies when the link is not captured in the housing.

A drawing of the mechanism in the initial position is shown in Figure 1. Note that the pistons and housing on one end of the link have been omitted for clarity. The link is perpendicular to the housing axis and is in contact with the end. The deployed configuration of the mechanism is shown in Figure 2. The link axis is now aligned with the housing axis and the pistons have retracted so that the link is in contact with both sides of the housing.

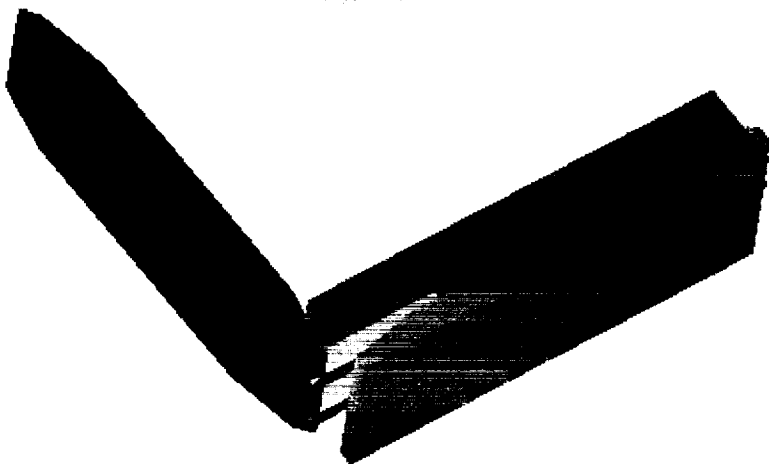


Figure 1. Mechanism in Initial Position

^{*} Mechanical Dynamics, Inc., Austin, TX

^{**} Orbital Sciences Corporation, Germantown, MD

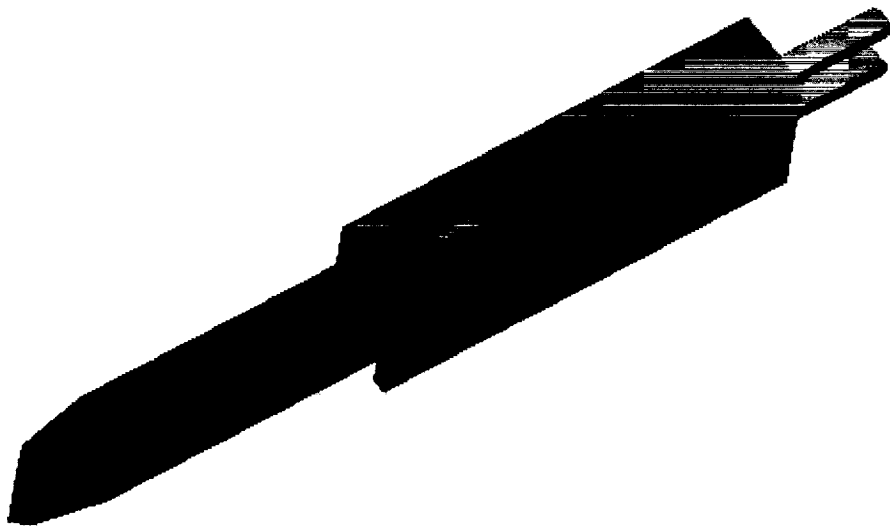


Figure 2. Mechanism in Deployed Position

The housings are embedded in solar panels for use in flight arrays. A variety of link designs have been used including straight and angled ones. An advantage of the design is that links between stowed panels are in contact with the attached housings resulting in a secure assembly for launch.

Analysis of Dynamics

Mechanical Systems Simulation technology was used to analyze the hinge/latch and solar array deployment dynamics. The goal was to correlate an analytical model with ground testing results then use the model to predict on-orbit behavior of the mechanisms. The tool used was ADAMS from Mechanical Dynamics, Inc [Reference 1].

A model of one hinge/latch connecting two panels was developed. It contains seven rigid parts: two panels, two housings, two pistons, and one link. The panels are representative of those used in various array configurations and are 55.9 cm by 28 cm and weigh 2.3 kg. One panel is attached to ground and the other panel is free to deploy. Each piston is connected to its housing with a translational joint; note that only one piston is necessary in this rigid model to represent the two pistons in the mechanism. The link is attached to each piston with a revolute joint. Figure 3 is an image of the ADAMS model.

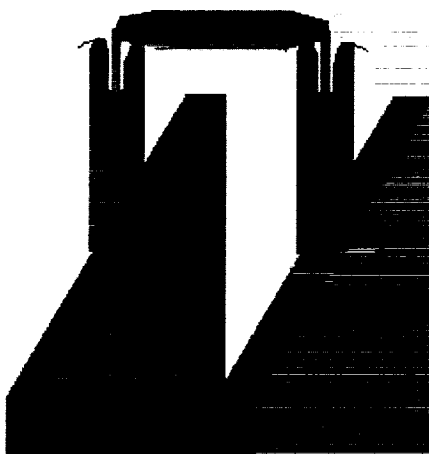


Figure 3. ADAMS Model of Mechanism

The springs that connect the pistons to the housings each have a rate of 158 N/m (17.9 lb/in). Each housing in the ADAMS model contains only one spring element so the effective rate is 317 N/m (35.8 lb/in). Each spring element has a preload in the initial position that starts the deployment motion.

Interaction between the link and housings is modeled with curve-to-curve contacts. Contact along smooth curves produces more accurate results for sliding motions than do contacts along faceted surfaces. Spline curves were added to each side of the housing and to the link. These curves follow the housing and link profiles more closely than the simple extrusion geometries used to model the parts. As shown in Figure 4, the curves actually extend beyond the edges of the housings. The extensions were used to help the curve-curve contact detection algorithm quickly resolve the point at which the two curves touch at the start of the simulation.

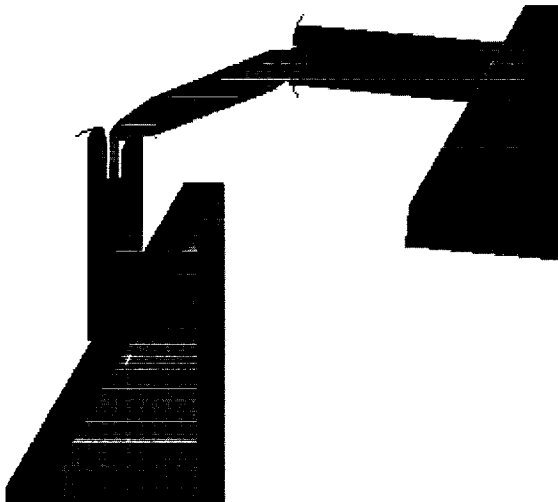


Figure 4. Model During Deployment

Each two-dimensional contact includes normal force (impact), transverse force (friction), and torque (also due to friction). In Figure 5, the model has reached the final deployed position. The springs pull the pistons, which in turn pull the ends of the link into the housing slots. There are normal forces on each side of each housing so there are also frictional forces at each location. These frictional forces provide the latching effect of the mechanism.

Engineering handbooks report the coefficients of friction between aluminum and mild steel as 0.61 static and 0.47 dynamic [Reference 2]. These values do not take into account the coatings used on the housings and link nor do they include the effects of vacuum that will be present in flight. The analysis effort focused on the dynamics with varying amounts of friction.

The model was run with dynamic coefficients of friction of 0.2, 0.3, and 0.4. The plots in Figure 6 show the angles between the piston and link. Angle1 is for the housing on the left that was attached to the grounded panel. Angle2 is the piston-link angle on the side with the panel that moved during the deployment simulation.

When the coefficient of friction is 0.2, the panel over-deploys almost 90 degrees and has not captured by the end of the run. In the high friction case, the panel over-deploys by approximately 10 degrees and is quickly captured into the final position. Higher friction coefficients would result in even less over-deployment. Note that the Angle2 curves are similar for all three cases. The link quickly settled in the housing on the deploying panel so that any over-deployment was due to motion in the housing on the grounded panel.

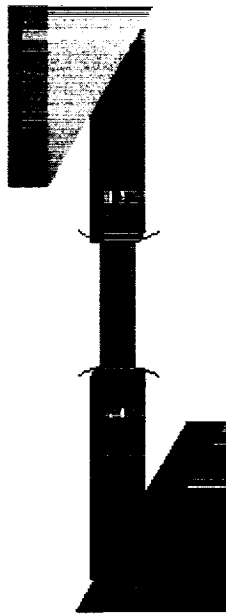


Figure 5. Model in Deployed Position

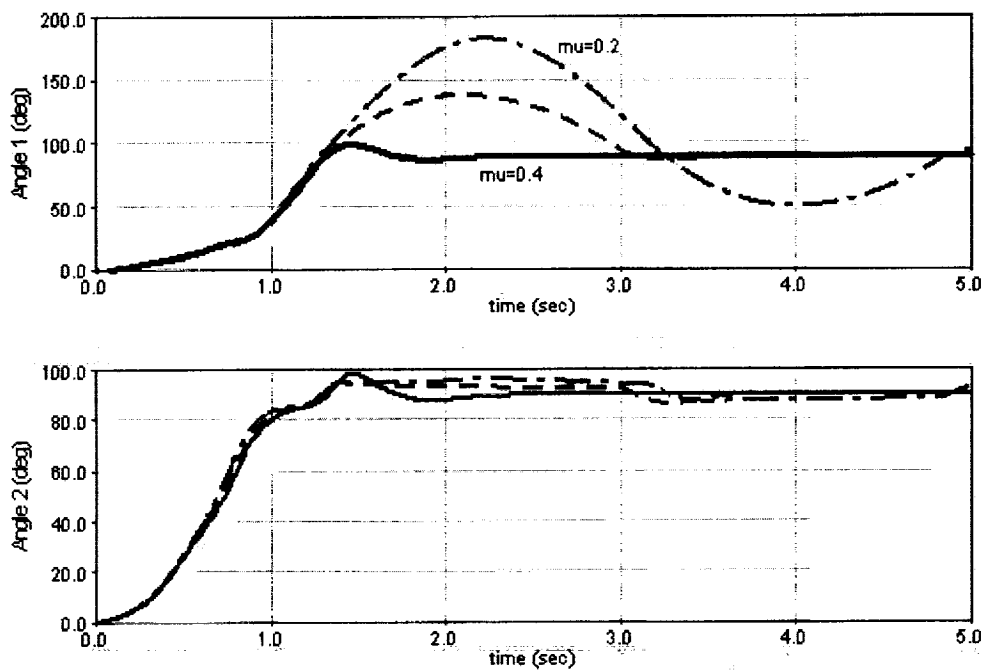


Figure 6. Angles Between Link and Pistons

Piston displacement is plotted in Figure 7. Piston1 is in the housing on the grounded panel while Piston2 is on the deploying panel. With low friction, the Piston1 curve shows how the link is pulled out of the housing by over-deployment. At a coefficient of friction of 0.4 the piston moves into the captured position. The Piston2 curves reflect the Angle2 curves in that the housing on the deploying panel quickly captures the link and does not experience any pullout motion.

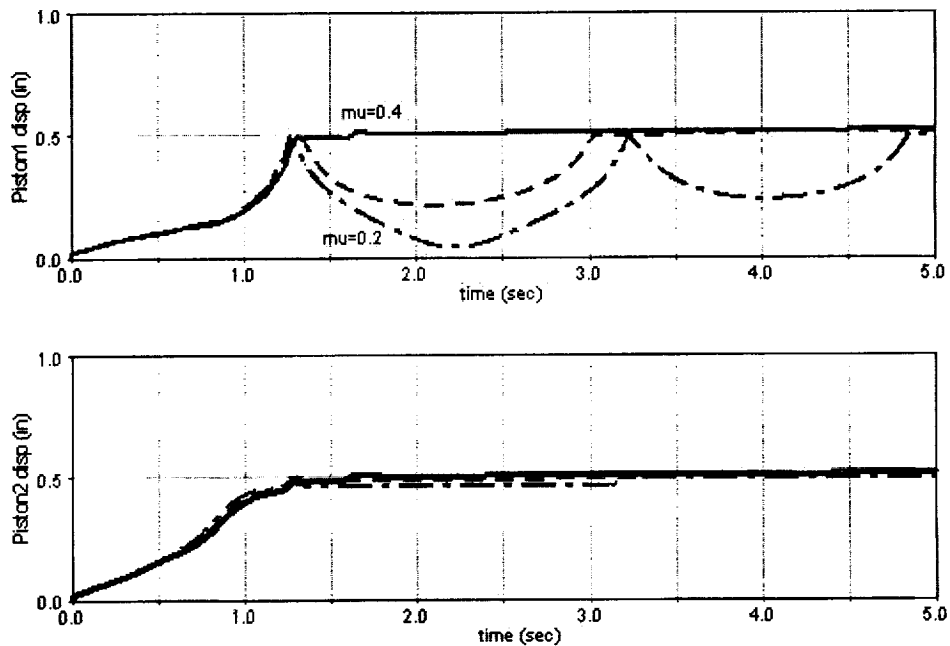


Figure 7. Piston Displacements

One concern with this mechanism design is the possibility of high loads being applied to the solar panels during deployment. This rigid body model predicts the deployment motion but the resulting contact forces can be high in magnitude (see Figure 8). In the actual solar array the panel can flex when the link is pulled into a housing that results in lower forces plus structural damping. Further work in this area will need to use flexible bodies for the panels to accurately find loads and stresses.

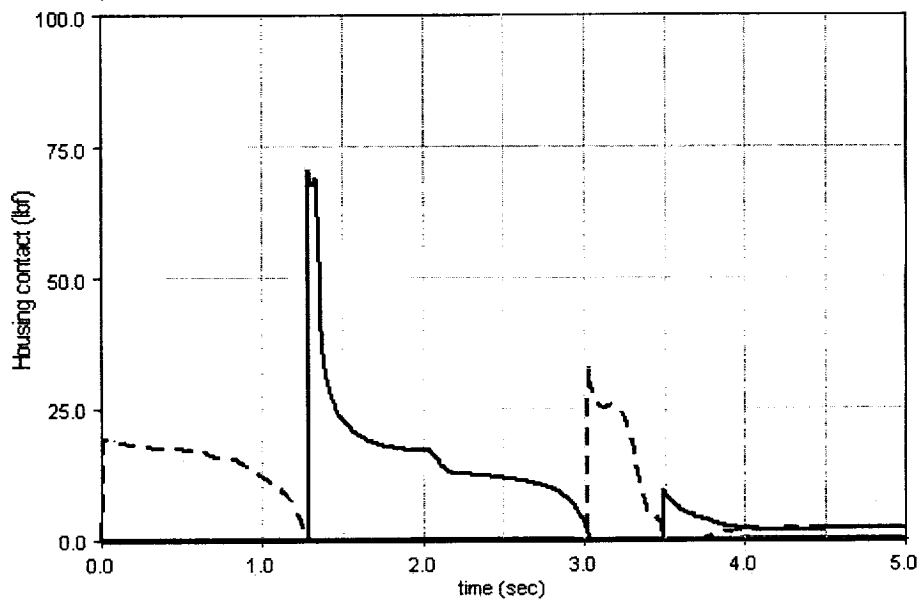


Figure 8. Contact Force Magnitude

The goal of this analysis effort was to extend the model to solar arrays with multiple panels and several hinges. Unfortunately, the approach described in this paper took a substantial amount of development and the execution times (several minutes even on a fast computer) were too long. An alternative approach would be to use the present model to develop an analytical representation of the link-housing interaction. For

example, a torque could be applied on the link that includes an impact function that is dependent upon piston position. Such a model would run substantially faster while accurately reflecting the deployment dynamics.

Ground Testing

A solar array that incorporates hinge/latch mechanisms has been fabricated and tested for the TSX-5 spacecraft [Reference 3]. Four different types of links were used in the design. Ground testing of this design was a significant challenge due to the complexity of the deployment motion. Tests were performed using cables and helium balloons to offset gravity. The tests were successful and provided confidence in the array design.

Flight Experience

An initial version of the hinge/latch mechanism was used on the EarlyBird spacecraft that CTA Space Systems (later part of Orbital Sciences Corporation) built for Earthwatch. The solar arrays deployed successfully but an unrelated power subsystem problem ended the mission after four days [Reference 4]. Figure 9 shows the EarlyBird spacecraft with the solar array deployed. The ADAMS models described earlier were based on one of the hinge types used on the TSX-5 solar array. The mission was scheduled for launch in late 1999 but has been postponed to March 2000 [Reference 5]. As a result flight deployment results were not available before the publication deadline.



Figure 9. EarlyBird Spacecraft

Conclusion

The hinge/latch design represents a unique approach to satisfying structural requirements for both the stowed and deployed configurations. Deployment dynamics of arrays using these mechanisms are challenging to analyze and test but flight experience to date has been positive. An analytical representation of the hinge/latch is being developed in order to build models of complex solar arrays.

Acknowledgements

The authors wish to acknowledge Walter Holemans who developed the hinge/latch mechanism design while at CTA Space Systems. He also directed the detailed design of the components that were used on the EarlyBird and TSX-5 missions.

References

1. *Building Models in ADAMS/View*, Mechanical Dynamics Inc., 1999.
2. Avallone, E. A. and Baumeister III, T., *Mark's Standard Handbook for Mechanical Engineers, Tenth Edition*. McGraw-Hill, 1996, page 3-23.
3. Details of the TSX-5 program are available at <http://www.te.plk.af.mil/TSX5HOME/TSX5.cfm>
4. For a description of EarlyBird spacecraft see <http://www.digitalglobe.com/company/spacecraft/earlybird.html>
5. The Vandenburg AFB launch schedule is available at <http://mocc.vandenberg.af.mil/launchsched.asp>

Inflatable Boom Controlled Deployment Mechanism for the Inflatable Sunshield In Space (ISIS) Flight Experiment

George H. Sapna III, John Folke, Charles R. Sandy, and David P. Cadogan*

Abstract

ILC Dover, Inc. has developed the wire brake Controlled Deployment Mechanism (CDM) for use in the Inflatable Sunshield In Space (ISIS) Shuttle flight experiment. The ISIS experiment is a 1/3-scale sunshield demonstration unit precursor to the Next Generation Space Telescope (NGST). The NGST sunshield is a 35 x 15 meter diamond-shaped multi-membrane sunshield that will be used to passively protect the telescope from thermal radiation and stray light. The ISIS requirements call for a smooth and predictable deployment of the sunshield by inflatable booms that are governed by the wire brake CDM. To deploy the sunshield, inflation gas is introduced into the inflatable booms, which gives them rigidity and causes them to unroll from the stowed position. As the boom is inflated, the torsional resistance of the wire brake device causes the pressure in the booms to increase until the point where it overcomes the torsional resistance of the wire brake and the boom unrolls. The wire brake operates by converting mechanical energy to heat through the plastic deformation of a ductile metal wire. Associated mechanisms react the torque from the wire brake to the inflated portion of the boom. Through use of the CDM, the boom maintains a constant internal pressure during deployment to provide sufficient structural stiffness. The wire brake governs the internal pressure of the tube such that the boom provides the required force to deploy the sunshade plus any contingency load. Technical information detailing the development, design, analysis, and testing of the CDM are described in this paper.

Introduction

Control of large space structures during deployment of articulated systems is of critical importance. Allowing portions of the structure to deviate from a prescribed path can result in snagging or impact between surfaces that can prevent the structure from properly deploying or may cause damage to satellite systems. In the case of large inflatable space structures, mechanisms and specific folding methods are used to provide the required control of various parts of the structure during deployment. These mechanisms and methods are typically simple in nature, low in mass, and small, keeping in line with general spacecraft design practices.

Inflatable structures offer the potential for lower mass and packing volume for large space structures such as antennas, solar arrays, and solar sails as compared to comparable mechanical systems. This has been demonstrated in studies for the Next Generation Space Telescope, conducted by NASA GSFC (Figure 1). The results of these studies lead to the development of the ISIS flight experiment, scheduled to fly in 2001, to verify performance of inflatable structures.

One of the critical objectives of the ISIS flight experiment is to evaluate the amount of control exhibited by the inflatable booms while they are deploying the sunshield membranes. The booms must deploy linearly, provide structural support during deployment, and provide an axial force to the membranes to extract them from their own deployment mechanism. This is accomplished by a mechanism that is embedded in the ends of each of the inflatable booms, called the wire brake. The wire brake was developed specifically for use with space inflatable structures.

* ILC Dover Inc., Frederica, DE



Figure 1. ISIS ½-Scale Model

Background

The wire brake was designed to enable the controlled deployment of an inflatable boom. In general, inflatable booms must act as structures during deployment, and they must deploy in a controlled manner. One way of creating an inflatable boom is to make a cylindrical tube with end caps. The unpressurized tube can be flattened and rolled on to a spool. By introducing inflation gas into the free end of the tube, the tube will unroll from the spool. The spool rotates as the boom is deployed. A controlled deployment mechanism is used to regulate the rotation rate of the spool. The resistance of the spool is set at a level that allows adequate pressure to be maintained in the inflated portion of the boom while the deployment envelope and rate remain predictable. Figure 2 shows the controlled deployment mechanism used for ISIS.

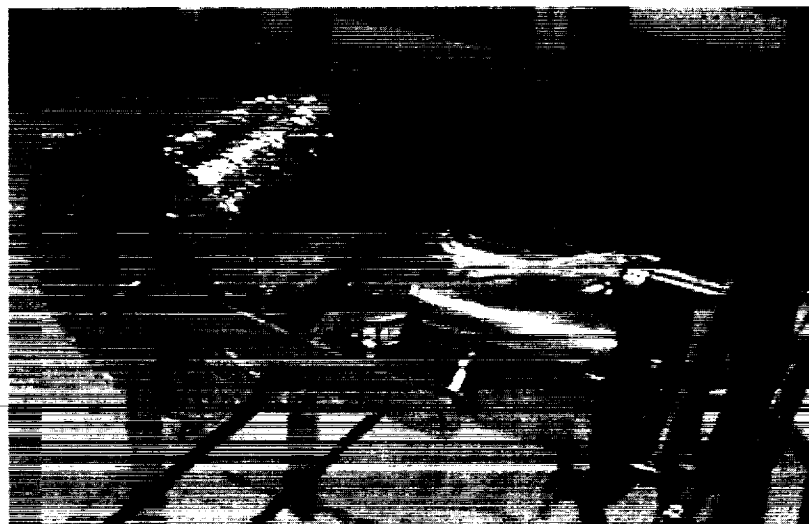


Figure 2. ISIS Controlled Deployment Device with Boom

This approach to deploying an inflatable boom is similar in principle to the workings of a common party favor. In a party favor, a wire torsion spring that runs along the surface of the paper tube in the axial direction is responsible for the controlled deployment and beam stiffness during inflation. The spring provides a balancing torque, which resists the torque introduced by the inflation pressure. In order for the party favor to deploy, the torque created by the inflation gas must be greater than the resisting torque of the spring. By changing the spring torque, the rate at which the party favor unrolls is adjustable for a given inflation pressure. Furthermore, the inflation pressure gives the paper tube enough stiffness to support itself as a structure.

In the case of a party favor, one of the advantages of the spring controlled deployment mechanism is that the torsion spring rolls up the paper tube after the inflation pressure is removed. However, in the case of a spacecraft or space structure, it is not usually desirable to re-pack an inflatable boom after it has been deployed in-orbit. The problem with an embedded spring is that it continues to apply torque even after the tube is deployed. This residual spring load reduces the stiffness of the boom because part of the skin tension that would otherwise be contributing to the structural stiffness is lost in the balance of the spring torque. Ultimately, this indicated that there was a need for a mechanism that dissipates energy, rather than storing it, while maintaining the same deployment characteristics of the party favor spring.

Many ideas have been investigated to design a mechanism that enables the controlled deployment of an inflatable boom. One example is a mechanism that uses friction to dissipate energy. This mechanism operates by sliding two surfaces together to generate heat as the spool is rotated. Frictional devices are very effective in providing resistance without storing energy and they are small, lightweight, and simple. The drawback of this approach is that frictional devices are generally not recommended for use in space because of the potential for variation of frictional characteristics when operating in the space environment.

Another example of a controlled deployment mechanism for an inflatable tube is Velcro®. When Velcro® is applied to the surface of an inflatable tube in a way that facilitates hook and pile interlocking during rollup, it is effective in producing a controlled deployment with adequate interim beam stiffness. However, Velcro® is bulky when applied to the entire length of a tube. A third controlled deployment mechanism is one that uses dampers to dissipate mechanical energy. The primary reason why a damper is not used, however, is because the damping torque is a function of the rate at which the boom is unrolled. When deploying inflatable booms, constant resistance regardless of deployment rate allows for smoother deployment. A fourth mechanism is being developed by ILC and AEC-Able, called a spring brake device. It uses radial sets of rollers and springs to dissipate energy through elastic work. The mechanism is configured such that the stored spring energy is released as the device rotates. Finally, a fifth solution, called a wire brake device, dissipates energy by plastically deforming metal. It works by transferring soft wire from one drum to another. In the process, the wire is bent to fit around the drum.

Explanation of the Wire Brake Device

Description

The wire brake is a simple device that dissipates energy by plastically deforming metal. The device is housed inside the hub of a spool, which is used to roll up a flattened inflatable boom. The wire brake is attached to a reaction arm through a central shaft, and the boom end cap inside the hub of the spool. The reaction arm is connected to a yoke, which straddles the inflated portion of the boom. The yoke prevents the reaction arm from rotating with the spool (Figure 3). As the boom unrolls, the spool rotates relative to the reaction arm. The wire brake resists motion of the spool, thus controlling the boom's rate of deployment.

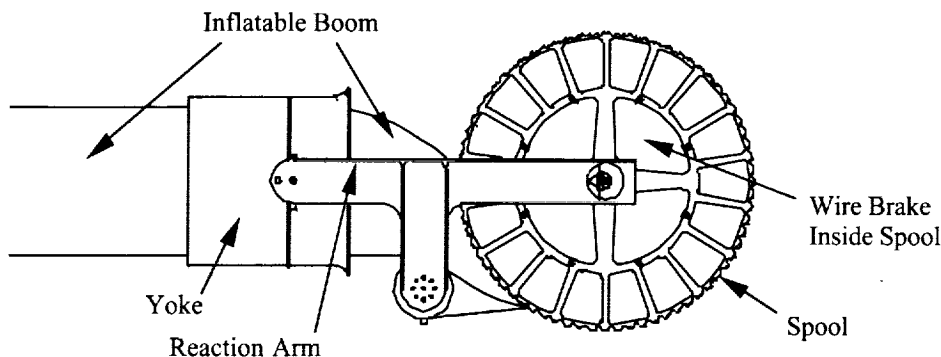


Figure 3. Controlled Deployment Device

The wire brake consists of an input shaft, a supply drum, a take-up drum, bearings, and a ductile wire (Figure 4). When the spool is rotated relative to the input shaft, ductile wire is wrapped around the take-up drum, as it unwraps from the supply drum. During the wire transfer, mechanical energy in the form of rotary motion is converted to heat energy. The bending and unbending of the wire as it unwraps from the supply drum and wraps onto the take-up drum accounts for the energy conversion.

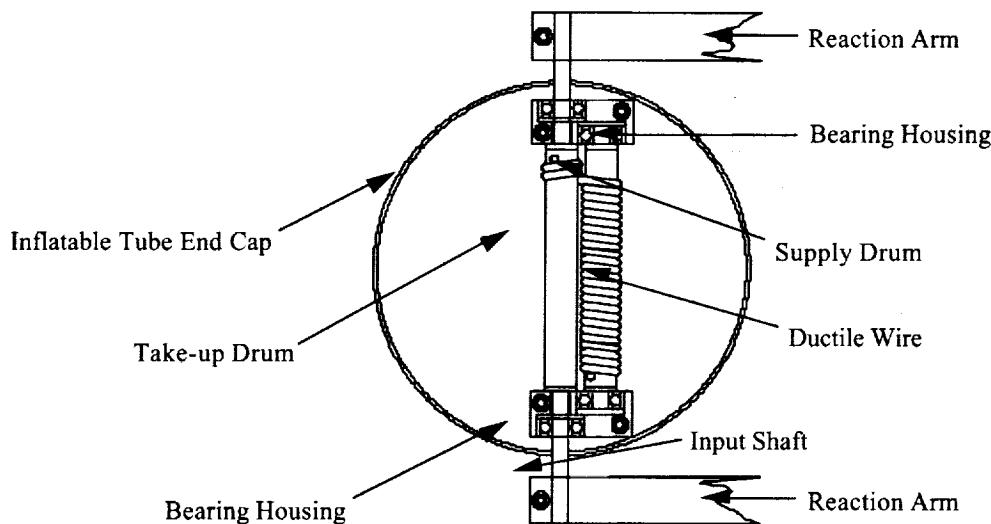


Figure 4. Wire Brake Mechanism Schematic

Theory of Operation

In order to select the wire material, wire diameter, and drum diameters, a simple theory was devised to calculate the approximate strain of the wire. Using the strain, the average stress of the wire could then be determined from the stress-strain curve. The average stress and cross-sectional area of the wire are used to compute the force in the wire, which is used to compute the torque required to wrap the wire on a drum. The success of the analysis, however, relies on the accuracy of the strain estimate.

The initial goal of the analysis is to predict the parameters that place the wire material in the plastic region of the stress-strain curve. Figure 5 shows a diagram of the model.

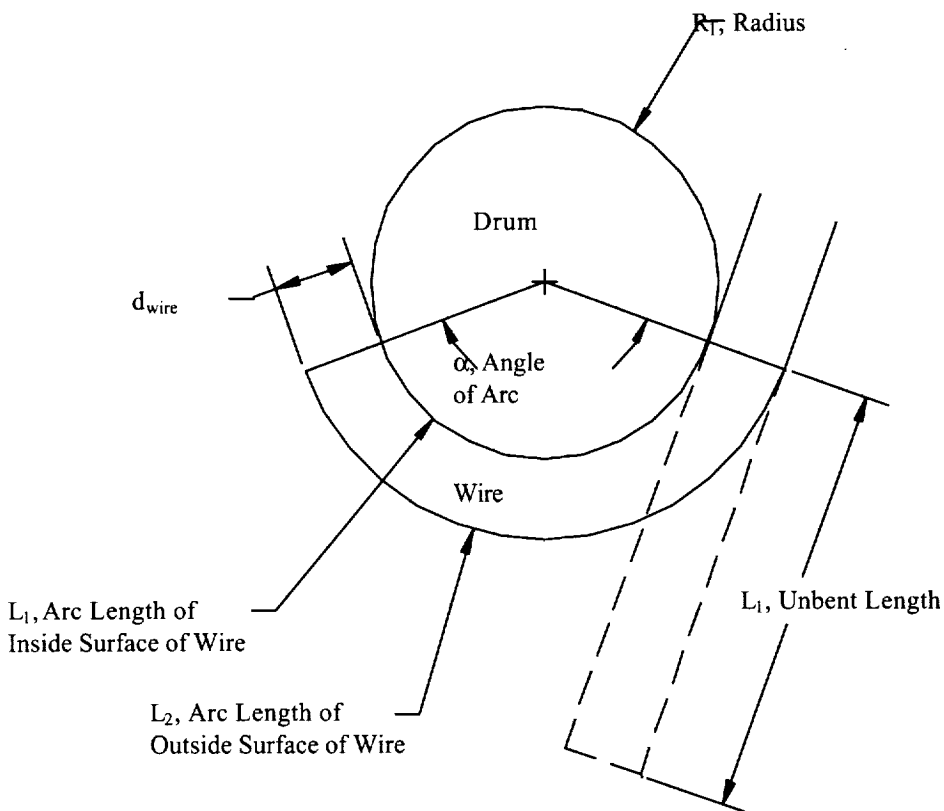


Figure 5. Wire Bending Model

As wire bends around a drum, it elongates to conform to the drum surface. In this model, the wire is assumed to bend around its inner surface rather than its neutral axis. This means that in bending there is only tensile stress and that the wire does not stretch or compress where it contacts the surface of the drum. The arc length of a wrapped segment of the wire, L , is proportional to the radius of curvature, R , and the angle, α , swept by the segment as shown below.

$$L = \alpha R \quad (1)$$

For the inside surface of the wire, the arc length is given by

$$L_1 = \alpha R_1, \quad (2)$$

where the radius of curvature is equal to the radius of the drum, R_1 . For the outside surface of the wire, the arc length is

$$L_2 = \alpha(R_1 + d_{\text{wire}}), \quad (3)$$

where the radius of curvature is equal to the sum of the radius of the drum and the diameter of the wire. Because it is assumed that the inside surface of the wire does not change length during bending, then the arc length of the wire segment after bending is equal to the original length of the wire segment before bending. Furthermore, the maximum strain of the wire occurs at the outside surface. Therefore, the maximum strain of the wire, ϵ_{\max} , can be written as the difference between the inside and outside arc lengths divided by the initial wire segment length. Thus, the equation follows from the principle of strain.

$$\epsilon_{\max} = \frac{L_2 - L_1}{L_1} \quad (4)$$

Substituting equations (2) and (3) into equation (4), the following expression is obtained.

$$\epsilon_{\max} = \frac{\alpha(R_1 + d_{\text{wire}}) - \alpha R_1}{\alpha R_1} \quad (5)$$

After simplification, the maximum strain of the wire, which occurs at the outside surface, is

$$\epsilon_{\max} = \frac{d_{\text{wire}}}{R_1}. \quad (6)$$

Since no strain occurs at the inside surface of the wire, then the average strain, ϵ_{avg} , in the wire is one half the maximum strain.

$$\epsilon_{\text{avg}} = \frac{d_{\text{wire}}}{2R_1} \quad (7)$$

Because this theory is very basic, experimental data was developed to correlate the analysis. Several versions of the mechanism were developed and tested for comparison to the analytical performance assessment.

Development and Results

Construction and Testing

For the ISIS setup, tests were conducted with the controlled deployment device in order to determine the torque, which provides the proper balance between tube stiffness, deployment rate and deployment force. The results indicated that the ISIS controlled deployment device must provide a resistive torque of 6.9 N-m. This is the torque that was used as the target value in the design of the wire brake.

The first wire brake was built and tested using commercially pure aluminum wire. The aluminum was selected mainly because of its commercial availability. Highly pure aluminum also provides greater elongation than aluminum alloys. In determining the wire diameter, a strain range was selected that bounded the wire diameter range. For 1100-0 aluminum, the plastic range lies between strains of 24% and 42%. This strain range was selected because it is outside of the elastic and failure regions for temperatures between 21 °C and –100 °C. The temperature range was selected because room temperature and the temperature at which the wire brake will operate inside the controlled deployment device bound it. Using equation (7), the wire diameter range was calculated for the strain range. A supply and take-up drum diameter was chosen as 12.7 mm. This resulted in a wire diameter range between 3 mm and 5.3 mm. The stress-strain curve also indicated that the load required to achieve high strain would be significantly higher at low temperatures as compared to room temperature. This indicated that low temperature testing was required.

Initially, a 3.18-mm diameter wire was installed into the mechanism. The torque that was required to rotate the input shaft was measured as 1.92 N-m. According to equation (7), the average strain in the wire should be approximately 25%. Although the wire brake is designed for only one bending cycle, the life of the device was tested. The 3.18-mm diameter wire broke after 6 cycles.

The second wire brake was built to operate over a wide range of torque. This was accomplished by adding an adjustment roller that would impose an additional bend in the wire. Figure 6, shows the second wire break mechanism.

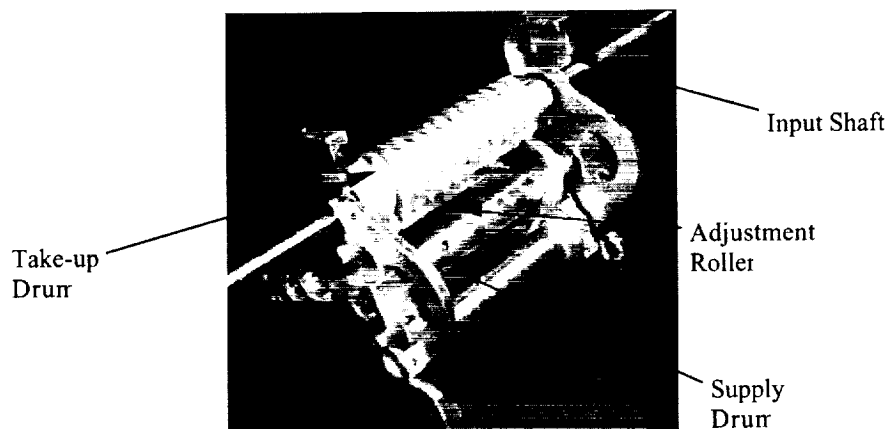


Figure 6. Wire Brake Mechanism

As in the first wire brake, the supply drum, take-up drum, and adjustment roller are 12.7 mm in diameter. With an adjustment roller, the torque is easily tuned without changing the wire. Two aluminum 1100-0 wires were tried in the adjustable wire brake mechanism; a 0.00476 m diameter wire and a 0.00635 m diameter wire. The tests were conducted at 20 °C and -100 °C. Table 1 shows the torque measured at the maximum and minimum adjustment points.

Table 1. Adjustable Wire Brake Test Results

Wire Diameter [m]	Torque [Nm]			
	20 °C		-100 °C	
	Minimum Adjustment	Maximum Adjustment	Minimum Adjustment	Maximum Adjustment
0.00476	3.39 - 3.73	-	-	-
0.00635	6.78 - 7.34	12.65 - 13.56	9.72 - 10.73	18.53 - 21.47

As Table 1 shows, the wire diameter of 0.00635 m at room temperature and with no adjustment met the 6.9 N-m torque requirement. Because the proper torque could be achieved by bending the wire only two times, the adjustable mechanism was abandoned. Subjecting the wire to 3 bends presented more risk of ultimate failure than the original two-drum design shown in Figure 3. As an alternative, multiple wires were wrapped next to each other to increase the torque from that of a single wire by a factor of the number of wires. This also reduced the overall mass of the mechanism.

Unfortunately, the preliminary analysis did not correlate well with the experimental results. According to equation (7), the 0.00635-m diameter wire chosen for the wire brake should have failed. The computed average strain significantly exceeded the published maximum strain of pure aluminum. This indicated that the principle by which the wire plastically bends to form around the drum could not be approximated by the simple theory presented here. More thought is necessary.

Ultimately, a design was chosen where 2 wires feed a central take-up drum. In the dual-feed device, the wire diameter is only half of the necessary wire diameter to produce the same torque on a single-feed device. Unlike that of a single wire design, the dual-feed wire brake mechanism will continue to provide half the nominal torque resistance in the event of a single wire breakage. Additionally, the take-up drum is relieved from bending because the bending loads are balanced by placing the supply drums in symmetry about the take-up drum. Compared to the single wire design, the risk of failure has been reduced in the dual-feed wire brake mechanism.

Conclusion

Space inflatable structures are showing promise for yielding large space structures with reduced mass and packing volume as compared to conventional structures. An important aspect of these structures is the incorporation of controlled deployment devices to ensure accurate and predictable deployments. Several mechanisms have been proposed for this purpose, including the wire brake mechanism, which uses the deformation of metal as a method of applying a retarding force to a rolled inflatable tube. The development work performed on the wire brake mechanism has lead to the conclusion that this unique approach to providing deployment control for inflatable tubular structures is viable.

References

- Cadogan, D. and M. Grahne. "Deployment Control Mechanisms for Space Inflatable Structures", 33rd Aerospace Mechanisms Conference, May 1999.
- Cadogan, D., Grahne, M., and Mikulas M. Inflatable Space Structures: A New Paradigm for Space Structure Design, 49th International Astronautical Congress, 1998.
- Sandy, C. "Next Generation Space Telescope Inflatable Sunshield Development", 2000 IEEE Aerospace Conference. March 2000.
- Popov, E. P. Engineering Mechanics of Solids. Prentice-Hall, Inc, New Jersey, 1990.

A Novel Mechanism using Shape Memory Alloy to Drive Solar Flaps of the INSAT-2E Satellite

N. Viswanatha* and T.P. Murali*

Abstract

An innovative drive mechanism developed by Indian Space Research Organisation for deployment and positioning of solar flaps is successfully working on the geosynchronous multi-purpose communication satellite INSAT-2E. The drive mechanism¹ works on linear actuators made of Shape Memory Alloy (SMA) wires and is capable of driving solar flaps in 2-degree steps, like a stepper motor. This paper describes the design of the mechanism, qualification testing and on-orbit experience.

Introduction

The second generation Indian National Satellite, INSAT-2E has a Very High Resolution Radiometer (VHRR) as payload and the passive cooler of this payload is mounted on the north side of the spacecraft. To provide a clear field of view for the cooler and to minimize IR heat radiation input into it, the solar array is mounted only on the south side of spacecraft. INSAT-2E on-orbit configuration is shown in Figure 1. A solar sail mounted on the tip of long deployable lattice boom is used to counteract the unbalance torque resulting from the solar radiation on the one sided solar array. Because of sun's changing declination over the year and conical shape of the sail, there is a change in the radiation torque produced by sail. The sail is slightly over sized to have comparatively higher torque on sail side in all the seasons. To fine balance the seasonal residual solar radiation unbalance torque, two solar flaps are mounted at the end of solar array and they are opened/closed to increase/reduce the projected area of array side to the solar incidence. This helps in improved spacecraft pointing and saving of onboard fuel.

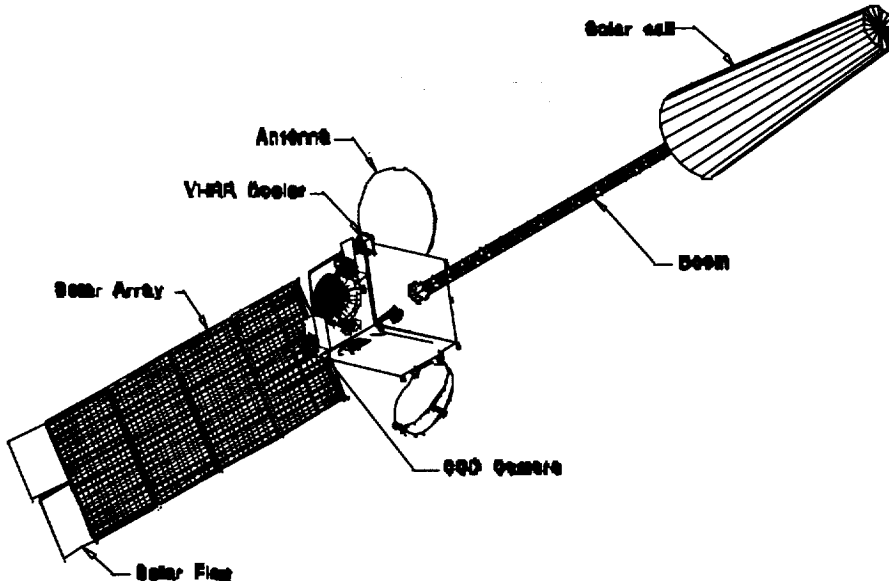


Figure 1. INSAT-2E Satellite on-orbit configuration

* ISRO Satellite Centre, Indian Space Research Organisation, Bangalore, India.

¹ Patent pending

For driving solar flaps, two drive motors, based on linear actuators of SMA are used. The use of SMA was decided over traditional electric motors and the final choice has met all the design requirements with the advantages of lower mass and cheaper cost. The motors are also magnetically clean.

Description of Solar Flap Mechanism

Two solar flaps, Flap-1 and Flap-2 of size 980 mm x 1250 mm are connected to the outermost solar panel with two hinges each (Figure 2). Each flap is independent and has a separate SMA drive motor mechanism for forward and reverse motion. When stowing the solar array to the launch configuration, the flaps are folded back to a position parallel to the backside surface of the last solar panel. The flaps are held by sandwiching them between the third panel and the last panel with elastomeric snubbers to apply hold down preloads. During the deployment of the solar array, the flaps move along with the last panel. After the deployment and locking of the solar array hinges, the flaps are opened in 2° steps to the required angle using SMA drive motor mechanisms. Up to the first 67.5° of their opening, the flaps will be

under panel shadow during all seasons. From this position, the flaps are opened farther to the required angle based on the need to fine balance the solar radiation torque. Since the daily change in the Sun's declination is very small, the flap(s) need to be moved by a step or two in a week. The flap movement is done by ground command and each command will move one step (~ 2°) in the commanded direction. The flap angle is indicated by the potentiometer built into the flap drive hinge. Each flap mechanism consists of one SMA drive motor mechanism, one Drive hinge, and an End hinge. The flaps are made by bonding two layers of Kapton film, which in turn is bonded onto a thin photo frame-like tubular CFRP frame structure.

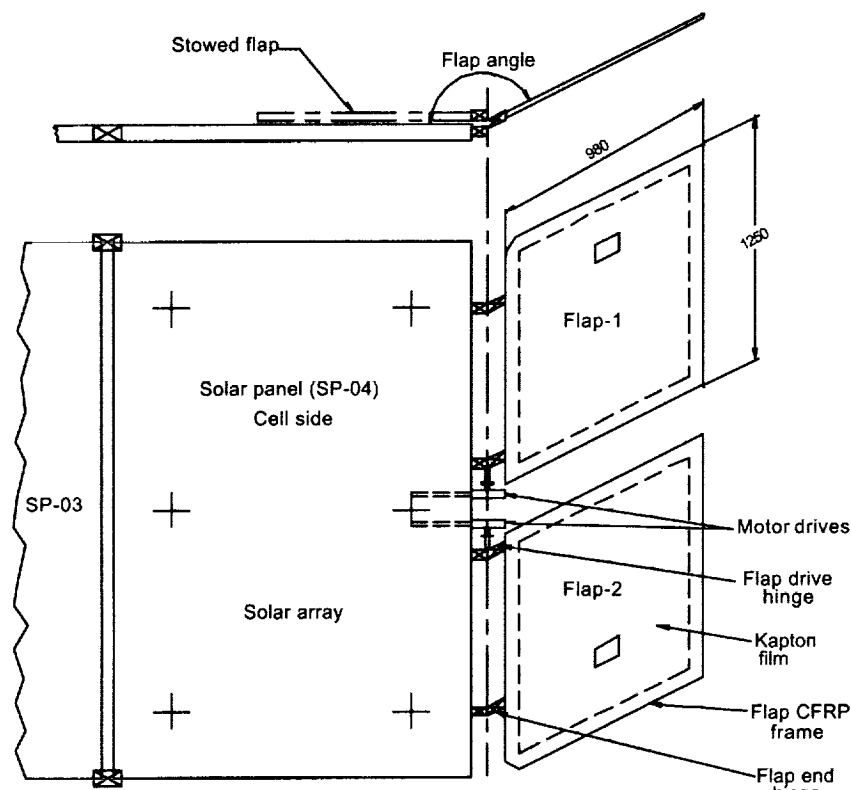


Figure 2. Schematic of solar flap drive mechanism

The Drive hinge and End hinge connect the flap and the outer solar panel. The drive hinge has a resistor disc-type angle potentiometer built in to indicate the flap angle. The hinge, as shown Figure 3, consists of two brackets with its shaft rigidly attached to the flap side bracket and the panel-end bracket is attached to solar panel. The panel-end bracket is fitted with a spherical monoball bearing. The shaft is connected to the output shaft of the SMA drive motor mechanism through a flexible shaft coupling, and this rotates the flap in steps whenever the mechanism is driven. The flap End hinge (Figure 4), is a simple idler hinge. It consists of two thin hinge brackets connecting the flap and panel with specified hinge spacing. The panel side eye-end bracket is fixed with a spherical monoball bearing. A mechanical stop is also

provided on this hinge to stop the flap from moving beyond 180 degrees position. Spherical bearings are used in the hinges to take care of any misalignment between the two hinges.

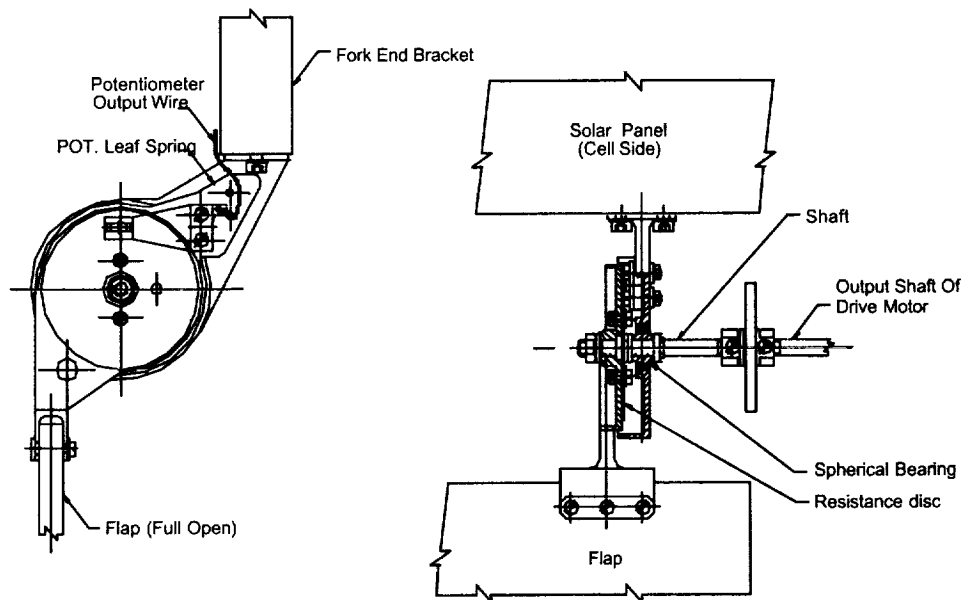


Figure 3. Flap drive hinge

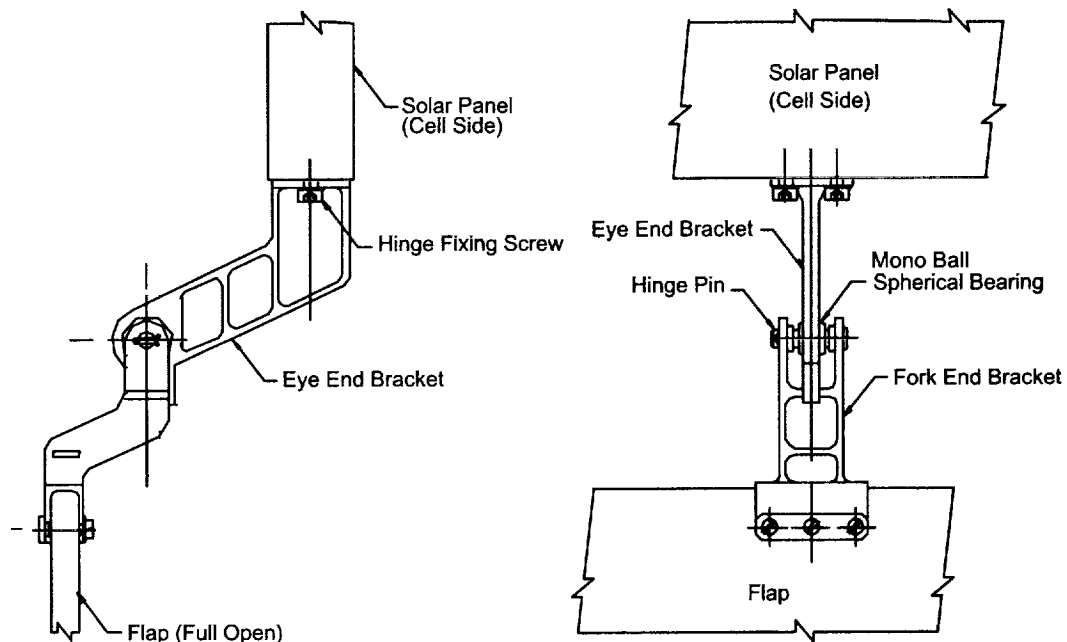


Figure 4. Flap end hinge

SMA Drive Motor Mechanism

The mechanism requirements/specifications are listed below:

Output Drive torque	: 0.2 N·m (minimum)
Drive step size	: 2 degree
No. of operations	: 10,000 steps of operations in both directions
Direction of rotation	: Both clockwise and anti clockwise
Drive angle	: 0 to 180°
Operating temperature	: -20° C to 70°C
Mass of flap	: 0.440 kg each
Inertia about rotation axis	: 0.15 kg·m ²
Drive mechanism Mass	: 0.190 kg each

The SMA drive motor mechanism mainly consists of: (a) SMA wire actuator elements, (b) Levers, Pawls and Ratchet wheels, (c) Detent mechanism, (d) Spur gear reducer, (e) Load limiting spring mechanism and other parts. Figure 5 shows the disassembled view of the mechanism. Two brackets, bracket 1 and bracket 2, give the necessary structural support to the mechanism. One aluminum alloy single-piece thermal cover is provided over the mechanism.

SMA wire actuators

Two SMA linear wire actuators of diameter 0.25 mm are used to generate the force required to drive the mechanism. One wire is used for the opening direction drive and the other for the closing direction drive. Linear wire actuators were preferred over spring-type SMA actuators as they are more efficient, require less electrical power, have faster heating and cooling rates, higher life for repeated operation, and low mass. The set memory in the wire actuator is shorter length. The SMA wire length shortens when heated above transformation temperature. Heating of the SMA wire is achieved by passing Pulse Width Modulated (PWM) electric current directly through the wire. PWM electric current heating was selected over DC heating for the improved life cycle of the SMA wire actuator. The SMA wire transformation temperatures were selected such that they are well above the estimated on-orbit temperature of the wire. The shape recovery temperature of the selected SMA actuator wire was ~90°C. The length of actuator wire was chosen to provide the required stroke within 3.5% recovery strain. The SMA wire also had two-way memory and returned to its longer length on cooling below its lower transformation temperature. Hence bias force was not required to stretch the SMA to its longer length (cold shape). This also had the advantage of higher net output force.

Levers, Pawls and Ratchet wheels

They are used to convert SMA actuator's linear stroke to rotary step motion. Two sets of lever, pawl and ratchet wheel assemblies (one set for opening and other set for closing direction) are mounted on the main shaft as shown in Figure 5. The ratchet wheels are fixed to the main shaft with their teeth in opposite direction to each other. The levers, fitted with bushing bearings are free to oscillate on the shaft. Each pawl is fitted with a bushing bearing and is mounted on to a pin fixed on one end of lever. A pawl torsion spring is also mounted on the pin to keep the pawl pressed. The pawls are provided with a guide contour to guide them for their engagement/disengagement with their ratchet wheels. The other end of the lever is connected to the wire rope terminal, which in turn links the SMA actuator. Pawl and ratchet wheel teeth are lubricated with bonded film molybdenum disulfide.

Detent mechanism

A detent wheel and a pair of spring-loaded levers provide the detent torque that is necessary for the ratchet wheels to hold them in their discrete tooth positions. The detent wheel mounted directly on the main shaft as shown in Figure 5, holds the main shaft in position when the lever and pawl are pulled back by the bias spring. The detent wheel is necessary, as after each drive step the shaft would have rotated back to the original position and might not produce any net rotation.

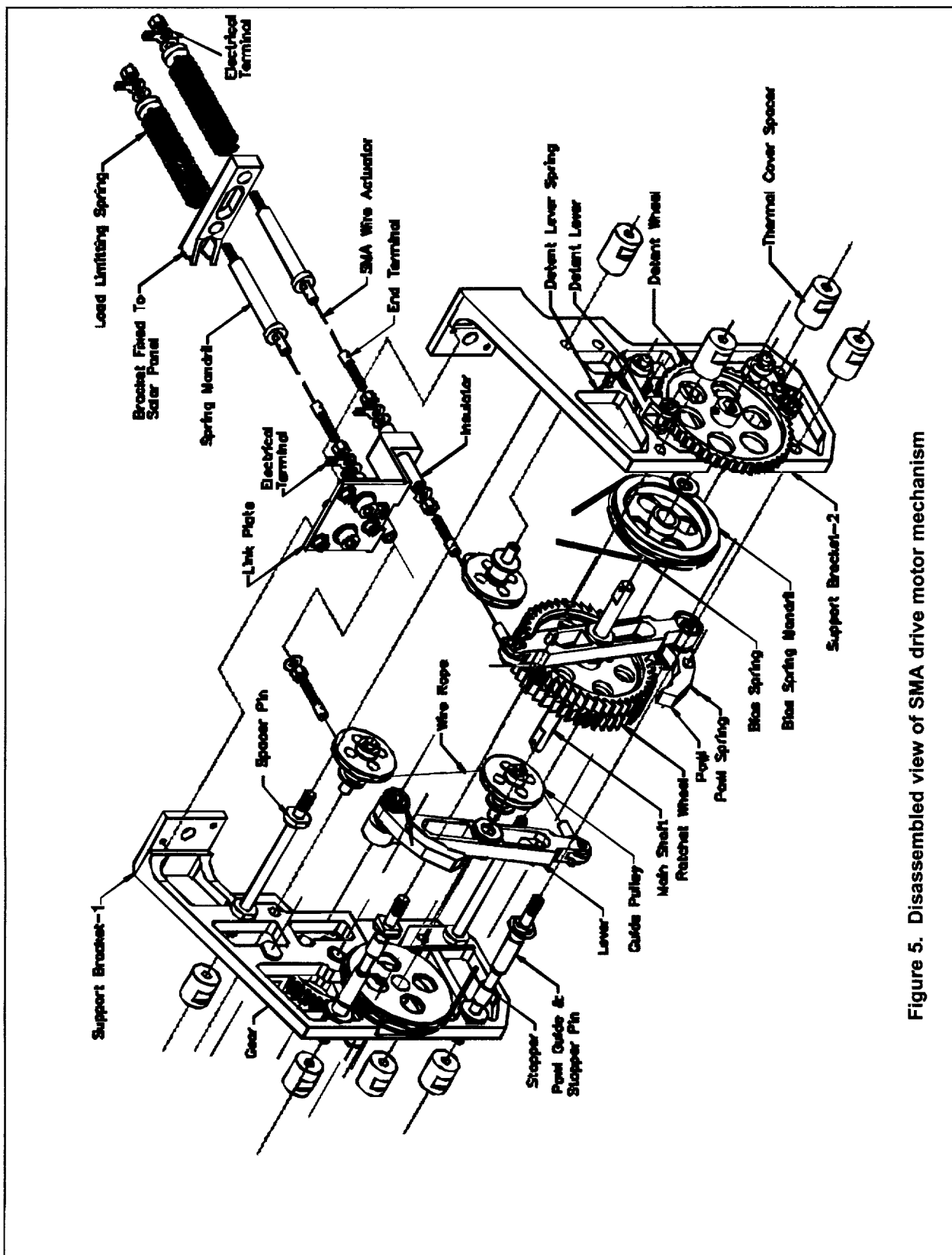


Figure 5. Disassembled view of SMA drive motor mechanism

The detent wheel has 'V'-shaped grooved teeth on its circumference and the teeth are spaced 8 degrees apart. Two detent levers, placed diametrically opposite over the detent wheel, exert load on to the wheel by using small torsion springs (detent springs). The detent mechanism also provides the holding torque to the flap, needed to keep it in the driven position against satellite attitude control disturbances.

Spur gear reducer

Spur gear reducer of 4:1 ratio is employed to reduce the 8-degree step motion of the ratchet wheel shaft to the 2-degree (approx.) step motion required to drive the solar flaps. The gear reducer also steps up the drive output torque and detent torque required at the flaps. The pinion is mounted on one end of main shaft, outside the support bracket-2 (Figure 6). The gear, supported on two bushing bearings, is integral to the output shaft.

Load-limiting spring mechanism

It is provided to limit the load build-up in the SMA wire actuator to a certain design limit, under all conditions of operations.

When the flaps reach end stops, further movement of flaps is not feasible. If the drive motor is operated in this configuration, the heated SMA wire can not contract to its full stroke as the output movement is arrested and hence the load in SMA wire would build-up leading to reduced operating life. To avoid this, a load-limiting compression spring is mounted at one end of each SMA wire with a set pre-compression (Figure 7). This spring deflects to allow the SMA wire contraction whenever the load in the SMA wire exceeds the set limit, thus limiting the load build-up in SMA wire.



Figure 6. Gear reducer assembly on mechanism

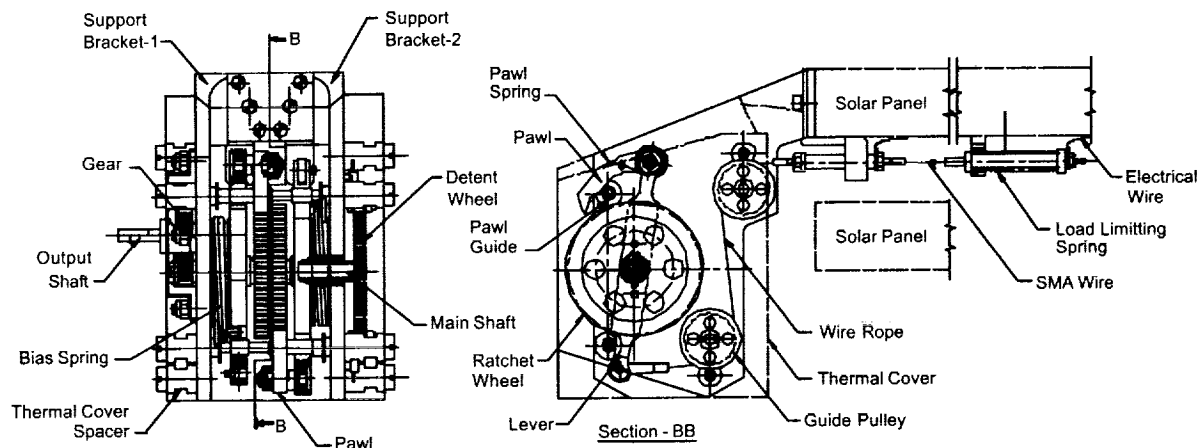


Figure 7. SMA Drive motor mechanism

In the transfer orbit of the satellite, the stacked solar array is pointed to sun. In this orientation, the panel and SMA actuators reach about 115° C. This will cause both forward and reverse SMA wires to actuate but the flaps are restrained from moving, as they are stacked. In this case, the load-limiting springs allow SMA wires to contract and limit the load in them to the set value.

Operation of the SMA drive motor mechanism

SMA wire actuators are mounted on backside of the outermost solar panel and their one end is connected to the lever through flexible wire rope link guided on pulleys (Figure 7). To step-drive the motor in the required direction, the corresponding SMA wire actuator is heated by passing electric current. The wire contracts in its length and pulls the lever to the right, turning it by 16 degrees until the lever is stopped by the stopper pin on the other end. At the same time, the pawl mounted and hinged on the lever rides over the pawl guide and gets engaged with the ratchet wheel teeth and turns it by one tooth pitch. The first half of lever stroke is used for pawl engagement and the rest for ratchet wheel rotation. The ratchet wheel, which is rigidly connected to the main shaft, rotates the shaft by ~8-degree step, equal to the ratchet wheel tooth pitch. The stroke of the lever in its operation is limited by two stepper pins, which also act as pawl guides. Once the current to the SMA actuator is removed, it cools down, becomes soft, and elongates to its original longer length by its two-way memory. At the same time, the bias torsion spring mounted on one side of lever will pull the lever back to its original place until it is stopped by the stopper pin at the bottom end. The pawl mounted on the lever is also pulled back. When the pawl is pulled back, it gets disengaged from the ratchet wheel. Disengaging the pawl is necessary for the next step motion of the flap. In the next actuation, the pawl engages to the next teeth of the ratchet wheel for another step movement. Heating the other SMA wire actuator will give an output step movement in the opposite direction as the ratchet wheel teeth orientation; lever and pawl are in reverse direction to the earlier as shown in Figure 5. The spur gear reducer steps down the main shaft rotation. The gear reducer output shaft is connected to the flap drive hinge shaft through a flexible shaft coupling to drive the flap.

Design details

Drive torque and detent torque

The net drive torque of the mechanism at the out put shaft is given by:

$$\text{Drive torque} = [(F_s \times L - T_d) \times N] - T_f$$

F_s = SMA wire pull force
 L = Lever length
 T_d = Detent torque
 N = Gear ratio
 T_f = System friction torque

The detent torque is at the flaps, after the gear reducer was specified for on-orbit condition. The detent mechanism was designed to withstand on-orbit disturbances with a margin of about 8 under lowest on-orbit assumed friction coefficient of 0.05. The drive torque calculations assume a worst-case friction coefficient of 0.3. With an SMA pull force of about 9 N, the mechanism provides 0.4 N·m drive torque at the output shaft over and above the maximum detent torque on the shaft.

Design of Shape Memory Alloy Actuator

SMA wire actuator was chosen with an operating strain level of ~3.5%. Actuator wire length was selected based on the stroke requirement for the ratchet wheel and pawl mechanism as under:

$$\text{SMA length} = \frac{100}{3.5} (\text{St} + \text{Sp} + \text{Sm}), \text{ where,}$$

St = Stroke required for one step of ratchet wheel rotation
 Sp = Stroke required for pawl engagement with Ratchet wheel
 Sm = Margin for memory loss and additional stroke margin.

The actuator wire diameter depends upon the torque requirement of the mechanism. SMA wire of 0.25 mm diameter and pull force of 9 N met all the requirements and provided sufficient design margin.

Design of load limiting spring

The spring is designed to provide 8.5-N preload with its pre-compression in assembly and limit the load in the SMA wire to 12 N when the mechanism is prevented from rotation.

Life requirement

Life requirement for the mechanism was 10,000 operation in both directions. With a factor of 10, the SMA wire actuator was tested for 10^5 cycles using a special PC-based test setup to understand memory fatigue/permanent loss of SMA wire stroke.

Electrical Heating Actuation

SMA wire can be assumed as electrical resistance wire having a defined resistance value per unit length. It can be actuated using Direct Current (DC) heating or PWM heating. DC heating was not preferred because of (i) uneven heating of SMA, and (ii) overheating resulting in hot spots, which can cause memory loss. PWM heating is provided for uniform heating and for increased life cycle time of the wires.

Each actuation of SMA wire for one step movement involves a heating period of T_1 seconds for actuation and after actuation the wire should be allowed a minimum cooling period of T_2 seconds, so that it returns to a martensitic state and is ready for the next operation. T_1 and T_2 periods vary depending on the thermal environment and electrical power. If T_1 is more than the required, then over-heating of the actuator may result, and if less, it may not heat the wire to its transformation temperature. The minimum cooling time T_2 could be 1 second to 180 seconds depending on the surrounding environment. Cooling time is kept large enough to take care of all environmental conditions. A provision to change the heating time for on-orbit operation is provided by programmable on-time command to cover variation in panel temperature and power generated. To ensure positive cooling of the SMA wire, a minimum of 5 minutes is specified between two actuation commands.

Instead of drawing power from spacecraft bus, a new concept is used in powering the SMA wire: a separate solar cell array is mounted on the first solar panel exclusively for flap SMA powering. This area on the panel was to be left blank otherwise to clear the shadow of spacecraft antennae. The power switching signals are given by satellite attitude control electronics as shown in Figure 8.

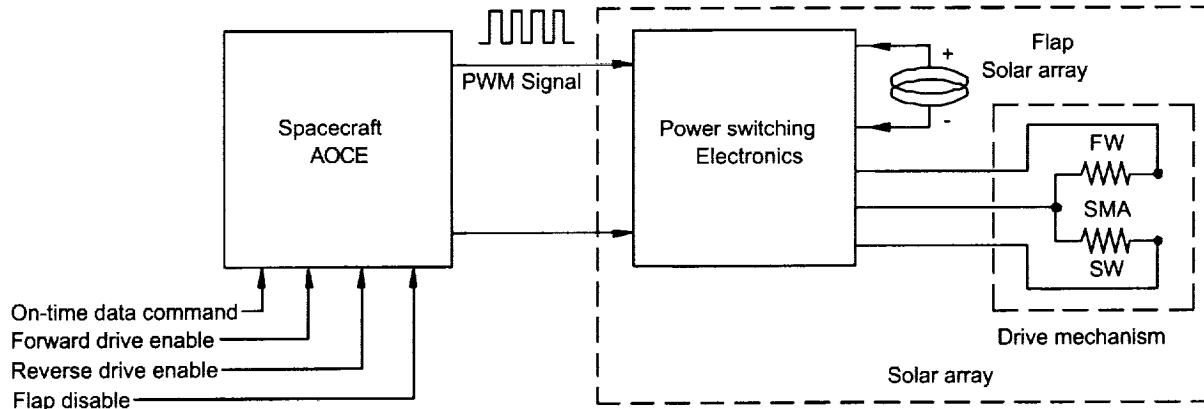


Figure 8. Flap drive electronics block diagram

Tests Conducted on Subsystem

Elaborate test plans were drawn at the component, subassembly and assembly levels to qualify the mechanism. One of the important tests is the life test on the SMA wire actuator to understand the memory/stroke loss. A special PC-based system was designed for conduct of the life test. The system setup, shown in Figure 9, consisted of a load simulation fixture, LVDT for stroke measurement, power supply, power switching box, and a PC for selection of number of cycles, heating time, cooling time, and number of cycles of operation.

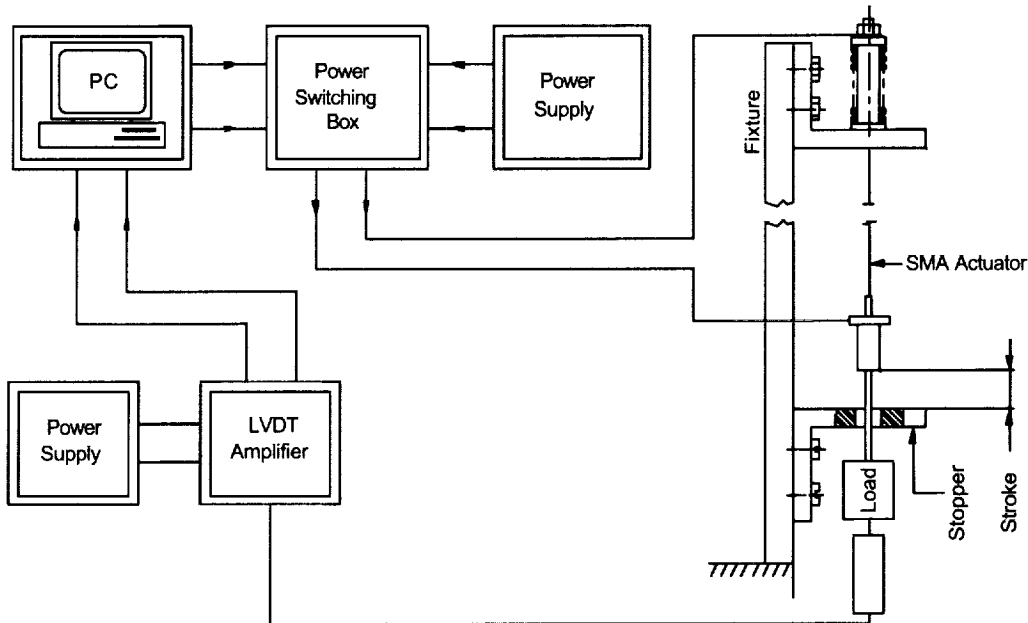


Figure 9. SMA actuator life test setup

Important tests conducted on the mechanism included:

- Load elongation tests, determination of transformation temperature, swage joint strength test, and life tests on the SMA linear actuator amounting to more than 10^5 cycles of operations. Life testing was done on the SMA drive motor mechanisms under thermal-vac.
- Transfer orbit condition simulation on SMA linear actuator and mechanism prior to life tests.
- Heating and cooling time evaluation at ambient and thermal-vacuum condition for the SMA wire actuator to arrive at optimum heating and cooling times for on-orbit operations.
- Drive testing of the mechanism with torque load simulation, with flap, and with spacecraft before and after vibration and acoustic tests.

On-Orbit Performance

The INSAT-2E spacecraft was launched successfully on April 2, 1999 onboard the Ariane Vehicle from Kourou, French Guyana. The solar array deployment was done successfully on April 11, 1999. As there was no need to move the flaps mounted on the outboard end of the array at that time, they were not moved immediately. Subsequently, the flap movement test was done on 14 July 1999. As an further precaution to avoid over-heating the SMA wires, the drive was attempted with a lower heating time of 0.9 second. The heating time was increased to 2.3 seconds in steps of 0.2 second, until the flaps started to move. The flaps started to move with a heating time of 2.3 seconds, which closely matched with the ground thermal-vac test data. Both the flaps (Flap-1 and Flap-2) forward and reverse movements were tested and all the movements occurred with same 2.3-sec heating time indicating the consistency of the mechanism. In addition to potentiometers indicating the changing angle with each step command, the flap movement was also indicated by the changes seen in satellite gyro-rate as shown in Figure 10. Since then, both the flap drives have been operated many times and are operating consistently.

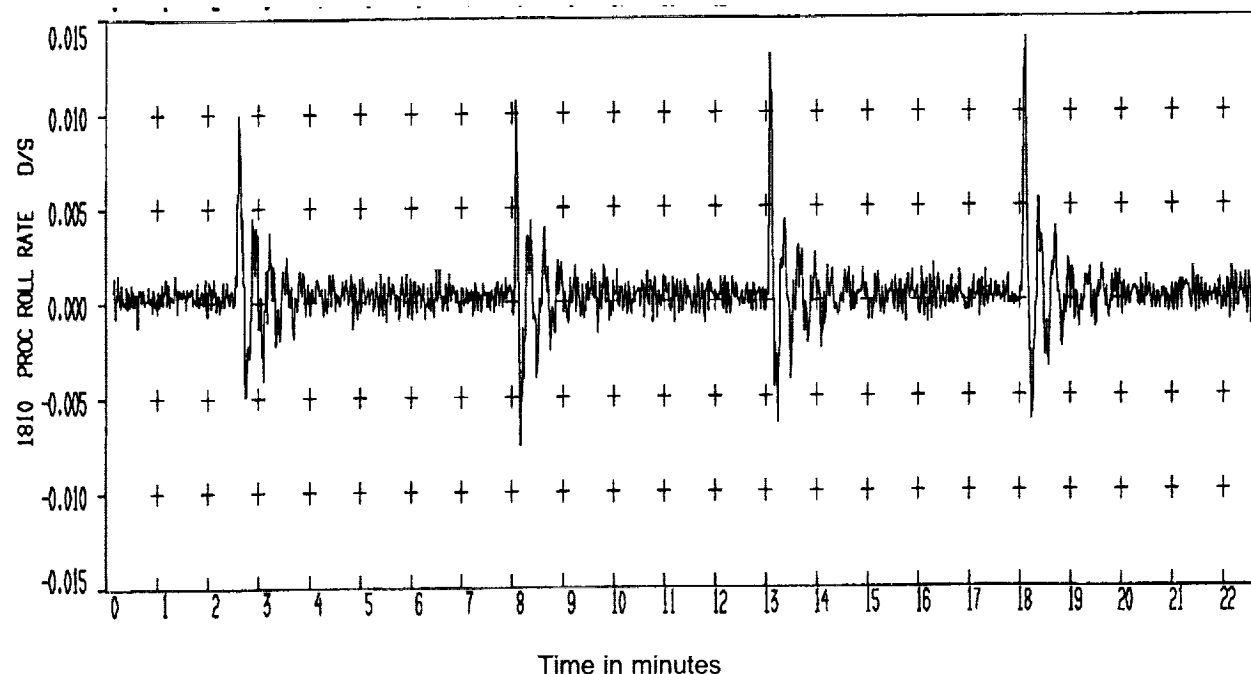


Figure 10. Satellite gyro-rates during flap deployment

The satellite attitude control rates disturbances were considered to arrive at the detent torque value (to hold the flaps in the driven position) with a margin of more than eight while designing the mechanism. Its adequacy was also proved with flaps holding to their position during orbit corrections. But when the south side (two) 22-N thrusters were fired in continuos mode for north-south station keeping operation, flap-1, which was opened to the full 180° position, hit the end stop and bounced back. From the dwell data of the flap movement, velocity of the flap at the time of hitting the end stop was computed. Using the velocity and bounce-back angle the on-orbit detent torque was estimated and found to be as per the design. A check on the thruster plume impingement torque on the flaps, which are 9 meters away from the thrusters, indicated very high plume torque. This high torque which was in excess of detent torque provided in the mechanism and caused the inadvertent movement of the flap.

Presently, north-south station keeping operations are being carried out after keeping the flaps in the fully closed position or in the fully open position to reduce projected area of flaps to the thruster plume. For future models, it is planned to increase the detent torque.

Lessons Learned

1. During repeated cycling, after about 50,000 cycles of operations, a loss in stroke or a memory fatigue of around 12 % was observed, and remained the same up to 10^5 cycles of operations.
2. Electrical actuation parameters are very important for long life operations of SMA, as over-heating/creation of hot spots could result in loss of memory. Memory/stroke loss due to cycling is small and can be accommodated in the design and memory loss due to over-heating results in total loss of stroke.
3. Direct heating of the SMA actuator utilizing higher resistance of NITINOL wires with pulse width modulated electric heating was found to be more suitable for uniform heating compared to direct electrical heating. This further ensures long life of the SMA actuator.
4. Provision for onboard programmable data command with adjustable on time for SMA electrical powering and actuation is necessary. This ensures that the SMA wire does not get over-heated and can actuate at different temperatures of on-orbit environment.
5. For on-orbit operation, a minimum cooling time of 5 minutes is provided to ensure complete cooling of SMA. Thermal-vac tests conducted on the wire actuator and on mechanism to determine SMA wire heating time and cooling times in vacuum proved to be very useful for on-orbit operation planning. Heating time cooling times seen in vacuum were totally different from ambient. Chances for over-heating were found to be more in vacuum than in ambient.
6. A PC-based test system was used for all ground tests. Software protection had to be included to avoid over-heating of SMA wires due to manual setting errors during thermal-vac tests, where as in ambient tests, with air present, over-heating problem was not seen.
7. Accurate teeth alignment between the two ratchet wheels is necessary in fixing the wheels on to the main shaft for matching of forward and reverse step positions.

Conclusion

A novel mechanism using a shape memory alloy linear actuator to drive solar flaps has been developed and is successfully operating on the INSAT-2E satellite. The mechanism is capable of driving the flap in 2° steps, and can sustain more than 10^5 cycles of repeated operations. Extensive testing of the mechanism at component, subsystems and system level has indicated that the mechanism is reliable for repeated operations. The mechanism is magnetically clean and has the capability to replace conventional electric stepper motor for slow-speed operations. Various lessons learned in the development; testing and on-orbit operations have been highlighted.

Evolution of an Actuator Family

Paul Stigell*, Pekka Kyrenius*, Tomi Ylikorpi*, Kai Viherkanto*

Abstract

VTT Automation got involved in spaceflight engineering in the mid-1980's and helped in the formation of the Finnish space industry. The first design was a worm gear mechanism that opened an auxiliary solar panel for the ASPERA instrument on board the Soviet Phobos spacecraft. Next came the Solar Wind ANisotropy (SWAN), including a 2-axis scanning mechanism, on board ESA's Solar and Heliospheric Observatory (SOHO). Two SWAN sensor units cover a field of view of nearly 4π . VTT Automation developed scanning mechanisms for two instruments on board NASA's Cassini spacecraft, namely the ACT actuator for the CAPS instrument and the TT turntable for the MIMI/LEMMS instrument. The actuator concept was further developed in ESA's MPRA project. A version of ACT actuator is currently being manufactured for NASA's Two Wide Angle Imaging Neutral Atom Spectrometers (TWINS) mission.

Introduction

ASPERA

In the mid-1980's, the Finnish Prime Minister was asked on a visit to Moscow about Finland's interest to have a Finnish Air Force officer fly as a cosmonaut in the Soviet manned space program. This was politically undesirable for Finland since most non-Russian cosmonauts came from the Soviet Union's satellite countries. The idea of a Finnish cosmonaut was converted into the co-operation between Finland and Russia in the field of scientific spacecraft and their instruments. This led Finns to participate in the Phobos, Mars-96, Interball, Spectrum-Röntgen-Gamma and Radioastron missions.

ASPERA (meaning "Difficulty") was a Swedish plasma instrument for the Phobos mission. It contained a "single shot" small solar panel opening mechanism. It used a small electric motor and a worm gear. The fact that this was the beginning of Finnish spacecraft engineering is manifested by the fact that hardly any project documentation can be found which is contrary to all later spacecraft projects. The Finnish-built hardware functioned well until the two spacecraft vanished near Mars in 1988.

SWAN

VTT started the design, manufacturing and testing of SWAN instrument's structures and mechanisms in 1989 for a French-Finnish science team. The mechanism design started from scratch since SOHO was Finland's first spacecraft assignment for ESA. SWAN's scan mechanism is shown in Figure 1.

The instrument's conceptual design freezing drifted after end of Phase B. Various mechanism concepts were investigated including the use of worm and bevel gears and even the possibility to manufacture the motors in-house was considered since knowledge of magnet technology was available. Finally, the mechanism design evolved around the French SAGEM toroidal hybrid stepper motors (35 PP 81 01 01 WW) and internally preloaded MoS₂ solid lubricant-coated thin 4-point bearings with a robotics textbook sort of configuration.

The motor has a maximum output torque of 0.4 N·m and a power-off detent torque of 0.040 N·m that is enough to keep the mechanism stationary even if the unit is unpowered and the spacecraft maneuvers. Because of ambitious scientific goals, which in the end were not sought after, a too wide optical path (DIA

* VTT Automation, Finland

40 mm) was built to the sensor unit. This led to a heavier and more expensive motor being selected. The design did become advantageous when VTT Automation started to build rotating actuators for Cassini.

The bearings are four-point internally preloaded ones by Kaydon [1]. Oil lubrication using Fomblin Z25, ceramic composite bearings and MoS₂ or lead plated bearings were considered. MoS₂ was selected because the bearings were close to optical elements and also because there was limited volume for seals. The friction of the bearings is nominally 15-25 mN-m (peak 35 mN-m). The MoS₂-coated bearings were procured by the European Space Tribology Laboratory (ESTL) [2] and that relationship has worked well ever since. For prototype testing, liquid lubricants have been used but moving from solid to liquid lubricants has never been considered for flight use because of the learning curve effect. "Whether to buy or develop components" question was solved the right way. This project led to a trip to Cannes for the 4th European Space Mechanisms and Tribology Symposium [3] to learn about vacuum tribology. Much later MIL-A-83577 [4] was read. Both confirmed that our thinking is right for space mechanism design. In those days, basic training (e.g., [5] and [6]) and European guidelines [7] were not available.

Resistive position sensors by Penny & Giles [8] were used because they fit mechanically the configuration best. The driving of the stepper motor is done in the microstepping mode that makes the disturbance torque small. Feedback control is used but in case the encoder (being one of relatively many non-redundant items in the design) information is lost, the motor can be driven in command mode counting the step.

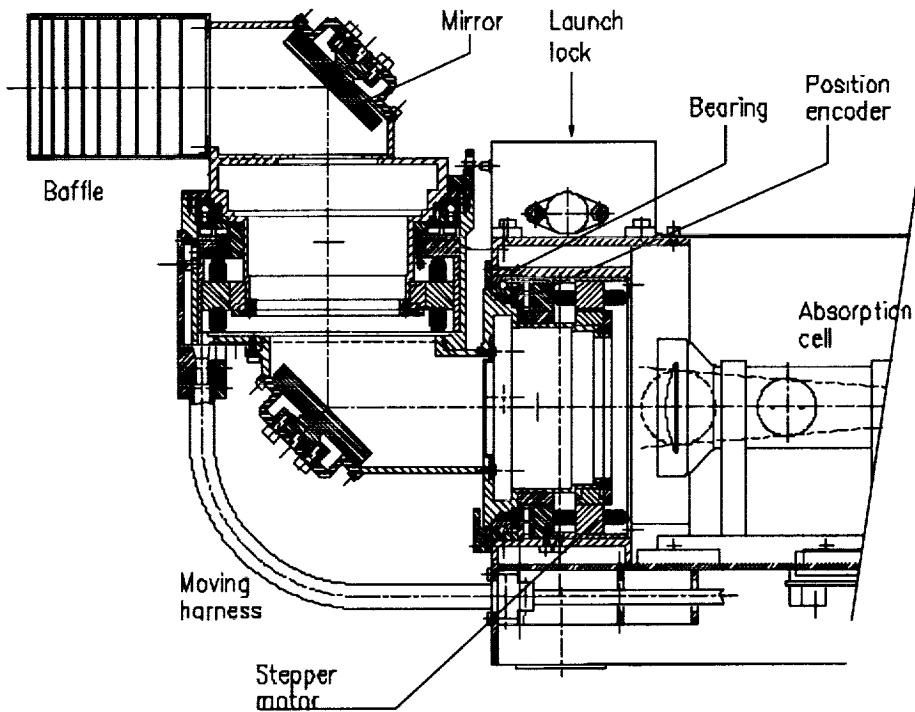


Figure 1. SWAN Sensor Unit's periscope mechanism.

SWAN's "periscope mechanism" was latched during the launch with pin-in-the-hole-mechanism that was released in-orbit by Starsys Research Corporation's [9] pin puller mechanism that is based on a High Output Paraffin (HOP) actuator. This usage of a resettable non-pyrotechnic actuator is believed to be the first of its kind in ESA flight projects. SOHO has stringent cleanliness requirements and therefore the issue of the paraffin wax was discussed at length until the actuator was shown to be hermetic. The lock and the actuator pin did tend to cold weld (metal-metal pair) or release debris (metal-plastic pair). After testing five different designs, a Nitronic steel pin with a Vespel lining was chosen.

During this project, VTT Automation got rid of drawing boards and started to use AutoCAD. Structural analysis was performed using I-DEAS and NASTRAN on a Cray-supercomputer. The engineering staff more than doubled because the Space Technology Group developed simultaneously three other space instruments, participated in feasibility study of a national satellite, etc. I-DEAS 3D-modelling was introduced first for faster (than ESATAN) thermal analysis (using TMG software) of the instruments and also the SWAN mechanism.

A spacecraft project requires work planning and cost follow-up. Typically 80% of the total cost is labor cost. Thus the extension of project, as in the case of SWAN, means added cost just to keep the knowledge within the team. VTT (a research center with personnel of 3000) has a computerized cost accounting system that allows multi-level cost breakdown (down to work packages). Actually, despite of this large system the project manager must handle the cost figures to gain real insight. Again Kelly Johnson's "Skunk Works" rules [10] are handy: the project manager must keep the core team so small that he knows who does/did what and when. Assembly, integration and testing may become easier and faster with more people, but design engineering does not unless the team is lacking some special knowledge.

SWAN mechanisms [11] are assumed to have gone way below their cold thermal limit temperature during the summer 1998 incident where flight control lost SOHO for several weeks and the spacecraft was in survival mode. Since recovery of SOHO, SWAN has been working well and started its 5th year of operation in December 1999.

Rotating Actuator Requirements and Properties

The actuator family described here rotates a payload that is mounted on top of the rotating actuator with a transition plate that allows adjustment of the payload center of gravity (CoG) to the axis of rotation. Typical requirements and properties of the different actuator models are summarized in Table 1. CoG offsets, mass, and limit load determine structural issues, especially for the Marman clamp. The rest of the parameter values determine the motion aspects, i.e. customer requirements.

Table 1. The actuator family - ACT, TT, MPRA and TWA - all have heritage from SWAN.

	SWAN	CAPS/ACT	LEMMS/TT	MPRA	TWINS/TWA
Mass, kg	2	4	3.2	3-4	3.6-4.0
Power, W	2	3	3	2-3	3
Rotated mass, kg	<1	18	6	5-20	17
CoG elevation from Marman clamp centerline, mm	<10	218	150	100-250	150
Design load, g	25	32	32	<40	28
Moment about axis of rotation, kg·m ²	small	0.4	0.3	0.2-0.5	0.5
Scan range, degrees	±90 per axis	±110	continuous	continuous	±90
Scan speed, deg/s	0-5	1	2-12	1-120	3
Pointing accuracy, degrees	±0.1	0.5	0.5	0.01	±0.05
Life, cycles	25000	250000	500000	3M	700000
Limit temperatures, °C, operational	-45 to +55	-35 to +50	-40 to +55	-45 to +55	-45 to +55
Radiation tolerance,	100	100	100	various	100

krad					
Magnetic disturbance, nT at 1 m	>2.5	2.5	2.5	various	10
Feedthroughs	optical	20 wires, cable wrap	slip ring	various	20 wires, cable wrap

CAPS/ACT and LEMMS/TT

Background

Originally the CAPS instrument for NASA's Cassini was designed to be located on a rotating platform (delivered by NASA) at the end of a boom. In 1992, the Cassini mission was de-scoped and the so-called platform instruments were mounted directly on the spacecraft. In order to restore the scientific capabilities of CAPS, the project team decided to add an actuator (ACT) that rotates the instrument in a windshield-wiper fashion [19]. VTT Automation did the development, design, fabrication and testing of the ACT including its drive electronics.

Another instrument on the Cassini Fields and Particles Platform, namely LEMMS, also suffered from the loss of the boom, and VTT Automation built an ACT-like actuator (called turntable, TT) for the LEMMS too. These two were "similar" and the design was to have lots of synergy. However, LEMMS required a slip ring and different motion control electronics. The heights, the payload masses, and launch loads were different. Also customer requirements were different. Two different designs evolved.

Motion

ACT, shown in Figure 2, rotates CAPS in a windshield-wiper fashion ± 110 degrees at an average scan speed of 1 deg/s. LEMMS/TT rotates continuously at variable speed in the range of 0 to 5 deg/s.

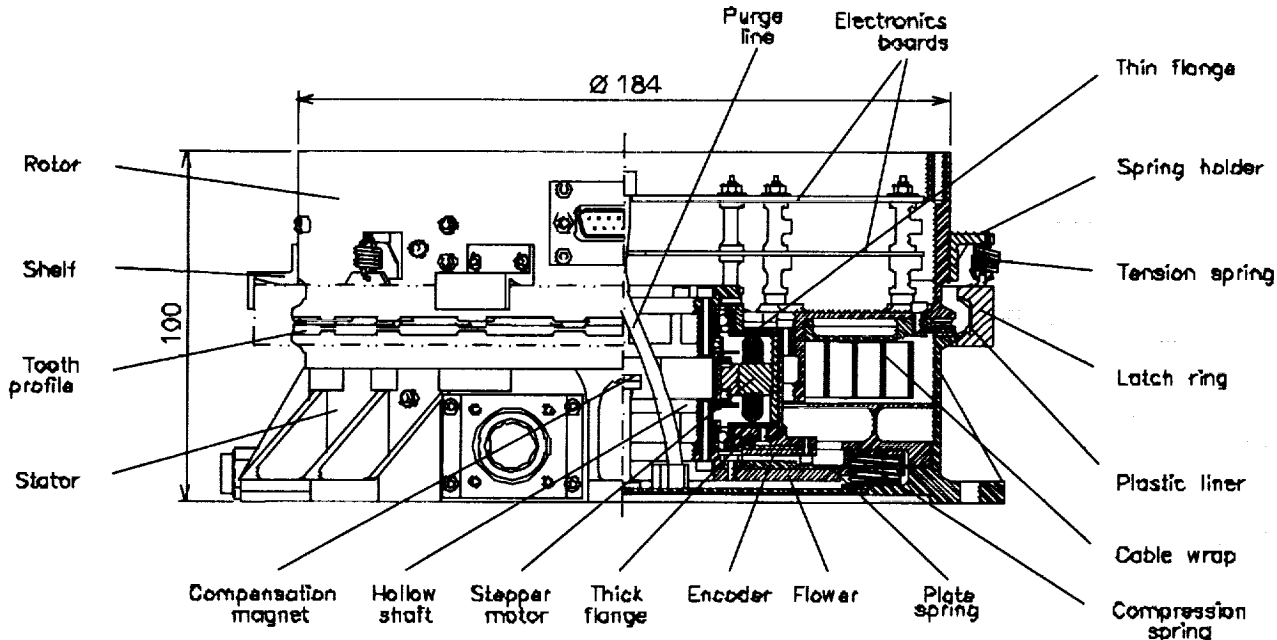


Figure 2. Cross section of CAPS/ACT.

The chosen stepper motor is the same as in the SWAN. Instead of a stepper motor, a DC-motor with a worm or bevel gears was considered, but these systems were abandoned because of high mass and

complicated gear configuration. The toroidal stepper motor gave also a good opportunity to place the purge tube (ACT) or a slip ring (TT) inside its hollow shaft.

Materials had to be non-magnetic in both housing and bearings. Aluminum alloys are avoided in the motor bearing assembly because of their high coefficient of thermal expansion. AISI 316 steel as housing material and CuBe bearings was found to be a good pair with similar coefficients of thermal expansion. The permanent magnet of the motor was of course unavoidable. Reducing the magnetic emission of Sagem's motor would have required new motor design with major cost penalty. To reduce the magnetic disturbance field outside the motor, μ -metal shields were mounted to both housing parts and to the shaft. Also a compensation magnet was mounted inside the hollow shaft to cancel the first order dipole field of the stepper motor. Residual magnetic moment of the shielded motor unit has been measured and found to be compliant with required less than 2.5 nT at 1 m. The μ -metal shielding reduces Sagem motor's maximum torque to 300 mN-m at 65 mA current (28 V).

Pointing direction of the CAPS is measured with a Novotechnik [12] resistive encoder mounted between the motor housing and a non-rotating flange (called 'flower' for its shape). Two additional calibration positions for the motor position are provided by two ABB's limit switches that give a signal at the ends of the $\pm 110^\circ$ sweep. The motion control electronics on two printed circuit boards in the actuator housing and in the CAPS-instrument DPU nominally drive the scan in a way that the limit switches and the mechanical end stops are not touched.

In order to minimize torque disturbances caused by the actuator motion, the CoG of the payload should be on the axis of rotation. Even in installing spacecraft hardware, Murphy's law may turn out to be still going strong: the payload unit was attached on top of a actuator in a way that moved the CoG further away from the axis of rotation. This was corrected, but the incident could be counted as a configuration control flaw.

Bearings

The SEUL 06050 non-separable angular contact ball bearings were selected. They are manufactured by SNFA [13] of beryllium copper, since common bearing steels are magnetic. Bearing rings are manufactured to High Precision Class ABEC 7, and the balls are of AFBMA-standard grade 16. Their material is also BeCu. The bearings were too fine quality when comparing their friction torque to that of the flex link (for data and power transmission through the actuator). For wear considerations, the bearings were a good choice.

The flex link has twelve shielded pairs of electrical lines in a laminated Kapton foil flat cable manufactured by Gore (for ACT). TT uses a slip ring assembly because its commanding unit is located in a box on the spacecraft panel. Sometimes slip rings are told to operate poorly in the beginning of their life. If the start-up command must go through it to a computer on top of the actuator, the mission of the experiment can be over before it started.

Bearings are mounted in an X configuration where they are pushed into seats by axial preload provided by the flexible flange of the housing (Housing II in Figure 3). The two bearing flanges of the unit are fitted together with three alignment pins to reach high concentricity requirements of the bearings. The thin bearing flange with a ~ 0.1 mm gap between the hard stop and the flange allows thermal expansion of the shaft. The bearing housing machining to the required tolerance has proven to be a very difficult task that is tolerable only in single unit production.

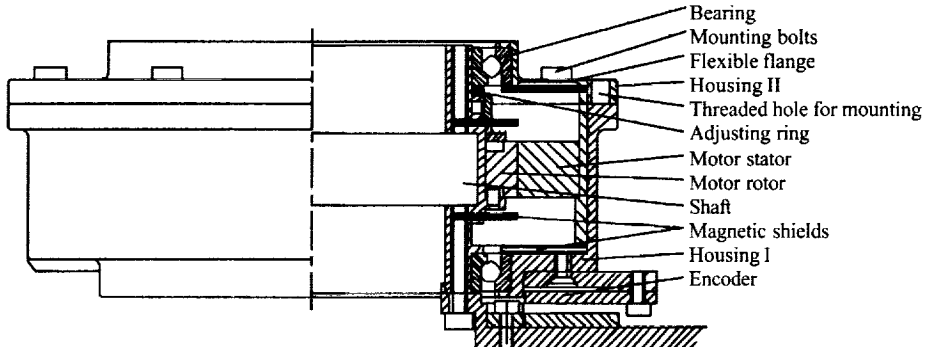


Figure 3. Cross section of CAPS/ACT motor bearing assembly.

The dry lubricant for the bearings is ion-plated lead as suggested by ESTL who also processed the coating. The lubricant and rolling surfaces easily suffer severe damage if the balls do not roll but skid along the ball track. ESTL used their special software that gives calculated values for minimum and maximum preload under given temperature difference between the housing and the shaft, and for given bearing seat axial stiffness. The software gives also an estimate for steady mean torque vs. preload. With the aid of this information the required bearing preload and housing stiffness were determined.

An adjusting ring that was placed between the bearing's inner rings tuned the preload. Thickness of the ring defines distance between the bearing inner rings, while the housing presses the outer rings towards each other. Bearing preload is determined by measuring the height of the motor housing with and without the bearings.

With 1 N/ μm bearing housing axial stiffness the nominal 68-N axial bearing preload stays between 45 N and 92 N when the thermal gradient over the bearings is below 10°C in either direction. The bearing axial static limit load is 1030 N and axial dynamic limit load is 290 N. The motor bearing assembly has been operated over the temperature range from -50°C to +60°C. During tests, their friction torque has been measured with a Kistler torque meter. The friction was demonstrated to vary only a little with respect to temperature.

Structural design of the Marman clamp

The bearings cannot carry any launch loads from the instrument mass loads during the launch. The loads are transferred between the upper and lower actuator parts through a Marman clamp. The first approach was to separate the ACT rotor and stator in the latched state with a W-shaped latch ring. The friction between the latch profile and ACT flanges was not enough to prevent payload rotation during vibration testing. It was difficult to add structural rotation locks since they might obstruct opening of the latch ring. The design was changed to press the ACT rotor and stator against each other with a V-shaped latch ring. Tooth-shaped PEEK-plastic ring placed between the bodies prevents rotation when latched.

Operating the latch requires a 2-mm axial separation between the rotor and stator, which is made possible by a flexible mounting between the motor shaft and the ACT stator. The stepper motor stator, the part with windings, is rigidly mounted to the ACT rotor. When latched, the rotor moves 2 mm down (Figure 1) and the motor assembly moves with it. The upper bearing mounted to the thin bearing flange presses the hollow shaft downwards. The shaft is mounted to the compression spring supported by the flower that also moves down against the compression springs. The flower part is mounted to the ACT stator also with a thin plate spring that allows axial movement but no lateral movement or rotation.

The compression springs keep the upper bearing preloaded and act against vibration loads of the shaft and flower during spacecraft lift-off. The lower bearing is unloaded during launch. This is permissible since it does not carry any external loads. When unlatched, the rotor, the shaft, and the flower move back to upper

position and the flower rests against the ACT stator structure. Therefore, the compression springs do not cause any loads on the bearings or motor assembly in the released state.

One design requirement change affected the Marman clamp design. The limit load arose from 28 g's to 56 g's and then, after the re-design effort of the Marman clamp, went back down to 28 g's.

The structure of the latch ring is significantly different from the common type of Marman-clamps. Usually several small clamps are pressed with the aid of a tensioned steel band but here we have a circular aluminum clamp that itself is tensioned. This is because the latch ring radius was limited to 92 mm, which is very small relative to external loads, and it is necessary to utilize the complete circumference. A similar design has been used in the attachment of small satellites to the OSC Pegasus rocket.

When unlatched, the latch ring is required to extend by itself and be 2 mm larger in diameter than the ACT flanges. This requires 31 mm tangential expansion. The expanded ring is pulled by tension springs to rest against the shelves (Figure 2). The shelves guarantee that the ring will not interfere with the ACT stator (the open Marman clamp rotates with the rotor).

During development, several materials were tested in vibration tests in which a representative latch configuration and a CAPS mass dummy with a correct CoG were shaken up to 15 g sinusoidal acceleration. The first fundamental frequency with the CAPS mass dummy was demonstrated to be above 100 Hz. This corresponded well with the eigenfrequencies solved from the FE-model by I-DEAS. During these two projects, the use of I-DEAS was widened from thermal design to mechanical design and structural analysis (eigenfrequencies, static stress analysis) using several UNIX workstations. More of the detail design work shifted from drafters to engineers.

The first latch configuration consisted of an anodized AA6061 W-band latch pressed against Alodine 1200 treated AA6061 flanges. The contacting surfaces of the Marman clamp were made convex with 5-mm radii while the flange surfaces were planar. This guarantees a smooth and continuous contact line around the entire ring. A vibration test showed that the anodized base material was not strong enough and the anodizing broke off. Also, the flange surfaces were damaged. Several material pairs with modified geometrical properties were tested. Results are shown in Table 2.

Table 2. Marman clamp materials and geometry.

Actuator flange material	Marman clamp inner surface	Problems	Comments
Alodine treated AA6061	Noryl GF30% plastic	Noryl is too brittle and generated debris	
Alodine treated AA6061	AISI 316 Steel		
60 µm Hard-Anodized AA2219	AISI 316 Steel	Steel surface broke, anodized surface broke off from the aluminum	Reduce surface pressure. Increase radii (R) of contact surfaces
60 µm Hard-Anodized AA2219	PEEK plastic, 1 mm thick	56 MPa surface pressure, some permanent depressions. OK	R = 25 mm
AA2219	PEEK plastic	56 MPa surface pressure, some permanent depressions. OK	R = 25 mm. The chosen design!

Locking mechanism

Another unusual character of the clamp ring is the locking mechanism. The clamp is fully re-latchable and opened by a HOP actuator from Starsys. The HOP actuator opens the latch actuating mechanism (LAM) by pushing a small hook forward and thus releasing a locking pin on a lever. The lever is a part of an over-

center mechanism that is used to reduce a 5000-N tension force in the Marman clamp down to 65 N at the locking pin. The movement of the hook is perpendicular to external forces at the pin and therefore it can not open by itself.

Analysis of the over-the-center mechanism revealed a problem of friction in mechanism joints. Small forces acting on the locking pin requires that the latch ring tensioning force must act very close to the pivot center. This makes the latch opening torque very small. At the same time, the tensioning force on the pivot and lever shaft remains at 5000 N that can have large friction torque. It is clear that no sliding bearing or bushing would work on this construction. Instead, three pieces of HK-type needle bearings were used. For these bearings, the manufacturer gives a coefficient of rolling friction of 0.003, which leaves a safety margin of 15 for bearing friction.

The Marman clamp is tensioned by tightening the tensioning screw with a pre-determined torque (Figure 4). During development tests torque versus tension curves were first calculated and then experimentally confirmed. In tests, several strain gages were glued along the Marman clamp circumference and tension was monitored while tightening the screw.

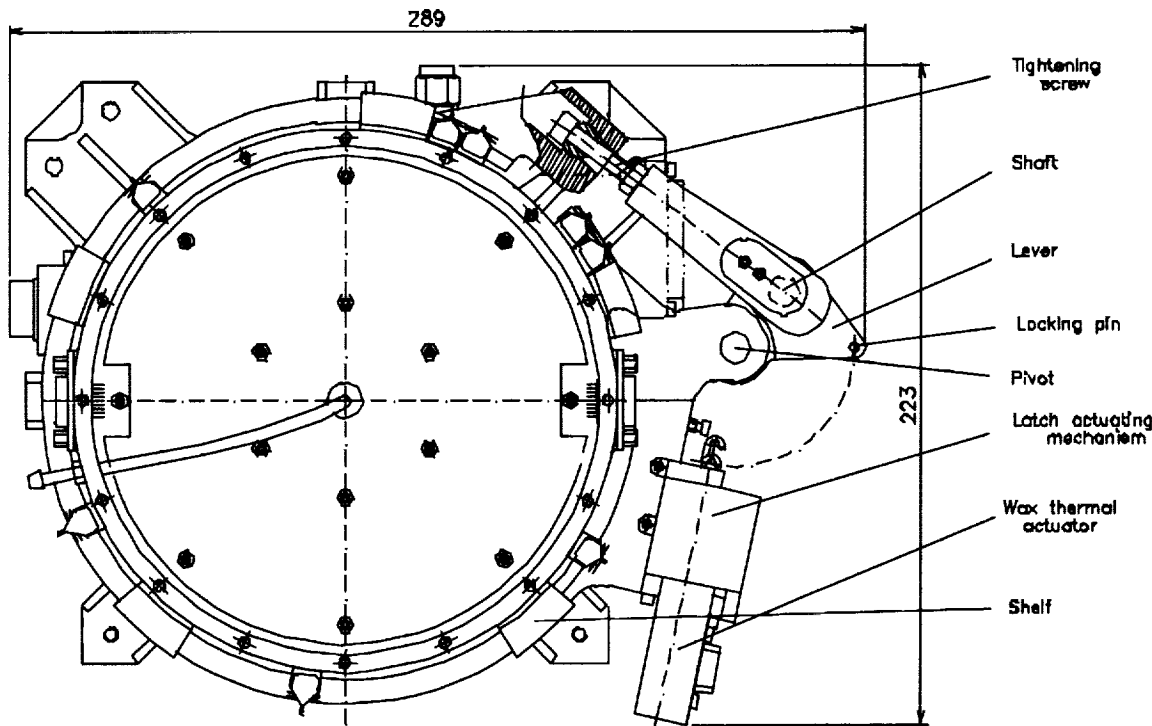


Figure 4. Top view of CAPS/ACT.

The temperature dependency of the triggering of the paraffin (that melts at +80 to +100°C) actuator has in other mechanisms applications been a drawback because sometimes the temperature limits have been specified to such values that pyrotechnics are the only acceptable actuators [18]. In space instrument applications, the temperature limits have been reasonable.

Testing

To qualify the actuator design, an extensive test program was executed. An engineering model (EM) was tested to full qualification levels. A separate lifetime testing assembly (LTA) was built in order to allow testing of life critical components (motor, bearings, position encoder and cable wrap) independently. Prior

to start of the lifetime test, the LTA was subjected to vibration and thermal cycling tests. This was to ensure that the LTA also experienced the "destructive effects" of qualification testing. ACT's LTA was tested to 500 000 cycles and TT's to 1.5 million cycles. The tests were accelerated by driving at 30 rpm. Tests were successful.

The test program for the EM included the following: mass properties (weight, CoG), magnetic cleanliness, friction torque and motor torque measurements, thermal cycling tests in nitrogen and vacuum (including functional tests of the motor, electronics, bearings, encoder, and launch lock), run-in and burn-in in vacuum, and vibration tests. All tests were performed at VTT Automation's facilities, except the magnetic field measurements that were performed at Finnish Meteorological Institute's magnetics measurement facility. Having machine shop, cleanrooms and environmental testing facilities has been a great benefit. Having people and facilities that are needed for the successful outcome nearby compensates for the fact that the customers and authorities are thousands of miles away that makes dialogue slower.

Changes

A typical VTT Automation's space mechanism project team has 2-6 members. Such projects can not afford to have a full-time product assurance manager nor does the project manager have much time for configuration control. However, both good PA and fully covering configuration control are worth the effort. The Finnish Mark vs. US dollar exchange rate fluctuated during the project in a fashion that engineers who negotiated the deal had not considered. This is one of the economics of scale effects: large organizations have infrastructure for doing many non-engineering tasks and in small ones the project manager (who also is the systems engineer) is responsible for a multitude of things. Currently the Euro vs. US dollar exchange rate seems to slide down in a fashion that may indicate trouble ahead for those who have international contracts.

In the latter part of ACT and TT projects in the mid-90's, VTT underwent a major restructuring. It did not affect the engineering staff, but did change the organizational structure of the Space Technology Group. The project manager left VTT Automation to become manager of much larger group at Nokia Corporation that has recruited a fair deal of all Finnish space technology engineers. The Space Technology Group was too large compared to the other groups. It was split into "Electronics and Optics" group and a "Structures, Mechanisms and Thermal Design" group. This meant also moving people from one place to another. The physical distance from the mechanical engineers to the electronics engineers grew from 20 m to 1000 m, which partly hinders the integrated product team approach. Also, the government research facility started to implement modern quality and management policies in continuous learning manner. A current reading [14] gave insight: organizational change does not only increase creativity but can also have negative effects. For the whole Finnish space industry, similar restructuring all over the world has been worse: more than 25% of the 20 satellite missions that have carried Finnish-made hardware have been lost in launch failures or in-flight mishaps!

MPRA

VTT Automation is finishing its study for ESA on the Multi Purpose Rotating Actuator (MPRA) (Figure 5). In this project, the ACT and TT actuator concept is developed to be easier to tailor for different payloads. Even in building on flight heritage, the customer, the instrument development team, and the satellite development team have ideas and concerns that become new requirements that cause design changes. This issue is not only a mass growth issue, but also more of a customer satisfaction issue. Structure and mechanism play a secondary role in space science instruments except in the mechanical design of the detectors. Thus the basic design should be flexible and that was sought after in MPRA project [20].

The solid aluminum Marman clamp is replaced by a lighter steel band Marman clamp to be more flexible for different sizes of payloads. A major part of the redesign concerns the control electronics and is not dealt with here.

In Cassini mission designs, the thermal analysis of all hardware was performed by the instrument system developer. In the MPRA project, the thermal analysis is done at VTT Automation. Finding data about the thermal conductivity of bearings is an interesting task.

MPRA is the first spacecraft mechanism that VTT Automation has developed using only the I-DEAS solid modeler. Earlier design was done using AutoCAD that allows fast generation of drawings but is cumbersome in a design process with a multitude of design changes. The tool has not fully been used as a team tool since the major part of the mechanical design has been done by just two engineers.

Unfortunately, the electrical design is still totally external, and even the introduction of waste heat of the electronics components to an I-DEAS thermal model requires manual operations.

TWINS

In 1999, VTT Automation started to build two scanning actuators of the CAPS/ACT-type for NASA's TWINS instrument [21]. The Critical Design Review of this project is in February 2000. MPRA and TWINS projects have led VTT Automation to a situation where its product is not necessarily unique every time but one that evolves from an earlier design. This is sensible economically and for technical risk. This is a novelty in all Finnish space industry (whose only series production has been hardware for 4 Cluster and 4 Cluster II satellites - a "payoff" of the sadly poor launch vehicle performance during the last decade).

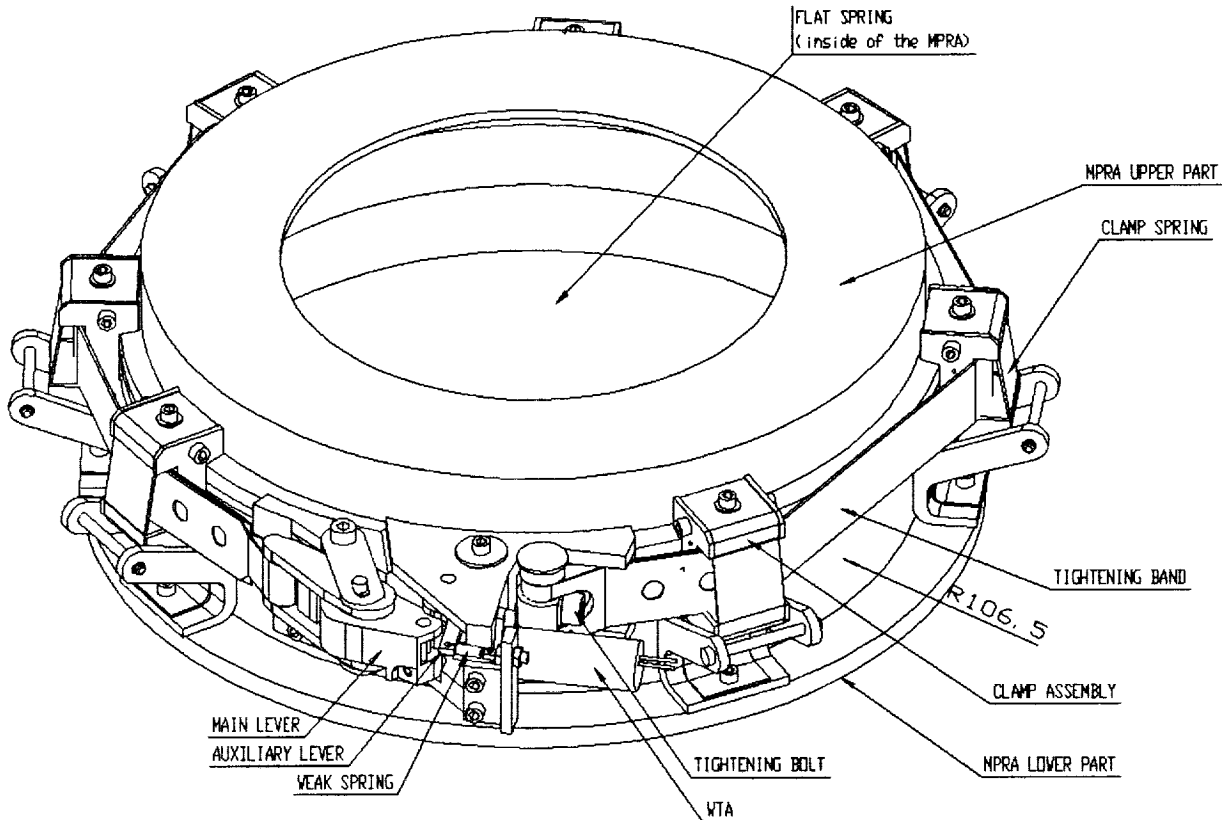


Figure 5. MPRA

Structural integrity

The question of what is the design load is a critical one for TWA, too. The structural integrity of the Marman clamp is always a major concern. The Marman clamp structural analysis has two difficulties: knowledge of load cases and the analysis itself. An instrument development team is given the following mechanical loads

- quasi-static limit load e.g. in the form of mass-acceleration-curve in axial and lateral directions
- sinusoidal vibration test loads along X-, Y, and Z-axis
- random vibration loads along X-, Y- and Z-axis
- shock loads along X-, Y- and Z-axis (both directions)
- acoustic load

Generally, mechanisms are compact and stiff entities that are not acoustically excited. In some cases, the acoustics on the panels the mechanisms support cause large loads on the mechanisms. Acoustic and shock loads have been handled by assessment and design so far. Sinusoidal vibration test is the strength test for instruments in place of a static load test. It and random vibration can be handled well by modern FEM-software packages such as I-DEAS. In Russian programs, the test loads are the worst load cases and this is a good approach: these loading cases are verified by testing. In ESA and NASA programs, the worst load case must be found from the first three cases. The direction and combination of the quasi-static limit load components has *never* been defined well and actually almost any combination will do. This case is not verified by testing, fortunately. The value of such static stress analysis is doubtful.

The structural analysis of the Marman clamp is difficult using FEM because there are contacts that are hard to model and contact elements prohibit eigenfrequency analysis. Marman clamps have been studied in recent years and some studies [17] indicate that the Marman clamps of launch vehicles have been grossly overdesigned for decades. In ESA, Saab has studied [16] Marman clamp structural analysis in detail. At VTT Automation, much of the analysis has been done using MathCAD and analytic methods. The issue of tension decrease caused by creep during the storage before has arisen in the TWINS project. Creep is hard to evaluate by analysis because of the lack of material properties. Testing can be done. One solution is tensioning the Marman clamp before the launch.

A HOP actuator opens the launch latch. The entire actuator with the latching mechanism is enclosed inside a cage that supports the multi-layer insulation (MLI). MLI gage, new connector locations and external limits by the spacecraft cause mere change from two to three spacecraft connectors into several design changes. The conflict could be found easily with a 3D-modeler but at the beginning of the project, ACT's old 2D drawings were used as the baseline.

EMC and mass growth

In the case of TWINS, the spacecraft tolerates higher magnetic emissions than Cassini did. 100 grams was intended to be decreased by removing the μ -metal shield around the motor. For TWA, potentially magnetic stainless steel bearings by Kaydon were ordered. Then the TWINS team realized that their detectors do have magnetic field requirements. Fortunately the requirement was loose enough. Stainless steel bearings are acceptable and maybe the μ -metal can be removed.

TWA's EMC emission limit is much lower than for ACT. Better electrical coupling between the static and the rotating part of the actuator is required to bring the actuator to a single potential. Printed circuit boards must be covered with metal shields. There is enough space for all this but the undesirable mass growth is evident even for a second-generation unit.

Motion control and lubrication

The pointing of the TWA is more accurate than that of ACT. This required a more accurate potentiometer. This time, the manufacturer, Betatronics [15], was found quickly. To some extent WWW has become a source of information but mainly faster procurement is caused by experience in the spacecraft mechanisms.

Cultural differences are seen occasionally. The Europeans are used to solid lubricants and the Americans have a vast experience in liquid lubrication. Liquid lubrication was used in the early space missions that the Europeans watched from the ground. Thus liquid lubrication has long flight heritage in the USA. ESA has invested on solid lubrication and it is thus popular in European missions. TWINS PDR review panel stated doubts on the life and debris issues of solid lubricants.

The fact that the temperature difference between the upper and lower bearing in ACT was limited to max 10°C in order to keep the preload in the right range caused some thermal design considerations for TWA. If the temperature difference would be something else, a new test program would have to be executed. The problem was solved by a thermal design using heaters and thermistors.

Conclusions

Finland should have gotten involved in spacecraft engineering in the 1970's. Despite the late start, VTT Automation and the Finnish space industry in general have gotten a tolerable number of flight references and gained know-how in the past ten years. For the first time, there is a possibility to deliver new flight units that have a Finnish heritage. VTT Automation's mechanisms experience has been limited to systems that use stepper motors and paraffin actuators as the prime movers. This experience has been enlarged to planetary drilling and sample acquisition "robotics" making the mechanisms side stronger within the space technology group.

References

1. <http://www.kaydon.com>, Kaydon, USA.
2. www.aeat-prodys.com/subdivisions/ESTL.html, European Space Tribology Laboratory, UK.
3. Fourth European Space Mechanisms and Tribology Symposium, ESA, SP-299. March 1990.
4. MIL-A-83577B, Assemblies, moving mechanical, for space and launch vehicles, General Specification for. USAF, USA. 1988.
5. www.launchspace.com
6. P.Conley, Space Vehicle Mechanisms, Elements of Successful Design, John Wiley, 1998
7. Space Mechanisms Standard Requirements Specification, draft 02, ESTEC, 1994.
8. www.penny-giles-controls.co.uk, Penny & Giles, UK.
9. <http://www.starsys.com/products.htm>. Starsys Research Corporation, Boulder, Colorado, USA.
10. Clarence "Kelly" Johnson, Maggie Smith, Leo Geary, Kelly - More Than My Share of It, Smithsonian Institution Press, 1990.
11. Heikki Huomo, Heikki Hannula, Kai Viherkanto, "Periscope Mechanism for SWAN Instrument", Proceedings of 'Fifth European Space Mechanism and Tribology Symposium', ESTEC, Noordwijk, The Netherlands, 28-30 October 1992, ESA SP-334, April 1993.
12. www.novotechnik.de, Novotechnik, Germany.
13. www.snfaf.com, SNFA, France.
14. Jay Alan Moody, William L. Chapman, F.David Van Voorhees, A. Terry Bahill, Metrics and Case Studies for Evaluating Engineering Designs, Prentice Hall PTR, New Jersey, 1997.
15. <http://www.betatrionics.com/>, Betatrionics, Inc., New York, USA
16. Separation Systems Technology Program, Phase A Final Report, ESA CR(X) 3910, Saab Ericsson Space, Sweden.
17. Robert DiTolla, Michael Ernst, "Allowable Design Loads for Marman Clamp Systems", Engineering, Construction and Operation in Space IV, Proceedings of Space '94, Volume 1, ASCE, 1994.
18. Low Shock Separation Mechanism, Final Report, VTT Automation and Rejlers, Finland. 1998.
19. Tomi Ylikorpi, Timo Luntama, Kai Viherkanto, Veli-Pekka Lappalainen, Heikki Hannula, Heikki Huomo, "Development of an Actuator for CAPS Instrument on Spacecraft Cassini", Proceedings Sixth European Space Mechanisms & Tribology Symposium, Zurich, Switzerland, 4-6 October 1995, ESA SP-374, August 1995.
20. H.Astola, K.Viherkanto, T.Ylikorpi, M.Verain, "Multi Purpose Rotating Actuator for Satellites", Poster presentation at 8th European Space Mechanisms and Tribology Symposium, 29 September - 1 October 1999 at Toulouse, France.
21. <http://nis-www.lanl.gov/nis-projects/twins/>, TWINS home page.

Coaxial Cable Failure in a Spacecraft Mechanism

Michael Chiu*

Abstract

After completing a life test, the Biaxial Assembly's (BA) coaxial cables failed their post-life RF performance testing. Further investigation into the cause of these failures revealed that the coaxial cables developed extensive damage to their outer shields, which resulted in unacceptable RF performance. This damage was caused by a phenomenon known as "cold welding", a type of adhesion between two similar material fretting surfaces that restricted the internal flexing of the cable.

This paper will summarize the testing environment to which the BA was exposed and describe the results of our investigation into the failures. Also, methods of preventing cold welding will be described, as well as lessons learned for coaxial cable construction and life testing of spacecraft mechanisms.

Introduction

The BA is equipped with a cablewrap assembly, essentially a controlled service loop consisting of flexible coaxial cables, a number of DC ribbon cable assemblies, and a copper ground strap. This cablewrap is divided into four chambers. One pair of chambers is counter-wrapped with respect to the second pair to provide even torque distribution as the output shaft rotates. Two of the four chambers house coaxial cables, which are loosely woven together using a polytetrafluoroethylene (PTFE) tape and are approximately 2.13 meters (7 feet) long inside the cablewrap. Essentially, the cablewrap behaves much like a clock spring, with the cables constrained as they enter and exit the cablewrap by two bridge clamps (Figure 1). The total travel of the cablewrap is greater than 360°.

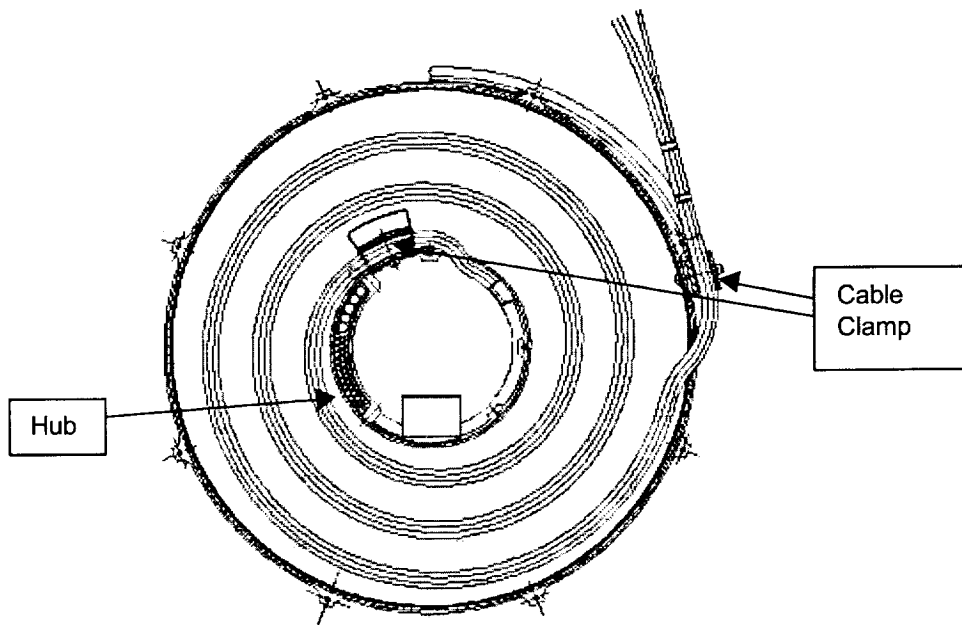


Figure 1. Cross-sectional view of the cablewrap assembly

* TRW Space and Technology Division, Redondo Beach, CA

The particular unit with the RF failures was an Engineering Qualification Model (EQM). Thus, it went through full qualification testing, including thermal cycling, random vibration, and thermal vacuum. Before and after every major stage of testing, the RF performance of the coax cables was measured and found to be within specification.

After completion of these environmental tests, the unit underwent a complete life test. As with many life tests, this particular one was performed at an accelerated rate when compared to the actual mission profile. By doing so, the requirements of 14×10^6 degrees of travel and 7×10^5 directional reversals was accomplished in three months instead of several years. To complete both the travel and reversal requirement at the same time, the BA was actuated in a "sawtooth" profile, as seen in Figure 2.

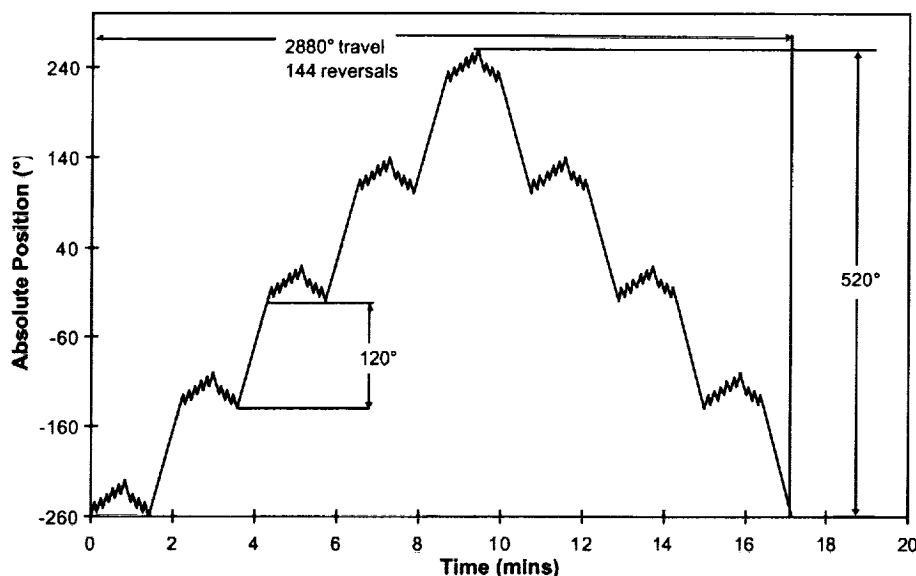


Figure 2. Life Test Travel Profile

This sawtooth profile consisted of a series of $+15^\circ/-10^\circ$ dithering motions, combined a $\pm 120^\circ$ slew, and was repeated approximately 5000 times. The BA slewed at its maximum operational rate of $\sim 3^\circ/\text{sec}$. The entire life test was performed under a vacuum of $< 6.6 \times 10^{-3} \text{ Pa}$ ($5 \times 10^{-5} \text{ torr}$) and at a variety of operating temperatures, from lab ambient to $\sim 60^\circ\text{C}$.

No RF testing was performed during the life test. The post-life RF performance test revealed that all the coaxial cables were failing voltage standing wave ratio (VSWR)¹ for frequencies $> 5 \text{ GHz}$, with increases as much as 120% from their pre-life values. Also, some had unacceptable insertion loss² values. The

¹ VSWR is one standard way to express the amount of reflected energy due to mismatches within the cable. For an ideal cable, there is no energy being reflected back to the source, resulting in a VSWR equal to 1. The equation for

VSWR is: $VSWR = \frac{1+\rho}{1-\rho}$, where $\rho = \frac{\text{Reflected Energy}}{\text{Incident Energy}}$

² Insertion loss is another standard expression involving how much energy is transmitted through the cable. Ideal cables transmit all incident energy, resulting in an insertion loss value of 0. Insertion loss is defined as:

magnitude of the insertion loss changed as a function of output shaft position, with the largest value occurring when the cables were fully "unwound" inside their respective chambers. However, the coax cables did have acceptable performance in both VSWR and insertion loss for frequencies < 5 GHz for all output shaft positions.

This type of coaxial cable is ~0.48 cm (0.19 inch) in diameter and is used in high frequency, low-loss applications. The cable consists of five components: an outer perfluoroalkoxy (PFA) jacket, a silver-coated flat copper wire braid, a silver-coated flat copper foil, a PTFE tape-wrapped dielectric core, and a stranded silver-coated copper inner conductor.

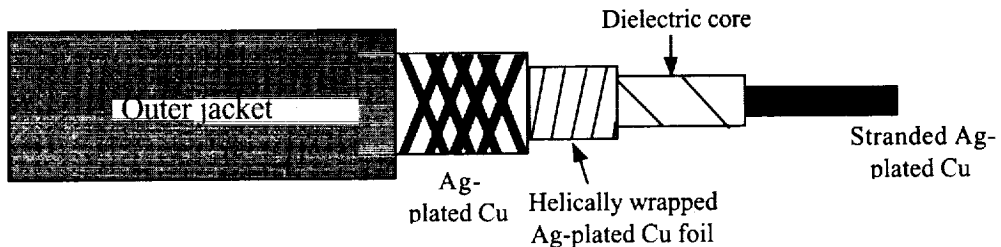


Figure 3. Construction of the coaxial cable used in the BA

Investigation

Investigation into these anomalous readings began with time domain reflectometry (TDR) testing, which provides an impedance versus cable length plot. These tests were performed at a number of output shaft positions because the insertion loss was observed to increase as much as 80% depending on the output shaft position. TDR plots showed a number of significant spikes in impedance of the cables, with the majority of the spikes occurring inside the cablewrap near the inner hub, at the smallest bend radius. The magnitude of these spikes were dependant on output shaft position (see Figures 4 and 5), with the greatest magnitude corresponding to the highest insertion loss readings. These higher insertion loss readings occurred when the cables were in the fully unwrapped condition.

The next step in the investigation was to physically inspect the cables themselves, which proved to be more dramatic. As the cable was removed from the cablewrap and straightened out, the cable had a number of dents, or kinks. At these locations, the wire braid appeared disturbed, or "bird caged" as viewed through the translucent jacket. The largest damage was concentrated within the first 0.9 meter (3 feet) from the inner hub, although damage was observed as much as 1.5 meters (5 feet) away. Also, some of the outer jacket and shield had been punctured, revealing the dielectric underneath (Figure 6).

$$\text{Insertion Loss(dB)} = -20 \log \frac{V_{\text{transmitted}}}{V_{\text{incident}}}, \text{ where } V \text{ is voltage}$$

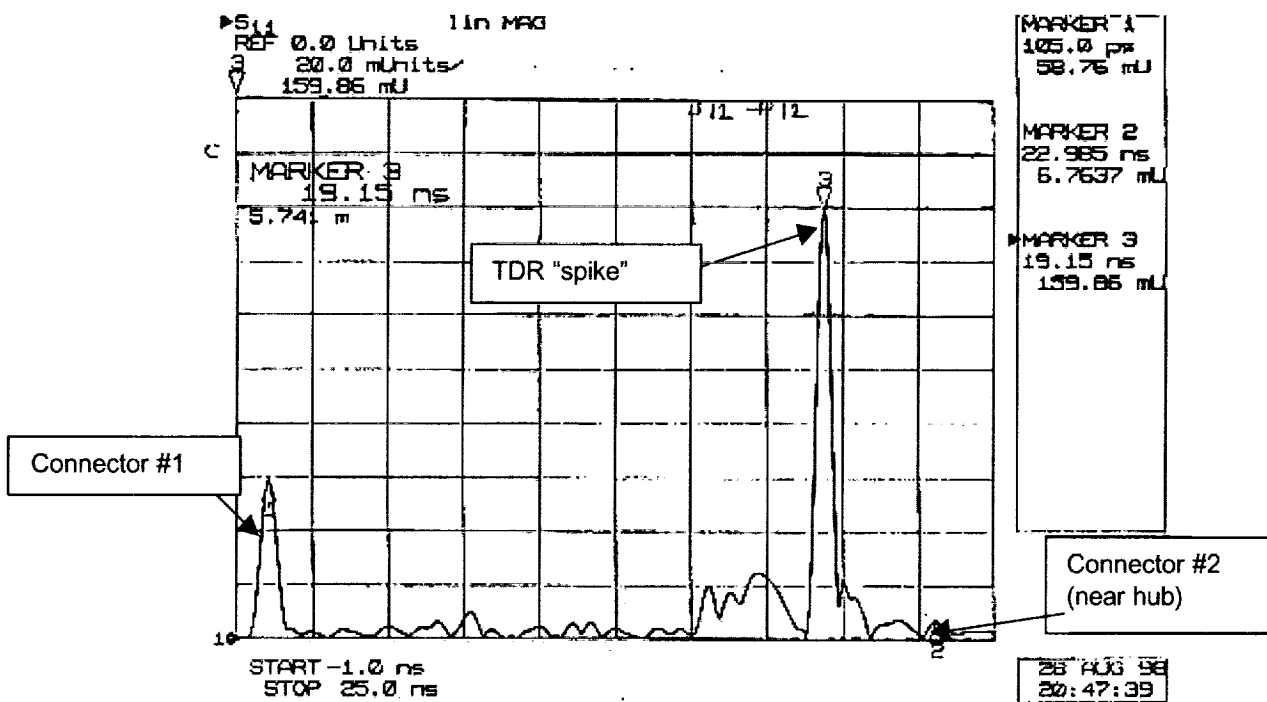


Figure 4. TDR plot of one of the BA's coaxial cables in the unwrapped position.

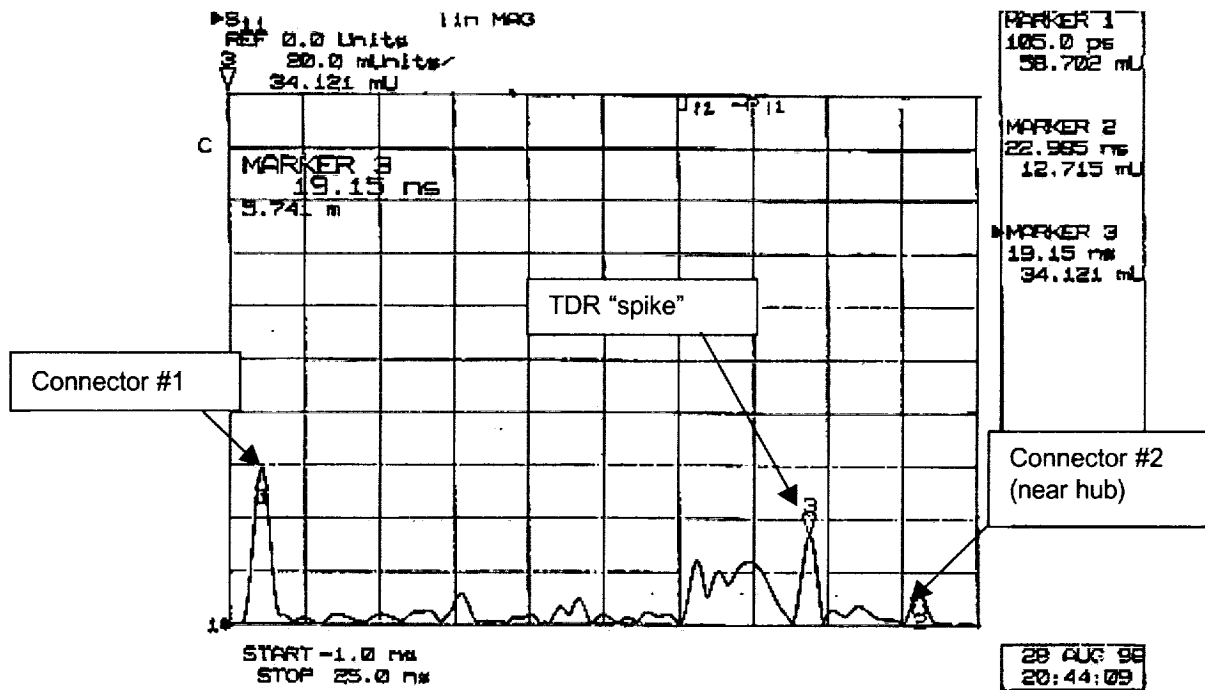


Figure 5. TDR plot of same cable in the wrapped position.

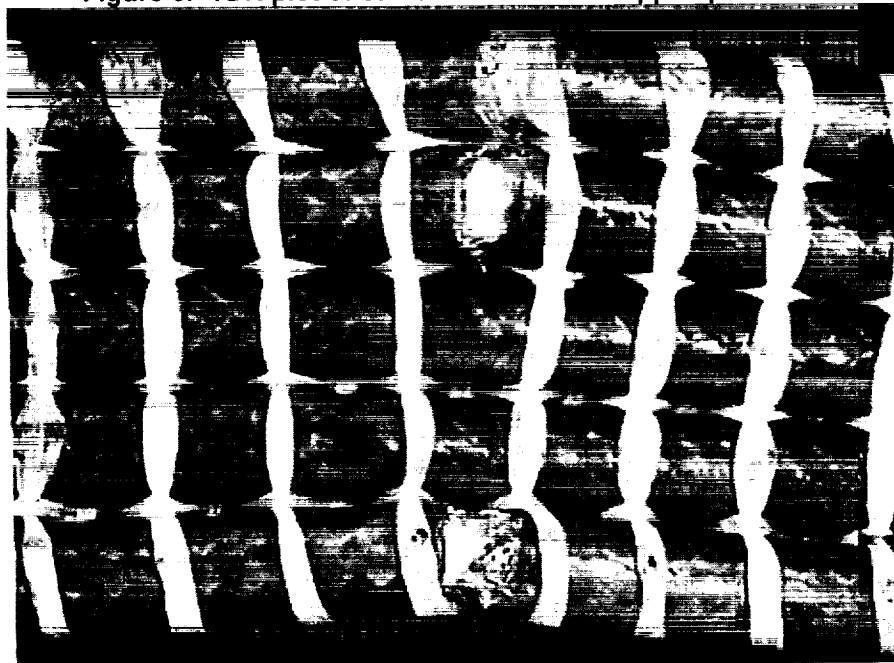


Figure 6. Photo of the coax cable after removal from the cablewrap

The location of the damage matched the spikes observed in the TDR measurements. Furthermore, when the BA was actuated, the gaps in the outer shields tended to close when the cablewrap wrapped tighter, explaining the dependence of the insertion loss on output shaft position.

Physical dissection of the cable pointed to the cause of the damage. Photos using a Scanning Electron Microscope (SEM) revealed that the wire braid had bonded to the foil shield at various locations (Figures 7 & 8).

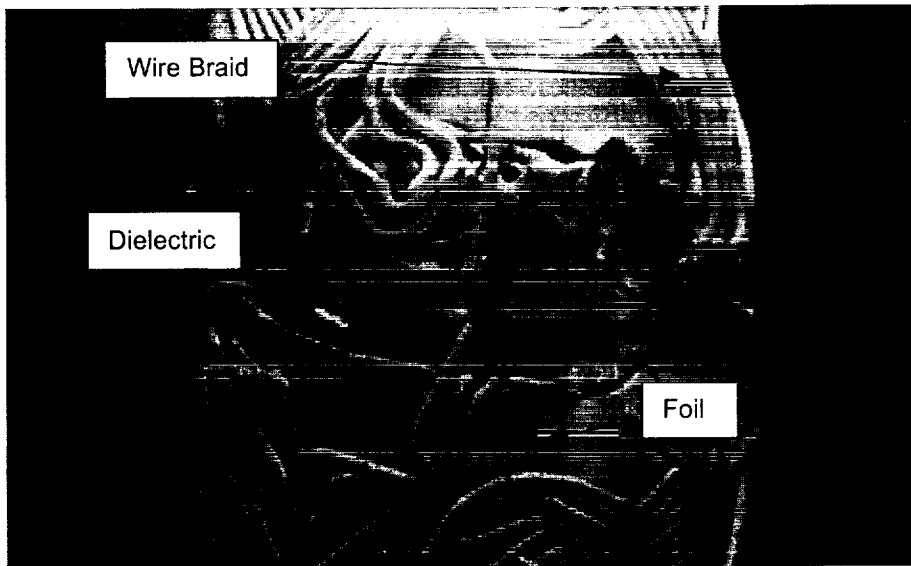


Figure 7. SEM photo of a typical damaged section of coaxial cable, with jacket removed

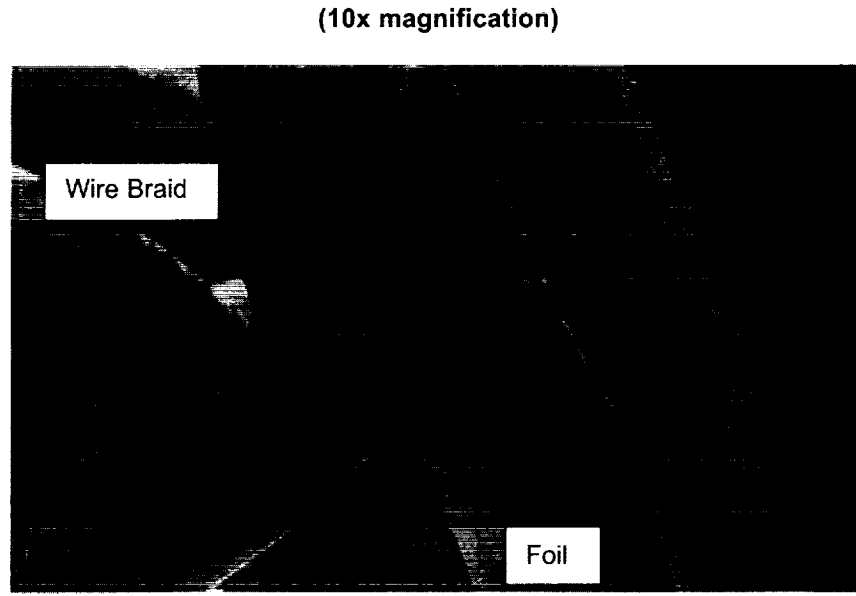


Figure 8. SEM photos of the coaxial cable show the wire braid and foil bonded together (200x magnification)

Study into how the wire braid bonded to the foil pointed to a phenomenon known as "cold welding". Cold welding is a molecular-level bonding that occurs when two atomically clean, smooth surfaces are in intimate contact. Silver is one material highly susceptible to cold welding, due to its high ductility. Cold welding occurs readily in a vacuum environment due to the lack of oxidation between the two surfaces. As its name suggests, cold welding does not require elevated temperatures to occur.

There were 3 types of cold welding found in the coax cables; foil-foil cold welding, foil-braid cold welding, and braid-braid cold welding, all involving similar metals (in this case silver) contacting each other. However, only one type of cold welding, the foil-to-braid cold welding, caused the localized deformation within the cable.

The wire braid and foil slide over each other as the cable is flexed. This motion removes the existing silver oxide layer, providing clean surfaces for cold welds to form. When the wire braid and foil cold weld together, this relative motion is prevented, and a hinge point is created. Eventually, the continued flexing fatigues the wire braid and foil, with the outer jacket now keeping the cable together. In locations of the most flexing, the outer jacket was also observed to fatigue. This failure mechanism was proven in subsequent flexure tests of isolated cables, as described in the next section.

Resolution

Was the BA, by being subjected to a life test unrepresentative of the actual mission profile, overtested or did the cables need to be replaced? As mentioned before, the life of the unit was condensed into a three-month test, where the BA slewed at a higher rate and different motion profile than the actual mission. By performing two flexure tests to determine how the rate of motion and amount of travel affected cold welding, the answer to the overtest question was found. Using fresh pieces of coaxial cables with the same construction as the failing ones, the flex tests were set up to simulate the cablewrap configuration in the BA. The cables were flexed around the same size hub as in the cablewrap and were bonded in two restraining fixtures which kept the cables in place yet did not subject them to any clamping forces (similar to the cablewrap). The test was setup per the drawing in Figure 9. All flex tests were performed in a vacuum of at least 1.3×10^{-2} Pa (1.0×10^{-4} torr).

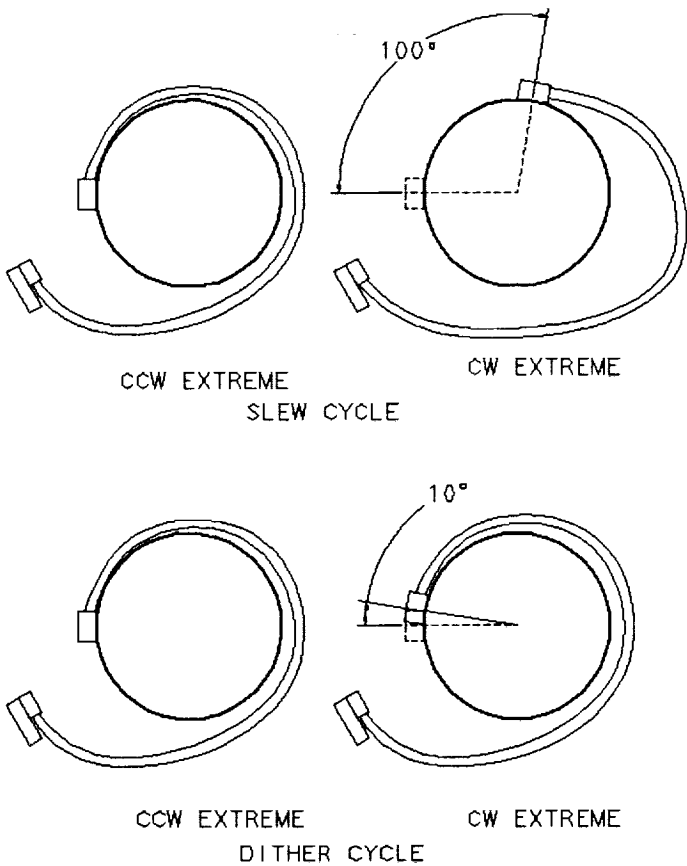


Figure 9. Sketch of flex test setup

Another purpose of these flex tests was to screen ways of preventing cold welding in coaxial cables. By identifying how cold welding occurs, methods of preventing its occurrence presented themselves. One such method is to place some type of barrier, made of materials different than the wire braid and foil, between the two components. PTFE tape, the same tape used in the dielectric core of the cable, was selected as a good candidate due to its low coefficient of friction. Another way to prevent cold welding is to have the wire braid and foil be of dissimilar materials. One such material proposed for the wire braid was a composite metal/fiber material, providing both strength and conductivity. Both such cable constructions were flex tested.

The flex tests were broken up into two different tests, both with different average velocity rates and degrees of flexure. The first test, herein referred to as the slew test, had the cables flexing at an average velocity of 6.7°/sec with a range of travel of $\pm 100^\circ$. There were six cables subjected to this test: two PTFE-barriered cables (referred to as PTFE-B cables), two composite wire braid (CWB) cables, and two cables of the old construction. All the cables were flexed a minimum of 264,000 slew cycles.

The second test, referred to as the dither/slew test, flexed the cables at an average velocity of 1.7°/sec with a combination of $\pm 10^\circ$ motions (dithers) and $\pm 100^\circ$ motions (slews). These flexing motions were alternated periodically throughout the test, which more closely represents the actual life test. A total of nine cables

(three of each type) underwent this test and were flexed for a minimum of 185,000 dither cycles and 20,000 slew cycles.

RF testing consisted of VSWR, Insertion Loss, and TDR's taken at frequencies between 1-15 GHz at various intervals throughout both tests. All cables were terminated with SMA connectors at both ends, similar to the BA. The RF testing was performed when the cables were in the full unwrapped configuration (CW extreme, see Figure 9), the same position as the worst RF results from the BA testing.

Results

Slew Test

Fairly early into the test (~500 cycles), the old cables exhibited signs of cold welding that affected RF performance. TDR traces showed spikes, indicating damage to the cables, at locations where the cables were seeing the most flexure, ~1 cm from the clamps. Visual examination confirmed the presence of cold welding of the braid to the foil, as indicated by the distortion of the wire braid. Eventually, the outer jacket separated in two places on one cable.

RF performance of the old cables remained in specification in the low frequency range of < 5 GHz. However, in the frequencies > 5 GHz, all the old cables saw increases in their VSWR and Insertion Loss resulting in out of specification conditions, which occurred starting at ~120,000 cycles.

Although the PTFE-B and CWB cables did experience cold welding of the foil with itself, neither developed the cold welding between the braid and the foil that damaged the old cable. TDR traces remained similar throughout the test, and RF performance stayed within specification.

Tables 1 and 2 summarize the worst case RF performance of the cables in the slew test at various frequencies. Each number represents the maximum or minimum value measured throughout the entire test, along with the expected value for this type of cable.

Table 1: RF Performance at ~2 GHz Range for slew test

Cable Type	Max VSWR	Min Insertion Loss (dB)
Nominal	1.2	-0.412
Old	1.19	-0.39
PTFE-B	1.10	-0.34
CWB	1.11	-0.38

Table 2: RF Performance at ~15 GHz Range for slew test

Cable Type	Max VSWR	Min Insertion Loss (dB)
Nominal	1.35	-1.08
Old	1.92	-3.74
PTFE-B	1.26	-0.91
CWB	1.24	-1.07

Dither/Slew Test

The dither/slew test began with the cables dithering for approximately 47,000 cycles, during which the cables exhibited no change in RF performance or in their TDR profiles. However, once the cables underwent slew cycles, the old cables developed spikes in the TDR traces and their wire braids distorted in a number of places. Eventually, all the old cables developed cracks in their outer jackets, as seen in Figure 10.



Figure 10. Picture of the old cables after removal from dither/slew test shows outer jacket splitting.

The old cables eventually went out of spec in the higher frequency ranges starting at 94,000 total cycles (87,000 dithers, 7000 slews). The RF performance at the lower frequency range never went out of spec. As for the PTFE-B and CWB cables that underwent the dither/slew test, their RF performances and TDR traces remained stable throughout. Tables 3 and 4 summarize the RF performance data for the dither/slew test.

Table 3: RF Performance at ~2 GHz Range for Dither/slew Test

Cable Type	Max VSWR	Min Insertion Loss (dB)
Nominal	1.2	-0.412
Old	1.11	-0.36
PTFE-B	1.08	-0.39
CWB	1.10	-0.40

Table 4: RF Performance at ~15 GHz Range for Dither/slew Test

Cable Type	Max VSWR	Min Insertion Loss (dB)
Nominal	1.35	-1.08
Old	1.88	-4.04
PTFE-B	1.15	-1.07
CWB	1.13	-1.2

Conclusions

The results of these two flex tests, as well as others performed prior to these tests, have proven that the mechanical discontinuities in the cables observed in the BA were an inherent design feature in the old cables rather than due to an overtest. Cold welding, which causes these discontinuities, has proven to be dependent on a number of factors, including the rate and travel that the cables are flexed. However, changing these two factors will not prevent cold welding in the old cables.

Looking at how the travel effects cold welding, the results suggest that a combination of small and large angle flexures develops the discontinuities faster than either motion by themselves. During the dither/slew test, the small angle motions developed cold welding of the braid and foil faster than the large angle motions, in part because the relative motion of the two components was large enough to create the clean surfaces needed for cold welding yet small enough not to break up these bonds, allowing them to strengthen. Then, the addition of the slews flexed the cold welded cables enough to create the hinge points. Thus, the dither/slew test, which better represents the actual life test than slewing alone, has proven that old cables are prone to RF-degrading mechanical discontinuities when subjected to flexing in a vacuum environment.

Although changing the rate of motion did not prevent the RF failures due to cold welding, there did seem to be some dependence on when the cold welding occurred. This dependence can be attributed to the duration of the contact between the wire braid and the foil. As the rate of motion is decreased, the time the wire braid and foil are in intimate contact increases, forming stronger cold welds. However, more rigorous flex testing is required to better understand this rate dependence.

Ultimately, the results of this extensive investigation into the RF failures resulted in the decision to refurbish the BA with different coaxial cables. Cables with the PTFE barrier between the wire braid and foil were selected as the replacement, due to their similarity to the old design.

Lessons Learned

Certainly, the lessons learned from this failure are valuable to any mechanism engineer who must contend with flexing of coaxial cable in a space environment. Due to the widespread use of coaxial cable to transmit RF signals in low-loss/high frequency applications, cold welding is a common spacecraft mechanism design consideration. Furthermore, these lessons extend beyond coaxial cable to any cable construction where similar metals are in contact.

Also, the importance of life testing fully configured spacecraft mechanisms is demonstrated by this example. Often, life tests are performed on drive modules (consisting of motors, bearings, gears, etc.) only, assuming that other components such as cables are stable throughout the life of the unit. But when sensitive components are involved, unexpected observations are sometimes encountered. Although the BA failed its life test, the purpose of a life test, to identify potentially mission threatening conditions, was fulfilled successfully.

Acknowledgements

The author would like to thank the members of the BA team for their hard work and dedication. Special thanks to Kathy Dacey and Raymond Liu for their perseverance and support. Also, I would like to thank Mark Carroll for persuading me to write this paper and helping it through the approval stage while I was exploring Europe.

The SeaWinds Scatterometer Antenna Subsystem on the QuikScat Spacecraft

Brian J. Workman^{*} and Eric Schwartzbaum^{**}

Abstract

In today's environment of "Better, Faster, Cheaper", the ability to produce reliable, flight-proven mechanisms for mission critical applications is more important than ever. Such a mechanism was produced for the QuikScat satellite. The Scatterometer Antenna Subsystem (SAS) is a spin mechanism that continuously rotates a scatterometer antenna, and includes the necessary features (rotary interfaces, drives, launch locks, etc) to allow collection of the scatterometry data that will insure mission success. This paper will discuss the evolution of the SAS from its design heritage on the GGS Polar mission to qualification on the ADEOS II satellite to being a key enabler for the rapid development of the QuikScat Satellite.

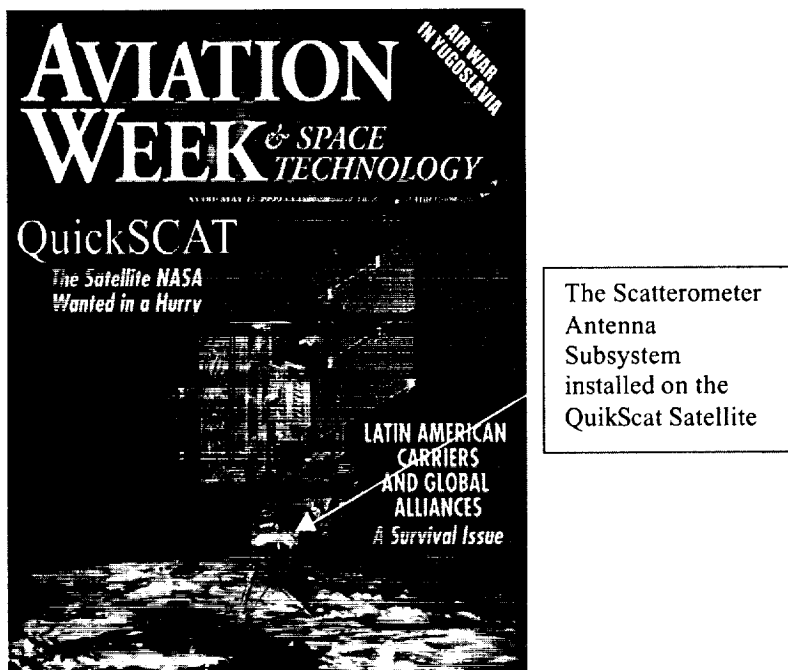


Figure 1. The SeaWinds Scatterometer Antenna Subsystem mounted on the nadir deck of the QuikScat spacecraft

Introduction

The QuikScat spacecraft is the first obtained under a new NASA program for rapid spacecraft acquisition, and was completed in just 12 months. Designed to acquire global, all-weather, high-resolution measurements of near-surface winds over the world's oceans, the spacecraft has been in the news repeatedly for its ability to track and measure wind speeds associated with hurricanes and even tracking a giant iceberg. The spacecraft was featured on the cover of *Aviation Week & Space Technology* in May of 1999. QuikScat was launched in June of 1999.

^{*}Honeywell Inc., Satellite Systems Operation, Glendale, AZ
^{**}Jet Propulsion Laboratory, California Institute of Technology, Pasadena, California

The SeaWinds instrument flying on the QuikScat Spacecraft and its near twin planned for launch on the ADEOS II spacecraft are composed of three major subsystems. Honeywell Satellite Systems Operation (SSO) designed, built, and tested the Scatterometer Antenna Subsystem, which is shown in Figure 1 mounted to the QuikScat nadir deck. The SAS includes the spin mechanism, drive motors, speed control, dish antenna, and RF rotary interfaces. Raytheon provided the Scatterometer Electronics Subsystem (SES), which generates the radar pulses transmitted to the ocean via the antenna as well as receiving and processing the radar echo. The SES and SAS interface via wave guides. The Command and Data Subsystem (CDS), which provides the command and telemetry interface with the spacecraft, was built by the Jet Propulsion Laboratory, which also integrated the three subsystems into the SeaWinds instrument.

The deployment and spin mechanism portion of the SAS traces its heritage to the despun platform mechanism on the Polar spacecraft of the Global Geospace Science (GGS) program. Launched in February of 1996, the Polar spacecraft has flawlessly completed its design life, and operation for another full lifetime is currently planned.

Description

Due to its size and complexity, a complete and detailed description of the Scatterometer Antenna Subsystem is beyond the scope of this paper. However, a brief description of the main mechanisms and components is useful prior to discussion of design evolution and lessons learned.

The SAS is shown in Figure 2. Overall height including the antenna is approximately 1.47 meters (58 inches). Total mass of the subsystem is about 60 kg. Design life is 4.5 years with a planned mission life of 3 years. The SeaWinds SAS consists of four major subassemblies: the Antenna Assembly (AA), the Base Structure Assembly (BSA), the Spin Actuator Assembly (SAA), and the Electronics Assembly (EA). These major subassemblies are identified in Figure 3.

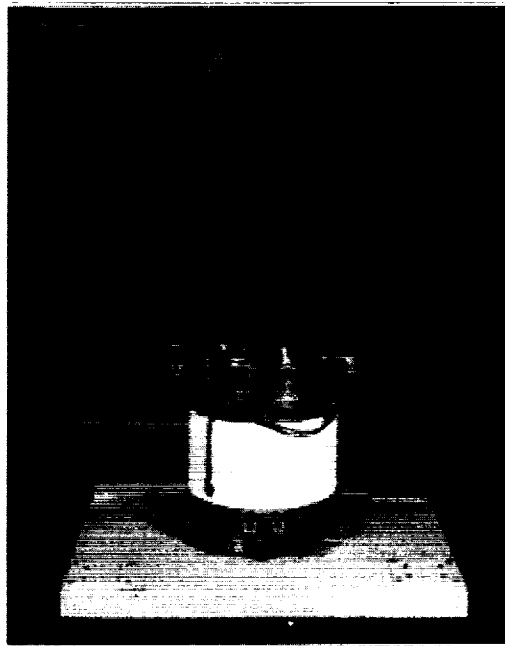


Figure 2. The SeaWinds Scatterometer Antenna Subsystem

The antenna assembly is a carbon graphite composite dish antenna, one meter in diameter, with a pair of linearly polarized feed horns that are supported by a tripod strut arrangement. These feed horns alternately transmit and collect the RF radar pulses generated by the instrument. Collected RF signals

are conducted through two composite WR75 wave guides attached to one of the support struts. The wave guides interface to a dual channel rotary joint housed within the SAA and mounted to the antenna plate, which interfaces with the antenna pedestal. The composite antenna assembly is bonded to a titanium mounting ring (for thermal isolation between the AA and SAA) that facilitates attachment to the SAA.

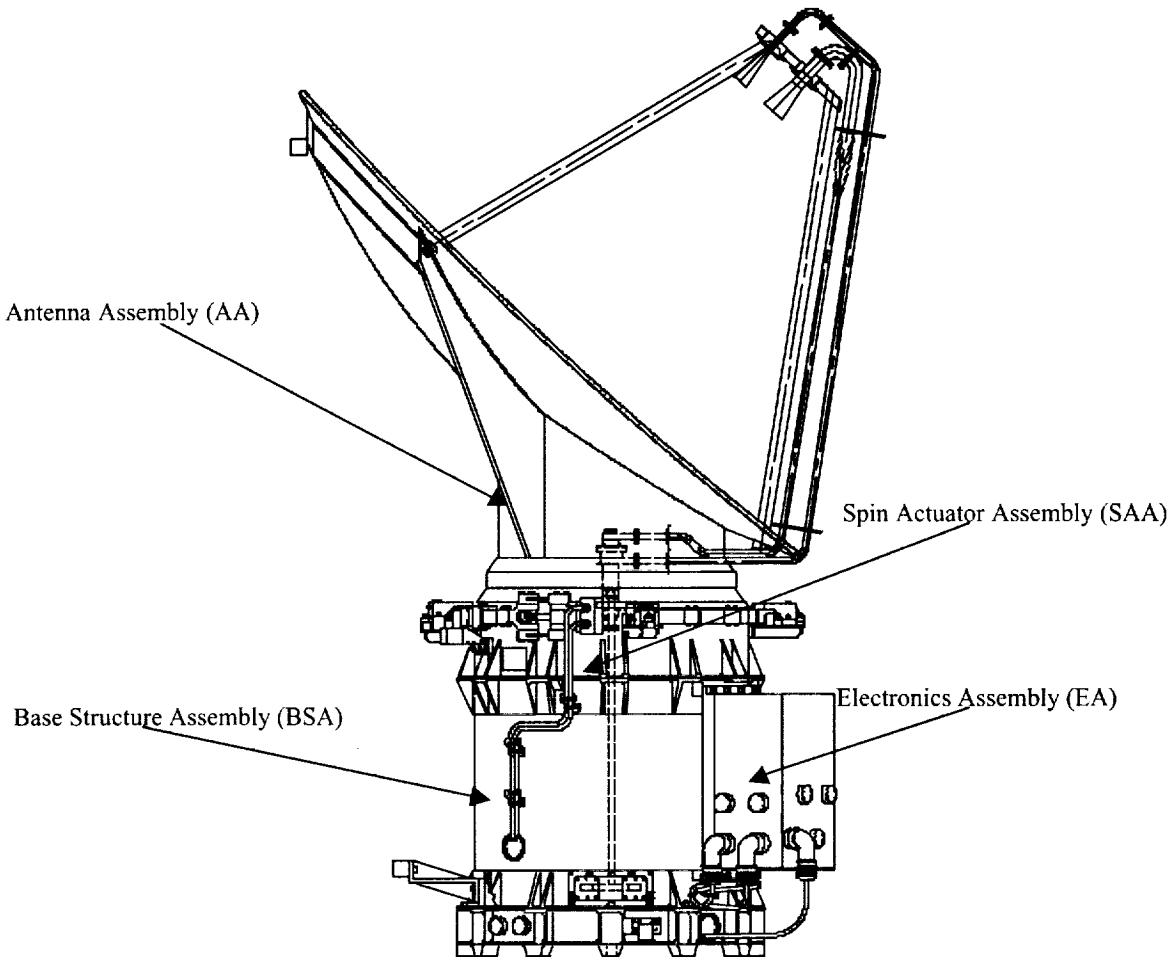


Figure 3. Major Subassemblies of the Scatterometer Antenna Subsystem

The BSA provides the structural interface between the spacecraft, the SAA, and the EA. It consists of a hollow aluminum cylinder approximately 48 cm (19 in) in diameter on a thermally isolating titanium base ring. The SAA mates to the upper mounting flange of the BSA with its lower portion extending down into the cylinder. Mounting points on the side of the cylinder provide for attachment of the EA. Interfaces are provided for connecting to the wave guide runs that are mounted to the spacecraft nadir deck and extend to the SES. Two bulkhead connectors at the bottom of the BSA provide for electrical connection to the pyrotechnic initiators on the SAA. Two white rectangles of thermal paint located at select locations on the outside of the BSA act as passive thermal radiators. The remainder of the surface of the BSA is covered with a multilayer insulation (MLI) thermal blanket. As will be discussed in the "Design Evolution" section, the outside of the BSA provided mounting locations for the later addition of the "survival" heaters that were necessary for adaptation of the design for operation on the QuikScat mission.

The SAA is the heart of the SeaWinds instrument. This assembly houses the motors, bearing system, encoder, launch lock and release mechanism, and heaters. These components are shown in Figure 4.

Redundant power conditioning, motor control, and bridge driver circuit card assemblies are located around the circumference of the SAA as shown in Figure 4. These electronics trace heritage to the GGS program. The SAA has two brushless DC motors that are offset slightly to help reduce cogging torque. The redundant, 24-pole brushless wye-wound motors are continuously commutated. A dual channel RF rotary joint provides the rotary interface between the wave guides of the antenna and those in the BSA.

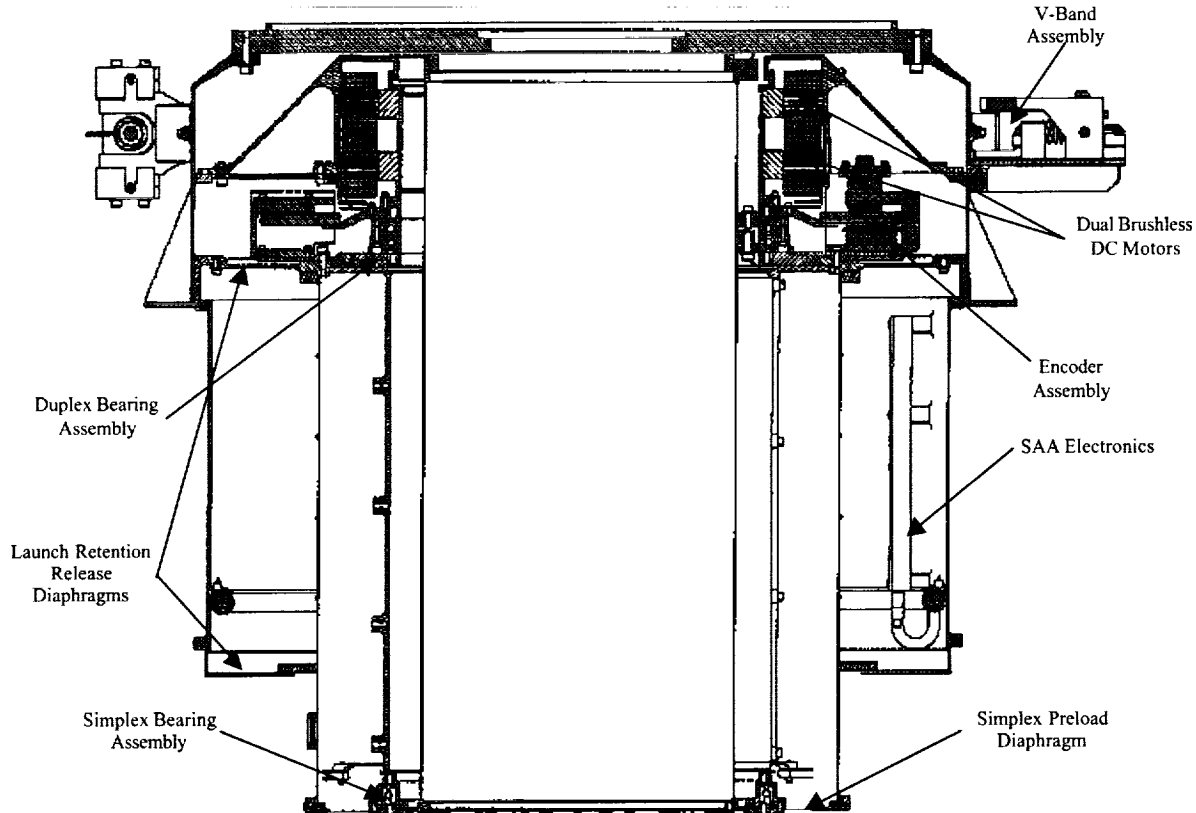


Figure 4. Cutaway view of the Spin Actuator Assembly

The 15-bit incremental optical encoder produces 32,768 pulses per revolution with an end-of-life incremental accuracy of approximately 10 arc seconds. These pulses, along with a once-per-revolution index pulse provide antenna azimuth position to the CDS, critical for ground signal processing and inferring of the ocean wind vectors. The optical encoder also produces two analog outputs, one sine and one cosine at 12 pulses per revolution used in the SAA electronics for commutation of the drive motors. The optical encoder is electrically redundant, using separate pick-off stations for each channel. Encoder electronics are packaged on four semicircular cards located underneath the disk.

Pointing knowledge and stability are critical requirements of the SAS. Antenna boresight pointing knowledge accuracy is critical for obtaining the required wind vector accuracy. Elevation angle calibration uncertainty includes all uncertainties in the measurement of beam angle from the electrical boresight to an optical reference cube on the BSA and must be less than 0.15 degree. Total azimuth uncertainty also includes uncertainties related to the encoder and command signal processing. Azimuth uncertainty must be less than 0.20 degree. Post-launch beam angle stability effects include thermal distortion, humidity, launch environment, rotation, gravity, life, and other time-varying, on-orbit effects. The requirements for elevation and azimuth beam angle stability are less than or equal to 0.15 degree and 0.25 degree, respectively. The required high precision pointing and stability requirements are maintained through employment of close tolerance interference fits. SAS elevation and azimuth pointing stabilities as

determined by analysis are better than 0.04 degree of which less than 0.02 degree is contributed by the SAA structure. Elevation and azimuth pointing calibration uncertainties of less than 0.10 degree and less than 0.16 degree, respectively, were achieved for the SAS, which exceed the requirements.

The bearing system consists of a preloaded DF duplex bearing pair at the upper end of the shaft, and an angular contact simplex bearing located at the bottom of the shaft. The duplex bearings are preloaded against each other to provide axial and radial stiffness. The simplex bearing is preloaded against the duplex pair with an axially compliant diaphragm to provide additional angular stiffness. The duplex bearing is basically a set of conventional thin section bearings machined directly into a bearing cartridge, eliminating several parts and the high tolerance fits usually required between them. The design features a one-piece inner race and separate outer races that are fastened together. Both the duplex and simplex bearings are 440-C steel with segmented phenolic cages and are manufactured to ABEC-7 equivalent tolerances. Preload sensitivities to fits and temperatures are minimized by mounting the bearing in a titanium sleeve that is structurally isolated from the surrounding aluminum structure by slots that are electrodischarge machined into the titanium. This almost completely eliminates preload changes due to fits and thermal expansion differences between the aluminum structure and the bearing. The duplex bearing is located several inches from the SAA/AA interface, which allows the use of a thin-walled hollow titanium shaft to provide thermal isolation. The high deflection diaphragm that provides preload to the simplex bearing keeps the bearing preload almost constant over the entire temperature range. The bearing lubrication system uses NYE 179A oil with sacrificial oil reservoirs and labyrinth seals to provide reliable lubrication over mission life.

The V-Band launch retention mechanism prevents antenna rotation and offloads the bearings from dynamic loads during launch (Figure 5). A marmon clamp arrangement that consists of a set of V-blocks on a titanium strap pulls the antenna mount down into contact with the structure of the SAA and against a spring force provided by two diaphragms. When dual pyrotechnic initiators are fired, a separation nut releases and tension is released in the band. The two diaphragms push the antenna mount apart from the main housing, forcing the V-blocks outward and allowing an axial gap of 1.5 millimeters (0.06 inch) between the rotating and non-rotating features. The V-Blocks are pulled out of contact with the structure by a set of coil springs and captured in a set of "catcher" mechanisms that positively lock them in place until they are manually released. When the band separates, a break wire opens sending a release telemetry signal. The interfaces between the V-blocks and structure are lubricated with a molydisulfide lubricant that is burnished into the surface of the structures.

The EA consists of a compact arrangement of electronics modules housed within an aluminum chassis. All electrical interfaces to the spacecraft, except those for the pyrotechnic actuators, are made through the circular bulkhead connectors on the EA. The EA contains all functions required for command, control, and telemetry of the SAS. Two isolated and redundant channels of power conversion, power conditioning, and speed control/telemetry modules are provided. The power conditioner/converter module receives a nominal primary 40 VDC bus voltage and generates the 15 and 5 VDC required internally by the EA as well as conditioned 28 VDC required for the SAA. Rate control electronics receive encoder pulses from the SAA and derive rate as an analog voltage. The signal is fed back and differenced with a reference voltage representative of 18 or 20 rpm, as selected by ground controllers. The choice of two slightly different operational speeds is provided as a contingency against the coincidence of rotational speed to a dynamic mode of the spacecraft. The rate error signal is compensated and output to the SAA as an analog torque command. The analog rate signal is also conditioned and output as active analog telemetry. Encoder pulses are accumulated in a 16-bit counter, which is reset by a zero index pulse. This data is representative of antenna azimuth angle and is conditioned and output as RS422 telemetry. The speed control loop circuitry ramps up the rotational speed of the antenna during start up at an artificially slow rate in order to minimize torques induced to the spacecraft. The circuit card modules of the EA represent all of the electronics that are "new" to the SeaWinds program. All electronics retained from the GGS heritage unit are contained within the SAA itself.

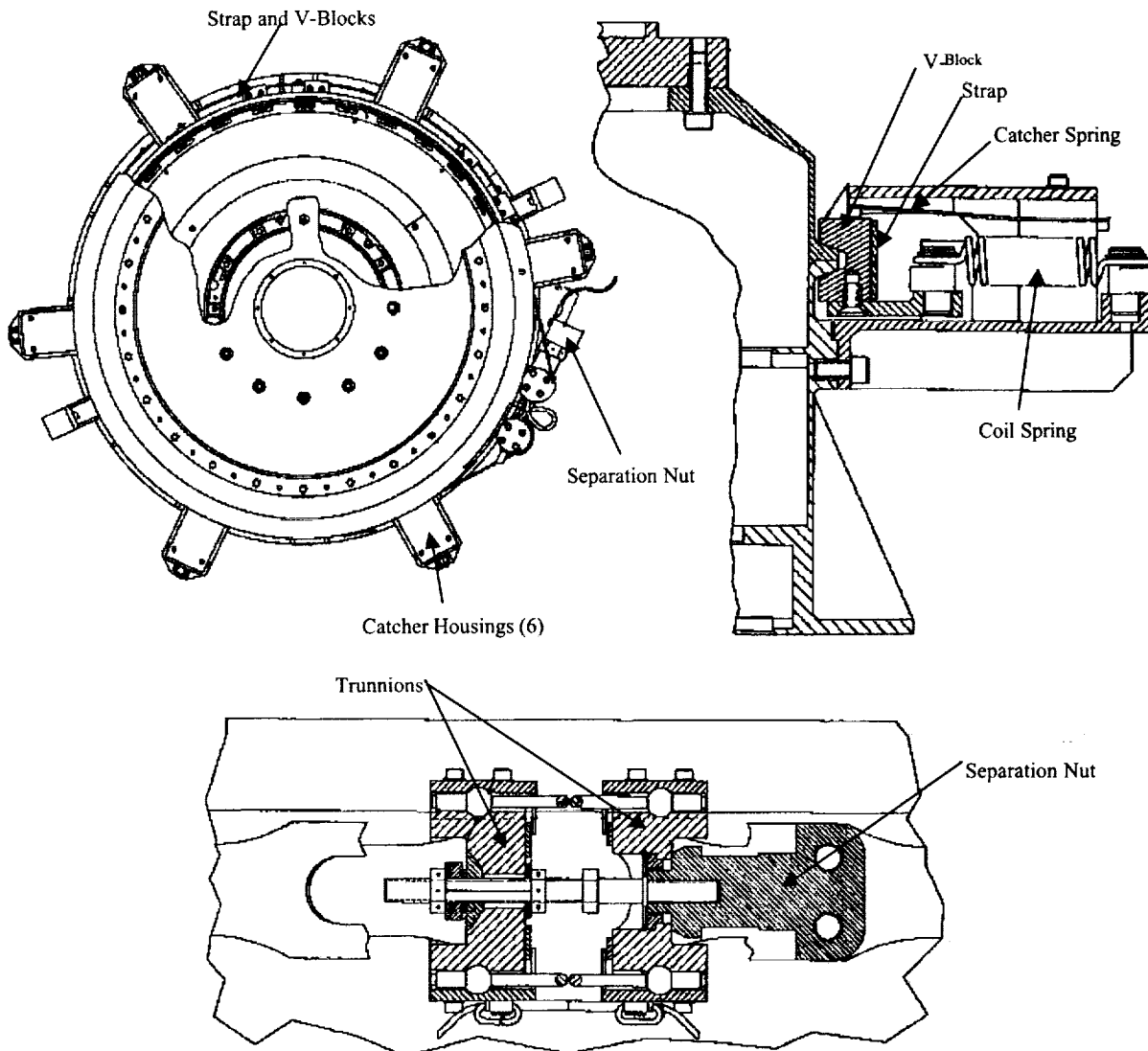


Figure 5. Pyrotechnically released V-Band launch lock mechanism

Thermal control is provided by the appropriate selection of radiator size and heater power. The SAA contains thermostatically controlled "replacement" heaters that are powered on when the electronics are not in order to maintain temperatures at the operational level. "Supplemental" heaters (also thermostatically controlled) maintain electronics and bearing temperatures when the instrument is in operation. In addition, the QuikScat version of the SeaWinds instrument adds externally mounted "survival" heaters that were necessary to accommodate differences between the QuikScat and ADEOS II electrical bus. The QuikScat survival heaters are powered on by the spacecraft automatically in survival or launch modes. Thermal isolation between the SAA and AA is maintained by virtue of the titanium antenna mounting plate, minimized physical contact with the titanium shaft, and a skirt of aluminum thermal shields mounted around the circumference of the base of the antenna plate. This thermal skirt is isolated from the titanium antenna plate by phenolic spacers and screens the titanium interface minimizing radiative heat transfer to deep space. Thermal isolation between the SAS and the spacecraft is maintained by use of a reduced contact area between the spacecraft and the titanium ring that makes up the lower portion of the BSA.

Design Evolution

The value of adapting previously developed hardware for quick missions can hardly be understated. Risk is minimized, especially if the heritage hardware has flown or is flying, and the design is open to adaptability. Such was the case between the GGS/Polar mission, the SeaWinds on ADEOS II mission, and the SeaWinds on QuikScat mission. Lessons learned from one mission can be applied directly to the design as it is adapted for its new mission.

The SAA portion of the SAS evolved directly from the GGS Polar spacecraft's Despun Platform Mechanism Assembly (DPMA). In that application, the speed loop is closed by spacecraft electronics in order to maintain an instrument platform stationary in inertial space while the cylindrical spacecraft rotates at 10 rpm to provide stability. In the DPMA, a 69-channel slip ring module inhabits the volume now occupied by the heaters in the SeaWinds SAS. The slip rings are required to provide a rotary electrical interface to the instruments on the platform.

The GGS DPMA launch lock design utilized customer-furnished separation nuts for actuation of the release mechanism. The customer on that program sought to minimize costs by using the same configuration separation nut for every pyrotechnically activated release mechanism on the spacecraft. Unfortunately, this configuration was not optimal for the V-band release mechanism on the DPMA. The nose of the separation nut contained a groove for a retaining c-clip. The forces involved in release and retraction of the V-Band assembly were occasionally greater than would be contained by the clip. This resulted in ejection of the c-clip, leaving the separation nut connected to the mechanism only by its ground strap. The solution at the time was to safety wire the nut and c-clip in place. For the SeaWinds device, the nose of the separation nut was redesigned by elimination of the groove and addition of a threaded feature. Thus, the separation nut was positively held in place by a spanner nut to one of the V-Band trunnions. This modification to the separation nut was made in such a way that the original qualification testing of the nut design was still valid, eliminating the cost of requalification.

The power budget available for operation of the GGS DPMA was very limited, precluding the use of heaters in the thermal design. In order to minimize viscous drag and assure adequate torque margin at cold temperatures, the bearing system was designed to operate with very little lubricant. 100 mg of Nye 179A oil was applied to each row. Sacrificial oil reservoirs supplied supplemental quantities of oil over the life of the mission. At 10 rpm, the bearing system operates in the margin area between EHD and non-EHD regimes. A life test was performed in order to gain confidence in the bearing and slip ring designs. The SeaWinds application has a much greater power budget, but operates at a faster speed and mission life is longer. Analysis of the GGS bearing in the SeaWinds environment indicated that the system would meet Honeywell SSO's internal design practice requirements for lube loss over life. Nevertheless, oil quantity was increased to 1.25 gram per row to add margin. This is close to the maximum quantity of free oil that the bearing would hold. The presence of heaters, the absence of drag from slip rings, and a more benign cold environment enabled this increase in free lubricant quantity yet still ensures significant torque margin at cold temperatures (about a factor of 2 at -20°C as determined during thermal vacuum testing). The increase in speed moves the bearing operation further into the EHD regime. This, coupled with a reduction in preload, yielded a better probability of success value in the fatigue analysis. The GGS instrument platform is approximately 118 kg (260 lb). The SeaWinds AA is approximately 6.8 kg (15 lb). This difference in payload mass results in a significant decrease in bearing loads and allowed the reduction in nominal unmounted preload from 980 N (220 lb) to 556 N (125 lb). Confidence in the successful heritage life test results and on-orbit performance data, extensive analysis, and the fact that all of the changes moved the bearing design in a favorable direction resulted in a decision to forego additional life testing.

SeaWinds successfully used a "red line" methodology for design changes. Flexibility of design allowed for inclusion of heater circuitry in the volume made available by removal of the slip rings. The large opening through the center of the shaft that was necessary to accommodate a large boom antenna on the Polar spacecraft provided the necessary space to allow installation of the wave guides and dual channel

rotary joint. These design changes were made by redlining the original drawings that were used to fabricate an engineering unit. Minor design corrections were captured on these redlines, which were then released for procurement of the flight hardware. This approach streamlined the design effort considerably.

NASA benefited from a contract requiring a deliverable engineering unit and spares. The original Honeywell SSO/JPL contract for the SeaWinds SAS called for construction of the engineering unit SAS, a flight unit SAS, and flight spare subassemblies for contingency. These included a spare SAA, BSA, EA, AA and rotary joint assembly. When the ADEOS I spacecraft, carrying the NASA Scatterometer (NSCAT), was lost in June of 1997, NASA directed JPL to initiate the QuikScat mission to quickly reinitiate the scatterometer data stream. JPL directed Honeywell SSO to integrate the spares into a second flight SAS unit. The spare SAS along with spare CDS and SES units were then integrated together onto the QuikScat spacecraft with the intent of launching the spare instrument as quickly as possible to fill the data gap left by the NSCAT loss.

The differences in the dynamic launch environments of the two SeaWinds missions were considered. The spin axis of the SAS as mounted to the QuikScat spacecraft bus was in line with the flight direction of the launch vehicle, whereas the spin axis of the ADEOS II mounting was perpendicular to the flight direction during launch. Thus, the direction of quasi-static loading due to acceleration during launch was different for the two missions. A Titan II launch vehicle was selected for the QuikScat mission. The ADEOS II spacecraft is scheduled for launch on an HII-A. The Titan II launch vehicle generally has lower acoustic and random vibration launch loads (no solid rocket propellant) than the H-IIA. From analysis it was determined that no structural design changes were required due to these differences in dynamic environments during launch.

The thermal environment of the QuikScat mission was determined to be more severe than that of ADEOS II for two main reasons. First, even though both the QuikScat and SeaWinds on ADEOS II missions utilize 800-km, sun-synchronous orbits, the relative spacecraft orientation with respect to the sun is significantly different (Beta angle). The result is that in the case of QuikScat the SAS -Y surfaces are continually sun pointed and the +Y surfaces always view deep space, a very different attitude than that which will be seen by SeaWinds on ADEOS II. Secondly, QuikScat is a dedicated mission housing only the SeaWinds instrument. Thus the SAS is mounted alone on the nadir deck, whereas in the ADEOS II configuration SeaWinds is surrounded by several other instruments, which both provide thermal shielding as well as radiate heat to it. This necessitated several thermal control design changes including radiator surface area reduction and location change, thermal blanket modifications, and the addition of external "survival heaters". The design of the survival heaters involved bonding RER65 resistors to the outside of the BSA with a thermally conductive epoxy in the proximity of the duplex bearings. The heater resistors were then wired in place to form two channels of series-parallel heater circuits.

Lessons Learned

V-Band

It was learned during the GGS program that a more secure method of retaining the separation nut was needed. The use of safety wire to prevent ejection of the c-clip was cumbersome, time consuming, and a "band-aid" solution at best. As discussed in the previous section, a much better solution was to incorporate a threaded nose into the separation nut design.

Another lesson learned came from unexpected embrittlement of titanium. During tensioning of the V-Band of the second flight unit (QuikScat) the (6Al-6V-2Sn) titanium strap of the V-Band suddenly fractured. Although no other damage was caused, the failure came as quite a surprise considering the maturity of the design. The fracture occurred at the thin, webbed portion of the strap at a location near the right trunnion. Analysis showed that the stress at the fracture was about 196 MPa (28,400 psi), far below the 1000 MPa (145,000 psi) yield strength of the material. No failures occurred in either the first

flight unit or the engineering unit in spite of the fact that all were from the same lot and the engineering unit was significantly exercised during qualification testing.

When the original strap drawing was generated and the straps were fabricated for the heritage GGS application, the most economical way to manufacture the straps was to have them stamped from a sheet and then formed on mandrels to their final shape. By the time procurement of the SeaWinds straps was initiated, advances in manufacturing techniques allowed numerically controlled laser cutting to become much more economical because the tooling required for stamping was no longer needed. Unfortunately, and unknown to the strap vendor, this less common titanium alloy is susceptible to embrittlement from localized heating. Honeywell SSO's failure analysis laboratory performed a failure analysis on the part. Investigation by scanning electron microscopy, microhardness testing, microstructure examination, and chemistry analysis revealed a heat affected zone containing recast layers and recrystallized alpha rich grains near the fracture origin. Secondary cracking was also detected at the same location.

Figure 6 is a photograph of the fractured web. The web is 7.37 mm (0.29 inch) in width and is the upper of two webs that wrap around the right (separation nut) trunnion. "Up" is to the right in this view and the fracture initiation point is identified by the arrow. A close up view of the fracture surface is shown in the scanning electron micrograph of Figure 7. It shows the crack initiation site in the recast layers (marked with an arrow) and the alpha-rich grain (marked with a double arrow). Both the recast layer and the alpha rich grain are prone to being brittle. The remaining area exhibits the characteristic features of a typical ductile fracture. Figure 9 represents the upper fracture section shown in Figure 7 with arrow, viewed in the longitudinal direction after polishing away 0.41 mm (0.016 inch) from the outside surface and etched with a reagent. The distinctive white and dark areas indicate the heat-affected zone where phase transformation and microstructural changes in the metal have occurred. The typical macroetched appearance of this titanium alloy can be observed on the right portion of the section. A pre-production material coupon from the same lot was subjected to the same processes to simulate the production experience of the failed strap, and it was verified that these embrittled areas were caused by localized overheating due to the laser cutting.

The solution to the problem was to replace the straps with new ones that had been cut by the abrasive water jet process. This process eliminates the heat effect completely. This conclusion was verified by processing a sample from the preproduction coupon, and is supported by published literature on the abrasive water jet process. Replacement straps were fabricated using this method and both the QuikScat and ADEOS II flight units had their straps replaced. As an added demonstration of confidence, these new straps were proof tested to levels significantly in excess of the nominal tension range.

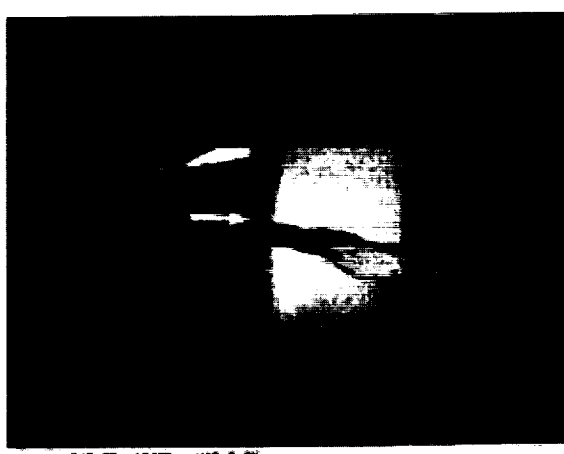


**Figure 6. A photographic view showing the location of the fractured web.
The inboard edge of the web is identified with an arrow.**

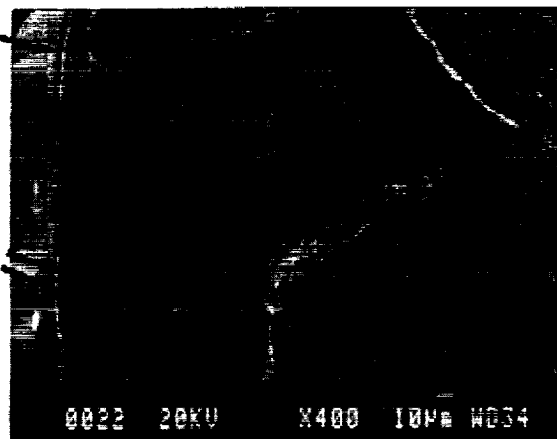


Figure 7. A Scanning Electron Micrograph of the fracture surface showing the crack initiation site in a recast layer (single arrow) and the alpha rich recrystallized grain (double arrows).



Figure 8. A macrograph of the fracture viewed longitudinally, showing the heat-affected-zone and recast layer identified with an arrow at the inboard edge.

Because the original manufacturing drawing for the strap was generated at a time when it was known that the parts would be stamped, no restrictions regarding localized heating of the part were included in the notes on the drawing. Engineering needs to maintain an understanding of the processes used during manufacture of parts, and need to remain cognizant during the procurement process so they become aware of changes in those processes. Significant drops in quotes from manufacturers to fabricate an established part should act as a flag to inquire about any changes in processes.

Circuit Card Stiffeners

One channel of the SAA electronics on the first flight unit failed to operate after a workmanship vibration test. Investigation of the failure led to the discovery that the screw holding down one of the large inductors on the power conditioning cards had not been torqued. This inductor had come loose and knocked a nearby transistor off the card, disabling operation of that channel. The apparently obvious solution was to not only torque these inductors down, but to also add a step to bond them to the circuit card as well. This seemed to solve the problem as the unit passed workmanship and acceptance level vibration at the subsystem level. However, when the second flight unit with bonded inductors was shaken during its acceptance test, a failure exhibiting the same symptoms as the first failure occurred.

Upon disassembly it was discovered that the card stiffener frame had fractured, allowing greater card deflections, which resulted in a fatigue failure of the leads of the same transistor that was knocked off the board on the previous unit. This time, a detailed investigation and analysis of the situation was performed.

The stiffener was originally designed and analyzed for the heritage GGS device. Initial analysis of the SeaWinds dynamic environments indicated that the heritage GGS design was sufficient to handle the somewhat higher SeaWinds levels. The resolution of this analysis was insufficient and failed to detect the narrow margin of the card stiffener to the new environment. When the inductor, which has a relatively large footprint, was bonded to the card, it resulted in a local increase in stiffness. This changed the fundamental mode of the card and directed the dynamic energy to the stiffener. The situation was made worse by a pre-stressed condition of the stiffener that resulted from the torques applied to the bolts used to fasten it to the card. This pre-stressed condition in particular would have been difficult to foresee during the original analysis.

The result of the investigation led to a redesign of the stiffener making it thicker and changing its cross section to make it stiffer in lateral bending in order to resist the stresses induced from assembly. Retrofit of the new card stiffeners to the power conditioning boards of both flight units finally solved the problem. There are several lessons learned here. First, make sure that analyses of "delta" environments are of sufficient resolution and provide adequate margins. Second, time must be taken to consider the consequences and possible impacts of even seemingly simple changes.

Conclusion

The SeaWinds Scatterometer Antenna Subsystem has been demonstrated to be a reliable, flight-proven mechanism for mission critical applications. Its on-orbit performance to date has been exceptional.

The SeaWinds SAS demonstrates that even a custom device, if it is robust and well designed, can evolve for use in entirely new applications. The end application of the SeaWinds device as a closed-loop antenna spinner is considerably different than that of the GGS despun platform mechanism. Yet the design was successfully developed through addition of new structure (the BSA), new electronics (the EA), modification of the existing design by eliminating the slip rings, adding an RF rotary joint and antenna, and adapting the design to new life and thermal requirements. Judicious use of "red line" drawing controls and an engineering unit were useful in this process. This example of re-use of previous flight hardware designs shows an effective way to reduce costs and meet the requirements of the "better, faster, cheaper" paradigm.

The redesign of existing hardware is not without hazards. When hardware is reordered from an earlier program, changes in manufacturing techniques can cause problems. Pay attention to the consequences of these manufacturing "improvements". Significant changes in quotes from manufacturers to fabricate an established part should act as a flag to inquire about changes in processes. The V-band problem described in this paper is an example of this from the SeaWinds effort. The specific lessons learned from this problem are to beware of localized heating of 6Al-6V-2Sn titanium during manufacturing, and that abrasive water jet techniques can be used in place of laser cutting to minimize localized heating.

The current successful flight of the SeaWinds instrument on the QuikScat spacecraft is a good example of a well-adapted design. This redesign of heritage hardware for a new and different application illustrates a cost-effective approach, while illustrating the need to consider hazards and learn from previous programs.

References

- 1.) *Aviation Week & Space Technology*, May 17, 1999. Aviation Week & Space Technology is a publication of The McGraw-Hill Companies, Inc.
- 2.) Ying Liu, "Failure Analysis Report 19406: V-Band Assembly", Honeywell Inc., Satellite Systems Operation, Product Assurance Labs
- 3.) H. R. Phelps, "AWJ Cutting of Titanium Vent Screens for the F-22 Advanced Tactical Fighter", Lockheed Martin Aeronautical Systems, Marietta Georgia

Antenna Pointing Mechanism for Steerable Spot Beam Antennas.

Manfred Schmid*

Abstract

The Antenna Pointing Mechanism (APM) was developed in the frame of a research and development program dedicated to geostationary Ka band communication antennas. At the end of the development phase, an APM qualification model was built and successfully tested. One of the main development goals was to establish a design not only accommodating the reference Ka band antenna, but fit for a range of potential applications and antenna configurations at low recurring costs. Figure 1 shows the Antenna Subsystem configuration that formed the basis for the APM development. This paper discusses the chosen technical approach and mechanism features on the basis of the established requirements as well as the issues encountered during the development and test phase.

Introduction

The Antenna Pointing Mechanism developed by DSS is a device to steer spot beam communication antennas. It is a compact and self-standing unit with simple interfaces to the satellite and also to the antenna. The unit tilts a complete antenna or antenna dish only, depending on the application, with two rotational degrees of freedom. The APM provides excellent pointing and performance repeatability over a wide temperature range and was already tested in an open-loop control configuration. The unit is able to accommodate a high-resolution encoder for closed-loop position control if required. Commercial sub-units and parts modified for space applications are used as far as possible.

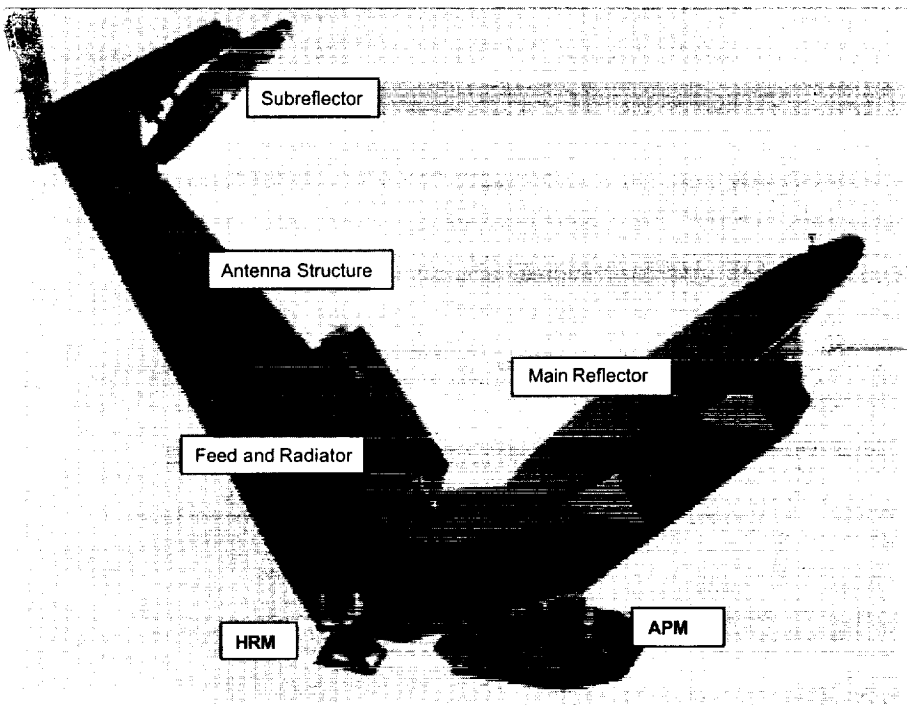


Figure 1: Steerable Ka Band Antenna Reference Configuration

* DaimlerChrysler Aerospace, Dornier Satellitensysteme GmbH (DSS), Friedrichshafen, Germany

Proceedings of the 34th Aerospace Mechanisms Symposium, Goddard Space Flight Center, May 10-12, 2000

Basic Set of Requirements

At the beginning of the development phase, a basic set of design, performance and environmental requirements was agreed upon and chosen as a working basis.

Table 1: Design Requirements

Design Requirements	Value	Comments
Number of Rotation Axes	2	
APM height	150 mm	
APM length / width	360 x 360 mm	
APM Mass	6 kg	mass budget had to be increased from 5 to 6 kg due to change of the required antenna mass to be supported in the course of the project
Antenna Mass to be supported	24 kg	requirement was changed from 15 kg to 24 kg during the project
Antenna Mol to be supported	15 kg·m ²	
APM Design Loads	in plane 15 g / out of plane 30 g	
Storage Life	7 Years	
Orbit life	15 years	at 4 repositionings / day
Waveguide Routing	possible to route up to 4 flexible Ku-or Ka-band waveguides along the APM	
Position Monitoring	provide I/F for position monitoring devices	potentiometers or encoders, depending on application.
Holddown and Release Mechanisms	2 pyrotechnically activated HRMs	mounted to the antenna structure

Table 2: Performance Requirements

Performance Requirements	Value	Comments
Pointing Range	10 deg halfcone	
Pointing Velocity	>5 deg / minute	
Pointing Accuracy / Repeatability	+/-0.01 deg	achieved value +/- 0.005 deg
Step Resolution	0.002 deg	at full step command
First System Eigenfrequency	50 Hz	(antenna with 24 kg mass and 15 kgm ² Mol, supported by APM and 2 HRMs)

Table 3: Environmental Requirements

Environmental Requirements	Value	Comments
Sinus Qual. Vibration Levels	12 to 15 g in plane (x, y) 6 to 30 g out of plane (z)	depending on frequency
Random Qual. Levels	17 grms in plane (x, y) 20.5 grms our of plane (z)	
Qualification Temperature Requirement	-40 to +60°C	Goal +107°C to -110°C was set on basis of thermal analysis results for an unprotected APM
Transportation Temperature	+60°C to -60°C	
Humidity max	85%	relative

APM Design Concept

A trade-off was performed at the beginning of the development phase in order to select the most appropriate design concept in view of the given set of requirements. Based on the key requirements such as:

- flexible design allowing to accommodate complete Antennas and Antenna Dishes as well
- geometric constraints (low overall height)
- possibility to rout flexible Ka (or Ku) band waveguides along or through the centre of the APM
- high antenna mass to be supported
- high stiffness
- simple and reliable design
- low recurring costs
- minimum possible mass

a two-axis gimbal system (cardan frame) was chosen as a baseline. In order to avoid static over-determination in the launch position and to avoid that the gimbal actuators have to take dynamic loads from the antenna, the APM actuator output is decoupled from the gimbal I/F during launch. By this concept the actuator can be sized as a lightweight unit of high output precision. The gimbal actuators are designed as linear actuators and during mission the actuator output transforms its linear motion into a rotational one at the gimbal level. An almost constant preload acting to the actuator I/F is provided by means of a spring package integrated to the gimbal. The gimbal system arranges both rotation axes in one horizontal plane so that a very compact and stiff configuration is achieved. The gimbal frame provides a central opening that can be used to accommodate a set of flexible waveguides, if required by the application.

The chosen APM concept allows adjustment to an initial operational pointing position of the Antenna already on ground. After release of the two separate Hold Down and Release Mechanisms (HRMs), the spring-loaded gimbal contacts the actuator output shaft, thus providing the pre-adjusted initial pointing position. All further pointing activities will then be performed by commanding the actuators to any arbitrary position.

Major Sub-units and Important APM Components

The overall APM layout consisting of the following main assemblies and sub-assemblies is shown in the next figure (Figure 2). A corresponding parts list is depicted in Table 4. Since the HRM's have no direct interface to the APM, these items are described in a separate section of this paper.

Gimbal Assembly

Gimbal Unit

The Gimbal Unit forms the central load carrying part and functional unit of the APM Gimbal Assembly. Its task is to provide the required rotational degrees of freedom about two axes, to allow the attachment of the antenna, and to take the launch loads. The Gimbal Unit comprises the two Base Brackets connecting the APM to the satellite, the two Frame Brackets forming the interface to the antenna, and the Cardan Frame interconnecting the Base Brackets and the Frame Brackets via the corresponding Bearing Units. The cardan frame is manufactured out of titanium for stiffness reasons. In order to compensate for thermal disturbances, each gimbal axis is designed with a fixed and a floating pair of bearings. The floating bearing pair of each axis is equipped with a double membrane element manufactured out of BeCu alloy.

At the beginning of the development phase, simple Gimbal Brackets manufactured out of aluminum and equipped with pairs of preloaded hybrid ball bearings in an X arrangement, wet-lubricated TiC balls, were considered as a baseline. In a late stage of the design, it was found that the temperature regime specified at the beginning of the development had to be significantly changed on basis of the outcome of the thermal analysis results. Based on these results, the qualification temperatures for the mechanism

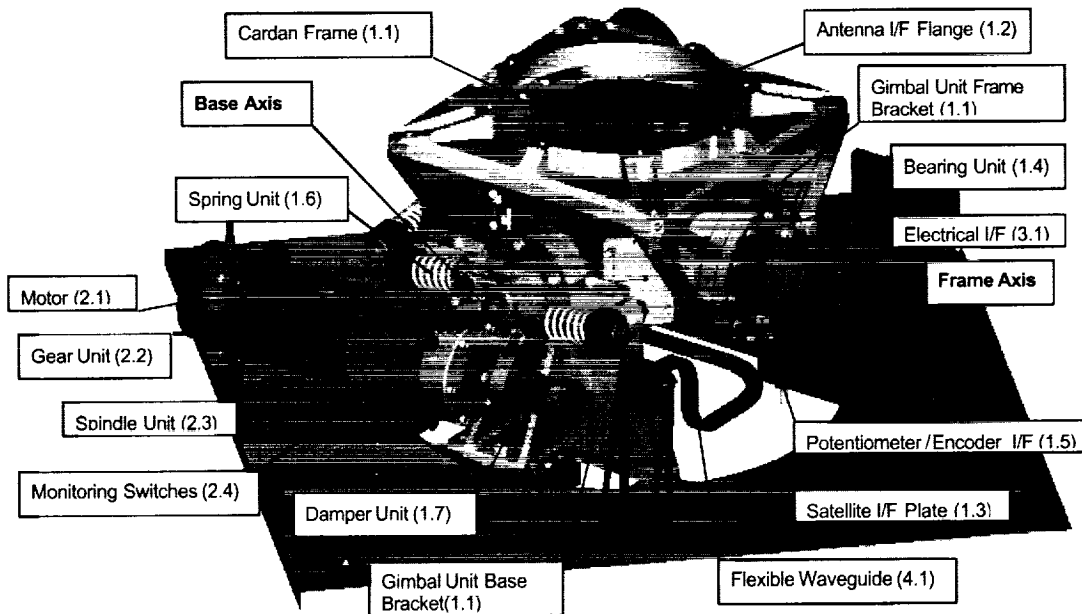


Figure 2: APM Configuration

Table. 4: Main Assemblies and Subassemblies Overview

Assembly	ID-No.
Gimbal Assembly	
Gimbal Unit/Cardan Frame	1.1
Antenna I/F Flange	1.2
Satellite I/F Plate	1.3
Bearing Unit	1.4
Potentiometer /Encoder I/F	1.5
Spring Unit	1.6
Damper Unit	1.7
Linear Actuator	
Motor	2.1
Gear Unit	2.2
Spindle Unit	2.3
Monitoring Switches	2.4
Electronics	
Electrical I/F	3.1
Rx, Tx Power Transmission	
Flexible Waveguide	4.1

changed from the assumptions of -40 up to $+60^{\circ}\text{C}$ made at the beginning, to calculated values reaching from -110°C up to $+107^{\circ}\text{C}$ for a worst-case orbit. It was found to be not an adequate solution to use MLI on the APM, since the mechanism has to perform a 2-axis motion leaving only a very small clearance underneath the antenna structure if tilted to an extreme position. Furthermore a strong interference with the HRMs was identified, so that for the further development activities a mechanism concept allowing to cope with the temperature extremes had to be considered as a baseline. Based on these facts, the

simple aluminum bracketry foreseen for the Gimbal Unit, combined with hybrid bearings was not longer feasible due the following reasons:

- In the low temperature case (ΔT about -130°C) the CTE between the Al bearing seat and the outer bearing ring caused unacceptable high stresses in the aluminum part.
- The high stresses in the Al-bracket caused in addition unacceptable radial deformations of the outer bearing ring.
- This negative effect is even increased due to the small CTE of the ceramic balls, keeping their diameter almost constant while cooling down the steel rings.
- The use of liquid lubricant at the expected low temperature regime is not adequate and the use of MoS_2 lubrication had to be considered.

In order to solve the problem, a trade-off between different potential solutions was performed. In a first approach, titanium brackets instead of aluminium were considered in order to deal with the CTE mismatch, however, a significant mass penalty had to be taken into account. The use of stainless steel for the brackets would have also solved the thermal mismatch problem, however, it was considered out of scope from the mass point of view. Table 5 shows the results of the thermal deflection analysis.

Table 5: Thermal Deflections for different Material Combinations

Material of bracket	ΔT [K]	ΔD_{in} [μm]	ΔD_{out} [μm]	ΔD [μm]	ΔD_{Ball} [μm]	ΔD_{res} [μm]
Aluminum	-110	-39,46	-79,96	-40,50	-5,34	-29,82
Titanium	70	25,10	28,40	3,30	3,40	-3,50
Dispal S225	70	25,10	31,30	6,20	3,40	-0,60

Assumptions and Explanations:

- Max allowable bearing diameter change $< 10 \mu\text{m}$
- Bearing balls and bearing rings in 440C
- No pre-stresses caused by bearing integration tolerances and bearing preload are assumed
- ΔT = Max. temperature difference between integration (ambient) and worst case operational temperature
- ΔD_{in} = Bearing inner diameter
- ΔD_{out} = Bearing outer diameter
- ΔD = Resulting diameter change between the bearing rings
- ΔD_{Ball} = Diameter change of the ball (multiplied by 2 for bearing diameter change)
- ΔD_{res} = Resulting negative bearing play

Based on these results and the fact that the detailed design drawings were already finished, the only quick and reliable way out of the problem was to switch from hybrid bearings to standard 440C steel bearings of the same dimensions, to choose dry lubrication as a baseline, and as a very important point, to use DISPAL S 225 Aluminum alloy (AlSi) as a baseline for the gimbal brackets instead of Aluminum 3.4364 alloy. DISPAL S 225 has the big advantage to provide a CTE that is close to steel at the specific weight of standard Aluminum. The major concern on the material was its potential stress corrosion cracking susceptibility expected due to the high amount of Si in the alloy and the sinter manufacturing process of the raw material. The material was already used in a space project (MHS) by DSS and in the frame of this project a stress corrosion crack test was performed. Based on this test, a material usage agreement was established by NASA for the project. The most important material properties of DISPAL S 225 (produced by PEAK) compared to alternative materials are summarized in Table 6.

Antenna to APM and APM to Satellite Interface

The mechanical I/F between Antenna and APM is realized by a hole pattern on top of the frame brackets that can either directly accommodate the antenna structure or allows the antenna to attach via a dedicated I/F adapter. In the actual design, the latter possibility is used to reduce the thermal interference between the metallic structure of the APM and the CFRP antenna structure to a minimum. By using the ring shaped I/F plate, a symmetric radial stress distribution can be achieved between the

Table 6: Material Properties of DISPAL S 225 Compared to Alternative Materials.

Mech. Property	DISPAL S 225	AL 3.4364 T 7351	Ti 3.7164.1	Steel 1.3543
Tension Strength	265 MPa	480 MPa	900 MPa	1970 MPa
Yield Strength	192 MPa	420 MPa	830 MPa	1900 MPa
Young's Modulus	93000 MPa	71000 MPa	110000 MPa	216000 MPa
Specific Mass	2620 kg/m ³	2890 kg/m ³	4490 kg/m ³	8000 kg/m ³
CTE (21-100°C)	$10.2 \cdot 10^{-6}$ 1/K	$23 \cdot 10^{-6}$ 1/K	$9 \cdot 10^{-6}$ 1/K	$10.1 \cdot 10^{-6}$ 1/K
Material	DISPAL S 225	AA 7075 T 7351	MIL-T-9046	AISI 440 C

Antenna and the APM I/F plate without producing significant deformations in the APM gimbal bracket. The I/F between the APM and Satellite panel consists of a 5-screw hole pattern (3 on one base bracket, 2 on the other). The attachment screws are equipped with thermal washers out of GFRP in order to limit the heat flux from the satellite to the APM and vice versa. An optional Baseplate with I/F to the APM only but not to the satellite panel can be used to accommodate accessories such as waveguide brackets, connector brackets, harness etc. without affecting the satellite I/F.

Bearing Unit

The Gimbal Brackets are equipped with pairs of 440C bearings in an X arrangement (Table 7). Each gimbal axis is equipped with a pair of fixed and a pair of floating bearings. The axial motion capability is realized by a pair of BeCu membranes, which interface with the corresponding bearing pair.

Table 7: Bearing Characteristics

Characteristics	Fixed Bearing	Floating Bearing
Material	X102CrMo7 (1.3543)	X102CrMo7 (1.3543)
Outer Diameter	37 mm	47 mm
Bore	20 mm	30 mm
Cage Material	PTFE	PTFE
Lubricant	Ion-sputtered MoS ₂	Ion-sputtered MoS ₂
Thickness of Lubricant Film	< 0.5 µm	< 0.5 µm
Arrangement	X arrangement	X arrangement
Preload	343 N	267 N

Potentiometer / Encoder Interface

In the baseline design, I/F flanges are foreseen on both APM axes in order to allow the accommodation of a customer-specific position-sensing device (potentiometer or high-resolution encoder). In the actual design, open-loop steering forms the baseline.

Spring / Damper Unit

The Gimbal Base Bracket as well as the Gimbal Frame Bracket is equipped with a Spring Unit allowing to force the Gimbal via a lever arm against the linear output I/F of the APM actuator during operation. By this concept, the actuator I/F is preloaded with an almost constant force over the operation angle so that hysteresis effects in the actuator can be limited. The concept implies that each gimbal axis is operated in one direction by moving the linear actuator against the spring force while in the other direction the spring force is used to tilt the gimbal simultaneously with the retracting actuator. During launch, the gimbal is locked by the HRMs in a position outside the nominal APM working range so that the actuators are out of the mechanical load path and decoupled from the antenna. After releasing the HRMs in orbit, the Spring Units force the gimbal against the actuators so that a pre-adjusted first mission configuration can be achieved without activation of the actuators. In order to reduce the shock loads in the actuator I/F due to gimbal release, a damper unit equipped with a set of Belleville washers is provided in the actuator I/F. The Belleville washer package is preloaded such that the maximum force applied by the Spring Unit is

always smaller than the preload of the damper unit. By this measure, a defined position of the damper system is always assured in operational conditions.

Linear Actuator

Besides the Gimbal Assembly, the Linear Actuator forms the second major assembly of the APM mechanism. One actuator comprises a two-phase stepper motor, a planetary gear, and a nut / spindle unit with linear guidance. Due to the cogging torque of the motor, the ratio of the gear and the chosen small spindle pitch, the actuator provides good backdriving torque capability so that the first mission pointing position can be pre-adjusted on ground without losing it during launch. Figure 3 shows the linear actuator design.

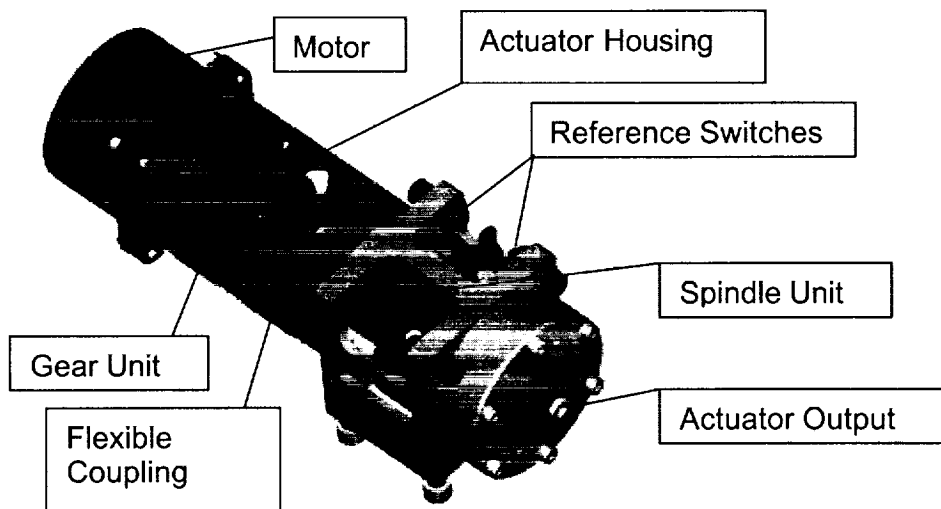


Figure 3: APM Linear Actuator

Motor

The motor is a two-phase disc rotor stepper motor on the basis of an industrially available type (Portescap P 532), but mechanically modified in order to adapt to the requirements and temperature environment of space missions. The motor consists basically of two stator parts containing the redundant windings and of the disc rotor. The device is mechanically overworked by DSS in order to make sure that all sizes and tolerances are according to the specified values. The motor is then equipped with dry lubricated bearings (RMB) and the axial backlash is adjusted to zero by means of PTFE washers, which also compensate for the axial thermal mismatch between the two bearings seats and the rotor shaft. A stepper motor of the same type was already qualified and delivered to ARTEMIS. The most important motor characteristics are listed in Table 8, and a cross-sectional view of the motor is shown in Figure 4.

Table 8: Characteristics of Stepper Motor

Characteristics	Value
Disc Rotor Mol	$12 \cdot 10^{-6} \text{ kg}\cdot\text{m}^2$
Motor mass	0.260 kg
Winding Resistance	12 Ω
Windings	Redundant
Phases	2
Cogging Torque	14 mN-m
Holding Torque	174 mN-m
Natural Step	3.6 deg
Phase Current	0.56 A

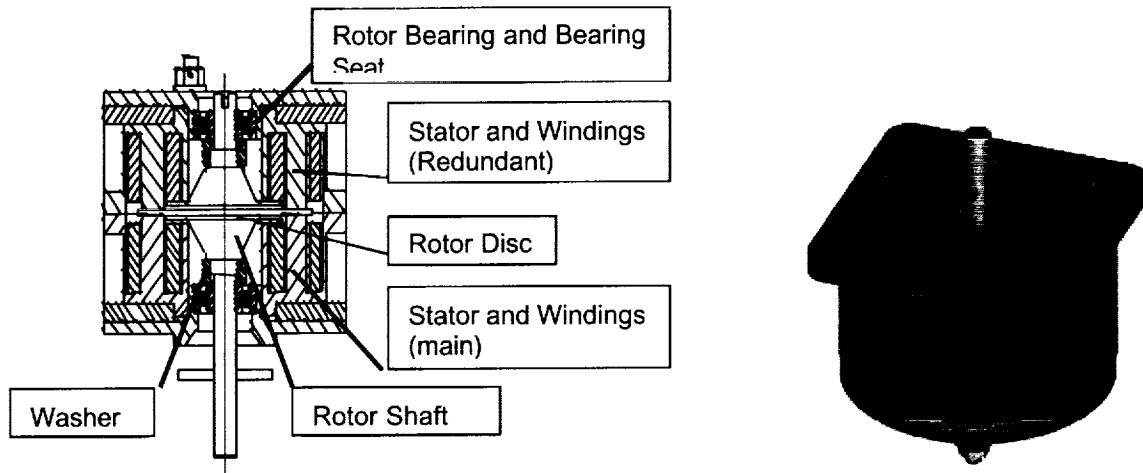


Figure 4: Motor Configuration

Gear Unit

The gear unit attached to the motor is a planetary gear from Gysin (GPL 32 -S) and its characteristics are listed in Table 9. The gear is lubricated with Bray 601. In order to deal with the low temperature environment, its outer surface is equipped with a redundant heater, a thermistor, and multilayer insulation so that the gear unit can be heated up to operational temperatures if it should cool down to unacceptable values (lower than -50°C) during the expected long non-operation phases. The operational low temperature limit is defined by the pour point of the lubricant.

Table 9: Gear Unit Characteristics

Characteristics	Value
Ratio	1:32
Mass	0.180 kg
Size	$L = 61\text{mm}$, $\varnothing 32\text{mm}$
Lubrication	Bray 601
Backlash	0.003 rad

Spindle Unit

The Spindle Unit is connected via a flexible metallic coupling to the motor / gear unit and comprises a bearing unit, which supports a planetary roller screw (Rollvis). Spindle unit characteristics are listed in Table 10. The screw nut is beared in a linear guidance bushing and carries the spherical actuator output I/F. The spindle is lubricated with Bray 601 and the nut is preloaded in order to avoid backlash.

Table 10: Spindle Unit Characteristics

Characteristics	Value
Type	Planetary Roller Screw
Pitch	1 mm
Diameter	8 mm
Lubricant	Bray 601
Mass	0.098 kg
Preload	60 N

Monitoring Switches

Each actuator is equipped with a set of 4 monitoring switches, two at each end of the working stroke. Two switches are nominally used to calibrate the zero position of the actuator; the other pair is for redundancy and to switch off the electronics in case that one switch should fail. The switches are

normally closed and open if approached by the spindle I/F. They are industrially procured (Baumer) and were qualified for the MSG/SEVIRI Project. The Switches provide a switching accuracy in the μm range and are adapted to space conditions by integrating a space proven harness. The switches characteristics are listed in Table 11.

Table 11: Precision Switch Characteristics

Characteristics	Value
Mass	0.003 kg
Size	\varnothing 8 mm, $l = 20$ mm
Switching Accuracy	$\pm 1 \mu\text{m}$ (ambient)

Electronics

The APM is controlled by dedicated electronics consisting of two cold redundant drivers, one of them interfacing the main windings of the APM actuators, the other the redundant ones.

Electrical I/F and Electronics

The APM electrical I/F is realized by a set of Cannon connectors attached to the APM Base Bracket. The APM Control Electronics has a mass of about 1.9 kg, at a dimension of 160x160x65 mm. The power dissipation is about 2.2 W and a primary voltage of 24 up to 52 V can be handled. The Electronics is able to drive the motor in microstepping mode. The command and data I/F is a serial R422 I/F or optionally a MACS Bus I/F.

Rx/Tx Signal and Power Transmission

Flexible Waveguides

The signal received and respectively transmitted by the antenna in the Ka- or Ku- band is guided from the moving antenna down to the satellite I/F by means of Flexible Waveguides. In the baseline design, the Flexguides are routed from the Satellite I/F through the center of the APM up to the Antenna I/F. The Flexguides are of the types WR 34 and WR 51 for the Ka band receivers and transmitters, and in case of a Ku-band application, the accommodation of WR 75 Flexguides is foreseen.

Since the thermal analysis has shown that a transmission power of some hundred watts as potentially required for future applications would cause Flexguide temperatures in the range of 300°C, a special routing was identified along the side of the APM for this application case in order to allow heat dissipation to cold space and not to produce hot spots and high gradients in the mechanism itself. The corrugated Flexguides are manufactured out of BeCu, are silver coated, and painted black with a high temperature Silicone Paint.

HRM

The two Holddown and Release Mechanisms which form together with the APM an isostatic three point support for the antenna during launch, are designed as pyrotechnic release units (ME 038 AA 055). The chosen design is derived from the LOCSTAR Antenna HRM. In order to achieve the S/S eigenfrequency requirement of 50 Hz at an antenna mass of 24 kg and an M_{ol} of $15 \text{ kg}\cdot\text{m}^2$, release bolts M10 are included into the design. Figure 5 shows the layout of the HRM.

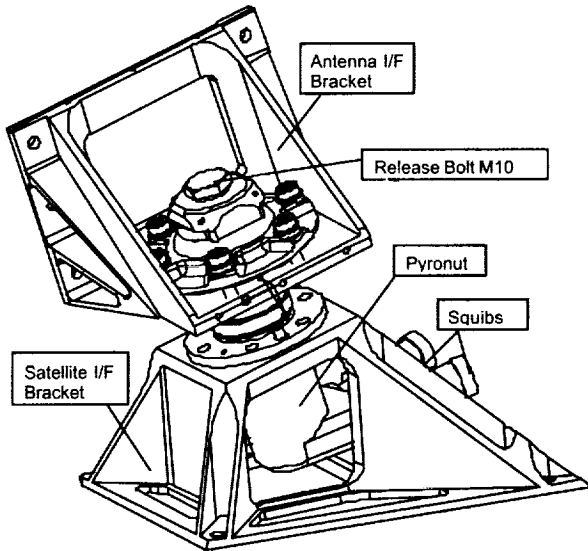


Figure 5: HRM Configuration

Development Status

An APM Qualification Model including Flexible Waveguides was built and tested. Tests performed are:

- Functional Performance
- Vibration
- TV
- Life
- EMC
- Functional Performance

- During functional performance testing, pointing accuracies and reproducibility of the commanded antenna I/F positions were verified.
- Vibration was performed together with the HRMs and with a dummy mass of 24 kg on top of the APM, simulating the worst-case antenna configuration.
- The TV qualification temperature was -110 to $+107^\circ\text{C}$. During test, the function of the APM and its performance was measured by means of a LDDM (Laser Doppler Displacement Meter).
- After TV testing, a life test with 90,000 random slews at a halfcone angle of 10 deg was performed.
- An EMC test (together with the control electronics) was performed and the test program was completed by a final functional performance test carried through in order to detect potential degradations of the mechanism over the whole test sequence.

Test Results of the Functional Test

The functional tests were performed on a 3D measuring facility from Leitz. The repeatability error of the machine (assuming the dimensions relevant for the APM measurements) is within 0.5 mdeg. In a first test step, the APM was adjusted on the measuring facility and the cross-coupling effect between the two (base and frame) axes was measured. Cross coupling means the angular shift of the frame axis if the base axis is commanded and vice versa. No measurable effect could be detected on the frame axis if the base axis was rotated. By rotation of the frame axis, a cross coupling effect of about ± 5 mdeg was found on the base axis. Since this effect is repeatable, it can be compensated by introducing an offset in the axis linearity deviation curves (nonlinearity curves) taken for the identification of the angular antenna I/F position as function of the commanded actuator steps. Arbitrary angles of the command I/F could be recovered with an accuracy of between 0 and 1 mdeg if the target angle is always approached from the

same direction. Similar results are obtained if a required angular value is commanded by using the non-linearity curve (antenna target angle as function of motor steps). Table 12 summarizes the functional test results, and the APM during functional test is shown in Figure 6.

Table 12: Functional Performance Test Results

Test Performed	Test Result	Comments
Angle of Motion	20.5 deg on Base Axis 20.6 deg on Frame Axis	depending on limit switch adjustment
Velocity of Motion	5.45. deg/min	
Position Reproduction Error	0 to 1 mdeg	overall 15 arbitrary positions were commanded
Position Error of the pre-adjusted position after Release from Launch Position	6 mdeg to 57 mdeg	5 tests with antenna inertia simulator performed at different target positions
Position Error after Release from Launch Position and active Position Recovery by means of Actuator	About 2 mdeg	actuator moved 100 steps forth and back after release from launch position

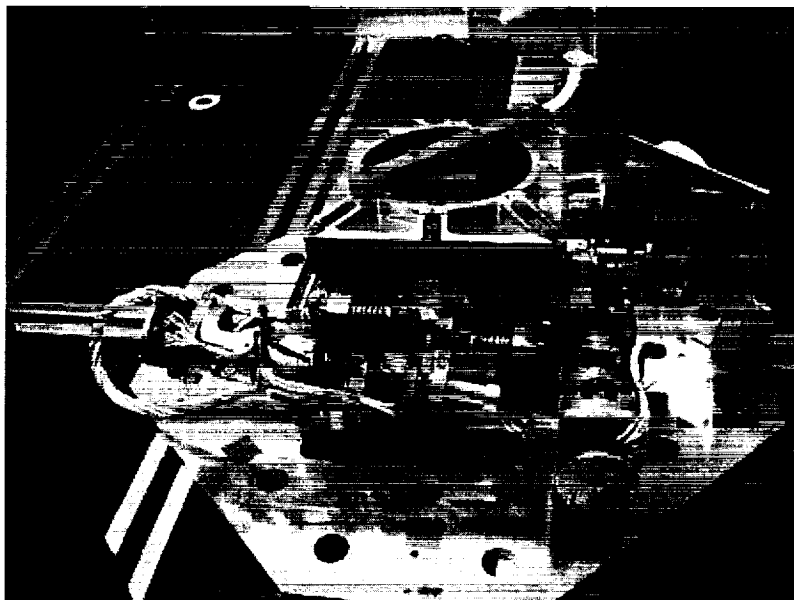


Figure 6: APM during Functional Performance Test

Vibration Test

The vibration test configuration consists of the APM and of the two HRMs attached to the vibration test adapter. In order to simulate the loads applied to the APM by the antenna structure, a dummy mass of 24 kg was mounted to the top of the APM and the two HRM I/F points. Lateral in plane loads (XY) are transferred by the APM and the HRMs, while axial out of plane (Z) loads are fully transferred via the APM. Sine qualification test levels of 12 to 15 g in plane and 6 to 30 g out of plane were applied up to 100 Hz. Random qualification was performed at 17 grms in plane and 20.5 grms out of plane. A sketch of the test setup and axis definition is shown in Figure 7. The first eigenfrequencies of the APM were about 160 Hz in plane and about 180 Hz out of plane with the dummy mass of 24 kg on top of the APM. In plane, the HRMs are partially supporting the APM while the Z(out of plane) loads are fully overtaken by the mechanism.

The vibration test was performed without degradation or malfunction of the H/W, the only minor NCR established was related to a damper unit, which got loose during test due to insufficient securing. The thread was refixed and the test was continued nominally. Adequate design measures to secure the dampers were then included into the APM design.

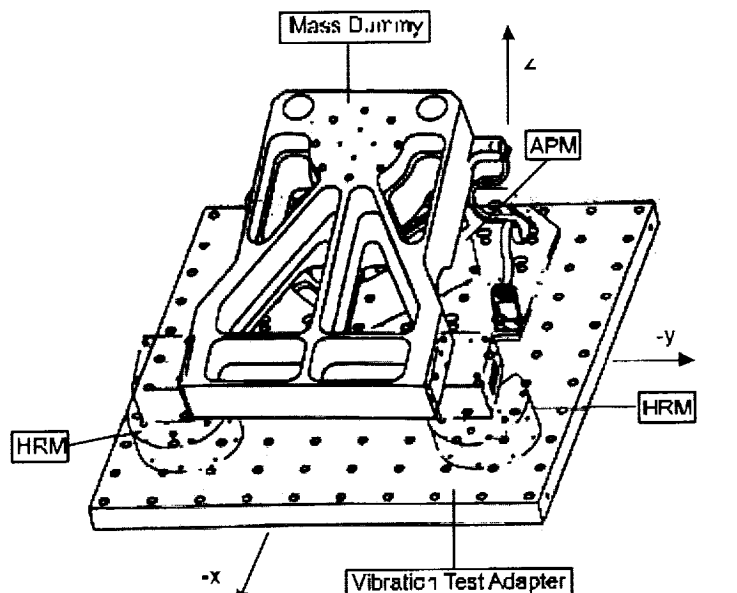
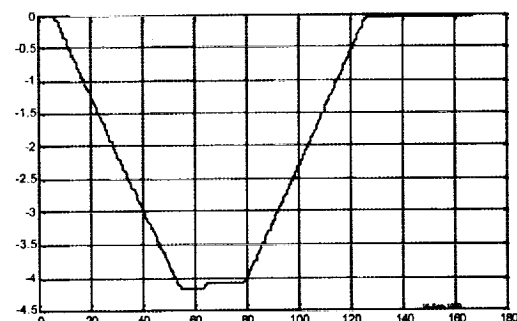
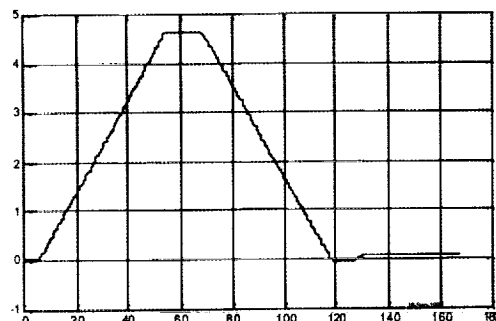
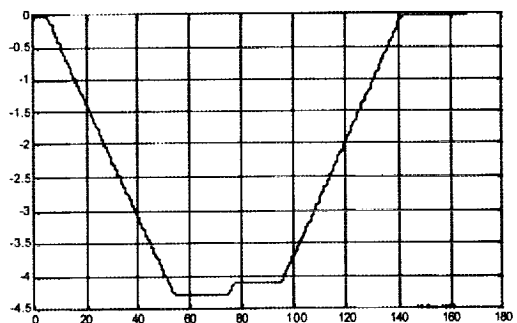
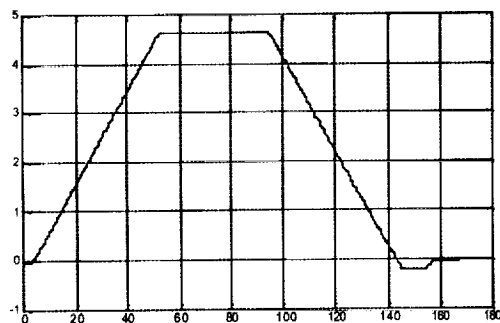


Figure 7: Vibration Test Setup



RUN A

Figure 8: APM Reproducibility Measurement Results at different Temperature Levels

Table 13: Overview over achieved TV-Test Results

Temperature <i>t</i> [°C]	Reproducibility	
	Run A [deg]	Run B [deg]
50	0,00039	$4,29 \cdot 10^{-5}$
60	0,00028	0,00027
70	0,00074	0,00080
80	0,00020	0,00090
90	0,00171	0,00027
100	0,00495	0,00663
-80	0,00031	0,00126
102	0,00469	0,00597
105	0,00781	0,00061
-100	0,02550	0,02144
-106	S/W error	0,00227
102	0,00050	0,00173
-95	0,00104	0,00013

TV Test

The TV test was performed at a qualification temperature range of between -110 to $+107^{\circ}\text{C}$. Overall 5 cycles were performed; the first temperature cycle was dedicated to the search of a potential functional limitation of the mechanism. For this purpose, a functional check (detection of the actuator limit switches function and motion of the gimbal frame, as well as a performance check) was carried through at different temperature levels. The performance checks were done by means of a Laser Doppler Displacement Meter (LDDM) arranged outside the TV chamber. A retro reflector attached to the gimbal base axis reflected the laser beam. The received signal was directly related to the tilt angle of the APM Antenna I/F. Some results of the reproducibility measurements performed during TV testing are shown in the Figure 8. Table13 depicts a summary of the measured reproducibility values for the temperatures during run A (positive angles) and run B (negative angles).

The APM passed the TV test successfully, however, during testing the following issues had to be solved. During the first cold cycle, the laser signal used for performance measurement got faint at about -80°C and it was observed that particles had condensed on the cold optical surface of the retro-reflector attached to the APM base axis. The problem could be solved by applying a small heater to the retro-reflector housing so that its temperature could be stabilized to temperatures above 0°C .

Despite the fact that the APM was mounted underneath an additional thermal shroud, it was very difficult to achieve well-balanced temperature extremes at all relevant APM parts within a reasonable working time. The main reasons for this behavior is that the APM Base Bracket is directly connected to a cold plate, while the Gimbal Bracket is coupled to the environment mainly by radiation. Based on this fact, a significant thermal gradient was built up during heating up and cooling down process over the gimbal bearings. In order to achieve performance measurements in the extreme temperature within a limited TV testing time, these measurements had partially to be performed at uncompleted temperature stabilization of all relevant APM parts, i.e., that gradients were still observed in the APM during measurements. One of the performance measurements was performed in the cold case at the beginning of the heat up phase. This measurement yielded decreased performance values due to extreme thermal gradients in the range of $\Delta T = 50^{\circ}\text{C}$, occurring between the APM Base Bracket and the Frame Bracket (over the gimbal bearings). These extreme gradients led to an increase of friction in the gimbal bearings, which jeopardized the APM performance by increased elastic effects in the bearings. Figure 9 summarizes the performance measurement results under TV conditions. The worst case reproducibility values of 0.026 and 0.021 deg are related to the high occurring gradient discussed above.

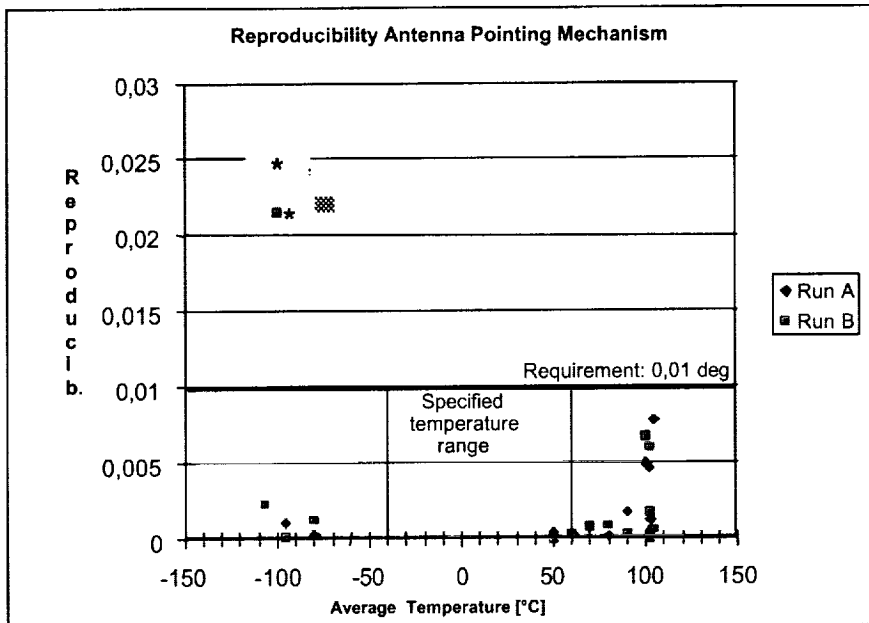


Figure 9: Summary of Reproducibility Measurements

Life Testing

After TV testing, a subsequent life test with 90000 random repositioning slews was successfully performed on the APM without degradation (verified in a final performance check). The random slews covered a half-cone angle of 10 deg with a minimum angle of about 0.175 deg. per slew.

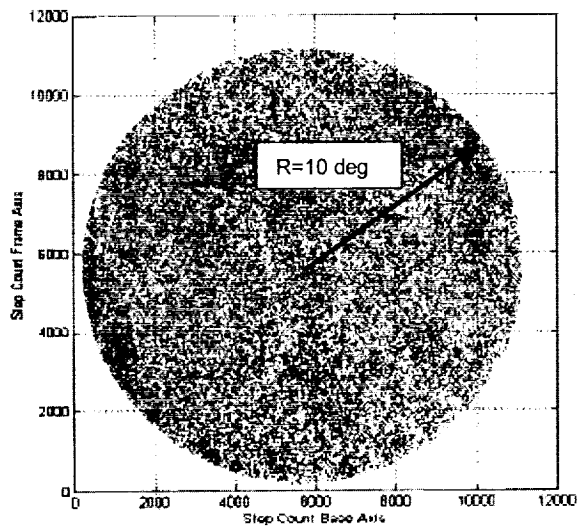


Figure 10: Life Test Random Slew Distribution

Summary and Conclusions

At the beginning of the development phase, an envelope specification was established in order to allow the application of the mechanism to a variety of applications. The operational qualification temperature of the APM was defined to -40 to $+60^{\circ}\text{C}$ and the design of the mechanism was based on this temperature regime.

The thermal analysis performed at the system level and later on the APM level under consideration of a chosen reference Satellite Platform and of a representative orbit yielded for some mission cases a much more severe thermal environment than specified. Therefore the goal was set to achieve the extreme qualification temperature range of -110 to $+107^{\circ}\text{C}$ with the existing design at minimum design changes. In order to adapt to the new temperature regime, not only the lubrication concept of the gimbal bearings had to be changed from liquid to solid lubricant, but also the bearing concept had to be changed from hybrid to 440 C bearings in order to not damage the hard preloaded bearing pairs at low temperatures due to the occurring thermal mismatch at maximum occurring temperature changes of 130°C ?T (change from $+20$ to -110°C). Furthermore, the bearing housing material, which was intended to be standard Aluminium before, had to be reconsidered in this context since the stresses in the aluminium housing and the subsequent deflections induced into the outer bearing ring were unacceptable high. The only way to solve the problem was found in using a special Al-Si alloy (DISPAL S 225) providing a CTE like steel at the specific weight of standard Aluminium. By manufacturing the bearing housings out of this alloy, an almost perfect match between the rotating steel gimbal shaft, the dry lubricated steel bearing, and the bearing housing could be achieved. The material performed well without any problem over the complete APM qualification cycle. Due to its CTE characteristics, the alloy is found to be an ideal material to be matched with ball bearings or other steel parts. Since the material is actually not widely used in space applications, the available material database is actually not on the same level as for standard space materials. Therefore it might be necessary to carry through project-specific material tests in order to qualify the material for a specific application.

In addition to the gimbal bearing issue, the actuator concept had to be reconsidered with respect to the temperature problem. The actuators are lubricated with Bray 601 and a confidence test has shown that the actuation temperature was limited to about -60 deg due to the increasing viscosity of the grease in this temperature range. Since it was not acceptable to change the chosen lubrication concept of the gear due to lifetime reasons, it was decided to apply a thermistor and a dedicated redundant heater mat to the planetary gear surface of the actuator in order to allow heating up to operational temperatures in the cold case.

The overall APM performance was much better than specified, even in the low and high temperature regime, however, it was found that significant gradients over the gimbal bearings strongly influence the performance. This is due to elastic effects caused in the bearings at the increased friction torque related to operational conditions at high gradients.

Earth Scanner Bearing Accelerated Life Test

Brian J. Dietz^{*}, Steven G. VanDyk^{**}, Roamer E. Predmore^{***}

Abstract

The Moderate Resolution Imaging Spectrometer (MODIS) optical instrument for NASA Goddard will measure biological and physical processes on the Earth's surface and in the lower atmosphere. A key component of the instrument is an extremely accurate scan mirror motor/encoder assembly. Of prime concern in the performance and reliability of the scan motor/encoder is bearing selection and lubrication. This paper describes life testing of the bearings and lubrication selected for the program.

Introduction

Five scan motor/encoders have been assembled and tested. These include an engineering model, qualification model and three flight models. The qualification scan motor/encoder has completed qualification testing and is currently undergoing life testing. The first flight mechanism was launched December 18, 1999 and is currently undergoing initial operating procedures. The second mechanism has been integrated on the PM spacecraft and is undergoing environmental testing.

As with most mechanisms, bearing life was determined to be a critical factor in the operation of the scan motor/encoder. Bearings and lubricant were chosen as the result of a previous (phase 1) screening program. Each scan motor/encoder contained two duplex bearing pairs. As the synthetic hydrocarbon lubricant (Pennzane SHF X-2000) was relatively new to space flight applications, accelerated and operational speed bearing life testing was required in parallel to verify the life of the Pennzane early in the program. The qualification life test mechanism was required to survive a ground test and five-year mission life of 57 million revolutions. This paper presents the results for one of four bearing life test stations. The other stations, including the qualification model, continue to operate.

This test station was an accelerated bearing life test running at 50 RPM (the operational speed of the scanner was 20.3 RPM). In order to compensate for the higher speed, heaters were added in order to decrease the viscosity of the lubricant. The original plan specified a life test duration of 57 million revolutions. After the bearing life test successfully achieved the required 57 million revolutions, the test torque data was reviewed and it was concluded that there was no indication of failure, so the test was allowed to continue.

Steel (440C), DF duplex pair bearings and Pennzane SHF X-2000 with 2.5% lead napthanate and 0.6% antioxidant additives were selected for the MODIS scanner assembly. Each bearing pair contained approximately 280 mg of total lubricant (approximately 75 mg of which was saturated into the retainers).

The decision to disassemble the test station was finally made after the test station had experienced equipment failure (heater control) and the life duration had been greatly exceeded. Upon disassembly of the test station, two of the three bearing pairs were dry and visible damage to the balls, races and retainers was observed. One of the three bearing pairs remained wet with lubricant and components of the bearing appeared to be in good condition. Bearing torque for all pairs remained well below the operational requirements of the system [0.13 N-m (18 oz-in) drag torque] throughout the life test.

^{*} Moog, Inc., Schaeffer Magnetics Division, Chatsworth, CA

^{**} Raytheon Systems Company, Santa Barbara Remote Sensing, Santa Barbara, CA

^{***} NASA Goddard Space Flight Center, Greenbelt, MD

Testing

As a first test phase, prior to initiation of the bearing life test stations, separate material and lubrication tests were performed. Based on the results of those tests, the best bearing material and lubricant were selected early in the program. As a third phase of the test program, after completion of the qualification program, life testing began on the qualification mechanism.

Bearing life test station III was initiated as part of the second test phase. Three flight quality 440C steel, 66.675 mm (2.625 inch) outer diameter, 50.800 mm (2 inch) inner diameter, 165 N (37 pound) preload, DF duplex pair bearings were used in the testing. The bearings, phenolic laminate retainers and sintered nylon reservoirs were lubricated in accordance with flight requirements. The test station is illustrated as Figure 1. Each bearing pair was contained in its own clamp/housing. The housings also contained lubrication reservoirs. Each housing was fitted with inner and outer race heaters. A strain gauge was mounted on a cantilever beam supporting each bearing enclosure to measure the torque. Instantaneous torque readings were recorded every 15 minutes. The monthly average of these readings was plotted over the life of the test (see Figure 2). One telemetry platinum resistance thermometer (PRT) was mounted to each bearing outer race housing for temperature measurement. Two control PRTs were also mounted to each bearing housing (one on the outer race and one for the inner race). All testing was performed under vacuum.

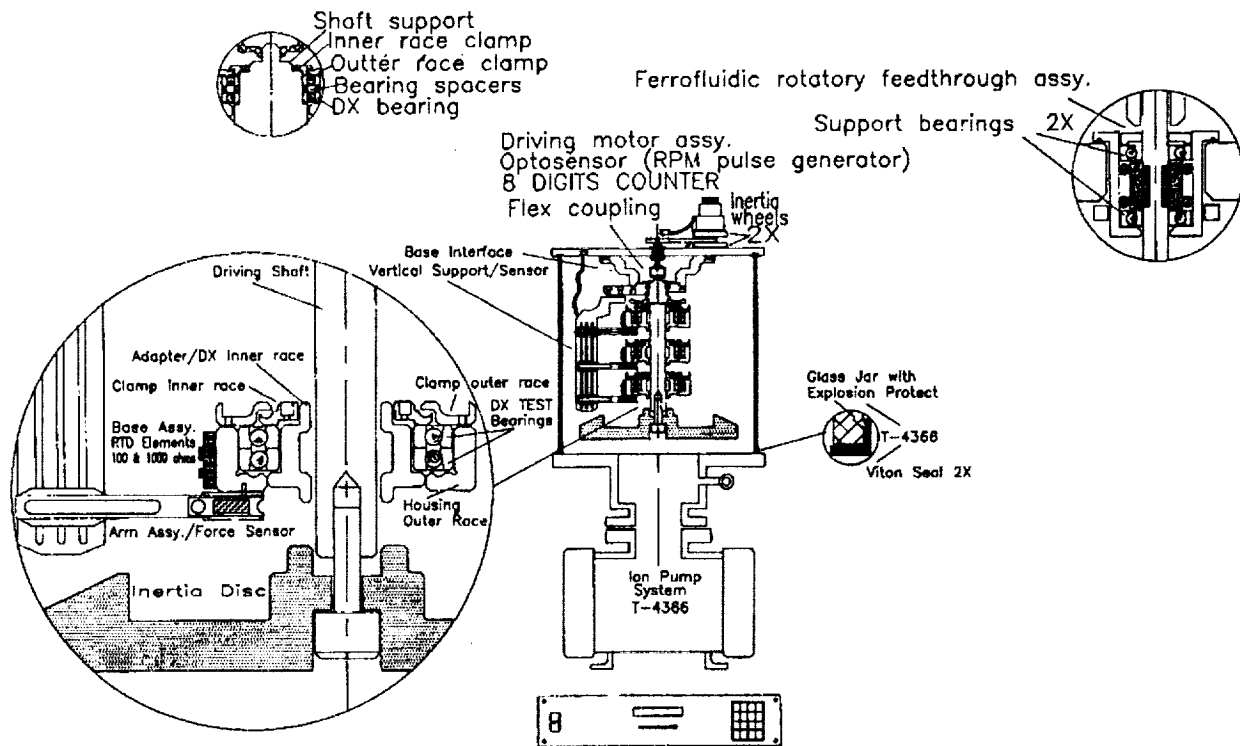


Figure 1 – Test Station

Test Data

Torque values over the complete test are presented in Figure 2.

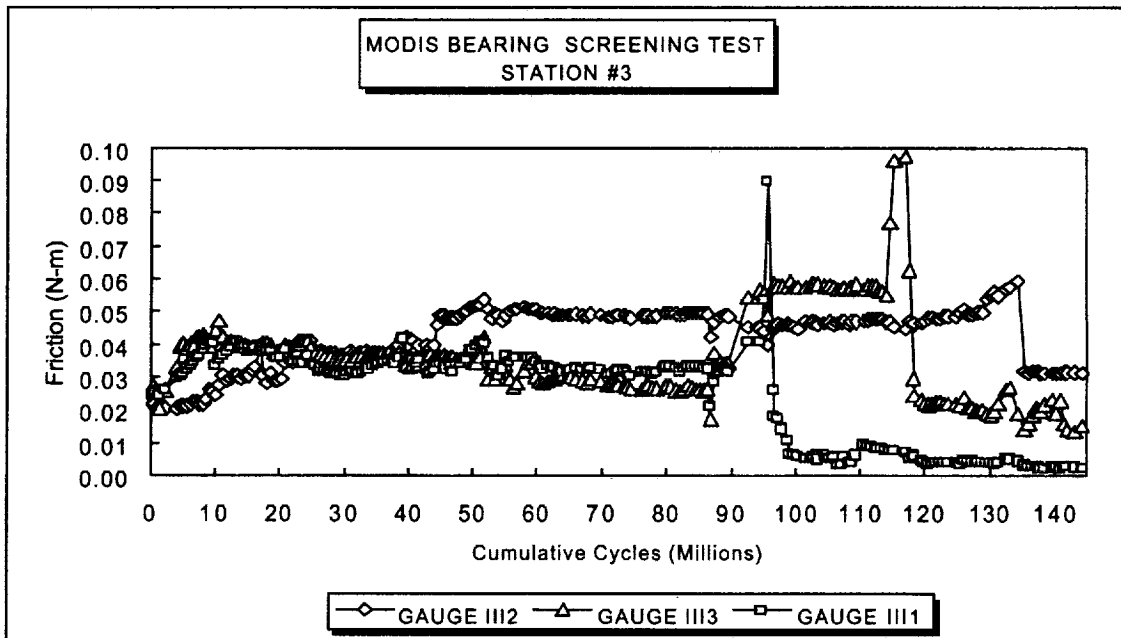


Figure 2 – Torque vs. Revolutions for Upper Pair Bearings (III1), Middle Bearings (III2) and Lower Bearings (III3)

At about 88 million cycles, a slight rise in indicated test temperature occurred. The indicated temperature of all three bearing pairs rose to approximately 48°C (118°F) [the nominal temperature was 37°C (99°F)]. It was not until the station was disassembled that delamination of the telemetry PRTs was observed. Analyses showed that the PRTs were functional, but the bond areas joining the telemetry PRTs to the outer race test fixtures were fractured. Bond areas for the control PRTs remained intact. The control PRTs were approximately 2-mm wide and 5-mm long while the telemetry PRTs were 3-mm wide and 12-mm long. The fractures may have resulted in lower indicated temperatures than the actual bearing temperatures. A corresponding drop in torque was observed at this time. The torque characterization plots indicated significantly lower values (approximately 1/4 of the previous values) for the upper and lower bearing pairs and a slightly lower value for the middle bearing pair. The drop in torque was likely due to a drop in lubricant viscosity and a drop in bearing preload as the aluminum housing expanded more than the steel bearings. This continued for approximately 4 weeks at which time the heaters were disabled. The torque values returned to a level slightly above (approximately 1/3 higher than) that prior to the temperature excursion. The rise in torque likely resulted from an increase in lubricant viscosity and a rise in bearing preload. The test continued without heaters until the conclusion.

At approximately 60 million revolutions, the torque characteristic plots showed considerable fluctuation due to jitter for all three bearing pairs. The cumulative trend data did not indicate this since data is averaged in the cumulative trend plot. The test station speed was increased to 60 RPM and the jitter ceased. The test was continued at 60 RPM.

Higher than normal torque readings were observed at approximately 95 million cycles for the lower bearing pair and at approximately 120 million cycles for the upper bearing pair. As the higher torque readings were

still within scan mechanism operating parameters, the test was continued. In each case the torque readings subsequently decreased below the normal level.

Testing was performed for a total of 144,263,692 revolutions or 2.5 specified mechanism lives. Torque characteristic plots were prepared monthly by Moog SMD and submitted to Raytheon SBRS. Figure 3 presents a typical characterization plot. Torque shown on the characteristic plots corresponded to the average torque values presented in the cumulative trend data.

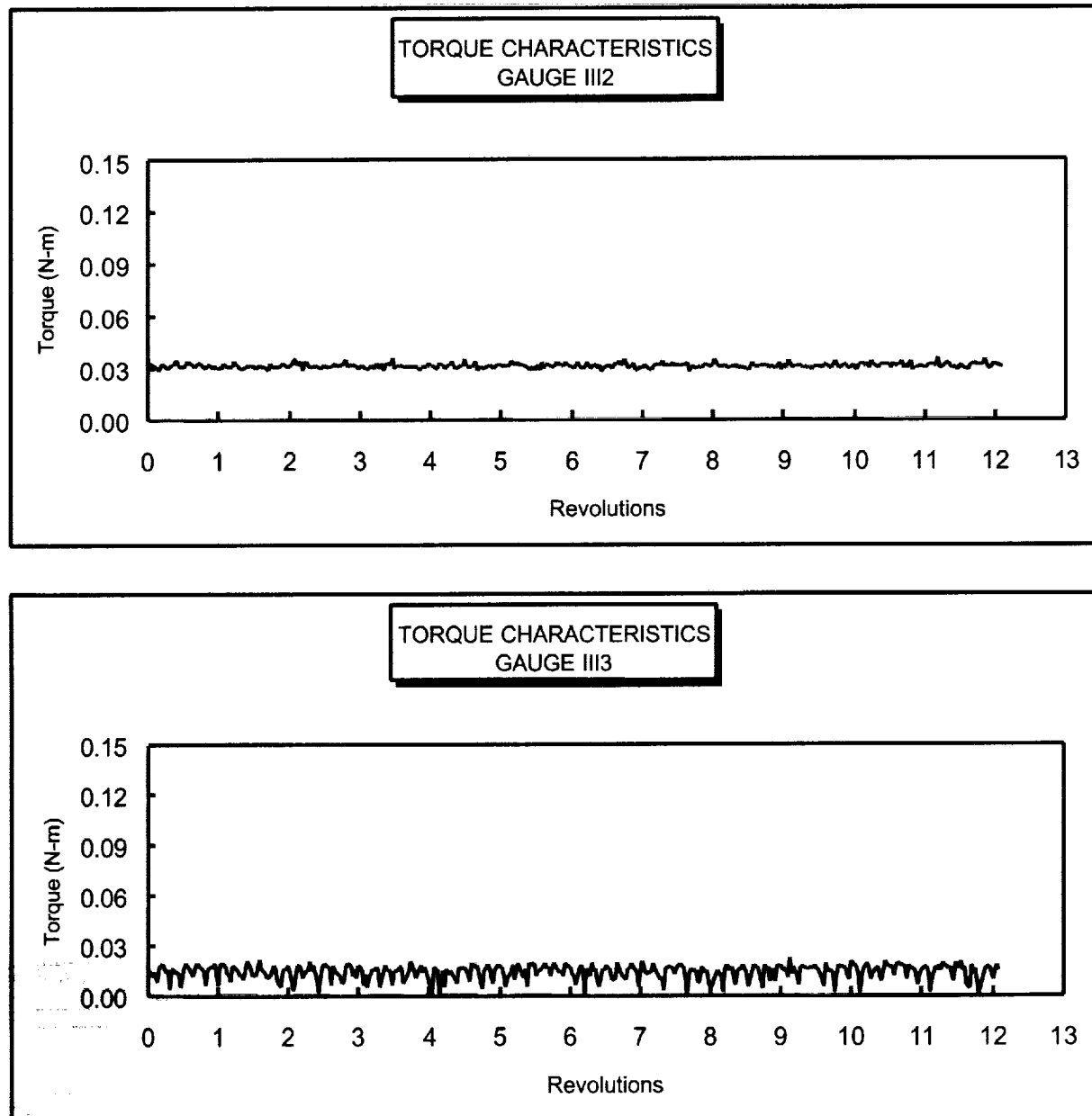


Figure 3 – Torque Characterization

(Note the lower torque and jitter present in the lower bearing pair, gauge III3. This occurred after the torque spikes seen at approximately 120 million revolutions in Figure 2.)

Disassembly and Inspection

Upon completion of 144,263,692 cycles, the station was disassembled. Photographs were taken throughout the disassembly and inspection process. Samples were also gathered during the disassembly.

A majority of the bearing analysis was performed at 5140/Tribology and Surface Science Branch of Glen Research Center.

Figure 4 presents the test station prior to disassembly. The drive motor, belt and test connector had previously been removed.

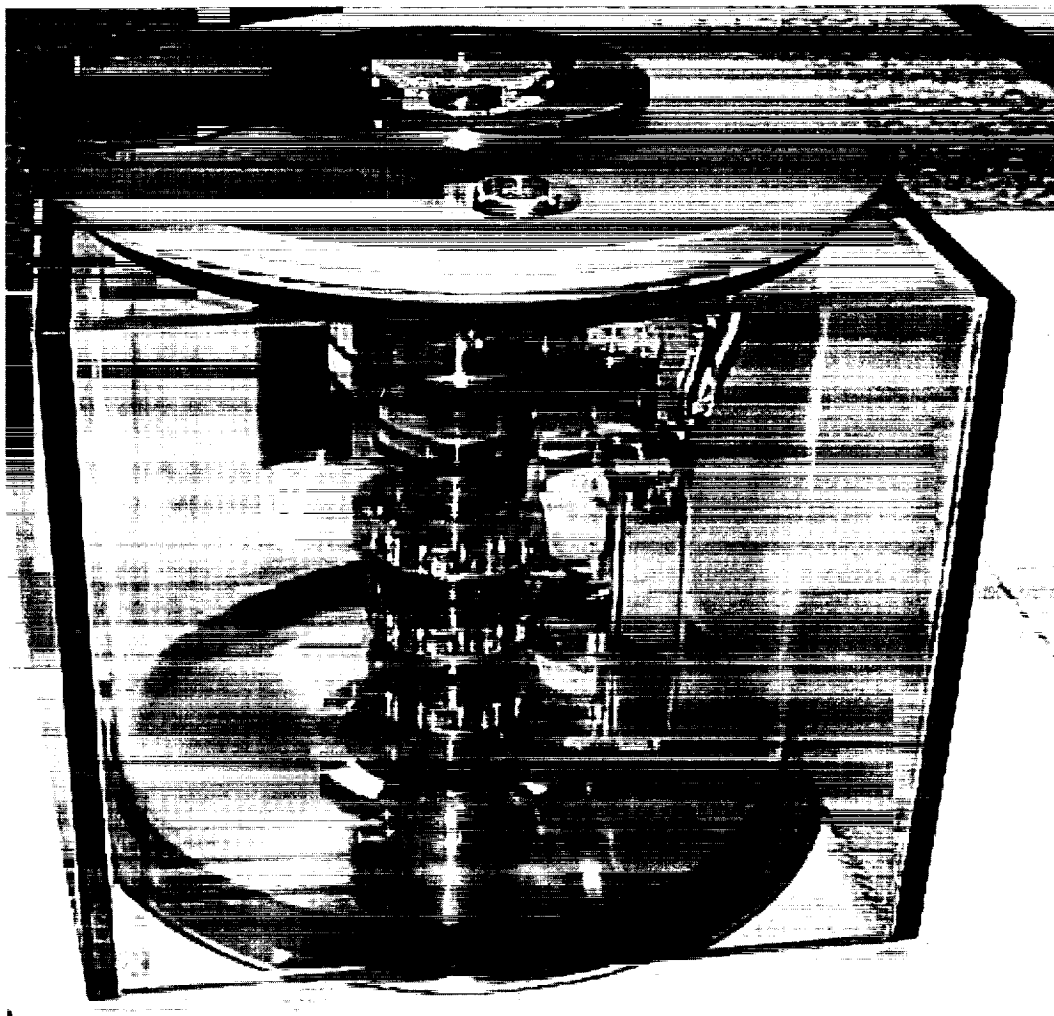


Figure 4 – Test Station III Prior to Disassembly

The complete shaft and all bearing components were removed from the test station and transported to a flow bench. Upon inspection of the test assembly, oil was seen on the lower flywheel and a ring above the slip ring (see Figures 5 and 6).



Figure 5 – Oil on Lower Flywheel

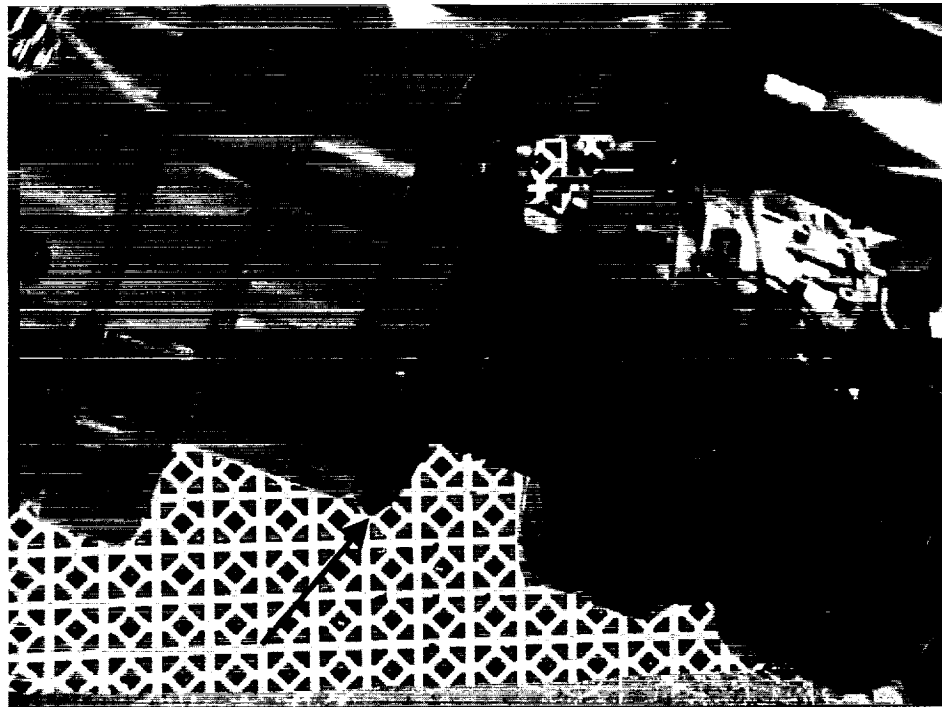


Figure 6 – Oil on Ring above Slip Ring

The strain gauges and PRTs were removed. Oil was seen under the bottom PRT mount and on all strain gauge mounts (see Figures 7 and 8). Samples were gathered for analysis.

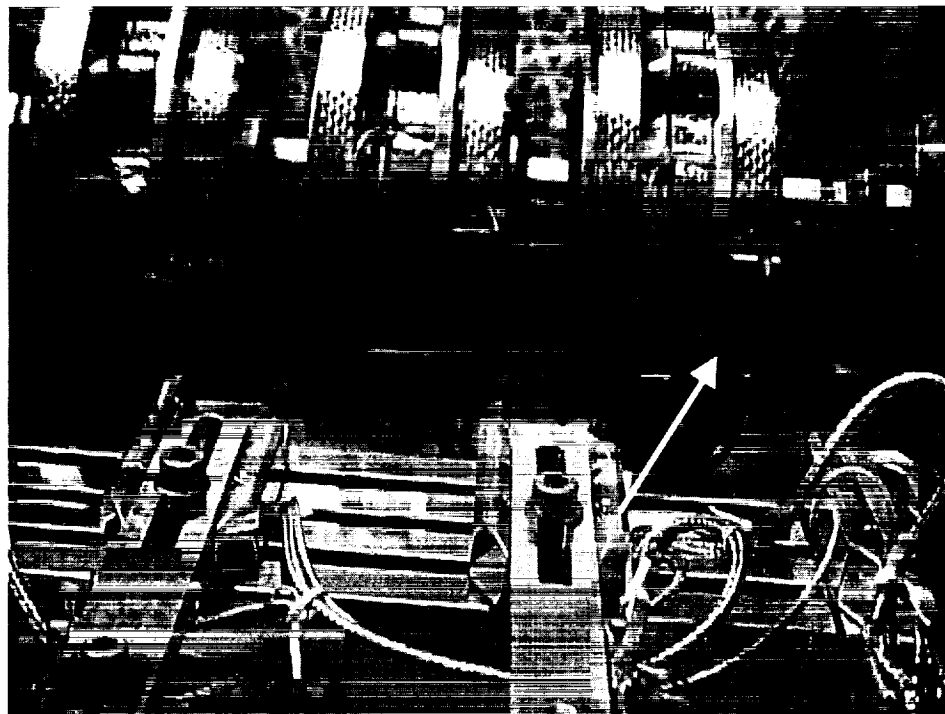


Figure 7 – Oil under Bottom PRT Mount



Figure 8 – Oil on Strain Gauge Mounts

The bearing housings were removed from the rotating shaft. Top and bottom views of a bearing housing are shown in Figures 9 and 10.

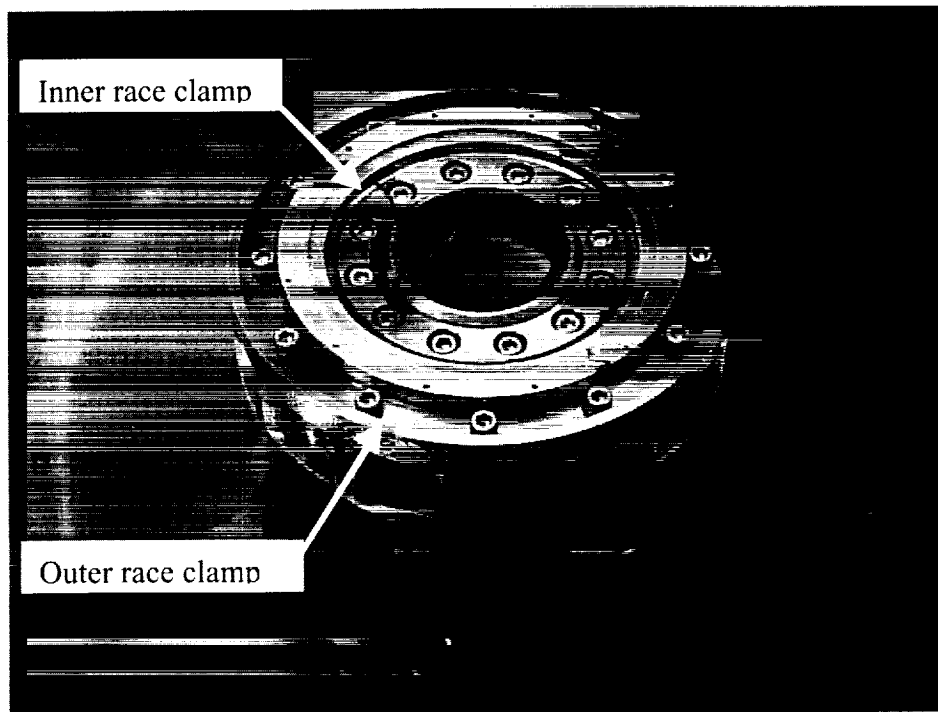


Figure 9 – Top View of Bearing Housing

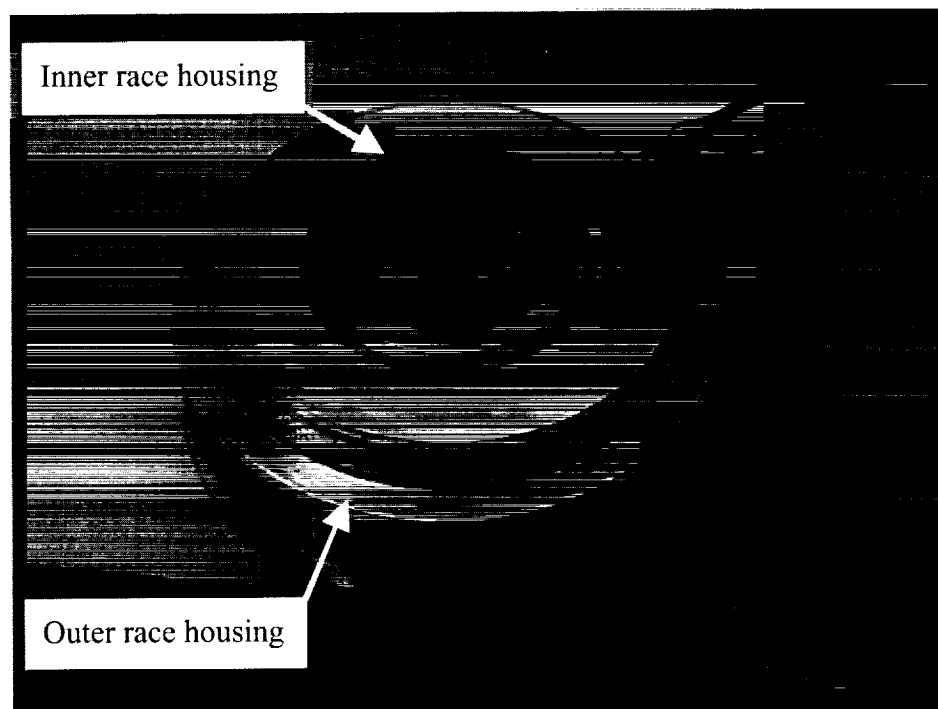


Figure 10 – Bottom View of Bearing Housing

Top and bottom bearing assemblies showed dry debris and worn races, balls and retainers. The top bearing assembly also showed silver debris from slip ring wear (see Figures 11 through 15).



Figure 11 – Lower Bearing Pair, Inner Race Clamp/Housing and Outer Race Clamp/Housing
(Note the black debris in the outer race clamp/housing and on the background cloth)

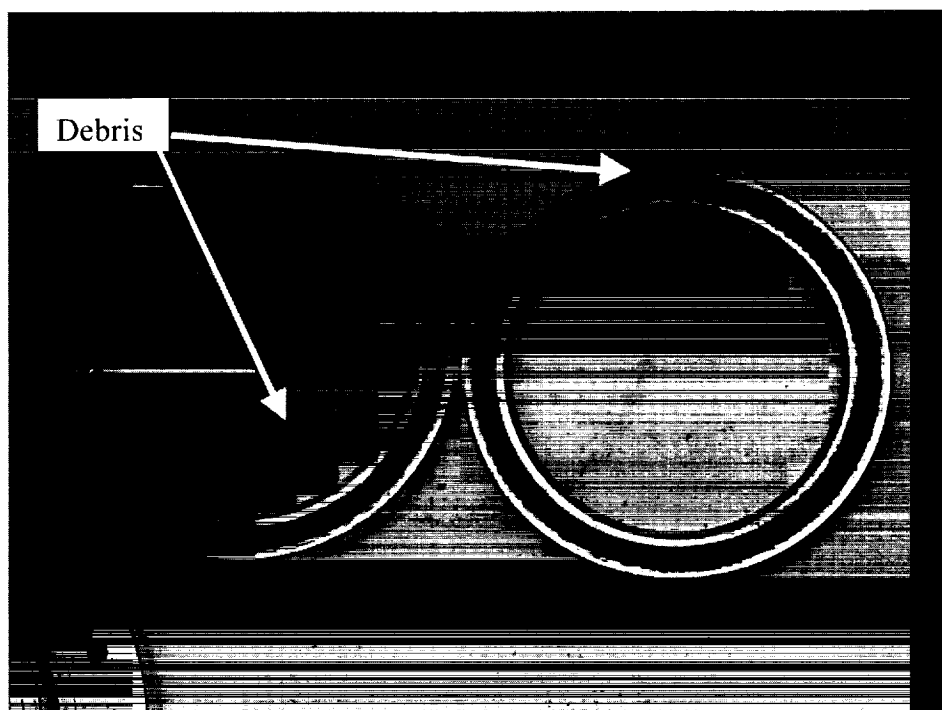


Figure 12 – Lower Bearing Pair
(Note the black debris on the bearings and on the background cloth)

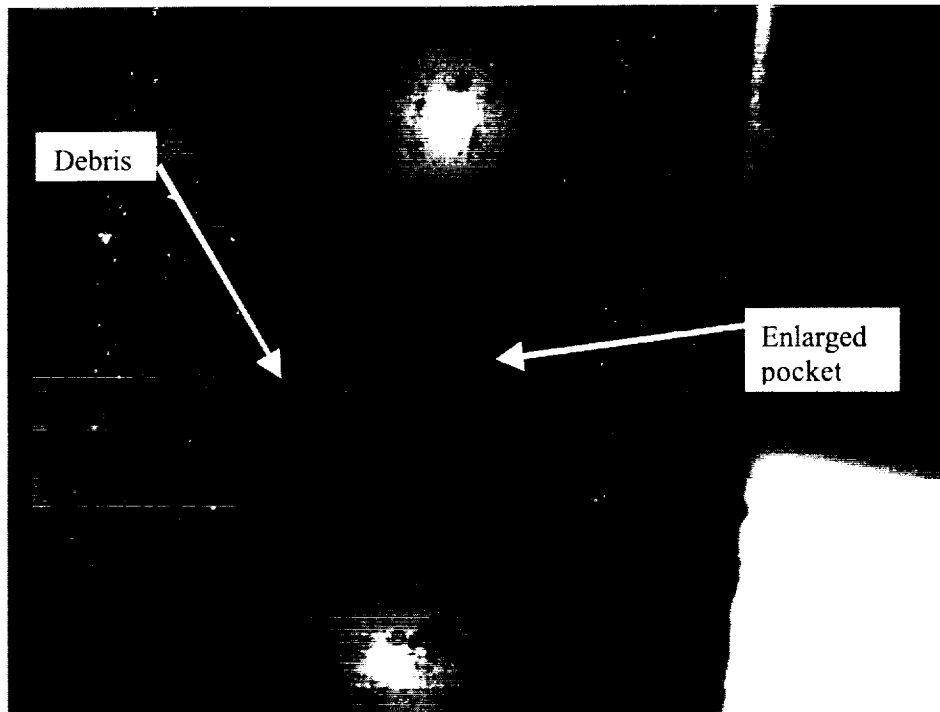


Figure 13 – Lower Bearing Balls, Retainer and Inner Race
(Note the black phenolic debris and enlarged retainer pockets)

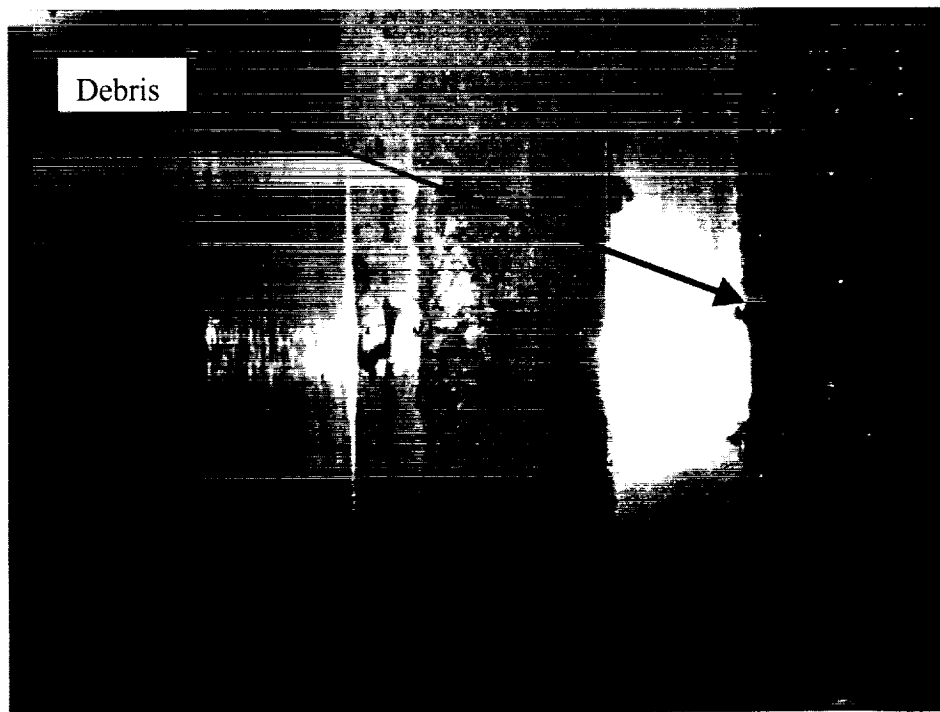


Figure 14 – Lower Bearing Inner Race
(Note the phenolic debris)

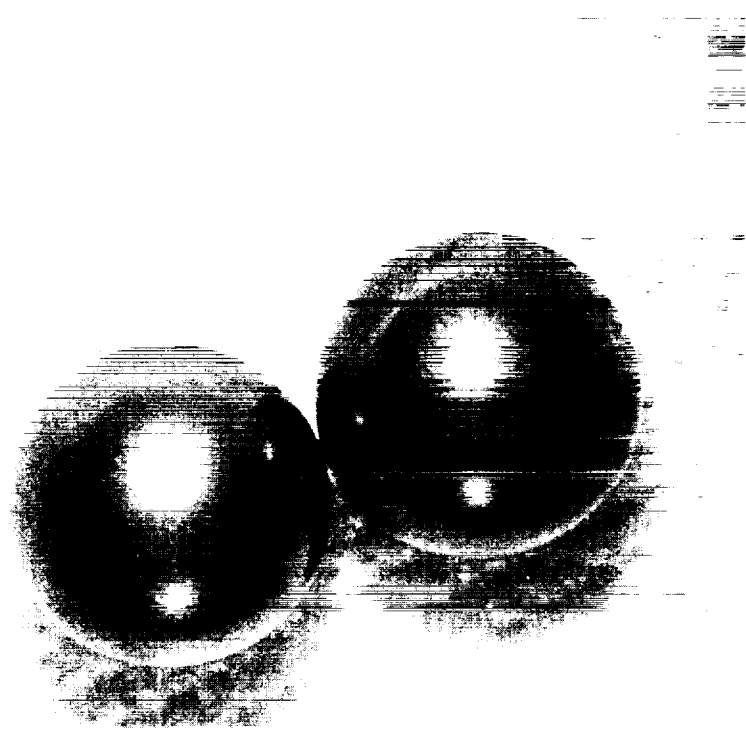


Figure 15 – Clean Balls From Lower Bearing
(Note the matte finish)

The middle bearing assembly showed wet lubrication and clean races, balls and retainers (Fig. 16 - 20).

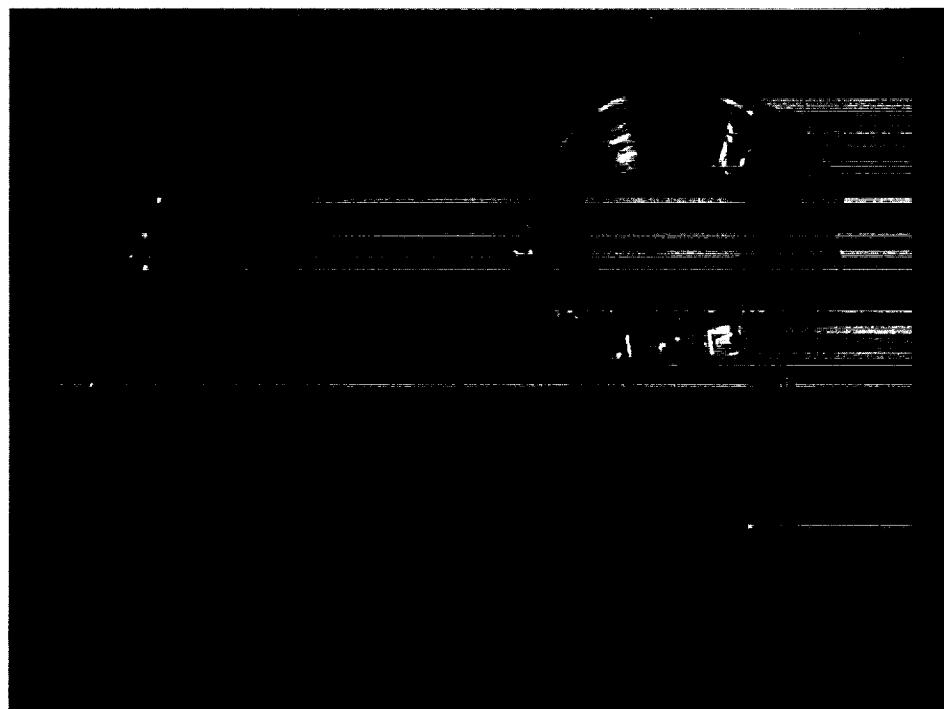


Figure 16 – Middle Bearing Pair, Housing and Shaft



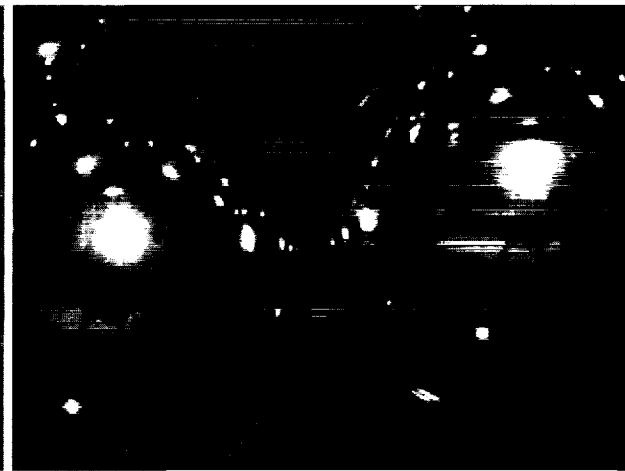
Figure 17 – Middle Bearing Retainer



Figure 18 – Middle Bearing Inner Race



Figure 19 – Middle Bearing Pair



**Figure 20 – Clean Balls from Middle Bearing
(Note the shiny finish)**

Results

Photographs clearly show that the top and bottom bearing assemblies were dry and worn. Damage of the balls and races were observed. X-ray photoelectron spectroscopy (XPS) analyses, performed at Glenn Research Center, indicated the presence of carbon, iron, chromium, oxygen and fluorine (an artifact).

The middle bearing assembly was seen to be well lubricated and wear was minimal. The oil was only slightly discolored. Micro Fourier transform infra red (Micro-FTIR) analysis of three balls, performed at Glenn Research Center, yielded the normal signature for undegraded Pennzane lubricant. Scanning electron microscope (SEM) analyses, also performed at Glenn Research Center, yielded the normal steel substrate elements.

Conclusion

Successful accelerated life testing of flight bearings with the flight lubricant in the boundary lubrication regime at elevated temperature was accomplished early in the program. This test result demonstrated that the flight lubricant would perform successfully in the flight scan mechanism.

Based on current information, it is likely that the elevated temperatures observed at 88 million revolutions (well beyond the specified mechanism life of 57 million revolutions) were actually higher than recorded (due to delaminated PRTs and/or heater control failure) and drove lubricant from the bearing pairs. Telemetry PRT delamination was likely caused by stresses created from the difference in thermal expansion of the PRT and the beryllium-copper mounting plate. The smaller size of the control PRTs resulted in lower bond-line stresses and did not cause delamination. Analysis of the heater control circuit revealed cycling of a relay near its specified life. An intermittently stuck relay could have caused the temperature excursion seen at 88 million revolutions. The conclusion of analyses performed at Glen Research Center was that loss of oil in the upper bearing pair was probably caused by an extended (i.e., 4 week) temperature excursion of more than 90°C. The upper and lower bearing pairs were probably heated beyond the temperature of the middle pair. Without the heater malfunction, the test could have proceeded considerably longer.

Two additional life test stations, one with 60 million accumulated revolutions (no heaters) and one with 200 million accumulated revolutions continue to run. The qualification model (QM), with 48 million accumulated cycles, also continues to run. Current measurements (directly corresponding to torque) of the QM performed monthly have shown a 29% increase over life. Investigation of an engineering model (EM), with several hundred thousand revolutions, and the QM, with 46 million revolutions, by NASA Goddard Space Flight Center has shown a beginning of life and end of life torque margin of greater than 20. Margin on phase lock (closed loop control) for both units was determined to be 200%. The beginning of life torque, measured with the EM, was 0.066 N-m (9.4 oz-in). The near end of life torque, measured with the QM, was 0.086 N-m (12.2 oz-in). This represented a 30% increase in torque over the 46 million revolution life of the unit. The bearing and lubrication system selected for the scanner has proven to exceed the life requirements of the MODIS program.

Lessons Learned

Criteria for determination of failure should be set and followed prior to the initiation of test. Had the test been terminated after 57 million revolutions or as soon as the torque spikes were observed, it is likely that results more similar to the actual mission would have been achieved.

Configuration and materials used in testing should match the production hardware as closely as possible. In this case, it is fortunate that the qualification unit (identical to the flight units) was added to the life testing in January, 1995 and has accumulated over 48 million revolutions. Recent testing of the qualification unit indicated performance within specification. Without the qualification unit, integrity of production hardware could be questioned.

As malfunctioning test equipment was the likely cause of lubrication loss in two of the three bearing pairs tested, the "keep it simple" theory certainly applies. The addition of heaters was of little benefit to the test. The bearings were operating in a boundary layer lubrication regime without heaters.

To life test a space mechanism, a flight mechanism should be tested rather than the bearings alone.

Acknowledgements

W. Jones, Glenn Research Center.

J. Uber, S. Cicchelli, M. Roberto and Rajeev Sharma, NASA Goddard Space Flight Center.

A. DeForrest, Raytheon Systems Company, Santa Barbara Remote Sensing.

L. Alegre, S. Natvipada, D. Owens, T. Phan, P. Tokeshi and H. Tsui, Moog SMD.

References

1. Jones, William R., "MODIS Scan Mirror Bearing Life Test Analysis", Letter dated 8/19/99 (Glen Research Center).
2. Uber, Joanne M., "MODIS Life Test Station III Thermistors", Letter dated 8/18/99 (NASA Goddard Space Flight Center)
3. Sharma, Rajeev, "Scanner Report", dated 11/4/99 (NASA Goddard Space Flight Center)

Measurements of Friction Coefficients between Oxidized and Contaminated Surfaces in Vacuum and in Air

Peter Frantz^{*} and Stephen V. Didziulis^{*}

Abstract

The successful operation of many moving mechanical assemblies is dependent upon controlling the coefficient of friction (COF) between sliding surfaces. However, the actual COF may deviate from expected values due to changes in surface composition during storage and testing. These effects are very important for low cycle devices that never establish a steady state operating condition. We have employed an ultra-high vacuum tribometer to measure the friction of common device materials in environmental conditions specific to space applications. The instrument provides for spectroscopic inspection of surface composition to correlate friction with surface chemistry. Extended tests were performed to determine the amount of cycles required to achieve steady state in the COF as oxides and contaminants were worn from the contacting surfaces.

Introduction

The successful design of many space mechanisms depends upon the appropriate choice of materials to control the coefficient of friction (COF) between sliding component surfaces. In many cases, a designer must rely upon values found in the literature for the COF of common material pairs. However, when a mechanism is tested or stored for extended periods, the composition of the interface may deviate from the composition of the materials that were used to determine the COF. As a result, the COF at the interface of the mechanism components may be greater or less than literature values, depending upon the type of materials. As the mechanism is cycled many times, or "run-in", the COF may gradually reach a steady state value that is equal to those found in handbooks. However, for mechanisms that are expected to operate for only a few cycles after storage, such as deployment devices, deviation of the COF during operation may be large enough to lead to anomalous performance characteristics. Furthermore, tribological properties measured in air are often different from those measured in vacuum and may be unreliable for space applications.

Deviations of the COF from expected values arise because of differences between the surface and bulk composition. The nature and origin of differences depend upon the history of the device. One must consider the manufacturing process, cleaning procedures, testing history, and the storage time and environment. The most common differences between the surface and bulk composition are the presence of a native oxide, and the unavoidable layer of adsorbed contaminants. Another consideration is the transfer of lubricants or wear debris during testing.

Consider a generic deployment latch (Figure 1) as an example of a mechanism that could fail due to surface properties that differ from those assumed in the design process. During deployment, the latch striker passes between two cams by sliding on the cam surfaces while it rotates the cams aside (figure 1B). As it reaches the deployed configuration (figure 1C), the cams rotate back towards their original position to hold the striker in place. A device such as this is often expected to be cycled only a few times during testing, and once during deployment. During operation, there is a sliding contact that is required to have low friction (so as not to oppose the motion of the striker through the cams). At this interface, one may wish to deposit a solid lubricant, such as a bonded film of MoS₂. When the deployment configuration is reached, the contact between the striker and the cams is required to have high friction, so that separation forces do not loosen the latch by rotating the cams. To achieve high friction, one may arrange for the contacting surfaces to be clean metals.

^{*} The Aerospace Corporation, El Segundo, CA

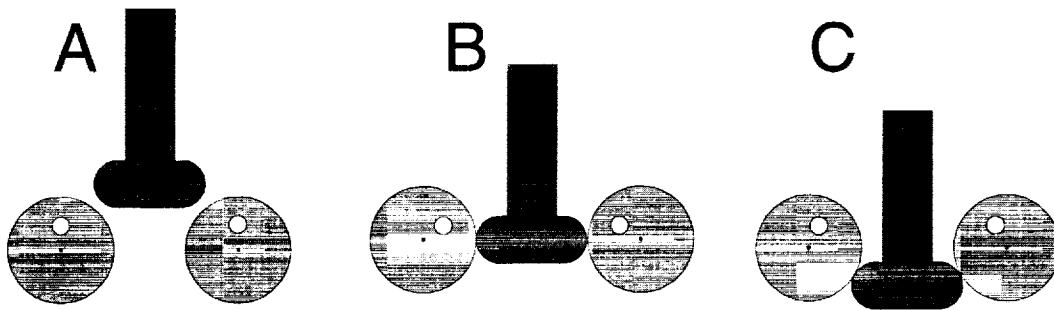


Figure 1. Schematic of a latch mechanism as the tab passes through the cams

This simple latch is designed for operation with the COF within certain limits, yet the device may require careful scrutiny if the surfaces are allowed to oxidize, collect adsorbed contaminants, or acquire lubricants from some other region of the sample in the proximity of the high-friction contact. For example, if a solid lubricant is applied to the sliding surfaces, the COF may be greater than specified by the manufacturer if it is not burnished or if it has oxidized. Similarly, the COF of the metallic interface may be less than expected if the surface has oxidized or if contaminants are present. The COF of the metal interface may also be lower than expected if the lubricant film had transferred to the clean metal surfaces during testing. Furthermore, both interfaces will exhibit differences between the COF measured in air and in vacuum.

To investigate the anomalous performance of a similar mechanism, we have conducted a series of tests to determine friction coefficients of common materials in a variety of different conditions. We directly measured friction forces between oxidized metal and solid lubricated surfaces as a function of time and load in air and in vacuum. We monitored the transfer of lubricant across a wear track and the effect it had on the COF. We also investigated the effect of thin layers of thin oil films on the surfaces of these materials. The results of these measurements are reported below.

Experimental

Test Samples

The materials used for the tribological tests included the following: 4.76 mm.-diam, grade 5 bearing balls made of 440C stainless steel; 14 mm.-diam superalloy disks with a 0.41 μm . surface finish; superalloy disks coated with a bonded film of MoS_2 ; and superalloy disks with half of the surface coated with the solid lubricant (see Figure 2). Prior to the tribological tests, the bearing balls were cleaned ultrasonically in ethyl acetate. To reproduce the surface treatment protocol used on an actual latch, the unlubricated superalloy disks were wiped with clean-room wipers soaked in ethyl acetate. The uncoated portion of the half-lubricated disks was also cleaned with an ethyl acetate-soaked wiper. The completely solid lubricated disks were used as received, without burnishing.

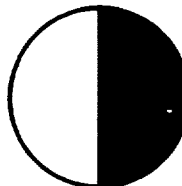


Figure 2. Schematic of the half-solid-lubricated sample

The surface of the superalloy material, MP35N, was determined by x-ray photoelectron spectroscopy (XPS) to be composed of Ni, Co, Cr, and Mo. The solid lubricant, Everlube 620C, was composed of MoS₂ in a phenolic binder. For the oil contamination tests, a solution of Bray 880 oil was prepared in heptane. The dilutions were calculated such that the residual oil left behind from a 20 μl aliquot would coat the substrate surface with a specified average film thickness after the solvent evaporated. For example, the 60-nm-thick film was created from a solution with a concentration of 0.453 mg/ml. The film thickness values investigated were nominally 15, 30, and 60 nm.

Friction Force Measurements

The device used to measure friction coefficients for this work is called the ultrahigh vacuum (UHV) tribometer. This tribometer is a custom ball-on-disk device that is housed in an ion-pumped vacuum chamber, enabling measurements to be obtained at pressures as low as 1×10^{-9} Torr. In the present study, the base pressure and operating pressure of the tribometer were $1\text{--}2 \times 10^{-8}$ Torr. Tests were also performed after the tribometer had been vented with laboratory air. Both the sample disks and balls could be transferred to and from the test positions under UHV conditions. The tribometer's vacuum chamber is directly connected to a surface analysis system, enabling chemical analysis with x-ray photoelectron spectroscopy (XPS) to be conducted on both ball and disk samples after test without exposing the samples to air.

A schematic of the UHV tribometer is provided in Figure 3. The main elements of this instrument are the rotating disk and the stationary ball. An external motor through a ferrofluidic feed-through drives the rotating disk. The stationary ball is mounted on an arm that possesses orthogonal flexures instrumented with strain gages to measure both the load and frictional forces. The tribometer is loaded by manually moving micrometers that position the arm such that the ball contacts the disk. Once contact is made, the load is controlled by the micrometers and measured by the strain gages on the load flexure that were calibrated before the tests. Tests were run at various durations, conditions of load, and speeds.

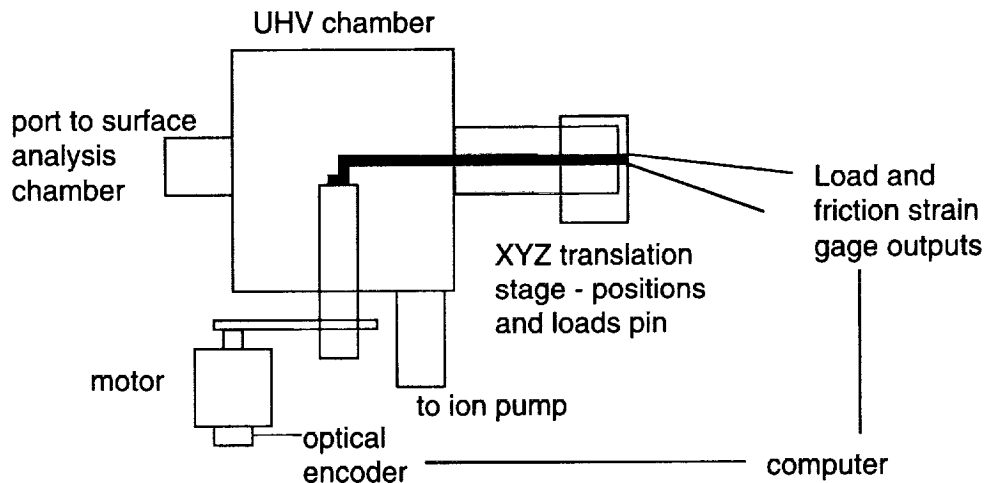


Figure 3. Schematic representation of the ball-on-disk UHV tribometer

Strain gage data obtained from the tribometer are recorded via microcomputer. This task is done with the use of a general-purpose analog-to-digital interface board and a custom acquisition program written in the LabView programming environment.

The friction coefficients of the clean and solid lubricated surfaces were determined by varying the loads from approximately 0.2–6 N. This range was selected to produce the expected range of contact stresses between the latch parts—up to 1.38 GPa maximum Hertzian contact stress. The calculated contact

stresses are appropriate for the unlubricated parts. The presence of the more compliant solid lubricant film could increase the effective contact area and thus decrease the stress.

To measure the steady state COF, the disk was rotated at a nominally constant speed of approximately 150 rpm while the load was increased incrementally. Some speed fluctuations were evident in the experiments, but previous work had shown that such fluctuations have little impact on the friction measured by the tribometer. Data were collected digitally at a rate of 15 Hz, and the time spent at each load was approximately 45 s.

To measure the COF as a function of time during the initial wear of the interfaces, samples were tested in a different fashion. For these experiments, we focused on obtaining data at a particular load (nominally either 3.0 or ~0.3 N) at a much higher collection rate of 250 Hz. Data were collected for approximately 1 min. As the results will show, these conditions were adequate to capture the desired friction behavior.

Surface chemical analysis was performed on selected samples to document the surface composition of the solid lubricant, the superalloy, and the lubricant transfer films formed on the half-lubricated disks. The XPS used was a Surface Science Instruments X-100 small spot spectrometer, with a 300 μm x-ray spot to examine the composition of the wear areas created by the tests.

Utility of the Surface Analysis Facility

Figure 4 is shown as an example of the benefit provided by locating surface spectroscopic probes within the chamber that houses the tribometer. In this figure, the friction coefficient versus time is plotted during testing of a TiC-coated ball against a 440C surface. The load was increased and decreased incrementally while the friction force was measured. The negative friction level reported is simply a function of the direction of the deflection of the strain gage flexure. At time $t=290$ s, we found that the friction decreased suddenly. In addition to the decrease in the COF, the amount of scatter in the data due to stick-slip motion of the fixture had decreased. When these surfaces were observed in the XPS it became apparent that a small amount of copper was acting as a lubricant in the wear track. The XPS spectrum shown in Figure 5, of the 440C surface after the friction measurement, shows the presence

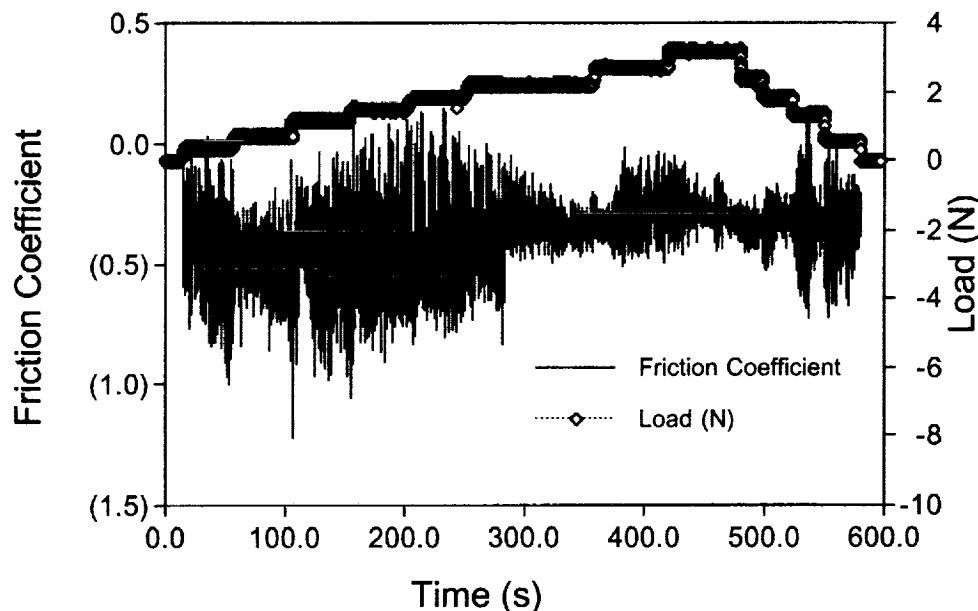


Figure 4. Friction coefficient vs. time while a titanium-carbide coated ball was held in a sliding contact against a 440C disk

of copper in the wear track. Evidently, a small amount of copper was transferred to the disk by an unknown mechanism from our test fixture components that are made of copper. This illustrates the importance of having a surface sensitive technique available to characterize and monitor the chemical integrity of the surfaces

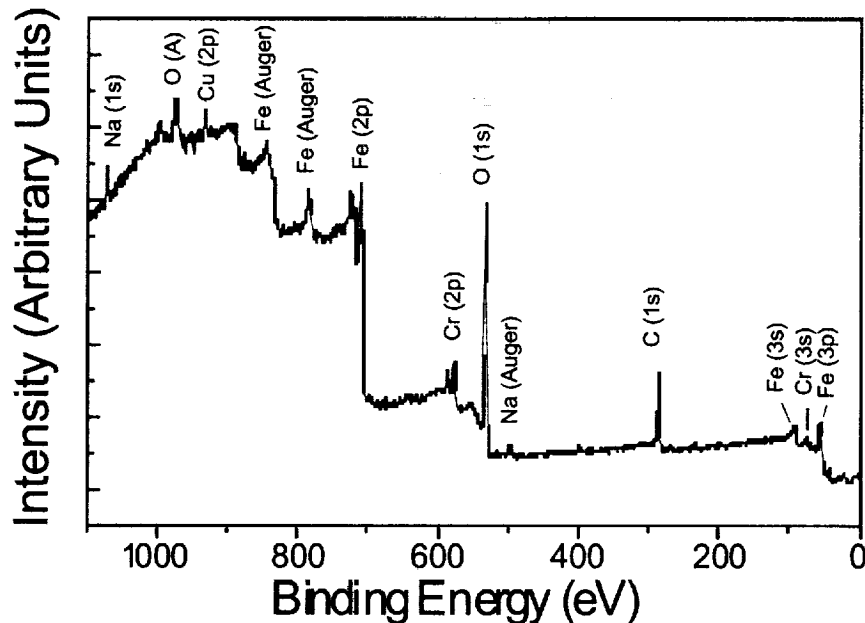


Figure 5. Photoelectron spectrum of the 440C surface after contamination with copper during tribological testing

Results and Analysis

Contact between oxidized 440C and a superalloy

The raw data from one of the vacuum tests of the clean, unlubricated 440C/superalloy pair are presented in Figure 6. These data show both the load and the friction channels from the test. The data show the expected trend of increasing frictional force in response to the increasing load force. The data also show the high noise level obtained in these tests, which results from the small sizes of the test disk required in this instrument and the erratic friction behavior often displayed in unlubricated systems. This behavior is due to the stick-slip motion that occurs in such contacts.

It is more instructive to present the data in a different format, which is done in the plot in Figure 7. In this plot, we have taken the average recorded friction obtained at a given load and plotted it against the average recorded load. In this form, the data clearly show the linear dependence of the friction force on the applied load, with the slope of the line representing the average friction coefficient for the material combination. In this particular experiment, the average friction coefficient was determined to be 0.76. Similar experiments were performed using the unlubricated materials tested in air, and the 440C/Solid-lube/superalloy material combination tested in both vacuum and air. At least two experiments for each test condition were performed. The average friction coefficients obtained are presented in Table 1.

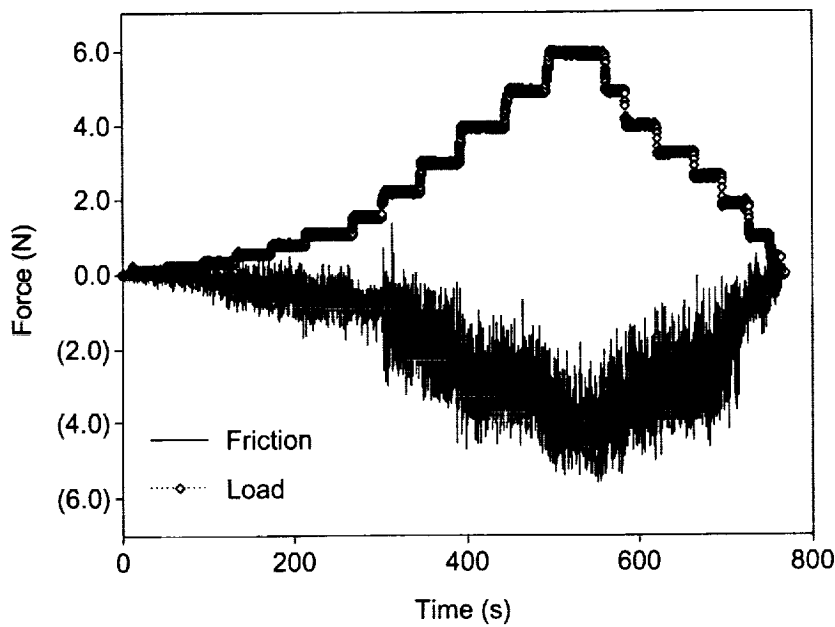


Figure 6. Raw data showing the friction force and load force vs. time during the sliding contact between a 440C ball and superalloy disk

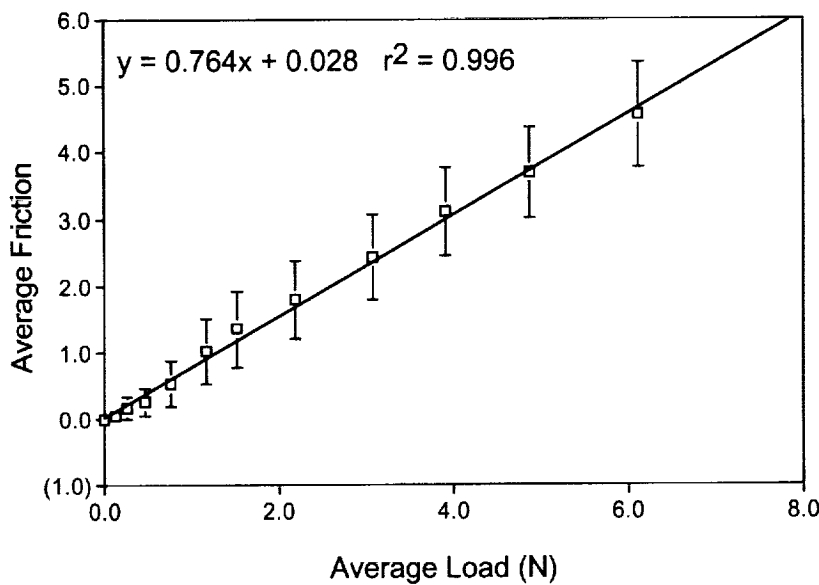


Figure 7. Averaged friction data from Figure 5 plotted vs. applied load

Table 1. Average Friction Coefficients of Clean 440C vs. superalloy

MP35N Sample	Vacuum, initial	Vacuum, steady state	Air, initial	Air, steady state
Clean	0.37	0.74	0.20	0.56
Solid-lube Coated	0.18	0.024	--	0.08 ^a

^aThis value varied with load between 0.17 and 0.06.

The friction coefficient obtained from the unlubricated samples in air averaged 0.56, which is significantly lower than that obtained under vacuum. This phenomenon is often observed for unlubricated metals, because reaction with the laboratory air forms surface oxides that usually have lower friction than the bare metals that are exposed under vacuum after the surface oxide wears away.¹ A large amount of wear debris was observed around the contact path during and after the tests in air, some of which were collected and analyzed with XPS to determine composition. We found the debris to be composed entirely of metallic oxides of the superalloy. This finding is consistent previous work,⁴ which has shown that oxide layers quickly reform in the presence of atmospheric gases and act to lower the friction.

The time dependent COF during the initial wear of the unlubricated 440C/superalloy contact in air is shown in Figure 8. In this figure, where the data were collected much more rapidly than is shown in Figure 6, the load (diamonds) and COF (solid line) are plotted as a function of time. The friction coefficient was obtained by dividing the friction force results by the load force results. The fluctuation in the load channel results from the sample disk not being completely flat (because of system run-out, disk variations, and sample mounting). While this oscillation was too small to affect the COF measurement, it provides a convenient measure for counting the number of revolutions. This figure reveals that for the first revolution the COF was approximately 0.2; less than half of the steady state COF between the clean metals in air (0.56). With each of the first three successive rotations the surface composition was changing to a state of higher COF until a steady state average value was achieved.

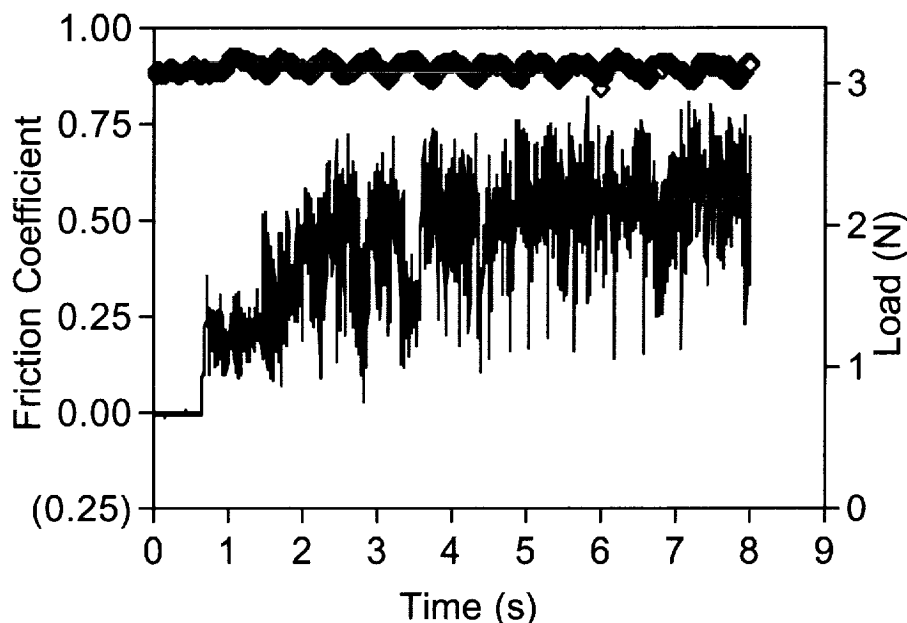


Figure 8. The COF and load vs. time during the initial run-in of 440C and superalloy in air

When this pair of materials was tested in vacuum, the initial and steady state friction values were both measurably larger. This experiment, not shown here, began with an average COF of 0.37 for the first revolution, and increased to 0.74 after approximately 10 revolutions. This suggests a difference in the surface composition at the beginning of the test, possibly due to fewer adsorbed contaminants in vacuum, and a difference in the steady state composition, as only the surface exposed to air continued to oxidize after the initial oxide layer had been worn away.

Contact between 440C and a bonded film of MoS₂ lubricant

The vacuum tests of the solid-lube coated specimens resulted in very low steady state friction coefficients, averaging 0.024. The lubricant within the solid-lube coating is MoS₂, which is an excellent vacuum lubricant. The tests of solid-lube conducted in-air were characterized by variable performance, as indicated in Table 1. We found that this variability is not due to a run-in burnishing process that solid lubricated systems usually display, but is related to load. The dependence of the COF on the applied load has been observed for many solid lubricant systems², including MoS₂.³ The effect has been explained by a load-dependent shear strength based on Hertzian contact mechanics. For the ball-on flat geometry, the friction coefficient should depend on the load (L) as L^{-(1/3)}, and our data show a L^{-0.39} dependence. The COF varied from a low-load (0.7 N) value of 0.17, to a high-load (6.2 N) value of 0.06. For comparison with our results, a handbook reports the in-air friction coefficient for the solid-lube as <0.10.³ Following tests in either air or vacuum, a track was plainly evident on all disks, but the coating did not appear to be worn through to the superalloy disks, consistent with the low friction measured during the tests.

The difference between steady state average friction coefficients in air and in vacuum is consistent with previous studies⁵, which showed the reaction of MoS₂ in atmospheric gases to produce oxides with lesser lubricating capability.

Tests were performed to determine the friction coefficient of the solid-lubricant before burnishing and the number of cycles required to achieve a steady state value of the COF. Figure 9 shows that the initial friction coefficient averaged 0.18, and quickly fell to a steady state average of 0.04 after approximately four revolutions. XPS spectra of the unburnished surface showed only carbon and oxygen within the escape depth of the photoelectrons (3-5 nm); no MoS₂ was detected on this surface. We conclude that this lubricant-depleted layer was worn away within the first few cycles, revealing subsurface MoS₂ crystals that were imbedded in the binder, which subsequently lowered the COF. This conclusion was supported by XPS spectra of the wear track after testing, which showed the presence of molybdenum and sulfur.

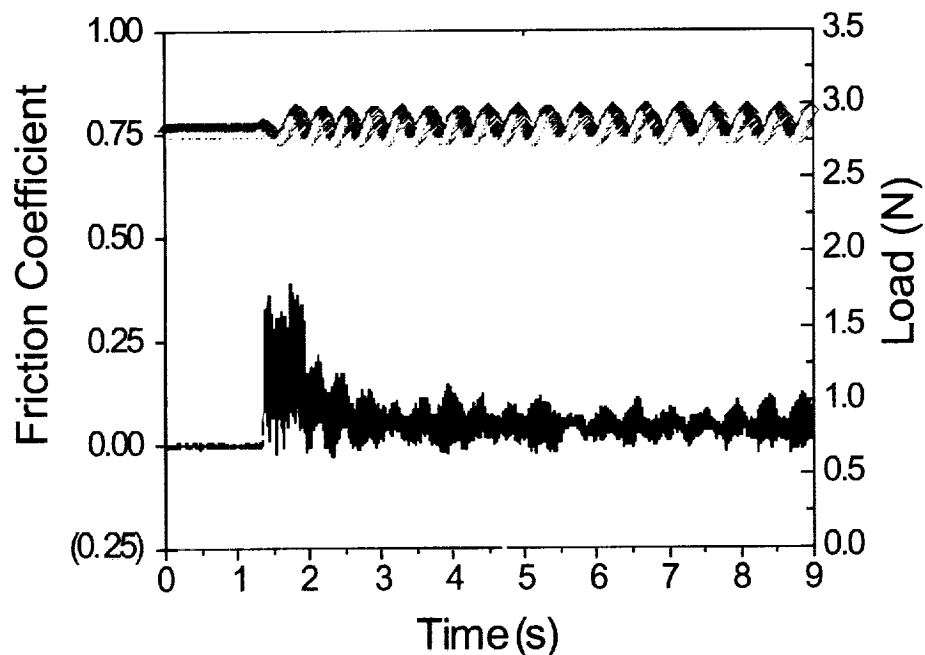


Figure 9. The COF and load vs. time during the initial run-in of 440C and Everlube 620C in vacuum

Lubricant Transfer Studies

To investigate the rate of transfer of lubricant along the wear track from one region of a sample to another, we performed a series of tests in which a 440C ball was held in sliding contact with one of the half-solid-lube-coated samples performed at the 3 N load under vacuum. In figure 10, the load channel is presented along with the friction coefficient, which was obtained by dividing the friction force results by the load force results. Again, we observed a periodic oscillation in the applied load. The load fluctuation does not account for the friction variation observed, as the load for this and other similar tests varied at most by $\pm 5\%$, while the friction changes were much greater and did not follow the same shape as the load channel. In this test, the ball was initially positioned on the lubricated half of the sample and the motor was started.

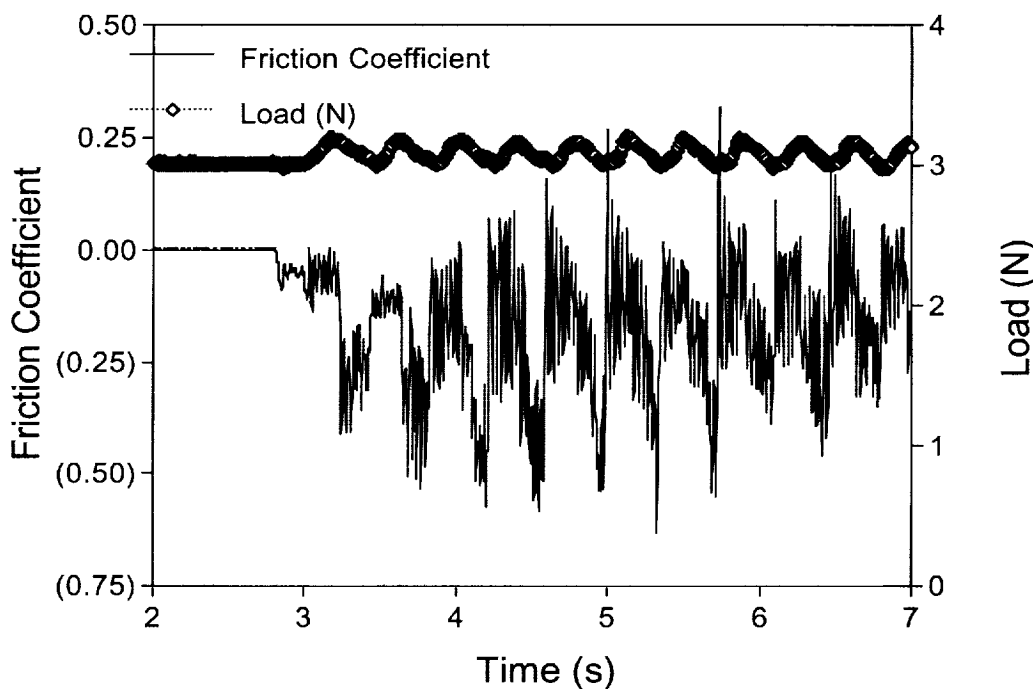


Figure 10. Plot of the COF and normal load at the start of a test of a half-solid-lube-coated superalloy disk against a 440C ball in vacuum. The disk began rotating just prior to the 3 s mark, as indicated by the friction measurement.

Many interesting observations can be made from these data. During the first few revolutions, the transition from the lubricated side of the sample to the unlubricated side is plainly evident by the step changes of the friction coefficient. The initial friction coefficient oscillates about 0.1 on the lubricated side of the disk, and increases abruptly to approximately 0.25–0.40 on the unlubricated side during the first revolution. In the second revolution, the friction measured on the lubricated side is somewhat higher, between 0.1 and 0.15. The average (~0.35) and maximum (~0.55) friction coefficients on the unlubricated side of the disk also increase on the second revolution, presumably because surface layers have been removed. By the third revolution, the unlubricated side of the disk is showing a trend of achieving higher maximum friction levels but is spending shorter time periods at these higher levels. The data clearly show that the duration of the time spent by the sample at higher friction levels grows shorter with each successive revolution. After seven cycles on this sample, the friction coefficient has decreased on the unlubricated side of the disk, reaching values ranging from 0.1 to 0.35 by the ninth cycle.

A second test run under these conditions showed a similar effect that occurred even faster: the friction on the entire unlubricated disk side was lowered after five cycles. This is exactly the type of behavior that would be expected if lubricant were being gradually transferred from the coated side of the disk to the uncoated side by the ball moving around the surface of the disk. The period of relatively high friction grew shorter with each revolution as the lubricant was spread farther around the track with each revolution of the sample. Under these test conditions, the rate of lubricant transfer was in the range of 0.2 to 0.4 cm/revolution, although such numbers are dependent on load and geometrical considerations.

Surface analyses were performed on the track and ball surfaces to look for evidence of the MoS₂ lubricant. Figure 11 presents the XPS data from a test where the disk had been rotated approximately 150 times in contact with the ball under a constant load of 3 N. The elemental compositions obtained from the superalloy disk include sulfur and excessive carbon and molybdenum. This is strong evidence for the transfer of lubricant because there are Mo and S peaks that indicate approximately 6% MoS₂. Spectra were also collected at a point further along the wear track, approximately 2 mm before the ball crossed over from the bare metal to the lubricated side of the disk. The concentration of MoS₂ in this area was approximately 3%. (Some of the detected Mo in each analysis results from the substrate.) The amount of MoS₂ detected relative to the C signal was much greater in the wear track (MoS₂:C = 6:45; 3:49 for the two data points) than on the fully coated sample (3:85). This indicates the preferential transfer of the MoS₂ lubricant in the wear areas, acting to reduce the friction more effectively than would transfer of the phenolic resin.

Further evidence of the transfer of lubricant was found by analyzing the contact area of the ball, which was used with the half-solid-lube sample during the test described previously. The surface of the contact area contained approximately 3% MoS₂ within the volume probed by XPS. After the detection of an MoS₂ transfer film on this surface, the ball was subjected to the surface preparation protocol that was applied to the latch surfaces: multiple wipes with a clean-room wipe saturated with ethyl acetate. The contact surface was again inspected with XPS. Still, we found the presence of a transfer film of MoS₂ representing 2%–3% of the surface material. The relative fraction of MoS₂ was very small, but very little MoS₂ is necessary to reduce the coefficient of friction. It is evident that through continued contact with the lubricant, a tenacious film of MoS₂ was burnished on to the 440C surface of the ball. It is expected that this film would reduce the friction between the ball and superalloy surface, as the levels of film were comparable to the levels found on the disk wear track.

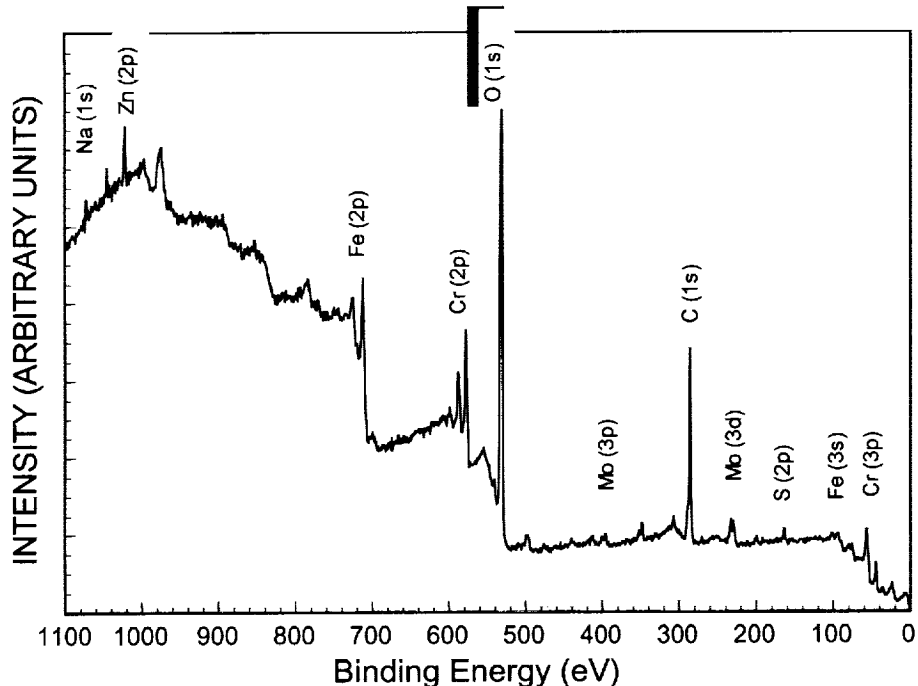


Figure 11. XPS data obtained from the wear track on the initially unlubricated side of a half-solid-lube-coated disk after test under vacuum. This shows the signature of the transfer of MoS₂.

Similar tests were performed in air to determine if atmospheric gases change the lubricant transfer phenomenon observed under vacuum. The results of one such test are shown in Figure 12. These results show the same fundamental behavior occurring over approximately the same time scale: the friction is gradually lowered on the unlubricated portion of the disk within the first 5–10 revolutions of the test disk. Following tests either in air or in vacuum, debris were evident visually in and around the track on the unlubricated disk side. In addition, the wear on the solid lubricant coating seemed much greater than in tests of the fully lubricated disks. Both of these observations can likely be explained by the transfer of the lubricant from the lubricated side to the unlubricated side of the disk.

One interesting difference on samples run in air compared to those run under vacuum is that once the lubricant was completely distributed across the sample, the difference in the friction coefficient between the lubricated and initially unlubricated surfaces was quite small for the air tests; also, the range of friction levels measured throughout the duration of the test stayed much lower than levels observed in the vacuum tests, as shown in Figure 10. Recall that the difference in the friction measured between the clean and unlubricated parts in air was less than that observed under vacuum (see Table 1), and the transfer experiment may be affected by this difference. However, this effect alone cannot explain the observations in Figure 12. This effect may also indicate that the lubricant transfer process is affected by the presence of air or surface oxides in a manner that makes transfer more uniform during tests in air, as described previously⁶. Further study would be required to understand this effect more completely.

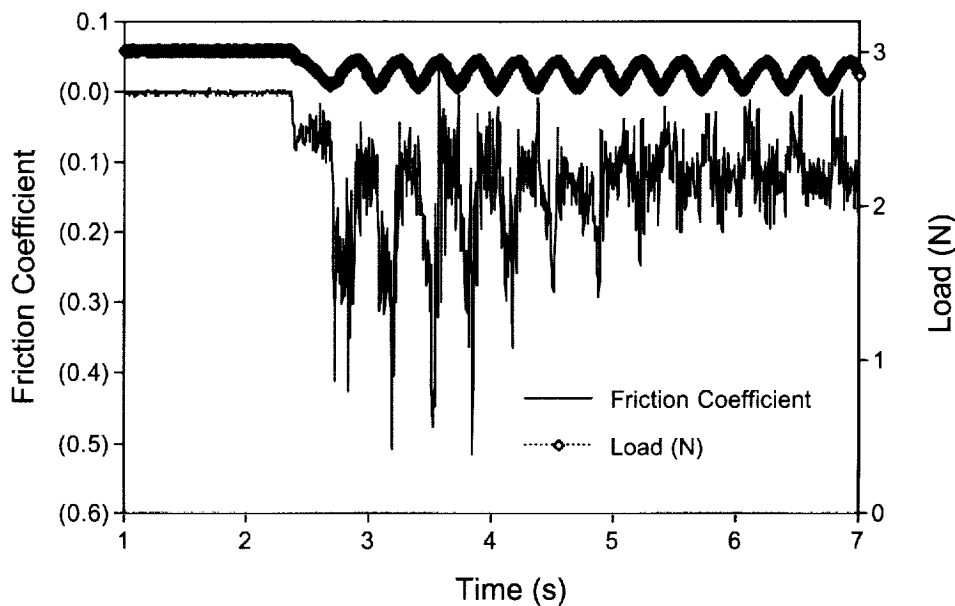


Figure 12. Plot of the COF and load at the start of a test of a half-solid-lube-coated superalloy disk against a 440C ball in air. The disk began rotating near the 2.4 s mark, as indicated by the friction measurement.

Dependence on Load

Two tests were conducted under vacuum with loads in the range of 0.2 to 0.5 N. The first test was performed with a half-solid-lube sample, and the second was performed with a clean superalloy sample.

The results of the first test, not shown here, indicate that the friction on the initially unlubricated side of the disk does not appear to be reduced by effective lubricant transfer under these lower load conditions. In particular, the friction coefficients stay high on the unlubricated portion of the disk, regularly exceeding 1.0 over the course of the test. However, from initial test measurements, it does appear that some reduction in friction is evident near the crossover point from the lubricated to the unlubricated side of the disk. The effect is not nearly as dramatic as that observed at higher loads, consistent with the premise that lower loads would be less efficient at transferring lubricant under the conditions studied. The transfer effect was more obvious with the tests conducted in air, which might also be true under the low load conditions.

The friction of a clean disk under the 0.3 N load showed that the friction under these conditions remains fairly low throughout the first 8 s of the test. In fact, the average friction coefficient determined from this one test was 0.47, a value that is much lower than the 0.74 obtained earlier. This result most likely occurs because of the light loads used in this particular test. The surface oxide layers would have a more prolonged effect under lower load conditions, as they wear away more slowly.

Oil Contamination Tests

Surface contaminants have the potential of changing the friction coefficient in a mechanical contact. In the present case, we investigated the effect of contamination by a thin film of an ester pump oil. This oil would be expected to alter friction if it existed in large enough quantities. We are exploring the extent to which a small amount of oil contamination impacts the friction coefficient.

Recall Figure 8, which presents the initial friction measurement obtained in air on a clean, uncontaminated 440C/superalloy pair. These results showed that the average, steady state friction coefficient for this combination in air was approximately 0.56, and that the friction coefficient on the very first revolution under similar conditions was approximately 0.2–0.25. The friction is observed to increase with each successive revolution, achieving the expected average values after 3 to 5 revolutions.

Figure 13 and Figure 14, present the same material pair coated with oil films of 15 nm and 60 nm thickness, respectively. These figures demonstrate the oil contamination effects on the friction. As expected, we found that the initial friction with the oil film present is lower than the friction obtained on the clean surface. However, the significant conclusions to be drawn from this data are that the initial friction coefficient was less than half of the steady state value, and that this condition persisted for many cycles. Specifically, on the 15 nm film, the friction coefficient is in the range of 0.15 to 0.20 for the first 3–4 cycles, then increases to values approaching nominal levels after 2 to 3 more cycles. In addition, during the first few cycles, the noise in the friction data is much reduced, as would be expected from a lubricated contact. These effects are even more pronounced in the data from the 60 nm film. This lower friction is a logical extension of what was observed in the 15 nm data, and shows that films in this thickness regime will impact the friction coefficient, potentially bringing it to values close to ~0.1. Some scatter is certainly to be expected in these results because the uniformity of the film coating cannot be guaranteed and because thicker coatings in areas where the test was running would lead to lower friction and more persistent low friction. At longer test times, the friction values do reach those expected for the clean materials, presumably after the lubricating surface layer has worn away. Experiments conducted with a varying load regimen showed similar results, with friction coefficients and noise levels greatly reduced early in the test, followed by higher and more erratic friction.

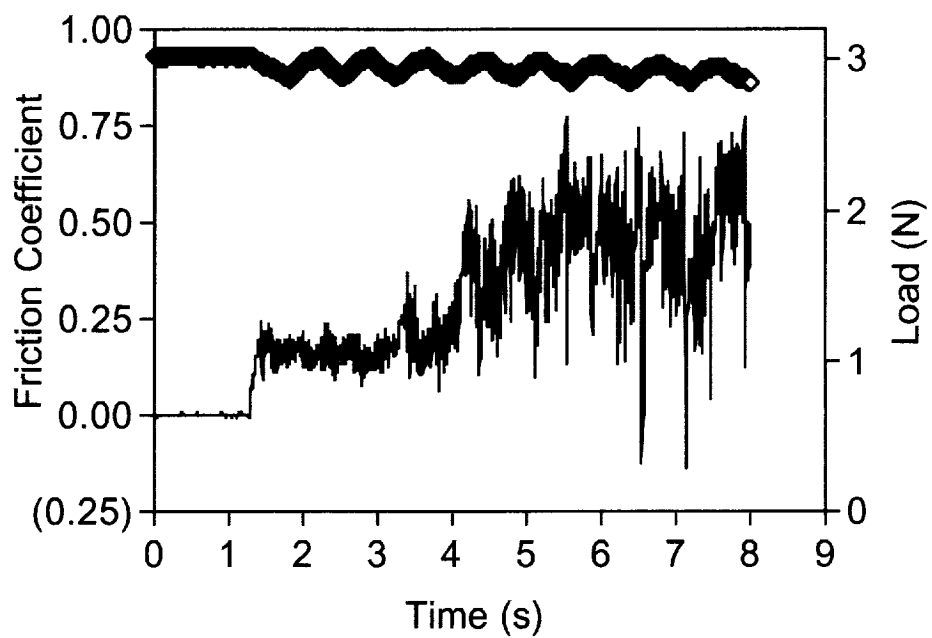


Figure 13. COF and load vs. time during the initial sliding contact between 440C and superalloy with a 15 nm film of Bray 880.

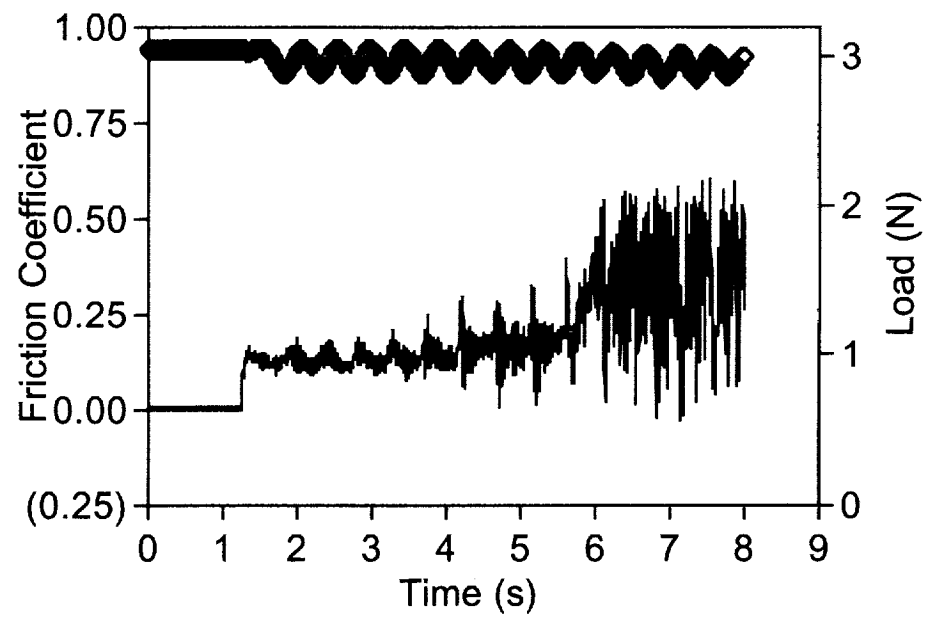


Figure 14. COF and load vs. time during the initial sliding contact between 440C and superalloy with a 60 nm film of Bray 880.

Lessons Learned

Measurements of the COF between common space mechanism materials have shown the importance of considering the composition of the surface layer when analyzing the performance of a mechanism. We have also shown that the mechanism environment during testing, storage, and operation can exert a strong influence on the COF between the component materials.

To summarize, for the materials tested in this study we have found that:

- The initial COF at a metal/metal interface was less than half of the steady state value, as the surface oxides and contaminants were worn away.
- The COF before and after wear removal of a metal oxide in air was approximately two thirds of the COF in vacuum.
- The initial COF at a metal/unburnished-solid-lubricant interface was four times the steady state COF because the MoS₂ was not yet present at the phenolic binder surface.
- The COF at a metal/solid-lubricant interface was greater in the presence of air due to the lesser lubricating qualities of oxidized MoS₂. The extent of this difference was dependent upon load.
- The COF at a metal/solid lubricant interface in air depended upon the applied load.
- The COF near the interface between a solid-lubricated region and a clean metal surface can decrease after very few cycles due to the transfer of lubricant during sliding across the interface.
- Only a small amount of transferred lubricant was necessary to reduce the COF, and these small amounts were difficult to remove by wiping with solvent saturated wipes.
- A small amount of oil contamination decreased the COF by more than 50% during the first several cycles.

These observations underscore the significance of obtaining an accurate and reliable quantity for the COF that is valid for the specific application environment. It is evident that the COF between oxidized materials may vary remarkably from the quantity determined for clean materials, and the COF can depend sensitively on the testing or application environment. Thus, when an application allows for only a narrow distribution of friction coefficients, it is imperative to carefully scrutinize the variability of the COF with the conditions of the testing, storage, and application. Furthermore, we assert that quantification of this environmental variability can only be obtained empirically.

In practice, attention must be given to the surface composition during storage and testing. For example, when a lubricant has been applied in the proximity of a region where high friction is required, a minimum number of device tests should be allowed to reduce the transfer of lubricants to other surfaces (particularly in air, where the spread is more effective). By contrast, in a situation where a bonded film is applied to provide a minimum COF, a large number of tests may be desired to burnish a wear track in the film. Finally, attention must always be given to the properties of the oxidized materials, which are ubiquitous until worn away in vacuum.

References

1. Buckley, D. H. "Surface Effects in Adhesion, Wear, and Lubrication." Elsevier Scientific, New York, NY, 1981.
2. Singer, I. L. "Solid Lubrication Processes," in *Fundamentals of Friction, Macroscopic and Microscopic Processes*, Singer, I. L. and Pollock, H. M. (eds.) pp 237-261, Elsevier, Amsterdam, 1992.
3. McMurtrey, E. L. "High Performance Solid and Liquid Lubricants: An Industrial Guide." Noyes Data Corporation, Park Ridge, NJ, 1987.
4. Claus, F. J. "Solid Lubricants and Self Lubricating Solids" Academic Press, New York, 1972.
5. Peterson, M. B. and Johnson, R. L. "Friction and Wear Characteristics of Molybdenum Disulphide. I. Effect of Moisture." NACA-TN-3055, 1953.
6. Fleischauer, P. D. and Bauer, R., "The Influence of Surface Chemistry on MoS₂ Transfer Film Formation," *ASLE Trans.*, 30 (1987), 160-166.

Marshall Space Flight Center High Speed Turbopump Bearing Test Rig

Howard Gibson¹, Chip Moore*, and Robert Thom*

Abstract

The Marshall Space Flight Center has a unique test rig that is used to test and develop rolling element bearings used in high-speed cryogenic turbopumps. The tester is unique in that it uses liquid hydrogen as the coolant for the bearings. This test rig can simulate speeds and loads experienced in the Space Shuttle Main Engine turbopumps. With internal modifications, the tester can be used for evaluating fluid film, hydrostatic, and foil bearing designs. At the present time, the test rig is configured to run two ball bearings or a ball and roller bearing, both with a hydrostatic bearing. The rig is being used to evaluate the lifetimes of hybrid bearings with silicon nitride rolling elements and steel races.

Introduction

Marshall Space Flight Center started bearing testing in the 1980's due to low lifetimes experienced in SSME turbopump bearings. The benchmark bearing life was set using the then used SSME turbopump bearings in a bearing tester designed for liquid oxygen coolant. As new bearing technologies developed, improved bearings were installed and evaluated. The best improvement was found to be hybrid bearings with silicon nitride rolling elements and steel races. The original baseline of fifteen minutes was improved greatly to four hundred and twenty minutes with this design.

In the 1990's, the need for testing high speed hydrostatic bearings and a change in supplier of turbopumps along with an emphasis in extending the lifetimes of bearings used in hydrogen, brought about the need for a new test rig. A tester was built that could be configured to run either ball/ball/hydrostatic, ball/roller/hydrostatic, or all hydrostatic bearings. The unit is powered by a gaseous nitrogen turbine, which gives it a very high-speed capability. Speeds of thirty-five thousand rpm are routinely reached with the capability to go higher. Axial and radial loading is possible with cycling capabilities. The test rig is simple to assemble and disassemble and has borescope ports to inspect the bearings without disassembly. The rig can also run using liquid nitrogen or oxygen as the coolant.

This test rig has completed five test series. These tests were used to evaluate ball/ball and ball/roller configurations using hybrid bearings. All tests were done in liquid hydrogen. Total time accumulated is approximately 75,000 seconds. After each test series, an inspection of the hardware is performed in the metrology lab. Traces of surface features are made, race curvatures are measured, roundness measurements are made, ball diameters are measured, and visual inspections are recorded.

This paper focuses on the results of the ball/roller bearing testing. Results of the ball/ball bearing testing were presented at the 32nd Aerospace Mechanisms Symposium by Chip Moore in May of 1998.

Test Requirements

The Test Rig

The test rig (Figure 1) is a vertical shaft oriented tester with a ball bearing at the top and either a ball or roller bearing in the middle position. Near the bottom of the shaft is a hydrostatic bearing. This rig was originally designed to be a hydrostatic bearing tester but was modified to test rolling element bearings also. At the bottom of the shaft is a turbine that spins the shaft. Gaseous nitrogen is forced into the inlet manifold and exits the bottom. Speeds of 35000 rpm are routinely used for testing. Radial loads are

* NASA Marshall Space Flight Center, Huntsville, AL

applied to the middle bearing through a cylinder attached to the tester squirrel cage. Axial loads are applied by changing the internal pressures either in the top cavity or in the thrust piston located at the bottom of the test rig. Liquid hydrogen is routed in series through the top bearing, through the middle bearing, and out of the rig. The hydrostatic bearing has a hydrogen supply of its own. Gaseous helium is routed thru the buffer seal to keep the liquid hydrogen and gaseous nitrogen separated.

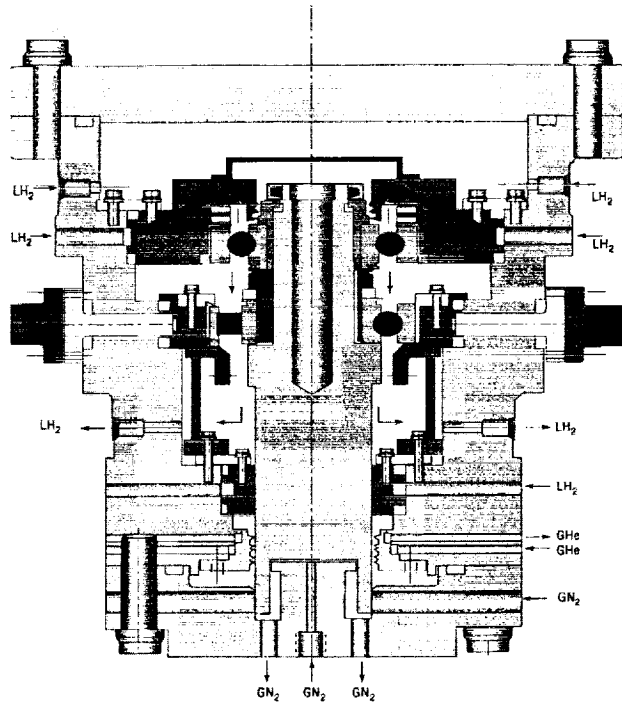


**Figure 1. Cross Section Of Bearing Test Rig
Ball/Roller configuration on left, Ball/Ball configuration on right,
flow paths as indicated**

Instrumentation is provided for monitoring the operation of the test rig and facility. Pressures, flow rates, and temperatures are recorded for the run tank, along the inlet piping, in the tester, and in the exit lines. Axial load, radial load, and speed are also recorded. During the testing, critical measurements are watched on monitors in the control room. Redline cuts are set on maximum and minimum limits of certain parameters. Because of the hazardous nature of hydrogen, no personnel are allowed on the test stand once testing starts. All tests are video taped and a fire suppression system is on line in case of an incident.

The Bearings

The bearings (Figure 2) that are run in the rig are the same bearings that are used in the developmental and certification turbopumps. For this build, the top bearing, called the reaction bearing, is a ball bearing with Cronidur 30 rings, Armalon cage with Salox inserts, and silicon nitride balls. The middle bearing called the load bearing, is a roller bearing with Cronidur 30 rings, Armalon cage, and silicon nitride rollers. The reaction bearing is 60 mm (2.36 inch) bore, 130 mm (5.12 inch) outside diameter, and has eleven 20.6 mm (0.81 inch) balls. The load bearing is 72.9 mm (2.87 inch) bore, 133 mm (5.23 inch) outside diameter, and has fourteen 17 mm (0.667 inch) diameter rollers.

The reaction bearing came from a hot-fired engine test and had 3,861 seconds of time on it. The load bearing came from an engine and also had test time on it for a total of 1,824 seconds. A visual inspection

and video taping of the components document the pre test conditions of the bearings. High precision dimensional and surface texture measurements are made before and after the test series. Typical measurements are diameter, roundness, surface texture, cross race curvatures, and wear. After testing, the components are inspected again and noted features can be relocated and inspected a second time to look for degradation.

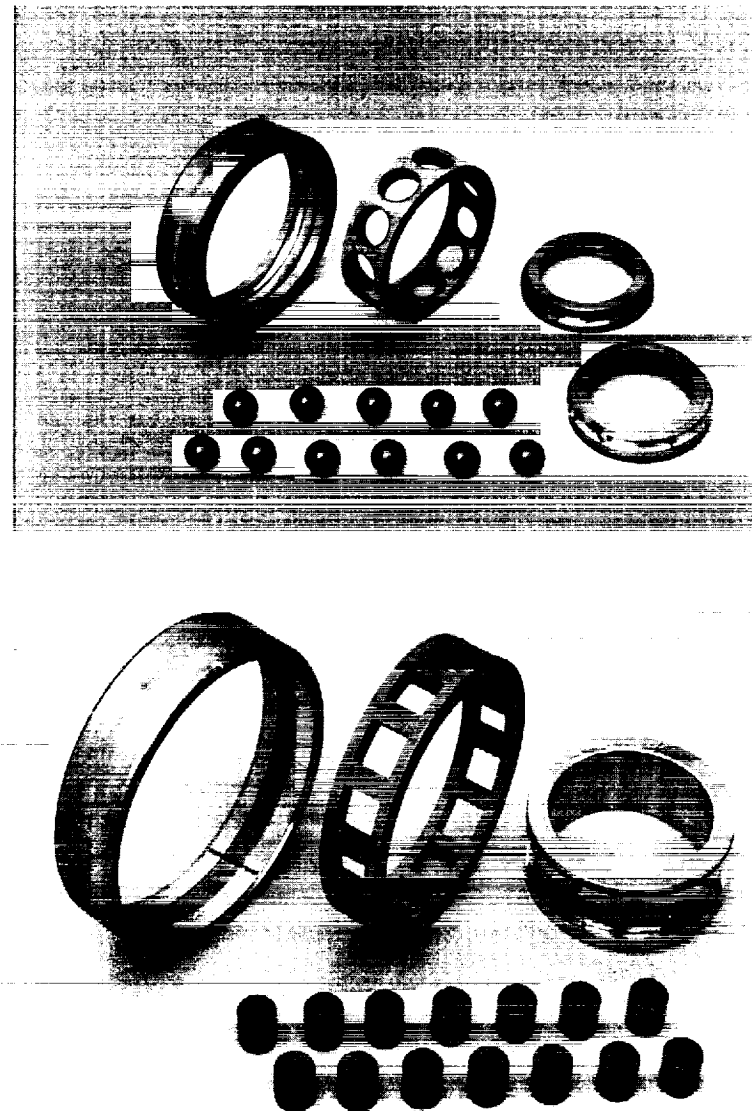


Figure 2 Typical Ball Bearing (top) and Typical Roller Bearing (bottom) used in Test Rig.

The rolling elements of both bearings had degradation in the form of river marks and other surface anomalies that were noted before installation into the test rig. These were formed in the hot-fired engine testing.

Objectives

There was an interest in documenting the performance of hybrid roller bearings running at high speeds in liquid hydrogen environments. Also, the surface anomaly that has been called "river marks" exists on

some silicon nitride balls and rollers and their effect on life needed to be studied. River marks (Figure 3) are seen on the surface of silicon nitride balls and rollers in bearings running in high load, cryogenic fluid applications. They are characterized by large width to depth ratios and run on the surface of the ball or roller with small tributaries leaving the main line. The walls or edges of the marks can be steep. Typical width and depth values seen are 0.14 mm and 0.005 mm, respectively. Fracture of the material has been a concern, however no fractures have occurred in any testing to date.

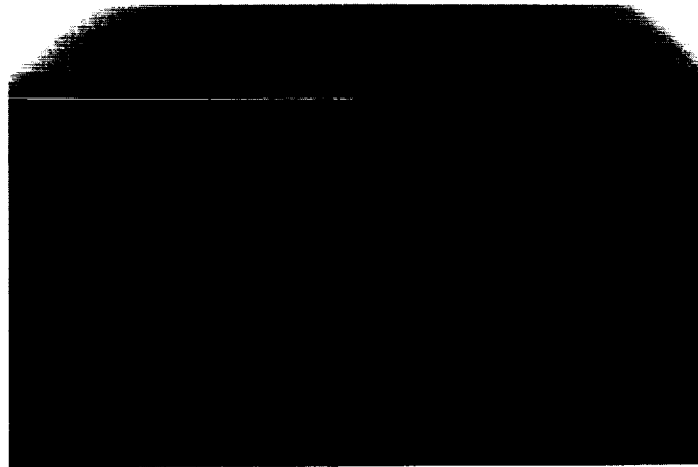


Figure 3. "River Mark" as seen on Silicon Nitride Balls and Rollers Run in Cryogenic Environments

To achieve the objective, the bearings installed in the test rig had river marking on the balls and rollers. The regions were documented for a before and after testing comparison. Previous testing¹ with hybrid ball bearings has shown that river marks tend to grow in length but not severity. The test program was started with the goal of accumulating 31,000 seconds of run time at high speed.

Test Procedure

A test consist of chilling the tester down to cryogenic temperature, flowing hydrogen through the bearings, spinning the tester, conducting any transient load cycles, and stopping the test rig. Run time is limited by a 5000 gallon tank that provides the liquid hydrogen. Test times average 800 to 1000 seconds, requiring 31 to 40 tests to complete a series.

Testing roller bearings presents a unique situation where as roller bearings do not take thrust loads. To hold the shaft in place and apply preload to the ball bearing, pressure must be balanced between the top cavity and the bottom thrust piston in the test rig. Automatic controls were set up to effectively control the valves that apply this pressure. A previous test series failed due to the shaft seizing to the thrust piston surface. No automatic control was used in this series. Pressure changes happen so rapidly that manual controls cannot be used.

A normal test sequence after the tester is chilled is to apply pressure in the thrust piston located at the bottom of the shaft to lift the shaft and apply a preload of 3113 newtons (700 lb) on the ball bearing. Instrumented strain gages on the preload spring give a real time read out of this value. The rig is brought up to a run pressure of 8.4 MPa (1225 psi). Rotation is started with a target speed of 35,000 rpm desired. During the speed ramp, radial loads are applied in steps up to 4.4 kN (1000 lb). The auto pressure control keeps the pressure differential between the top cavity of the tester and thrust piston constant so as not to allow the shaft to drop and rub the top of the thrust piston. The temperature of the coolant is normally in the 28 K (-410°F) range. The flow rate into the bearings is 0.25 kg/sec (0.5 lb/sec) with 0.45

kg/sec (1.0 lb/sec) flowing through the hydrostatic bearing. A temperature sensor monitors tester inlet temperature and when it reaches a redline, the test is automatically terminated. This prevents gas from entering the test rig, which would be detrimental to the bearings. Throughout the tests, sensors monitor temperatures, pressures, speeds, and loads and are capable of stopping the test when any redline value is reached.

After the test is over, personnel are allowed back into the area to secure the valves and controls. It takes approximately 18 hours for the test rig to "thaw out". When the ice has cleared, a borescope inspection can be performed of the bearings and internal hardware. After 15,000 seconds have been accumulated, the test rig is removed from the stand and taken to a disassembly room for a mid point inspection. If the hardware and bearings show no degradation, the tester is reassembled and taken back for further testing. At the end of 31,000 seconds, the rig is removed for final disassembly and inspection.

Results

Test Program

This test series consisted of fifteen rotational attempts. Twelve tests were successful in that 35,000 rpm was reached. In one attempt, facility problems aborted testing. In another, the rotor did not break away and come up to speed, and in the last attempt, the speed was very erratic and the rig was shut down manually. Speed fluctuations had been seen in other test as well, but the target speed was reached. The erratic speed was attributed to the rollers becoming skewed in the bearing and acting as wedges that slowed or locked the rotor. An effort was made to re-orient the rollers by raising and lowering the shaft in the test rig but problems still persisted on a random basis. The test time in the rig was 10,894 seconds with a total time at speed including previous turbopump time of 15,975 seconds on the ball bearing and 12,635 seconds on the roller bearing. The tester was removed from the stand (Figure 4) for an inspection of the bearings to check for damage.

Bearing Inspections

The bearings were visually inspected and examined under a microscope. No obvious evidence was seen for the locking of the rotor or speed fluctuations. Some light rubbing was visible on the upstream faces of the rollers and some wear in the cage pockets had occurred due to the radial loading. Surface metrology was done on the rollers and balls. The areas that were highlighted earlier were re-examined for degradation. The analysis showed that the major river marking did not grow, but smaller "tributaries" branched out from the main features.

Figure 5 shows a ball with two surface features that were mapped. In the post test pictures, the smaller surface cracks can be seen running from the main features. Figure 6 is another ball with one area that was watched. The same degradation happens on this ball. Figure 7 is a roller with small surface distress features. The post test photo shows that the surface resisted cracking better than the balls. The roller did show signs of parallel grooving, thought to be from the fiberglass fibers in the Armalon™ cage pockets. This grooving was seen on several of the rollers. Figure 8 shows another roller with surface features. The post test photograph shows some smoothing of the surface and debris scoring. In general, all of the rollers resisted the surface cracking better than the balls.

Marshall Space Flight Center has some of the best surface metrology equipment available. Two examples of this are Figure 9 and 10. The WYKO NT2000 instrument can look at surfaces and provide valuable information on all Rq, Ra, Rt, Rp, and Rv values. A three dimensional map can be made of the surface that provides depths and widths of selected areas. Color is used to represent differing depths and heights of features. Figures 9 and 10 are of the two balls in Figures 5 and 6. The X (horizontal) and Y (vertical) profiles can be compared along with the 3D color plots for before and after results. The X and Y coordinates can be changed for an overall look at the surface.



Figure 4. Installed Test Rig.

Tester mounted on stand, inlet and outlet piping is above to allow access to ports and instrumentation. Fire suppression system is overhead. Hydrogen burn off stacks are in background. All piping and valves are insulated before test series begins to conserve hydrogen.

Conclusions

After examinations of the hardware and test data reviews were complete, the rig was reassembled. No obvious reason for the speed fluctuation was found. The action of river mark growth has continued in this test series just as it has in other bearing testing at Marshall². No definite mechanism for river mark formation has been determined. The degradation of the surface has not caused any premature failures in the bearings to date. The testing will continue with the goal of accumulating the needed 20,000 seconds that will complete this program.

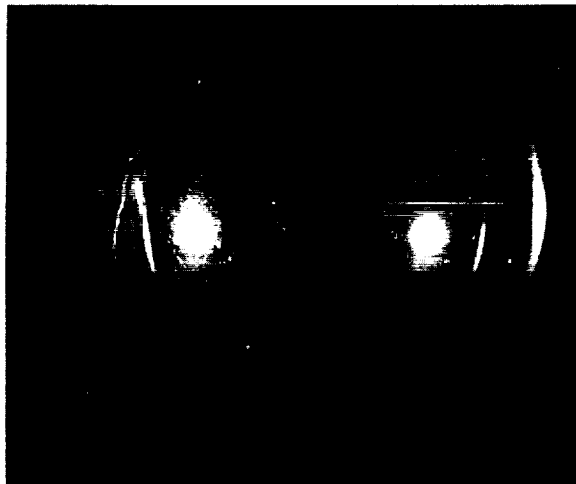
Acknowledgements

The primary author would like to thank Chip Moore of MSFC for the metrology measurements and test support, Dr. Robert Thom of MSFC for the determination in investigating the safety of hybrid bearings, Jim Moore of SRS Technologies and Phillip Benefield of USA for the test support and data reviews, Steve Allums of MSFC for conducting the test, and the technicians of LB&B for continuing test stand support.

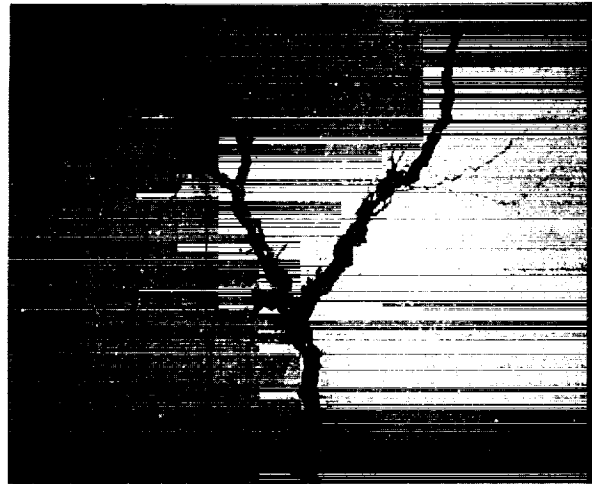
References

1. Moore, Chip, Howard Gibson, and Dr. Robert Thom, "Liquid Hydrogen Testing of Silicon Nitride Bearings for Use in High Speed Turbomachinery", Proceedings from the 32nd Aerospace Mechanisms Symposium, May 1998

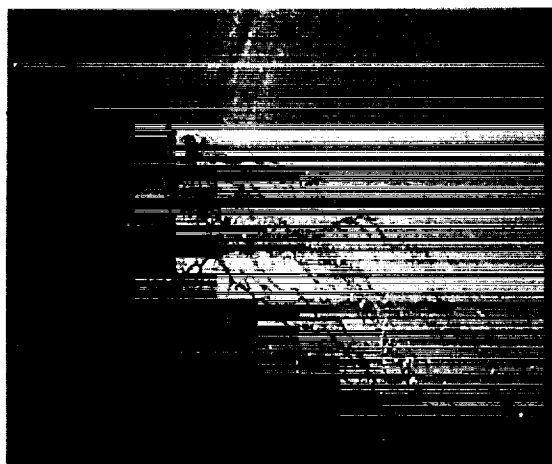
2. Gibson, Howard, and S. Fears, "Bearing Testing Performed in Liquid Oxygen", Proceedings from the Advanced Earth To Orbit Propulsion Technology Conference, MSFC, 1992



Silicon Nitride Ball With River Mark On Left
And Surface Anomaly In Middle



Close Up Of River Mark On Ball



Surface Anomaly In Middle Of Ball



Close Up Of Mark After 10,894 Seconds

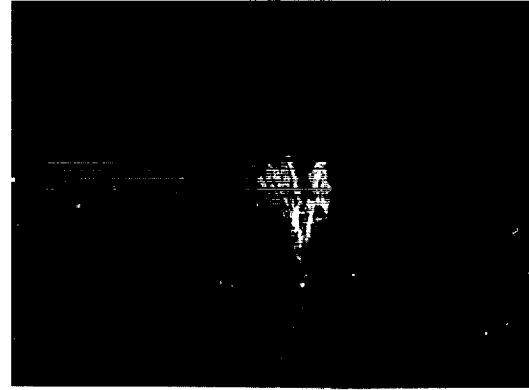


Surface Anomaly After 10,894 Seconds

Figure 5. Ball Number 1 From Test Rig



Three Fingered Hand Surface Anomaly



Close Up Of Surface

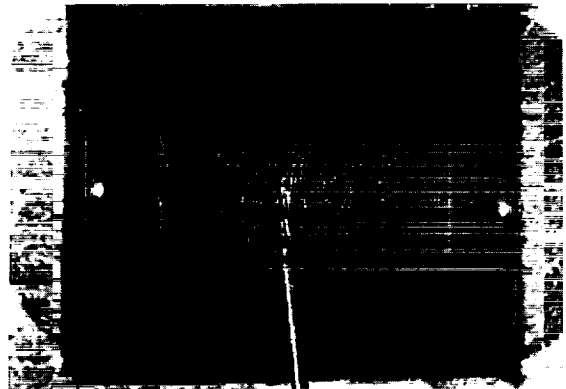


Surface Before Running In Tester



Surface After 10,894 Seconds

Figure 6. Ball Number 7 From Test Rig



Surface Feature On Roller Number 5



Close Up Of Surface



Close Up Of Surface

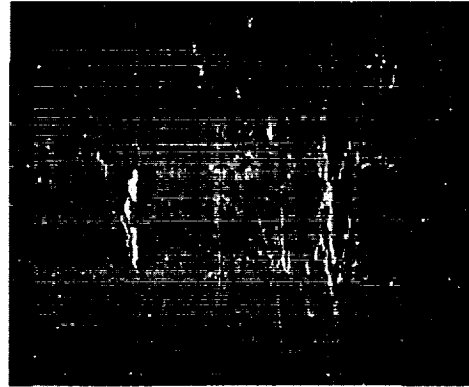


Surface After 10,894 Seconds

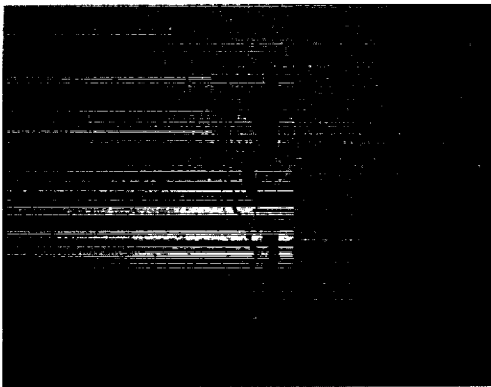
Figure 7. Roller Number Five From Tester



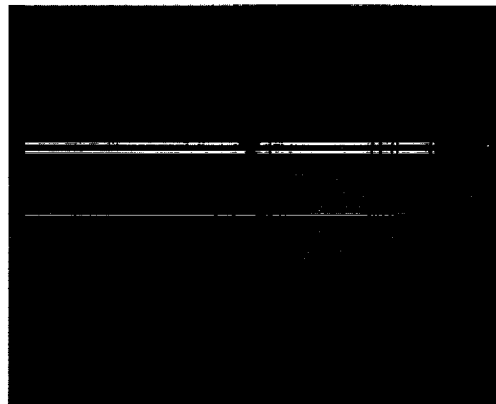
Surface Of Roller



Closer View Of Surface



Close Up Of Anomaly Pre Test



Anomaly After 10,894 Seconds

Figure 8. Roller Number 8 From Test Rig

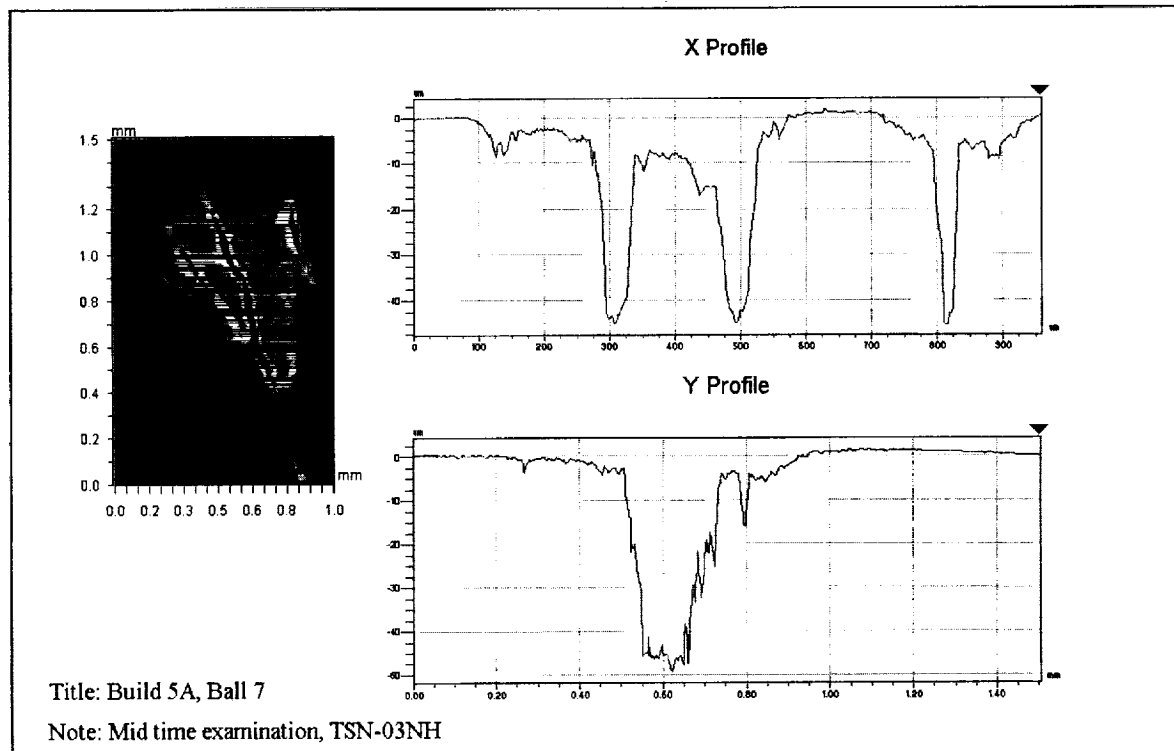
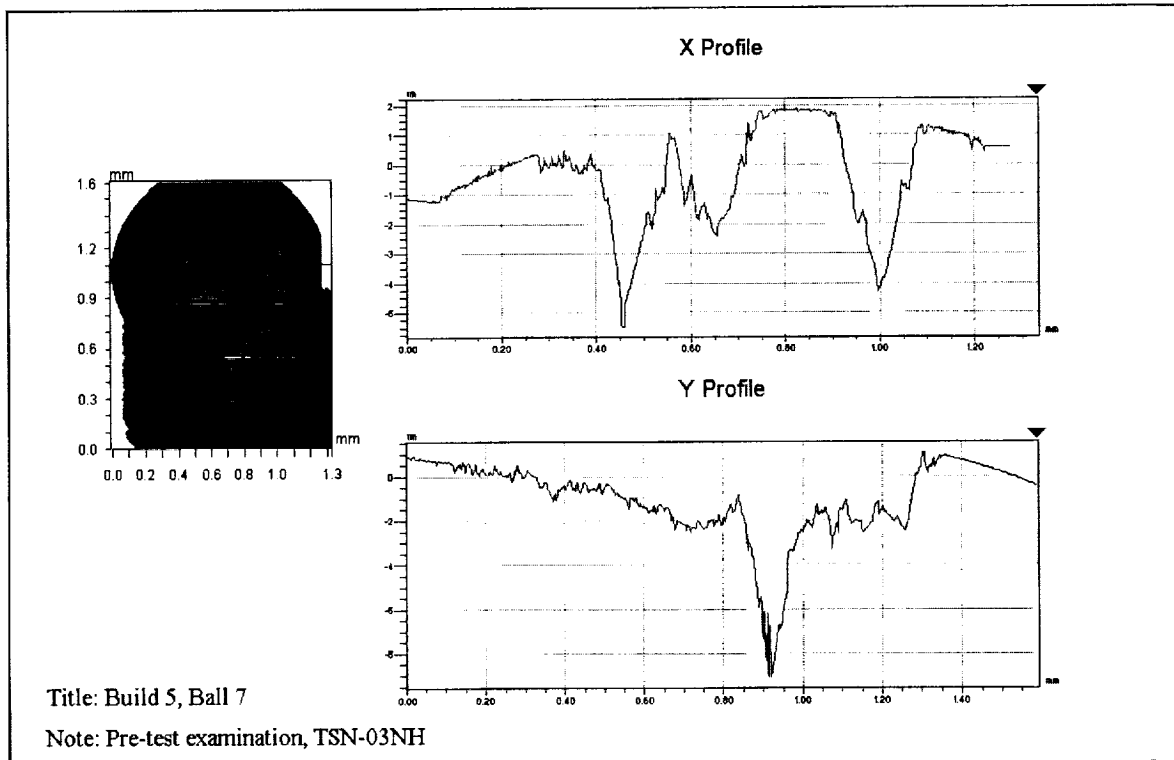


Figure 9. WYKO NT-2000 Surface Inspection

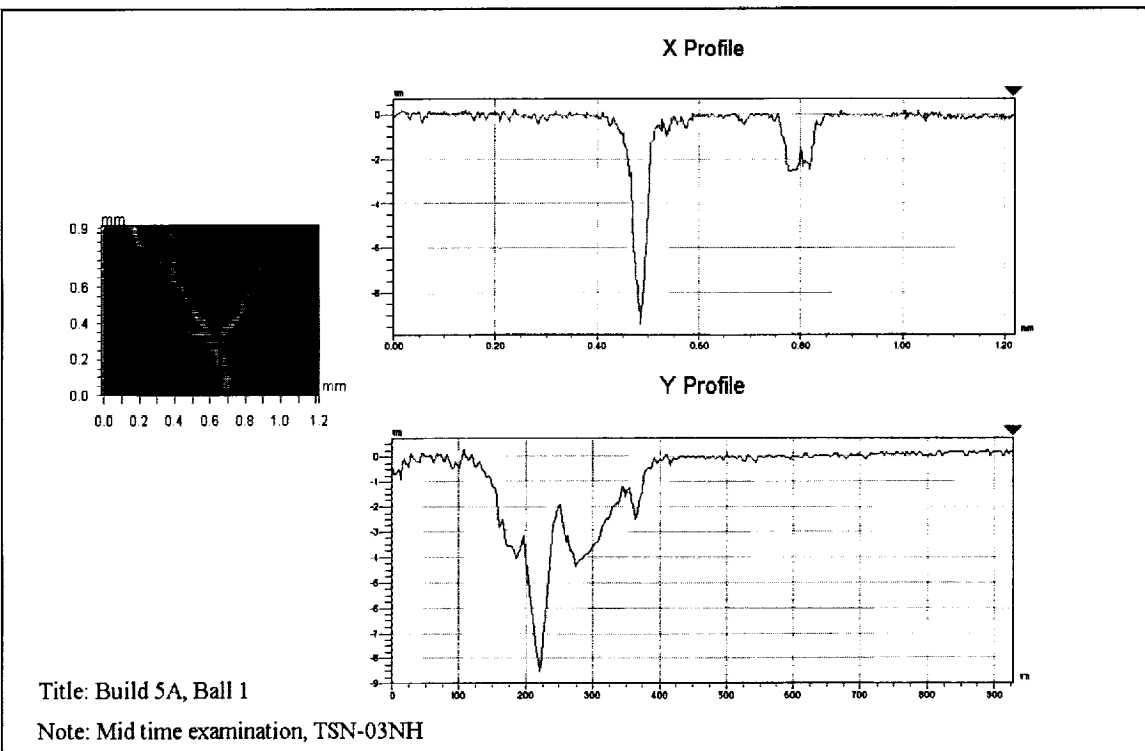
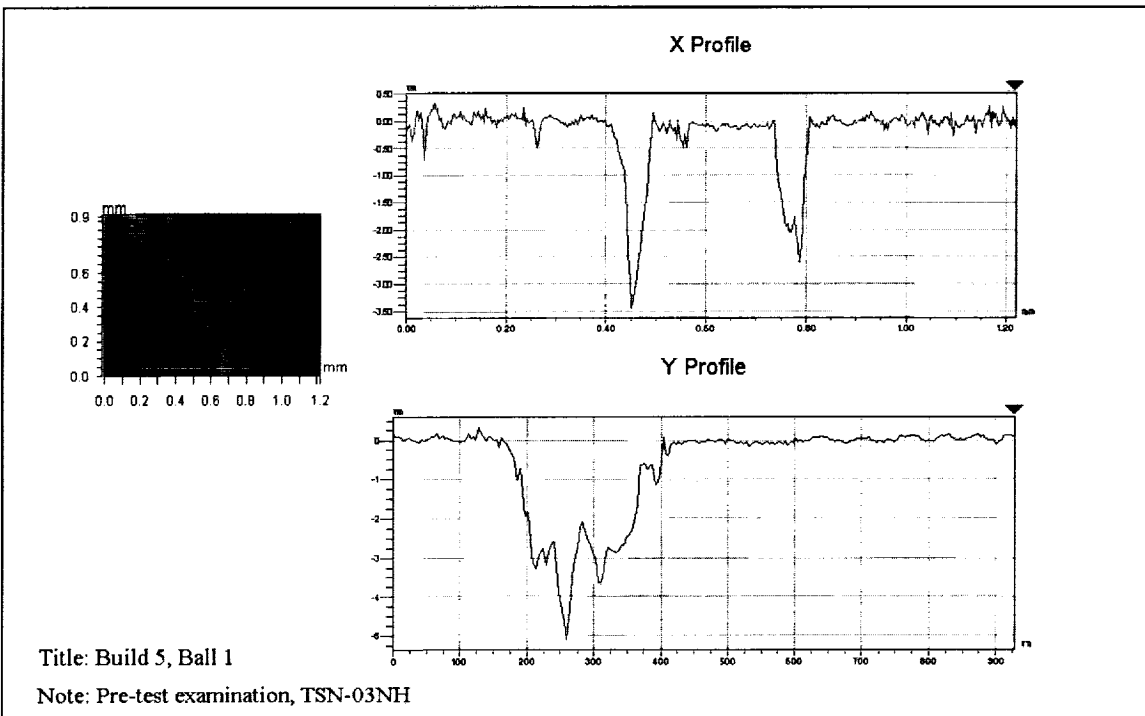


Figure 10. WYKO NT-2000 Surface Inspection

Design, Development, And Testing of Umbilical System Mechanisms for the X-33 Advanced Technology Demonstrator

Alan C. Littlefield^{*} and Gregory S. Melton

Abstract

The X-33 Advanced Technology Demonstrator is an un-piloted, vertical take-off, horizontal landing spacecraft. The purpose of the X-33 program is to demonstrate technologies that will dramatically lower the cost of access to space. The rocket-powered X-33 will reach an altitude of up to 100 km and speeds between Mach 13 and 15. Fifteen flight tests are planned, beginning in 2000. Some of the key technologies demonstrated will be the linear aerospike engine, improved thermal protection systems, composite fuel tanks and reduced operational timelines. The X-33 vehicle umbilical connections provide monitoring, power, cooling, purge, and fueling capability during horizontal processing and vertical launch operations. Two "rise-off" umbilicals for the X-33 have been developed, tested, and installed. The X-33 umbilical systems mechanisms incorporate several unique design features to simplify horizontal operations and provide reliable disconnect during launch.

Introduction

The two ground-to-flight umbilical connections for the X-33 vehicle are located facing aft on either side of the linear aerospike engines (Figure 1). The fuel umbilical provides thirteen connections to the vehicle, including liquid hydrogen supply and bleed lines, as well as high-pressure gases (up to 21 MPa), environmental control, hazardous gas sampling, electrical power, and data. The oxidizer umbilical provides seventeen connections to the vehicle, including liquid oxygen supply, high-pressure gases, environmental control, hazardous gas sampling, avionics cooling, electrical power, and data. The umbilicals are connected after the vehicle is mated to the rotating launch mount in the horizontal configuration and remain connected through rotation to vertical, tanking, and launch. The aft mounting of the umbilicals results in a "rise-off" type of disconnect that quickly subjects the ground half of the connection to the engine exhaust plume. Traditional vehicle configurations (with minimal aft area) have favored side-mount umbilical configurations, which complicate the disconnect but provide additional time to protect the ground system from damage. The X-33 umbilicals are the largest rise-off umbilicals developed for any U.S. space system.

Umbilical System Requirements

The requirements for the X-33 umbilicals were driven by the general vehicle configuration and design, as well as specific safety and operational requirements. The aft-mounted umbilical "rise-off" configuration and fast acceleration of the X-33 off of the pad (0.9g) resulted in an available operating time of 1.4 seconds from first motion of the vehicle until the engine exhaust plume impinges on the ground umbilical. The umbilical must be disconnected and stored within a protective enclosure before the plume reaches any sensitive components. Operational timelines allotted only one hour to accomplish the entire mating operation. This resulted in a requirement for semi-automatic connection and leak check capability. The quick turnaround requirement for successive launches (24 hours) leaves little time available for refurbishment of ground systems. Misalignment of the vehicle on the launch mount, dynamic deflections of the structure, and drift of the vehicle during liftoff required accommodating relative motions between the ground and flight components of up to 4 cm. Early in the design, the customer imposed several additional requirements on the system. In order to reduce costs and refurbishment time, no pyrotechnic devices

* NASA Kennedy Space Center, Florida

were allowed. To simplify the ground control systems and software, no T-0 signal from the vehicle or ground would be provided. This required the disconnect sequence to be initiated by liftoff motion of the vehicle only. Finally, all systems must operate on stored energy (springs, compressed gas, or gravity).

Umbilical System Description

The X-33 Umbilical system consists of a flight panel assembly and a ground umbilical assembly. The nominal size of the ground and flight connector panels is 89 cm by 127 cm. The fluid and electrical connectors are rigidly mounted to the panels. The flight panel assemblies (Figure 2) attach to the vehicle aft thrust structure adjacent to the engines and consist of a structural aluminum panel supporting the flight halves of the various connectors as well as receptacles for the panel alignment and locking mechanisms. A sliding door on each assembly closes after disconnect to protect the panel and connectors from heating and contamination during flight. The ground umbilical assemblies (Figure 2) attach to the rotating launch mount on the pad. The ground assembly is a protective tunnel structure containing the ground panel and mating, release, and retraction mechanisms. The umbilical tunnel weldment supports and protects the ground umbilical mechanisms. Blast doors on the tunnel close to protect the umbilical mechanisms from launch blast damage. A translating frame structure within the tunnel supports the ground panel on a six degree-of-freedom compliance mechanism and retracts into the tunnel during the disconnect. Fluid and electrical lines are routed through the translating frame and tunnel to an interface plate on the launch mount.

Umbilical System Operation

The operation of the umbilical can be divided into three phases. The first operational phase is mating of the umbilical in the horizontal mode (or vertical mode as a contingency). The second phase is the use of the various fluid and electrical systems throughout processing, rotation and tanking operations. The third phase is the actual disconnect of the umbilical following liftoff.

Mating Operations

The mating operation begins after the vehicle is attached to the launch mount. First, the flight door is manually opened and pinned to allow access to the flight panel. Next, the blast doors are opened and the translating frame assembly is extended using pneumatic jacks. As the jacks are extended, alignment pins on the ground panel engage the flight panel while the compliance mechanism supports the weight of the ground panel, hoses, and cables and allows the panels to align for mating. As the jacks are fully extended, the translating frame latches in the extended position. The jacks are then retracted to allow the latches to support the translating frame. Next, the alignment pins are retracted in parallel to mate all the fluid and electrical connectors. Finally, quick-release locks are pneumatically engaged to rigidly connect the panels.

Processing Operations

Throughout horizontal, rotational, and vertical operations, the compliance mechanism continues to support the ground panel, hoses, and cables (with a total mass of over 800 kg) to limit loads transferred to the vehicle. The quick release locks prevent separation of the panels due to fluid pressure forces between the connectors (up to 71 kN total).

Disconnect Operations

Following completion of tanking operations, the cryogenic lines are drained, and power is removed from the electrical connectors in preparation for launch. Several pneumatic lines and the environmental control system remain fully or partially pressurized through disconnect.

The launch sequence begins as the vehicle engines are started. As the engines cause the vehicle and launch mount to deflect from their nominal position, the compliance mechanism absorbs relative motion (up to 2.5 cm) between the vehicle and the mount. The umbilical must remain connected during these deflections to ensure the capability to de-tank in the event of an abort. After the engines are verified to be at proper operational levels, the vehicle initiates the pyrotechnic charges in the hold-down system to release the vehicle from the pad. The vehicle rises off of the pad with the umbilicals still connected. After

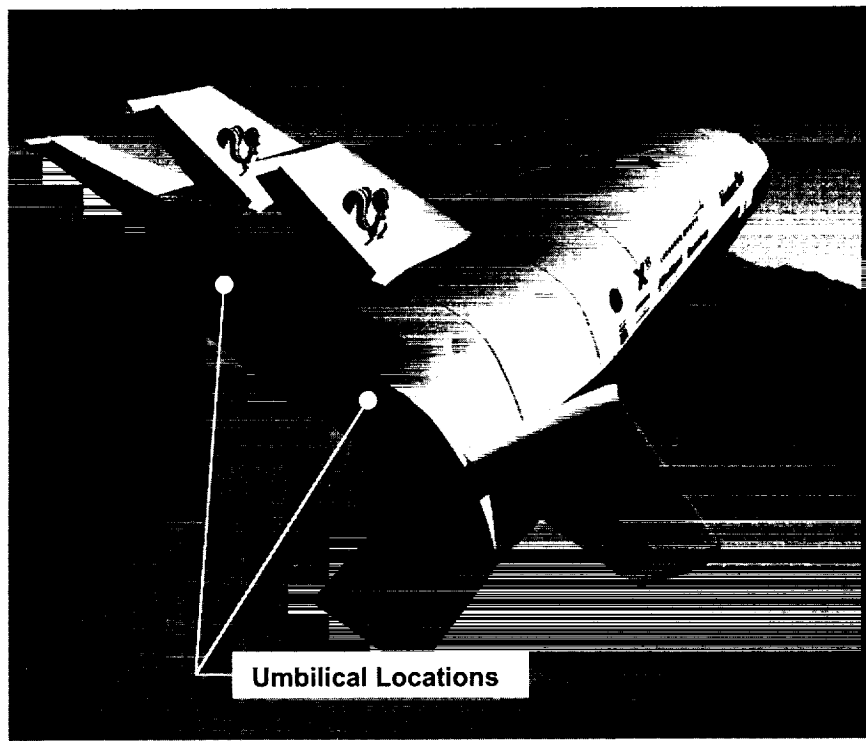


Figure 1. X-33 Vehicle Umbilical Locations

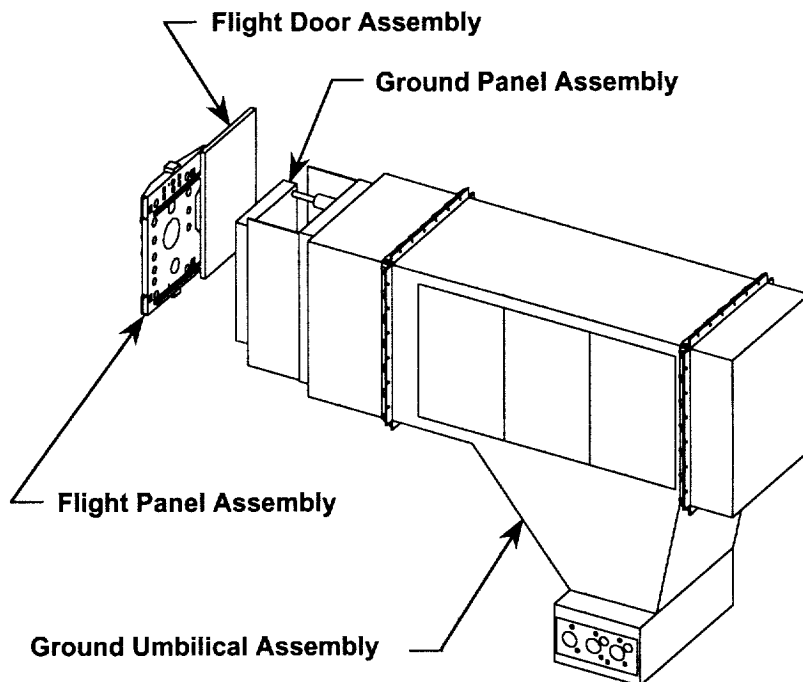


Figure 2. Ground and Flight Umbilical Assemblies

rising 4 cm, release lanyards actuate the quick-release locks, and valves in the compliance mechanism open to actuate the latches supporting the translating frame. Next, the translating frame drops 110 cm into the tunnel as the compliance mechanism decelerates and centers the ground panel, hoses, and cables. Shock absorbers then decelerate the translating frame at the bottom of the tunnel. Finally, blast doors on the tunnel close to protect the ground panel assembly and mechanisms.

Passive Compliance Mechanism

The key to the operation of the umbilical system is the self-centering, counterbalanced, six degree-of-freedom passive compliance mechanism that supports the ground panel assembly with hoses and cables during horizontal and vertical operation (Figure 3). The compliance mechanism must support the ground panel and adjust for misalignment during mating. It also provides the axial force required to mate the connectors. Finally, it must decelerate, center, and support the ground panel, hoses, and cables during the high-speed disconnect. The passive compliance mechanism uses a variety of specially-designed and commercial off-the-shelf components to accomplish these tasks.

Passive Compliance Mechanism Requirements

Some of the significant design requirements for the passive compliance mechanism were:

- Provide six degree-of-freedom capability
- Support the 800 kg panel assembly in horizontal and vertical modes
- Provide positive centering to nominal position
- Limit lateral centering forces to 1 kN transferred to vehicle while aligning
- Generate nominal axial centering force of 11 kN to assist mating
- Provide latch actuation via integral valves
- Maximize access to center of panel (support at perimeter)
- Provide lateral compliance ± 3 cm
- Provide Axial compliance +16 cm, -4 cm
- Provide angular compliance within limits of lateral and axial compliance

Passive Compliance Mechanism Description

The compliance mechanism uses a simple arrangement of eight spring-centered struts to maintain the ground panel in the proper position for mating while allowing for misalignment and vehicle motions during mating, engine buildup, and launch.

The four axial strut assemblies (Figure 4) were designed specifically for the X-33 umbilical. A large (9-cm diameter) compression spring is used to generate the design preload of 2.75 kN on the strut piston to resist strut compression. The spring rate was minimized in order to provide a relatively constant force throughout the 16 cm compression stroke. This resulted in a significant initial compression of 19 cm required for assembly. (The stored energy in the spring created a significant risk to technicians if proper assembly or disassembly steps were not followed. The engineering team took great care to ensure that the hardware and procedures contained adequate safety warnings.) The second spring, nested within the first for space savings, resists strut extension by reacting between the strut rod and the piston. This configuration provides a self-centering strut with different strokes, preloads, and spring rates for each operating direction. Spherical rod ends allow for end rotation and strut length adjustment. An elastomeric stop is provided for the compression stroke in the unlikely event that the maximum strut compression occurs simultaneously with the translating frame maximum deceleration. Air transfer ports in the piston provide a limited degree of cushioning and damping. No additional damping was added to the system. The strut piston, in addition to providing the centering function, actuates an integral pneumatic control valve for the retract latches (discussed later).

The four lateral strut assemblies center the ground panel with respect to the translating frame. One pair of struts provides spring centering only; the other pair of struts provides spring centering for vertical operation and has additional pneumatic counterbalance capability to support the ground panel, hoses, and cables for horizontal operation. The design of the lateral strut uses a back-to-back pair of

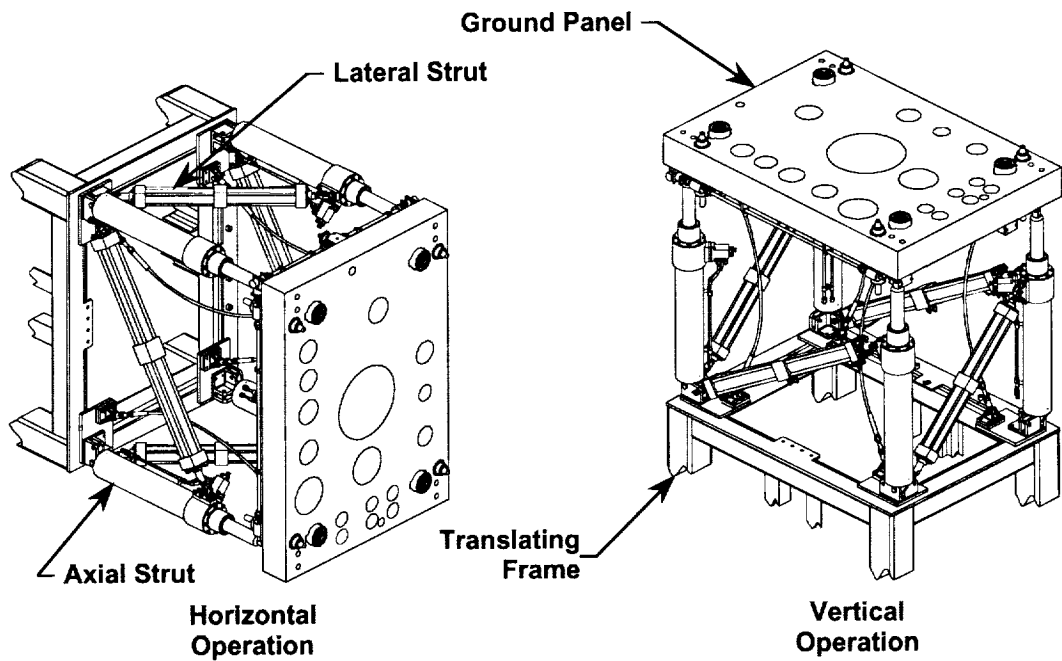


Figure 3. Umbilical Compliance Mechanism

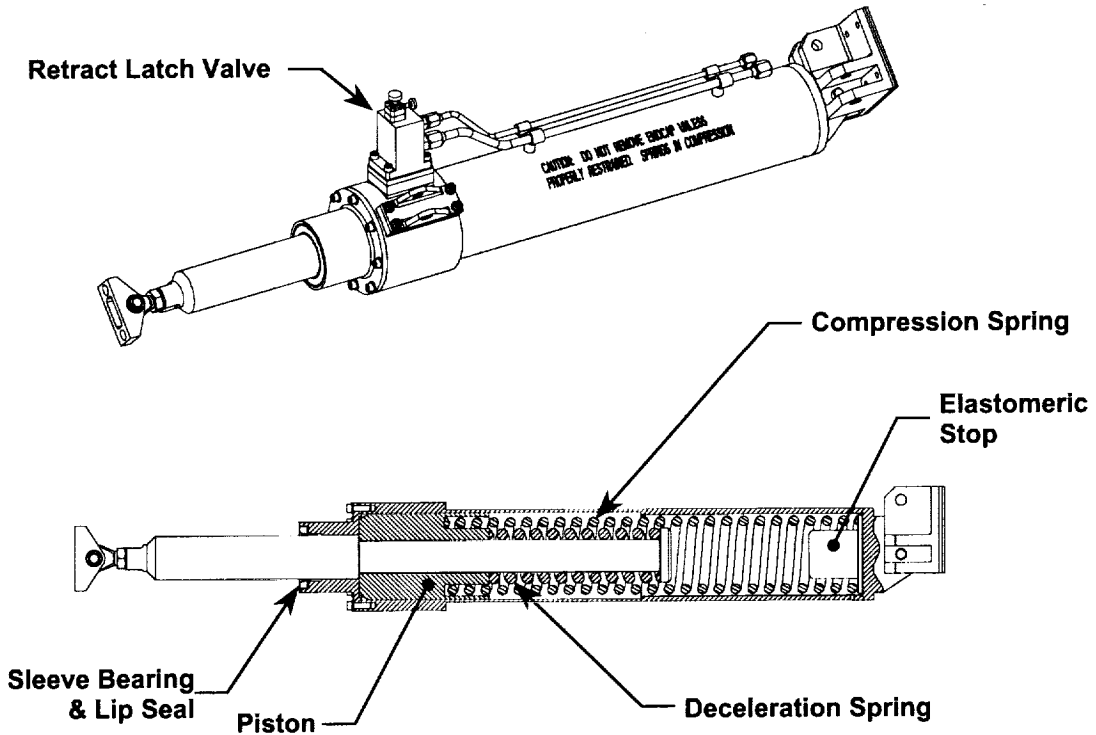


Figure 4. Compliance Mechanism Axial Strut Assembly

commercial high-pressure pneumatic cylinders (Figure 5). One cylinder of each pair is spring retracted (extension cylinder) and the second is spring extended (compression cylinder). Together, they provide the spring centering capability required for the struts. Spherical rod ends allow for end rotation and strut length adjustment. Internal seal friction, airflow through the vent ports, and integral cushions provide a limited degree of damping. The counterbalancing capability is created by applying equal pneumatic pressure to the rod ends of both cylinders. At the proper pressure setting, the struts support the weight of the panel while the springs provide the bias force necessary to overcome seal friction and center the strut. The pressure is removed from the struts after the vehicle is rotated to vertical. It should be noted that the strut system is "over-constrained," that is, only three of the lateral strut assemblies are required for stability. The fourth strut assembly was added to eliminate moments induced into the panel assembly by lateral accelerations and prevent unwanted rotation of the plate following disconnect.

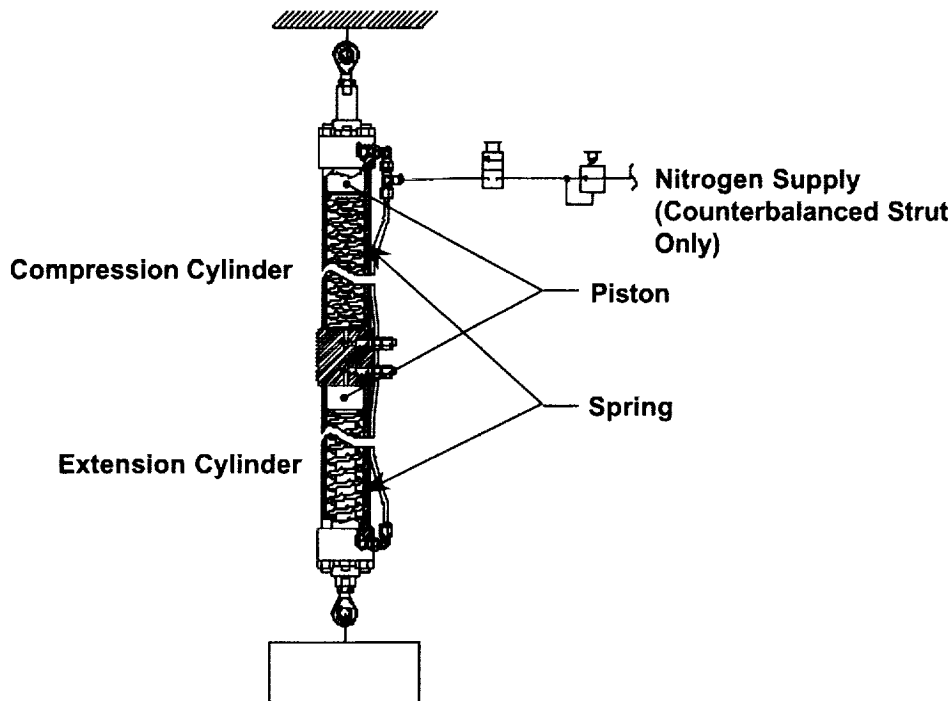


Figure 5. Compliance Mechanism Lateral Strut Assembly

Panel Alignment Mechanism

The panel alignment mechanism guides the ground panel into alignment with the flight panel for mating. After aligning the panels, the mechanism mates all of the umbilical connectors by guiding the panels together while maintaining alignment and parallelism. The alignment mechanism consists of a retractable pin system on the ground panel and mating receptacles on the flight panel.

Panel Alignment Mechanism Requirements

Some of the significant design requirements for the panel alignment mechanism were:

- Correct for six degree-of-freedom initial misalignment of panels
- Eliminate possibility of binding during alignment or disconnect
- Align panels within ± 0.015 mm
- Maintain panels parallel within ± 0.03 mm throughout mating operation
- Operate with cordless drill or manually
- Provide nominal lateral alignment force of 1 kN, fail safe at 8 kN
- Provide maximum axial load capacity of 18 kN
- Accommodate maximum initial lateral misalignment of 2 cm
- Accommodate initial angular misalignment within limits of lateral misalignment
- Provide mating stroke (parallel motion) of 5 cm

Panel Alignment Mechanism Description

The alignment mechanism uses four retractable tapered pins located at the corners of the ground panel. Four mating receptacles are located at the corners of the flight panel. The tapered pins and receptacles, in conjunction with the compliance mechanism, align the panels to the desired accuracy. After the panels are aligned, the four pins are retracted in unison to maintain parallelism as the connectors engage.

The tapered pin assemblies (Figure 6) are comprised of a housing, a commercial jack assembly, the tapered pin, and support bearings. The four pin assemblies are installed on the ground panel and linked with a system of shafts and gear drives for parallel operation (Figure 7). The tapered pin has a 10-degree half-angle cone and a flat end (Figure 8). The flat end prevents binding and accommodates thermal distortions and manufacturing tolerances (see next paragraph). The housing is aluminum, the bearings are plain bronze, and the pin is 15-5 PH stainless. The machine screw jack assembly is internally keyed to prevent screw rotation, the rated capacity is 4.5 kN and the lead is .127 mm / turn.

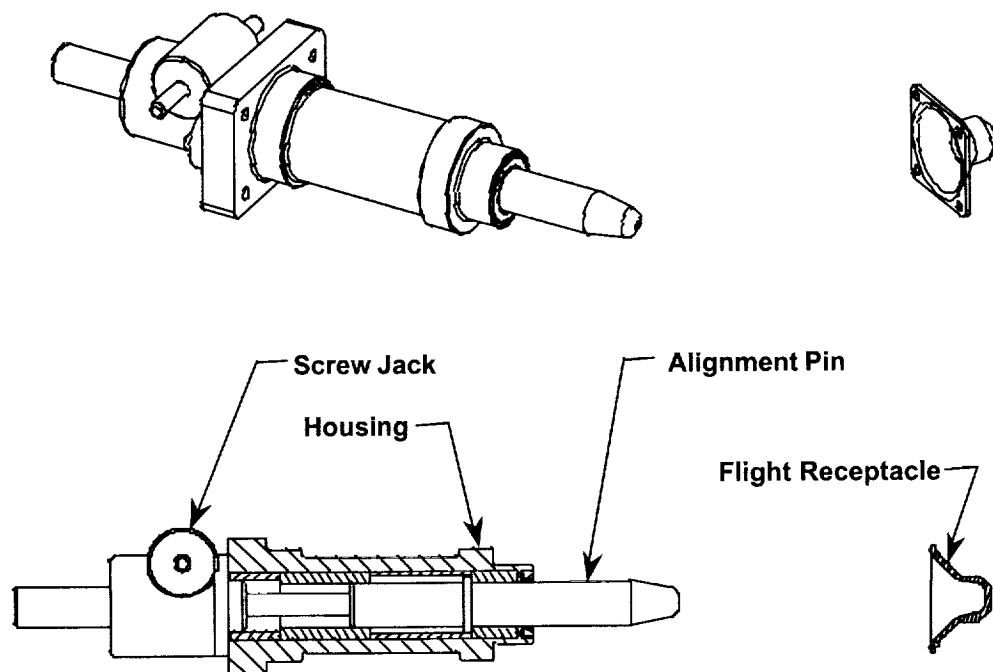


Figure 6. Alignment Pin and Receptacle

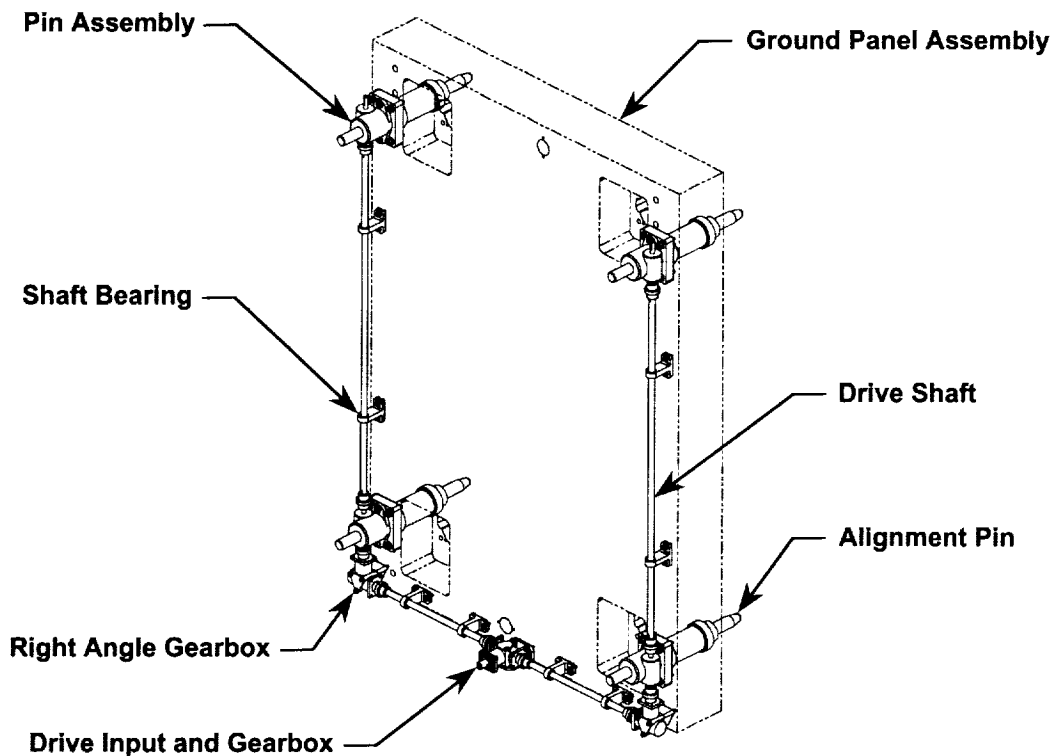


Figure 7. Alignment pin Assembly

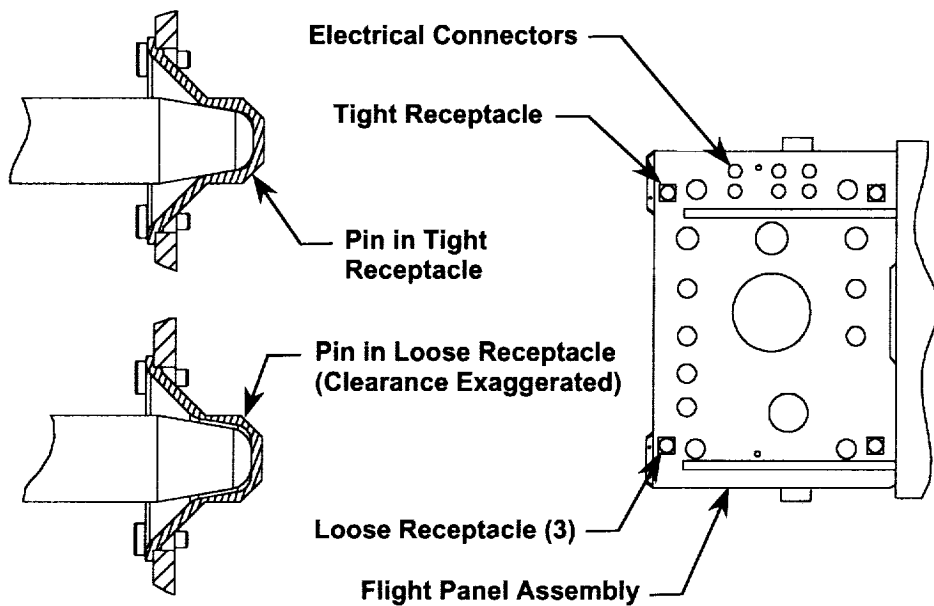


Figure 8. Alignment Pin Receptacle Details

The flight panel receptacles (Figure 6) are machined from A286 stainless. The pin and receptacle materials combination was selected to minimize the possibility of galling as the pin was guided into the receptacle. The internal geometry of the receptacle consists of an outer 45-degree half-angle cone and an inner 10-degree half-angle cone with a flat bottom. The inner cone matches the pin, the larger angle outer cone accommodates greater initial misalignment with less total insertion length. The use of two different flat-bottomed receptacles and the flat ended pins prevents binding or locking of the pins and accommodates thermal distortions and manufacturing tolerances. Plate-to-plate alignment was most critical for the electrical connectors. To reduce the alignment error at the electrical connectors, the inner cone of the receptacle nearest the connectors was tolerated to become tight simultaneously with the flat of the pin bottoming in the receptacle. The inner cone of the other three receptacles was tolerated to allow a slight radial clearance with the pins bottomed in the receptacles (Figure 8). This small radial float (0.127 mm) accommodates the expected panel-to-panel variations, yet allows only a slight relative rotation between the panels. The geometry of the alignment system locates the critical electrical connectors within 0.04 mm when the plates are in thermal equilibrium.

Retract Latch Mechanism

The umbilical retract mechanism supports the ground umbilical panel, compliance mechanism, translating frame, hoses, and cables in the extended position. Following liftoff, the latch mechanism is released, allowing the translating frame and the rest of the umbilical to free-fall into the umbilical tunnel. The latch mechanism must be fast acting and reliable for both remaining latched and unlatching on command.

Retract Latch Mechanism Requirements

Some of the significant design requirements for the panel alignment mechanism were:

- Provide load capacity when latched of 18 kN
- Unlatch in less than 250 ms from vehicle first motion
- Tolerate a single failure for latch and unlatch
- Latch automatically on frame extension
- Use stored energy for actuation

Retract Latch Mechanism Description

The retract latch mechanism uses four spring-extend, pneumatic retract latch assemblies arranged in mating pairs. One half of each pair is mounted to the translating frame. The other half of each pair is mounted to the umbilical tunnel (Figure 9). Each latch assembly is actuated by a dedicated control valve located on one of the axial struts of the compliance mechanism. The latch valves are supplied from a gaseous nitrogen accumulator charged to 17 MPa. The latch arrangement shown is single failure tolerant for supporting the load and also for ensuring release. Since any latch pair will support the entire load, the inadvertent release of any single latch will not allow the translating frame to drop. Similarly, only one latch of each pair must release in order to allow the translating frame to drop. The 250 ms maximum operating time is somewhat misleading. Due to the fact that the vehicle may lift off from any point over a 8 cm range, the latch valve may not be actuated until the vehicle has risen over 8 cm. This results in an available operating time of only 150 ms. Analysis showed that, with proper pneumatic flow capacities, the 150 ms target was achievable.

The latch assembly (Figure 10) is comprised of a structural steel housing, steel latch, bronze pivot bearings, and a specially designed pneumatic cylinder. The latch profile is circular to prevent lifting of the assembly during unlatching. The spring return pneumatic cylinder (5 cm bore, 8 cm stroke) was designed with oversize ports for high speed operation. In order to obtain the desired latch speed (30 ms stroke time), the cylinder working pressure was approximately three times the pressure required to operate the latch statically. This, combined with the fact that load is zero at the end of stroke and some latches operate with no resisting force, created the need for significant cushioning in the cylinder. Both pneumatic and elastomeric cushioning were included in the design. Space constraints dictated that for each latch pair, one cylinder would extend to operate, the other would retract. Otherwise, all four latches are identical.

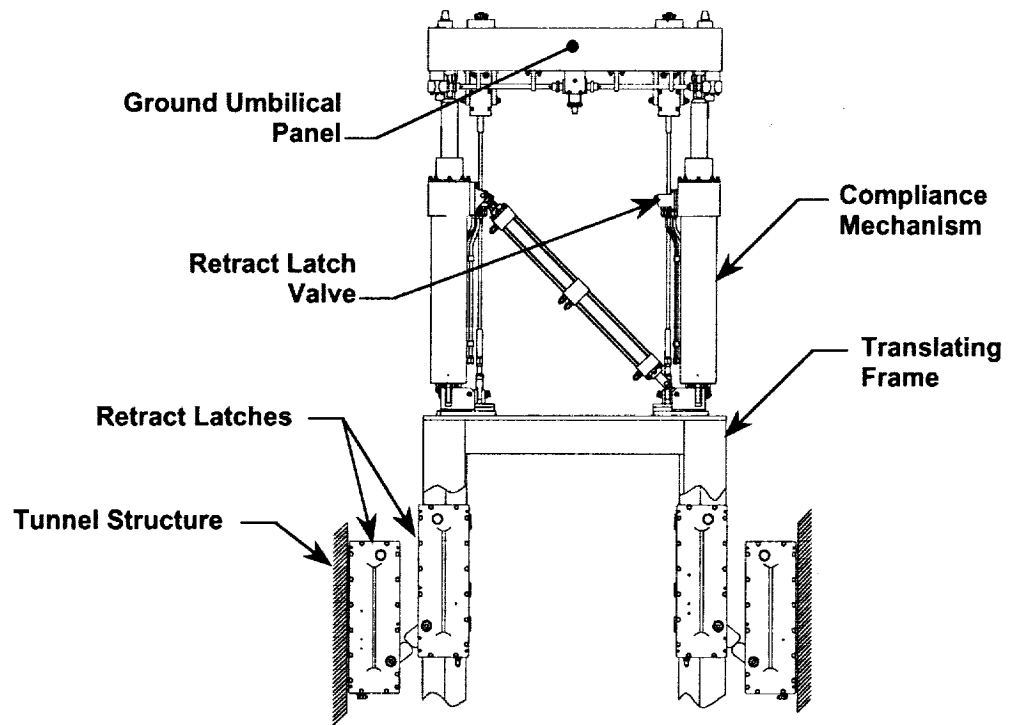


Figure 9. Retract Latch Mechanism Installation

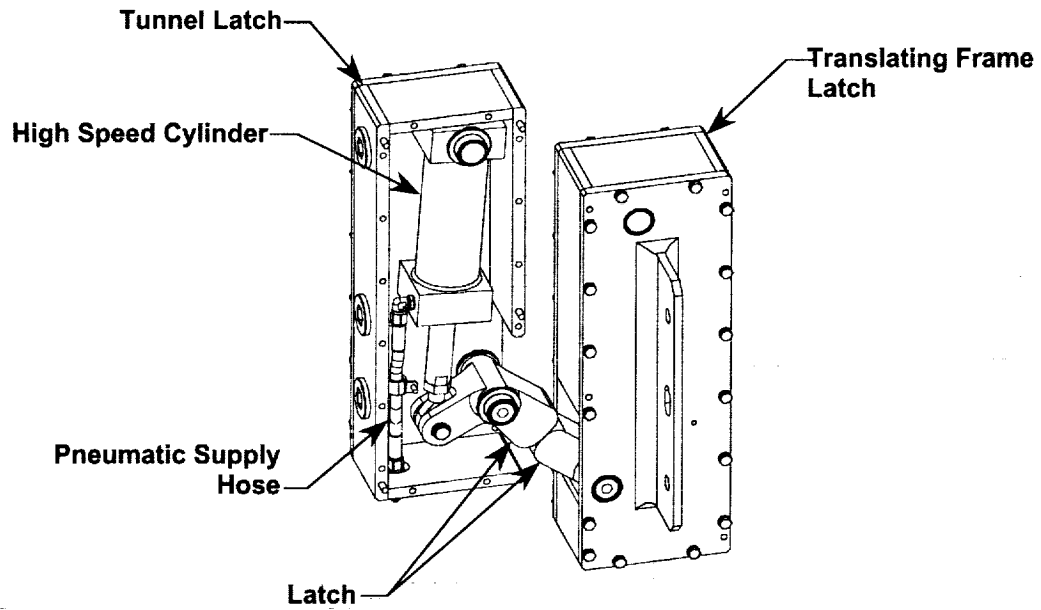


Figure 10. Retract Latch Mechanism

The latch valves (located on the axial struts) are direct-acting and sense vehicle liftoff from the axial strut piston. Each valve is dedicated to a latch assembly in order to prevent a valve failure from causing a premature disconnect of the umbilical or a failure of the umbilical to retract into the tunnel following liftoff. The valve-to-latch connections were arranged to minimize actuating time in the event that the vehicle pitches or yaws significantly during liftoff. As mentioned previously, 30 ms operating time was allotted to the latch itself for operation. The remaining 120 ms delay arises from valve actuation and pneumatic system "fill" time. The system drivers were the latches located on the umbilical tunnel. The latches on the translating frame are located within 1.5 m of the valves. The line lengths to the tunnel latches were nearly 10 m and accounted for most of the total delay. When operating normally, the latches on the translating frame will actuate well before the tunnel latches, resulting in faster system operation.

Quick-Release Lock Mechanisms

The quick-release lock mechanisms resist the separation forces between the umbilical panels generated by fluid pressures and vibration. The mechanisms remain locked until they are released by lanyards following liftoff. The quick-release lock system consists of four collet locks located at the corners of the ground panel and four mating receptacles on the flight panel.

Quick-Release Lock Mechanisms Requirements

Some of the significant design requirements for the quick release lock mechanisms were:

- Resist panel separation force 71 kN (17.75 kN per lock)
- Support axial load only, shear forces resisted by shear pins
- Provide automatic locking and preload generation
- Provide single failure tolerance for release
- Minimize loads transferred to vehicle
- Prevent ice formation in mechanism

Quick-Release Lock Mechanisms Description

The quick-release lock mechanisms use a pin-expanded collet on the ground panel to engage a conical receptacle on the flight panel. A disconnect lanyard, connected to the translating frame, pulls the pin to release the lock. If the collet does not release, a cam mechanism on the ground mechanism shears the flight receptacle from its mount to release the panels.

An assembly view and details of the ground mechanism (collet lock) are shown in Figure 11. An aluminum housing interfaces with the ground panel through a bolted flange connection. The expanding collet is fabricated from beryllium copper. Threads in the housing and on the exterior of the collet allow for adjustment of joint preload by rotating the collet either prior to or after locking. The 15-5 PH stainless expansion pin has an integrally machined piston to allow the collet to be locked pneumatically. A key on the pin engages the collet. This key allows the collet to be rotated and locked from the exterior of the mechanism using the pin. The housing is bored for the piston seals and an aluminum end cap and rod seal close the cylinder. A bias spring in the cylinder maintains the collet in the locked position. A sliding aluminum sleeve is located on the front of the housing. The sleeve seats against the flight panel and resists the compression in the joint. Two roller assemblies are mounted to the back of the sleeve. An adjustable trunnion is attached to the expansion pin. Two A286 stainless steel release cams pivot on the trunnion and ride on the sleeve rollers. A lanyard bracket attached to the cams completes the mechanism. An ambient temperature helium purge through the joint prevents ice formation.

The flight receptacle (Figure 11) is comprised of an attachment bolt with a tapered head, a threaded housing with a tapered bore, a conical mating sleeve for interfacing with the collet, and a shear pin for

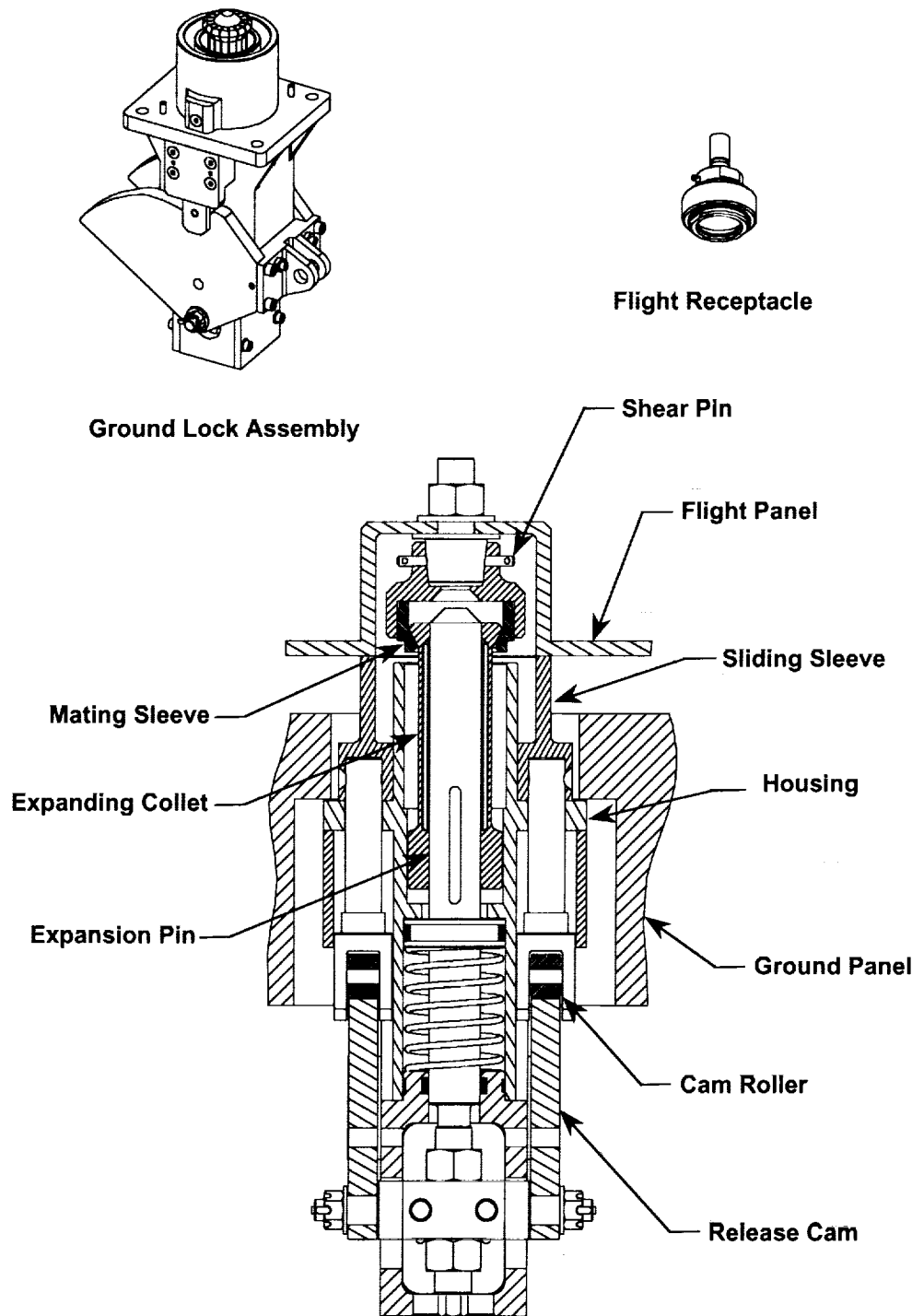


Figure 11. Quick Release Lock Mechanism

attaching the housing to the bolt for secondary release. All components, except for the shear pin, are fabricated from A286 stainless steel, and the conical sleeve is dry-film lubricated. The design shear-out load for the 17-7 PH stainless drawn wire pin is 24.5 kN (total in double shear), which is 150% of the design static load on the lock. The pin stock (all from a single lot) was ordered slightly oversize and pull tested to obtain a shear strength. The final pin diameter was determined from the shear tests. The flight pins, test pins, and spares were then ground to final size. Five pins were sheared for acceptance testing. All of the test pins sheared within 50 N of the design target. There was some concern about wedging the receptacle together and increasing the shear-out force. To eliminate this possibility, an assembly tool was used to control the axial force applied to the tapered connection during match drilling and pinning.

The lock mechanism is mated (locked) by inserting the collet into the conical sleeve until the sliding sleeve is firmly seated against the flight panel. Pneumatic pressure is applied to the cylinder to drive the pin into the collet and expand the fingers. The tapers in the sleeve and on the collet fingers generate the desired joint preload. Pin insertion pressure is used to verify proper preload generation. Figure 11 shows the mechanism in the locked configuration.

For a primary release of the mechanism, the lanyard pull causes the cams to rotate and react between the trunnion and the sleeve rollers to retract the pin and collapse the collet fingers (Figure 12). Additional pull on the lanyard drives the sleeve forward on the housing to provide a kick-off force for separation.

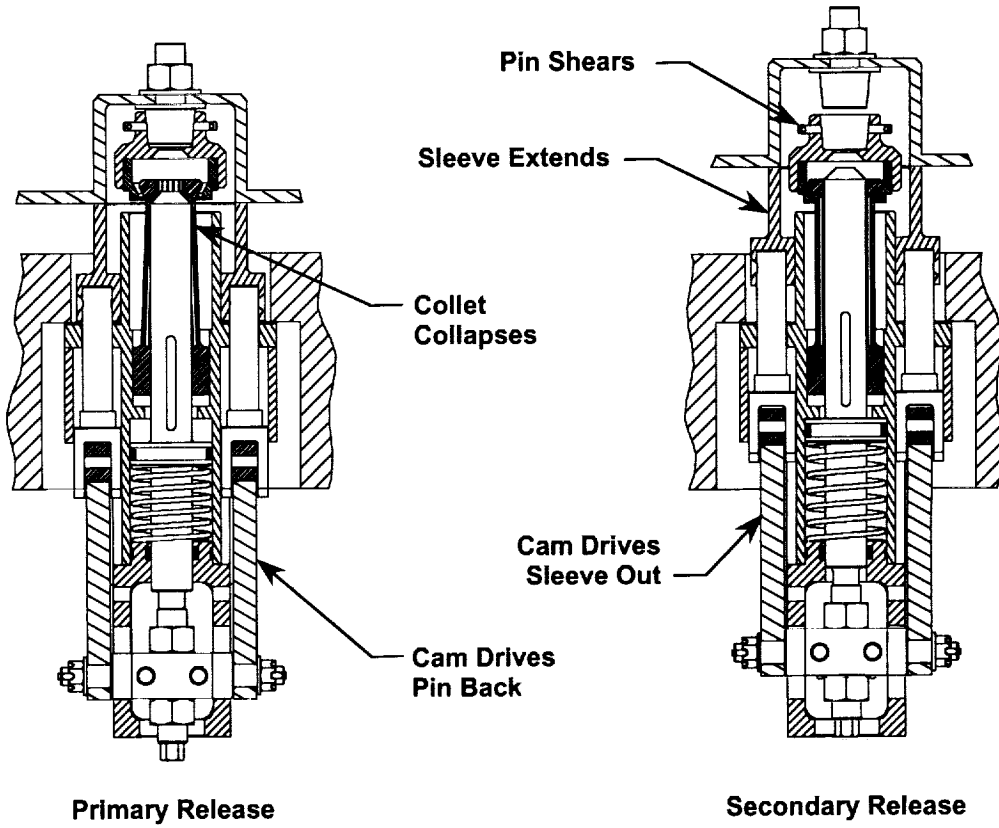


Figure 12. Lock Mechanism Release Modes

The lock mechanism can tolerate several different failures of the primary operation. If the cam bearings were to seize and prevent rotation, the pin will still be pulled (with a loss of the mechanical advantage of the cam) to release the joint. The kick-off force will not be applied in this case. In the event that the pin does not retract, the cams immediately force the sleeve forward to separate the joint by breaking the

shear pin in the flight receptacle (Figure 12). Note that the force to shear the pin is reacted internally in the lock and the only external force applied to the vehicle is the lanyard load. The system mechanical advantage reduces the lanyard load to approximately 33% of the shear-out load. Similarly, if the pin is retracted but ice or debris prevents the collet from collapsing, the sleeve will still shear the flight pin as noted above. Finally, if the entire mechanism or the lanyard were to fail, the weak link in the system is still the shear pin. This case would, however, transfer the entire shear-out force (24.5 kN) to the vehicle.

Verification Testing

A verification test program was performed to demonstrate proper operation of the X-33 umbilicals in processing and launch modes. Testing was divided into two phases for each umbilical. The first phase tests were performed with the umbilical in the horizontal processing configuration. The second test phase was performed with the umbilical in the vertical launch configuration. Rotation testing was performed at the launch site.

The horizontal tests verified umbilical mating (connection), de-mating, and leak tightness. The counter-balanced struts in the compliance mechanism worked well. The ground panel was held centered but could be easily deflected by a technician. The return to center was somewhat sluggish. The seal friction on the piston and rod increased significantly when the cylinder was pressurized. A slightly higher force in the return springs would have helped eliminate this problem. Each umbilical was mated with nine different initial alignment offsets. The compliance mechanism and alignment system accurately mated the panels. The quick-release locks (collets) consistently generated the desired preload. With the exception of a seal that was damaged during shipping, there were no out-of-specification leaks detected. Figure 13 shows an umbilical during horizontal testing and gives a good idea of the size of the systems. The umbilical mate time was reduced to less than one hour from more than eight hours required for the Space Shuttle. Most of the time is used for cleaning, inspection, and verification. The actual mate process only takes a few minutes.

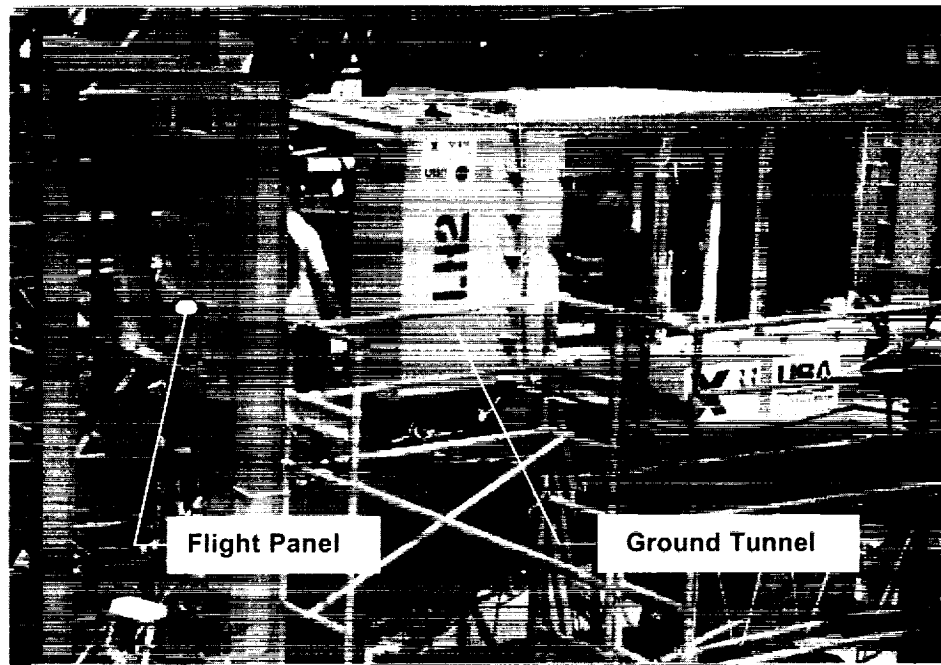


Figure 13. Horizontal Test Setup

Vertical testing of the umbilical verified proper leak tightness and launch disconnect dynamics. The umbilicals were mated and translated to a worst case misalignment for disconnect. Liquid nitrogen and liquid hydrogen (hydrogen umbilical only) were circulated through the appropriate connectors to simulate vehicle tanking. Liquid nitrogen was used instead of liquid oxygen to reduce the hazard while testing at a temperature slightly lower than required. Leak tests were performed in the cryogenic condition. Finally, the cryogens were drained and a launch simulation was performed by raising the flight panel at the launch acceleration rate. All leaks were within specification. Minor frost developed in several areas of the panels but was not significant. Each panel was disconnected four times, one test for each umbilical involved disabling the lock expansion pin to force a secondary disconnect. All tests were successful.

The quick-release locks worked extremely well. All four locks typically disconnected within 5 ms of each other. Lanyard loads were as expected. Primary release dynamic loads were typically around 1.8 kN. The secondary release worked smoothly without damaging any components. The lanyard dynamic load for secondary release was 16 kN. The compliance mechanism smoothly centered and decelerated the ground panel and hoses. The system was under-damped (as expected) but this did not affect operation in any way. Total operation time for the umbilical was less than 1.1 seconds with all four latches operating. The translating frame latches released between 70 and 150 ms after first motion, depending on the vehicle starting position. Test data indicated that the failure of a translating frame latch would delay operation an additional 50 ms. The failure of a latch was not simulated during test. Figure 14 shows an overall view of an umbilical during vertical testing. Figure 15 shows a close-up view of the ground and flight panels mated for a vertical test.

Conclusions and Lessons Learned

Although the entire program went relatively smoothly, there were several lessons learned that may prove useful to others. The most significant problem encountered during the program involved a simple purge seal located around the perimeter of the ground panel. The seal compression force was erroneously assumed to be minimal due to the soft material being used. The problem occurred because, although the seal was soft, its length was nearly 6 m. The seal was actually capable of generating several hundred newtons of separation force and preventing the plates from fully mating under certain contingency conditions. Lubricating the seal allowed it to compress adequately for mating. Another problem encountered was that, due to the short schedule, the effects of late design changes were not thoroughly analyzed. A guide track for the flight door was added at the end of the design. This track was located too close to a quick-release lock and actually impacted the lock sliding sleeve during disconnect. No hardware changes were made as the impact occurred from a worst case disconnect position and damage was minimal. Leakage from one of the seals on the retract latches was noted during one of the tests. After about a minute, the leak stopped. The piston seal was apparently not seating properly when suddenly pressurized with nitrogen at 17 MPa. The latched still released properly, even with the leak. The cylinder was cycled several times, and the problem never recurred. As discussed previously, the friction in a dynamic fluid seal can vary considerably with pressure. Testing may be required to determine the actual seal friction under pressure.

The final lesson learned involved the test stand. It is imperative that the engineers understand the possible failure modes of the test equipment and how they might impact the test or the test hardware. There also needs to be good communication between the test technicians and the engineering team. Prior to one of the tests, a technician noticed a small leak on the hydraulic system for the lift-off simulator. He simply tightened a loose fitting and did not inform the test team. Toward the end of the next cryogenic test, as the liftoff simulator was being pressurized for disconnect, the air that had entered the system through the leaky fitting slowly compressed and allowed the umbilical to rise slightly and initiated an inadvertent disconnect. The data acquisition systems were not yet operating and all test data were lost.

In conclusion, the X-33 umbilicals were successfully tested and have been installed on the vehicle and at the launch site. The umbilicals utilize several new mechanisms to significantly reduce operational timelines.

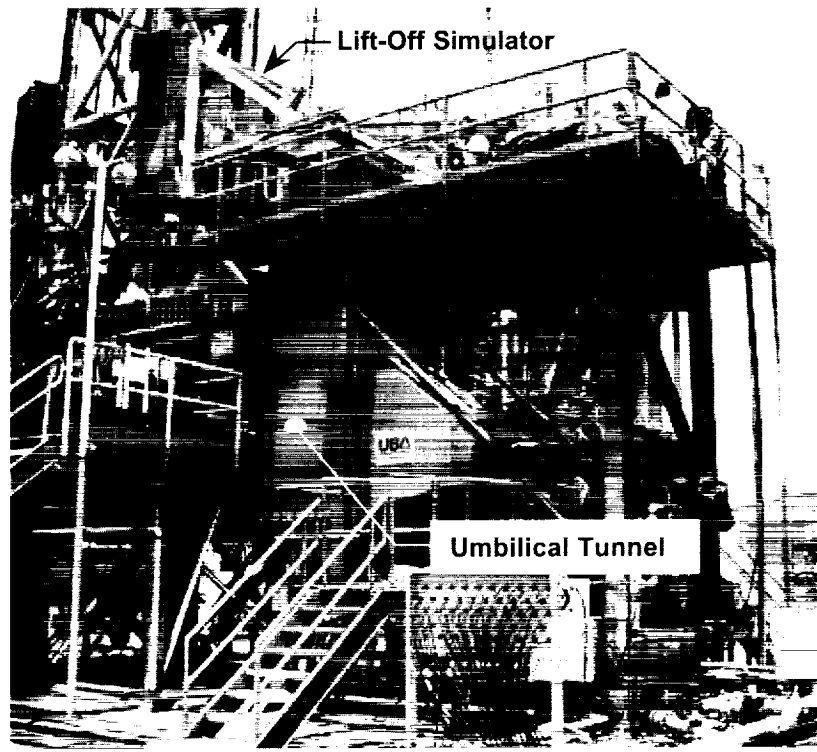


Figure 14. Vertical Test Setup

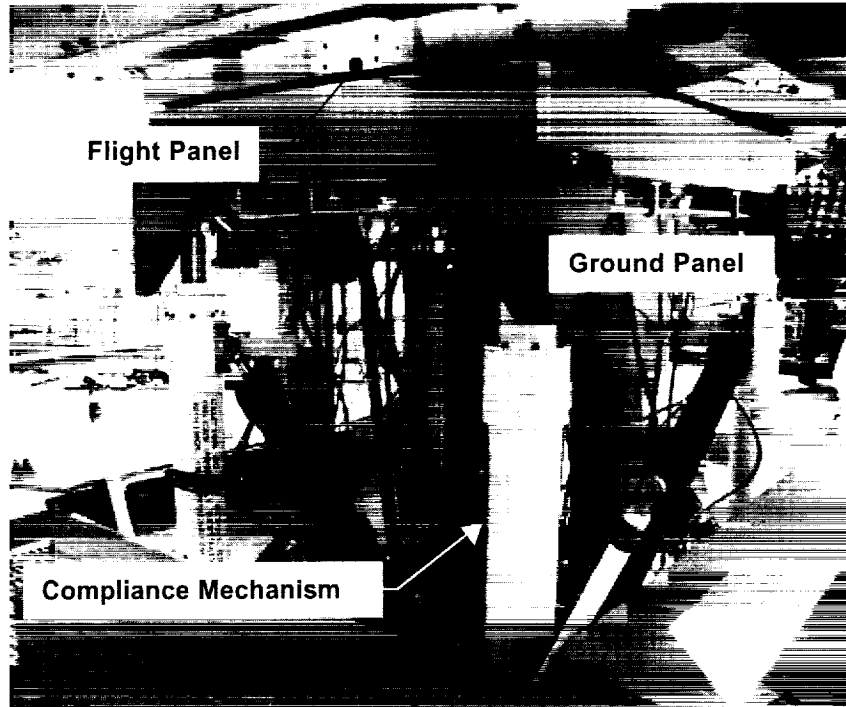


Figure 15. Detail of Vertical Mate

Development of a Flywheel for Energy Storage and Attitude Control of an Exoatmospheric Interceptor

Doug Havenhill^{*}, Frank Nimblett^{**}, Steve Nichols^{**} and John Young^{**}

Abstract

SatCon Technology Corporation is developing a unique subsystem that controls the attitude and trajectory of an exoatmospheric kinetic weapon (KW) while supplying power to the weapon's subsystems. The Missile Integrated Power and Roll Control System (MIPARS) uses SatCon-developed flywheels and control electronics in conjunction with a multiple ignition solid fuel gas generator to provide rotational and translational control of the KW. Energy stored in the rotating flywheels is used to supply power to the KW throughout its flight.

Introduction

Kinetic weapons are designed to intercept and destroy incoming missiles. With closing velocities approaching 5 km/s, translational and attitude control play a key role in a successful intercept. Current KW systems use continuously burning, solid propellant, gas generators with divert thrusters for translational control, offset thrusters for attitude control, and thermal batteries for power. Drawbacks inherent with this approach include

- Short flight times due to limited fuel capacity
- Structural excitation due to bang-bang thruster control
- Preflight testing of the power source is impossible
- Obscuration of sensor by burnt fuel

SatCon, under contract from the U.S. Navy, was tasked with developing an innovative approach to the divert and attitude control system (DACS) for a KW. Our approach uses three flywheels as attitude control torque actuators and power sources and a multiple-ignition solid-propellant gas generator to provide divert thrust and to spin up the flywheels. Our specific goals were to

- 1) Enable a 300-second KW flight
- 2) Improve KW accuracy
- 3) Reduce DACS cost
- 4) Improve KW reliability

The MIPARS is required to perform three major functions:

- Supply power to the KW systems during flight
- Provide KW attitude control torque
- Provide KW divert thrust for translational control

Under our current contract we established requirements, performed a conceptual design of a DACS system, and designed, built, and tested bench model (proof of concept) flywheels. Figure 1 illustrates the MIPARS conceptual design.

^{*} SatCon Technology Corporation, Peoria, AZ

^{**} SatCon Technology Corporation, Cambridge, MA

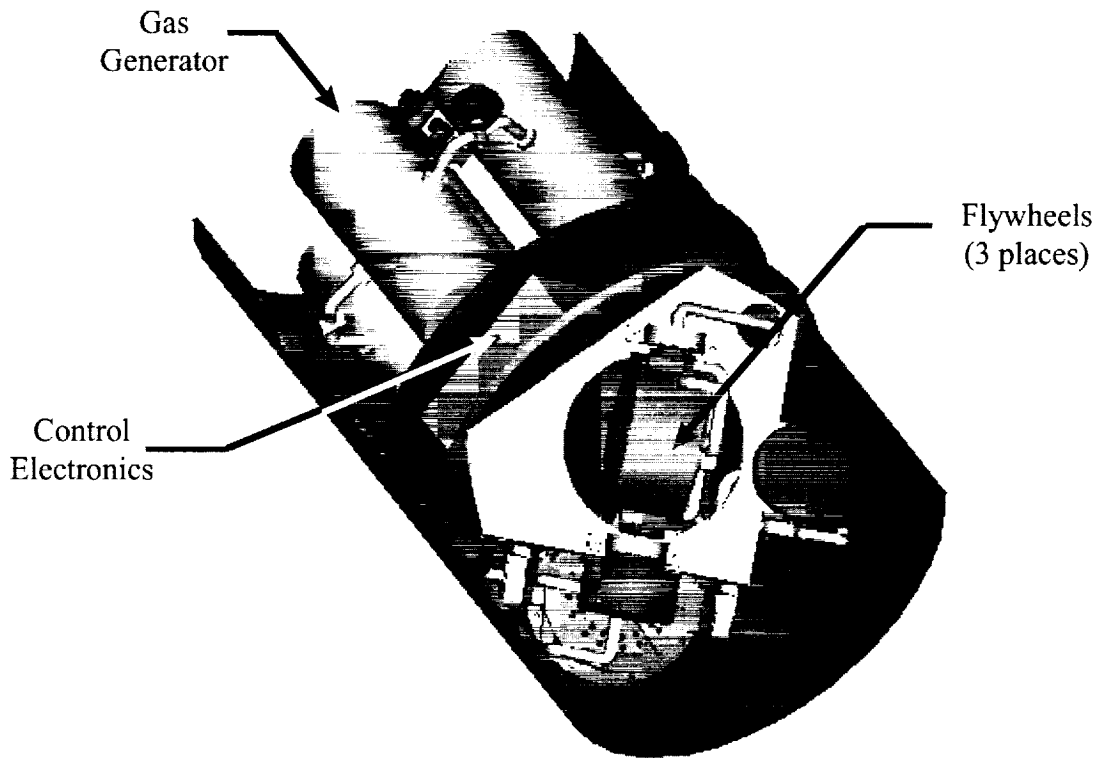


Figure 1. Missile Integrated Power and Roll System

Background

MIPARS consists of a three-flywheel array, control electronics, and a multiple-ignition solid-propellant gas generator. The gas generator supplies high-pressure hot gas to 1) spin up the flywheels and 2) provide divert maneuvering thrust for translational control of the KW. The flywheels provide control torques for attitude control by rotating the momentum vectors with a gimbal, and provide electrical power by extracting energy from the flywheel using an electrical generator.

The block diagram in Figure 2 illustrates how the system works. The KW is the fourth stage of the Navy's standard missile. Two seconds prior to fourth-stage separation, the gas generator is started and the flywheels are spun up. After separation, the guidance computer issues torque commands to the flywheels to control the KW attitude and force commands to the thrusters to control the trajectory of the KW. During periods when trajectory adjustment is unnecessary, the gas generator is extinguished and then it is reignited later when thrust is required. Throughout the flight, the flywheels supply power to all the KW subsystems and attitude control torque to the KW. Table 1 summarizes the MIPARS requirements.

Flywheel

The emphasis of this paper is on the gimbaled flywheel. The flywheel has two functions 1) provide attitude control torque and 2) provide power to the kinetic weapon throughout its 300-second flight. It replaces conventional thermal batteries and bang-bang attitude control valves.

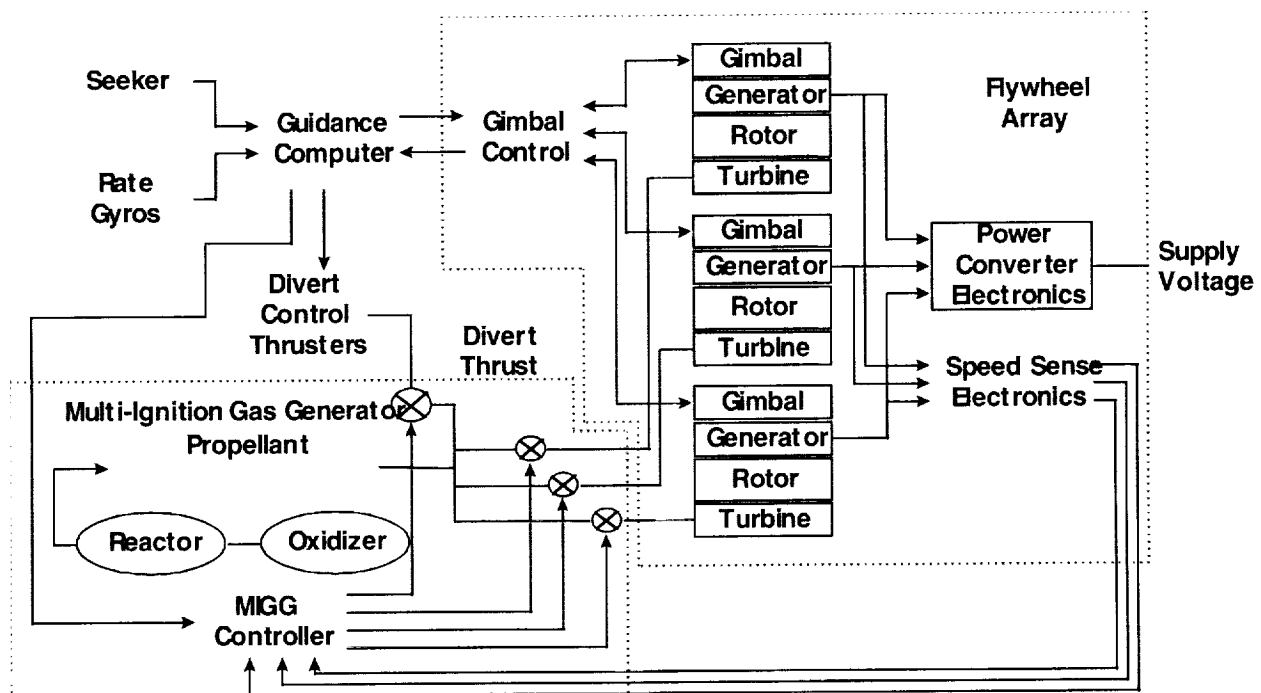


Figure 2. MIPARS Block Diagram

Table 1: MIPARS Specification

Parameter	Requirement
Energy Storage	150 kJ
Peak Power	650 W
Mission Duration	300 s (maximum)
Steering Torques	45.2 N·m (pitch, yaw) 22.6 N·m (roll)
Divert Thrust	1557 N (two axes)
Thrust Duration	10 seconds
Weight	< 27.3 kg
Envelope	25.4 – 50.8 cm (diameter) 38.1 – 63.5 cm (length)
Non-operational Temp	-29 to +54 deg C
Magazine Temp	+7 to +32 deg C
Altitude	70 - 200 km

From the system power and attitude control requirements, the flywheel requirements in Table 2 were derived. The approach to deriving the requirements is as follows:

- Selected the speed range of 2:1 for efficient operation of the electronics.
- Selected the required energy storage based on conservative energy loss estimates due to the bearing drag torque, the eddy current losses in the motor, and the efficiency of the electronics.
- Selected a rotor size that would fit within envelope and weight requirements.
- Derived the rotor speed to achieve the desired energy storage.
- Calculated the average spin up torque needed to achieve full speed in two seconds.
- Calculated the range of angular momentum available for momentum exchange with the KW.
- Calculated the maximum gimbal rate required to achieve maximum attitude control torque at minimum rotor speed.

- Calculated the maximum gimbal holding torque to hold the flywheel in position when maximum cross axis rates are present
- Calculated the maximum required gimbal acceleration to achieve adequate full power bandwidth.
- Calculated the gimbal torque from the required acceleration and the holding torque.
- Set the gimbal rate loop bandwidth for use with a 5 to 10 Hz KW attitude control bandwidth.

Table 2: Flywheel Requirements

Parameter	Requirement	Units
Maximum Rotor Speed	42000	rpm
Maximum Rotor Energy	120	kJ
Useable Energy Storage	50.0	kJ
Maximum Momentum	54.6	N·m·s
Minimum Momentum	27.3	N·m·s
Peak Gimbal Rate	± 1.8	rad/s
Gimbal Rate Loop BW	75	Hz
Holding Torque	19.0	N·m
Maximum Gimbal Acceleration	400.0	rad/s ²
Gimbal Angle Range	± 180	deg
Spin-up torque	27.3	N·m
Spin-up time	2	sec
Weight	3.8	kg

The flywheel consists of a hub and rotor assembly, an electrical generator, a turbine, a housing, a motor-driven gimbal, and an electronics package. The turbine is used to spin up the flywheel to 42000 rpm two seconds prior to fourth stage separation. The energy stored in the rotor during spin up is extracted from the flywheel to power the KW during flight. To supply torque the flywheel is rotated on a gimbal whose axis of rotation is perpendicular to the spin axis. The torque applied by the flywheel is then given by

$$T = \omega \times H$$

where,

ω is the gimbal rate, and

H is the momentum of the flywheel!

The electronics package, depicted in Figure 3, consists of a spin up controller, a power supply, a gimbal controller, and a command and telemetry processor. The spin up controller is used during spin up to solicit the turbine gas flow and shuts off the gas when the wheels reach speed. The power supply takes the output of the generator and converts it to dc voltages used by the KW. The gimbal controller accepts commands from the attitude control system and controls the gimbal rate to provide the desired attitude control torque. The command and telemetry processor provides the necessary interfaces to other on board systems and any KW test equipment.

Flywheel Rim

The initial design effort of the MIPARS bench model hardware was aimed at utilizing a simple turbine design as an "add-on" to the shaft on the outside of the housing. It appeared that this would be the most economical use of design effort. Several concerns led us to re-evaluate that decision and proceed to design an integrated flywheel and turbine for the test hardware. Rotor-dynamics studies of potential turbine/flywheel configurations illustrated the difficulty in having two large masses at the ends of the support shaft. This caused a 1st mode bending critical speed ranging from 15k to 25k rpm, which is in the middle of the operating range of the flywheel for both power generation and attitude control torque application. In addition, the mechanical configurations were becoming ungainly and the assembly of the parts more difficult. As a result we arrived at integrated turbine and rim design. The result is the hardware pictured in Figure 4.

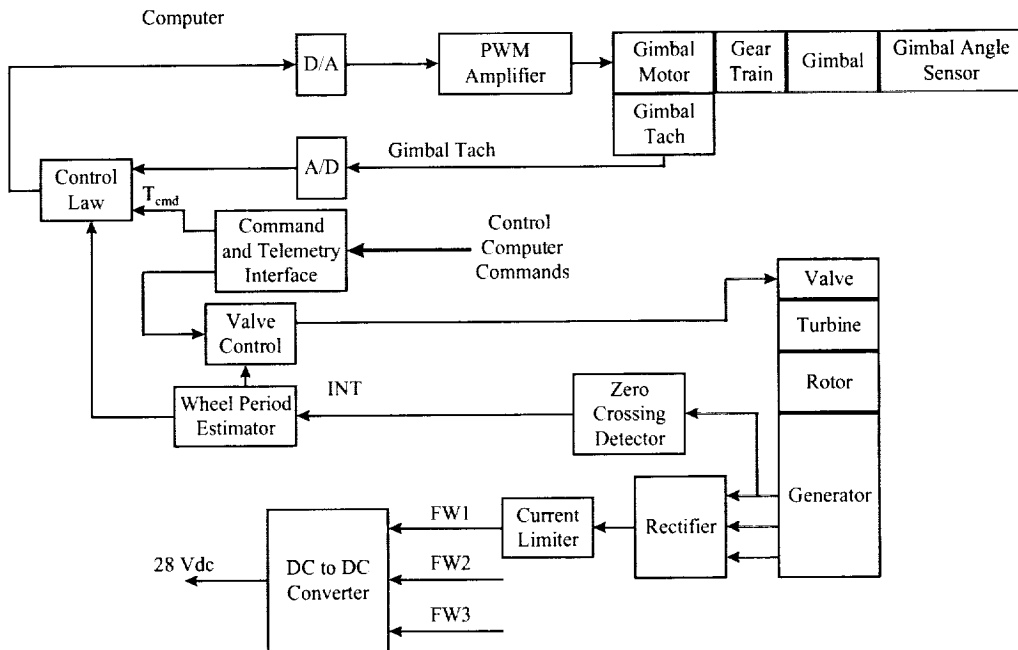


Figure 3. Block Diagram of Flywheel Electronics

The rotor, with integrated turbine blades (Figure 4), was designed to provide the blade design and appropriate nozzle and blade tip clearances. The flywheel/turbine is fabricated from 4340-HS steel and hardened to RC 53 to provide both high strength (1862 MPa (270 ksi)) and good ductility (11% elongation). All machining except for the interface diameter with the hub was done prior to hardening, greatly reducing potential production costs. Comments from the fabricators of the hardware indicated that the heat treat process created very little distortion thus opening the possibility of having no final grinding operations, which could further reduce costs.

Similarly, the nozzle design was iterated to create a design that was compatible with the flywheel layout. The bench model nozzle, shown in Figure 5, is a two-piece assembly with a rectangular nozzle cross-section. Screws attach the two components.

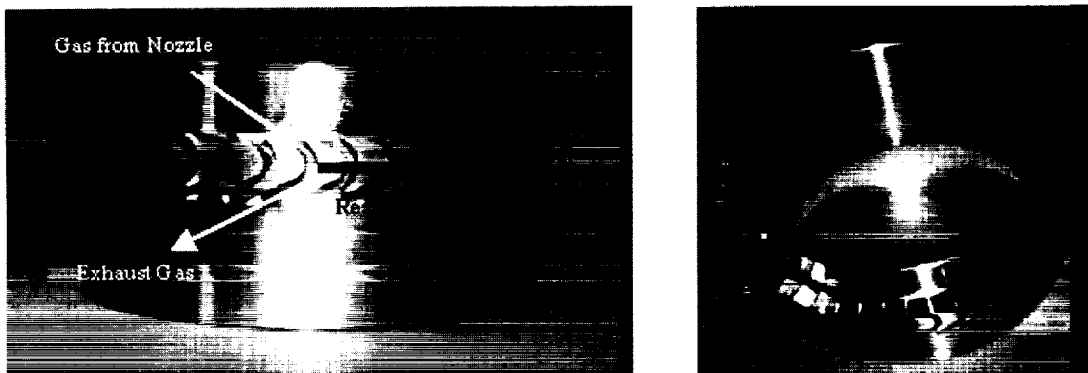


Figure 4. Flywheel Rim



Figure 5: Turbine Nozzle

Hub Design

Initial design direction for this flywheel anticipated an integral hub and flywheel. Detailed FEA analysis of the concepts quickly revealed that such a design would not leave adequate safety margin for a test bed device. An alternative design using a separate hub was analyzed (Figure 6). The hub/flywheel interface is an interference fit (0.2 mm (0.008 inch) radial interference) that provides radial compressive stress to maintain contact between the parts up to approximately 54,000-rpm. Although this results in additional hoop stress in the flywheel and compressive hoop stress in the hub, the overall balance is to improve the stress seen by the hub, the original problem area.

Since the tendency for the flywheel is to grow faster than the hub as the speed increases, the compressive radial interface stress decreases with increasing speed until the parts actually separate. A design objective was to incorporate radial separation of the flywheel and hub prior to any catastrophic hoop failures yet still have this speed be well above planned operational speeds. This design has, in effect, a built in safety valve where the flywheel becomes loose on the hub. This permits the flywheel to translate axially to contact either the end housing or the nozzle assemblies. Friction resulting from this contact would then slow the rotation; essentially it is a built-in over-speed brake. In a production design, this feature can be easily adjusted or eliminated if desired. Due to the high stresses seen by the hub, it, like the flywheel, was hardened to RC-53. Size and concentricity tolerances were maintained through the hardening procedure and no final grinding was required.



Figure 6. Flywheel Rotor Parts

Rotor Assembly:

Attachment of the Rotor Shaft to the hub was accomplished with the use of shrink fit, freezing the shaft in liquid nitrogen (LN_2) to -184°C (-300°F) and heating the hub to $+149^\circ\text{C}$ ($+300^\circ\text{F}$). The 0.038 mm (0.0015 in) interference between shaft and hub bore diameters is relatively easy to overcome. The hub/shaft subassembly is then chilled in LN_2 to -184°C and the Turbine/Flywheel is heated to $+149^\circ\text{F}$. Again this permits a relatively easy assembly for the 0.4 mm (0.016 in) interference of the interface diameters. Finally, the motor rotor is pressed into position with the rest of the assembly being cooled to -73°C (-100°F). The interference is such that this operation could be replaced by pressing the motor rotor onto the shaft, but the thermal shrink method eliminates any shaft scoring. At this point, the rotor assembly looks like the solid model shown in Figure 7.

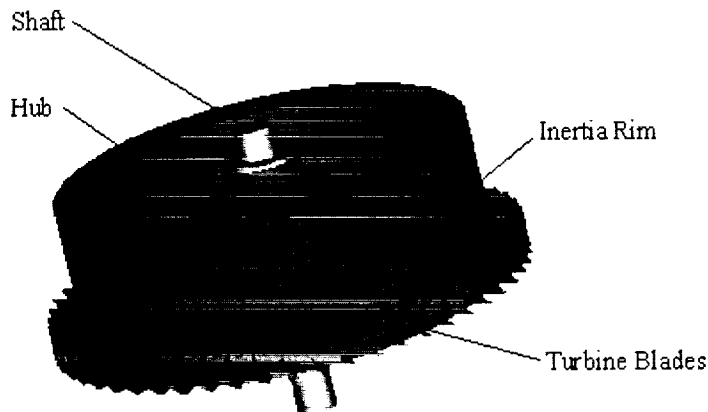


Figure 7. Model of rotor assembly

Generator/Motor:

A 6-pole slotless, brushless DC motor, manufactured by Elinco Motors, was selected for use as the generator. The major design consideration other than providing power at the design voltage was to minimize the eddy current losses caused by the passage of the high-speed rotating magnets on the rotor past the stator metal. In this particular test bed application, it is the testing and utilization of the generator to "motor-up" the flywheel rotor to the operating speed of 42,000 rpm that was the key driver of the motor design. This slotless design was selected after having reviewed numerous other brushless motor options and weighing the cost of designing a custom motor from scratch to do this job.

The rotor consisted of a steel inner ring, a non-magnetic outer sleeve to contain the 6 magnet arcs and a brass insert to provide a sacrificial mass to be used to balance the motor rotor assembly. The motor rotor is shrunk onto the shaft to provide adequate interface pressure to operate at $>50,000$ rpm without coming loose. This is the final part assembled onto the rotor following the shrinking of the hub/shaft and turbine/flywheel together.

The stator is the unique feature of this motor that provides low eddy current losses. The windings fill essentially all of the space on the inside diameter of the stator; there is no magnetic material at the motor air gap. There is a slotless lamination stack (simple discs) outside of the windings. The effect of this is to increase the space to the lamination stack and reduce the potential to generate eddy current losses due to the high-speed passage of the magnets by the stator laminations. Figure 8 illustrates these design features.

Finally, when the stator is installed into the motor housing cavity, there is an interference fit to provide a good passive thermal link to the housing to help dissipate the stator power losses when the flywheel is motoring up to speed in particular. This is an adequate solution for the test phase since it provides adequate time to accelerate to speed before we exceed the 150°C temperature limit on the stator

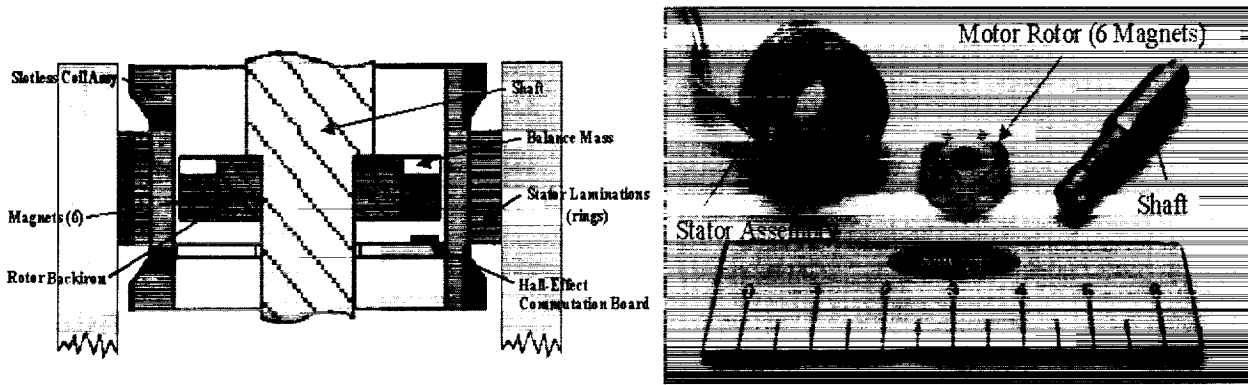


Figure 8. Slotless Generator/Motor

windings. A thermocouple was attached to the end turns so that this temperature could be monitored during the operation of the motor. The anticipated temperature rises for the flight units operating as a generator only are much less severe than for the long-term vacuum test sequence where the electric machine was used as both a motor and a generator.

Flywheel Bearings

Torrington Superprecision stainless steel angular-contact ball bearings (2MM201WI-CR with a 15° contact angle; ABEC-7) were used with a phenolic retainer to be able to handle the high speed. These bearings have a limiting PD x N value (PD in mm times RPM) of 1,400,000 for oil lubrication. For this application, we have a maximum value of 1,000,000 for PD x N. Lubricant will be either a vacuum-compatible oil lubricant or a solid-film lubricant such as Diacronite to provide good shelf life and cold start-up characteristics with low friction during high-speed operation. The bench model utilized Nye Synthetic Oil 2001A to provide protection to the bearings for the long duration testing in a vacuum environment (<1 millitorr). The bearings are axially preloaded through the shaft with a force of approximately 133 N (30 lb) by the use of wave spring washers on the outer race of one bearing. Only one set of bearings was used for all of the testing and no observable performance change was noted over the test duration.

The two bearings are "soft-mounted" into the end housings with the use of two greased O-rings for each bearing. These O-rings are located between the bearing outside diameter and the mounting cavities in the end housings and provide an effective bearing stiffness of 35-52 kN/m (200-300 lb/in). Figure 9 illustrates this bearing interface concept. This design limits the forces that can develop as a result of any structural resonance excited by wheel frequency. It allows radial motion of ± 0.05 to 0.076 mm (± 0.002 to 0.003 in) of "soft-mount" before the bearing outer race contacts the aluminum bearing housing. This level of radial freedom is more than adequate to reduce the interface forces between the rotor and the housing to very low levels. While within this "soft-mount" region, unbalance forces are limited to less than 4.5 N (1 lb). In addition, these grease lubricated O-rings provide some radial damping as well as low axial friction force to maintain the axial preload forces. However, there is a need for an axial stop to limit the motion of the outer race on the spring-loaded end. Due to an extremely high gimbal input rate, contact of the housing with the rotational stop, enough axial force was generated to translate the outer race to the point where enough radial clearance was created to permit interference between the rotor and the case at the turbine blade outside diameter. This can be easily resolved with an axial stop that limits this travel to 0.13 to 0.25 mm (0.005 to 0.010 in).

Finally, this bearing interface system permits the outer races to seek their most desirable operating attitude that is determined by the average planes of the inner and outer bearing races rather than by the outer dimensions of the outer race. This feature further lessens bearing power losses and improves bearing life. Although bearing life is not a significant issue for the MIPARS flight systems, other longer duration systems could well benefit from these bearing system features.

Test Rig Design

The function of the gimbal test rig for the bench model flywheel is to provide the capability of putting in an angular rate about an axis of rotation, the trunnion axis, that is normal to the flywheel axis of rotation. This results in an output torque vector orthogonal to both the spin axis and the trunnion axis that has a magnitude equal to the product of the flywheel angular momentum and the trunnion angle rate in rad/s. It is this reaction-torque that is used to redirect the flight path of the missile. The entire test rig is attached to a torque sensor so that the reaction torque can be measured and the performance of MIPARS evaluated. Figure 10 illustrates the flywheel in its housing mounted to the gimbal test rig with a stub-shaft attached to each side of the housing. These shafts define the axis of rotation normal to the flywheel spin-axis. A radial bearing in one of the uprights supports one trunnion shaft and other trunnion shaft attaches to the Gimbal torquer and uses its output bearing. The gimbal torquer is attached to the other upright. Finally, there is a simple angular stop with two rubber pads to limit the angular motion about the gimbal axis to approximately $\pm 30^\circ$ by contacting the corner of the lower bearing housing.

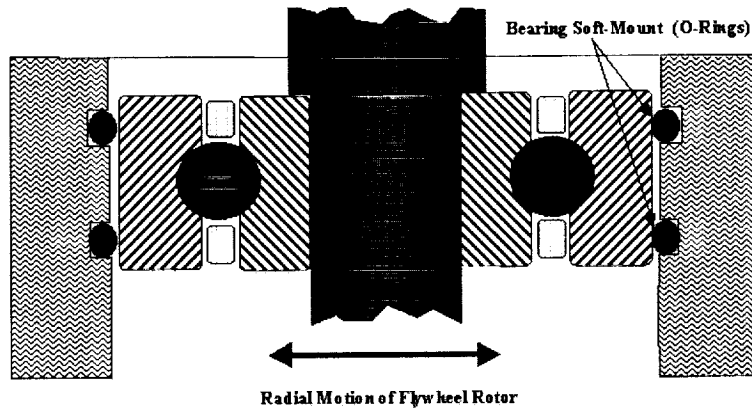


Figure 9. Bearing Soft-Mount Design

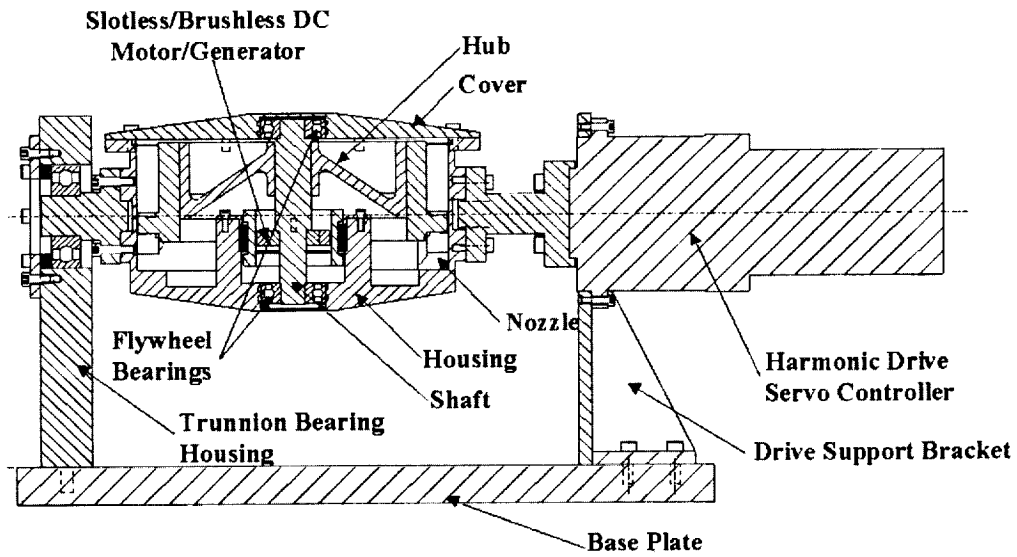


Figure 10. Test Rig

Test

Tests were conducted to demonstrate compliance to the specifications. Specific tests included

- Spin up tests
- Attitude torque tests
- Power and energy tests
- Efficiency tests

Figure 11 is a photograph of the test unit.

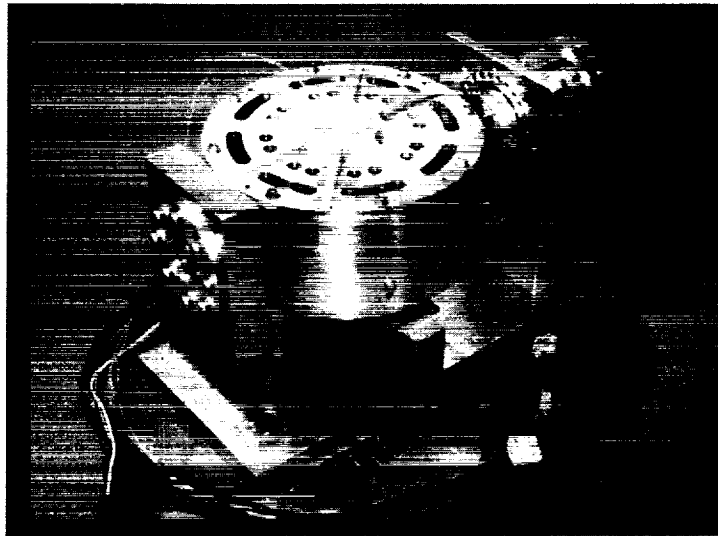


Figure 11: Bench Model Flywheel

Gimbal Test Configuration

The flywheel hardware is assembled into the gimbal bracket, coupled to the gimbal torquer and then attached to the top mounting face of a six-degree-of-freedom force/torque sensor. The sensor used is a strain gage sensor manufactured by Assurance Technologies Inc. (Model FT 3224 Theta 550/3300). The sensor has a torque limit of 373 N-m (3300 in-lb) about all three instrumented axes and a resolution of 0.2 N-m (2 in-lb) over that range. This torque sensor is first attached to the interface plate in the vacuum chamber; this interim assembly is pictured in Figure 12. The gimbal test rig is then attached to the movable top surface of the sensor in the vacuum chamber as shown in Figure 13 prior to the vacuum-tight cover being attached. All internal electrical connections are made and all functions are verified. The end cover is then secured, a roughing vacuum pump is attached to the outlet of the turbo-pump and all external electrical connections are made and operation verified. This test chamber provides a pressure during testing of less than 1 millitorr. This is equivalent to the pressure at an altitude of 90 km and provides a good representation of the end use windage losses to be expected in the actual flight system once the hot gasses, used to accelerate the flywheel, are vented from the flywheel housing.

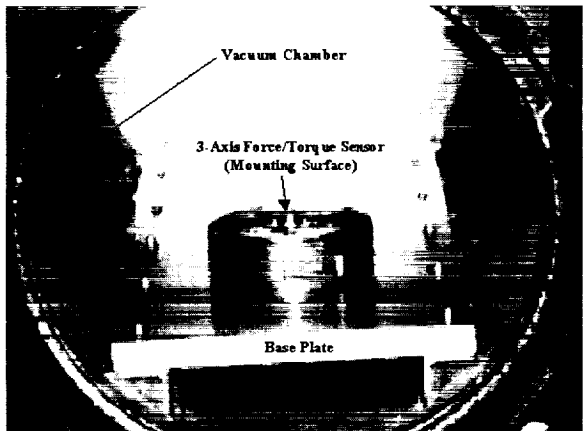


Figure 12. Torque Sensor

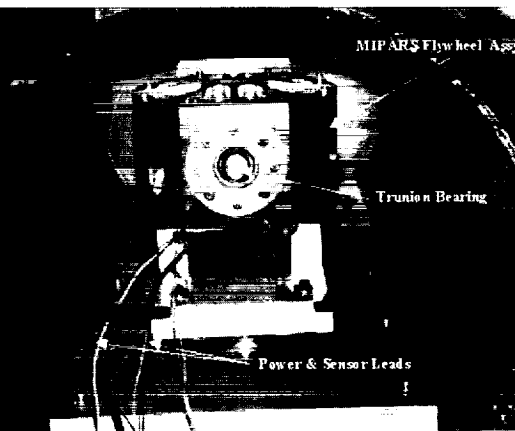


Figure 13. Gimbal Test Rig

Spin Up Test

Figure 14 below shows a spin-up event. Spin up is achieved by diverting hot gas ($1038\text{-}1371^{\circ}\text{C}$ ($1900\text{-}2500^{\circ}\text{F}$)) from the kinetic warhead's gas generator onto a turbine mounted on the flywheel rim. The hot gas drives the turbine until the top speed is achieved at which time a valve closes and a dump valve extinguishes the solid gas generator.

Rotor Speed, Torque, & Drive Pressure vs Time
(RPM, ft-lbf x 1000, PSIA x 100)

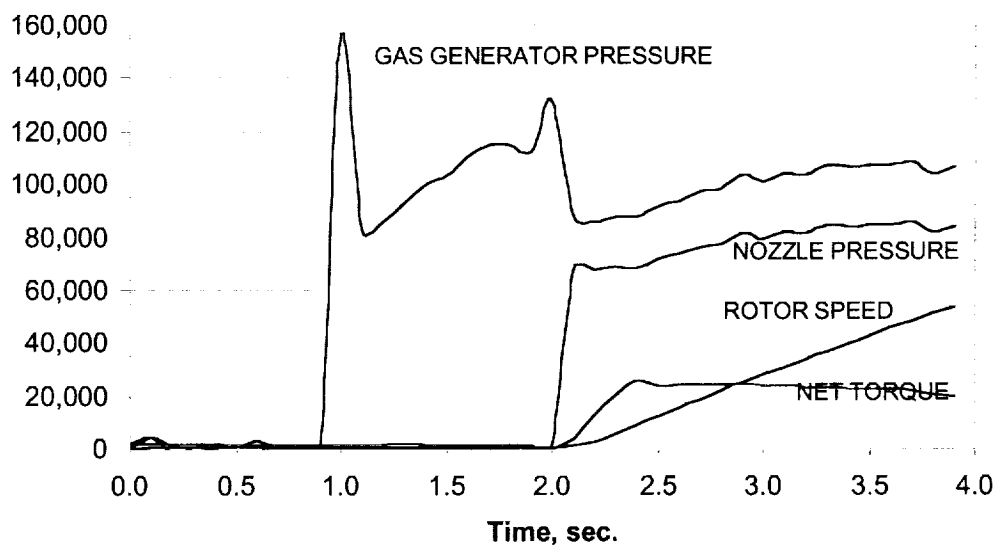


Figure 14. Results of Hot Gas Spin Up Test

Discharge Test

The discharge test demonstrated MIPARS ability to supply power to the KW during its flight. The wheel was spun up to 37000 rpm and then discharged into a 250-ohm resistor. The voltage across the resistor was held constant by the voltage regulator. This results in a constant power discharge. Figure 15 illustrates the energy usage during the discharge cycle. The lower curve represents the energy dissipated in the 250-ohm resistor during the discharge. The center curve represents the energy dissipated in the motor and bearings due to the drag torque added to the load energy. The top curve shows the energy removed from the wheel as function of time. The difference between the energy removed from the wheels and the loss plus load energy represents the energy lost in the electronics and additional energy lost in the motor due to resistance losses. As can be seen, the losses are higher than expected. We recovered only 21 kJ of energy from the flywheel. Our failure investigation revealed there was a viscous loss caused by excessive eddy current losses in the generator. A custom generator design is required to overcome these losses.

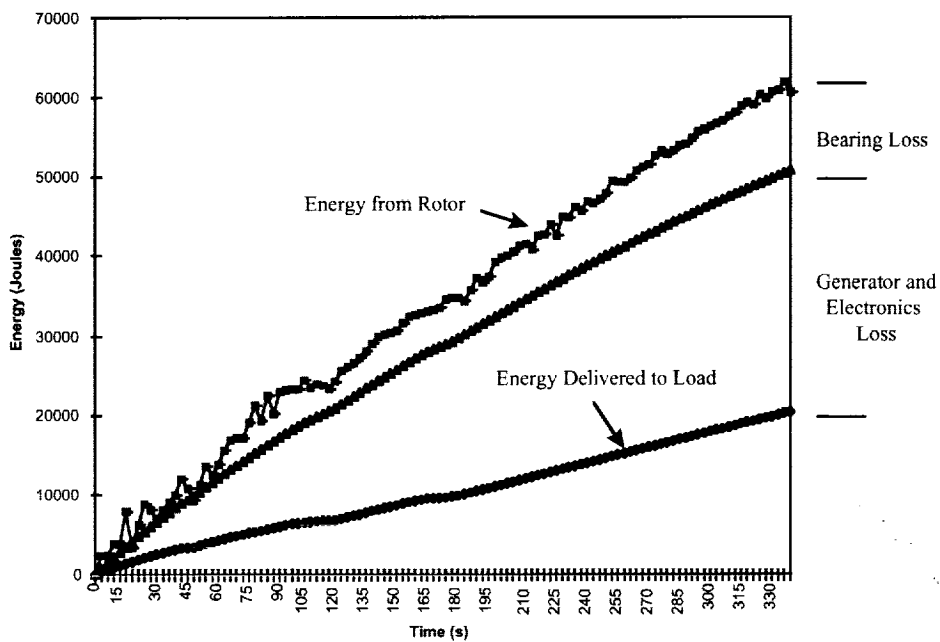


Figure 15. Results of Discharge Test

Attitude Torque Test

The purpose of the attitude torque test is to directly measure the gyroscopic torque applied by the flywheel. The flywheel is mounted on a torque measurement platform and the entire assembly is mounted in the vacuum chamber. The wheel is spun up to about 21000 rpm and a gimbal rate is commanded. The momentum of the wheel multiplied by the gimbal rate yields a gyroscopic torque, which is measured by the three-axis torque platform. A plot of the vector sum of the measured torques is shown in Figure 16. Notice that the torque response is quite noisy. This noise is mostly caused by structural resonances due to gear train compliance and by backlash and other nonlinearities in the gear train. It does not appear in the rate response since the rate is measured at the input of the gear train. Depending on the torque requirements of the KW, more work will be required in phase 3 to design a suitable gear train. A summary of the torque tests appears in Table 3. The torque error is quite small and would be very acceptable for a KW attitude control system.

Inadvertent Rotor Crash Test

The final test involved simultaneously delivering power and applying attitude control torque. The control system was configured so that the input to the torque loop was a torque command. The control system then used the measured wheel speed to calculate the required gimbal rate. The wheel speed was measured using the same Hall effect devices used to commutate the motor. Unfortunately, the motor currents affect the motor magnetic field that disrupts the Hall sensor outputs. As a result the motor speed measurement was quite noisy resulting in a noisy gimbal rate command. The noise saturated the gimbal rate loop causing the gimbal to travel from stop to stop (~ 60 degrees) at about 20 rad/s. When this happened the rotor was spinning at about 40000 rpm. The combination of the high rate and hitting to stops caused the rotor to touch down inside the case. The inside of the housing was slightly scored but the rotor was not damaged. In future designs an axial stop will be added to limit rotor motion due to an unexpected gimbal overrate. Also, a separate rotor speed sensor will be added.

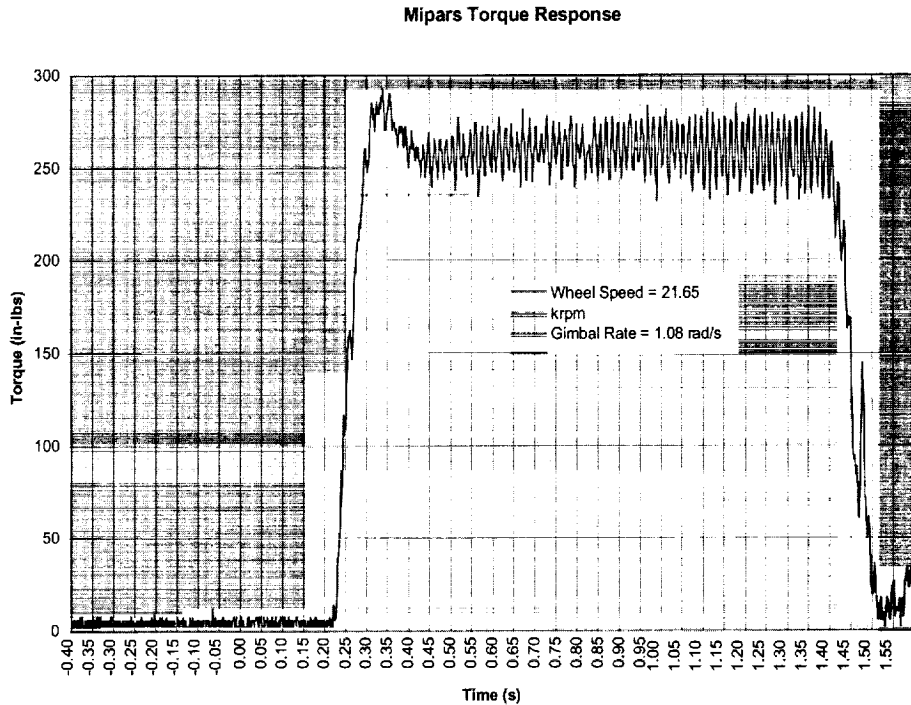


Figure 16. Attitude Torque Response of the MIPARS Flywheel

Table 3. Attitude Torque Performance Summary

Gimbal Rate (rad/s)	Wheel Speed (krpm)	Predicted Torque (N-m) (in-lb)	Average Torque (N-m) (in-lb)	Error
0.09	22.4	2.53 (22.4)	2.49 (22.0)	-1.8%
0.18	21.6	4.88 (43.2)	4.88 (43.2)	0.0%
0.36	21.6	9.76 (86.4)	9.47 (83.8)	-3.0%
0.54	21.7	14.7 (130)	14.9 (132)	1.4%
0.72	21.6	19.5 (173)	19.1 (169)	-2.2%
0.9	21.7	24.5 (217)	24.4 (216)	-0.5%
1.08	21.7	29.4 (260)	29.3 (259)	-0.6%
1.08	27.7	37.5 (332)	38.3 (339)	2.0%
1.26	21.8	34.5 (305)	34.5 (305)	-0.1%
1.44	21.2	38.3 (339)	38.4 (340)	0.2%
1.62	21.2	43.2 (382)	42.9 (380)	-0.4%

Conclusion

The work done on MIPARS shows the concept of providing attitude control and energy storage using flywheels is viable and attractive. The flywheels offer significant performance advantages over attitude control thrusters including

- Continuously variable and smooth torque delivery resulting in more precise and stable sensor-on-target pointing
- Efficient and reliable energy storage
- Ability to provide attitude control torque and power when the gas generator is shut down
- Enables long duration (> 300 seconds) flight using multiple ignition gas generators

Our testing demonstrated the feasibility of the concept and also uncovered some deficiencies in the design. These deficiencies and their mitigation are summarized in Table 4.

Table 4: Lessons Learned

Problem	Cause	Mitigation
Poor efficiency	Excessive motor eddy current losses	Custom high speed motor design
Large attitude control torque noise	Gear train noise due to backlash and compliance	Stiffer gear train with antibacklash gearing
Rotor touchdown after stop contact	Excessive axial rotor motion allowed	Add axial stop
Noisy wheel speed measurement	Interaction of the motor current with the motor magnetic field cause Hall effect devices to produce a noisy output	Use an independent optical or magnetic rate sensor

Overall the flywheel performed very well and as a result the MIPARS concept is seriously being considered for inclusion in future generations of exoatmospheric interceptors.

Acknowledgements

The authors would like to thank the Naval Air Warfare Center Weapons Division for the support of this work. In particular we thank Arnie Danielson, Martin Minthorn, Jerry Kong, and Dr. Pashang Esfandiari for their inputs and guidance.